ABSTRACT

Title of Dissertation: FUNCTIONALIZED ACYCLIC CUCURBIT[N]URIL MOLECULAR CONTAINERS AS REVERSAL AGENTS FOR DRUGS

Shweta Ganapati, Doctor of Philosophy, 2017

Dissertation directed by: Professor Lyle Isaacs,
Department of Chemistry & Biochemistry

The study of molecular containers has a prominent place in the scientific literature with many applications, including drug reversal. The clinical use of the cyclodextrin based reversal agent Bridion™ has greatly improved the post-operative safety of patients who undergo surgery aided by NMBAs such as rocuronium.

Chapter 1 introduces molecular containers, CB[n], and reports the use of the acyclic CB[n] known as Calabadion 2 as a broad spectrum reversal agent for NMBAs in rats. It also proposes the potential use of molecular containers as reversal agents for the treatment of overdose of illicit drugs in the context of available therapies.

Chapter 2 establishes that Calabadion 2 displays good to high levels of selectivity toward the NMBAs rocuronium, vecuronium, and cisatracurium both *in vitro* and based on simulations designed to capture the essence of the biological

system. The excretion profile of Calabadion 2 after NMBA reversal in rats was studied by a ^{1}H NMR assay. It is reported that more than 50% of Calabadion 2 is eliminated intact by the kidneys within 1 hour.

Chapter 3 establishes that CB[n] based molecular containers - Calabadion 1, Calabadion 2, and CB[7] display higher affinities than *p*-sulfocalix[4]arene and HP-β-cyclodextrin toward a panel of illicit drugs for which there are currently no USFDA approved pharmacotherapies. Calabadion 2 but not CB[7] is able to ameliorate the hyperlocomotive activity of rats treated with methamphetamine. The excretion profile of fentanyl and Calabadion 1 post reversal in rats was studied by HPLC and ^{1}HNMR. It is reported that on an average 24 % fentanyl and 40% Calabadion 1 are eliminated by the kidneys within 1 hour.

Chapter 4 discusses the synthesis and molecular recognition properties of three new acyclic CB[n] hosts **IV-2a** – **IV-2c** which incorporate alkyl linkers of varying lengths- ethyl, hexyl, and decyl; capping one end of Calabadion 1. These hosts were less water soluble than Calabadion 1 due to the loss of two sulfonate groups and did not undergo intermolecular self-association. However, the intramolecular self-inclusion of the alkyl linkers inside the cavity of these hosts led to decreased binding affinities toward guests compared to Calabadion 1.

FUNCTIONALIZED ACYCLIC CUCURBIT[N]URIL MOLECULAR CONTAINERS AS REVERSAL AGENTS FOR DRUGS

by

Shweta Ganapati

Dissertation submitted to the Faculty of the Graduate School of the
University of Maryland, College Park, in partial fulfillment
of the requirements for the degree of
Doctor of Philosophy
2017

Advisory Committee:
Professor Lyle Isaacs, Chair
Professor Neil Blough
Professor Jeffery Davis
Professor Philip DeShong
Professor Srinivasa Raghavan, Dean's Representative

Dedication

To my parents, Raji Ganapati and S. Ganapati, sister, Swechcha Ganapati, and fiancé Sumon Chatterjee; who give me the strength to endure failure and keep moving forward.

Acknowledgements

The past five years spent in the Isaacs lab at the University of Maryland (UMD) have been the most challenging and rewarding years of my life thus far. I extend my sincere gratitude to my adviser Professor Lyle Isaacs for teaching me chemistry, how to do research, and most all for holding me to high standards and serving as an example to follow.

I would like to acknowledge Professor S.V. Eswaran, Professor Rene Saksena, and Professor Ashok K. Prasad for their mentorship during my undergraduate years; and Ms. Nandini Dasgupta and Ms. Rajalakshmi Karthikeyan for my most memorable lessons in chemistry from high school.

I would like to thank senior Isaacs group members- Dr. Ben Zhang, Dr. Brittany Vinciguerra, Elizabeth Robinson, Dr. Liping Cao, Dr. Mingming Zhang, Dr. Xiaoyong Lu, Dr. David Sigwalt, and Dr. Soumen Samanta for teaching me laboratory skills, helping me troubleshoot experiments and for their advice on matters beyond chemistry. Steve Murkli, Kim Brady, Sandra Zebaze, and Wenjin Liu- thank you for support in lab and also for asking good questions that taught me new things in trying to answer them.

I would like to thank our collaborators- Professor Matthias Eikermann, Stephanie Grabitz, and Tharusan Thevathasan for their contributions to my projects and for translating our *in vitro* work into animal experiments.

The instrumentation facilities at UMD have been crucial to my work and I thank Dr. Yu-Fai Lam, Dr. Yinde Wang, Dr. Peter Zavalij, and Dr. Yue Li for their invaluable help.

My friends, classmates, and housemates in Maryland- thank you for your friendship and encouragement through the many milestones in graduate school and life that we have passed together!

My friends from back home in India- thank you Monalisa Goswami and Sunaina Gupta for being my sounding boards and cheerleaders. And most of all my family- parents, Swechcha, and Sumon; thank you for always pointing out the silver lining.

Table of Contents

Dedication ii
Acknowledgements iii
Table of Contents v
List of Tables vii
List of Figures ix
List of Schemes. ixiv
List of Abbreviations xv
Chapter 1: Introduction to Molecular Containers and their Application in Drug Reversal 1
1.1 Introduction 1
1.2 Molecular Containers 2
1.3 Introduction to Cucurbit[n]urils 4
1.4 Functionalization of Cucurbit[n]urils and Development of Acyclic Analogues. 9
1.5 Drug Reversal Using Molecular Containers 15
1.5.1 Reversal of Neuromuscular Blocking Agents 16
1.5.2 Reversal of Drugs of Abuse 21
Chapter 2: Calabadion 2 as a Reversal Agent for Neuromuscular Blocking Agents . 25
2.1 Introduction 25
2.1 In Vivo Selectivity of Calabadion 2 towards Neuromuscular Blocking Agents Relative to Commonly Used Drugs 26
2.2.1 Binding Properties of **II-2** towards Drugs **II-3** – **II-29** Investigated by ^{1}H NMR 29
2.2.2 Stoichiometry of the Complexes between **II-2** and Drugs **II-3** – **II-29** 31
2.2.3 X-ray Crystal Structure of the **II-2·II-29** Complex 33
2.2.4 Measurement of K_as between **II-2** and Drugs **II-3** – **II-29** 35
2.2.5 Commentary on the Tabulated K_a Values 38
2.2.6 Assessment of the Potential for Displacement Interactions 40
2.2.7 Simulation of In Vivo Equilibria uding Modeling Software Gepasi 42
2.2.8 In Vitro Selvectivity of Calabadion 2 for Rocuronium 42
2.2.9 In Vitro Selvectivity of Calabadion 2 for Cistracurium 45
2.2.10 Influence of K_1 46
2.2.11 Influence of [AChR] 49
2.2.12 Summary 50
2.3 Renal Elimination of Calabadion 2 in Rats Post Reversal of Neuromuscular Blockade 51
2.3.1 ^{1}H NMR Based Assay for Quantification of **II-2**, Rocuronium, **II-2**·Rocuronium Complex for Rocuronium Reversal Samples 52
2.3.2 ^{1}H NMR Based Assay for Quantification of **II-2** for Cisatracurium Reversal Samples 55
2.3.3 Summary 56
2.4 Conclusions 57

Chapter 3: Molecular Containers As Reversal Agents for Drugs of Abuse 58
3.1 Introduction 58
3.2 Molecular Containers Bind Drugs of Abuse in Vitro and Reverse the Hyperlocomotive Effect of Methamphetamine in Rats. 60
3.2.1 Qualitative Binding Study of Containers **III-1** – **III-5** toward Drugs of Abuse by ^{1}H NMR Spectroscopy. 61
3.2.2 Stoichiometry and X-ray Crystal Structures of the Drug•Container Complexes 63
3.2.3 Measurement of K_as between Containers **III-1** – **III-5** and Drugs of Abuse **III-6** – **III-12**. 64
3.2.4 Commentary on the Tabulated K_a Values 67
3.2.5 In Vivo Reversal of Methamphetamine by Calabadion 2 69
3.2.6 Summary 73
3.3 Renal Elimination of Calabadion 1 and Fentanyl in Rats Post Reversal Application 74
3.3.1 Fentanyl Calibration Curve. 74
3.3.2 Fentanyl Excreted by Rats Injected with Fentanyl and Placebo. 76
3.3.3 Fentanyl Excreted by Rats Injected with Fentanyl and Calabadion 1. 78
3.3.4 Calabadion 1 Excreted by Rats Injected with Fentanyl and Calabadion 1 79
3.3.5 Summary 81
3.3 Conclusions 81
Chapter 4: Synthesis and Molecular Recognition Properties of Acyclic Cucurbit[n]urils with Alkyl Linkers 83
4.1 Introduction 83
4.2 Design and Synthesis of Hosts **IV-2a** – **IV2c**. 85
4.3 Solubility Properties of Hosts **IV-2a** – **IV2c**. 87
4.4 Self-Association Properties of Hosts **IV-2a** – **IV2c**. 87
4.5 Binding Properties of Hosts **IV-2a** – **IV-2c** and **IV-1** towards Guests **IV-6** – **IV-10** Investigated by ^{1}H NMR. 90
4.6 Measurement of Binding Affinities between Hosts **IV-2a** – **IV-2c** and **IV-1** and Guests **IV-6** – **IV-10** by Isothermal Titration Calorimetry. 93
4.7 Commentary on the Tabulated K_a Values. 94
4.8 Conclusions 96
Appendix 1 98
Appendix 2 167
Appendix 3 248
Appendix 4 318
Bibliography 320

List of Tables

Chapter 1

Table I.1. Binding constants measured for some guests that form 1:1 complexes with CB[n].

Table I-2. Binding constants (K_a, M^{-1}) for the host–guest complexes formed in aqueous solution.

Chapter 2

Table II-1. Binding constants determined by direct or competitive UV/Vis assays or direct ^{1}H NMR titrations for the interaction between **II-2** and drugs **II-3**-**II-29**, drug dosages in the rat model, estimated plasma concentrations, and binding constants toward **II-1**.

Table II-2. Excretion of II-2, NMBA, II-2•NMBA complex measured by 1H NMR assay for rats injected with 3.5 mg kg-1 rocuronium or 0.6 mg kg-1 cisatracurium (values for cisatracurium and II-2•cisatracurium complex excreted were not measured).

Chapter 3

Table III-1. Binding constants (K_a, M^{-1}) determined for the various container•drug complexes.

Table III-2. Excretion of **III-7** and **III-1** measured by HPLC and ^{1}H NMR assays for rats injected with 12.5 μg kg^{-1} **III-7** (0.83 μg kg^{-1} min^{-1} infusion over 15 minutes) and placebo or 50 mg kg^{-1} **III-1** (bolus).

Chapter 4

Table IV-1. Binding constants determined by ITC for the interaction between molecular containers **IV-1**, **IV-2a** – **IV-2c** and guests **IV-6 – IV-10**.

List of Figures

Chapter 1

Figure I-1. Chemical structures of some molecular containers.

Figure I-2. a) Structure of CB[6]•**I-1** complex, and b) structures of some typical alkyl ammonium guests for CB[n].

Figure I-3. Schematic representation of the onset and reversal of neuromuscular blockade.

Figure I-4. Chemical structures of molecular containers CB[7], Calabadion 2 (**I-16**), Sugammadex, and guests rocuronium, vecuronium, cisatracurium, and acetylcholine.

Figure I-4. Chemical structures of some commonly abused drugs.

Figure I-5. Schematic representation of the pharmacokinetic and pharmacodynamic strategies for disrupting the effects of drugs of abuse.

Chapter 2

Figure II-1. Chemical structures of CB[n], Sugammadex (**II-1**), Cb 2 (**II-2**); and NMBAs cisatracurium, rocuronium, vecuronium.

Figure II-2. Chemical structures of drugs used in this study.

Figure II-3. ^{1}H NMR spectra recorded (400 MHz, RT, 20 mM NaH_2PO_4 buffered D_2O, pH = 7.4) for a) **II-26**, b) **II-2**, c) an equimolar mixture of **II-2** and **II-26** (12.5 mM), and d) a 1:2 mixture of **II-2** (12.5 mM) and **II-26** (25 mM).

Figure II-4. Job plot constructed for mixtures of **II-2** and **II-26** ([**II-2**] + [**II-26**] = 1 mM) by monitoring the change in ^{1}H NMR (400 MHz, RT, 20 mM NaH_2PO_4 buffered D_2O, pH = 7.4) chemical shift of H_u (7.72 ppm) of **II-2**.

Figure II-5. Cross-eyed stereoscopic representation of the geometry of one molecule of **II-2•II-29** from the x-ray crystal structure. Color code: C, grey; H, white; N, blue; O, red; S, yellow; hydrogen bond, red–yellow striped.

Figure II-6. Cross-eyed stereoscopic representation of the packing of **II-2•II-29** in the x-ray crystal structure. Color code: C, grey; H, white; N, blue; O, red; S, yellow.

Figure II-7. a) ^{1}H NMR (400 MHz) stack plot of the titration of **II-2** (0.976 mM) with guest **II-6** (0 – 6.57 mM) in 20 mM NaH_2PO_4 buffered D_2O (pH = 7.4); b) plot of the chemical shift of H_v as a function of guest concentration. The solid line represents the best non-linear fit of the data to a 1:1 model ($K_a = (3.0 \pm 0.6) \times 10^{3\ M-1}$).

Figure II-8. a) UV/Vis spectra recorded during the titration of a mixture of II-2 (9.92 μM) and dye rhodamine 6G (10.0 μM) with guest II-28 (0 – 1.21 mM) in 20 mM NaH_2PO_4 buffer (pH = 7.4), b) plot of absorbance at 550 nm as a function of the concentration of II-28. The solid line represents the best non-linear fit of the data to a competitive binding model ($K_a = (3.3 \pm 0.5) \times 10^6\ M^{-1}$).

Figure II-9. Illustration of the equilibria considered in the simulations using Gepasi.

Figure II-10. Three dimensional surface plots of the concentration of AChR•NMBA at equilibrium versus log [Drug] and log K_3 for **II-2**•Drug) for: a) rocuronium at [rocuronium] = [AChR] = 160 μM, [**II-2**] = 320 μM (2 eqv.), $K_1 = 10^5\ M^{-1}$, $K_2 = 3.4 \times 10^9\ M^{-1}$; b) cisatracurium at [cisatracurium] = [AChR] = 18 μM, [**II-2**] = 1.2 mM (64 eqv.), $K_1 = 10^5\ M^{-1}$, $K_2 = 4.8 \times 10^6\ M^{-1}$. The red dots mark the points corresponding to each of the 27 drugs (**II-2** – **II-29**).

Figure II-11. Plot of the mole fraction of AChR•rocuronium versus log (K_1) for drugs **II-3** – **II-19** present at their estimated plasma concentrations from Table II-1. a) $[\mathbf{II\text{-}2}]_{initial}$ = 320 μM (2-fold higher than $[Rocuronium]_{initial}$), and b) $[2]_{initial}$ = 960 μM (6-fold higher than $[Rocuronium]_{initial}$).

Figure II-12. Plot of mole fraction of AChR•rocuronium versus log [AChR].

Figure II-13. ^{1}H NMR spectra (600 MHz, RT, 20 mM NaH_2PO_4 buffered D_2O, pH = 7.4) of: a) free rocuronium (2 mM) shows two resonances (a and b) for the steroidal methyl groups, b) an equimolar mixture of **II-2** and rocuronium (2 mM), a' and b' are resonances for steroidal methyl groups rocuronium bound in the **II-2**•rocuronium complex, and c) urine sample from a rat taken 1 h after reversal of rocuronium (3.5 mg kg^{-1}) with **II-2** (10 mg kg^{-1}), a' and b' are resonances for steroidal methyl groups rocuronium bound in the **II-2**•rocuronium complex.

Chapter 3

Figure III-1. Chemical structures of: a) molecular containers, and b) drugs of abuse used in this study.

Figure III-2. ^{1}H NMR spectra recorded (400 MHz, RT, 20 mM sodium phosphate buffered D_2O, pH 7.4) for: a) **III-6** (2 mM), b) **III-1** (1 mM), c) a mixture of **III-6** (1 mM) and **III-1** (1 mM), and d) a mixture of **III-6** (2 mM) and **III-1** (1 mM).

Figure III-3. Cross-eyed stereoviews of individual complexes of: a) **1•6**, and b) CB[7]•**6** in the crystal. Color code: C, grey; H, white; N, blue; O, red; S, yellow; H-bond, red-yellow striped.

Figure III-4. a) UV/Vis spectra recorded during the titration of a mixture of III-2 (4.97 μM) and rhodamine 6G (4.97 μM) with methamphetamine (6, 0 – 219 μM) in

20 mM NaH_2PO_4 buffered water (pH 7.4). b) Plot of absorbance versus [2] fitted to a competitive binding model with K_a = (4.3 ± 1.0) x 10^6 M^{-1}. c) ITC thermogram recorded during the titration of III-2 (87 μM) in the cell with III-12 (0.93 mM) in the syringe. d) Fitting of the data to a 1:1 binding model with K_a = (6.8 ± 0.1) x 10^5 M^{-1}.

Figure III-5. Results from behavioral tests in the open field. a) Bar graph showing distance traveled in percent of the placebo + methamphetamine activity level within 20 minutes; error bars represent the standard error of the mean. *$p<0.01$ compared to methamphetamine + placebo. **$p<0.001$ compared to methamphetamine + placebo. #interaction term indication × Calabadion 2 dose: $p<0.001$, indicating effect modification by time of administration of Calabadion 2. Tracking plots illustrating the traveled distance of one rat within 20 minutes in the open field: b) Baseline, no methamphetamine given, c) following methamphetamine (0.3 mg kg^{-1}) + placebo, d) following methamphetamine (0.3 mg kg^{-1}) + Calabadion 2 (65 mg kg^{-1}), and e) following methamphetamine (0.3 mg kg^{-1}) + Calabadion 2 (130 mg kg^{-1}).

Figure III-6. HPLC spectrum of a standard solution of **III-7** (14 μM) showing a retention time of 13.8 minutes for III-7 at 229 nm. The peak at 2.7 minutes is from trimethylamine in the buffer.

Figure III-7. Calibration curve for fentanyl using working standard solutions.

Figure III-8. HPLC spectra of: a) blank urine spiked with fentanyl, and b) one of the representative urine sample following the fentanyl injection to rat. The fentanyl peak can be seen at 14.4 and 14.3 minutes respectively.

Figure III-9. ^{1}H-NMR spectrum of a representative urine sample following the injection of **III-7** and **III-1** to a rat (600 MHz, D_2O).

Figure IV-1. Chemical structures of: a) cucurbit[n]urils (CB[n]) and Calabadion 1, (**IV-1**) and b) guests used in this study.

Figure IV-2. ^{1}H NMR spectra recorded (400 MHz, RT, 20 mM sodium phosphate buffered D_2O, pH 7.4) for: a) **IV-8** (1 mM), b) **IV-2b** (1 mM), c) a mixture of **IV-8** (0.5 mM) and **IV-2b** (0.5 mM), and d) **IV-8** (1.0 mM) and **IV-2b** (0.5 mM).

Figure IV-3. a) ITC thermogram recorded during the titration of **IV-2b** (0.1 mM) in the cell with **IV-8** (1.0 mM) in the syringe. d) Fitting of the data to a 1:1 binding model with $Ka = (1.6 \pm 0.1) \times 10^{6}\ M^{-1}$.

List of Schemes

Chapter 1

Scheme I-1. Synthesis and structure of CB[n].

Scheme I-2. Synthesis of Me_{10}CB[5] from **I-6** and formaldehyde.

Scheme I-3. Synthesis of mono and fully hydroxylated CB[n].

Scheme I-4. Templated synthesis of hexamer (**I-7**) and building-block synthesis of monofunctionalized CB[7] (**I-8**) and functionalized CB[8] (**I-9**).

Scheme I-5. Synthesis of acyclic CB[n] congeners: a) **I-11**, and b) **I-12**.

Scheme I-6. Building block synthesis of: a) glycoluril tetramer precursor (**I-13**), b) acyclic CB[n] congener **I-14**, c) Calabadion 1 (**I-15**), and d) Calabadion 2 (**I-16**).

Chapter 4

Scheme IV-1. Synthesis of hosts **2a** – **2c**.

List of Abbreviations

^{1}H NMR	proton nuclear magnetic resonance
^{13}C NMR	carbon-13 nuclear magnetic resonance
Å	angstrom
Ach	acetylcholine
AChE	acetylcholine esterase
AChR	acetyl choline receptor
$AgNO_3$	silver nitrate
API	active pharmaceutical ingredients
br	broad
C	carbon
Cb	Calabadion
CB[n]	cucurbit[n]uril
CD	cyclodextrin
d	doublet
D_2O	deuterium oxide
DMSO	dimethylsulfoxide
ESI-MS	electrospray ionization-mass spectrometry
EtOH	ethanol
g	gram
GRAS	generally recognized as safe
H	hydrogen
h	hour

HCl	hydrochloric acid
HP-β-CD	hydroxypropyl-β-cyclodextrin
Hz	hertz
IR	infrared
ITC	isothermal titration calorimetry
J	coupling constant
K	kelvin
K_a	binding affinity
kg	kilogram
$KMnO_4$	potassium permanganate
M	molar
m	multiplet
M.p.	melting point
m/z	mass to charge ratio
M+	molecular ion
mAchR	muscarinic acetyl choline receptor
MeOH	methanol
mg	milligram
MHz	megahertz
min	minute
mL	milliliter
mM	millimolar
MW	molecular weight

N	binding stoichiometry
$NaAuCl_4$	sodium tertrachloroaurate
NaH_2PO_4	sodium monophosphate
NaO_2CCD_3	deuterated sodium acetate
NaOH	sodium hydroxide
NMBA	neuromuscular blockade
o	ortho
p	pentuplet
p	para
PD	pharmacodynamic
PK	pharmacokinetic
pKa	negative logarithm of acid dissociation constant
ppm	parts per million
RT	room temperature
s	singlet
SWNT	single-walled carbon nanotubes
t	triplet
t-BuOK	potassium tert-butoxide
TFA	trifluoroacetic acid
TMSP	2,2,3,3-d(4)-3-(trimethylsilyl)propanoic acid sodium salt
USFDA	Food and Drug Administration
UV/Vis	Ultra violet/ visible
$\Delta\delta$	change in chemical shift

ΔH	change in enthalpy
ΔS	change in entropy
μg	micrograms
μM	micromolar
π	pi
χ	mole fraction

Chapter 1: Introduction to Molecular Containers and their Application in Drug Reversal

1.1 Introduction.

Interactions formed between atoms or ions lead to chemical bonds such as covalent, ionic, or metallic bonds to form molecules or crystals. There can also be associations between molecules which cause them to assemble in specific ways- which is the realm of supramolecular chemistry. These interactions between molecules are called non-covalent interactions and consist of weaker forces than the chemical bond, such as ion-dipole interactions, hydrogen bonding, π-π interactions, and the hydrophobic effect. [1] Non-covalent interactions are widespread in natural systems and despite being individually orders of magnitude weaker than the chemical bond; they can collectively exert a significant influence over the properties of the system. In proteins and nucleic acids they are responsible for maintaining the three dimensional structure of macromolecules, and they form the basis for the recognition between enzyme-substrate, antibody-antigen, and hormone-receptor pairs.[2] The first synthetic systems with molecular recognition ability were designed by Pederson, Lehn, and Cram who made crown ethers and cryptands which bound alkali metal ions in their cavity and more complex molecular hosts which could encapsulate guest molecules within their structures through non-covalent interactions.[3] Since their seminal work, the scientific literature has been flooded with many synthetic molecular

containers and their unique applications. This chapter discusses some of the most popular containers, with a focus on CB[n] and their therapeutic use as drug reversal agents.

1.2 Molecular Containers.

Just like everyday containers, molecular containers hold and protect their cargo –except they do so at the molecular level. The container molecule is referred to as the molecular host and the cargo, generally a smaller molecule that is encapsulated within the structural cavity of the host, is called the guest. The chemical environment within the host cavity can be quite different from the environment outside (such as that of the solvent) and has the ability to stabilize and even alter the properties of the guest; including its pK_a, conformation, and optical properties. [4]

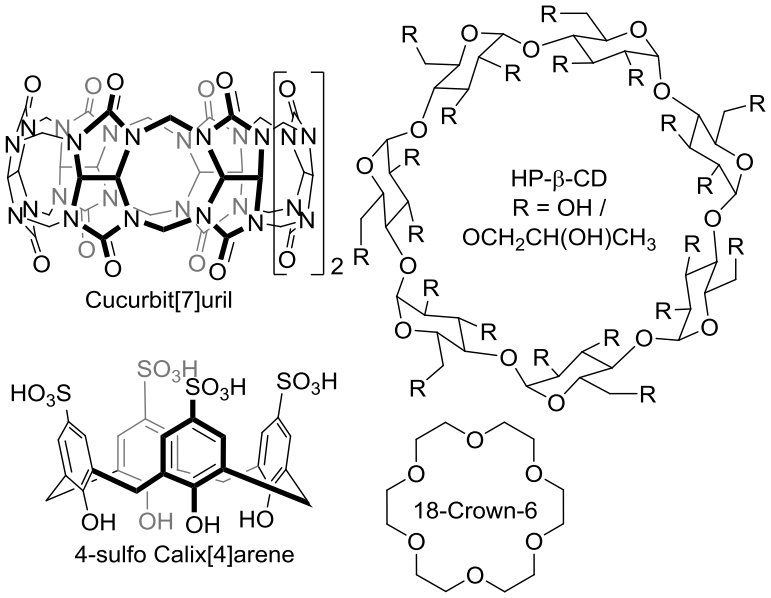

Figure I-1. Chemical structures of some molecular containers.

Host-guest chemistry has led to exciting applications in molecular machines, sensors, catalysis, separation techniques, and the formulation, delivery and sequestration of drugs and other guests. Some well-known containers in the literature include crown ethers, calixarenes, cyclodextrins, and cucurbiturils (Figure I-I).

Crown ethers are polyethers arranged in the shape of a ring and were first reported by Pedersen in 1967.[3] The oxygen atoms in their structure act as Lewis bases that bind to and stabilize alkali metal cations within the ring through ion-dipole interactions. The size of the ring can be synthetically varied to accommodate a range of cations with varying size and charge densities. Crown ethers have been used as phase transfer catalysts. Over the next few decades, much more complex molecular hosts have emerged in the literature with more sophisticated molecular recognition features.

For example, calixarenes are composed of phenols linked by methylene bridges at the meta position with bulky alkyl groups in the para position. This creates a bowl-shaped hydrophobic cavity that is able to bind hydrophobic guests and ions with moderate affinities on the order of 10^4 M^{-1}. Calixarenes have been studied for their use as ionophores for membrane transport, extractants, stationary phases, electrode ionophores and in optical, electrochemical, biological sensing applications.[5]

Cyclodextrins (CDs) are currently the most widely used molecular containers for commercial applications.[6] CDs are water soluble hosts made of linked glucose units which bind hydrophobic guests in water with moderate

affinities (very few > 10^4 M^{-1}). They have been classified as "generally recognized as safe" (GRAS) by the United Sates Food and Drug Administration (USFDA), and can be synthesized in various sizes (α = 6 sugar units, β = 7 sugar units, δ = 8 sugar units) and with varied functionalization. Some CDs currently in the market include Captisol®, a functionalized β-CD used to formulate insoluble active pharmaceutical ingredients (APIs), Bridion® or Sugammadex a δ-CD used as a reversal agent for neuromuscular blocking agent (NMBA) rocuronium, and Febreze™ a household odor eliminator with HP-β-CD as the active ingredient.

1.3 Introduction to Cucurbit[n]urils.

Over the last two decades, a newer class of containers called cucurbit[n]urils (CB[n], n = number of glycoluril units) has gained the attention of chemists.[7] Their outstanding molecular recognition ability far surpasses other synthetic molecular containers in terms of binding affinity (K_a routinely 10^8 – 10^9 M^{-1}), and even reaches and exceeds affinities observed in biological receptors.[8]

CB[n] are composed of glycoluril units linked together by methylene bridges to form closed rings. They were synthesized for the first time in 1905 by Behrend and co-workers. The resulting material of unknown structure came to be known as "Behrend's Polymer," and was recrystallized from sulfuric acid, to give a white crystalline product. Behrend's Polymer was found to form complexes with various metal salts such as $KMnO_4$, $AgNO_3$,

and $NaAuCl_4$ as observed by the induced color change in these salt solutions upon complexation.[9]

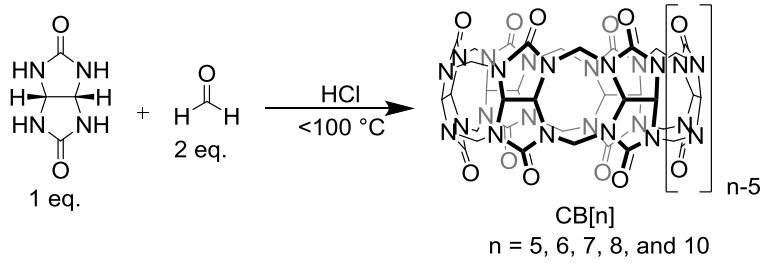

Scheme I-1. Synthesis and structure of CB[n].

It was only in 1981 that Mock et al. elucidated the structure of this molecule by X-ray crystallography as cucurbit[6]uril, consisting of 6 glycoluril units linked by 12 methylene bridges (Scheme I-1). The highly symmetrical molecule had a pumpkin-like shape and was named "cucurbituril" after the Latin name for the gourd family-*cucurbitaceae*.[10] Since then several research groups have worked towards the synthesis and isolation of other members of the cucurbit[n]uril family. The work of Mock,[10] Day,[11] Kim,[12] Tao,[13] and Isaacs[14,15] has led to the synthesis of CB[5], CB[6], CB[7], CB[8], CB[10], and CB[14]. The Day and Isaacs groups have intensively studied the mechanism of CB[n] formation and their recognition properties.[16]

There are a few different structural features of the CB[n] family which contribute to its unprecedented molecular recognition ability. The cavity of CB[n] (lined with methine groups) is hydrophobic and is well suited to stabilize the hydrophobic parts of a guest such as alkyl and aromatic groups

in water by the hydrophobic effect. Additionally, the inclusion of a hydrophobic guest within the host cavity expels high energy water molecules previously occupying the cavity (in aqueous solution) further stabilizing to the complex. In contrast to the cavity, the CB[n] portal is lined with electrostatically negative carbonyl groups which stabilize the cationic (such as ammonium groups) parts of the guest, when they are appropriately positioned for ion-dipole interaction. The host structure is relatively rigid, making size and shape complementarity necessary for guest inclusion.[17] Figure I-2a illustrates these interactions between CB[6] and guest **I-1**. The K_a for this complex in 50 mM NaO_2CCD_3-buffered D_2O (pD 4.74) is $(8.97 \pm 1.43) \times 10^7$ M^{-1}.[18] The height of CB[n] homologues is uniformly 9.1 Å, and therefore having six carbon atoms as linker positions the ammonium groups in **I-1** at the appropriate distance from the two portals to benefit from ion-dipole interactions.

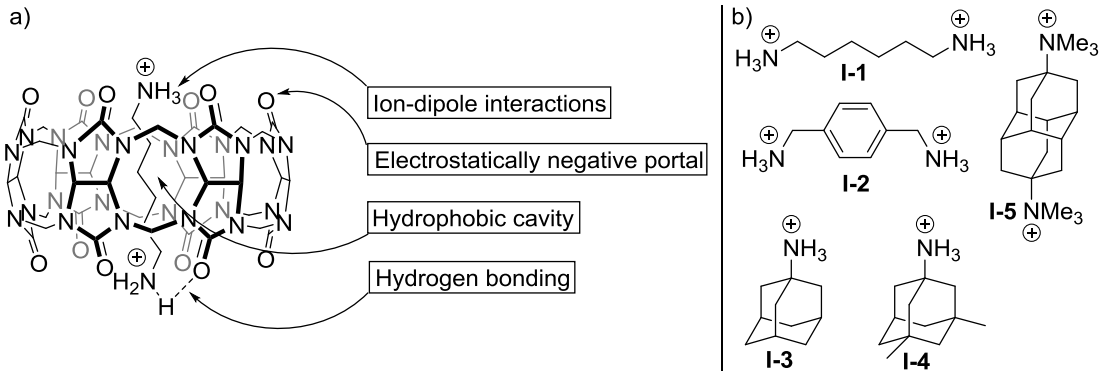

Figure I-2. a) Structure of CB[6]•**I-1** complex, and b) structures of some typical alkyl ammonium guests for CB[n].

While cavity depth is constant across CB[n] homologues, cavity volumes and diameters increase systematically with the increase in *n*, which is the number of glycoluril units.[17] CB[5] has the smallest cavity with a volume of 68 $Å^3$ which makes it an appropriately sized host for small gases such as Kr, CO_2, CO, O_2, and N_2, and organic solvents such as methanol and acetonitrile.[19] CB[6] is larger (142 $Å^3$) and shows high affinity for guest **I-1** ($K_a = (4.49 \pm 0.84) \times 10^8\ M^{-1}$), but its volume can just about accommodate the larger guest **I-2** ($K_a = (550 \pm 30\ M^{-1}$), upon heating. Still larger adamantyl guests such as **I-3** and **I-4** cannot be included within CB[6]. However, CB[7] with a volume of 242 $Å^3$ is an excellent host for **I-3** ($K_a = (4.23 \pm 1.00) \times 10^{12}\ M^{-1}$). The larger guest **I-4** packs more tightly into the larger (367 $Å^3$) cavity of CB[8] ($K_a = (4.33 \pm 1.11) \times 10^{11}\ M^{-1}$) as compared to CB[7] where it can only be partially included ($K_a = (2.50 \pm 0.39) \times 10^4\ M^{-1}$). Table I-1 summarizes the K_a values of guests **I-1** – **I4** toward CB[6], CB[7], and CB[8].[18]

Table I.1. Binding constants measured for some guests that form 1:1 complexes with CB[n].[18]

Guest	CB[6]	CB[7]	CB[8]
I-1	$(4.49 \pm 0.84) \times 10^8$	$(8.97 \pm 1.43) \times 10^7$	-
I-2	$(550 \pm 30$	$(1.84 \pm 0.34) \times 10^9$	-
I-3	-	$(4.23 \pm 1.00) \times 10^{12}$	$(8.19 \pm 1.75) \times 10^8$
I-4	-	$(2.50 \pm 0.39) \times 10^4$	$(4.33 \pm 1.11) \times 10^{11}$

In 2014, the Isaacs group published a CB[7]-diadamantane guest (**I-5**) complex with an attomolar dissociation constant (K_a = 7.2 x 10^{17} M^{-1}, D_2O), comparable to and exceeding the avidin-biotin affinity ($K_a \approx 10^{15}$ M^{-1}).[20] The optimal packing, 14 ion-dipole interactions, and desolvation of the CB[7] portal in the complex and the resultant thermodynamic stabilization demonstrated the scope of optimizing host-guest interactions to meet and exceed affinities compared to their biological counterparts.

CB[8] with an even larger cavity volume could further expand the scope of high affinity host-guest complexes and even forms ternary complexes with two identical or different guests.[21] However applications of CB[8], especially in biological systems are severely limited by its poor (< 50 μM) aqueous solubility which is ascribed to its extensive self–association through CH•••O hydrogen bonding between methine protons of one CB[8] molecule with the ureidyl carbonyl portal of another.[22,23] CB[10] is also insoluble in water, whereas CB[14] has a 360° twisted cavity; neither are suitable for encapsulation of biologically relevant molecules.

There is a need for improving the properties of CB[n] such as aqueous solubility, facile synthesis, and incorporation of additional recognition features while retaining their impressive molecular recognition features. Thus, research in CB[n] field has branched out to functionalization approaches to make a diverse array of CB[n]-type receptors.

1.4 Functionalization of Cucurbit[n]urils and Development of Acyclic Analogues.

Syntheses of functionalized derivatives of cyclic CB[n] have involved the use of the following strategies: (a) homomeric/ heteromeric cyclization of functionalized glycolurils with formaldehyde to obtain fully or partially functionalized CB[5] and CB[6] (Scheme I-2), (b) direct functionalization of preformed CB[n] to give mono and fully functionalized (n=5-8) derivatives (Scheme I-3), and (c) the building block approach using glycoluril oligomers to give monofunctionalized CB[n] (n = 6-8) (Scheme I-4).

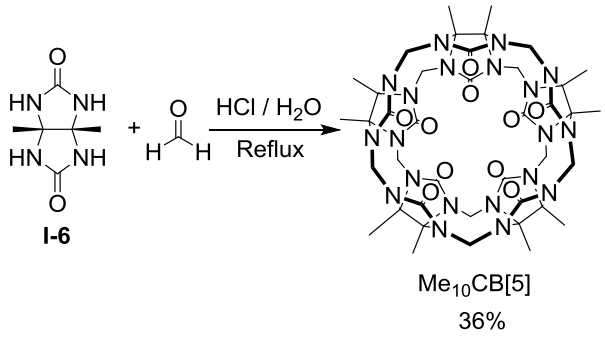

Scheme I-2. Synthesis of $Me_{10}CB[5]$ from **I-6** and formaldehyde.

The first fully characterized functionalized derivative of CB[n]-decamethylcucurbit[5]uril ($Me_{10}CB[5]$) was reported by the Stoddart group in 1992.[24] It was synthesized by the homomeric cyclization of dimethylglycoluril with formaldehyde in hydrochloric acid and water (Scheme I-2). The cyclization approaches from functionalized glycolurils have succeeded in improving the solubility of CB[6] derivatives in water and organic solvents.[25,26] However, the reactions of substituted glycolurils tend to favor

smaller CB[n] homologues, CB[5] and CB[6] due to 1,5-diaxial interactions between substituents on adjacent glycoluril rings that comprise the methylene bridged eight-membered rings. Such 1, 5-diaxial interactions are expected to increase as the size of the CB[n] increases. [27]This issue can be circumvented by starting with preformed CB[n] including CB[7] and CB[8]. The direct hydroxylation of CB[n=5-8] with $K_2S_2O_8$ was introduced by Kim in 2003.[28]

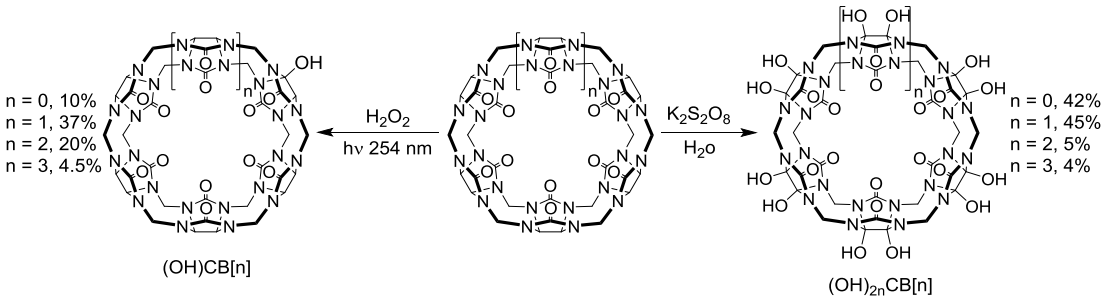

Scheme I-3. Synthesis of mono and fully hydroxylated CB[n].

The resulting fully hydroxylated CB[n] could be modified to provide tailored CB[n] derivatives with different functional groups, frequently accompanied by enhanced solubility in common organic solvents.

Monofunctionalized CB[n] present an exciting advance in the CB[n] field as they give more regiochemical control for further modifications. In 2011, the Isaacs group reported the templated synthesis of the glycoluril hexamer (**I-7**)[29] which led to the synthesis of the first monofunctionalized CB[7] with enhanced aqueous solubility in 2012.[30] Monofunctionalized CB[7] has been used for targeted delivery application[31-33] and covalently attached to Fujita type cages for stimuli responsive drug release.[34] Functionalized CB[8] with

enhanced aqueous solubility was also synthesized in a later work using a related strategy (Scheme I-4).[35]

In 2015 Bardelang and co-workers reported a direct photochemical monohydroxylation of CB[n] (n = 5- 8) using hydrogen peroxide in one step under mild reaction conditions.[36] Functionalization approaches for closed CB[n] have led to improved solubilities of CB[6] and CB[8], improved ease of synthesis and purification, and the ability to chemically attach CB[n] to various scaffolds.

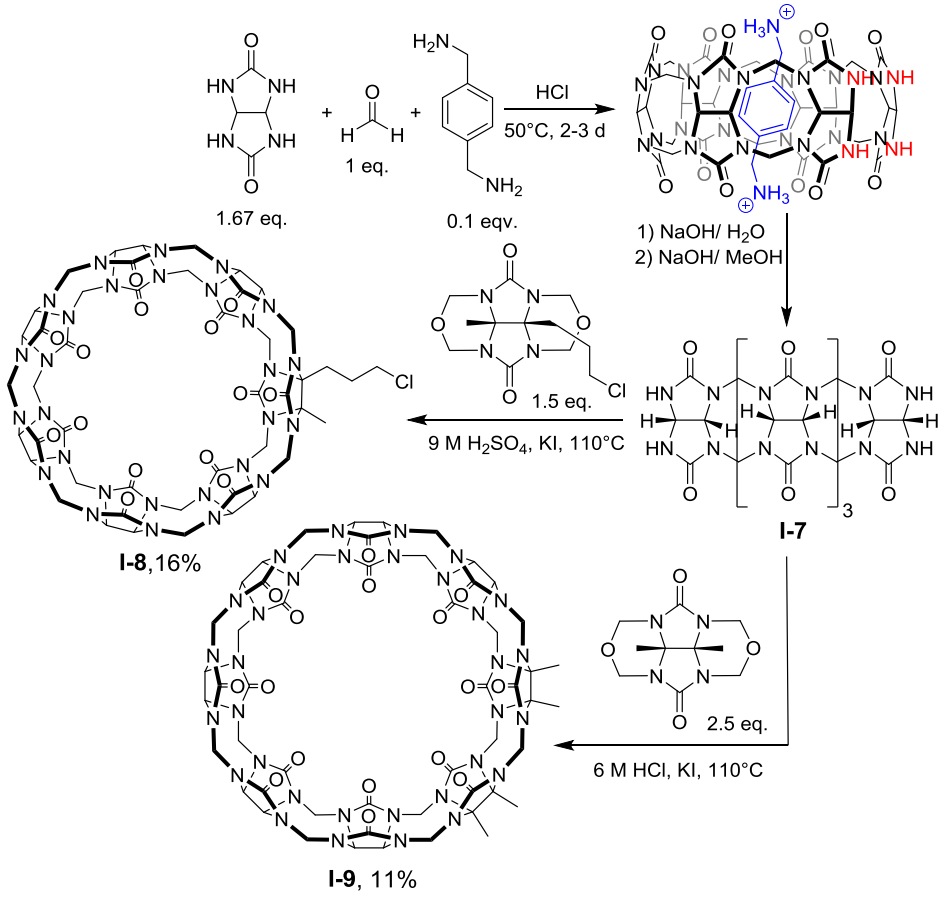

Scheme I-4. Templated synthesis of hexamer (**I-7**) and building-block synthesis of monofunctionalized CB[7] (**I-8**) and functionalized CB[8] (**I-9**).

Simultaneous development of water soluble acyclic CB[n] analogues, most notably by Isaacs and co-workers has opened up new avenues in CB[n] modification. The first acyclic congener of CB[6] was reported by the Isaacs group in 2003 (Scheme I-5a).[37] Compound **I-11** was synthesized by the alkylation of functionalized glycoluril (**I-10**) to introduce an *ortho*-xylelene linker, circumventing the difficulties in CB[6] synthesis. Carboxylic acid groups were incorporated on the convex face of the structure to improve water-solubility. Remarkably, the C-shaped preorganized compound **I-11** showed recognition properties towards alkyldiammonium ions similar to CB[6], with only a moderate reduction in affinity.

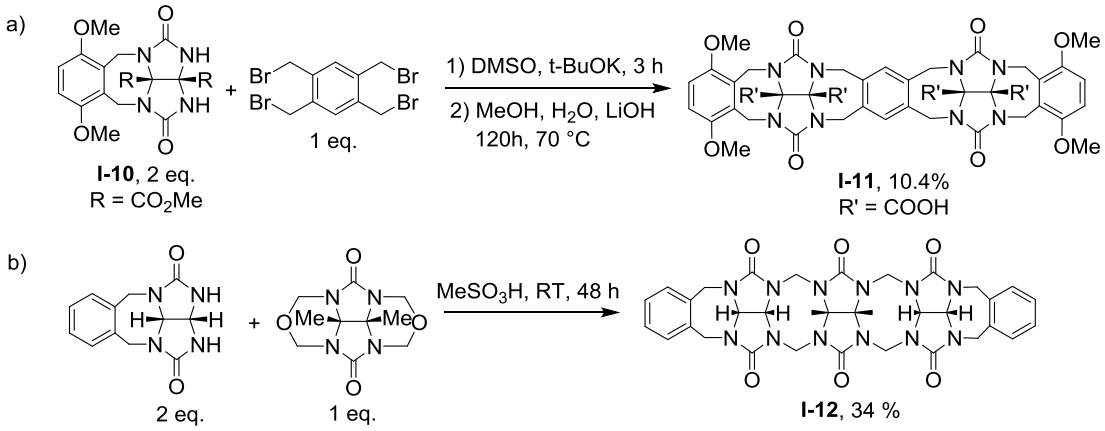

Scheme I-5. Synthesis of acyclic CB[n] congeners: a) **I-11**, and b) **I-12**.

This was followed by the development of compound **I-12** by Sindelar, which retained the glycoluril trimer backbone while incorporating aromatic walls.[38] Compound **I-12** was able to bind bispyridinium ethylene and methylviologen guests with moderate (10^4 M^{-1}) affinities. Through their experience with the

synthesis and study of molecular clips and glycoluril oligomers, Isaacs and co-workers recognized the importance of the carbonyl portal in CB[n] recognition. This led to the design of compound **I-14**, with a glycoluril tetramer backbone and aromatic walls with carboxylic acid groups to facilitate aqueous solubility (Scheme I-6).[39] The affinity of host **I-14** towards dialkyl ammonium, adamantyl ammonium, and aromatic ammonium guests was comparable to that of CB[6] and CB[7], and ranged from 10^5 -10^9 M^{-1}.

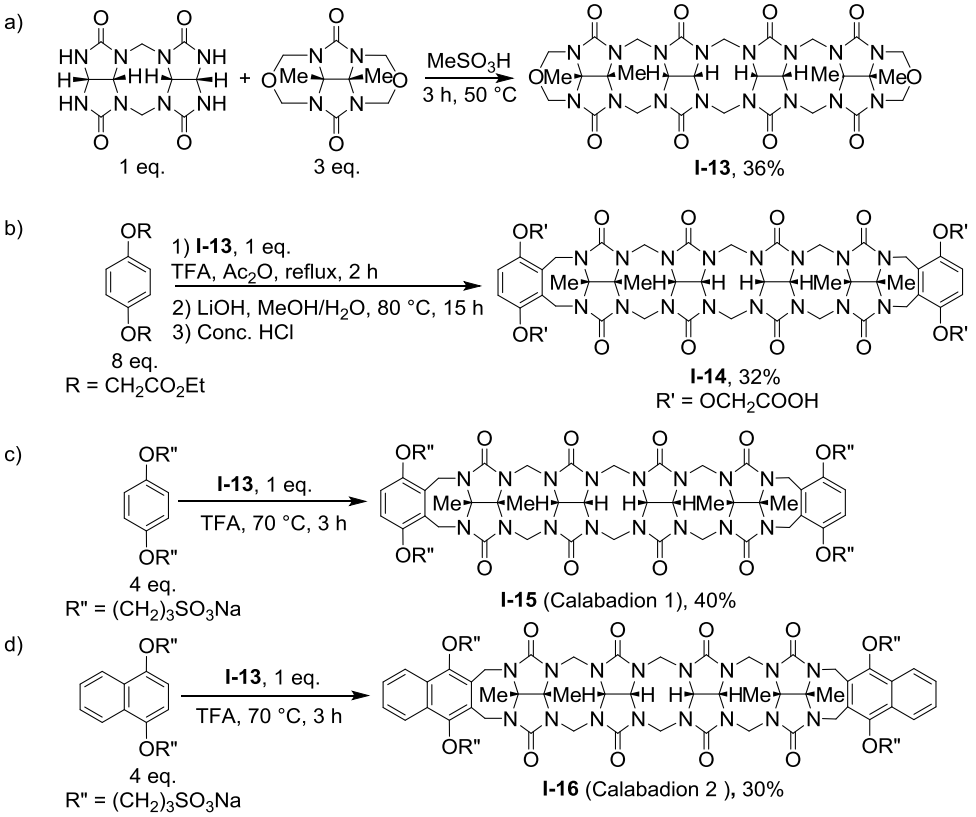

Scheme I-6. Building block synthesis of: a) glycoluril tetramer precursor (**I-13**), b) acyclic CB[n] congener **I-14**, c) Calabadion 1 (**I-15**), and d) Calabadion 2 (**I-16**).

A further modification to the design of **I-14**, involved the replacement of the carboxylic acid groups by sulfonate groups to obtain Calabadion 1 (**I-15**). The solubility of **I-15** was 346 mM in water and 105 mM in phosphate buffer (pH 7.4) which is significantly higher than either CB[7] (20-30 mM) or compound **I-14** (1-2 mM). Calabadion 2 (**I-16**) was designed by incorporating naphthalene walls in place of the benzene walls of Calabadion 1, and its solubility in water and buffer was 18 mM and 14 mM, respectively. Compounds **I-15** and **I-16** demonstrated excellent affinity towards poorly water soluble active pharmaceutical ingredients (APIs) and were able to increase their bioavailability in mice by acting as solubilizing agents.[40] While **I-16** has lower inherent water solubility than **I-15**, its larger aromatic walls allowed it to enhance the solubility of insoluble drugs at lower concentrations. Compounds **I-15** and **I-16** have also been reported as solubilizing agents for single walled carbon nanotubes (SWNTs) at 1000 times lower concentrations than surfactants while maintaining their optical properties,[41] and as hosts for hydrocarbons for their uptake into water for potential application in separation, sequestration, and transformation of gaseous and liquid hydrocarbons.[42]

The enhanced aqueous solubility and comparable or in some cases improved affinities of the Calabadion hosts (when compared to the cyclic CB[n]) prompted the Isaacs group to carry out numerous structural modifications to them in order to better understand the structure-affinity relationships. Some modifications include changing the solubilizing group,[43]

aromatic group,[44] length of the alkyl arm,[45] and size of the glycoluril backbone.[46,47] Chapter 4 discusses the effect of introducing alkyl linkers of varying sizes to Calabadion 1.

Another application of **I-16** was reported in 2012. It was found that **I-16** binds neuromuscular blocking agents (NMBAs) with affinities ranging from 10^6 – 10^9 M^{-1}, and reverses their effects *in vivo*.[48] The application of molecular containers as reversal agents for different classes of drugs is described in detail in the following section.

1.5 Drug Reversal Using Molecular Containers.

As described in the previous sections, molecular containers can alter the property of the guest encapsulated within their cavities. The biological activity of a drug is one such property. A drug exhibits its activity in the free state, however when it is completely bound within the cavity of a host, it can lose its ability to interact with its biological target(s) (Scheme I-7).

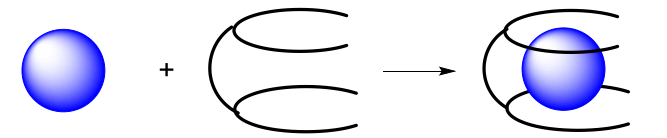

Scheme I-7. Schematic representation of drug reversal by encapsulation within a molecular container.

This effect can be used to sequester drugs *in vivo* whose activity is no longer desired. Factors such as the relative binding affinity between drug•container and drug•biological receptor, the concentrations of drug, container, and

binding sites on biological receptor, and the selectivity of the container toward the drug relative to other molecules in the system play a role in determining the feasibility of this reversal. Sections 1.5.1 and 1.5.2 discuss the scope for using molecular containers as reversal agents for two different classes of drugs- NMBAs and drugs of abuse respectively.

1.5.1 Reversal of Neuromuscular Blocking Agents.

Annually, more than 400 million patients receive curare-type NMBAs during surgical procedures in operating rooms, intensive care units, and emergency medicine departments.[49] NMBAs such as rocuronium and cisatracurium are often used as an essential adjunct to general anesthesia to block neuromuscular transmission (muscle relaxation) dose-dependently. This facilitates endotracheal intubation, optimizes surgical conditions, prevents potentially harmful movements during surgery, and also requires that the patient be put on mechanical ventilation. To speed up the recovery of the muscle function of the patient and to prevent residual neuromuscular block, it is often necessary to reverse the biological effect of NMBAs at the end of the surgery.[50,51] This can be achieved by a few different mechanisms: (1) natural metabolism / excretion of the NMBA, (2) displacement of the NMBA from the acetylcholine receptor (AChR) by an increased local acetylcholine (ACh) concentration resulting from the inhibition of acetylcholine esterase (AChE) by drugs such as neostigmine, or (3) the encapsulation of the NMBA by a molecular container (Figure I-3). The first mechanism can be too slow or unreliable, especially in cases of deep

neuromuscular blockade. This results in muscle spasms and breathing problems in the patient from incomplete reversal, leading to increased healthcare costs from readmission to ICU and in some cases, mortality. In the second mechanism, there can be cardiovascular side-effects from neostigmine itself due to an agonistic effect at muscarinic acetylcholine receptor (mAChR) and may even induce a (depolarizing) neuromuscular block via agonistic effects at nicotinergic receptors (nAChR).[52] Hence this mechanism also does not improve respiratory safety.

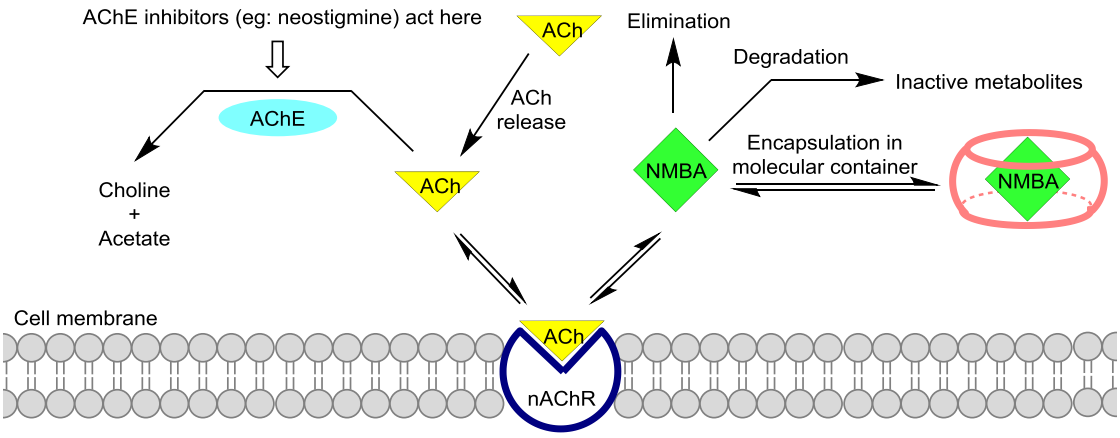

Figure I-3. Schematic representation of the onset and reversal of neuromuscular blockade.

A major advance in the clinical practice of anesthesia was made by the introduction of a γ-cyclodextrin-derived molecular container known as Sugammadex, marketed as Bridion™ by Merck with sales of more than $340 million in 2014 (Figure I-4); which binds rocuronium with high affinity (K_a = 1.79×10^7 M^{-1}) in water and reverses the effects of rocuronium *in vivo*.[53-55] Sugammadex reverses neuromuscular block by sequestering rocuronium in the

bloodstream, thereby depleting its concentration at the neuromuscular junction.[56] The Sugammadex•rocuronium complex is subsequently excreted in the urine. Sugammadex has had a major impact on the clinical practice of anesthesia in Europe since it came into use in 2008. Its use in the United States was delayed by the US FDA because of hypersensitivity events, but the drug was approved for clinical use in 2015.[57-59] While Sugammadex is able to reverse steroidal NMBAs such and rocuronium, it is not useful for reversing benzylisoquinolinium NMBAs such as cisatracurium due to weak binding affinity. As a result, there is a real need to develop alternative classes of molecular containers that function as reversal agents for the full range of clinically important NMBAs.

Given the high K_a values typically observed for CB[n] for alkyl ammonium guests,[18] their low toxicity[60] and ability to cross cell membranes ,[61] CB[n]-type receptors represent a potential alternative to the γ-cyclodextrin derivative Sugammadex for the reversal of neuromuscular block. Among the known CB[n], only CB[8] and CB[10] are large enough to encapsulate the steroidal nucleus of NMBAs like rocuronium, but unfortunately the water solubility of these containers is poor (<50 μM) which severely limits their potential to function as *in vivo* reversal agents for NMBAs. Conversely, water-soluble CB[7] is neither voluminous enough to encapsulate the steroidal ring system nor is its C=O···O=C distance of ~ 6.1 Å appropriate to electrostatically complement the N···N separation (~ 11.0 Å) of the steroidal NMBAs rocuronium and vecuronium. In fact, Macartney has shown that CB[7] binds to the ammonium ends of the steroidal NMBAs rather than the steroidal ring system. In

addition to this, CB[7] has poor selectivity for NMBAs compared to acetylcholine which implies that it could preferentially bind ACh instead of NMBA in *vivo*, further hindering NMBA reversal (Table I-2.). [62]

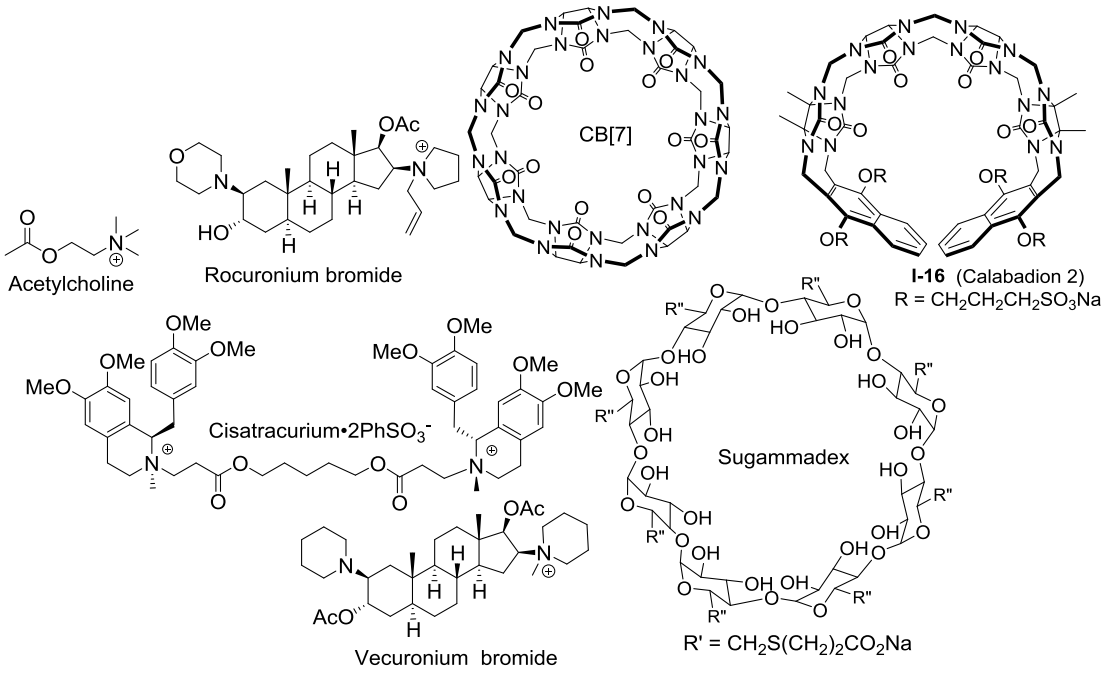

Figure I-4. Chemical structures of molecular containers CB[7], Calabadion 2 (**I-16**), Sugammadex, and guests rocuronium, vecuronium, cisatracurium, and acetylcholine.

In 2012, the Isaacs group reported that acyclic CB[n]-type receptor **I-6** binds steroidal NMBAs 100-fold stronger and the benzylisoquinoline type NMBA cisatracurium 1000-fold stronger than Sugammadex in water (Table I-2.).[48] *In vivo* experiments in rats showed that **I-16** reverses deep neuromuscular blockade induced by steroidal NMBAs rocuronium and vecuronium in a dose dependent

manner and restores the train-of-four ratio to 0.9 faster than placebo and Sugammadex.[48,63,64]

Table I-2. Binding constants (K_a, M^{-1}) for the host–guest complexes formed in aqueous solution.

Guest	CB[7]	Sugammadex	Calabadion 2
Acetylcholine	$(7.0 \pm 1.3) \times 10^5$	-	$(1.8 \pm 0.2) \times 10^5$
Cisatracurium	-	4.89×10^3	$(4.8 \pm 0.9) \times 10^6$
Vecuronium	$(2.2 \pm 0.3) \times 10^5$	5.72×10^6	$(1.6 \pm 0.2) \times 10^9$
Rocuronium	$(1.5 \pm 0.2) \times 10^4$	1.79×10^7	$(3.4 \pm 0.6) \times 10^9$

The same trend is observed for recovery of spontaneous breathing, which is also rapid with **I-16** as compared to experiments using placebo or Sugammadex.[48] Unlike Sugammadex, Calabadion 2 (**I-16**) displays a high *in vitro* binding affinity towards cisatracurium and also causes the *in vivo* reversal of the benzylisoquinolinium NMBA cisatracurium.[63,64] These previously published *in vivo* and *in vitro* results together indicate the potential of **I-16** to act as a broad spectrum reversal agent of NMBAs. However, there is the possibility that a patient who has been or is being treated with NMBAs during surgery may have previously taken other drugs and/or need to be treated with other drugs post-

surgically. For example, many surgical patients are treated with a variety of other drugs including antibiotics, antihistamines, and antiarrhythmics.[65] Accordingly, for the further development of **I-16** it is important to assess whether the binding of **I-16** toward rocuronium, vecuronium, or cisatracurium can be compromised by the presence of other drugs. The toxicity or other adverse effects of the host molecule and / or the host•NMBA complex are also important considerations. Chapter 2 addresses these issues of selectivity of Calabadion 2 toward NMBAs relative to other drugs and the pharmacokinetics of the excretion of container and drug in rats.

1.5.2 Reversal of Drugs of Abuse.

The recreational use of drugs of abuse is a major problem worldwide and overdoses and the associated mortality are common.[66] For example, the Substance Abuse and Mental Health Services Administration (SAMHSA) estimated that 10.2% of the US population 12 and older (27 million) had used an illicit drug in the past month.[67] Illicit drugs include methamphetamine, cocaine, marijuana, heroin, hallucinogens (ketamine, phencyclidine), inhalants, or prescription-type psychotherapeutics (pain relievers, tranquilizers, stimulants, and sedatives) when used non-medically (Figure I-4.).

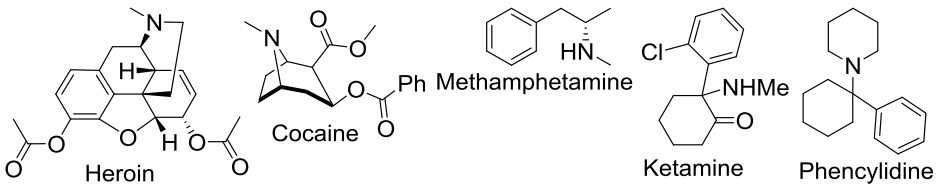

Figure I-4. Chemical structures of some commonly abused drugs.

The heathcare costs of emergency room visits related to illicit drugs was ≈ $11 billion in 2011 and overall costs associated with crime and lost work productivity was ≈ $193 billion.[68] Accordingly, the treatments for illicit drug overdose and addiction is an important biomedical problem with significant socioeconomic consequences.

Current treatments for drug overdose and addiction are based on either pharmacodynamic (PD) or pharmacokinetic (PK) strategies. PD strategies aim to disrupt the effects of the illicit drug at its site(s) of action (e.g. drug receptors) in the body. This approach is being used clinically for treating opioid overdose and addiction.[69] Some examples of anti-opioid drugs that work by the PD strategy include: opioid receptor antagonists naloxone and naltrexone which are used to treat overdose and addiction; methadone, levomethadyl acetate (LAAM), and buprenorphine which are used to treat withdrawal; and non-opioid agents (such as α2 adrenergic agents) clonidine and lofexidine which are used for managing withdrawal.[70] While this treatment approach has been successful for opioids, there are currently no pharmacotherapies approved by the US FDA to treat cocaine, methamphetamine, or cannabis use disorders.[71] In contrast, the PK strategy does not require a precise molecular level knowledge of the drug-receptor interaction needed in the PD strategy, but only the ability to decrease drug concentration below its effective concentration.[72] For example, enzyme based therapeutics (e.g. human butyrylcholine esterase) are being explored that can hydrolyze cocaine into its inactive metabolites (ecgonine methyl ester and benzoic acid), thereby creating a negative concentration gradient between the brain and

blood which results in a reduced concentration of the drug at its receptor in the brain.[69,73-75] Immunotherapeutics are also being developed for cocaine, methamphetamine, and fentanyl, most notably by Janda,[76-79] which act as peripheral blockers by binding and sequestering the "antigenic" drug and preventing it from crossing the blood brain barrier.[80,81]

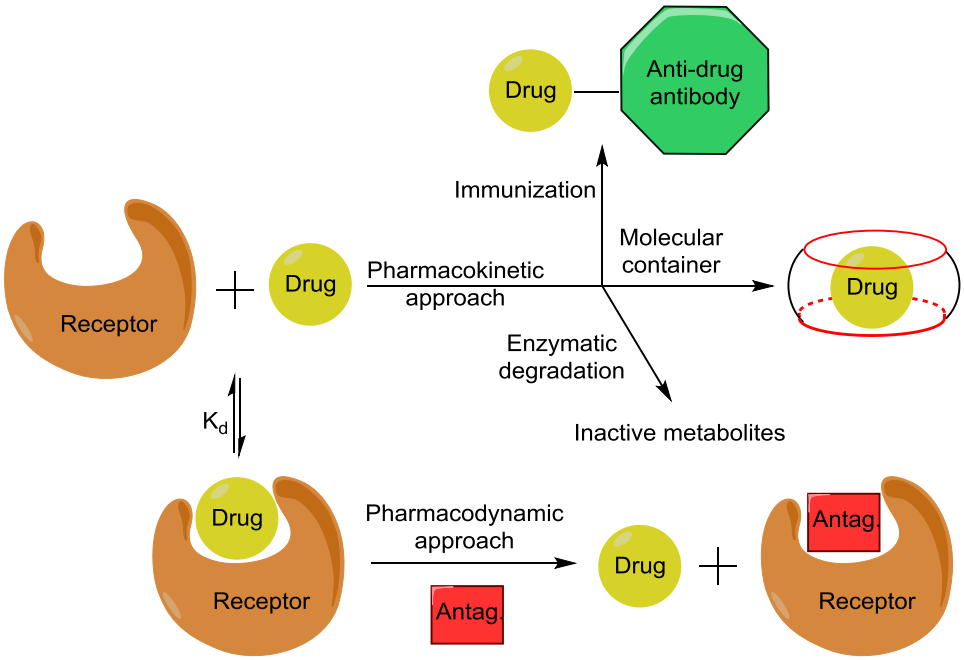

Figure I-5. Schematic representation of the pharmacokinetic and pharmacodynamic strategies for disrupting the effects of drugs of abuse.

The PK strategy has also been implemented using synthetic molecular container compounds to directly compete with biological molecular recognition events for the reversal of NMBAs as outlined in section 1.5.1. However in the context of molecular recognition of drugs of abuse by molecular containers only

sensing applications[82] have been reported for some amphetamine type molecules using phosphonate cavitands[83,84] and CB[n] derivatives.[85] Chapter 3 describes the recent work on the recognition properties of some common molecular containers towards a panel of frequently abused drugs. The *in vivo* reversal of methamphetamine by Calabadion 2 is reported as well as the pharmacokinetics of excretion of Calabadion 1 and fentanyl after the reversal of fentanyl in rats.

Chapter 2: Calabadion 2 as a Reversal Agent for Neuromuscular Blocking Agents

The work presented in this chapter was take from Ganapati, S.; Zavalij, P. Y.; Eikermann, M.; Isaacs, L., In Vitro Selectivity of an Acyclic Cucurbit[n]uril Molecular Container towards Neuromuscular Blocking Agents Relative to Commonly Used Drugs. *Org. Biomol. Chem.* **2016**, *14*, 1277-1287 and Haerter, F.; Simons, J. C. P.; Foerster, U.; Moreno Duarte, I.; Diaz-Gil, D.; Ganapati, S.; Eikermann-Haerter, K.; Ayata, C.; Zhang, B.; Blobner, M.; Isaacs, L.; Eikermann, M., Comparative Effectiveness of Calabadion and Sugammadex to Reverse Non-depolarizing Neuromuscular-blocking Agents. *Anesthesiology* **2015**, *123*, 1337-1349.

2.1 Introduction.

Muscle relaxant drugs such as rocuronium, vecuronium (steroidal neuromuscular blocking agents- NMBAs) and cisatracurium (benzylisoquinolinium NMBA) are widely used pre-surgically to block the patients muscle function and optimize surgical conditions.[49] Post-surgical reversal of neuromuscular blockade through the use of AChE inhibitors such as neostigmine is not optimal due to side effects arising from incomplete reversal of NMBAs and cardiovascular issues.[52] The γ-cyclodextrin based molecular container- **II-1** marketed by Merck as Bridion™ has greatly improved the safety of NMBA reversal for rocuronium and vecuronium in Europe, and has recently been approved by the United States Food and Drug Administration after

concerns regarding hypersensitivity were addressed in clinical trials.[57,59] Isaacs et al. have designed and synthesized the acyclic CB[n] based container **II-2**, which has shown faster reversal of steroidal NMBAs such as rocuronium and vecuronium. Container **II-2** also shows a broader scope and also reverses the structurally distinct benzylisoquinolinium NMBA cisatracurium. The faster rate of reversal and broader scope can both be attributed to the order(s) of magnitude higher K_as shown by **II-2** toward these three NMBAs compared to **II-1**.[48] For the further development of **II-2** as a broad spectrum reversal agent for NMBAs in the clinic, we have addressed two important issues in this chapter: (1) the *in vitro* selectivity of **II-2** toward different NMBAs in the presence of other drugs commonly found on anesthesia trays in hospitals and (2) the pharmacokinetic profile of **II-2** after NMBA reversal in rat urine.

2.2 *In Vitro* Selectivity of Calabadion 2 towards Neuromuscular Blocking Agents Relative to Commonly Used Drugs.

The superior K_as and faster / broader scope of *in vivo* reversal of NMBAs by **II-2** compared with **II-1** is a promising preliminary result for its development for clinical use. However, there is the possibility that a patient who has been or is being treated with NMBAs during surgery may have previously taken other drugs and/or need to be treated with other drugs post-surgically. For example, many surgical patients are treated with a variety of other drugs including antibiotics, antihistamines, and antiarrhythmics.[65]Accordingly, for the further development of **II-2** it is important to assess whether the binding of **II-2** toward rocuronium,

vecuronium, or cisatracurium can be compromised by the presence of other drugs.

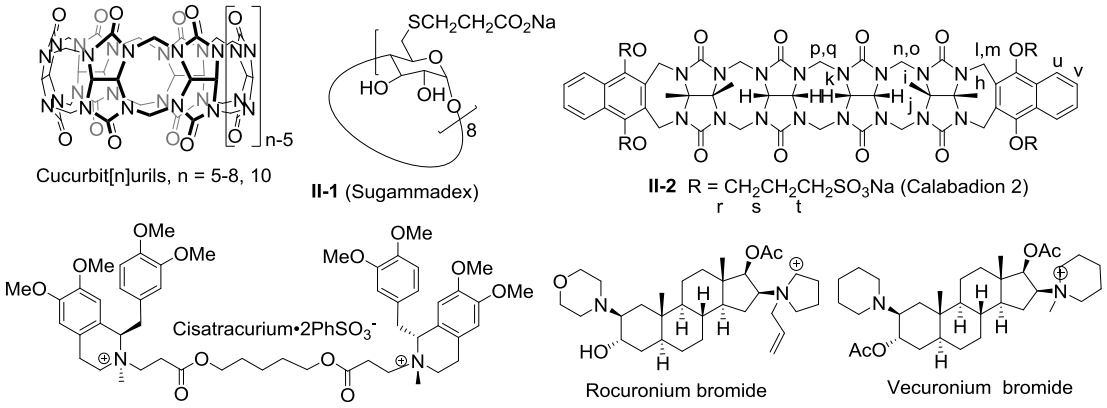

Figure II-1. Chemical structures of CB[n], Sugammadex (**II-1**), Cb 2 (**II-2**); and NMBAs cisatracurium, rocuronium, vecuronium.

In this study, we determine the binding constant of **II-2** toward 27 drugs that are commonly used during and after surgery. We use the experimentally determined values of K_a and used them as known inputs to explore by simulations (Gepasi^{TM}) the behavior of the multicomponent system comprising **II-2**, rocuronium or vecuronium or cisatracurium, acetylcholine receptor (AChR), and drug using estimated or known values of clinical drug concentration ranges and AChR binding constants.

Thus we assessed the potential for these 27 drugs to induce displacement of rocuronium, vecuronium, or cisatracurium from the cavity of **II-2**. The results of these simulations are presented in the form of three dimensional plots that connect the K_a of the **II-2**•drug complex and the dosage of drug with the equilibrium concentration of the AChR•NMBA complex. These drugs were selected to include a variety of drug classes such as antibiotics, antiarrythmics, analagesics,

etc. which are typically present on standard anesthesia trays at hospitals. Cationic drugs were selected specifically as they are expected to have higher affinity towards our anionic acyclic CB[n]-type container **II-2**, and therefore pose the highest potential for displacing NMBAs from the **II-2**•NMBA complexes.

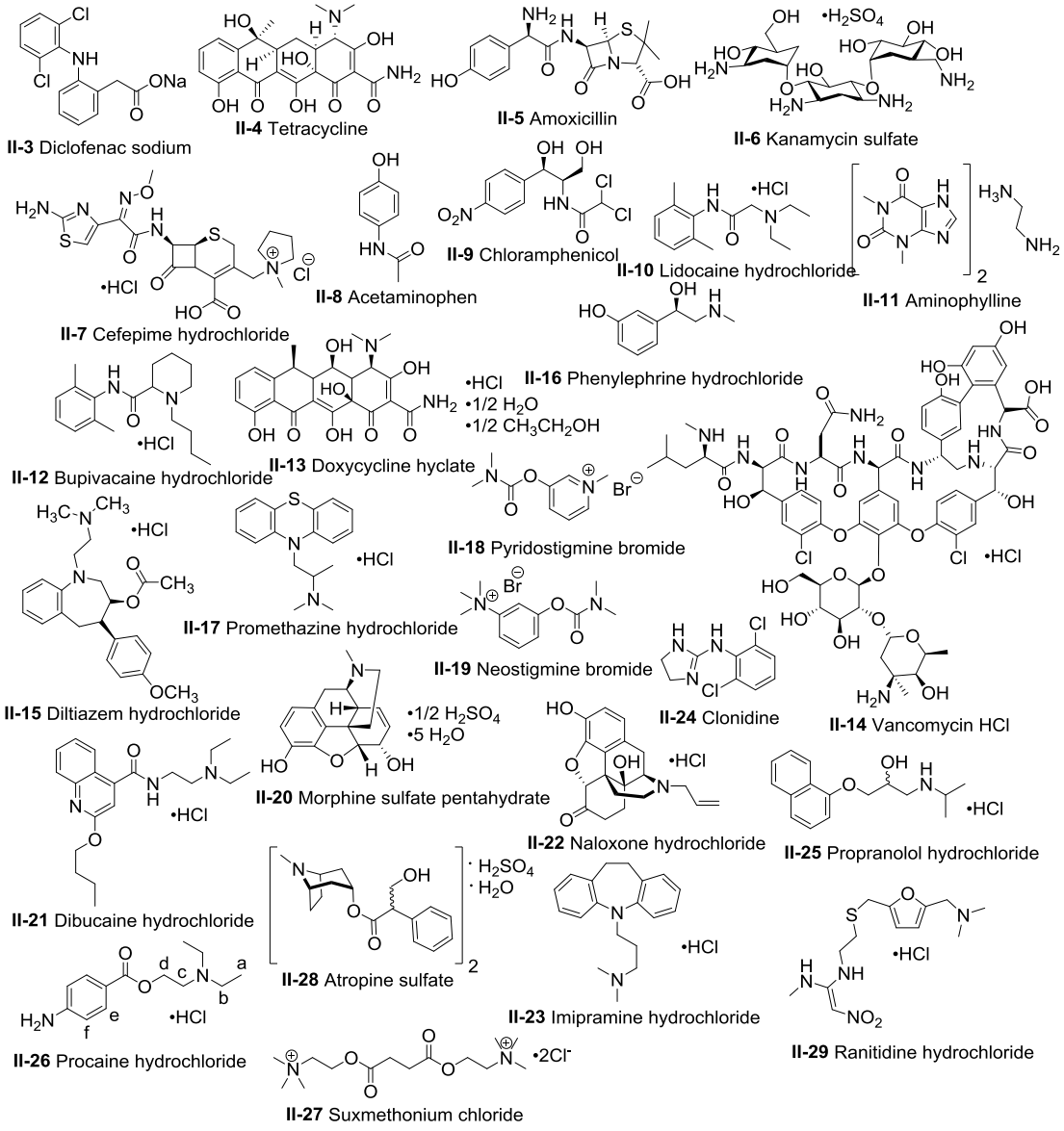

Figure II-2. **Chemical structures of drugs used in this study.**

2.2.1 Binding Properties of II-2 towards Drugs II-3 – II-29 Investigated by ^{1}H NMR.

Initially, we investigated the ability of container II-2 to bind drugs II-3 – II-29 by ^{1}H NMR spectroscopy. For complexes between II-2 and drugs II-3 – II-29 we commonly observed upfield shifting of guest resonances which indicates that these protons on the guest (drug) are located in the cavity of II-2. All of the II-2•drug complexes display intermediate to fast kinetics of exchange on the ^{1}H NMR timescale.

These preliminary ^{1}H NMR observations suggested that complexes between container **II-2** and drugs **II-3** – **II-29** would be of moderate stability in water. In contrast, complexes between **II-2** and NMBAs cisatracurium, rocuronium and vecuronium exhibit slow exchange on the chemical shift timescale. To facilitate further discussion of the NMR results we present the ^{1}H NMR spectra recorded for **II-26** (procaine), **II-2**, the **II-2•II-26** complex, and a mixture of **II-2•II-26** with excess **II-26** present (Figure II-3). These ^{1}H NMR spectra display a number of interesting features, which provide insight the nature of the **II-2•II-26** complex. For example, the aromatic peaks H_e, and H_f of **II-26** shift considerably upfield (> 1 ppm) upon binding to one equivalent of **II-2** (Figure II-3c). This dramatic upfield shift reflects the anisotropic shielding environment provided by the two aromatic naphthalene sidewalls of **II-2**. Given the aromatic nature of drug **II-26**, we surmise that π-π interactions are formed within the **II-2•II-26** complex. In the spectrum containing two equivalents of **II-**

26 to one equivalent of **II-2** (Figure II-3d) H_e and H_f shift back downfield (relative to Figure II-3c) to a position that is the average of the completely bound and completely free form of **II-26**. This indicates a fast kinetics of exchange between free guest **II-26** and the **II-2•II-26** complex relative to the ^{1}H NMR chemical shift time scale.

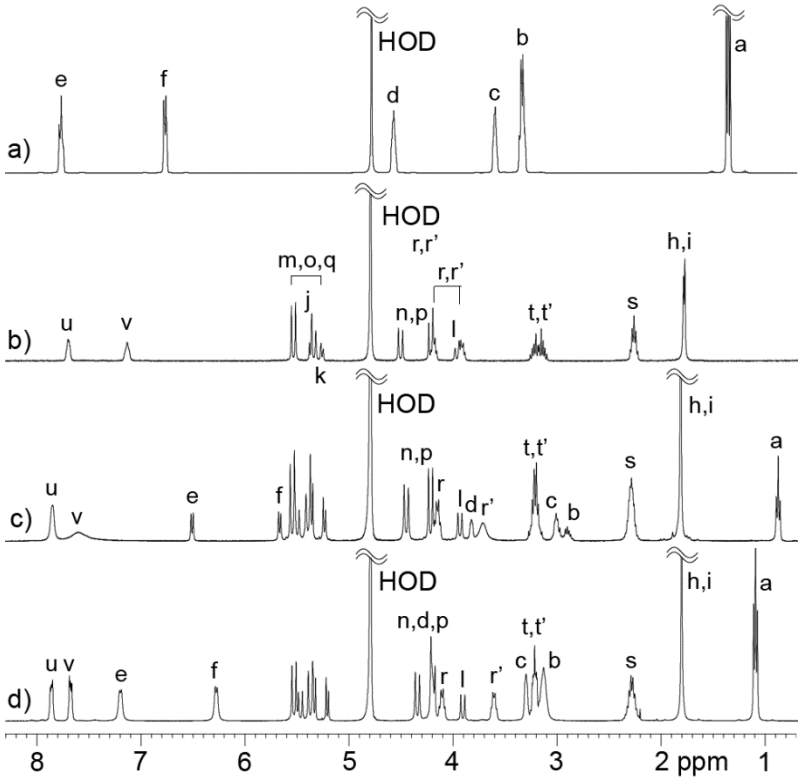

Figure II-3. ^{1}H NMR spectra recorded (400 MHz, RT, 20 mM NaH_2PO_4 buffered D_2O, pH = 7.4) for a) **II-26**, b) **II-2**, c) an equimolar mixture of **II-2** and **II-26** (12.5 mM), and d) a 1:2 mixture of **II-2** (12.5 mM) and **II-26** (25 mM).

In contrast, the aromatic protons H_u and H_v of host **II-2** undergo a downfield shift (H_u, 7.72 ppm; H_v, 7.17 ppm) upon formation of the **II-2•II-26** complex. The observed downfield shift is due to the disruption of edge-to-face π-π interactions between the tips of free host **II-2** which are disrupted upon formation of the **II-2•II-26** complex. Addition of a second equivalent of **II-26** results in little additional shifting and sharpening of the resonances for H_u and H_v because the **II-2•II-26** complex is largely formed at both stoichiometries.

Interestingly, the resonances for H_a, H_b, and H_c of 2-diethylaminoethyl sidechain also show significant upfield shifts upon binding to **II-2** which is probably reflects partial inclusion of the sidechain in the shielding region defined by the glycoluril tetramer backbone and the aromatic naphthalene sidewalls. Analogous phenomena were seen in the ^{1}H NMR spectra recorded for the remaining **II-2**•drug complexes in accord with the previously established preferences of CB[n]-type receptors to bind the hydrophobic portions of guests within the hydrophobic cavity whereas the cationic ammonium groups reside at the ureidyl carbonyl portals and benefit from ion-dipole interactions.[86,18]

2.2.2 Stoichiometry of the Complexes between II-2 and Drugs II-3 – II-29.

It is well known that CB[n]-type receptors generally form host•guest complexes with 1:1 stoichiometry. In order to confirm the 1:1 stoichiometry of the complexes between **II-2** and drugs **II-3** – **II-29** we created Job plots.

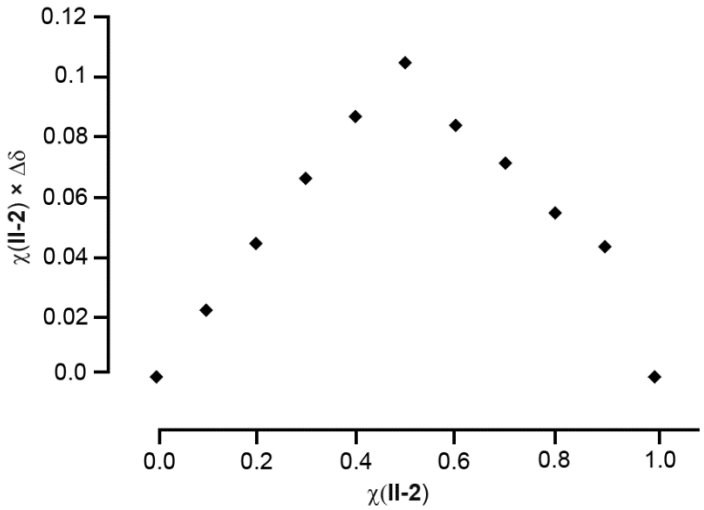

Figure II-4. Job plot constructed for mixtures of **II-2** and **II-26** ([**II-2**] + [**II-26**] = 1 mM) by monitoring the change in ^{1}H NMR (400 MHz, RT, 20 mM NaH_2PO_4 buffered D_2O, pH = 7.4) chemical shift of H_u (7.72 ppm) of **II-2**.

In Job plots, a series of samples containing host and guest at a constant total concentration ([host] + [guest] = constant) are prepared and are investigated by an appropriate spectroscopic technique. A plot of the change in spectroscopic signal versus mole fraction displays a maximum at the mole fraction that corresponds to the stoichiometry of the host•guest complex. Figure II-4 shows the Job plot constructed using **II-2** and **II-26** at a total concentration of 1 mM. The Job plot displays a maximum at a mole fraction of 0.5 which confirms the 1:1 stoichiometry of the **II-2•II-26** complex. Job plots were constructed for several additional drugs and are given in Appendix 1.

2.2.3 X-ray Crystal Structure of the II-2•II-29 Complex.

We were fortunate to obtain single crystals of the **II-2•II-29** complex by slow evaporation of an aqueous solution of the complex and to solve its x-ray crystal structure.

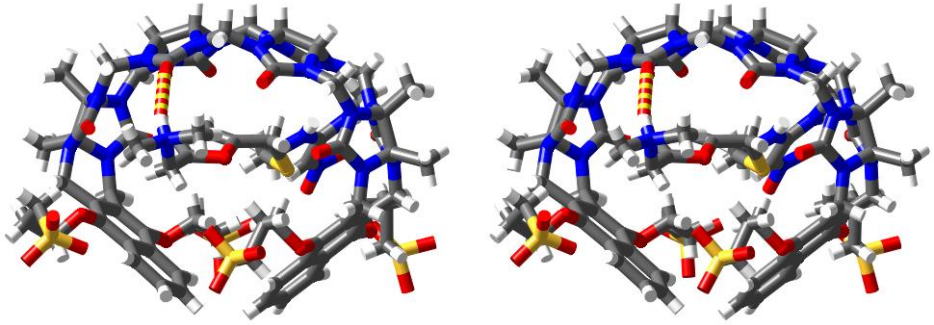

Figure II-5. Cross-eyed stereoscopic representation of the geometry of one molecule of **II-2•II-29** from the x-ray crystal structure. Color code: C, grey; H, white; N, blue; O, red; S, yellow; hydrogen bond, red–yellow striped.

Figure II-5 shows a cross-eyed stereoview of one molecule of **II-2•II-29** in the crystal which displays a number of interesting features. As described previously, the glycoluril tetramer backbone of **II-2** imparts an overall C-shape to the receptor whereas the terminal naphthalene sidewalls help to define a hydrophobic box-like cavity. Interestingly, host **II-2** within the **II-2•II-29** complex adopts a helical (chiral) conformation where the two naphthalene sidewalls are splayed out-of-plane with respect to the glycoluril tetramer backbone; both senses of handedness are observed in the crystal in a 1:1 ratio. Furthermore, the ammonium ion unit of guest **II-29** engages in an N-H•••O=C hydrogen bond (N•••O distance = 2.803 Å; N-H•••O angle = 160.9˚) with the carbonyl portal. The furan ring is

enclosed within the cavity of **II-2** but does not engage in π-π stacking interactions with naphthalene sidewalls. In addition, one of the amidine N-H groups at the opposite carbonyl portal appears to engage in a weak hydrogen bond (N•••O distance = 3.231 Å; N-H•••O angle = 147.2˚)

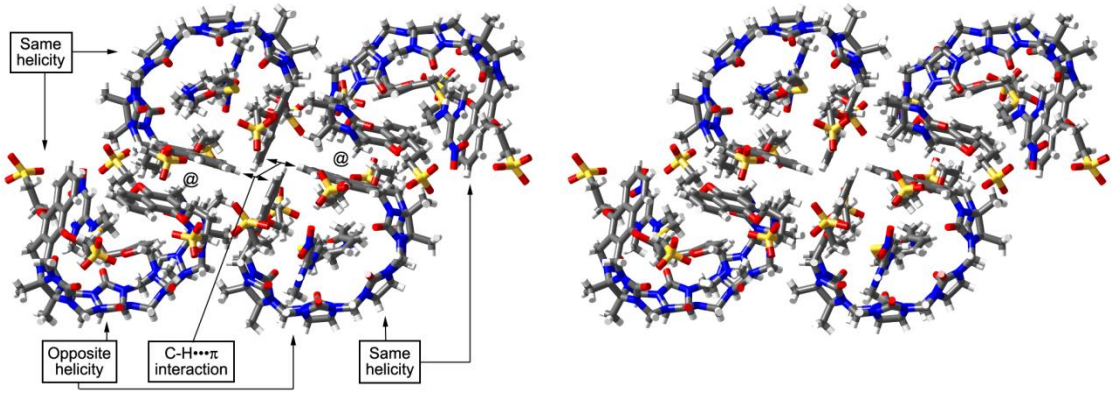

Figure II-6. Cross-eyed stereoscopic representation of the packing of **II-2•II-29** in the x-ray crystal structure. Color code: C, grey; H, white; N, blue; O, red; S, yellow.

Finally, Figure II-5 shows that the naphthalene sidewalls of **II-2** in the **II-2•II-29** complex do not undergo edge-to-face π-π interactions which is in accord with the downfield shift observed for H_u and H_v upon complex formation.[48,44] The three dimensional packing of the individual molecules of **II-2•II-29** complex in the crystal is also intriguing (Figure II-6). As shown in Figure II-6, two molecules of the **II-2•II-29** complex of the same helicity pack next to one another by interactions between the convex faces of the aromatic sidewalls (marked with @ symbol). Additional homochiral pairs of the **II-2•II-29** complex extend along the z-axis with alternating sense of helicity. Quite interestingly, adjacent pairs of

the **II-2•II-29** complex are held together by reciprocal pairs of close CH•••π interactions (CH•••π distance = 2.798, 2.868 Å; CH•••π angle = 161.7˚, 149.1˚) between molecules of complex **II-2•II-29** of opposite helicity.

2.2.4 Measurement of K_as between II-2 and Drugs II-3 – II-29.

After having established the inclusion binding of drugs **II-3** – **II-29** inside container **II-2** by ^{1}H NMR spectroscopy, we decided to measure the binding affinity (K_a, M^{-1}) for the **II-2•II-3** – **II-2•II-29** complexes. For this purpose, we employed three different strategies: (1) direct UV/Vis titrations (for UV/Vis active drug **II-4**), (2) direct ^{1}H NMR titrations (for drugs **II-3**, **II-5** – **II-7**, **II-9**, **II-11**, and **II-13** with K_a < 5000 M^{-1}), and (3) UV/Vis competition titrations (for UV/Vis inactive drugs with Ka > 5000 M^{-1}). The detailed procedures and models used to analyze the data using Scientist™ are given in Appendix 1. For example, Figure II-7a shows the ^{1}H NMR spectra recorded during the titration of a fixed concentration of **II-2** (0.976 mM) with **II-6** (0 – 6.57 mM). As described above, upon formation of the **II-2•**guest complexes, we generally observe a downfield shift of H_u and H_v because the tips of the naphthalene sidewalls are no longer engaged in edge-to-face π-π interactions. Figure II-7b shows a plot of chemical shift of H_v versus [**II-6**] which was fitted to a standard 1:1 binding model using Scientist™ (Appendix 1) which allowed us to determine $K_a = (3.0 \pm 0.6) \times 10^3$ M^{-1} for the **II-2•II-6** complex. Similar ^{1}H NMR titrations were performed for guests **II-3**, **II-5** – **II-7**, **II-9**, **II-11**, and **II-13** (Appendix 1) and the results are presented in Table II-1.

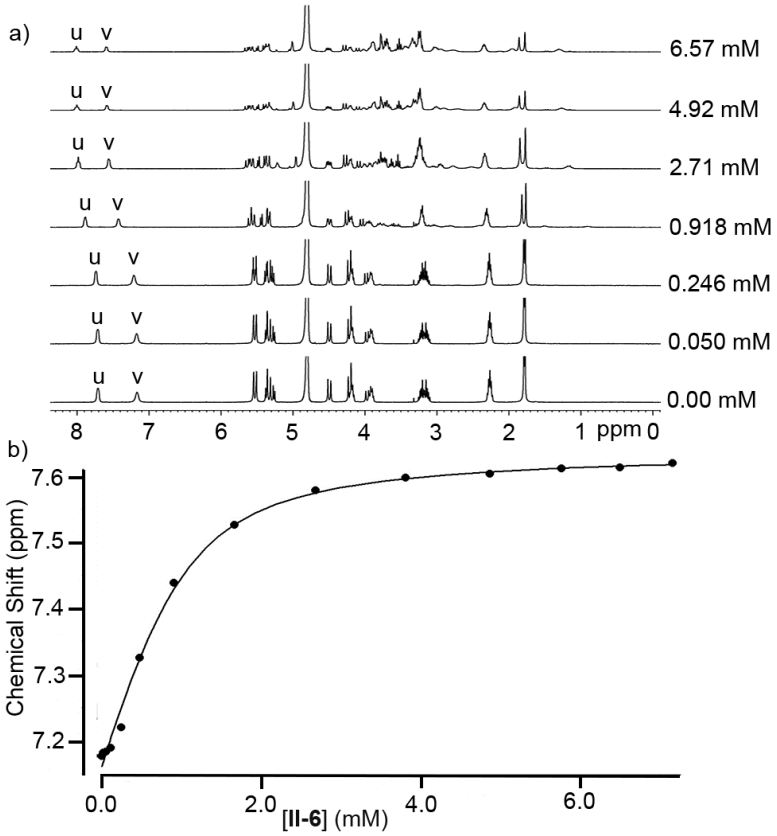

Figure II-7. a) ^{1}H NMR (400 MHz) stack plot of the titration of **II-2** (0.976 mM) with guest **II-6** (0 – 6.57 mM) in 20 mM NaH_2PO_4 buffered D_2O (pH = 7.4); b) plot of the chemical shift of H_v as a function of guest concentration. The solid line represents the best non-linear fit of the data to a 1:1 model (K_a = (3.0 ± 0.6) × $10^{3\ M-1}$).

Next, to determine the K_a values for the stronger **II-2**•guest complexes we performed competition experiments monitored by UV/Vis spectroscopy.[87] For this purpose, we employed Rhodamine 6G which undergoes significant changes in its UV/Vis spectrum upon formation of the II-2•Rhodamine 6G complex (K_a = 2.3 ± 0.2 × 10^6 M^{-1}).[48] Addition of competitive guests displace indicator

Rhodamine 6G from the **II-2**•Rhodamine 6G complex and reverse the observed UV/Vis changes.

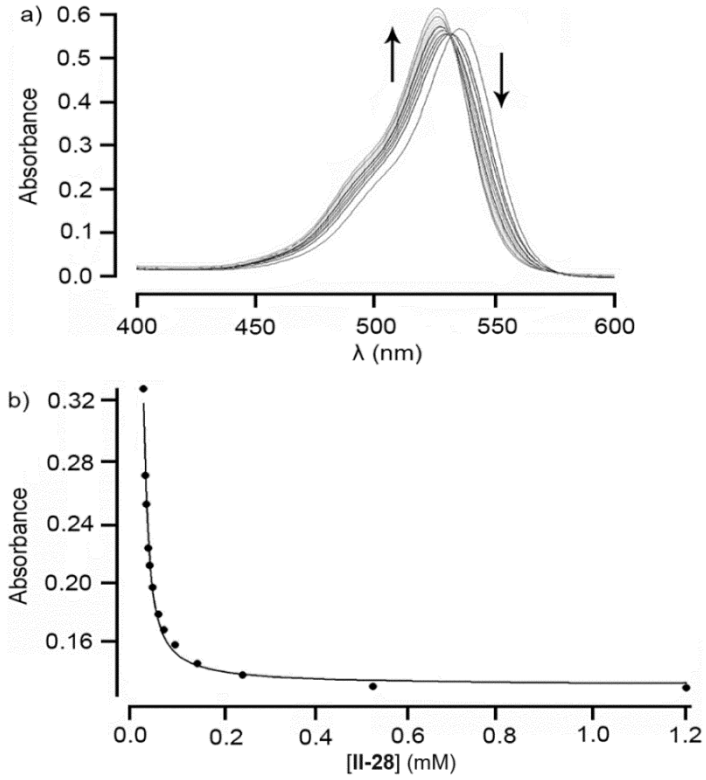

Figure II-8. a) UV/Vis spectra recorded during the titration of a mixture of **II-2** (9.92 μM) and dye rhodamine 6G (10.0 μM) with guest **II-28** (0 – 1.21 mM) in 20 mM NaH_2PO_4 buffer (pH = 7.4), b) plot of absorbance at 550 nm as a function of the concentration of **II-28**. The solid line represents the best non-linear fit of the data to a competitive binding model ($K_a = (3.3 \pm 0.5) \times 10^6\ M^{-1}$).

Figure II-8 shows the absorbance data obtained from the competitive UV/Vis titration of **II-2**•Rhodamine 6G with II-28 (0 – 1.21 mM). We fit a plot of absorbance versus [**II-28**] to the standard competitive binding model

(Appendix 1)[48,39] to determine the K_a for the **II-2•II-28** complex (K_a = (3.3 ± 0.5) × 10^6 M^{-1}) using the known K_a of **II-2**•rhodamine 6G ((2.3 ± 0.2) × 10^6 M^{-1})[48] as input. Analogous UV/Vis competition experiments were performed which allowed us to measure the remaining K_a values given in Table II-1. For purposes of comparison, the K_a values for Sugammadex (**II-1**) toward drugs **II-3** – **II-29** as reported by Zwiers are also given in Table II-1.[65]

2.2.5 Commentary on the Tabulated K_a Values.

An examination of the binding constants given in Table II-1 reveals that the K_a values for this set of 27 drugs ranges from a low of 2.0 x 10^3 M^{-1} for diclofenac **II-3** to a high of 4.5 x 10^6 M^{-1} for ranitidine **II-29**; 13 out of 27 drugs have $K_a > 10^5$ M^{-1} whereas 14 out of 27 have $K_a < 10^5$ M^{-1}.

Some of the trends can be readily understood given the well-known binding preferences of CB[n] and acyclic CB[n]-type receptors for hydrophobic and (di)cationic guests.[86,18] For example, among the weaker binders ($K_a < 10^5$ M^{-1}) we find neutral or anionic compounds like diclofenac (**II-3**), acetaminophen (**II-8**), chloramphenicol (**II-9**), and aminophylline (**II-11**) as well as highly hydrophilic and hydroxylated compounds like tetracycline (**II-4**), kanamycin (**II-6**), doxycycline (**II-13**), and vancomycin (**II-14**).Other weak binders include the zwitterionic compounds amoxicillin (**II-5**) and cefepime (**II-7**). Conversely, among the stronger binders ($K_a > 10^5$ M^{-1}) we find compounds that better satisfy the binding preferences of **II-2**.

Table II-1. Binding constants determined by direct or competitive UV/Vis assays or direct ^{1}H NMR titrations for the interaction between **II-2** and drugs **II-3**-**II-29**, drug dosages in the rat model, estimated plasma concentrations, and binding constants toward **II-1**.

Drug	K_a with **II-2** (M^{-1})	Dosage in rat model (mg kg^{-1})[88]	Est. Plasma Concentration in Rats (μM)	K_a with **II-1** (M^{-1})[65]
Acetylcholine	$(1.8 \pm 0.2) \times 10^{5}$ d)	-	-	-
Cisatracurium	$(4.8 \pm 0.9) \times 10^{6}$ d)	0.7	18.3	4.89×10^{3}
Vecuronium	$(1.6 \pm 0.2) \times 10^{9}$ d)	0.7	26.7	5.72×10^{6}
Rocuronium	$(3.4 \pm 0.6) \times 10^{9}$ d)	3.5	160	1.79×10^{7}
II-3	$(2.0 \pm 0.4) \times 10^{3}$ a)	10	763	2.50×10^{4}
II-4	$(2.3 \pm 0.2) \times 10^{3}$ b)	10-20	819	$<1.00 \times 10^{3}$
II-5	$(3.0 \pm 0.4) \times 10^{3}$ a)	10-20	997	$<1.00 \times 10^{3}$
II-6	$(3.0 \pm 0.6) \times 10^{3}$ a)	10-20	752	$<1.00 \times 10^{3}$
II-7	$(4.6 \pm 0.5) \times 10^{3}$ a)	10-40	1040	$<1.00 \times 10^{3}$
II-8	$(5.9 \pm 0.5) \times 10^{3}$ c)	100-300	32122	$<1.00 \times 10^{3}$
II-9	$(5.9 \pm 1.8) \times 10^{3}$ a)	45-80	4696	$<1.00 \times 10^{3}$
II-10	$(8.6 \pm 0.8) \times 10^{3}$ c)	0.5-1	63.1	$<1.00 \times 10^{3}$
II-11	$(1.4 \pm 0.4) \times 10^{4}$ a)	3-100	5948	$<1.00 \times 10^{3}$
II-12	$(2.1 \pm 0.2) \times 10^{4}$ c)	0.5-2	88.5	-
II-13	$(3.3 \pm 1.0) \times 10^{4}$ a)	5-10	355	2.40×10^{4}
II-14	$(4.4 \pm 0.3) \times 10^{4}$ c)	20	335	1.78×10^{4}
II-15	$(4.8 \pm 0.3) \times 10^{4}$ c)	20-40	1615	1.12×10^{4}
II-16	$(8.3 \pm 0.6) \times 10^{4}$ c)	0.001	0.12	-
II-17	$(1.9 \pm 0.1) \times 10^{5}$ c)	6.25-12.5	709	1.02×10^{4}
II-18	$(1.9 \pm 0.1) \times 10^{5}$ c)	0.018	1.67	$<1.00 \times 10^{3}$
II-19	$(2.5 \pm 0.1) \times 10^{5}$ c)	0.005-0.015	1.60	$<1.00 \times 10^{3}$
II-20	$(5.3 \pm 0.4) \times 10^{5}$ c)	0.2-0.4	9.60	2.44×10^{4}
II-21	$(5.9 \pm 0.7) \times 10^{5}$ c)	-	-	-
II-22	$(8.0 \pm 0.7) \times 10^{5}$ c)	0.01-0.1	3.04	1.84×10^{4}
II-23	$(8.2 \pm 0.9) \times 10^{5}$ c)	20	1532	-
II-24	$(9.3 \pm 0.9) \times 10^{5}$ c)	0.1-0.3	18.2	$<1.00 \times 10^{3}$
II-25	$(9.7 \pm 1.1) \times 10^{5}$ c)	0.02-0.15	14.0	2.61×10^{4}
II-26	$(9.8 \pm 0.5) \times 10^{5}$ c)	1-2	133	-
II-27	$(2.8 \pm 0.1) \times 10^{6}$ c)	0.25-0.45	21.4	$<1.00 \times 10^{3}$
II-28	$(3.3 \pm 0.5) \times 10^{6}$ c)	0.02-0.05	1.22	$<1.00 \times 10^{3}$
II-29	$(4.5 \pm 0.7) \times 10^{6}$ c)	6-10	553	5.40×10^{3}

a) measured by direct ^{1}H NMR titration. b) measured by direct UV/Vis titration, c) measured by UV/Vis competition assay using rhodamine 6G, d) reference.[48]

For example, the two linear dications procaine (**II-26**) and suxmethonium chloride (**II-27**) are among the strongest binding drugs. In accord with the preference of CB[n]-type receptors for hydrophobic bicyclic and polycyclic cations,[19,86,18,89,90] compounds like morphine (**II-20**), naloxone (**II-22**), atropine (**II-28**) are among the better binders for **II-2**. Recently, we reported that **II-2** is an outstanding solubilizing agent for insoluble drugs that are aromatic cations due to the formation of π-π interactions between the insoluble drug and the naphthalene walls of **II-2** which define a hydrophobic box.[44] The observed stronger binding between **II-2** and aromatic ammonium ions dibucaine (**II-21**), propranolol (**II-25**), and imipramine (**II-23**) are consistent with the previously delineated binding preferences of **II-2**.

2.2.6 Assessment of the Potential for Displacement Interactions.

We undertook the measurement of the binding constants for the complexes between **II-2** and drugs **II-3** – **II-29** with the goal of assessing the potential for these drugs to interfere with the *in vivo* use of **II-2** as a reversal agent for neuromuscular block induced by rocuronium, vecuronium, or cisatracurium. Given the high level of complexity of the *in vivo* system (e.g. metabolism, excretion, biodistribution, other binding partners) we created a minimalist model that is amenable to appropriate simulations. Figure II-9 shows the three equilibria that we decided to consider, namely the binding of NMBA to the acetylcholine (AChR) receptor and to Calabadion 2 as well as the binding of drug to Calabadion 2. With a knowledge of the three K_a values (K_1 – K_3) and the total concentrations

of NMBA, AChR and drug it is possible to calculate the concentrations of each species present at equilibrium. It should be noted that the total concentration of displacing drug in this model represent an upper limit to what would be observed in vivo because drugs can also be bound to plasma proteins and are subject to rapid distribution to peripheral compartments such as the intercellular space. Accordingly, our model is a conservative screening technique that will generally overestimate the displacement potential of a given drug. Our goal of the simulations was to systematically explore the influence of the different K_a values and total concentrations on the equilibrium concentration of the AChR•NMBA complex since the occupation of the biological receptor by NMBA is ultimately what controls the biological function. The simulations are meant to inform and serve as a stepping stone toward future *in vivo* selectivity experiments which will ultimately determine the selectivity of **II-2** towards NMBAs over other drugs in the actual biological system.

$$\text{AChR} + \text{NMBA} \overset{K_1}{\rightleftharpoons} \text{AChR•NMBA}$$

$$\text{Calabadion 2} + \text{NMBA} \overset{K_2}{\rightleftharpoons} \text{Calabadion 2•NMBA}$$

$$\text{Calabadion 2} + \text{Drug} \overset{K_3}{\rightleftharpoons} \text{Calabadion 2•Drug}$$

Figure II-9. Illustration of the equilibria considered in the simulations using Gepasi.

2.2.7 Simulation of In Vivo Equilibria Using modelling Software Gepasi.

We decided to perform the simulations using the freely available software package Gepasi[91-93] which is capable of performing both kinetic and thermodynamic simulations of user defined interaction networks. The Gepasi software is very powerful and capable of performing multiple simulations where one or more variables are scanned sequentially (using the scan function), which allowed us to develop insight into the influence of each variable. The equilibrium concentrations of each species determined by the Gepasi simulations were exported to and visualized using Microsoft Excel. Below we present simulations using values derived from the data for rocuronium and cisatracurium. An analogous simulation for vecuronium is presented in Appendix 1.

2.2.8 In Vitro selectivity of Calabadion 2 for Rocuronium.

For the simulations using **II-2**, rocuronium, and drugs **II- 3** – **II-29** we fixed the equilibrium constants K_2 (3.4 x 10^9 M^{-1}) and K_3 using the values in Table 1. We set the total concentration of rocuronium equal to 160 μM to mimic the initial *in vivo* plasma concentration in the rat; this value was calculated based on the known dosage (3.5 mg kg^{-1}, twice the ED90), the average mass (370 g) and the average plasma volume (15.2 mL) of the male *Sprague-Dawley* rats used in our previous experiments.[94] The initial concentration of AChR was defined as equal to the initial concentration of NMBA (160 μM) for simplicity. Figure II-10

shows a three dimensional plot of the mole fraction of AChR•Rocuronium (z–axis) as a function of the total concentration of drug (e.g. **II-3** – **II-29**, x-axis), and log K_3 (y-axis) obtained from the simulations.

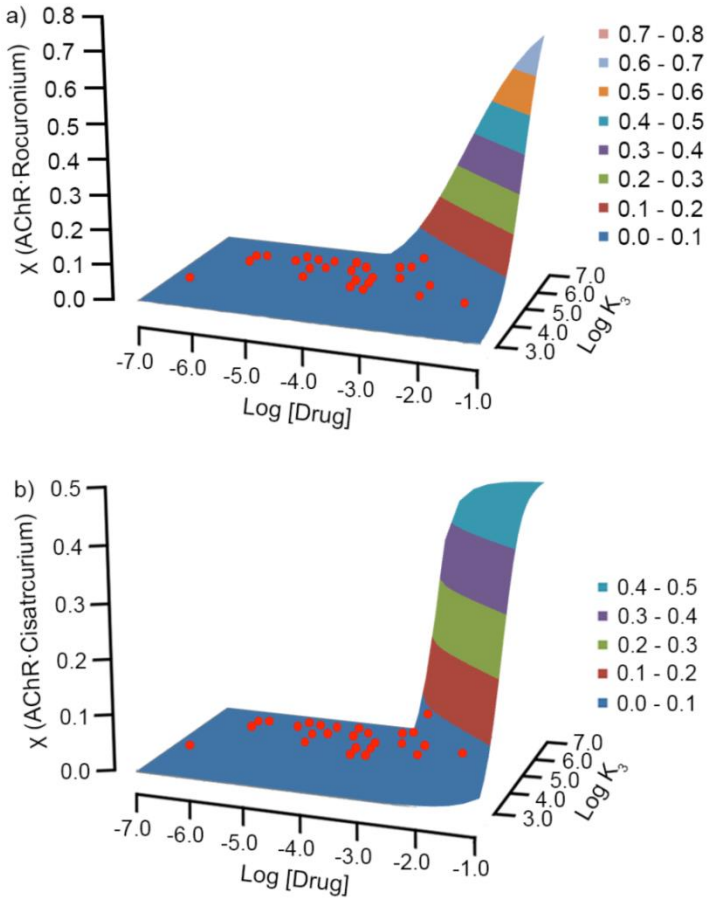

Figure II-10. Three dimensional surface plots of the concentration of AChR•NMBA at equilibrium versus log [Drug] and log K_3 for **II-2**•Drug) for: a) rocuronium at [rocuronium] = [AChR] = 160 μM, [**II-2**] = 320 μM (2 eqv.), K_1 = 10^5 M^{-1}, K_2 = 3.4 × 10^9 M^{-1}; b) cisatracurium at [cisatracurium] = [AChR] = 18 μM, [**II-2**] = 1.2 mM (64 eqv.), K_1 = 10^5 M^{-1}, K_2 = 4.8 × 10^6 M^{-1}. The red dots mark the points corresponding to each of the 27 drugs (**II-2** – **II-29**).

The range of the x-axis from 0.1 μM to 100 mM was chosen to span the range of plasma concentrations of drug **II-3** – **II-29** given in Table II-1 whereas the range of the y-axis from 10^3 to 10^7 M^{-1} was chosen to span the range of K_3 values given in Table II-1 for drugs **II-3** – **II-29**. This surface plot represents the general behavior of $[AChR•Rocuronium]_{equilibrium}$ over the full range of dosages and K_3 of potentially interfering drugs studied in this work. As can be readily seen, there is a plateau region in the lower left region of the plot that corresponds to situations where the drugs do not display any ability to displace rocuronium from the II-2•rocuronium complex and therefore [AChR•rocuronium] is low.

Conversely, as [Drug] and/or log K_3 is increased the [AChR•rocuronium] increases. The region in the upper right hand side of the plot corresponds to situations where drugs with these combinations of [Drug] and log K_3 values are expected to display the ability to displace rocuronium from the **II-2**•rocuronium complex resulting in the increase in the concentration of AChR•rocuronium. The data points corresponding to the individual combinations of plasma concentrations and K_3 values for each drug are marked on the 3D surface of Figure II-10a as red dots. According to the constraints of this simulation, none of the drugs possess any substantial ability to displace rocuronium from **II-2**•rocuronium. From the shape of Figure II-10a, it is easy to see that drugs with a combination of a high value of K_3 and a large dose are most likely to displace rocuronium from **II-2**•rocuronium.

2.2.9 In vitro selectivity of Calabadion 2 for Cisatracurium.

The binding affinity of **II-2** toward the NMBA (K_2) relative to potentially competing drugs plays a major role in influencing how much NMBA is bound to the AChR at equilibrium. Calabadion 2 (**II-2**) binds cisatracurium (K_2 = (4.8 ± 0.9) x 10^6 M^{-1}) approximately 103-fold weaker than rocuronium (K_2 = (3.4 ± 0.6) x 10^9 M^{-1}) and therefore we would expect that the potential for displacement of cisatracurium from the **II-2**•cistracurium complex by drugs **II-3** – **II-29** would be more significant than for rocuronium. For the purpose of the simulations, we created a three dimensional plot of the equilibrium concentration of AChR•cisatracurium (z-axis) as a function of the concentration of the potentially interfering drug over a range of concentrations (1 μM – 100 mM, full range of average dosage of drugs **II-3** – **II-29**, Table II-1, x-axis), and the change in K_3 over the range 10^3 – 10^7 M^{-1} (range of K_a values measured for drugs **II-3** – **II-29** with **II-2**, Table II-1, y-axis) as shown in Figure II-10b. For this simulation, we fixed the total concentration of cisatracurium at 18.3 μM (Table II-1) and the concentration of Calabadion 2 at 1183 μM (64 equivalents) which is derived from our previous *in vivo* experiments which found that a dose of 80 mg kg^{-1} was effective at reversing cisatracurium. As for the case of rocuronium, we fixed K_1 = 10^5 M^{-1} and [AChR] as 18.3 μM. Figure II-10b represents the general behavior of [AChR•cisatracurium] over the full range of drug concentrations and K_3 values of potentially interfering drugs studied in this work. Similar to the case of rocuronium, there is a large plateau region where [AChR•Rocuronium] is low and

displacement of cisatracurium from the **II-2**•cisatracurium complex is not significant. The upper right side of the Figure II-10b is the region where both drug concentration and K_3 are high and where the displacement of cisatracurium from the **II-2**•cisatracurium complex is most significant. The data points corresponding to the individual concentrations and K_3 values for each drug are marked on the 3D surface of Figure II-10b as red dots. Once again, all of the drugs lie in the plateau region which indicates that they do not displace cisatracurium from the **II-2**•cisatracurium complex. Simulations using lower doses of **II-2** (32 or 16 equivalents) display higher equilibrium mole fractions of AChR•cisatracurium for drugs **II-29** and **II-23** (Appendix 1). Of course, the dramatic simplifications introduced into our model means that future *in vivo* experiments are needed to determine if drugs with high combinations of K_3 and dosage (e.g. ranitidine (**II-29**) and imipramine (**II-23**)) nearby the edge of the plateau result in displacement of **II-2**•cisatracurium in practice. In this regard, it is worth mentioning that we previously found that the *in vivo* onset and duration of action of succinylcholine (**II-27**) with its high K_3 value (2.7×10^6 M^{-1}) is unaffected by prior treatment with **II-2**.[64] Accordingly, the fact that a drug possesses a high K_3 value toward **II-2** is insufficient to conclude that undesirable displacement interactions will occur.

2.2.10 Influence of K_1.

The simulations described above assessed the influence of a range of [Drug] and K_3 values on [AChR•rocuronium] or [AChR•cisatracurium] but were

conducted at a single value of K_1 (10^5 M^{-1}) that was not drawn from experimental data, but rather based on the known *in vivo* ability of **II-2** to function as a reversal agent for rocuronium and cisatracurium. Accordingly, we thought it was important to study the influence of K_1 on the equilibrium concentration of AChR•rocuronium.

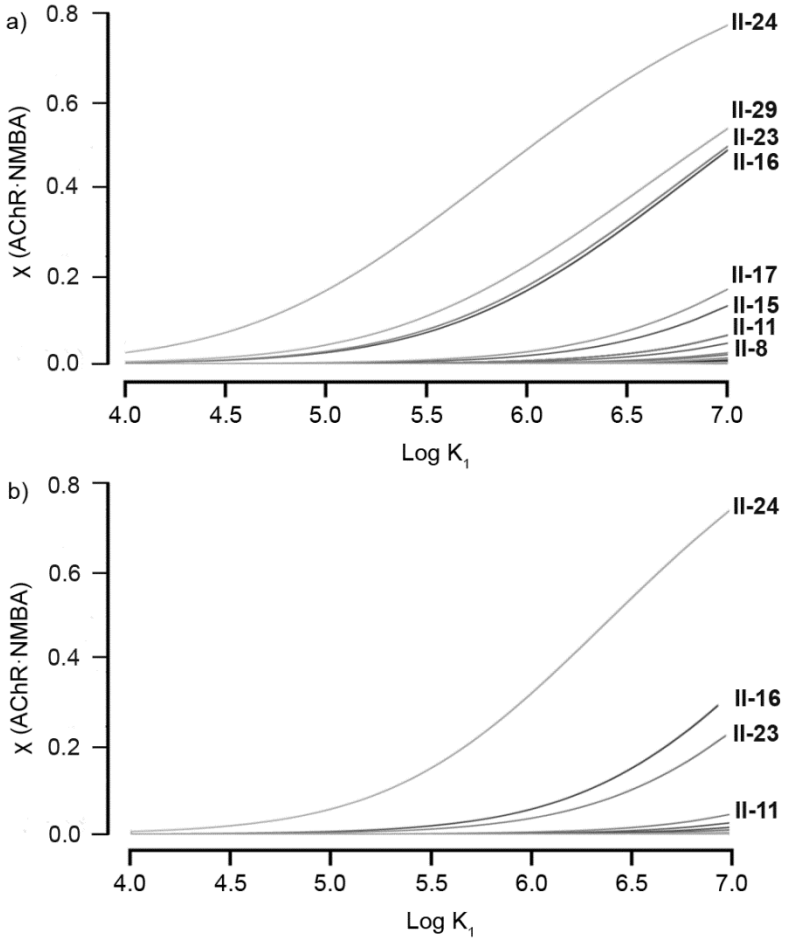

Figure II-11. Plot of the mole fraction of AChR•rocuronium versus log (K_1) for drugs **II-3** – **II-19** present at their estimated plasma concentrations from Table II-1. a) $[\textbf{II-2}]_{initial}$ = 320 μM (2-fold higher than $[Rocuronium]_{initial}$), and b) $[2]_{initial}$ = 960 μM (6-fold higher than $[Rocuronium]_{initial}$).

Figure II-11a shows the simulations performed where K_1 is scanned from 10^4 to 10^7 M^{-1} and where [**II-2**] = 320 μM, [rocuronium] = 160 μM, K_2 = 3.4 x 10^9 M^{-1}, and [drug] and K_3 are taken from Table II-1. As can be readily seen, as K_1 is increased the concentration of AChR•rocuronium increases because the difference in free energy between AChR•rocuronium and **II-2**•rocuronium decreases. At high values of K_1 the concentration of AChR•rocuronium is most significant for ranitidine (**II-29**). The reason ranitidine possesses the highest potential to displace rocuronium from **II-2**•rocuronium to form **II-2•II-29** is due not only to its relatively high binding constant (K_3 = (4.5 ± 0.7) x 10^6 M^{-1}) but also due to its high therapeutic dose (6-10 mg kg^{-1}) which served as inputs to the simulation.

Three other drugs that display significant amounts of AChR•rocuronium at high K_1 values are **II-23**, **II-17**, and **II-15** (Figure II-11a) which similarly possess a combination of moderate to large K_3 and high therapeutic dose values. Figure II-11b shows the simulation of the system when [**II-2**] is increased to 960 μM (6-fold higher than rocuronium). As can be seen, the concentration of AChR•rocuronium at equilibrium is decreased in all cases relative to Figure II-11a. However, the effect is most dramatic for compound **II-29** which has the highest K_a value but the lowest therapeutic concentrations among **II-29**, **II-23**, **II-17** and **II-15**. The excess of **II-2** therefore sequesters more significant amounts of **II-29** as its **II-2•II-29** complex than is possible for **II-23**, **II-17**, and **II-15** with their higher therapeutic concentrations. Overall, this simulation establishes that:

(1) the potential for displacement of NMBA from the **II-2**•NMBA complex is reduced by maximizing the difference between K_2 and K_1, and (2) that the use of concentrations of **II-2** at the level of the therapeutic concentration of the competing drug can be used to reduce displacement of the **II-2**•NMBA complex.

2.2.11 Influence of [AChR].

Lastly, in the simulations described above, we have somewhat arbitrarily fixed [AChR] as being equal to the concentration of NMBA. Therefore, we decided to investigate the influence of [AChR] on [AChR•rocuronium] in the presence of ranitidine ([**II-29**] = 553 μM) by performing simulations with [AChR] spanning the 1.6 μM to 16000 μM range. The other variables were fixed as follows: [rocuronium] = 160 μM, [**II-2**] = 320 μM, $K_1 = 10^5\ M^{-1}$, $K_2 = 3.4 \times 10^9\ M^{-1}$, and $K_3 = 4.5 \times 10^6\ M^{-1}$.

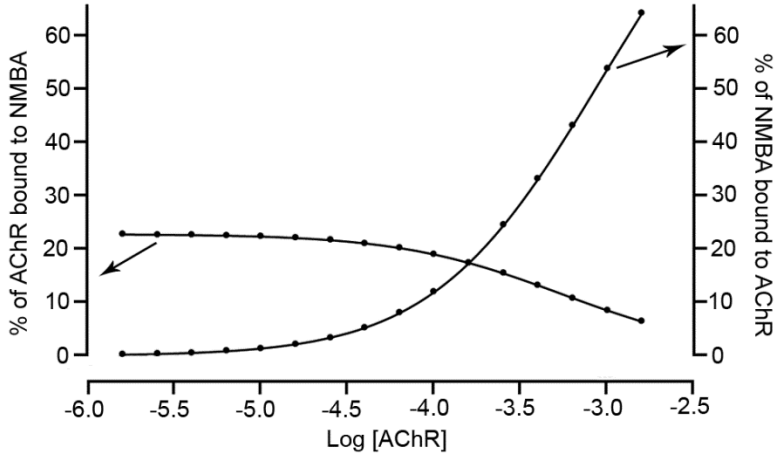

Figure II-12. Plot of mole fraction of AChR•rocuronium versus log [AChR].

Figure II-12 shows plots of the mole fraction of AChR•rocuronium relative to [AChR] (left axis) and relative to [Rocuronium] (right axis) as a function of [AChR]. These two curves cross when [AChR] = [rocuronium] = 160 μM. At low [AChR] the mole fraction of AChR•rocuronium is ≈ 5%; as [AChR] increases beyond the fixed concentration of rocuronium (160 mM) the mole fraction of AChR•rocuronium drops by necessity. Conversely, if [AChR] is high then the mole fraction of AChR•rocuronium increases because of Le Chateliers principle.

2.1.12 Summary

In summary, we measured the binding constants for the complexes between **II-2** and drugs **II-3** – **II-29** by a combination of direct ^{1}H NMR titrations, direct UV/Vis titrations, and competitive UV/Vis binding assays using the **II-2**•rhodamine 6G complex. The binding constants range from 2000 M^{-1} (for **II-3**) to 4.5 x 10^{6} M^{-1} (for **II-29**). The 1:1 stoichiometry of the complexes were confirmed by Job plots whereas the complexation induced changes in ^{1}H NMR chemical shift were used to shed light on the geometry of selected **II-2**•drug complexes. The x-ray crystal structure of the **II-2**•ranitidine complex showed: (1) the expected inclusion of the furan ring in the cavity of **II-2**, (2) the ammonium ion bound at the C=O portal, and (3) an end-to-end helical twist of the acyclic CB[n] receptor **II-2**. Simulations were performed to assess the potential for drugs **II-3** – **II-29** to displace NMBA from the **II-2**•NMBA complex resulting in the formation of AChR•NMBA complex. Global simulations reveal that drugs that

possess high values of K_3 and/or high therapeutic concentrations have the highest potential to display displacement interactions. For rocuronium and vecuronium none of the drugs display significant displacement potential although ranitidine (**II-29**) should be assessed in future *in vivo* studies. For cisatracurium, drugs **II-29** and **II-23** display both high dose and high K_3 and lie near the edge of the plateau in Figure II-10b and consequently must be closely evaluated in future *in vivo* studies. The more significant potential for displacement seen in the cisatracurium simulations can be traced to fact that K_2 for **II-2**•cisatracurium (K_2 = (4.8 ± 0.9) x 10^6 M^{-1}), is 700-fold lower than for **II-2**•rocuronium (K_2 = (3.4 ± 0.6) x 10^9 M^{-1}).

2.3 Renal Elimination of Calabadion 2 in Rats Post Reversal of Neuromuscular Blockade.

An important issue in the development of **II-2** as a reversal agent for NMBAs is establishing that it can be safely administered and gets eliminated rapidly without forming harmful metabolites. *In vivo* studies in *Swiss Webster* mice and *Sprague-Dawley* rats by the Briken and Eikermann groups respectively, have shown that **II-2** displayed low cytotoxicity in 3-(4,5-dimethylthiazol-2-yl)-5-(3-carboxymethoxyphenyl)-2-(4- sulfophenyl)-2H-tetrazolium (MTS) based cell viability and adenylate kinase release cell necrosis assays, did not inhibit the human ether-à-go-go-related channel, and was not mutagenic (Ames test). A cumulative dose of 1.6g kg^{-1} (well above the therapeutic dose needed for NMBA reversal) of **II-2** over three consecutive days (100, 500, and 1,000 mg kg^{-1})

proved to be well tolerated and nonlethal in adult male *Sprague-Dawley* rats.[48,64,95]

In the following study we describe the quantification of the urinary elimination of **II-2** and rocuronium in *Sprague-Dawley* rats after compound **II-2** was used to reverse the neuromuscular blockade induced by rocuronium and cisatracurium. Our collaborator Professor Eikermann and co-workers at Massachusetts General Hospital injected *Sprague Dawley* rats with varying doses of **II-2** to reverse rocuronium or cisatracurium induced NMB. One hour after administration of the reversal agent, all the urine was collected from the bladder of these rats, and stored at -80 °C. We designed a ^{1}H NMR based assay to get a preliminary understanding of the pharmacokinetic profile of **II-2**.

2.3.1 ^{1}H NMR Based Assay for Quantification of II-2, Rocuronium, and II-2•rocuronium complex for Rocuronium Reversal Samples.

When rocuronium binds within the cavity of **II-2** in water, the steroidal skeleton of the drug is encapsulated within the hydrophobic cavity of **II-2**. As a result of the shielding effects of the cavity, the axial steroidal methyl protons of rocuronium undergo a dramatic upfield shift in their ^{1}H NMR resonance. The signals for the methyl proton of bound rocuronium are detected at 0.23 and -0.32 ppm. Fortunately, none of the other compounds excreted in the urine of *Sprague-Dawley* rats had signals which could be observed at less than 0.8 ppm. By using a suitable internal standard (2,2,3,3-d(4)-3-(trimethylsilyl)propanoic acid sodium salt) of known concentration which also has ^{1}H NMR signal in this upfield and uncluttered region, we could quantify the rocuronium bound to **II-2** in solution.

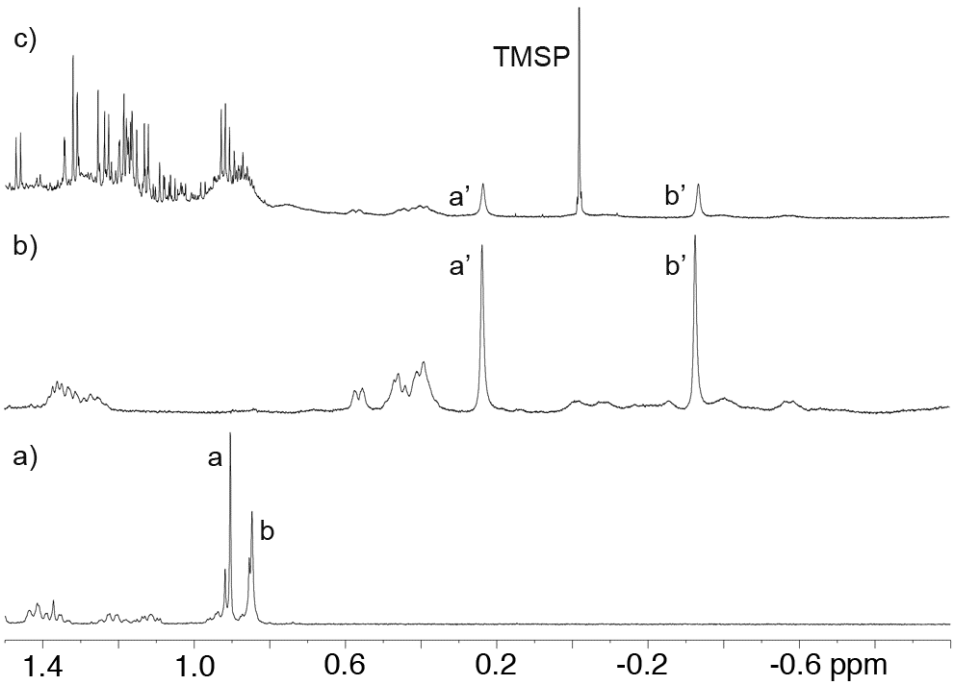

Figure II-13. ^{1}H NMR spectra (600 MHz, RT, 20 mM NaH_2PO_4 buffered D_2O, pH = 7.4) of: a) free rocuronium (2 mM) shows two resonances (a and b) for the steroidal methyl groups, b) an equimolar mixture of **II-2** and rocuronium (2 mM), a' and b' are resonances for steroidal methyl groups rocuronium bound in the **II-2**•rocuronium complex, and c) urine sample from a rat taken 1 h after reversal of rocuronium (3.5 mg kg^{-1}) with **II-2** (10 mg kg^{-1}), a' and b' are resonances for steroidal methyl groups rocuronium bound in the **II-2**•rocuronium complex.

From the urine samples of rats injected with 3.5 mg kg^{-1} of rocuronium, 0.1 mL aliquots were withdrawn and evaporated under high vacuum. The residue was dissolved in a solution containing a known concentration of 2,2,3,3-d(4)-3-(trimethylsilyl)propanoic acid sodium salt (TMSP) as internal standard

and the sample was diluted to a total volume of 0.6 mL with 20 mM phosphate buffered D_2O (pH = 7.4). The concentration of the **II-2**•rocuronium complex was determined by ^1H NMR spectroscopy (Figure II-13) by comparing the integral for diagnostic peaks of the complex (methyl groups at 0.23 ppm and -0.32 ppm, 3H each) relative to the internal standard (-0.02 ppm, 9H).

Concentrations of free **II-2** and rocuronium were measured by adding a two-fold molar excess of rocuronium or **II-2** respectively to the above mentioned solution. Addition of excess **II-2** bound any free rocuronium as the **II-2**•rocuronium complex, whereas addition of excess rocuronium bound any free **II-2** which allowed the determination of free **II-2** and free rocuronium in the original sample by using the mass balance expressions. When administered in low dosage (5 to 10 mg kg^{-1}), 62 ± 17 % (mean ± SD) of **II-2** was detected in urine. The excretion of rocuronium was proportionate to the equivalents of **II-2** administered. For samples Rocuronium1 - Rocuronium4 (Table II-2), 3.5 mg kg^{-1} rocuronium was reversed with 5 mg kg^{-1} (0.5 equivalents) of **II-2**. This resulted in the excretion of 56 ± 8 % of rocuronium in the form of the **II-2**•rocuronium complex. Whereas for samples Rocuronium5 - Rocuronium8, 3.5 mg kg^{-1} rocuronium was reversed with 10 mg kg^{-1} (1.0 equivalent) of **II-2**. This resulted in a higher percentage of rocuronium excreted- 73 ± 21 % in the form of the **II-2**•rocuronium complex. Rocuronium was eliminated in the form of the **II-2**•rocuronium complex due to the high K_a of the **II-2**•rocuronium complex ((3.4 ± 0.6) x 10^9 M^{-1}) which prevents other weaker binding substances in urine from

displacing rocuronium from its complex with **II-2**. The results are summarized in Table II-2.

2.3.2 ^{1}H NMR Based Assay for Quantification of II-2 for Cisatracurium Reversal Samples.

For the samples of rats injected with 0.6 mg kg^{-1} of cisatracurium, it was only possible to measure the total concentration of **II-2** eliminated because we could not detect any diagnostic resonances for bound or free cisatracurium. The degradation of cisatracurium via Hoffmann elimination under physiological conditions further complicates the analysis (see Appendix 1).

Table II-2. Excretion of **II-2**, NMBA, **II-2**•NMBA complex measured by ^{1}H NMR assay for rats injected with 3.5 mg kg^{-1} rocuronium or 0.6 mg kg^{-1} cisatracurium (values for cisatracurium and **II-2**•cisatracurium complex excreted were not measured, *n.m. = not measured.).

Rat I.D. (NMBA, rat number)	**II-2** Dosage (mg kg^{-1}), equivalents of NMBA	NMBA Dosage (m kg^{-1})	Urine Volume (mL)	**II-2** Excreted (%)	**II-2** Excreted (mg)	NMBA Excreted (%)	**II-2**•NMBA Complex Excreted (%)
Rocuronium1	5, 0.5	3.5	0.87	51.4	0.77	51.4	51.4
Rocuronium2	5, 0.5	3.5	0.85	46.6	0.67	46.6	46.6
Rocuronium3	5, 0.5	3.5	1.4	54.6	0.83	59.9	45.5
Rocuronium4	5, 0.5	3.5	1.08	69.2	0.96	66	53.8
Rocuronium5	10, 1.0	3.5	1.69	37.5	1.00	56.3	37.5
Rocuronium6	10, 1.0	3.5	0.52	87.4	2.30	87.4	87.4
Rocuronium7	10, 1.0	3.5	0.69	76.6	2.04	76.6	76.6
Rocuronium8	10, 1.0	3.5	0.68	90.4	2.41	90.4	90.4
Cisatracurium1	40, 32	0.6	1.32	100	10.91	n.m.*	n.m.
Cisatracurium2	60, 48	0.6	0.64	34.2	5.42	n.m.	n.m.
Cisatracurium3	60, 48	0.6	0.71	10.7	1.68	n.m.	n.m.
Cisatracurium4	60, 48	0.6	0.75	76.9	13.80	n.m.	n.m.
Cisatracurium5	80, 64	0.6	0.87	27.6	5.65	n.m.	n.m.
Cisatracurium6	80, 64	0.6	0.69	60.5	13.31	n.m.	n.m.
Cisatracurium7	80, 64	0.6	0.94	35.5	8.14	n.m.	n.m.
Cisatracurium8	80, 64	0.6	1.08	0	0	n.m.	n.m.

The total amounts of **II-2** eliminated in the samples from rats treated with cisatracurium were obtained using the analytical technique described in section 2.2.1 This assay relies on the addition of an excess of rocuronium to form a tight **II-2**•rocuronium complex which displays diagnostic resonances in the ^{1}H NMR spectrum (Figure II-13). When administered in moderate doses (40 to 80 mg kg^{-1}), 49 ± 31% (mean ± SD) of the **II-2** was detected in the urine samples. The results are summarised in Table II-2.

2.3.3 Summary.

In summary, we designed a ^{1}H NMR based assay for the quantification of **II-2** eliminated in the urine of *Sprague-Dawley* rats, taking advantage of the diagnostic steroidal methyl peaks of rocuronium which shift dramatically upfield when bound in the cavity of **II-2**. We used this property to measure the amount **II-2** excreted when administered at low doses (5-10 mg kg^{-1}) for the reversal of rocuronium as 62 ± 17%. We were also able to measure the amounts of free and bound rocuronium excreted by this assay and found that most of the rocuronium is excreted as its complex with **II-2**. When 0.5 equivalent of **II-2** is used to reverse rocuronium, 56 ± 8 % of rocuronium is excreted and when 1.0 equivalent of **II-2** is used for the reversal of rocuronium 73 ± 21 % of rocuronium is excreted. For samples in which cisatracurium was reversed with moderate dosages of **II-2** (40-80 mg kg^{-1}), 49 ± 31% of **II-2** was detected in the urine samples.

2.4 Conclusions.

In conclusion, we have established that **II-2** displays good to high levels of selectivity toward the NMBAs rocuronium, vecuronium, and cisatracurium both *in vitro* and in simulations designed to capture the essence of the biological system. The studies serve as a guide that allows us to prioritize the investigation of the efficacy of **II-2** as a reversal agent for neuromuscular block when other drugs (e.g. **II-3** – **II-29**) have already been or need to be subsequently administered.

By studying the excretion profile of **II-2** after NMBA reversal in *Sprague-Dawley* rats, we have established that more than 50% of **II-2** (and rocuronium) is eliminated intact by the kidney within 1 hour of reversal administration.

Taken together, the results of the selectivity studies and pharmacodynamic studies serve to establish the high potential for the further development of Calabadion 2 (**II-2**) as a broad spectrum reversal agent for both amino-steroidal as well as benzylisoquinolinium type NMBAs.

Chapter 3: Molecular Containers as Reversal Agents for Drugs of Abuse

The work presented in this chapter was taken from Ganapati, S.; Grabitz, S. D.; Murkli, S.; Scheffenbichler, F.; Rudolph, M. I.; Zavalij, P. Y.; Eikermann, M.; Isaacs, L., Molecular Containers Bind Drugs of Abuse in Vitro and Reverse the Hyperlocomotive Effect of Methamphetamine in Rats. *Chembiochem* **2017**, In press: http://dx.doi.org/10.1002/cbic.201700289. All experiments discussed in this chapter were carried out by me except the *in vivo* studies presented in section 3.2.5, which were carried out by Professor Eikermann and his students.

3.1 Introduction.

The recreational use and abuse of illicit drugs is a major societal and healthcare issue worldwide.[66]The cost of emergency department visits due to drug overdose runs into billions of dollars per annum.[68]Many patients do not survive drug-overdose.

Current treatment strategies in the clinic include pharmacodynamic (PD) approaches for opioid overdose using drugs such as naloxone and naltrexone which block the effect of opioids at their biological receptors.[69] For non-opioid drugs such as cocaine and methamphetamine, the clinical treatment strategies involve treating the adverse effects of overdose (such as elevated heart rate, hyperthermia, psychosis, etc.) rather than disrupting the effect of the drug itself.[71] Research efforts have been underway to develop pharmacokinetic (PK) strategies such as immunotherapeutics[81] and enzyme based therapeutics[74] which would

lower the concentration of the illicit drug at its receptors and thus prevent or reverse its biological effects. The key advantage of the PK approach over the PD approach is that it does not require a detailed understanding of the interaction of the drug with its biological receptor(s).

The PK strategy has also been implemented using synthetic molecular container compounds to directly compete with biological molecular recognition events. For example, Sugammadex which is a γ-cyclodextrin derivative that is marketed worldwide by Merck under the trade name Bridion™ acts as a reversal agent for NMBAs such as rocuronium and vecuronium by sequestering them *in vivo*.[54]

In the studies reported in this chapter we have investigated the potential use of different classes of molecular containers such as cyclodextrins, CB[n], and calixarenes as reversal agents for opioid and non-opioid drugs of abuse. We started by investigating which class of molecular hosts would serve as good lead compounds for structural optimization for this application, based on the *in vitro* binding affinity measurements (section 3.2). This was followed by *in vivo* studies of methamphetamine reversal by molecular host **III-2** guided by the *in vitro* binding data (section 3.2.5), and finally pharmacokinetic studies for the renal elimination of **III-1** and **III-7** post reversal of fentanyl in *Sprague-Dawley* rats.

3.2 Molecular Containers Bind Drugs of Abuse *in Vitro* and Reverse the Hyperlocomotive Effect of Methamphetamine in Rats.

We chose to screen the affinity of the five molecular containers (Calabadion 1 and 2, CB[7], **III-4**, and HP-β-CD) toward a panel of drugs of abuse (**III-6** – **III-12**) in order to inform and prioritize subsequent *in vivo* work. The molecular containers used in this study were selected for several reasons. First, all of these classes of containers are known to bind to hydrophobic cations (e.g. for sensing, drug delivery, and reversal applications)[54 ,96] which is a common structural element in drugs **III-6** – **III-12**. Second, these molecular containers possess good levels of aqueous solubility (≥ 10 mM) which is required for efficient formulation. Third, all of these containers are easily synthesized on large scale by efficient procedures which make them viable scaffolds for further medicinal chemical optimization.

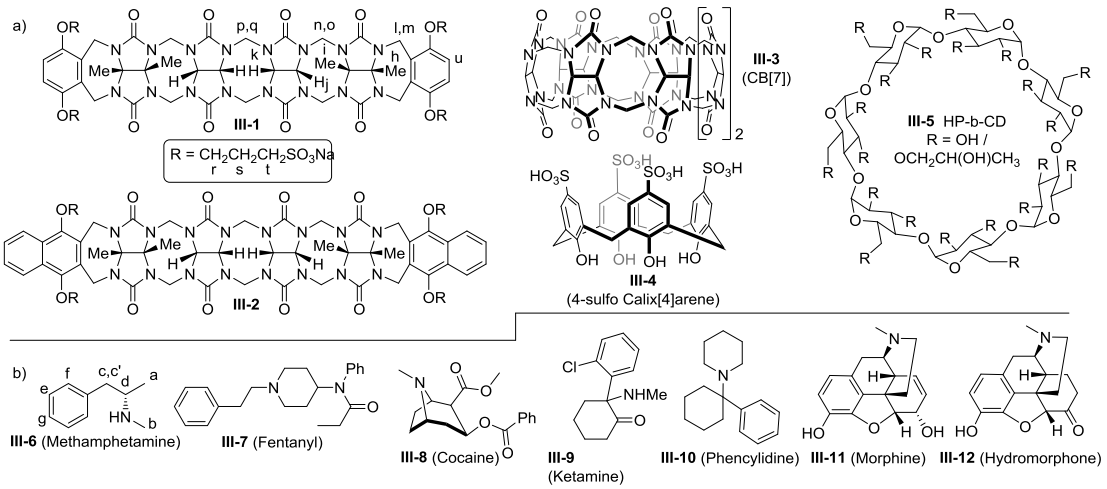

Figure III-1. Chemical structures of: a) molecular containers, and b) drugs of abuse used in this study.

Finally, all of these containers display good biocompatibility (*in vitro* and *in vivo*) and one (HP-β-CD) has even been used to formulate drugs administered to humans (e.g. Janssen's formulation of Itraconazole (Sporonox^{TM}). The disparate molecular structures of the five containers will result in different binding modes and types of interactions (ion-dipole, ion-ion, hydrophobic, π–π, etc.) between container and drug; an important goal of our study was to determine which class of molecular containers serves as the best lead scaffold for further medicinal chemistry optimization in the future. In particular, the use of molecular containers to treat intoxication with drugs of abuse – as opposed to addiction where long circulation times would be needed – seems most promising. The drug panel includes stimulants (**III-6**, **III-8**), hallucinogens (**III-9**, **III-10**), and prescription-type psychotherapeutics used for pain relief (**III-7**, **III-11**, **III-12**). All these drugs contain the amino functional group which is protonated at physiological pH.

3.2.1 Qualitative Binding Study of Containers III-1 – III-5 toward Drugs of Abuse by ^{1}H NMR Spectroscopy.

For containers **III-1** – **III-4** whose cavity constitutes an NMR shielding region we typically observe upfield shifts in the ^{1}H NMR resonances of included drugs **III-6** – **III-12**, although the kinetics of exchange is generally fast on the chemical shift timescale (Appendix 2) for **III-1** – **III-4**. For example, Figure III-1a-d shows the ^{1}H NMR spectra recorded for methamphetamine (**III-6**), Calabadion 1, a 1:1 mixture of **III-1** and **III-6**, and a 1:2 mixture of **III-1** and **III-6**.

The ^{1}H NMR resonances for the aromatic ring of **III-6** (H_e – H_g) shift significantly upfield within **III-1•III-6** (Figure III-1c) and appear as sharp resonances at 1:1 stoichiometry. When 2 equivalents of **III-6** are present (Figure III-1d) the resonances for H_e – H_g shift back toward the chemical shifts the resonances for H_e – H_g shift back toward the chemical shifts for free **III-6** due to the fast kinetics of guest exchange on the chemical shift timescale.

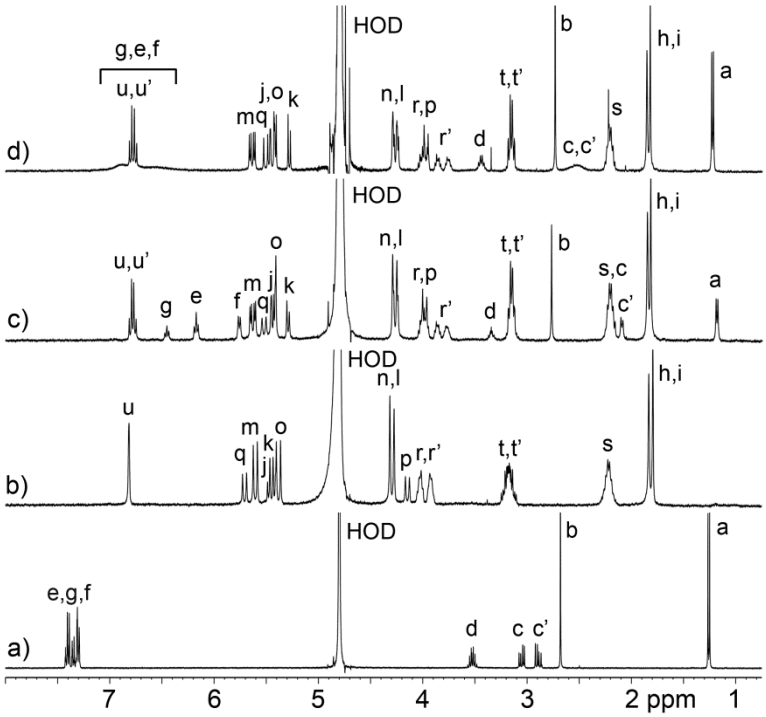

Figure III-2. ^{1}H NMR spectra recorded (400 MHz, RT, 20 mM sodium phosphate buffered D_2O, pH 7.4) for: a) **III-6** (2 mM), b) **III-1** (1 mM), c) a mixture of **III-6** (1 mM) and **III-1** (1 mM), and d) a mixture of **III-6** (2 mM) and **III-1** (1 mM).

The resonances for the aromatic wall of **III-1** (H_u) appear as a pair of doublets due to the chiral nature of the guest which renders these protons

diastereotopic (u, u') in the complex. For HP-β-CD, ^{1}H NMR was not a useful analytical tool because only very minor changes in guest chemical shift are typically observed upon HP-β-CD•guest binding.

3.2.2 Stoichiometry and X-ray Crystal Structures of the Drug•Container Complexes.

The 1:1 nature of the various host•guest complexes was established by either Job plots (Appendix 2), x-ray crystallography, ^{1}H NMR, isothermal titration calorimetry (ITC), or literature precedent. We were fortunate to obtain single crystals of CB[7]•**III-6** and **III-1**•**III-6** that were suitable for structure determination by x-ray crystallography.[17]X Figure III-2 shows stereoscopic representations of individual structures of the CB[7]•**III-6** and **III-1**•**III-6** complexes in the crystal.

In accord with the NMR studies, the aromatic ring of **III-6** is bound within the cavity of **III-1** featuring π−π stacking (Figure III-2a). The ammonium ion is H-bonded to one of the ureidyl C=O groups (H•••O=C, 2.093 Å; N-H•••O angle, 140.0°) and also benefits from ion-dipole interactions with the carbonyl portal. The C-shaped backbone of **III-1** undergoes a helical distortion within the **III-1**•**III-6** complex as observed previously with different guests.[40,43,44,46]

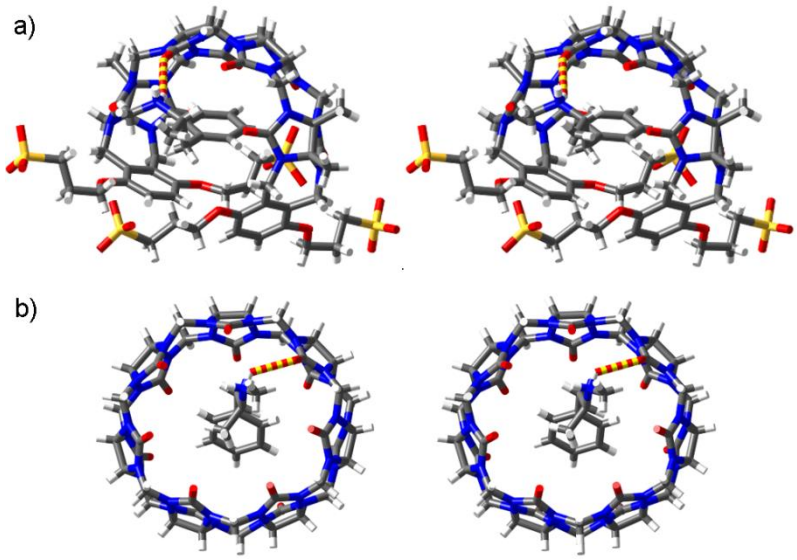

Figure III-3. Cross-eyed stereoviews of individual complexes of: a) **1•6**, and b) CB[7]•**6** in the crystal. Color code: C, grey; H, white; N, blue; O, red; S, yellow; H-bond, red-yellow striped.

The crystal structure of CB[7]•**III-6** (Figure III-2b) also shows a deep penetration of the aromatic ring of **III-6** into the cavity of CB[7] along with ion-dipole and H-bonding interactions at the ureidyl C=O portal. Interestingly, four CB[7]•methamphetamine complexes pack into a square in the crystal driven by interactions between the C-H groups on the convex face of CB[7] and the C=O portal on an adjacent CB[7].

3.2.3 Measurement of K_as between Containers III-1 – III-5 and Drugs of Abuse III-6 – III-12.

After having qualitatively investigated the binding between **III-1** – **III-5** and **III-6** – **III-12** by ^{1}H NMR and confirming the binding mode for **III-6** toward

CB[7] and **III-1** by x-ray crystallography we set out to measure the K_a values of the various complexes initially using NMR and UV/Vis methods and later incorporating isothermal titration calorimetry (ITC) when this instrument became available to us in the later stages of our study. For this purpose, we employed various binding assays as appropriate. For example, for the weaker complexes (K_a < 5000 M^{-1}) formed between hosts **III-3** and **III-4** whose cavities constitute NMR shielding regions and drugs **III-6** and **III-8** – **III-11** we used direct ^{1}H NMR titrations of guest with host and fitted the change in chemical shift to a standard 1:1 binding model (Table III-1, Appendix 2). Based on our extensive experience measuring CB[n]•guest binding constants, we chose a ^{1}H NMR competition assay[18,90,20] to determine K_a = 1.2 x 10^8 M^{-1} for CB[7]•methamphetamine. For stronger complexes involving **III-1** and **III-2** we employed UV/Vis competition assays developed by us previously.[39] For this purpose, we form the **III-1**•rhodamine 6G or **III-2**•rhodamine 6G complexes which show different UV/Vis spectra than free rhodamine 6G and then titrate those complexes with drug which induces the reverse UV/Vis change. Based on a knowledge of the total concentrations of container, rhodamine 6G and the **III-1**•rhodamine 6G and **III-2**•rhodamine 6G binding constants we fitted the change in UV/Vis absorbance versus [drug] to a competition binding model[39] to extract the unknown container•drug complex K_a value (Table III-1). For example, Figure III-3a shows the UV/Vis spectra recorded when a solution of **III-2** (4.97 μM) and rhodamine 6G (4.97 μM) was titrated with a solution of methamphetamine (0 – 219 μM)

whereas Figure III-3b shows the fitting of the data to the competition binding model to extract $K_a = 4.3 \times 10^6\ M^{-1}$ for **III-2**•methamphetamine.

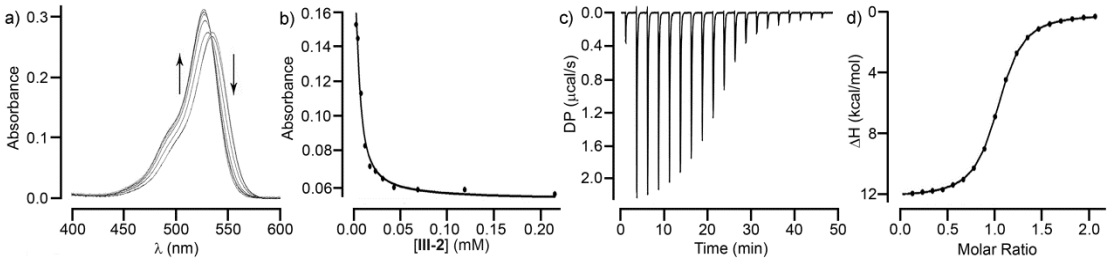

Figure III-4. a) UV/Vis spectra recorded during the titration of a mixture of **III-2** (4.97 μM) and rhodamine 6G (4.97 μM) with methamphetamine (6, 0 – 219 μM) in 20 mM NaH_2PO_4 buffered water (pH 7.4). b) Plot of absorbance versus [2] fitted to a competitive binding model with $K_a = (4.3 \pm 1.0) \times 10^6\ M^{-1}$. c) ITC thermogram recorded during the titration of **III-2** (87 μM) in the cell with hydromorphone (0.93 mM) in the syringe. d) Fitting of the data to a 1:1 binding model with $K_a = (6.8 \pm 0.1) \times 10^5\ M^{-1}$.

The remaining complexes – mainly HP-β-CD•drug but also container•fentanyl and container•hydromorphone – were measured by ITC when the instrumentation became available in the lab (Table III-1, Appendix 2). For example, Figure III-3c,d shows the thermogram recorded for the titration of **III-2** (87 μM) with hydromorphone **III-12** (0 – 200 μM) which was fitted with the MicroCal PEAQ-ITC analysis software to deliver $K_a = (6.8 \pm 0.1) \times 10^5\ M^{-1}$ and $\Delta H = -2.1 \pm 0.3$ kcal mol^{-1} for the **III-2•III-12** complex.

Table III-1. Binding constants (K_a, M^{-1}) determined for the various container•drug complexes.

Guest	**III-1**	**III-2**	**III-3**	**III-4**	**III-5**
III-6	$(7.5 \pm 2.9) \times 10^{6}$ a)	$(4.3 \pm 1.0) \times 10^{6}$ a)	1.2×10^{8} c)	$(3.8 \pm 0.6) \times 10^{4}$ b)	$(1.9 \pm 0.3) \times 10^{2}$ d)
III-7	$(1.1 \pm 0.04) \times 10^{7}$ d)	$(7.6 \pm 0.5) \times 10^{6}$ d)	$(1.8 \pm 0.1) \times 10^{7}$d)	$(1.1 \pm 0.1) \times 10^{4}$ d)	$(3.0 \pm 0.5) \times 10^{3}$ d)
III-8	$(6.6 \pm 0.4) \times 10^{5}$ a)	$(1.0 \pm 0.1) \times 10^{6}$ a)	$(2.3 \pm 0.2) \times 10^{3}$ b)	$(4.3 \pm 1.5) \times 10^{4}$ b)	$(1.7 \pm 0.3) \times 10^{2}$ d)
III-9	$(1.1 \pm 0.1) \times 10^{4}$ a),e)	$(2.1 \pm 0.1) \times 10^{5}$ a),e)	$(6.4 \pm 1.2) \times 10^{2}$ b)	$(2.0 \pm 0.2) \times 10^{4}$ d)	$(1.1 \pm 0.2) \times 10^{2}$ d)
III-10	$(4.7 \pm 0.5) \times 10^{4}$ a)	$(2.1 \pm 0.1) \times 10^{5}$ a)	$(4.4 \pm 0.9) \times 10^{3}$ b)	$(4.5 \pm 0.3) \times 10^{4}$ d)	$(1.0 \pm 0.03) \times 10^{3}$ d)
III-11	$(5.3 \pm 0.3) \times 10^{5}$ a)	$(5.3 \pm 0.4) \times 10^{5}$ a),f)	n.b.	$(4.9 \pm 0.3) \times 10^{4}$ b)	n.b.
III-12	$(1.8 \pm 0.03) \times 10^{5}$ d)	$(6.8 \pm 0.1) \times 10^{5}$ d)	n.b.	$(1.0 \pm 0.04) \times 10^{4}$ d)	$(2.8 \pm 0.5) \times 10^{2}$ d)

a) Measured by UV/Vis competition assay. b) Measured by direct ^{1}H NMR titration. c) Measured by ^{1}H NMR competition assay. d) Measured by ITC. n.b. – no binding detected by ITC. e) Reference.[95] f) Reference.[97]

The other ITC derived thermodynamic parameters given in Table III-1 were carried out analogously. Previously, we have shown that the results of UV/Vis competition assays and direct ITC titrations involving Calabadions 1 and 2 and guests give comparable values which gives us confidence in comparisons between K_a values measured by the different techniques.[97]

3.2.4 Commentary on the Tabulated K_a Values.

An examination of the K_a values given in Table III-1 reveals that they span a wide dynamic range from no binding to over 10^8 M^{-1}. HP-β-CD, which is well known as a promiscuous and low affinity host, unsurprisingly displays modest K_a values in the $0 – 10^3$ M^{-1} range. The lack of charge complementarity

between neutral HP-β-CD and cationic drugs as well as the absence of typical high affinity binding epitopes (e.g. adamantyl residue) on the drugs is presumably responsible for the weaker binding. In contrast, the tetraanionic calix[4]arene derivative **III-4** displays larger K_a values but they cluster in the narrow range of $1.0 \times 10^4 - 4.9 \times 10^4$ M^{-1}. The lack of selectivity in this case may be due to the relative importance of the electrostatic contributions to the binding free energy. Most interesting, and encouraging as lead compounds for the further development of reversal agents for *in vivo* intoxication with drugs of abuse, are the three CB[n]-type molecular containers Calabadion 1 and 2 and CB[7]. These three containers bind to selected drugs of abuse with K_a values that fall in the $10^4 - 10^8$ M^{-1} range. Given the presence of phenethylammonium binding epitopes it is not surprising that CB[7] displays high affinity toward both methamphetamine ($K_a = 1.2 \times 10^8$ M^{-1}) and fentanyl ($K_a = 1.8 \times 10^7$ M^{-1}). Furthermore, CB[7] discriminates against the more sterically encumbered drugs ($K_a < 4400$ M^{-1}) due to unfavorable steric interactions in the CB[7]•guest complexes. In contrast, the acyclic CB[n]-type containers Calabadion 1 and Calabadion 2 have a more flexible cavity which can flex to accommodate a range of guest sizes and display both good levels of affinity (K_a from $10^4 - 10^7$ M^{-1}) and some selectivity toward the panel of drugs of abuse. The complexes between the tetraanionic Calabadions and cationic drugs benefit from electrostatic interactions and π–π interactions between guest aromatic rings and host aromatic walls. Similar to CB[7], Calabadion 1 and Calabadion 2 display highest affinity toward methamphetamine and fentanyl with K_a values in the $10^6 - 10^7$ M^{-1} range. Among Calabadions 1 and

2 and CB[7], CB[7] displays the highest levels of affinity and selectivity toward the drugs of abuse panel. However, the affinity and selectivity of **III-1** and **III-2** seen herein and also documented in the context of neuromuscular block reversal,[97] is substantial and suggests that **III-1** and **III-2** could serve as core scaffolds for further structural optimization. We are mindful of the fact that metabolites of amino acids, especially phenylalanine, will likely display similar binding affinity toward Calabadion 2 as methamphetamine does which could compromise *in vivo* efficacy. Accordingly, and given the fact that Calabadion•guest complexes are eliminated in the urine over several hours,[63,64] we do not envision the use of Calabadion 2 for long term treatment of methamphetamine addiction. However, such consideration of circulation time and discrimination against related metabolites are less relevant in the context of treatment of drug overdose and intoxication where dose can simply be adjusted to prevent mortality.

3.2.5 In Vivo Reversal of Methamphetamine by Calabadion 2.

Accordingly, we decided to test the ability of an acyclic CB[n]-type receptor and unfunctionalized CB[7] as an *in vivo* reversal agent for methamphetamine intoxication. We choose Calabadion 2 as the acyclic CB[n] test compound because of its documented high biocompatibility (e.g. low *in vitro* cytotoxicity, high in vivo maximum tolerated dose, passed Ames test, no hERG ion channel inhibition)[95] and because of its generally higher binding affinity toward its guests.[48,44] With the help of our collaborators Eikermann and co-workers, we set out to determine whether the high *in vitro* binding affinities of

Calabadion 2 and CB[7] toward methamphetamine could prevent or reverse its *in vivo* biological effects. For this assay, Eikermann and co-workers took advantage of the known increase of locomotor activity (e.g. movement) of rats upon treatment with methamphetamine.[98] A total of 21 male *Sprague-Dawley* rats (weight, mean ± SD: 288 ± 14 g) were tested repeatedly in a randomized controlled crossover setting. A single bolus of methamphetamine (0.3 mg kg^{-1}) or placebo was injected intravenously via a tail vein catheter to assess baseline locomotor activity. Two types of studies were performed. In the treatment studies, Calabadion 2 (65 or 130 mg kg^{-1}) or CB[7] (45 or 90 mg kg^{-1}) was administered 30 seconds after methamphetamine whereas in the prevention studies, rats were pretreated with Calabadion 2 (Figure III-5) 30 seconds before methamphetamine treatment via tail vein catheter. The catheter was flushed with 1 mL normal saline in between injections to ensure that methamphetamine was not simply complexed by Calabadion 2 inside the catheter. The animals were placed in the center of a 100 x 100 x 40 cm open field and their locomotor activity was video recorded for 20 minutes. The location of the rat and the total distance traveled was analyzed using the ANYmaze (version 4.5, Stoelting, Wood Dale, IL, USA) software. Values are given in percent of the placebo + methamphetamine activity level and reported as mean ± standard error of the mean. As expected, the rats only treated with placebo in addition to methamphetamine exhibit enhanced levels of locomotor activity relative to their baseline: (n = 21; 26.5 ± 4.9) m vs. (5.8 ± 1.5) m; $p<0.001$. Encouragingly, the preventive use of Calabadion 2 (65 or 130 mg kg-1) significantly decreased the traveled distance by (64.1 ± 8.4)% (p=0.001) and

(74.4 ± 3.8)% ($p<0.001$), respectively, compared to placebo + methamphetamine (Figure III-5a).

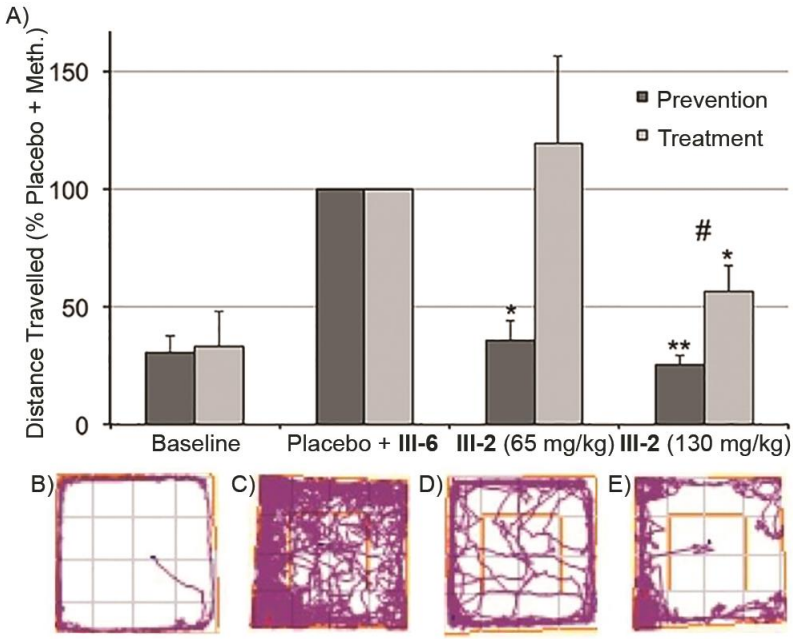

Figure III-5. Results from behavioral tests in the open field. a) Bar graph showing distance traveled in percent of the placebo + methamphetamine activity level within 20 minutes; error bars represent the standard error of the mean. *$p<0.01$ compared to methamphetamine + placebo. **$p<0.001$ compared to methamphetamine + placebo. #interaction term indication × Calabadion 2 dose: $p<0.001$, indicating effect modification by time of administration of Calabadion 2. Tracking plots illustrating the traveled distance of one rat within 20 minutes in the open field: b) Baseline, no methamphetamine given, c) following methamphetamine (0.3 mg kg^{-1}) + placebo, d) following methamphetamine (0.3 mg kg^{-1}) + Calabadion 2 (65 mg kg^{-1}), and e) following methamphetamine (0.3 mg kg^{-1}) + Calabadion 2 (130 mg kg^{-1}).

Similarly, the treatment study with Calabadion 2 (130 mg kg^{-1}) significantly decreased the traveled distance by (43.8 ± 11.2)% compared to placebo + methamphetamine (p=0.004), whereas no significant reduction of methamphetamine induced hyperlocomotion was observed when treated with 65 mg kg-1 of 2 (p=0.625). As a control, it was determined that a bolus of Calabadion 2 alone (130 mg kg^{-1}) without methamphetamine did not affect the locomotion compared to baseline (33.5 ± 17.7% vs. 32.9 ± 15.0%; p = 0.982). A smaller dose of Calabadion 2 was required in a prevention setting compared to a treatment setting to reverse methamphetamine-induced hyperlocomotion (interaction effect of indication × Calabadion 2 dose for locomotor activity: p<0.001), indicating effect modification. In our previous studies of the use of Calabadion 1 and 2 to reverse neuromuscular block, we found that the majority of the drug was eliminated in the urine of the rats as the non-metabolized Calabadion•drug complex within two hours.[63,64,95]

We posit that Calabadion 2 functions in a similar way to modulate the hyperlocomotive effect induced by methamphetamine described herein. The substantially higher doses of Calabadion 2 required for methamphetamine reversal than for neuromuscular block reversal likely reflects the tighter binding of methamphetamine to its biological targets and/or kinetic issues of intravenous sequestration of methamphetamine once it has crossed the blood-brain barrier. We expect that the Calabadion framework will enable a medicinal chemistry structural optimization to enhance both binding affinity and selectivity. In

contrast, treatment with CB[7] (45 mg kg^{-1} or 90 mg kg^{-1}) did not affect the distance traveled compared to placebo + methamphetamine: (87.0 ± 42.6)%, p=0.773 and (119.5 ± 55.4)%, p=0.739, respectively). As a control, it was verified that injection of CB[7] alone had no significant effect on locomotion compared to baseline (19.3 ± 6.0% vs. 21.6 ± 6.9%; p =0.546).

3.2.6 Summary.

In summary, we have screened the binding affinity of molecular containers III-1 – III-5 toward seven drugs of abuse by a combination of direct and competitive ^{1}H NMR, UV/Vis, and ITC binding assays. The structures of the III-1•methamphetamine and CB[7]•methamphetamine complexes were solved by single crystal x-ray diffraction. Calabadion 1 and Calabadion 2, in particular, display very good levels of affinity across the full range of drugs and display highest affinity toward methamphetamine and fentanyl. We find that the hyperlocomotive activity of rats given methamphetamine could be both prevented and treated by Calabadion 2 (65 or 130 mg kg^{-1}). The documented biocompatibility of the Calabadions[40,95,99] and their convergent building block synthesis[44] suggest fruitful pathways toward their further structural optimization for development as reversal agents for intoxication with non-opioid drugs of abuse for which no treatments are currently available.

3.3 Renal Elimination of Calabadion 1 and Fentanyl in Rats Post Reversal Application.

In order to gain insight into the *in vivo* reversal capability and pharmacokinetic profiles of the drugs of abuse and Calabadion type reversal agents studied in section 3.2, our collaborator Professor Eikermann and co-workers are performing *in vivo* reversal studies for the most promising drug container•complexes using the K_as in Table III-1 as a guide.[100] Fentanyl (**III-7**) is a potent surgical anesthetic as well as a recreationally abused opioid drug.[76] The **III-7•III-1** complex has a K_a of (1.1 ± 0.04) x 10^7 M^{-1} and is one of the tightest complexes determined in this work.[100] Accordingly, the Eikermann group treated two groups of 6 male *Sprague-Dawely* rats with an infusion of **III-7** (0.83 μg kg^{-1} min^{-1} over 15 minutes), followed by a bolus dose of placebo (saline) or test reversal agent (**III-1**, 50 mg kg^{-1}). One hour after placebo or reversal agent administration, bladder surgeries were performed; the urine was collected, and subsequently was analyzed by us. The quantification of **III-7** was achieved with an HPLC based assay[99] and that of **III-1** was done by ^{1}H NMR.[63,64]

3.3.1 Fentanyl Calibration Curve.

The dosage of **III-7** used for the two rat groups was too low (12.5 μg kg^{-1}) to be detected by ^{1}H NMR. Therefore a more sensitive HPLC based assay for measuring the μM concentrations of **III-7** in the urine was designed. Based on the literature precedent for the pharmacokinetics of intravenously administered **III-7** in rat muscle and plasma[101] and a further 10-20% loss expected due to metabolism

of **III-7** being eliminated in urine, [102] we estimated that about 24-34 % of **III-7** should be excreted unmetabolized. We modified an assay previously published by the Isaacs group for the detection of albendazole and its metabolites in mouse plasma by HPLC[99] to obtain a calibration curve for fentanyl.

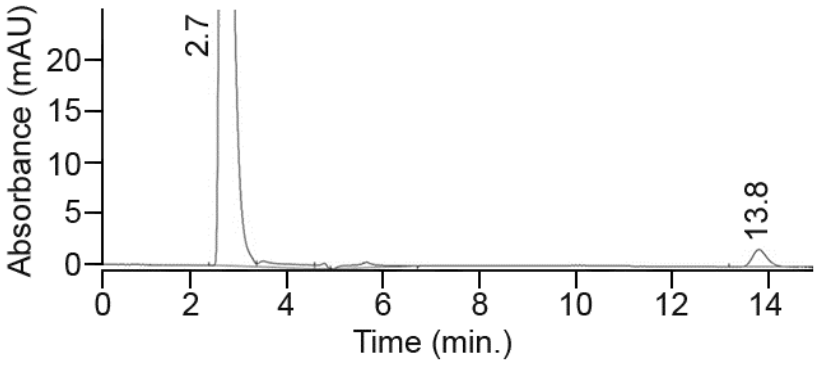

Figure III-6. HPLC spectrum of a standard solution of **III-7** (14 μM) showing a retention time of 13.8 minutes for III-7 at 229 nm. The peak at 2.7 minutes is from trimethylamine in the buffer.

For this purpose, a 13.13 mM stock solution of **III-7** was prepared by dissolving 11.8 mg **III-7** in 1.7 mL HPLC grade water. This stock solution was diluted, evaporated, and reconstituted in the HPLC mobile phase (1.3% v/v trimethylamine in 60% water, 27% methanol, 13% acetonitrile) to obtain solutions with a concentration range of 5.7 μM – 19 μM. These solutions were injected (20 μl injection volume) onto a Microsorb-MV 100-5 C18 column (5 μm, 250 × 4.6 mm) and the area under the peak at 13 – 14 min. was plotted against the gravimetric concentrations to obtain a linear calibration curve ($R^2 = 0.99$).

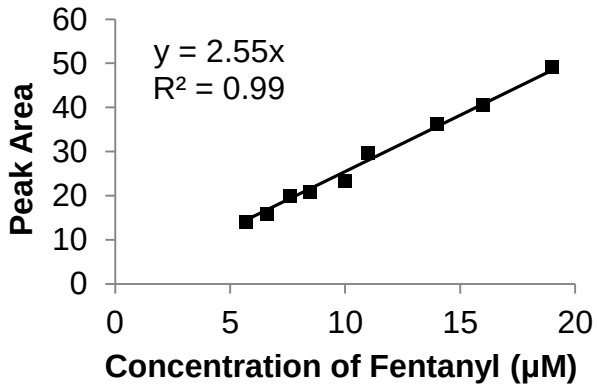

Figure III-7. Calibration curve for fentanyl using working standard solutions.

3.3.2 Fentanyl Excreted by Rats Injected with Fentanyl and Placebo.

For the urine samples of rats injected with fentanyl and placebo (saline), we expected about 24-34 % of **III-7** to be excreted. Accordingly, the samples with Rat I.D. 1, 2, 3, 7, 8, and 9 were analyzed by HPLC. A measured volume of urine sample from these rats was evaporated under high vacuum. These samples were reconstituted in a smaller volume of mobile phase in order to make the concentrations of **III-7** higher than the detection limit of our protocol. The concentrated samples were injected (20 μL) and the fentanyl peak was observed at 14 - 15 minutes. Since the retention time for fentanyl fluctuated by ± 1 minute between samples, and there were other peaks from substances present in the urine sample adjacent to the fentanyl peak, we needed to confirm the identity of the fentanyl peak. For this purpose, we ran each sample two times. First we obtained a spectrum of the original sample, followed by injecting the same sample spiked with a 2-fold excess of fentanyl. Based on comparing the retention time and position of the peak whose area increased by 2–fold in the second run to the

corresponding peak in the first run, we were able to confidently identify the fentanyl peak in the first run and distinguish it from the other substances present in the urine sample. The area of this fentanyl peak was used to calculate the corresponding gravimetric concentration of fentanyl using the calibration curve in Figure III-7.

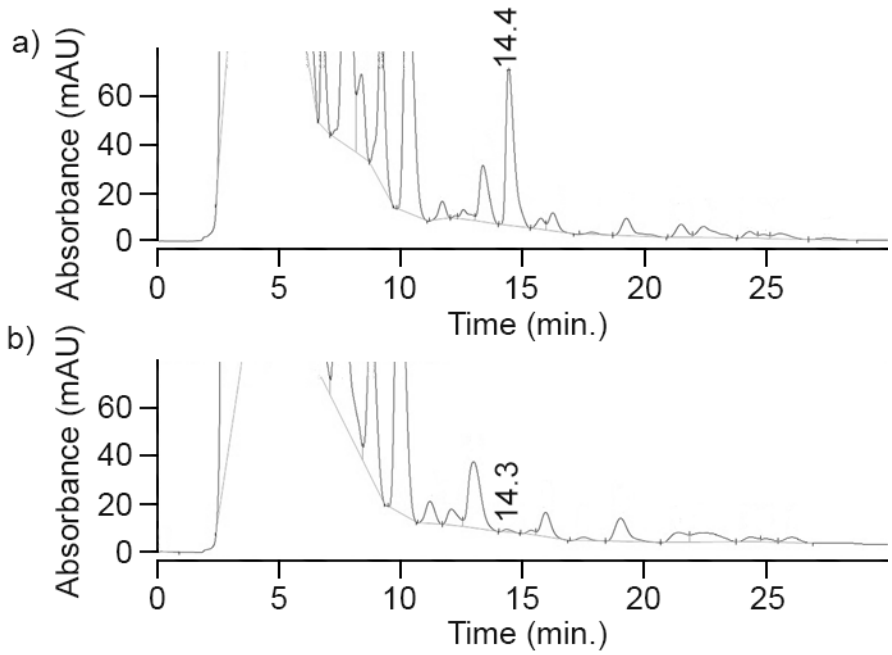

Figure III-8. HPLC spectra of: a) blank urine spiked with fentanyl, and b) one of the representative urine sample following the fentanyl injection to rat. The fentanyl peak can be seen at 14.4 and 14.3 minutes respectively.

The concentration of **III-7** in urine and the urine volume were used to calculate the weight and the weight percentage of **III-7** excreted. The average percent excretion of **III-7** in rats injected with **III-7** + placebo was (17 ± 9) %, the results are summarized in Table III-2.

Table III-2. Excretion of **III-7** and **III-1** measured by HPLC and ^{1}H NMR assays for rats injected with 12.5 μg kg^{-1} **III-7** (0.83 μg kg^{-1} min^{-1} infusion over 15 minutes) and placebo or 50 mg kg^{-1} **III-1** (bolus).

Rat I.D.	Rat Wt. (kg)	**III-7** Injected (μg)	**III-1** Injected (mg)	Urine Volume (mL)	**III-7** Excreted (μg)	**III-7** Excreted (%)	**III-1** Excreted (mg)	**III-1** Excreted (%)
1	0.357	4.46	0	0.344	0.225	5.1	-	-
2	0.342	4.27	0	0.470	0.199	4.7	-	-
3	0.361	4.15	0	0.527	0.759	18.3	-	-
7	0.303	3.79	0	0.657	1.090	28.8	-	-
8	0.301	3.76	0	1.080	0.764	20.3	-	-
9	0.284	3.55	0	0.860	0.875	24.7	-	-
4	0.380	4.75	19.00	0.860	0.914	19.2	4.317	22.7
5	0.360	4.50	18.00	0.890	1.135	25.2	7.127	39.6
6	0.342	4.27	17.10	1.250	1.238	29.0	7.049	41.2
10	0.301	3.76	15.05	0.900	0.905	24.1	7.405	49.2
11	0.304	3.80	15.20	0.505	0.553	14.5	6.978	45.9
12	0.307	3.84	15.35	0.915	1.224	31.9	6.000	39.1

3.3.3 Fentanyl Excreted by Rats Injected with Fentanyl and Calabadion 1.

The second group of rats were injected with **III-7** followed by reversal with **III-1**. For these samples we designed a protocol to first separate the excreted **III-7** from its **III-1** complex so that we could quantify the drug and reversal agent separately. For this purpose, a known volume of urine from Rat I.D. 4, 5, 6, 10, 11, and 12 (500 μL) was evaporated under high vacuum. Each sample was mixed with 2 mL methanol, sonicated and vortexed in order to extract **III-7** into solution and leave behind the insoluble compound **III-1** as precipitate. These samples were

centrifuged to separate the supernatant from the precipitate. The supernatant methanol solutions were dried under high vacuum and reconstituted in 125 μL of mobile phase and injected into the HPLC system and quantified as described in section 3.3.2. The average percentage excretion of **III-7** in these samples was found to be (24 ± 6) %. The results are summarized in Table III-2.

3.3.4 Calabadion 1 Excreted by Rats Injected with Fentanyl and Calabadion 1.

The urine samples from rats injected with **III-1** as reversal agent (Rat I.D. 4, 5, 6, 10, 11, and 12) were analysed for the quantification of **III-7** by the HPLC assay described in section 3.3.3. Since the dosage of **III-1** in these samples was high enough (50 m kg^{-1}) to obtain mM quantities in urine,[63] we designed a ^{1}H NMR based assay to quantify compound **III-1**. The precipitate obtained from methanol in the previous step (section 3.3.3) was dried and reconstituted in 2 mL deuterium oxide, and centrifuged. The concentration of compound **III-1** in this solution was measured by ^{1}H NMR by comparing the peak area of the methyl protons of **III-1** at 1.8, 1.76 ppm with the methyl protons of a known concentration 3-(Trimethylsilyl)propionic-2,2,3,3-d_4 acid sodium salt (TMSP) internal standard at -0.05 ppm (Figure III-9). TMSP was chosen as the internal standard because it is a negatively charged molecule which does not bind to **III-1**, resulting in a single sharp peak at -0.005 ppm corresponding to 9 methyl protons.[64] Additionally the position of its resonance in ^{1}H NMR appears very upfield (at -0.05 ppm) in a region uncluttered by any other peaks from **III-1** or any other substances present in the urine sample.

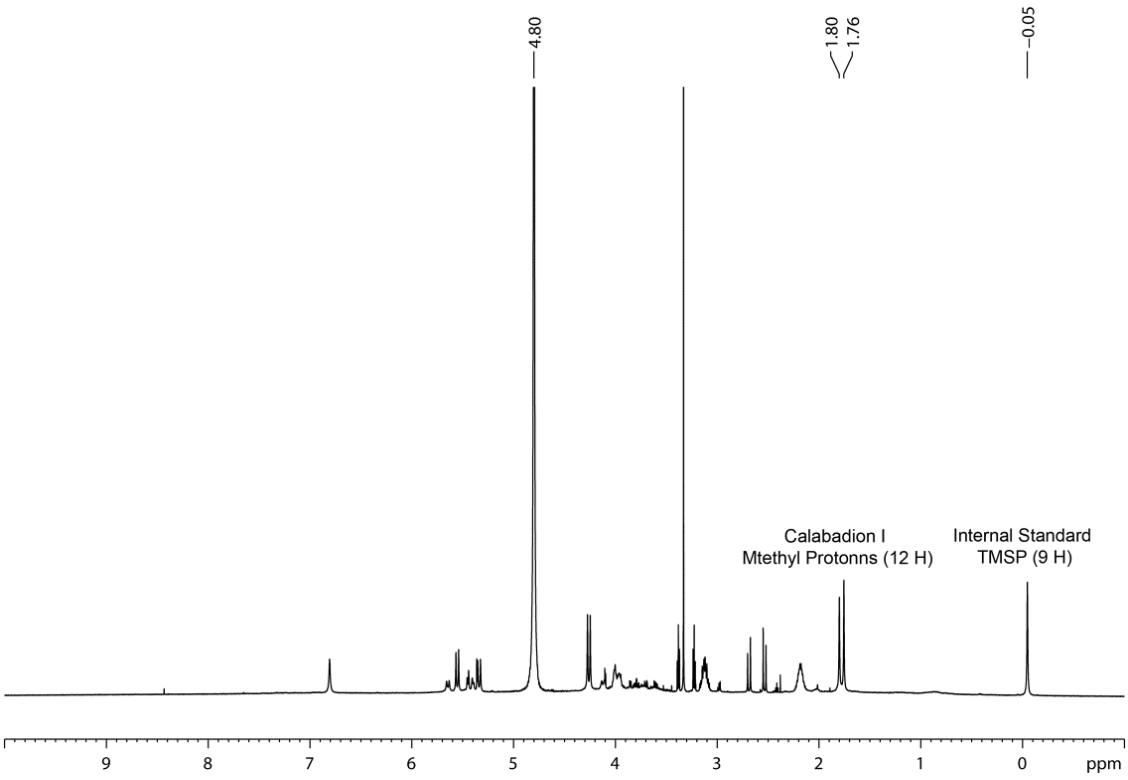

Figure III-9. ^{1}H-NMR spectrum of a representative urine sample following the injection of **III-7** and **III-1** to a rat (600 MHz, D_2O).

This separation of peaks in ^{1}H NMR allows us to obtain reliable peak integrals which are correlated to its known concentration in the solution. We were fortunate that the methyl protons of **III-1** (at 1.80 ppm and 1.76 ppm, corresponding to 12 protons) were also free from overlap from other signals in the ^{1}H NMR spectrum and could be integrated reliably. Integrals of the methyl peaks of **III-1** and TMSP were obtained by line shape fitting using the Gaussian model in TopSpin^{TM} software. We also adjusted the acquisition parameters for collecting the ^{1}H NMR data, such that a long delay time (D1) of 74 s was chosen so that it was approximately 5-times the T1 (relaxation time) for TMSP. This long D1

ensured that TMSP was fully relaxed between successive scans, and **III-1** was also expected to be fully relaxed since larger molecules have shorted relaxation times. The concertation of **III-1** calculated in urine and urine volume were used to calculate the weight percentage of **III-1** excreted as (40 ± 8) %.

3.3.5 Summary.

The reversal of fentanyl was effected in *Sprague-Dawley* rats using molecular container **III-1**. The renal elimination of **III-7** was analyzed by an HPLC assay for comparison between rats injected with placebo (saline) vs rats injected with reversal agent **III-1**. In case of placebo administration, (17 ± 9) % of **III-7** was eliminated and in case of reversal by **III-1**, (24 ± 6) % of **III-7** was eliminated in urine in 1 hour. A significant difference in renal elimination of **III-7** was not observed between the two cases taking into account the errors in measurement. The elimination of **III-1** by the kidneys was found to be (40 ± 8) % as measured by ^{1}H NMR.

3.4 Conclusions.

In conclusion, we have established that CB[n] based molecular containers- **III-1**, **III-2**, and **III-3** display higher affinities than calixarene (**III-4**) and cyclodextrin (**III-5**) based containers toward the panel of drugs of abuse (**III-6** – **III-12**) studied in this work. In particular CB[7] shows the highest selectivity for smaller phenethylammonium containing drugs **III-6** and **III-7**, whereas the Calabadion scaffold seems to be the most suitable for binding the full range drugs in this study and for further optimization of the lead reversal agents. The *in vivo*

reversal of methamphetamine by **III-2** and not CB[7] further establishes the Calabadion scaffold as promising for further development. By studying the excretion profile of **III-7** and **III-1** post reversal in *Sprague-Dawley* rats, we have found that on an average 24 % fentanyl and 40% Calabadion 1 are eliminated by the kidneys in 1 hour.

These results serve as encouraging preliminary data for the further development of molecular containers, especially CB[n] as reversal agents for drugs of abuse. They also point to the need for the further optimization of the Calabadion scaffold to develop reversal agents with higher *in vitro* K_a values for more potent *in vivo* efficacies for the sequestration of illicit drugs. Along with other PD and PK strategies being developed for the treatment of drug overdose, molecular containers show great promise to expand the toolbox of treatment options for tackling the social and healthcare issues associated with drug abuse and overdose.

Chapter 4: Synthesis and Molecular Recognition Properties of Acyclic Cucurbit[n]urils with Alkyl Linkers

4.1 Introduction.

Cucurbit[n]urils (CB[n]) are a class of molecular containers well-known for their high affinities, selectivities, and stimuli responsiveness towards various guests, especially hydrophobic diammonium cations.[18,103] Accordingly, CB[n] compounds have been used in a wide range of applications, including drug delivery, drug reversal, molecular machines, and sensing ensembles.[104] In order to expand the scope of CB[n] applications and improve their properties such as aqueous solubility, functionalization approaches to obtain modified CB[n] is an active area of research.[105,30,36,35]

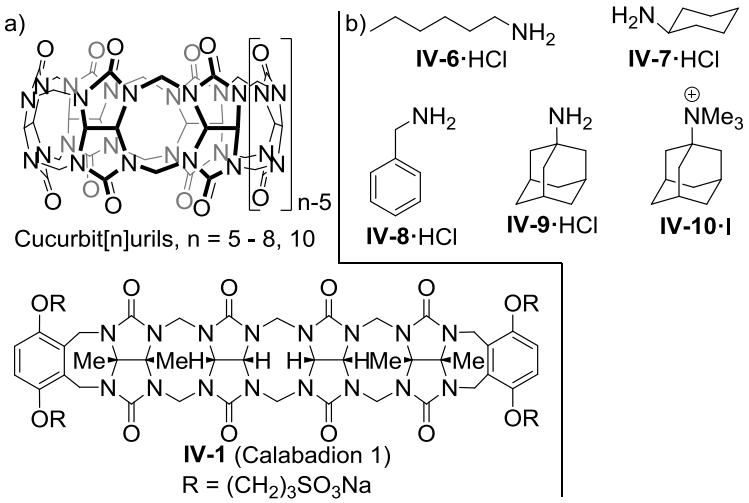

Figure IV-1. Chemical structures of: a) cucurbit[n]urils (CB[n]) and Calabadion 1, (**IV-1**) and b) guests used in this study.

In 2012, Isaacs and co-workers reported the synthesis of an acyclic CB[n] Calabadion 1 (Figure IV-1 a) which contains a glycoluril tetramer backbone while incorporating aromatic side walls with solubilizing sulfonate groups attached via alkyl chains. Calabadion 1 was reported as an effective solubilizing excipient for poorly water soluble drugs[40] and as a reversal agent for neuromuscular blocking agents (NMBAs).[48] Subsequently, the Isaacs and Sindelar groups have reported many host compounds which are structurally related to **IV-1**. The modular synthesis of **IV-1** and related compounds has facilitated the synthesis of analogues with different solubilizing groups,[43] aromatic walls,[44] glycoluril oligomer lengths,[46] and length of the alkyl chain connecting the solubilizing group to the glycoluril backbone.[45] The effect of these structural modifications on the ability of these new hosts to bind guest molecules as compared to **IV-1** has also been previously studied. From these studies, it has been found that generally a larger glycoluril oligomer (e.g.: tetramer as compared to trimer, dimer, or monomer), larger aromatic walls (e.g.: substituted naphthalene as compared to substituted benzene), and negatively charged solubilizing groups (e.g.: sulfonate as compared to neutral or positive groups) lead to more potent molecular hosts with higher binding affinities towards guests such as hydrophobic diammonium cations. The binding affinity of **IV-1** toward drugs of abuse such as fentanyl and methamphetamine is also notable ($\sim 10^7$ M^{-1}) as discussed in Chapter 3, and renders it as a promising scaffold for further medicinal chemistry optimization for the purpose of developing a reversal agent for sequestering drugs of abuse.[100] In this chapter we present the synthesis of three new hosts **IV-2a** – **IV-2c**, with alkyl

linkers of varying lengths capping one side of **IV-1**. We have also studied their aqueous solubility, self-association properties and molecular recognition properties toward guests (**IV-6** – **IV-10**) and compared them to those of **IV-1**.

4.2 Design and Synthesis of Hosts IV-2a – IV2c.

The synthesis of host **IV-1** was previously reported by the double electrophilic aromatic substitution reaction of the glycoluril tetramer bis(cyclic ether) building block (**IV-5**) with the corresponding dialkoxyaromatic sidewall **IV-4** in trifluoroacetic acid.[40] The high binding affinity of **IV-1** toward various hydrophobic ammonium cations has been attributed to its ureidyl carbonyl portals resulting from the glycoluril tetramer backbone which is preorganized into a C-shape facilitating guest encapsulation. The cavity of **IV-1** is in part defined by aromatic walls which facilitate π-π interactions with guests containing aromatic groups, further stabilizing the complex. The sulfonate arms enhance the solubility of host **IV-1** in water and also provide favorable electrostatic interactions with positively charged guests. In designing congeners of **IV-1** we wanted to preserve the carbonyl portals, aromatic walls, and sulfonate solubilizing groups to maintain the recognition properties and aqueous solubility of **IV-1**, while improving the preorganization of the cavity size of the acyclic host by locking the distance between sidewalls and providing additional binding sites to the hydrophobic parts of larger guest molecules which could protrude from the host cavity.

Accordingly we hypothesized that the binding affinity of **IV-1** toward hydrophobic cations could be increased by incorporation of a covalent capping group such as an alkyl linker, on one face of the host. We reacted dibromoalkanes

of varying chain lengths (ethyl, hexyl, and decyl) with hydroquinone under basic conditions to obtain precursors with alkyl linkers, compounds **IV-3a, IV-3b**, and **IV-3c** in 13%, 50%, and 33% yield respectively (Scheme IV-1a).[106,107] Precursor **IV-3** was alkylated with 1,3-propanesultone to obtain the aromatic sulfonate walls with alkyl linkers, **IV-4a**, **IV-4b**, and **IV-4c** in 87%, 77%, and 47% yield respectively (Scheme IV-1b).

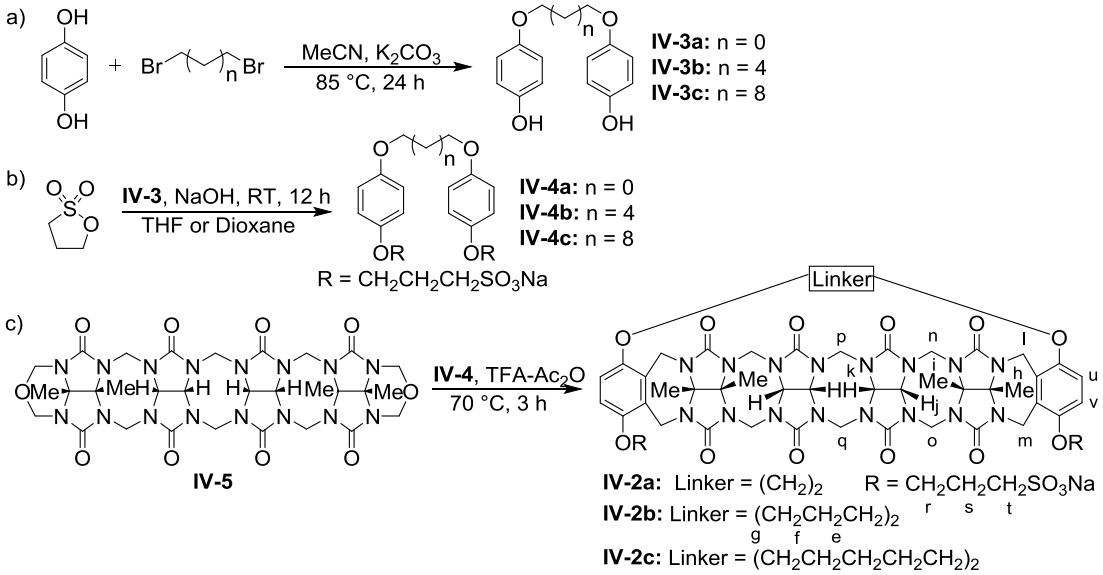

Scheme IV-1. Synthesis of hosts **2a** – **2c**.

Compound **IV-5** was refluxed with **IV-4** (analogous to the synthesis of **IV-1**)[40] in a mixture of trifluoroacetic acid and acetic anhydride, to obtain alkyl capped congeners of **IV-1**, compounds **IV-2a**, **IV-2b**, and **IV-2c** in 33%, 13%, and 26% yield respectively. Compounds **IV-2a** – **IV2c** were purified by Dowex ion exchange chromatography (Dowex® 1X2 chloride form, 200-400 mesh ion exchange resin) to isolate the hosts with the alkyl linker joining the same side of

the aromatic walls as is confirmed from the ^{1}H NMR splitting patterns of the methylene protons of the glycoluril backbone on the same and opposite sides of the alkyl linker (Figure IV-2b and Appendix 3).

4.3 Solubility Properties of Hosts IV-2a – IV2c.

The use of molecular containers for biological applications such as drug reversal and drug solubilization requires their good inherent solubility in water as well as the aqueous solubility of their complexes with relevant guest molecules. The solubility of **IV-1** was reported as 105 mM in 20 mM monosodium phosphate buffer at pD 7.4 in deuterium oxide.[40] We used the same technique as that reported for **IV-1** for measuring the solubility of our hosts and found that the solubilities of **IV-2a**, **IV-2b**, and **IV 2c** are 1.8 mM, 1.5 mM, and 1.7 mM respectively in 20 mM monosodium phosphate buffer at pD 7.4 in deuterium oxide. This dramatic drop in aqueous solubility by two orders of magnitude was unexpected, but can be attributed to the loss of two sulfonate groups per host while incorporating linkers into **IV-2a** – **IV-2c**. While this reduced aqueous solubility makes **IV-2a** – **IV-2c** less attractive for use in biological systems as compared to **IV-1**, we decided to investigate the effect of the alkyl linker on the self -association properties and the molecular recognition properties of these hosts toward some common guests for CB[n].

4.4 Self-Association Properties of Hosts IV-2a – IV2c.

The self-association of **IV-1** has been previously studied by dilution experiments monitored by ^{1}H NMR spectroscopy. It was found that the observed change in chemical shift with change in concentration of **IV-1** fit well to a 2-fold

self-association model, and the corresponding self-association constant (K_s) of 47 M^{-1} was obtained.[40] In general the K_s of acyclic CB[n] which are structurally related **IV-1** (in that they have a glycoluril backbone and aromatic walls with sulfonate arms) have been reported as less than 1000 M^{-1}. This low tendency to self –associate has been attributed to the electrostatic repulsion between the tetraanionic molecules.[47]

Fortunately our dianionic hosts **IV-2a** – **IV-2c** also showed no significant changes in chemical shift in ^{1}H NMR dilution studies over the accessible concentration range (1.0 – 0.1 mM) in deuterium oxide buffered to pD 7.4. This low tendency for self-association is a desirable property for molecular hosts as it leaves their cavity accessible for guest binding.

While the intermolecular association in **IV-2a** – **IV2c** is low, we did note some concentration independent intramolecular features in the ^{1}H NMR spectra of our hosts which suggest the partial inclusion of the alkyl linker within the hydrophobic cavity of each host molecule. Figure IV-2b shows the ^{1}H NMR spectrum of host **IV-2b** in which the resonances of the methylene protons of the linker H_f, $H_{e'}$, and H_e are shifted upfield by 0.5 ppm relative to their resonances in **IV-4b** (Appendix 3). This can be explained by the shielding effect of the hydrophobic cavity of **IV-2b** which stabilizes the alkyl linker of the host in water by the hydrophobic effect. The resonance for H_g is not significantly different between **IV-2b** and **IV-4b** indicating that its magnetic environment is unchanged and it does not enter the cavity of **IV-2b**. The same effect is observed for host **IV-2c**, in which the resonances of all the methylene protons of the alkyl linker

(except the ones directly attached to the aromatic wall) are upfield shifted by 0.2 - 0.6 ppm relative to their resonances in **IV-4c** (Appendix 3).

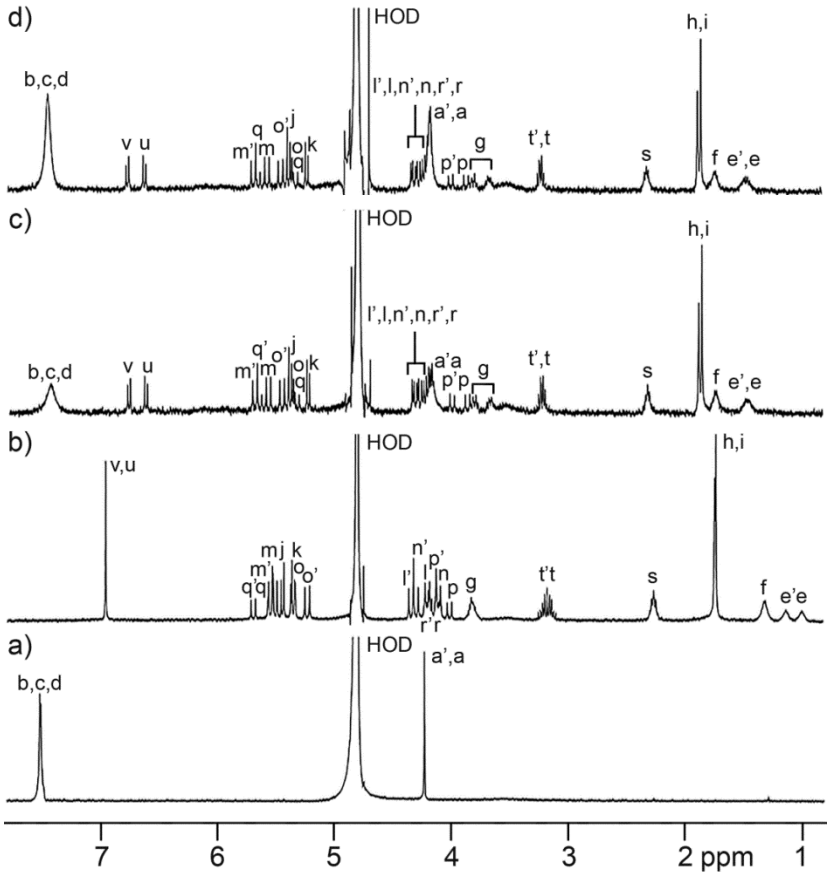

Figure IV-2. ^{1}H NMR spectra recorded (400 MHz, RT, 20 mM sodium phosphate buffered D_2O, pH 7.4) for: a) **IV-8** (1 mM), b) **IV-2b** (1 mM), c) a mixture of **IV-8** (0.5 mM) and **IV-2b** (0.5 mM), and d) **IV-8** (1.0 mM) and **IV-2b** (0.5 mM).

Since the decyl linker is longer and has more degrees of freedom than the hexyl linker we observed a broadening of the ^{1}H NMR signals of the protons in the linker of **IV-2c** as compared to the sharper resonances of those in **IV-2b**. The

decyl linker also penetrates more deeply into the its cavity relative to the hexyl linker on account of its longer length, as is evidenced by the larger upfield shifts of its methylene protons at the mid-point of the linker. In case of host **IV-2a**, the linker is shortest (ethyl group) and the methylene groups are both directly attached to the aromatic walls of the host. Two well-resolved resonances are observed for the linker protons in **IV-2a** at 4.47 ppm and 3.87 ppm respectively. The resonance at 3.87 ppm is shifted upfield by 0.5 ppm relative its position in the ^{1}H NMR spectrum of **IV-4a** (Appendix 3) which indicates that this set of protons is experiencing a different magnetic environment, potentially from the anisotropic effect of the aromatic walls of the host. The other set of protons whose chemical shift is observed at 4.47 ppm are out of the plane of the aromatic walls and therefore do not experience any shielding effect.

This phenomenon of the alkyl linker of the hosts **IV-2**a – **IV-2c** interacting with or being partially included within their cavities is expected to create an energetic penalty for guest molecules to be included within their cavities. In the following sections we investigate the thermodynamic costs of this phenomenon qualitatively and quantitatively.

4.5 Binding Properties of Hosts IV-2a – IV-2c and IV-1 towards Guests IV-6 – IV-10 Investigated by ^{1}H NMR.

Initially, we tried to investigate the ability of hosts **IV-2a** – **IV-2c** to bind typical dicationic guests known to bind to CB[n] such as 1,6-diamino hexane, 1,6-diamino cyclohexane, and *p*-xylene diamine. We found that the complexes of these dicationic guests with our dianionic hosts **IV-2a** – **IV2c** precipitated out

from water. We rationalize this precipitation as a consequence of the formation of a zwitterionic host-guest complex which would have lower aqueous solubility. Therefore we decided instead to study the water soluble complexes of monocationic guests **IV-6** – **IV10** with hosts **IV-2a** – **IV-2c** and **IV-1** by ^{1}H NMR spectroscopy. For all these complexes we commonly observed upfield shifting of guest resonances which indicates that these protons on the guest are located in the cavity of the host molecule. The upfield shifting of guest resonances in the complexes with hosts containing alkyl linkers (**IV-2a** – **IV-2c**) was generally less than or equal to the upfield shifting of the same resonances in the complexes with host **IV-1**. This preliminary observation indicates that in most cases the cavity of host **IV-1** better accommodates guests **IV-6** – **IV-10** as compared to the cavities of **IV-2a** –**IV2c** which are more constrained due to the presence of the alkyl linkers. All of the host guest complexes display fast kinetics of exchange on the ^{1}H NMR timescale which suggests that these complexes would be of moderate stability in water. In general, the binding of guests **IV-6** – **IV-10** to hosts **IV-2a** – **IV-2c** resulted in the downfield shifting of the resonances of the linker protons of the host molecule indicating that guest binding displaces the linkers from within the cavity of the host. The ^{1}H NMR spectrum of the **IV-2b·IV-8** complex is presented in Figure IV-2 to facilitate discussion of the binding features of this complex. The resonances of the aromatic protons H_b, H_c, H_d of **IV-8** undergo upfield shifting in its complex with **IV-2b** as a result of the anisotropic environment of the aromatic walls of the host when the host and guest are combined in a 1:1 ratio. Upon adding excess guest (2:1 ratio) we observe that the

peak corresponding to H_b, H_c, and H_d protons shifts to a position which is the average between the free (Figure IV-2a) and bound (Figure IV-2c) forms of the guest. This indicates a fast kinetics of exchange between free guest **IV-8** and the **IV-2a·IV-8** complex relative to the ^{1}H NMR chemical shift time scale. The same trend is observed for the H_a methylene protons of **IV-8** in free and bound form which experience the shielding effect of the cavity of the host when bound to **IV-2b**. The resonances of the aromatic protons of host **IV-2b**, H_v and H_u also undergo upfield shifting in the **IV-2b·IV-8** complex as a result of the anisotropic effect of the aromatic group of **IV-8**. The resolution of the H_v, H_u multiplet peak of **IV-2b** (Figure IV-2b) into two sharp doublets (J =9.0) in the **IV-2b·IV-8** complex instead of four peaks or broadening indicates the facial selectivity of the guest **IV-8** in binding to the cavity, presumably with the aromatic end of **IV-8** facing the alkyl linker of **IV-2b** and the ammonium group of **IV-8** facing the sulfonate groups of **IV-2b**. The other noteworthy change in the spectrum of **IV-2b** occurs to the resonances of the H_f, $H_{e'}$, and H_e protons of the linker. In the spectrum of the **IV-2b·IV-8** complex these protons are shifted downfield by 0.5 ppm relative to their positions in free **IV-2b**, at the same positions where they were observed in the spectrum of **IV-4b** (Appendix 3). This downfield shift indicates that the presence of guest **IV-8** in the cavity of host **IV-2b** necessitates the displacement of the hexyl linker from the cavity of **IV-2b**. Analogous phenomena were seen in the ^{1}H NMR spectra recorded for the remaining host-guest complexes.

4.6 Measurement of Binding Affinities between Hosts IV-2a – IV-2c and IV-1 and Guests IV-6 – IV-10 by Isothermal Calorimetry (ITC).

The binding affinities (K_a) of the hosts **IV-2a** - **IV-2c** and **IV-1** with monocationic guests **IV-6** – **IV-10** were measured by ITC (Table IV-1).

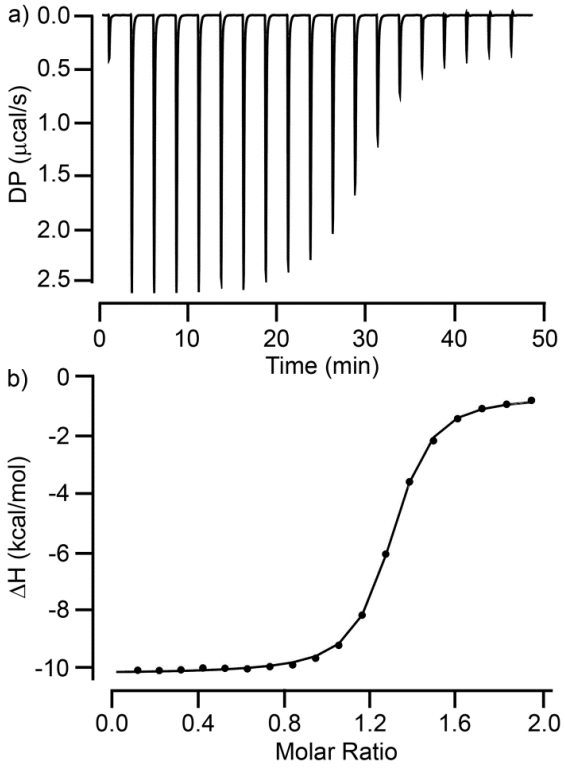

Figure IV-3. a) ITC thermogram recorded during the titration of **IV-2b** (0.1 mM) in the cell with **IV-8** (1.0 mM) in the syringe. d) Fitting of the data to a 1:1 binding model with Ka = $(1.6 \pm 0.1) \times 10^6\ M^{-1}$.

For example, Figure IV-3 shows the thermogram recorded for the titration of **IV-2b** (100 µM) with **IV-8** (0 – 200 µM) which was fitted with the MicroCal PEAQ-ITC analysis software to deliver $K_a = (1.6 \pm 0.1) \times 10^6\ M^{-1}$and ΔH = - 9.5

± 0.1 kcal mol^{-1} for the **IV-2b•IV-8** complex. The other ITC derived thermodynamic parameters given in Table IV-1 were carried out analogously.

Table IV-2. Binding constants determined by ITC for the interaction between molecular containers **IV-1**, **IV-2a** – **IV-2c** and guests **IV-6 – IV-10**.

Guest	Binding Constants (M^{-1}), ΔH (kcal mol^{-1}) with various molecular containers			
	1	**2a**	**2b**	**2c**
6	$(2.4 \pm 0.1) \times 10^6$, -8.7	$(6.2 \pm 0.9) \times 10^3$, -3.9	$(1.3 \pm 0.1) \times 10^5$, -5.5	$(2.3 \pm 0.2) \times 10^4$, -5.0
7	$(1.7 \pm 0.1) \times 10^6$, -8.2	$(2.3 \pm 0.2) \times 10^4$, -8.7	$(7.9 \pm 0.1) \times 10^5$, -8.6	$(3.2 \pm 0.3) \times 10^4$, -6.0
8	$(3.9 \pm 0.2) \times 10^6$, -10.5	$(2.1 \pm 0.1) \times 10^4$, -11.3	$(1.6 \pm 0.1) \times 10^6$, -9.5	$(7.1 \pm 0.4) \times 10^4$, -8.5
9	$(4.9 \pm 0.2) \times 10^5$, -7.1	$(2.7 \pm 0.6) \times 10^4$, -4.5	$(7.2 \pm 1.0) \times 10^5$, -3.9	$(1.5 \pm 0.04) \times 10^4$, -6.5
10	$(6.2 \pm 0.6) \times 10^6$, -9.0	$(6.9 \pm 0.3) \times 10^4$, -6.9	$(1.3 \pm 0.03) \times 10^6$, -9.6	$(2.7 \pm 0.2) \times 10^5$, -5.7

Conditions: 20 mM sodium phosphate buffered water, pH 7.4, room temperature.

4.7 Commentary on the Tabulated K_a Values.

The K_a values measured for the various hosts and guests in this study ranged from $6.2 \times 10^3 – 6.2 \times 10^6$ M^{-1}, with **IV-1** being the highest affinity host toward each guest. In general, the presence of an alkyl linker and the loss of two sulfonate groups led to a decrease in binding affinity of **IV-2a** - **IV-2c** toward **IV-6** – **IV-10** relative to **IV-1** by one or two orders of magnitude. The lowered electrostatic attraction between the dianionic hosts and monocationic guests as compared to that between the tetraanionic **IV-1** and the same guests; as well as the energetic penalty of displacing the alkyl linker from within the cavities the new hosts/ decreased cavity volume led to significant losses in binding affinities. The preference for CB[n] hosts to bind hexyl diammonium ions is well known, due to the size complementarity which leads to the positioning of the hydrophobic

hexyl chain to span the full height of the cavity of the CB[n] while the ammonium groups are appropriately placed for ion-dipole interactions with the carbonyl portals on each end.[18] The same preference has been reported for **IV-1** and its analogues.[37] Accordingly, **IV-1** binds **IV-6** with an affinity of 2.4×10^6 M^{-1}. However, hosts **IV-2a** – **IV-2c** show a drastically lowered preference for **IV-6**. In case of **IV-2b** and **IV-2c** the 19- and 104-fold loss in affinity respectively, can be explained by the cost of displacing the hexyl and still longer decyl linkers from the cavity to accommodate the hexyl chain of **IV-8**. In case of **IV-2a**, the shorter ethyl linker brings one end of the aromatic walls close together reducing the cavity volume. Therefore, guest **IV-6** has to be accommodated within the cavity of **IV-2a** of reduced volume, leading to a 387-fold decrease in affinity relative to **IV-1**. Guest **IV-7** being shorter and wider than **IV-6** is preferred by **IV-2a** and **IV-2b** over **IV-6** on account of their decreased cavity depths due to the presence of the alkyl linker. Predictably, host **IV-1** which has no such factors decreasing its cavity volume shows little preference between **IV-6** and **IV-7**. Interestingly, **IV-2c** also shows little preference for **IV-7** over **IV-6**. This lack of selectivity can be attributed to the larger decyl linker, which would need to be pushed out from the cavity to accommodate either guest **IV-6** or **IV-7** and the energetic penalty is same for both.

For each of the hosts in this study, guest **IV-8** results in one of the tightest complexes from group of guests **IV-6** – **IV-10** due to its aromatic ring which can undergo favorable π-π interactions with the aromatic walls of each host molecule. All hosts also display a preference for the quaternary ammonium adamantyl guest

IV-10 over the primary ammonium adamantyl guest **IV-9**. This selectivity is most pronounced for **IV-1** (13-fold). We rationalize this selectivity based on the improved ion-dipole interactions between the N-methyl ammonium groups with the ureidyl carbonyl portal of the host. For hosts **IV-2a** – **IV-2c** we only observe a 2-3 fold selectivity for **IV-10** over **IV-9**. This can be explained based on the partial encapsulation of **IV-9** and **IV-10** in the cavities of **IV-2a** – **IV-2c** on account of the decreased cavity volumes of these hosts. The evidence for partial encapsulation comes from the ^{1}H NMR resonance of the methyl protons of **IV-10** when bound to **IV-2a – IV-2c**. This resonance does not undergo upfield shifting in their host-guest complexes (Appendix 3), indicating that **IV-10** is not encapsulated within the host cavities. In contrast, the ^{1}H NMR resonance of the same N-methyl protons when bound to **IV-1** undergoes a substantial upfield shifting potentially due to the out of plane helicity for **IV-1** leading to a shielding effect by one of its aromatic walls. Therefore, the presence or absence of methyl groups on the ammonium nitrogen protruding outside of the cavities of **IV-2a – IV-2c** does not significantly affect their binding affinities.

4.8 Conclusions.

Three new hosts **IV-2a** – **IV-2c** were synthesized with alkyl linkers of varying lengths- ethyl, hexyl, and decyl; capping one end of the previously reported host **IV-1**. These new hosts were less water soluble than **IV-1** due to the loss of two sulfonate groups and did not undergo intermolecular self-association. However, the intramolecular self-inclusion of the alkyl linkers inside the cavity of these hosts led to decreased binding affinities toward guests relative to **IV-1**. Future

work will try to overcome these disadvantages in the solubility and molecular recognition properties of **IV-2a** – **IV-2c** by incorporating linkers with more rigidity and/or hydrophilic groups that do not undergo self-inclusion processes, such as aromatic walls connected by oligoethylene glycol units. Such linkers would lead to entropic gains from the improved preorganization of the acyclic CB[n] cavity and enthalpic gains from the favorable interactions between the capping linker and encapsulated guest; without the energetic penalty of self-inclusion or loss in aqueous solubility.

Appendix 1

Calabadion 2 as a Reversal Agent for Neuromuscular Blocking Agents: *In Vitro* Selectivity of an Acyclic Cucurbit[n]uril Molecular Container towards Neuromuscular Blocking Agents Relative to Commonly Used Drugs[97] and Renal Elimination of Calabadion 2 in Rats Post Reversal of Neuromuscular Blockade.[64]

Table of Contents **Pages**

General experimental details 99

Procedures and binding models for UV/Vis titrations 100-101

UV/Vis spectra and plots of absorbance data for K_a determination of various drugs with **II-2** 102-121

Binding model for ^{1}H NMR titrations and plots of chemical shift data for K_a determination by direct ^{1}H NMR titrations 122-129

^{1}H NMR stack plots for drugs with **II-2** 130-156

Job plots of selected drugs with **II-2** 157-161

Three dimensional surface plot of [AChR•NMBA] versus log [Drug] and log K_3 for vecuronium with 2 equivalents of Calabadion 2 162

Three dimensional surface plot of [AChR•NMBA] versus log [Drug] and log K_3 for cisatracurium with 32 equivalents of Calabadion 2 162

Three dimensional surface plot of [AChR•NMBA] versus log [Drug] and log K_3 for cisatracurium with 16 equivalents of Calabadion 2 163

Study of Hoffmann Degradation of Cisatracurium 164-166

General experimental details. Drugs used for measuring binding constants with **II-2** were purchased from commercial suppliers and used without further purification. Compound **II-2** was prepared according to the literature procedure.[40] ^{1}H NMR spectra were measured on commercial spectrometers operating at 400 or 600 MHz. UV-Vis absorbance was measured on a Varian Cary 100 UV spectrophotometer.

Determination of K_a between Host II-2 with various drugs using UV/Vis spectroscopy. K_a values up to 10^4 M^{-1} can be measured reliably by ^{1}H NMR spectroscopic methods. For values that exceed this level it is necessary to use other techniques such as UV/Vis, fluorescence, or isothermal titration calorimetry. UV/Vis spectroscopy was used in this work.

The K_a between **II-2** and **II-4** (tetracycline, UV/Vis active drug) was determined by direct titration of a fixed concentration of **II-4** with increasing concentrations of **II-2**. The K_a value was determined by fitting the change in absorbance as a function of host concentration to a 1:1 binding model. In order to determine the K_a value for **II-2** toward guests which were not UV/Vis active, an indicator displacement assay involving the addition of guest to a solution of **II-2** and dye Rhodamine 6G was used. The change in UV/Vis absorbance as a function of guest concentration was fitted to a competitive binding model which allowed determination of the K_a values based on the known total concentrations of **II-2**, Rhodamine 6G, and drug. The known K_a value of the **II-2**•Rhodamine 6G complex (2.3×10^6 M^{-1}) was used as input in the competitive binding model.[48]

Binding Models Used to Determine Values of K_a with Micromath Scientist

1:1 Binding Model for UV/Vis.

// Micromath Scientist Model File
// 1:1 Host:Guest binding model
//This model assumes the guest concentration is fixed and host concentration is varied
IndVars: ConcHostTot
DepVars: SpectroscopicSignal
Params: Ka, ConcGuestTot, SpectroscopicSignalMin, SpectroscopicSignalMax
Ka = ConcHostGuest/(ConcHostFree*ConcGuestFree)
ConcHostTot=ConcHostFree + ConcHostGuest
ConcGuestTot=ConcGuestFree + ConcHostGuest
SpectroscopicSignal = SpectroscopicSignalMin + (SpectroscopicSignalMax - SpectroscopicSignalMin) * (ConcHostGuest/ConcGuestTot)
//Constraints
0 < ConcHostFree < ConcHostTot
0 < Ka
0 < ConcGuestFree < ConcGuestTot
0 < ConcHostGuest < ConcHostTot

Competitive Binding (Indicator Displacement) Models.

Competitive Model Fitting Absorbance at One Wavelength.

// MicroMath Scientist Model File
IndVars: ConcAntot
DepVars: Absorb
Params: ConcHtot, ConcGtot, Khg, Kha, AbsorbMax, AbsorbMin
Khg = ConcHG / (ConcH * ConcG)
Kha = ConcHAn / (ConcH * ConcAn)
Absorb = AbsorbMin + (AbsorbMax-AbsorbMin)*(ConcHG/ConcGtot)
ConcHtot = ConcH + ConcHG + ConcHAn
ConcGtot = ConcHG + ConcG
ConcAntot = ConcAn + ConcHAn
0 < ConcHG < ConcHtot
0 < ConcH < ConcHtot
0 < ConcG < ConcGtot
0 < ConcAn < ConcAntot
***

Competitive Model Fitting Absorbance at Two Wavelengths.

// MicroMath Scientist Model File
IndVars: ConcAntot
DepVars: Absorb1, Absorb2

Params:Khg, Kha, AbsorbMax1, AbsorbMin1, AbsorbMax2, AbsorbMin2
Khg = ConcHG / (ConcH * ConcG)
Kha = ConcHAn / (ConcH * ConcAn)
Absorb1 = AbsorbMin1 + (AbsorbMax1-AbsorbMin1)*(ConcHG/0.00001)
Absorb2 = AbsorbMin2 + (AbsorbMax2-AbsorbMin2)*(ConcHG/0.00001)
0.00001 = ConcH + ConcHG + ConcHAn
0.00001= ConcHG + ConcG
ConcAntot = ConcAn + ConcHAn
0 < ConcHG < 0.00001
0 < ConcH < 0.00001
0 < ConcG < 0.00001
0 < ConcAn < ConcAntot
***

(A)

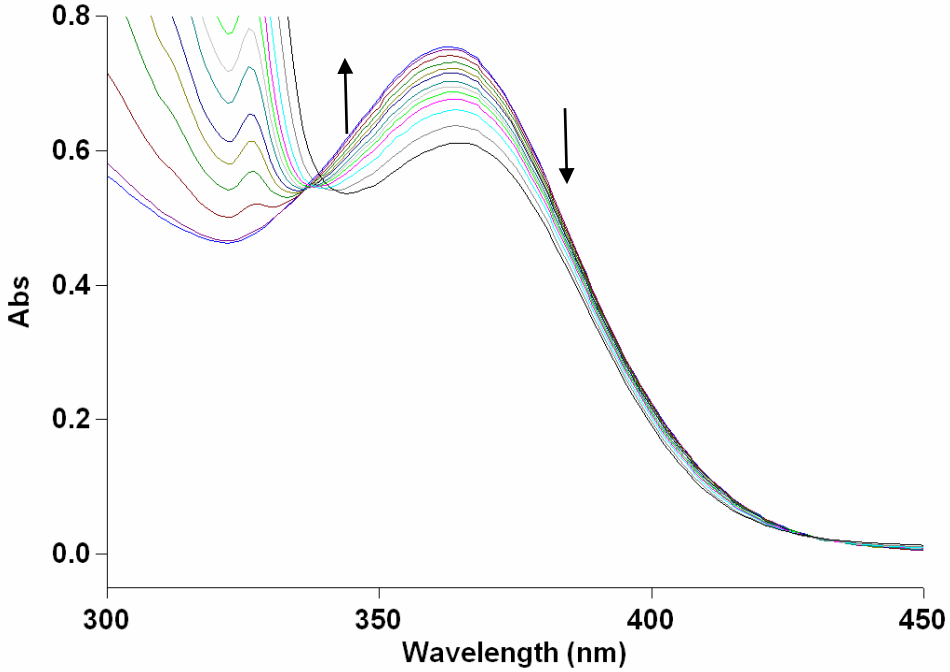

(B)

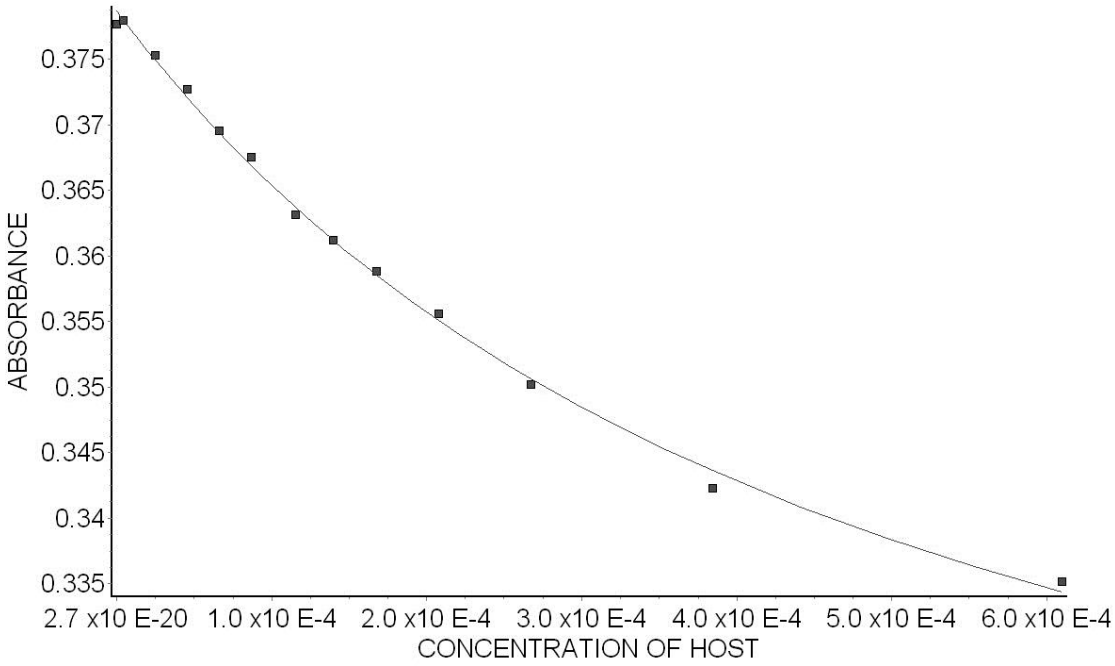

Figure II-S1. (A) UV/Vis spectra from the titration of **II-2** (0–610 µM) with guest **II-4** (57.3 µM) in 20 mM NaH_2PO_4 buffer (pH = 7.4); (B) plot of the A_{390} as a function of the concentration of **II-2**. The solid line represents the best non-linear fit of the data to a 1:1 binding model ($K_a = (2.3 \pm 0.2) \times 10^3\ M^{-1}$).

(A)

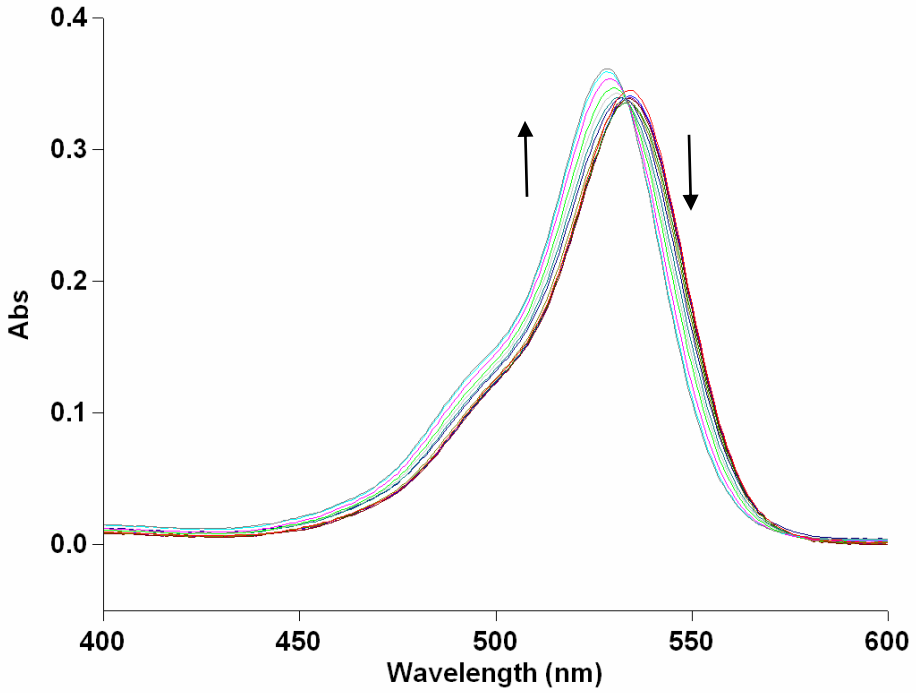

(B)

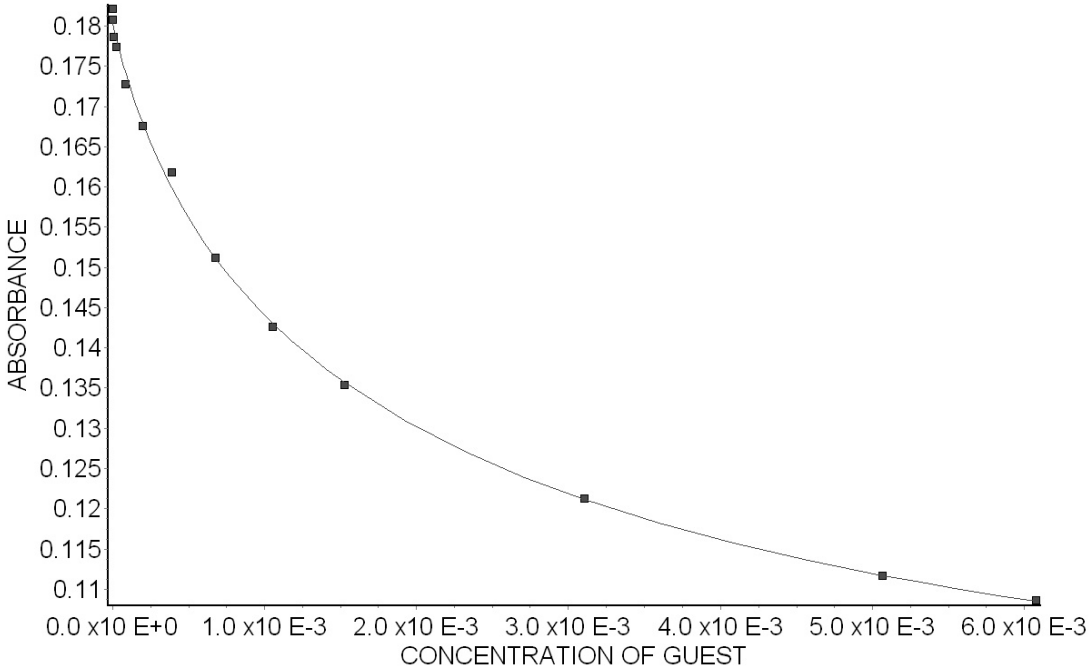

Figure II-S2. (A) UV/Vis spectra from the titration of **II-2** (5.07 µM) and Rhodamine 6G (5.01 µM) with guest **II-8** (0 – 6.08 mM) in 20 mM NaH_2PO_4 buffer (pH = 7.4); (B) plot of the A_{550} as a function of the concentration of **II-8**. The solid line represents the best non-linear fit of the data to a competitive binding model ($K_a = (5.9 \pm 0.5) \times 10^3\ M^{-1}$).

(A)

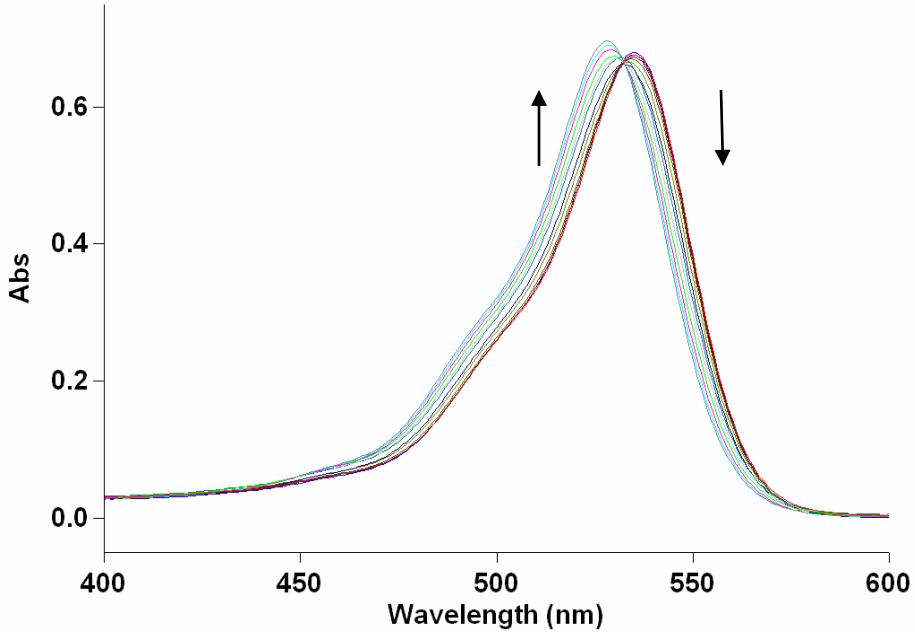

(B)

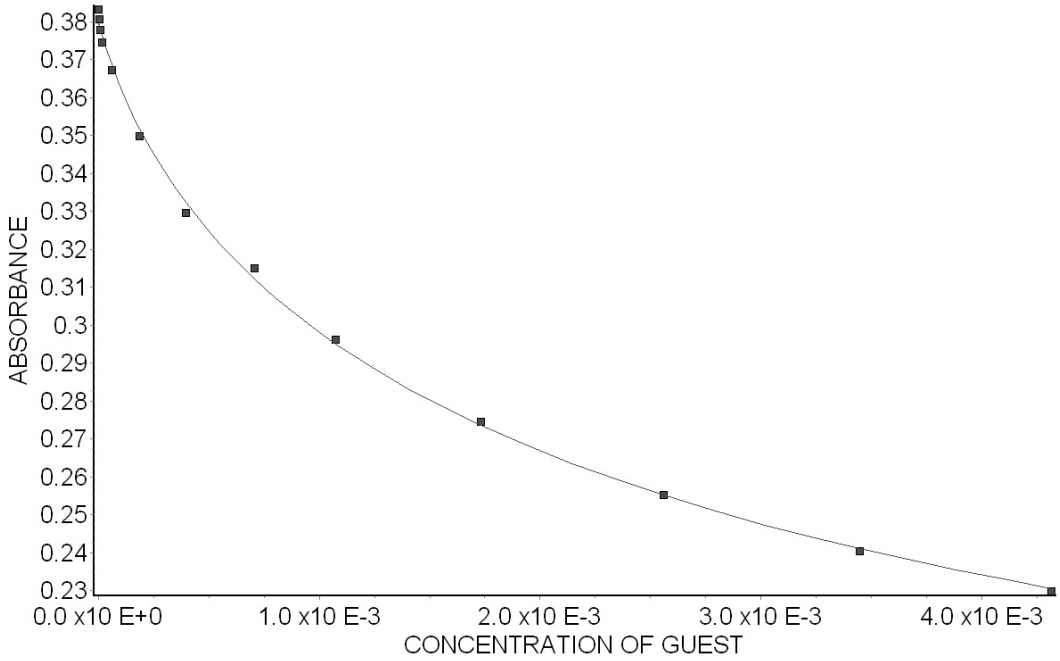

Figure II-S3. (A) UV/Vis spectra from the titration of **II-2** (10.1 µM) and Rhodamine 6G (9.96 µM) with guest **II-10** (0 – 4.32 mM) in 20 mM NaH_2PO_4 buffer (pH = 7.4); (B) plot of the A_{550} as a function of the concentration of **II-10**. The solid line represents the best non-linear fit of the data to a competitive binding model ($K_a = (8.6 \pm 0.8) \times 10^3\ M^{-1}$).

(A)

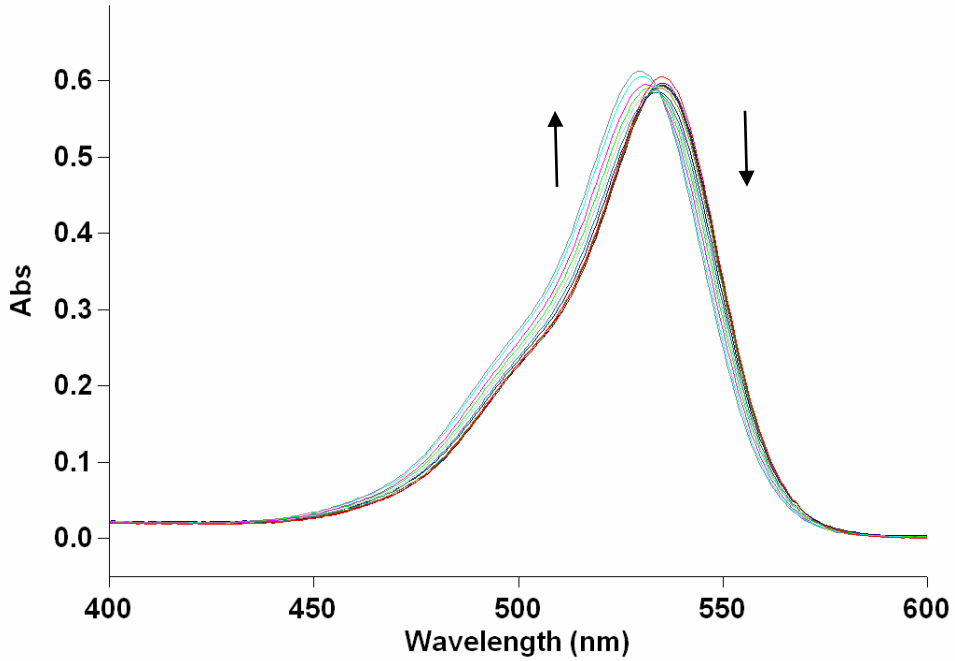

(B)

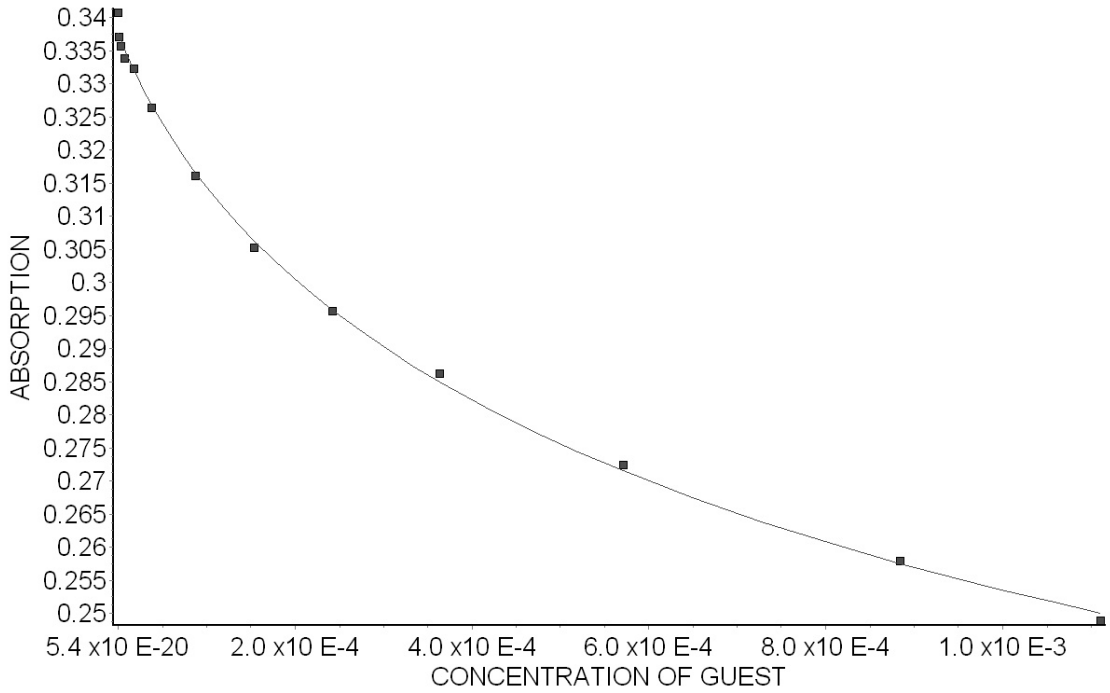

Figure II-S4. (A) UV/Vis spectra from the titration of **II-2** (9.98 µM) and Rhodamine 6G (9.96 µM) with guest **II-12** (0 – 1.11 mM) in 20 mM NaH_2PO_4 buffer (pH = 7.4); (B) plot of the A_{550} as a function of the concentration of **II-12**. The solid line represents the best non-linear fit of the data to a competitive binding model ($K_a = (2.1 \pm 0.2) \times 10^4\ M^{-1}$).

(A)

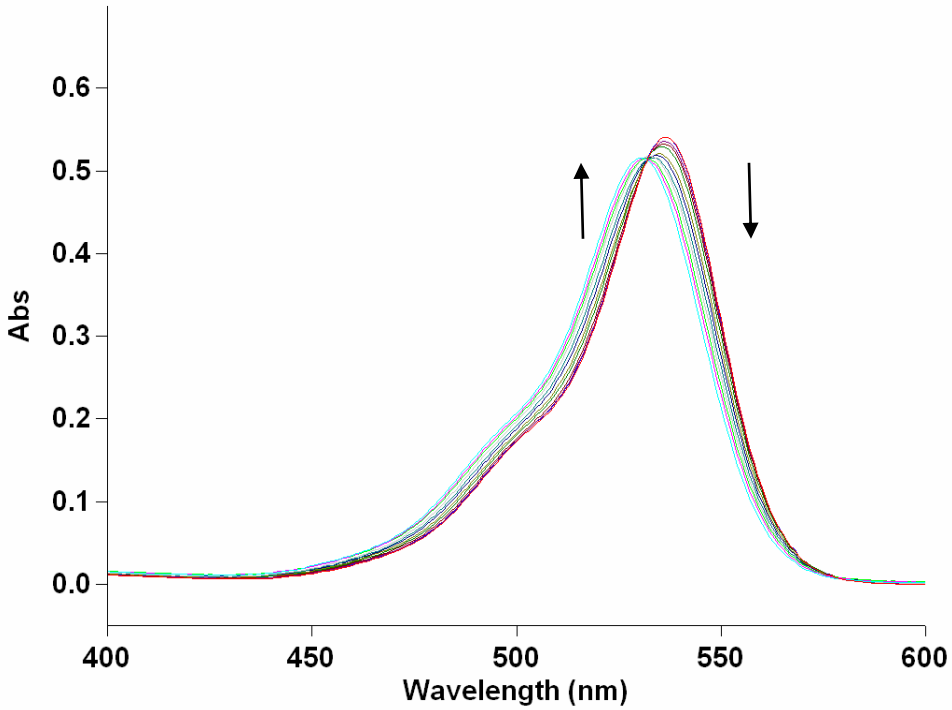

(B)

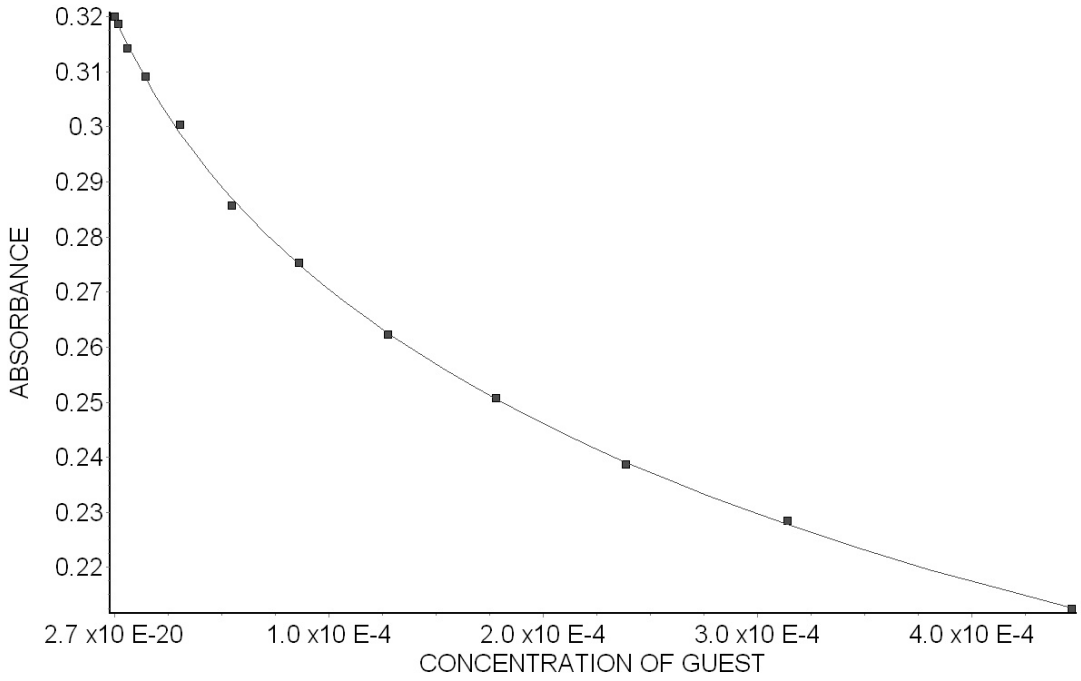

Figure II-S5. (A) UV/Vis spectra from the titration of **II-2** (10.2 μM) and Rhodamine 6G (9.96 μM) with guest **II-14** (0 – 447 μM) in 20 mM NaH_2PO_4 buffer (pH = 7.4); (B) plot of the A_{550} as a function of the concentration of **II-14**. The solid line represents the best non-linear fit of the data to a competitive binding model ($K_a = (4.4 \pm 0.3) \times 10^4\ M^{-1}$).

(A)

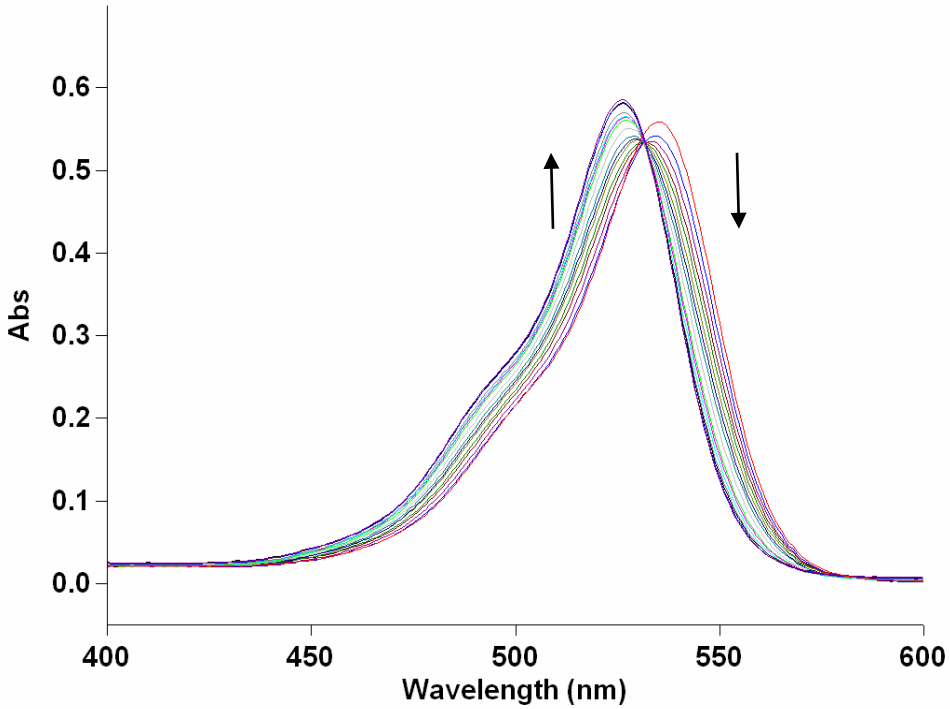

(B)

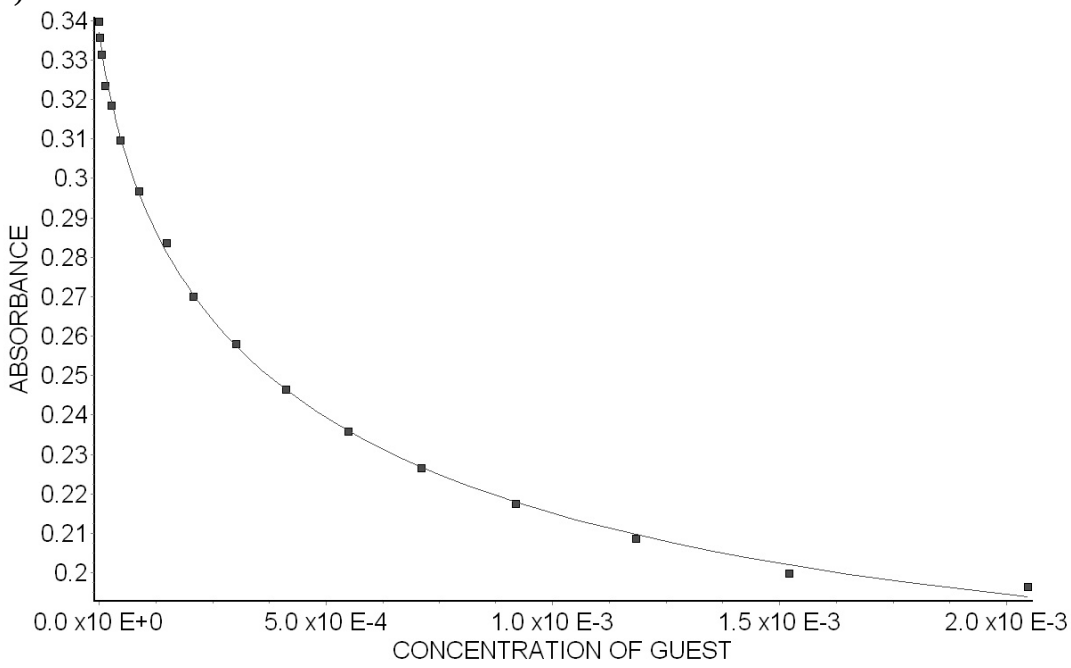

Figure II-S6. (A) UV/Vis spectra from the titration of **II-2** (9.92 µM) and Rhodamine 6G (10.0 µM) with guest **II-15** (0 – 2.05 mM) in 20 mM NaH_2PO_4 buffer (pH = 7.4); (B) plot of the A_{550} as a function of the concentration of **II-15**. The solid line represents the best non-linear fit of the data to a competitive binding model ($K_a = (4.8 \pm 0.3) \times 10^4\ M^{-1}$)

(A)

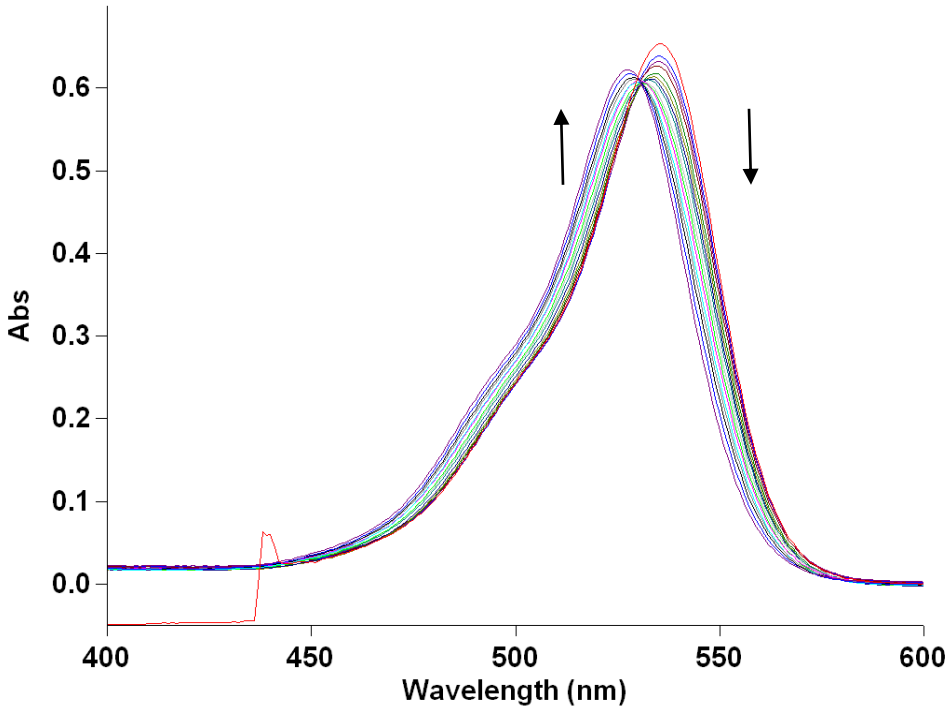

(B)

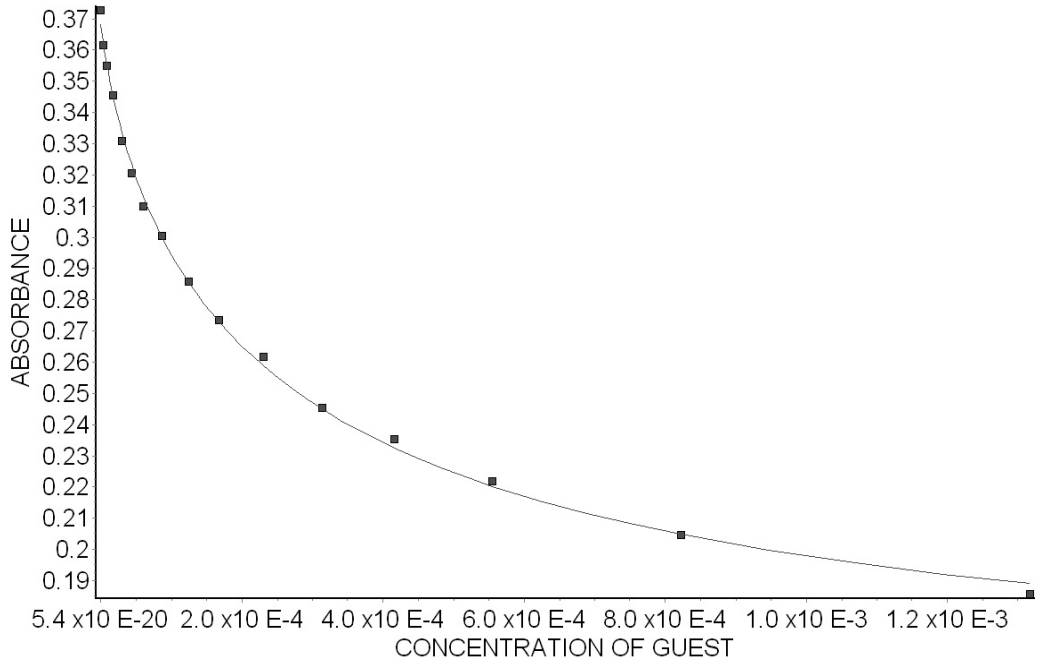

Figure II-S7. (A) UV/Vis spectra from the titration of **II-2** (9.92 µM) and Rhodamine 6G (10.0 µM) with guest **II-16** (0 – 1.32 mM) in 20 mM NaH_2PO_4 buffer (pH = 7.4); (B) plot of the A_{550} as a function of the concentration of **II-16**. The solid line represents the best non-linear fit of the data to a competitive binding model ($K_a = (8.3 \pm 0.6) \times 10^4\ M^{-1}$).

(A)

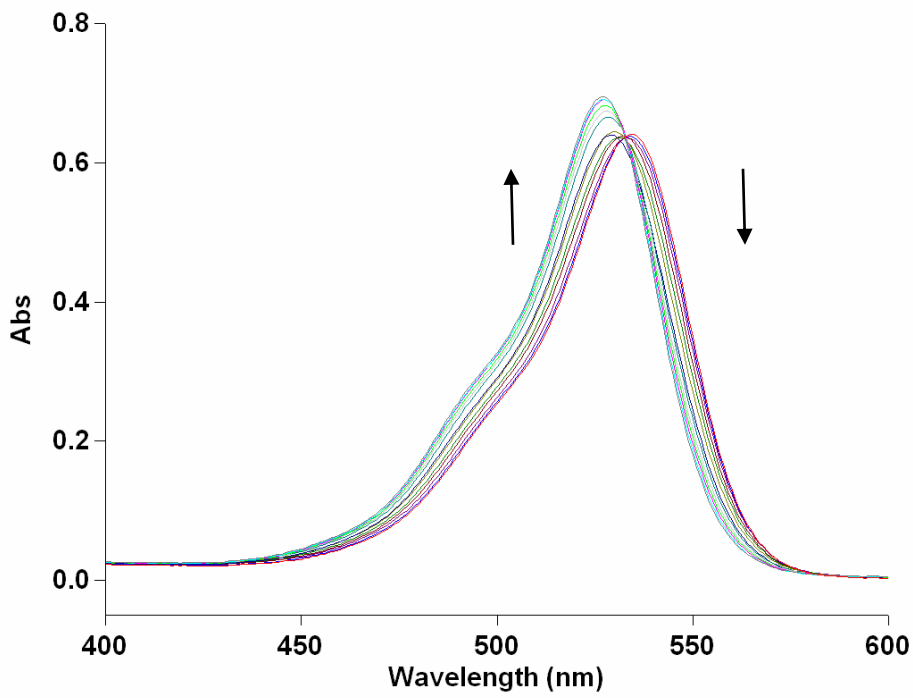

(B)

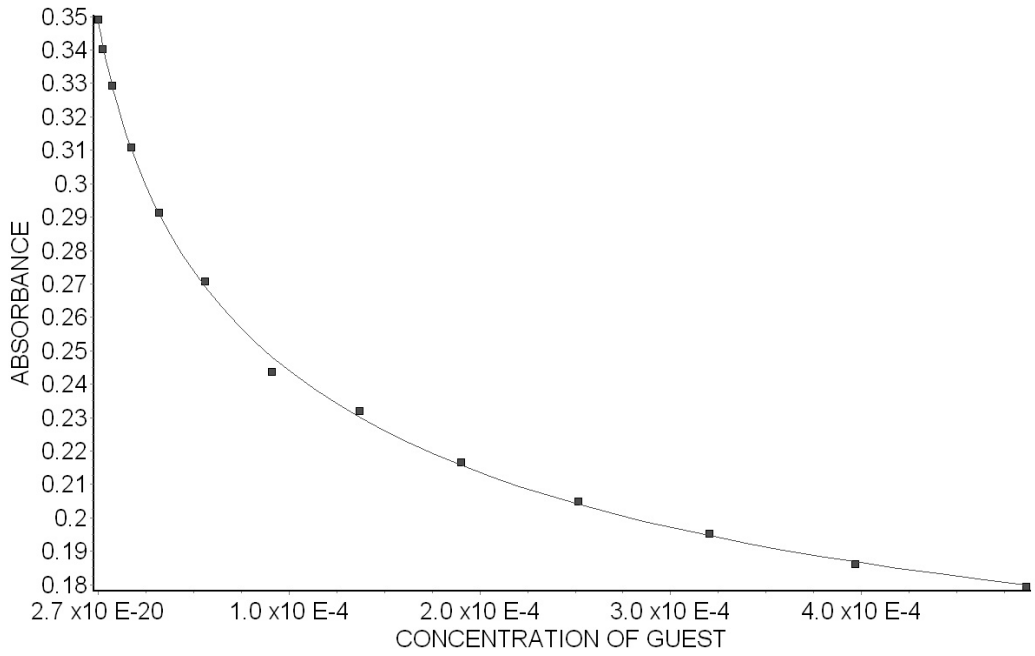

Figure II-S8. (A) UV/Vis spectra from the titration of **II-2** (10.1 µM) and Rhodamine 6G (9.96 µM) with guest **II-17** (0 – 486 µM) in 20 mM NaH_2PO_4 buffer (pH = 7.4); (B) plot of the A_{550} as a function of the concentration of **II-17**. The solid line represents the best non-linear fit of the data to a competitive binding model ($K_a = (1.9 \pm 0.1) \times 10^5\ M^{-1}$).

(A)

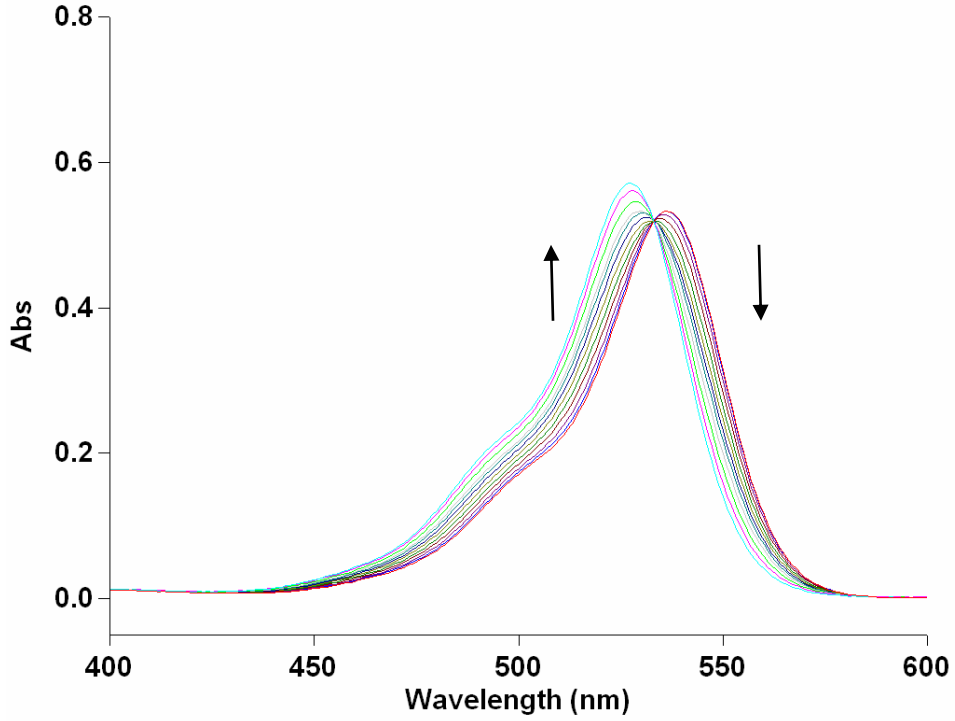

(B)

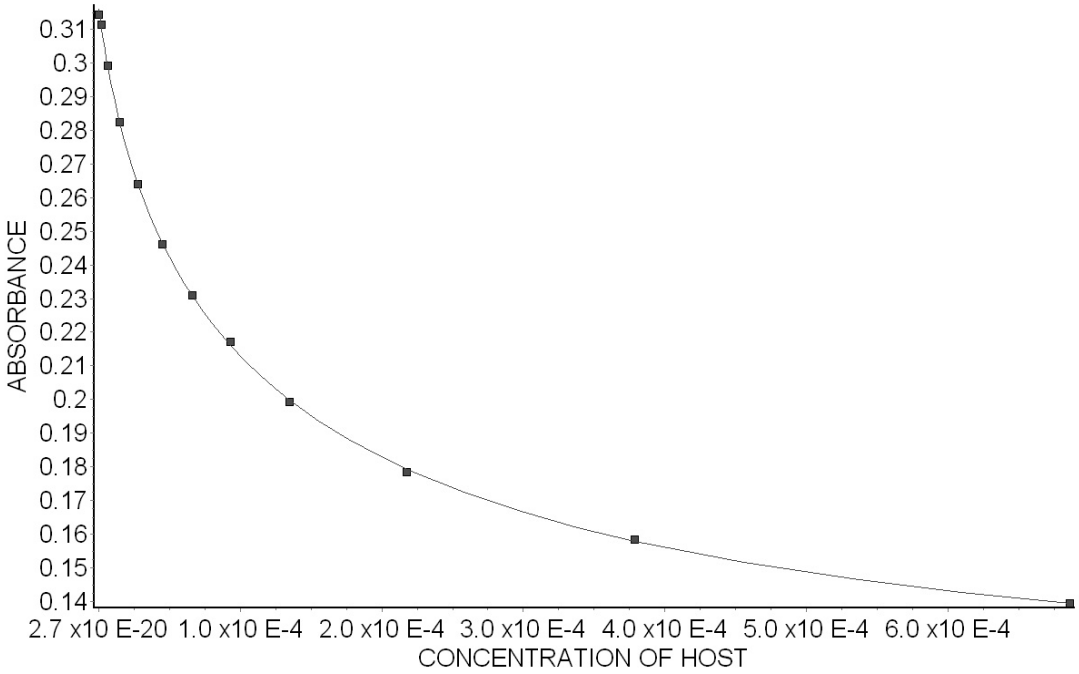

Figure II-S9. (A) UV/Vis spectra from the titration of **II-2** (10.2 µM) and Rhodamine 6G (9.96 µM) with guest **II-18** (0 – 686 µM) in 20 mM NaH_2PO_4 buffer (pH = 7.4); (B) plot of the A_{550} as a function of the concentration of **II-18**. The solid line represents the best non-linear fit of the data to a competitive binding model ($K_a = (1.9 \pm 0.6) \times 10^5\ M^{-1}$).

(A)

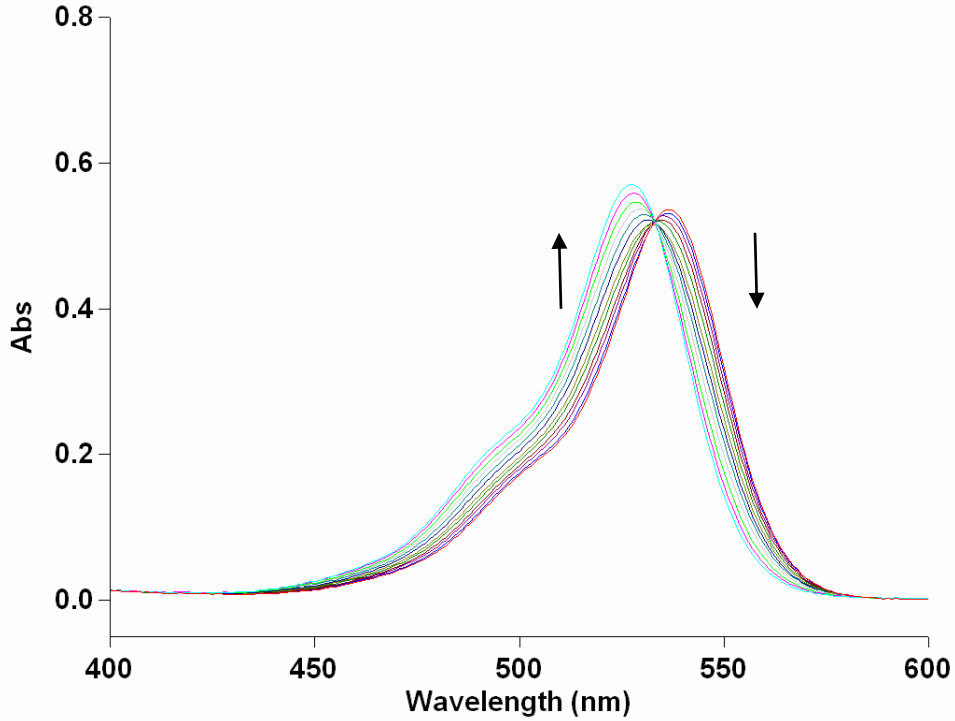

(B)

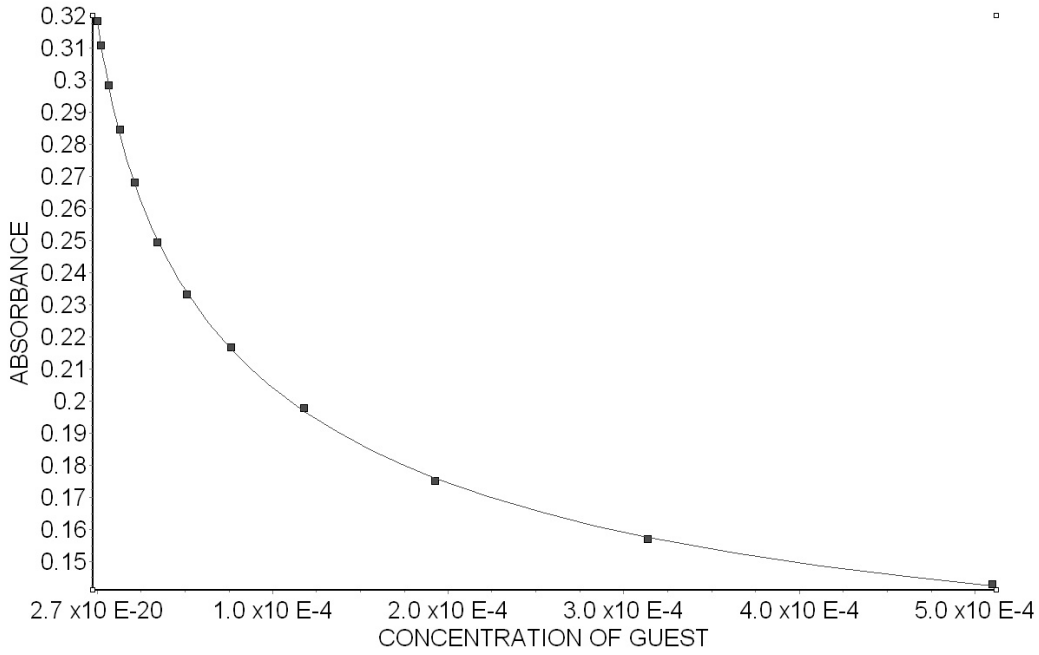

Figure II-S10. (A) UV/Vis spectra from the titration of **II-2** (10.2 μM) and Rhodamine 6G (10.3 μM) with guest **II-19** (0 – 510 μM) in 20 mM NaH_2PO_4 buffer (pH = 7.4); (B) plot of the A_{550} as a function of the concentration of **II-19**. The solid line represents the best non-linear fit of the data to a competitive binding model ($K_a = (2.5 \pm 0.7) \times 10^5\ M^{-1}$).

(A)

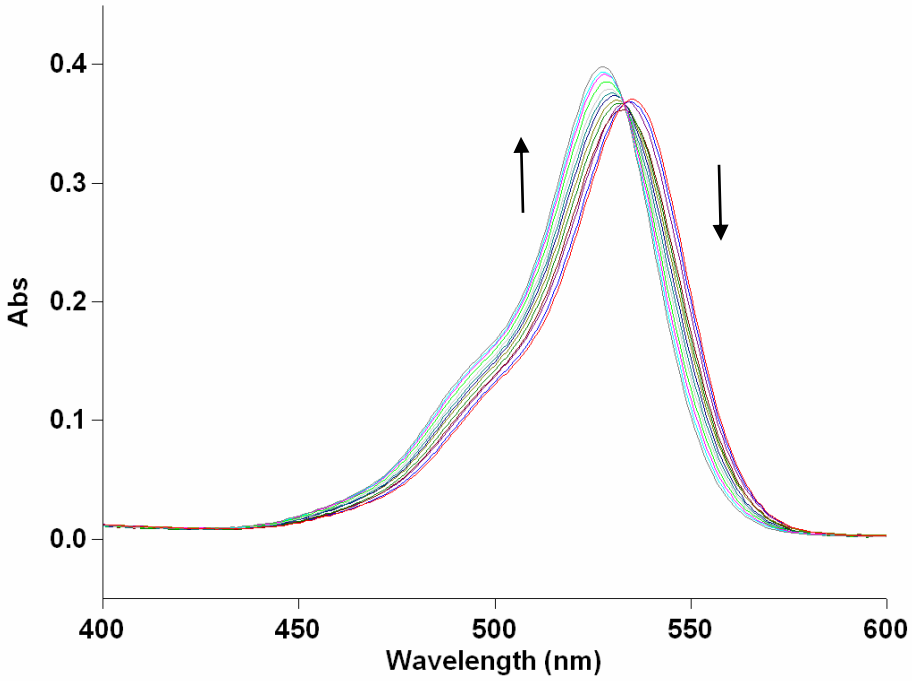

(B)

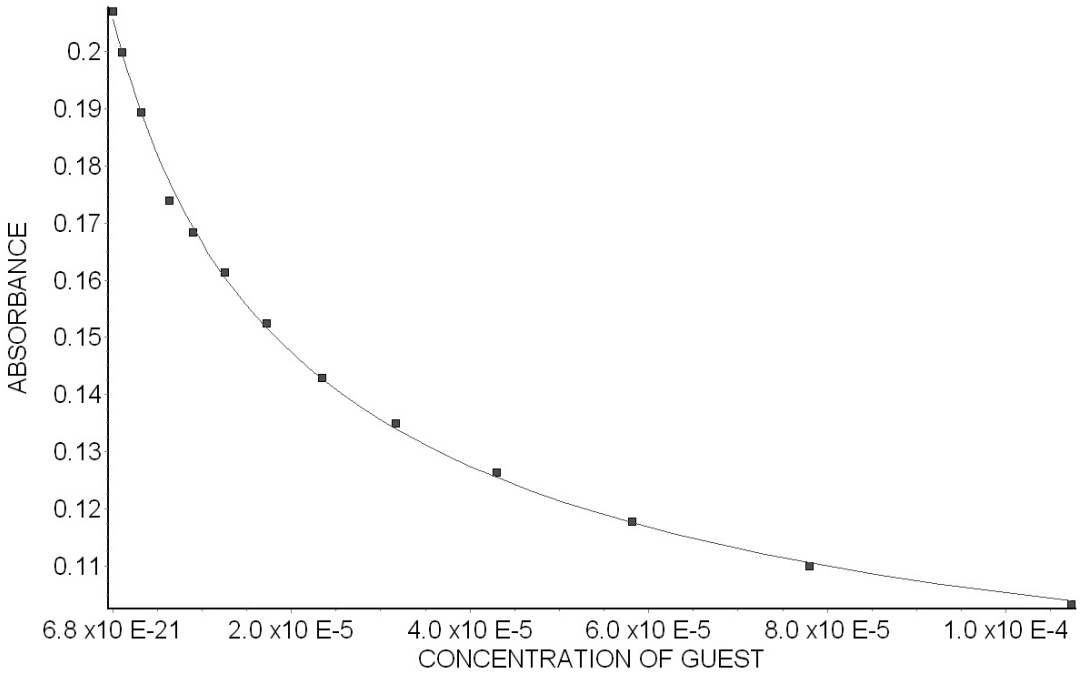

Figure II-S11. (A) UV/Vis spectra from the titration of **II-2** (5.07 μM) and Rhodamine 6G (5.01 μM) with guest **II-20** (0 – 107 μM) in 20 mM NaH_2PO_4 buffer (pH = 7.4); (B) plot of the A_{550} as a function of the concentration of **II-20**. The solid line represents the best non-linear fit of the data to a competitive binding model ($K_a = (5.3 \pm 0.4) \times 10^5\ M^{-1}$).

(A)

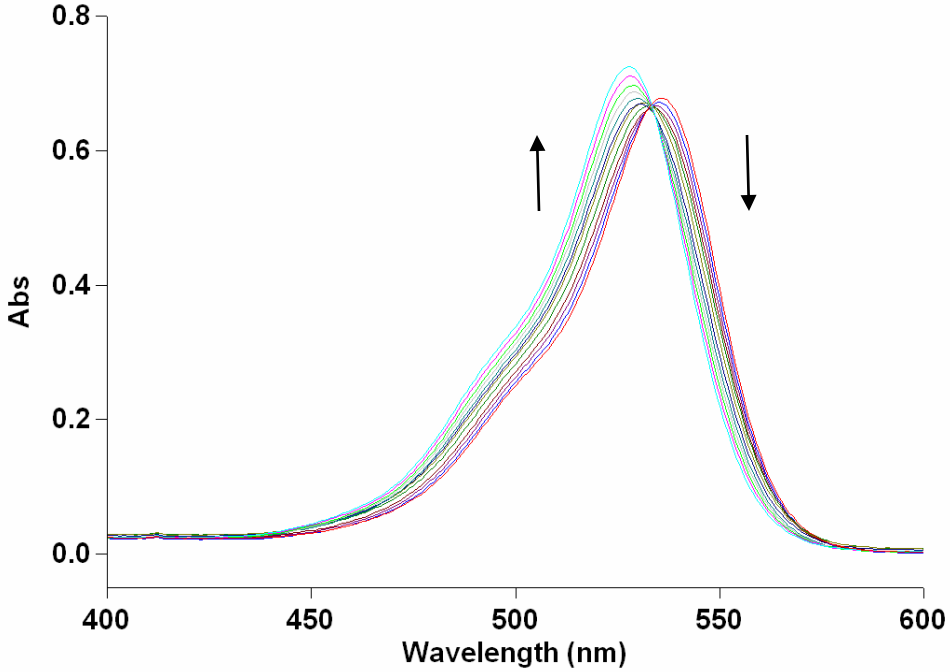

(B)

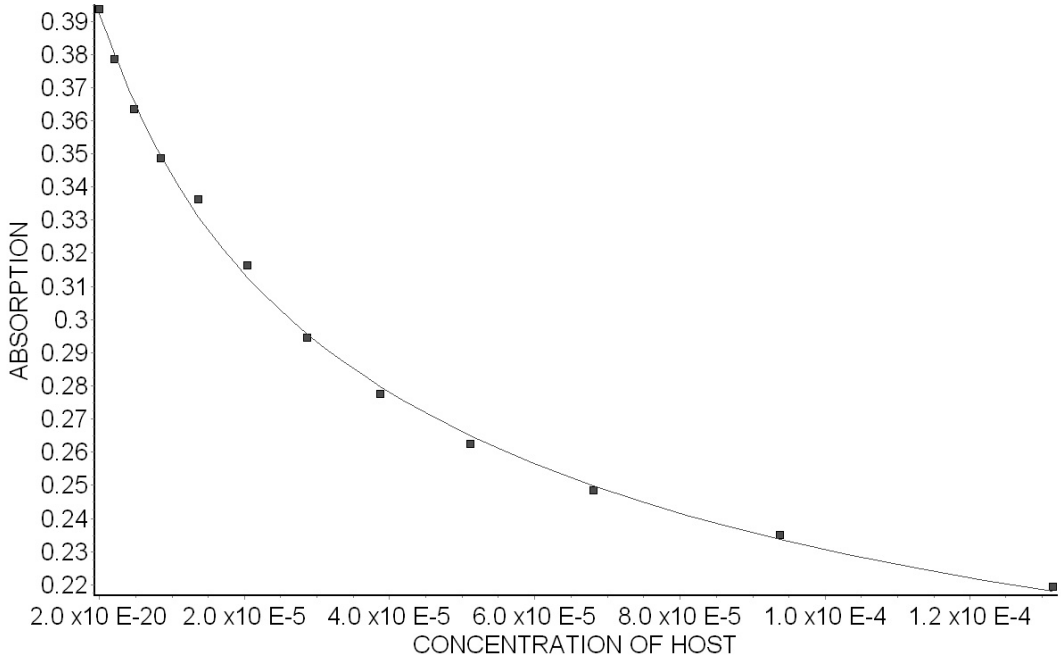

Figure II-S12. (A) UV/Vis spectra from the titration of **II-2** (12.5 µM) and Rhodamine 6G (12.4 µM) with guest **II-21** (0 –131µM) in 20mM NaH_2PO_4 buffer (pH = 7.4); (B) plot of the A_{550} as a function of the concentration of **II-21**. The solid line represents the best non-linear fit of the data to a competitive binding model ($K_a = (5.9 \pm 0.7) \times 10^5\ M^{-1}$).

(A)

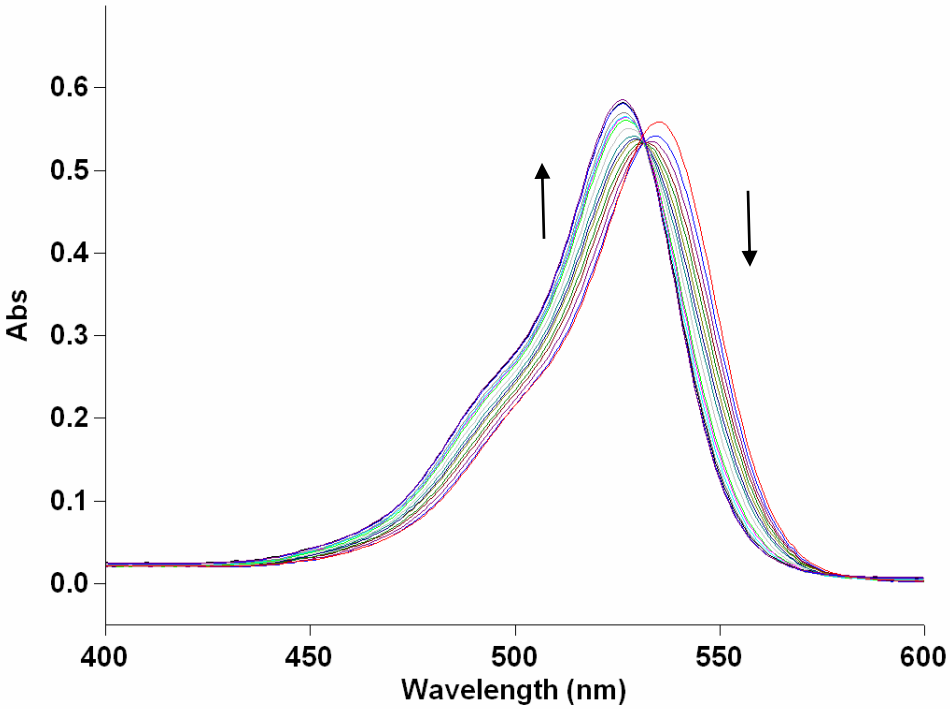

(B)

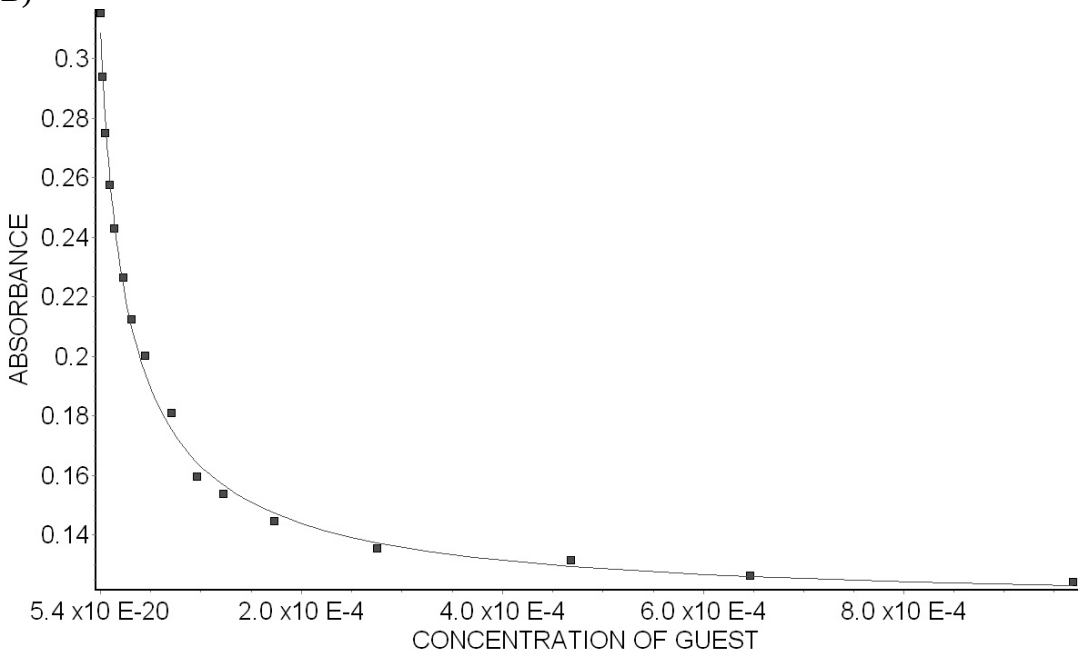

Figure II-S13. (A) UV/Vis spectra from the titration of **II-2** (9.92 µM) and Rhodamine 6G (10.0 µM) with guest **II-22** (0 – 968 µM) in 20 mM NaH_2PO_4 buffer (pH = 7.4); (B) plot of the A_{550} as a function of the concentration of **II-22**. The solid line represents the best non-linear fit of the data to a competitive binding model ($K_a = (8.0 \pm 0.7) \times 10^5\ M^{-1}$).

(A)

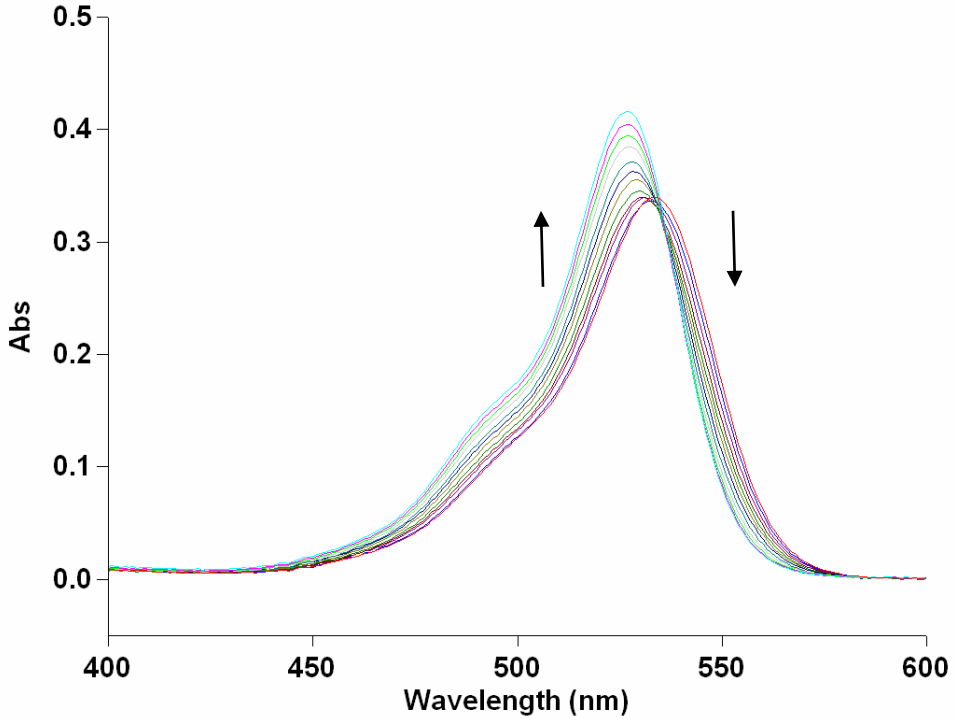

(B)

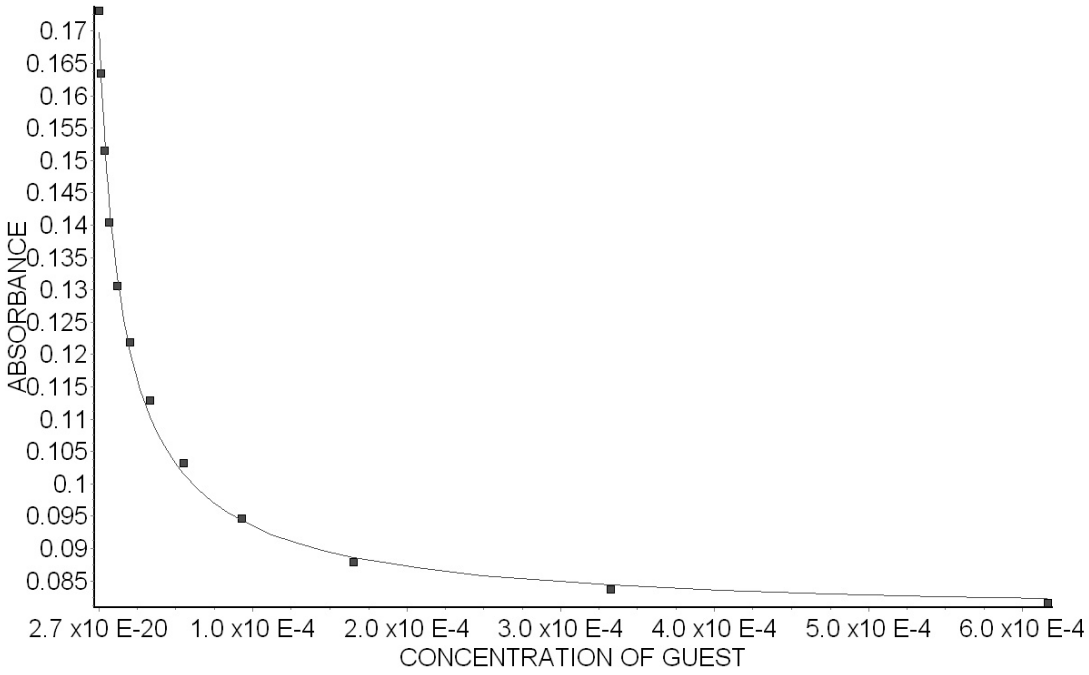

Figure II-S14. (A) UV/Vis spectra from the titration of **II-2** (5.07 µM) and Rhodamine 6G (5.01 µM) with guest **II-23** (0 – 616 µM) in 20 mM NaH_2PO_4 buffer (pH = 7.4); (B) plot of the A_{550} as a function of the concentration of **II-23**. The solid line represents the best non-linear fit of the data to a competitive binding model ($K_a = (8.2 \pm 0.9) \times 10^5\ M^{-1}$).

(A)

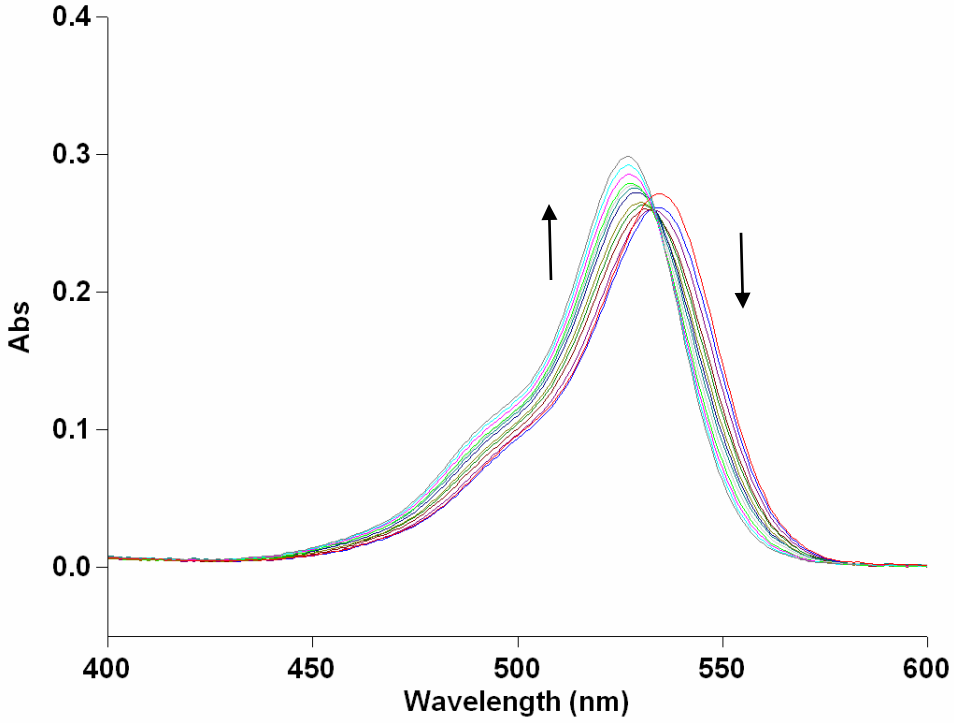

(B)

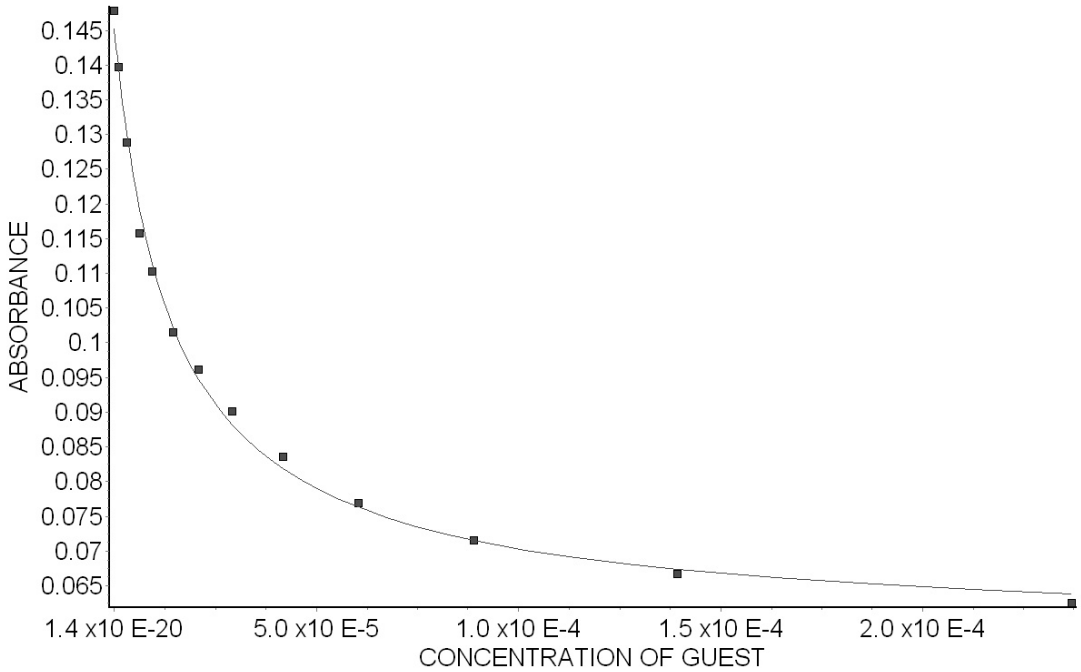

Figure II-S15. (A) UV/Vis spectra from the titration of **II-2** (5.07 μM) and Rhodamine 6G (5.01 μM) with guest **II-24** (0 – 237 μM) in 20 mM NaH_2PO_4 buffer (pH = 7.4); (B) plot of the A_{550} as a function of the concentration of **II-24**. The solid line represents the best non-linear fit of the data to a competitive binding model ($K_a = (9.3 \pm 0.9) \times 10^5\ M^{-1}$).

(A)

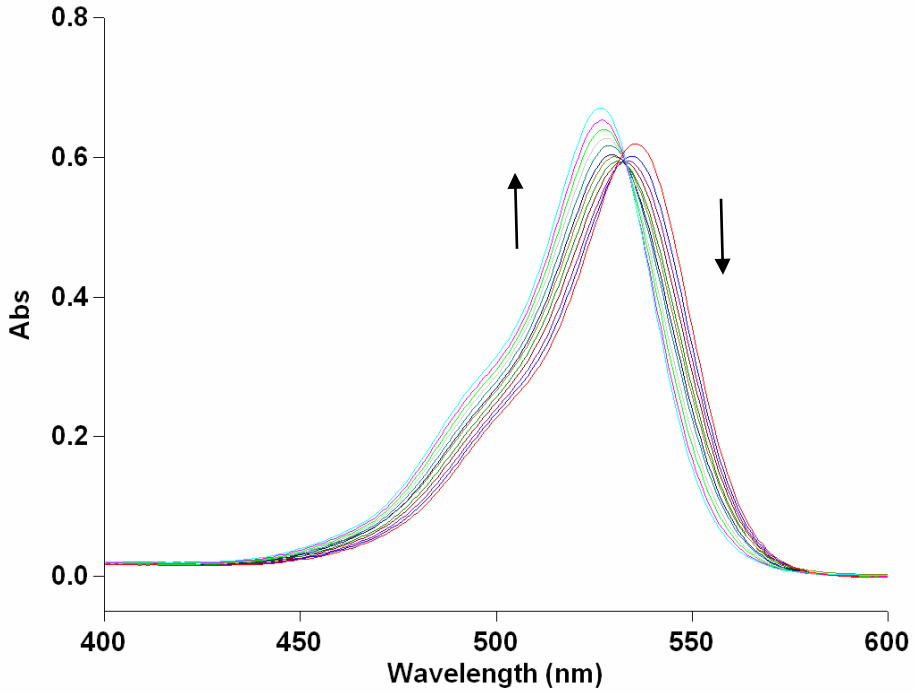

(B)

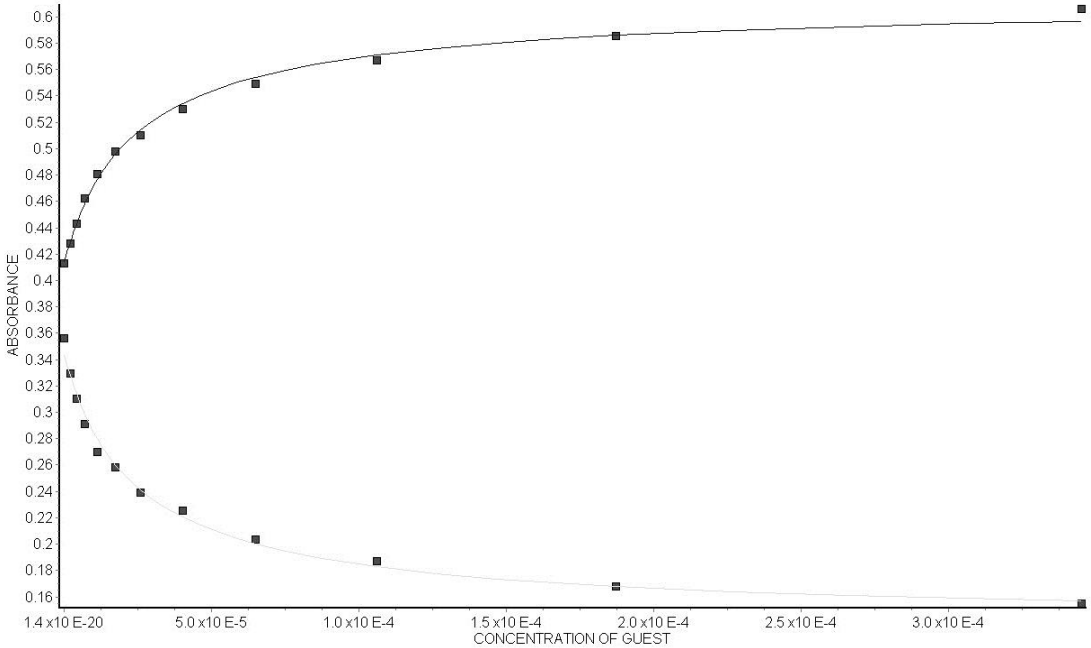

Figure II-S16. (A) UV/Vis spectra from the titration of **II-2** (10.1 µM) and Rhodamine 6G (9.96 µM) with guest **II-25** (0 – 345 µM) in 20 mM NaH_2PO_4 buffer (pH = 7.4); (B) plot of the A_{550} as a function of the concentration of **II-25**. The solid line represents the best non-linear fit of the data to a competitive binding model ($K_a = (9.7 \pm 1.1) \times 10^5\ M^{-1}$

(A)

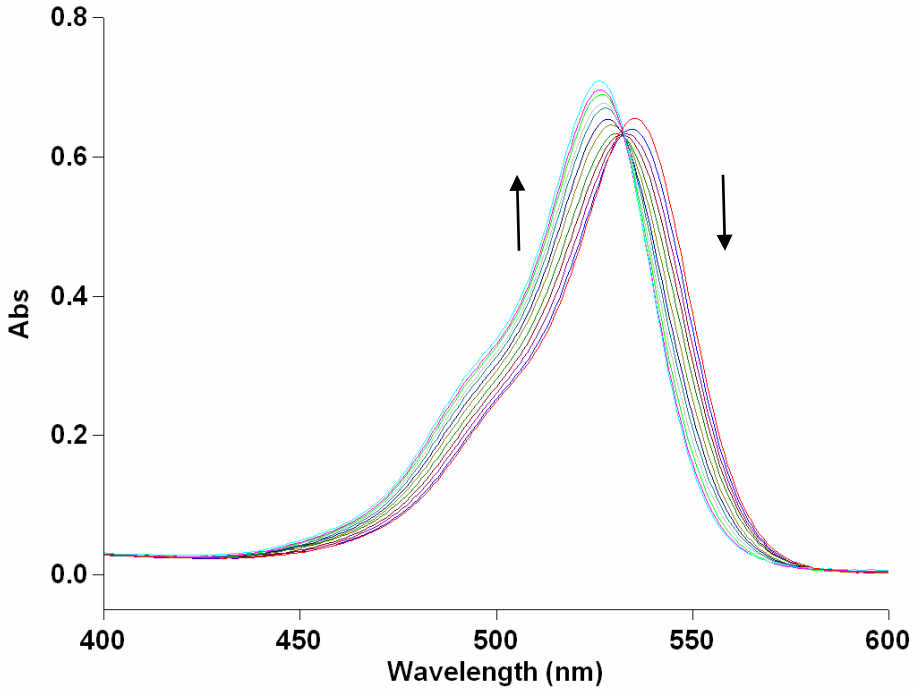

(B)

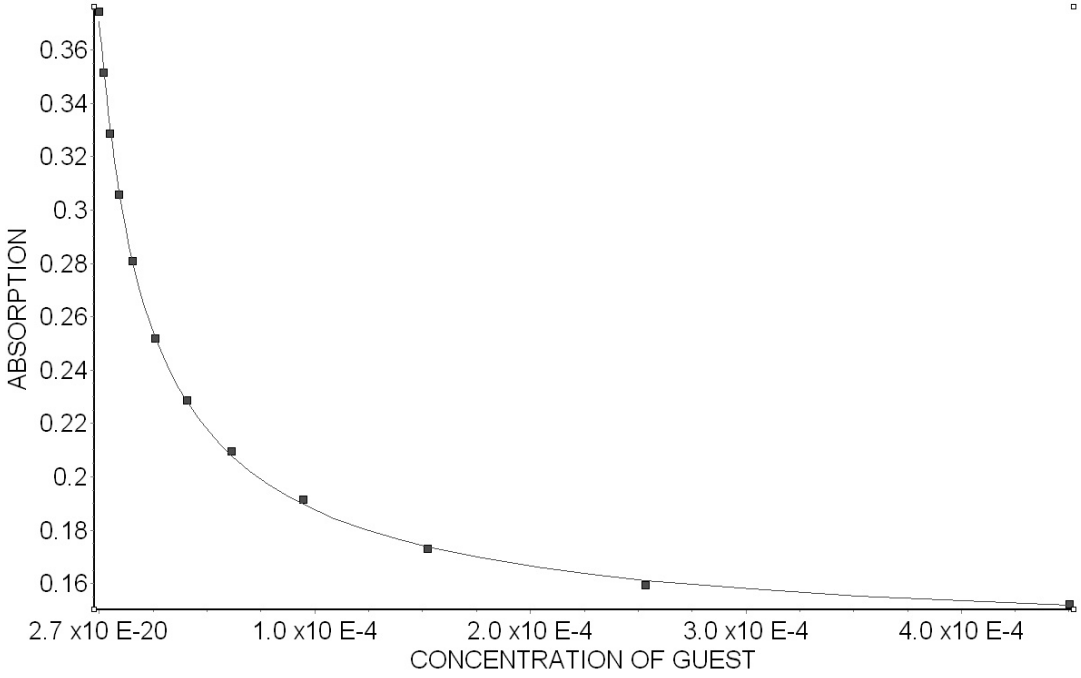

Figure II-S17. (A) UV/Vis spectra from the titration of **II-2** (10.1 µM) and Rhodamine 6G (9.96 µM) with guest **II-26** (0 – 450 µM) in 20 mM NaH_2PO_4 buffer (pH = 7.4); (B) plot of the A_{550} as a function of the concentration of **II-26**. The solid line represents the best non-linear fit of the data to a competitive binding model ($K_a = (9.8 \pm 0.5) \times 10^5\ M^{-1}$).

(A)

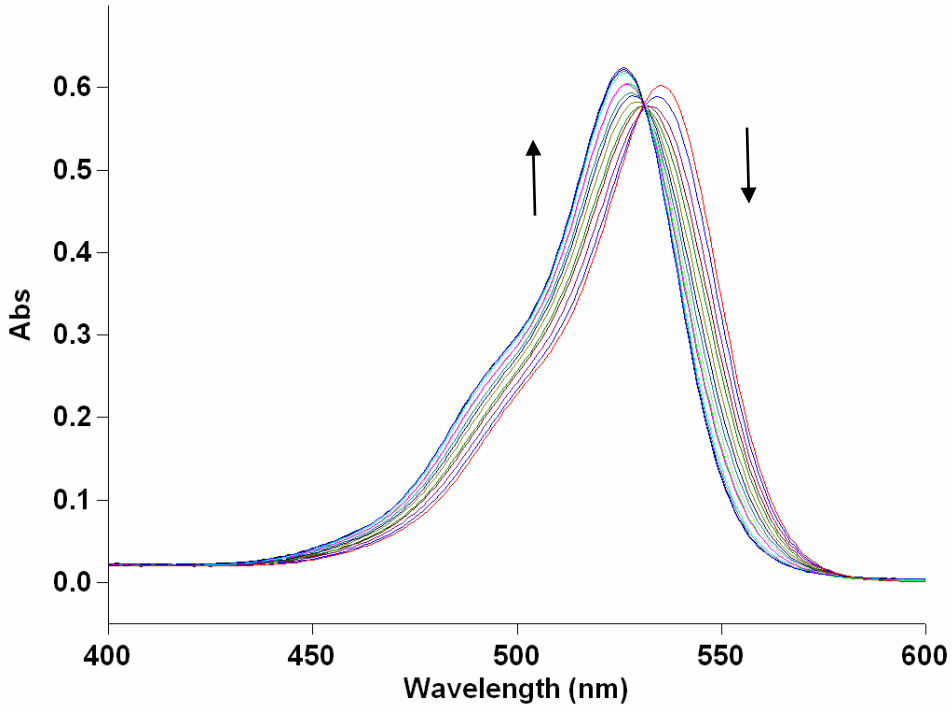

(B)

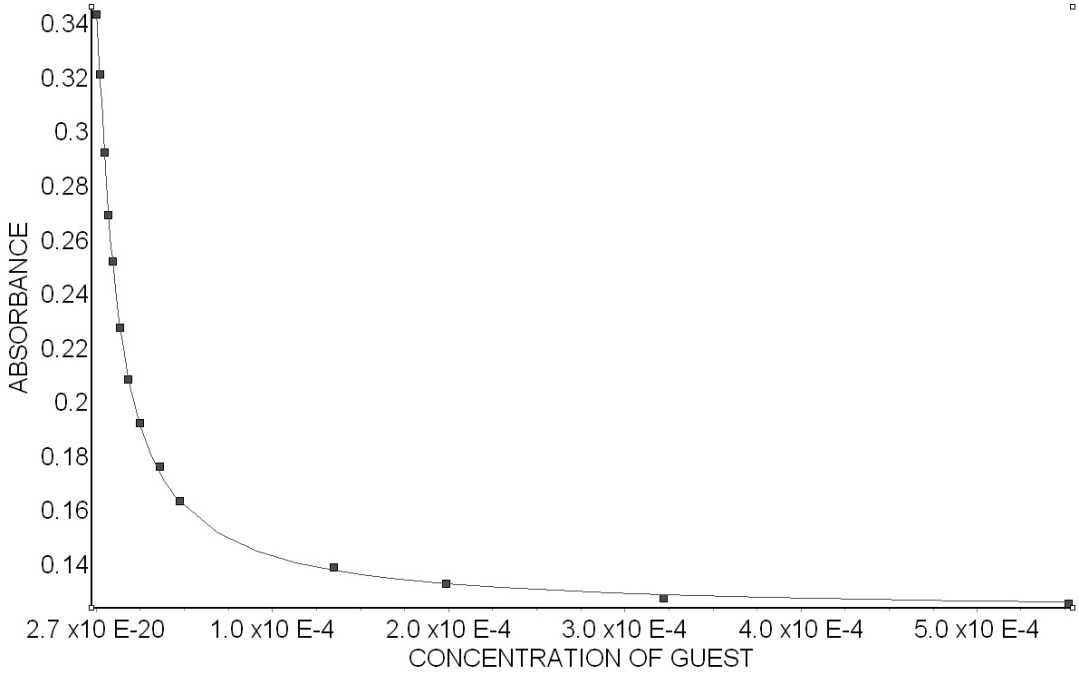

Figure II-S18. (A) UV/Vis spectra from the titration of **II-2** (9.92 μM) and Rhodamine 6G (10.0 μM) with guest **II-27** (0 – 552 μM) in 20 mM NaH_2PO_4 buffer (pH = 7.4); (B) plot of the A_{550} as a function of the concentration of **II-27**. The solid line represents the best non-linear fit of the data to a competitive binding model ($K_a = (2.8 \pm 0.1) \times 10^6\ M^{-1}$).

(A)

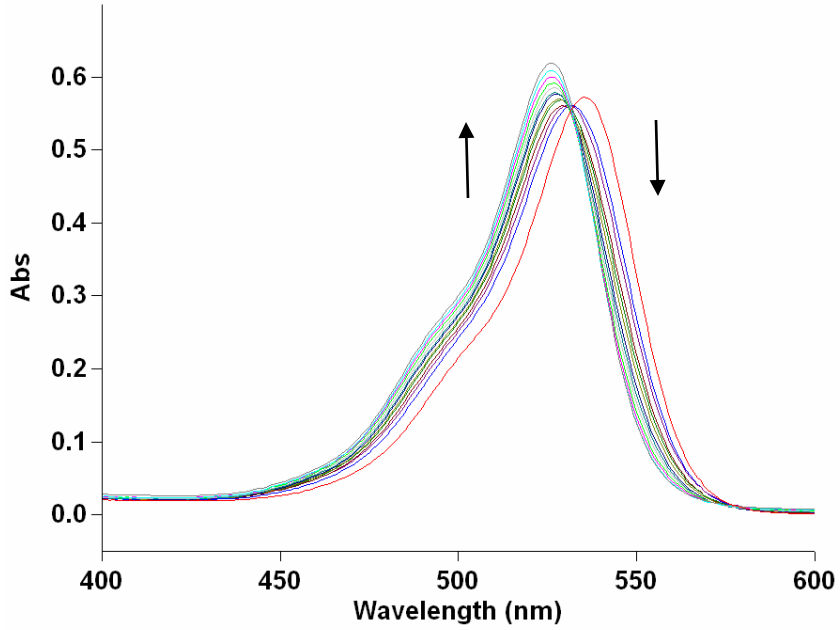

(B)

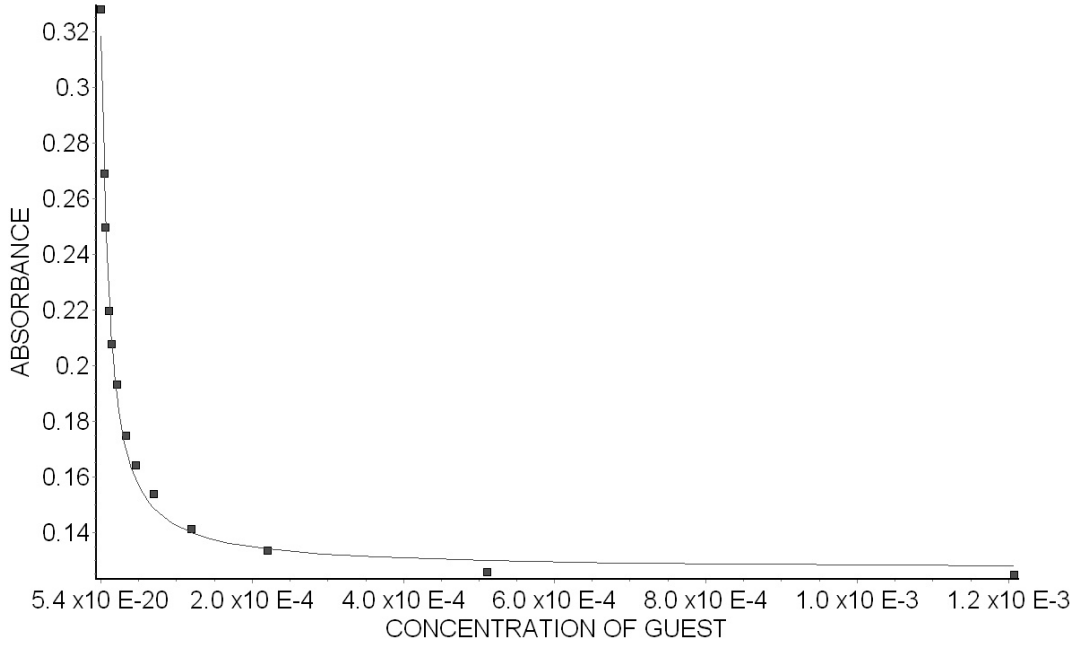

Figure II-S19. (A) UV/Vis spectra from the titration of **II-2** (9.92 μM) and Rhodamine 6G (10.0 μM) with guest **II-28** (0 – 1.21 mM) in 20 mM NaH_2PO_4 buffer (pH = 7.4); (B) plot of the A_{550} as a function of the concentration of **II-28**. The solid line represents the best non-linear fit of the data to a competitive binding model ($K_a = (3.3 \pm 0.5) \times 10^6\ M^{-1}$).

(A)

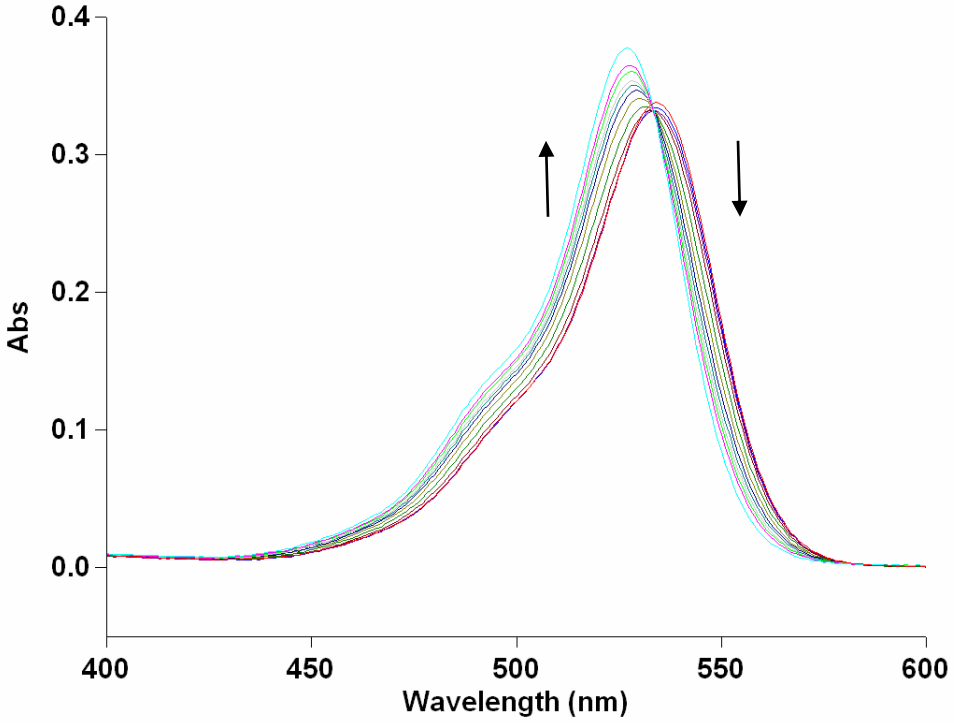

(B)

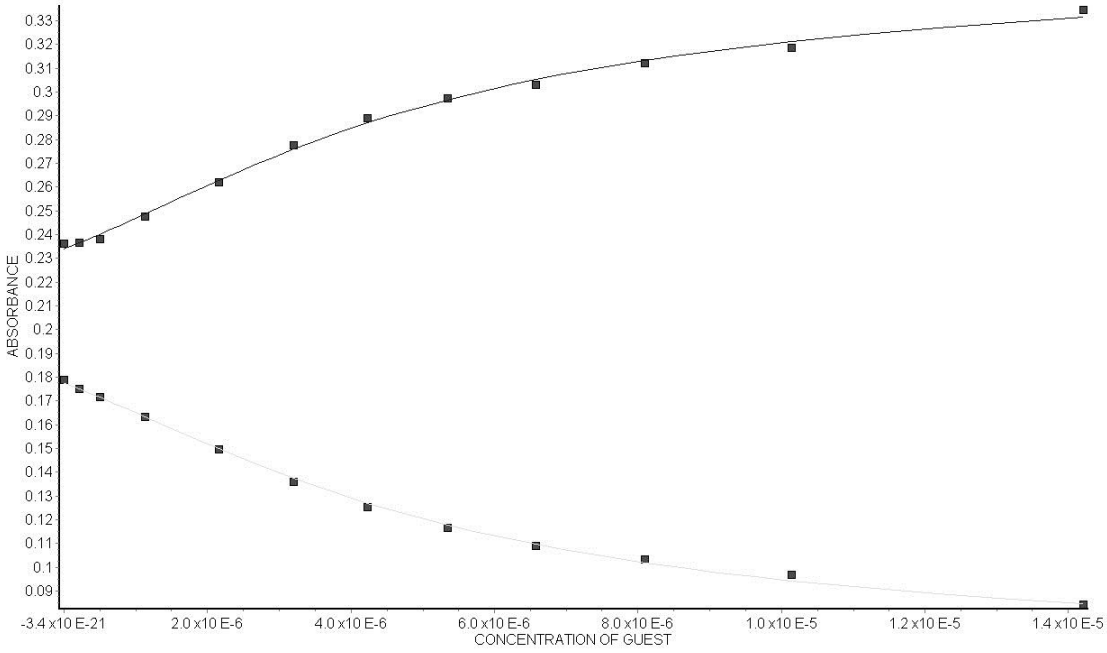

Figure II-S20. (A) UV/Vis spectra from the titration of **II-2** (5.07 μM) and Rhodamine 6G (5.01 μM) with guest **II-29** (0 – 14.2 μM) in 20 mM NaH_2PO_4 buffer (pH = 7.4); (B) plot of the A_{550} as a function of the concentration of **II-29**. The solid line represents the best non-linear fit of the data to a competitive binding model ($K_a = (4.5 \pm 0.7) \times 10^6\ M^{-1}$).

1:1 Binding Models for NMR

Model Fitting Absorbance at One Chemical Shift.

// Micromath Scientist Model File
// 1:1 Host:Guest binding model for NMR
//This model assumes the guest concentration is fixed and host concentration is varied
IndVars: ConcHostTot
DepVars: Deltaobs
Params: Ka, ConcGuestTot, Deltasat, Deltazero
Ka = ConcHostGuest/(ConcHostFree*ConcGuestFree)
ConcHostTot=ConcHostFree + ConcHostGuest
ConcGuestTot=ConcGuestFree + ConcHostGuest
Deltaobs = Deltazero + (Deltasat - Deltazero) * (ConcHostGuest/ConcGuestTot)
//Constraints
0 < ConcHostFree < ConcHostTot
0 < Ka
0 < ConcGuestFree < ConcGuestTot
0 < ConcHostGuest < ConcHostTot
***

Model Fitting Absorbance at Two Chemical Shifts.

// Micromath Scientist Model File
IndVars: ConcHost
DepVars: CSA, CSB
Params: Ka, CSAzero, CSAsat, CSBzero, CSBsat
Ka = ConcHG/(ConcHfree*ConcGfree)
ConcHost=ConcHfree+ConcHG
0.0001=ConcGfree+ConcHG
CSA = CSAzero + ((CSAsat-CSAzero)*(ConcHG/0.0001))
CSB = CSBzero + ((CSBsat-CSBzero)*(ConcHG/0.0001))
0<ConcHfree<ConcHost
0<ConcGfree<0.0001

(A)

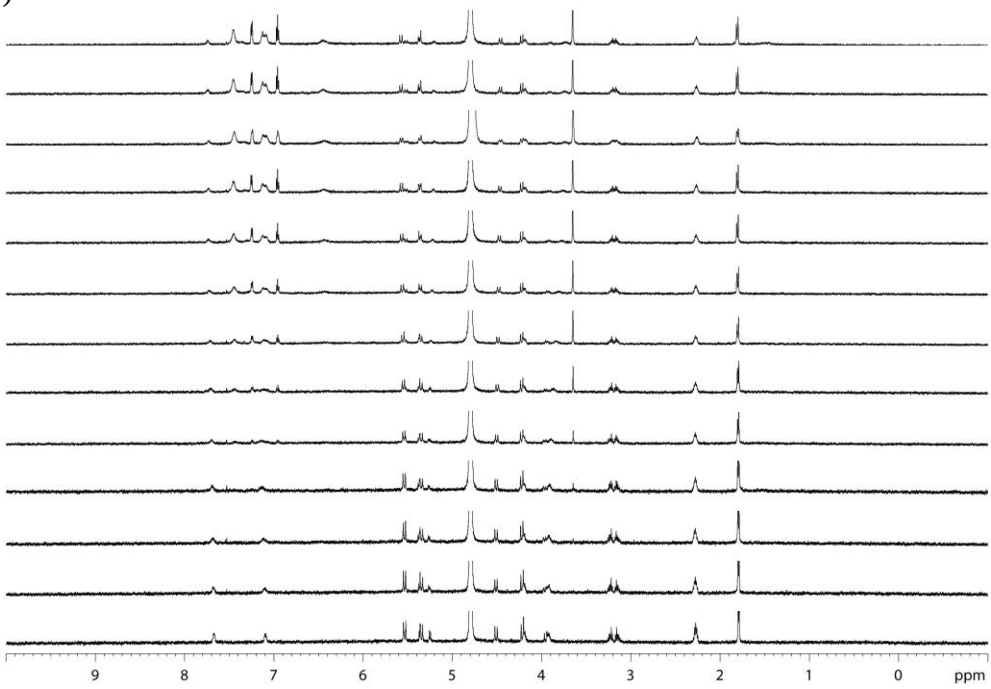

(B)

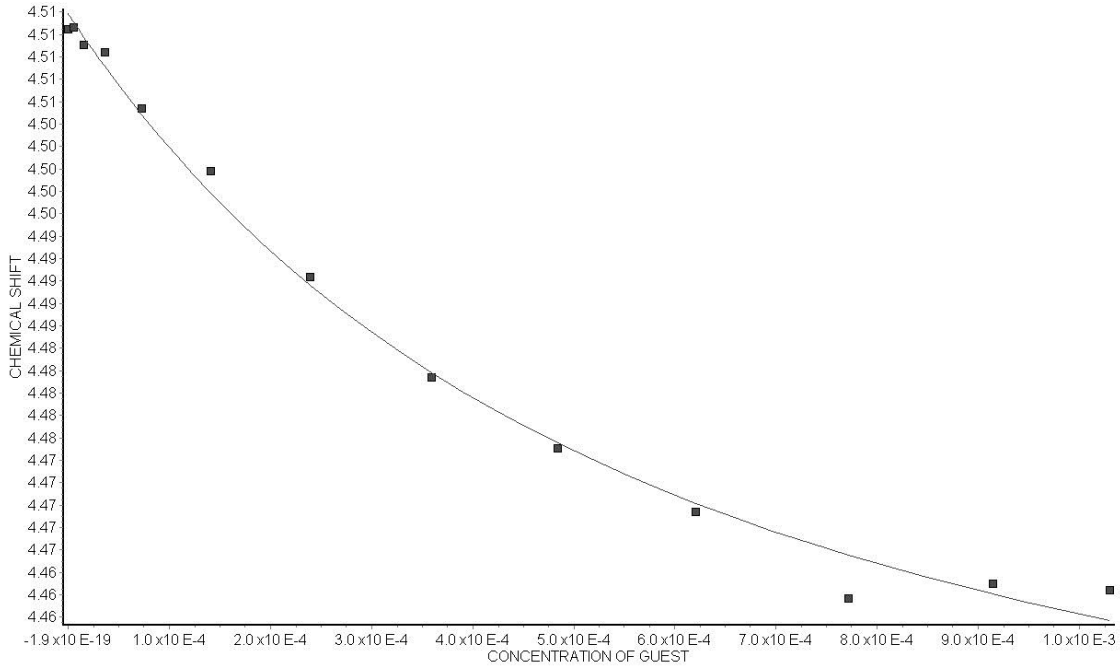

Figure II-S21. (A) ^{1}H NMR (600 MHz) stack plot of the titration of **II-2** (0.104 mM) with guest **II-3** (0 - 1.03 mM) in 20 mM NaH_2PO_4 buffered D_2O (pH = 7.4); (B) plot of the chemical shift at 7.67 ppm as a function of guest concentration. The solid line represents the best non-linear fit of the data to a 1:1 model (K_a = $(2.0 \pm 0.4) \times 10^3$ M^{-1}).

(A)

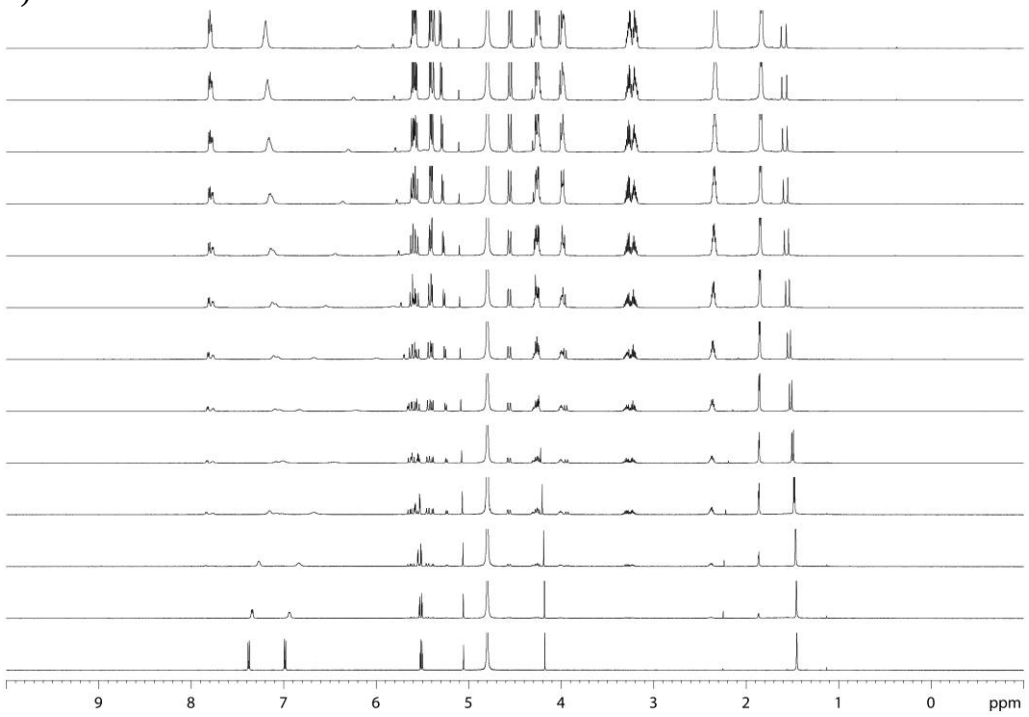

(B)

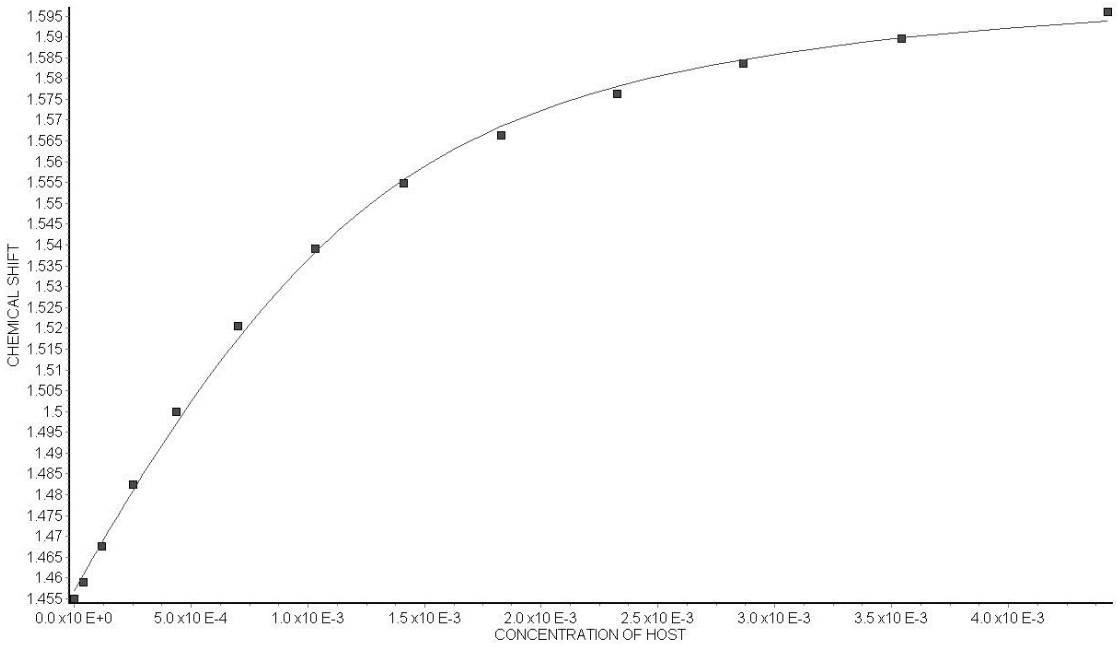

Figure II-S22. (A) ^{1}H NMR (600 MHz) stack plot of the titration of **II-2** (0 - 4.5 mM) with guest **II-5** (1.86 mM) in 20 mM NaH_2PO_4 buffered D_2O (pH = 7.4); (B) plot of the chemical shift at 1.46 ppm as a function of host concentration. The solid line represents the best non-linear fit of the data to a 1:1 model (K_a = (3.0 ± 0.4) × 10^3 M^{-1}).

(A)

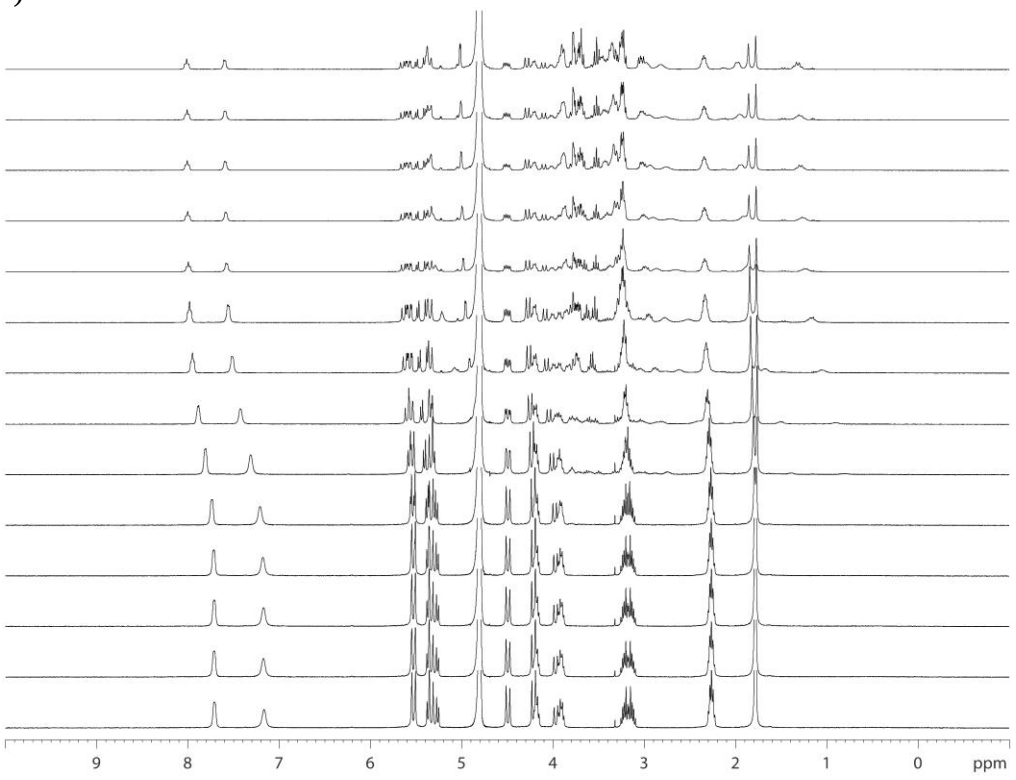

(B)

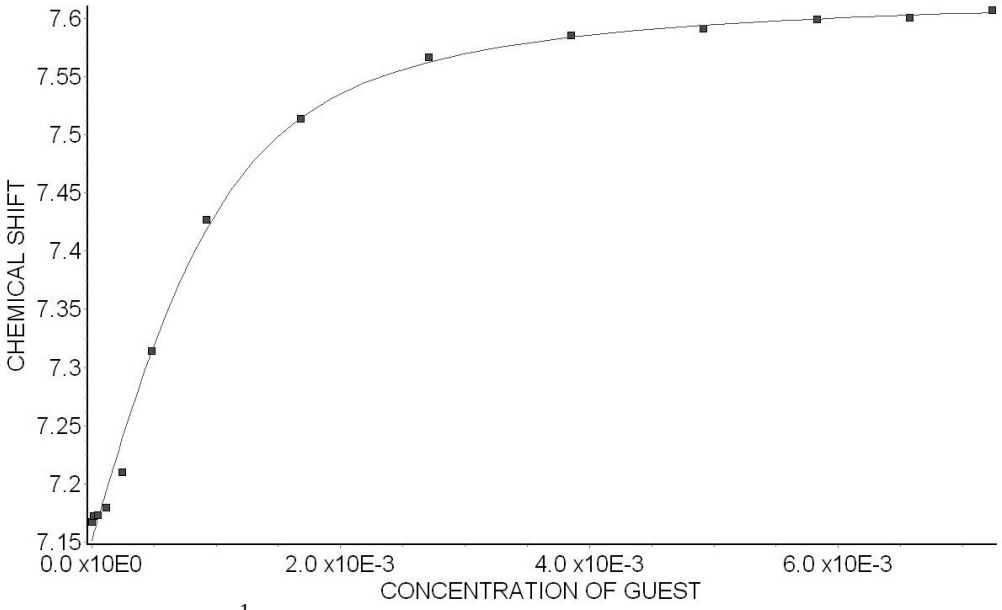

Figure II-S23. (A) ^{1}H NMR (400 MHz) stack plot of the titration of **II-2** (0.976 mM) with guest **II-6** (0 - 7.24 mM) in 20 mM NaH_2PO_4 buffered D_2O (pH = 7.4); (B) plot of the chemical shift at 7.17 ppm as a function of guest concentration. The solid line represents the best non-linear fit of the data to a 1:1 model (K_a = $(3.0 \pm 0.6) \times 10^3$ M^{-1}).

(A)

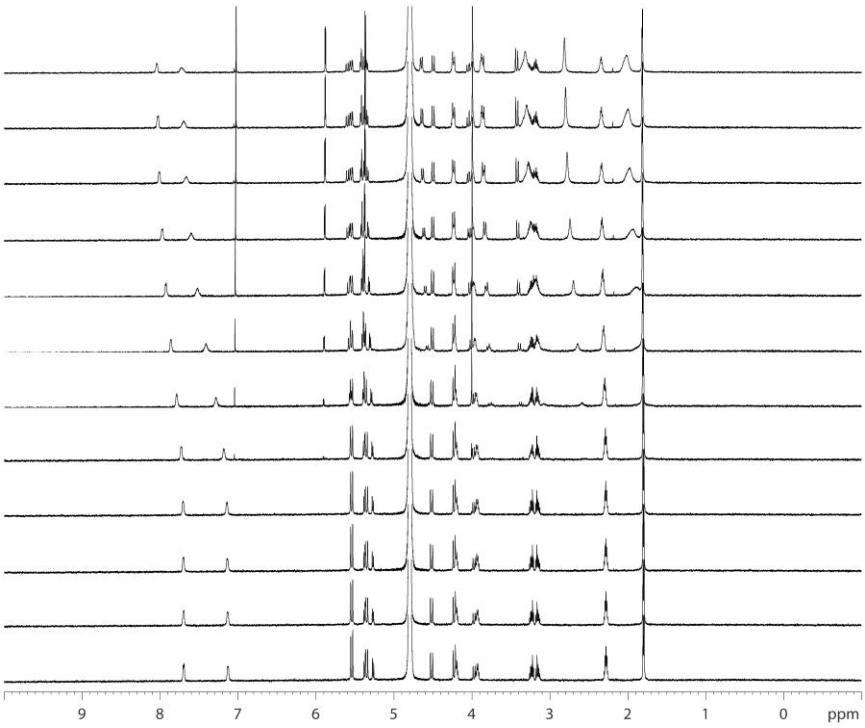

(B)

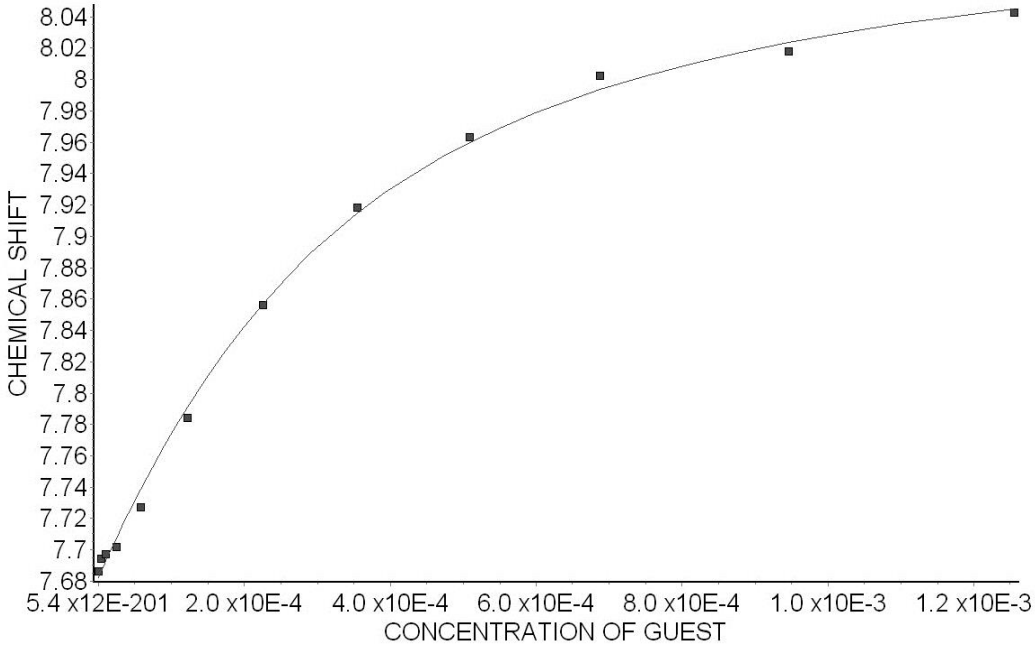

Figure II-S24. (A) ^{1}H NMR (600 MHz) stack plot of the titration of **II-2** (0.199 mM) with guest **II-7** (0 - 1.26 mM) in 20 mM NaH_2PO_4 buffered D_2O (pH = 7.4); (B) plot of the chemical shift at 7.69 ppm as a function of guest concentration. The solid line represents the best non-linear fit of the data to a 1:1 model (K_a = $(4.6 \pm 0.5) \times 10^3$ M^{-1}).

(A)

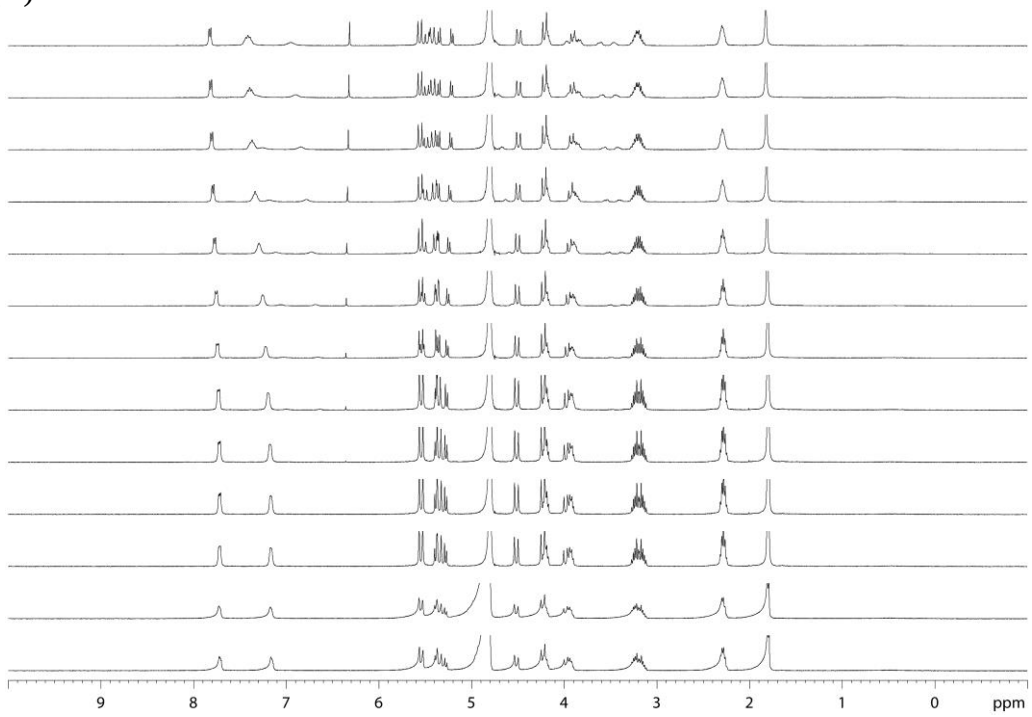

(B)

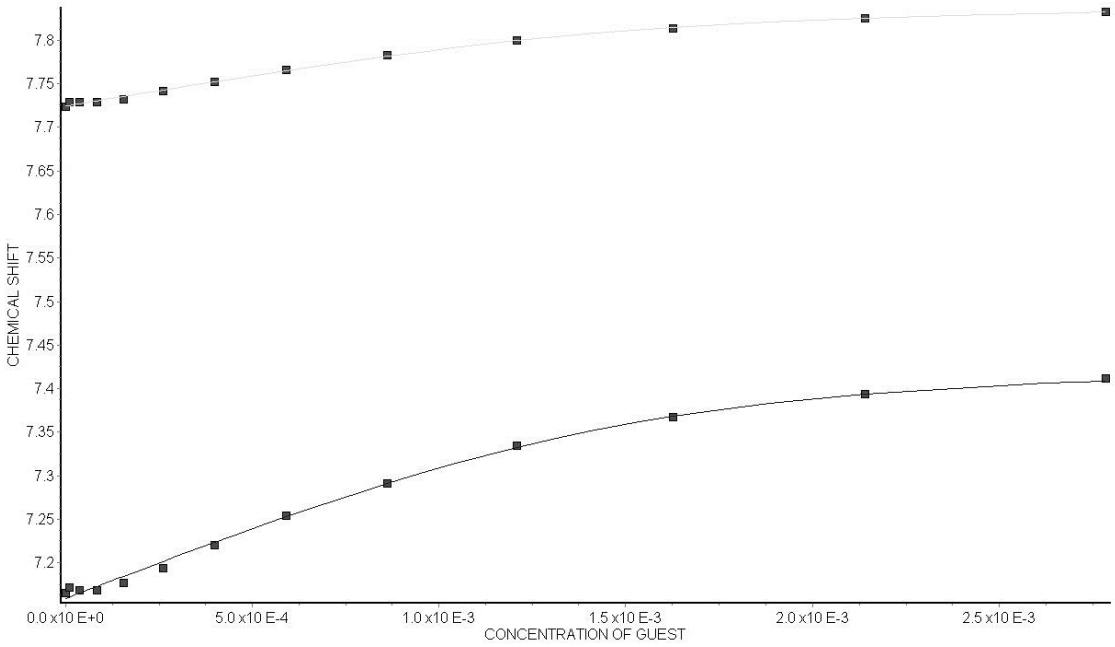

Figure II-S25. (A) ^{1}H NMR (600 MHz) stack plot of the titration of **II-2** (1.50 mM) with guest **II-9** (0 - 2.7 mM) in 20 mM NaH_2PO_4 buffered D_2O (pH = 7.4); (B) plot of the chemical shift at 7.15 and 7.72 ppm as a function of guest concentration. The solid line represents the best non-linear fit of the data to a 1:1 model ($K_a = (5.9 \pm 1.8) \times 10^3\ M^{-1}$).

(A)

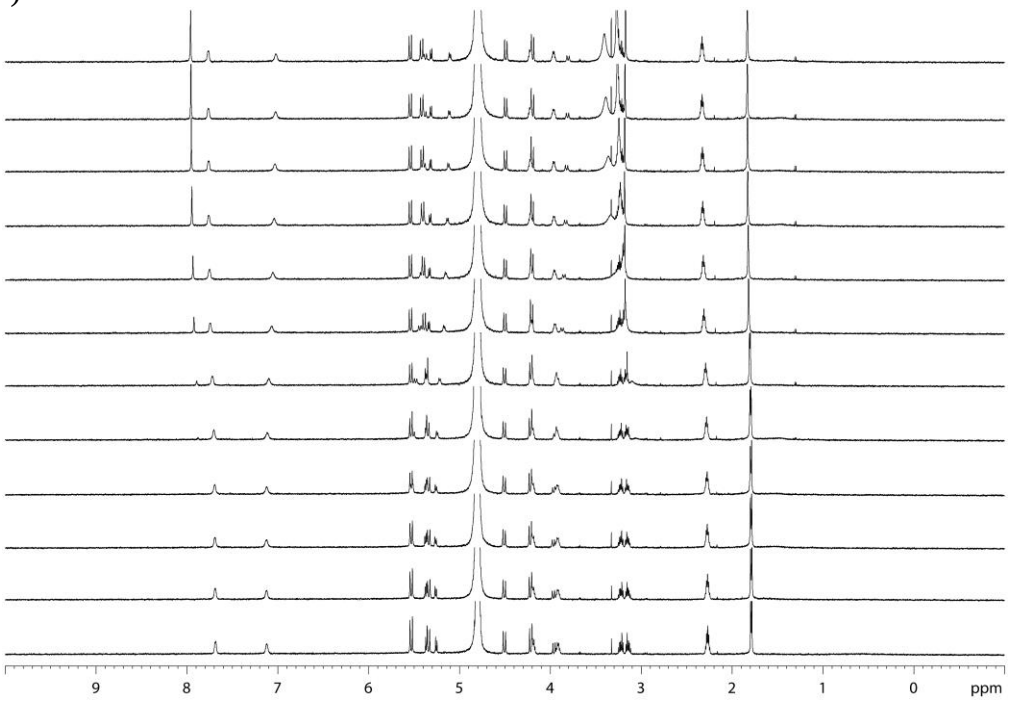

(B)

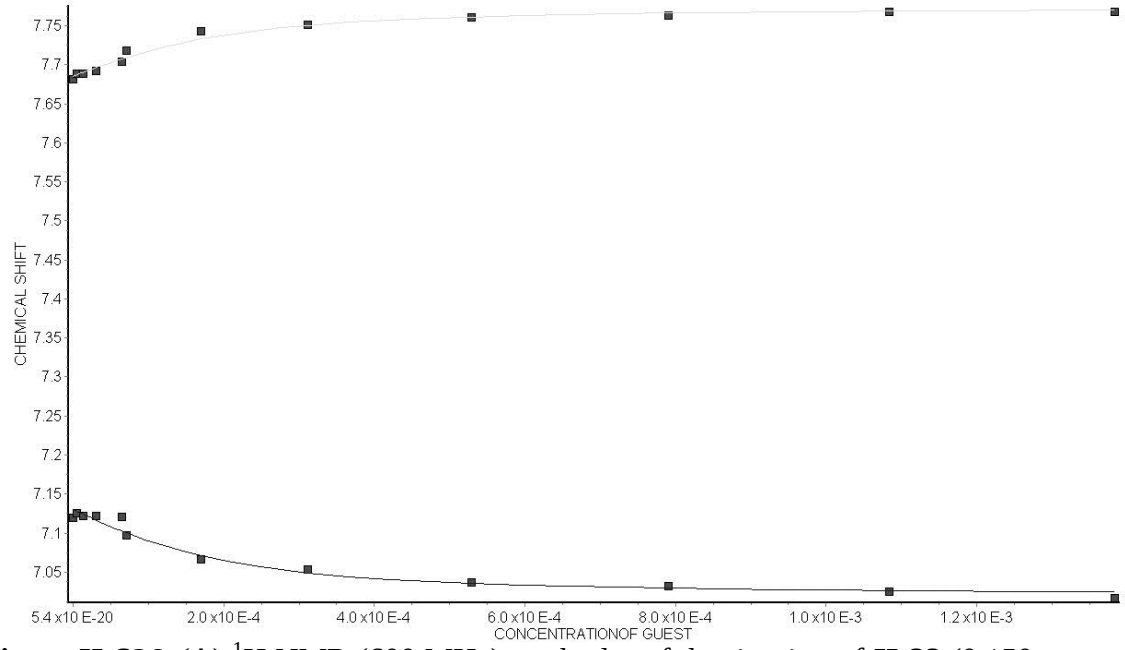

Figure II-S26. (A) ^{1}H NMR (600 MHz) stack plot of the titration of **II-22** (0.150 mM) with guest **II-11** (0 - 1.3 mM) in 20 mM NaH_2PO_4 buffered D_2O (pH = 7.4); (B) plot of the chemical shift at 7.12 and 7.68 ppm as a function of guest concentration. The solid line represents the best non-linear fit of the data to a 1:1 model ($K_a = (1.4 \pm 0.4) \times 10^4\ M^{-1}$).

(A)

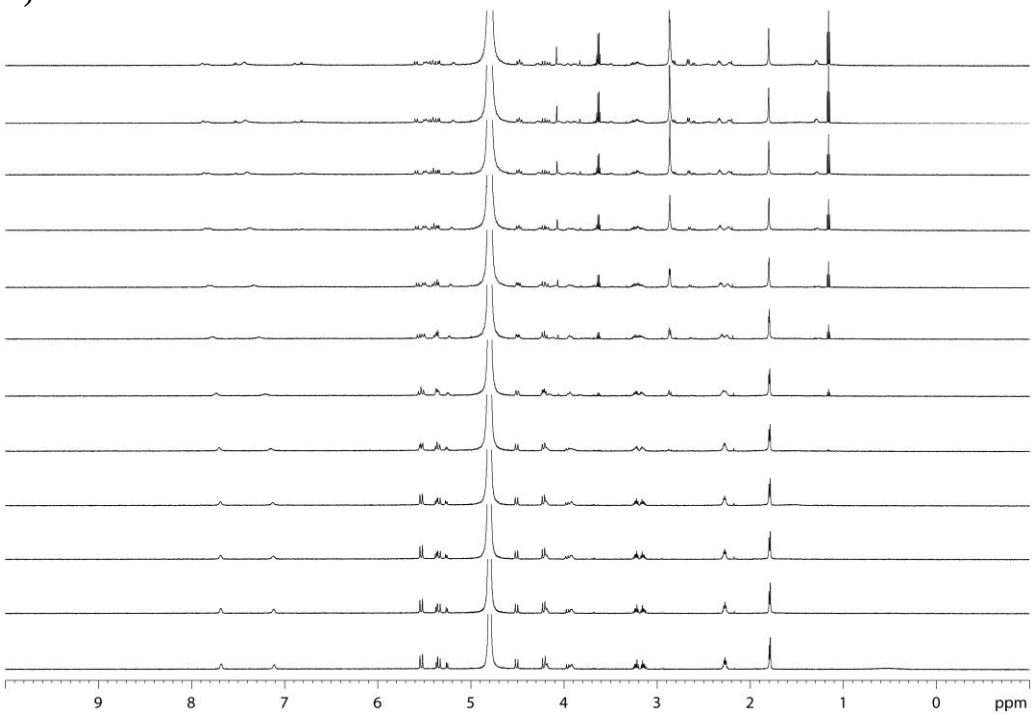

(B)

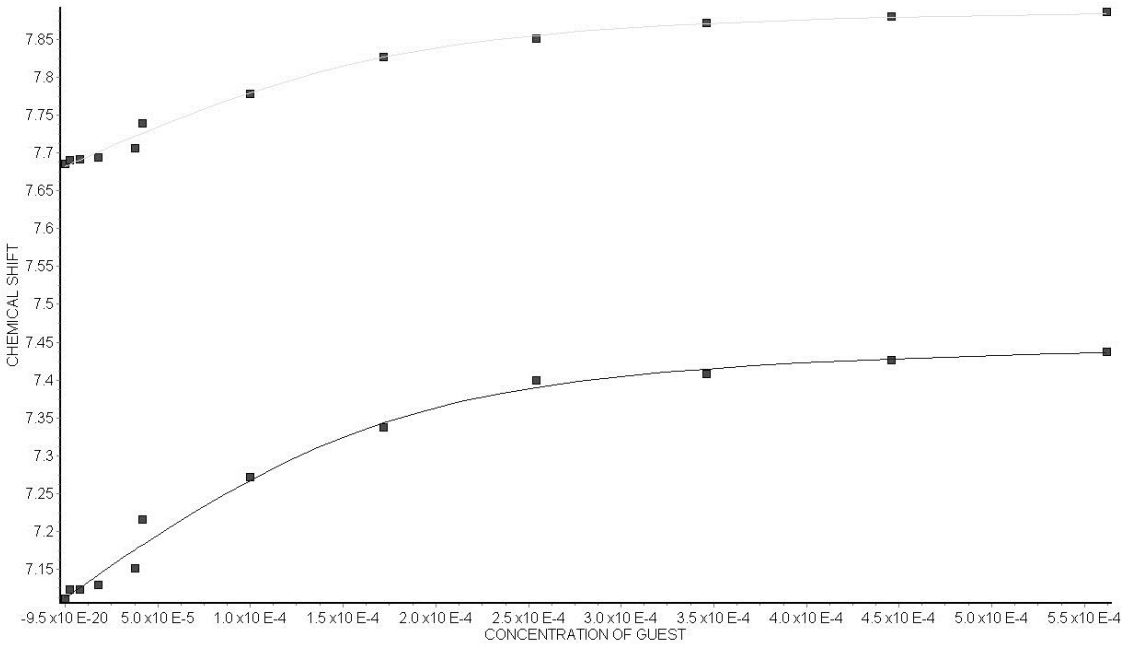

Figure II-S27. (A) ^{1}H NMR (600 MHz) stack plot of the titration of **II-2** (0.150 mM) with guest **II-13** (0 - 1.26 mM) in 20 mM NaH_2PO_4 buffered D_2O (pH = 7.4); (B) plot of the chemical shift at 7.12 and 7.68 ppm as a function of guest concentration. The solid line represents the best non-linear fit of the data to a 1:1 model ($K_a = (3.3 \pm 1.0) \times 10^4\ M^{-1}$).

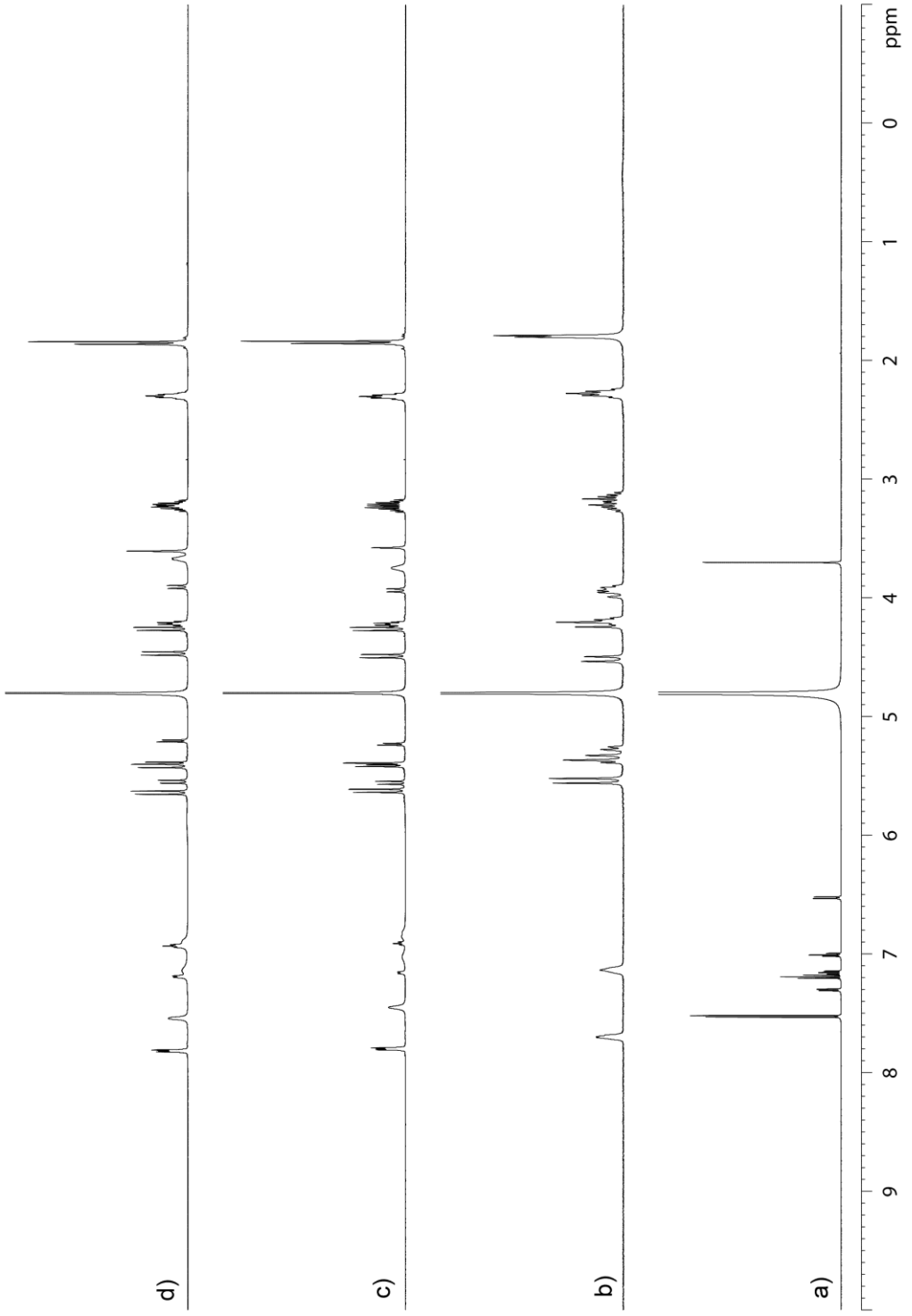

Figure II-S28. ^{1}H NMR spectra recorded (400 MHz, RT, D_2O) for a) **II-3**, b) **II-2**, c) an equimolar mixture of **II-2** and **II-3** (5 mM), and d) a 1:2 mixture of **II-2** (5 mM) and **II-3** (10 mM).

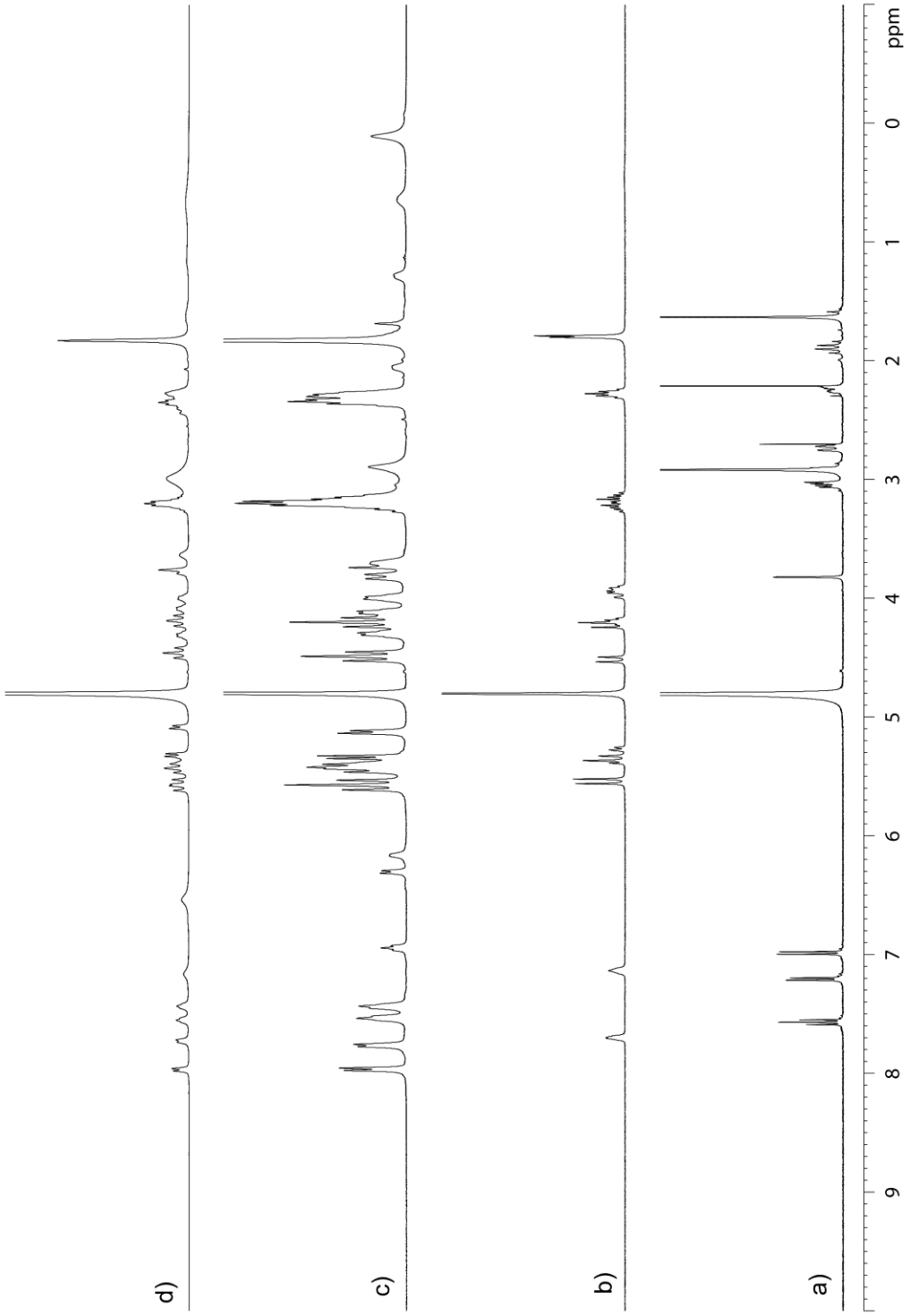

Figure II-S29. ^{1}H NMR spectra recorded (400 MHz, RT, D_2O) for a) **II-4**, b) **II-2**, c) an equimolar mixture of **II-2** and **II-4** (12.5 mM), and d) a 1:2 mixture of **II-2** (12.5 mM) and **II-4** (25 mM).

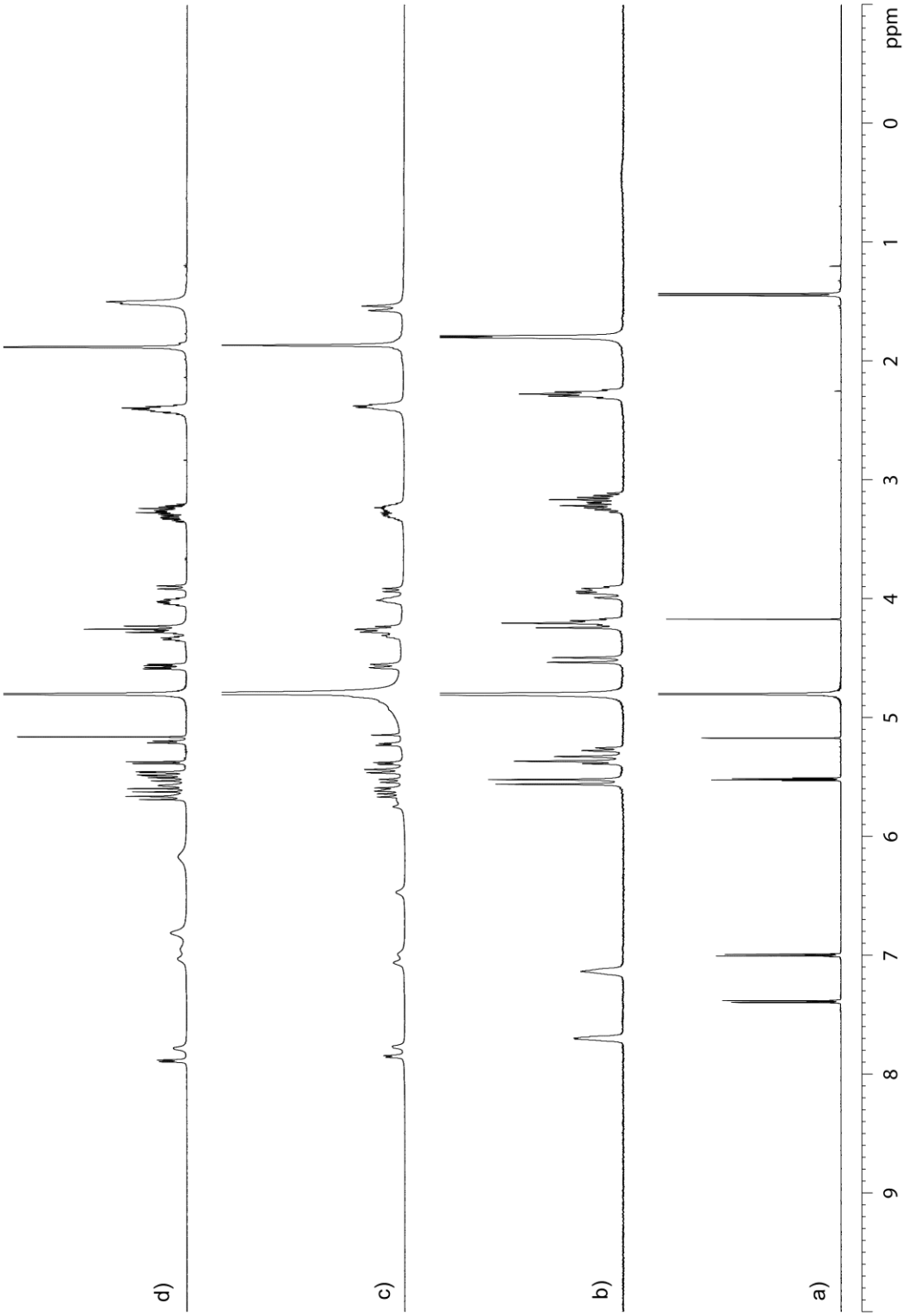

Figure II-S30. ^{1}H NMR spectra recorded (400 MHz, RT, D_2O) for a) **II-5**, b) **II-2**, c) an equimolar mixture of **II-2** and **II-5** (5 mM), and d) a 1:2 mixture of **II-2** (5 mM) and **II-5** (10 mM).

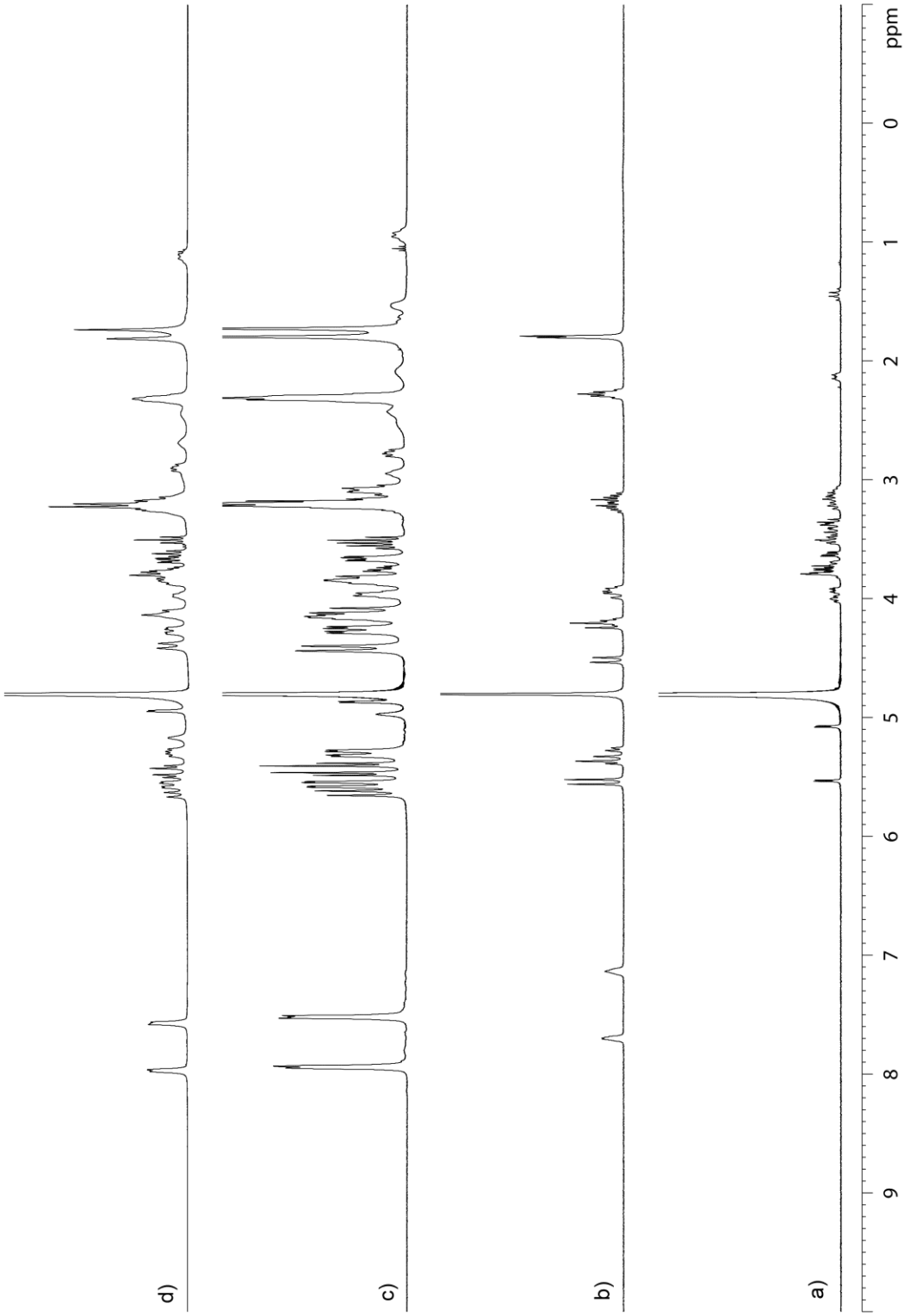

Figure II-S31. ^{1}H NMR spectra recorded (400 MHz, RT, D_2O) for a) **II-6**, b) **II-2**, c) an equimolar mixture of **II-2** and **II-6** (12.5 mM), and d) a 1:2 mixture of **II-2** (12.5 mM) and **II-6** (25 mM).

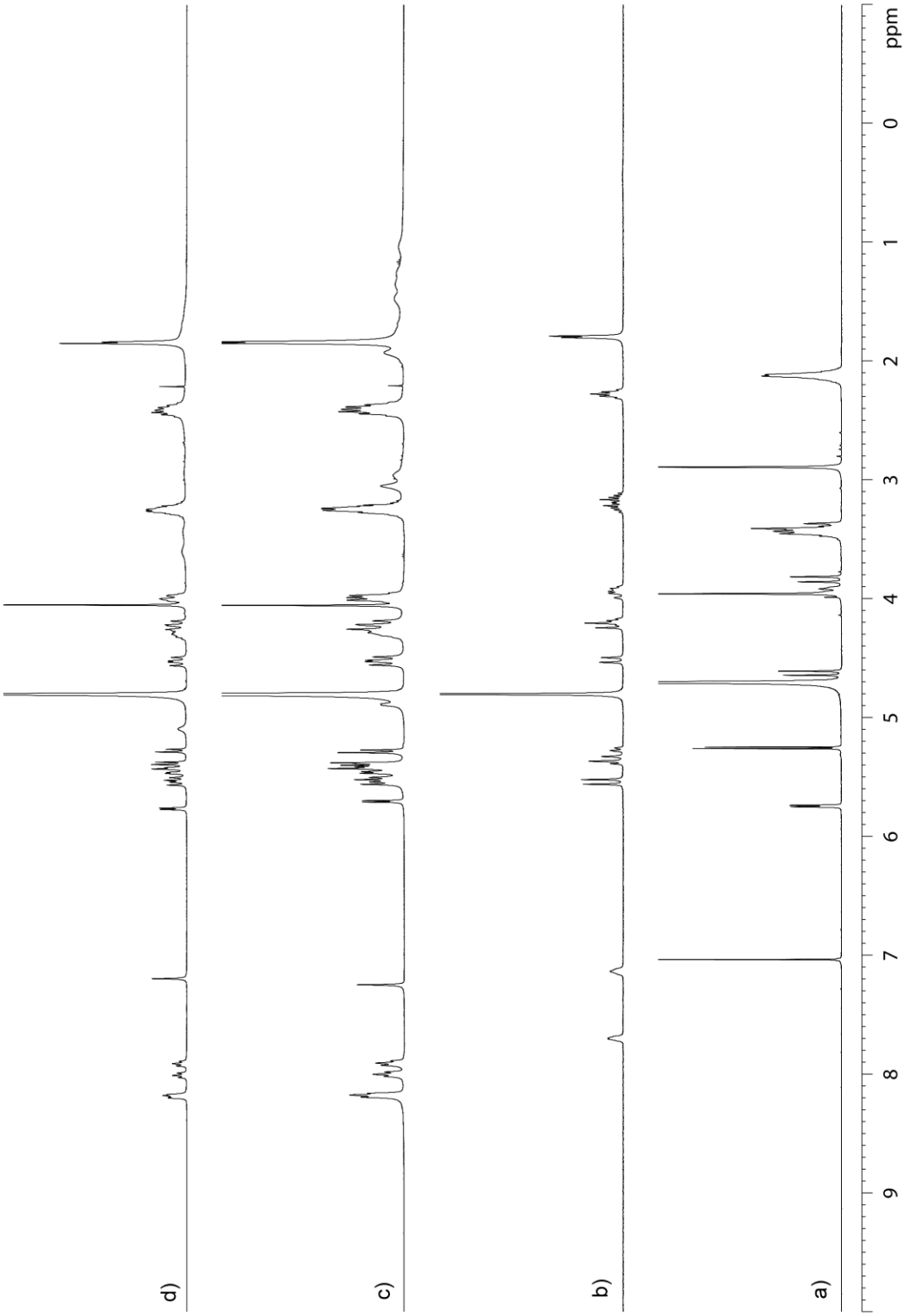

Figure II-S32. ^{1}H NMR spectra recorded (400 MHz, RT, D_2O) for a) **II-7**, b) **II-2**, c) an equimolar mixture of **II-2** and **II-7** (5 mM), and d) a 1:2 mixture of **II-2** (5 mM) and **II-7** (10 mM).

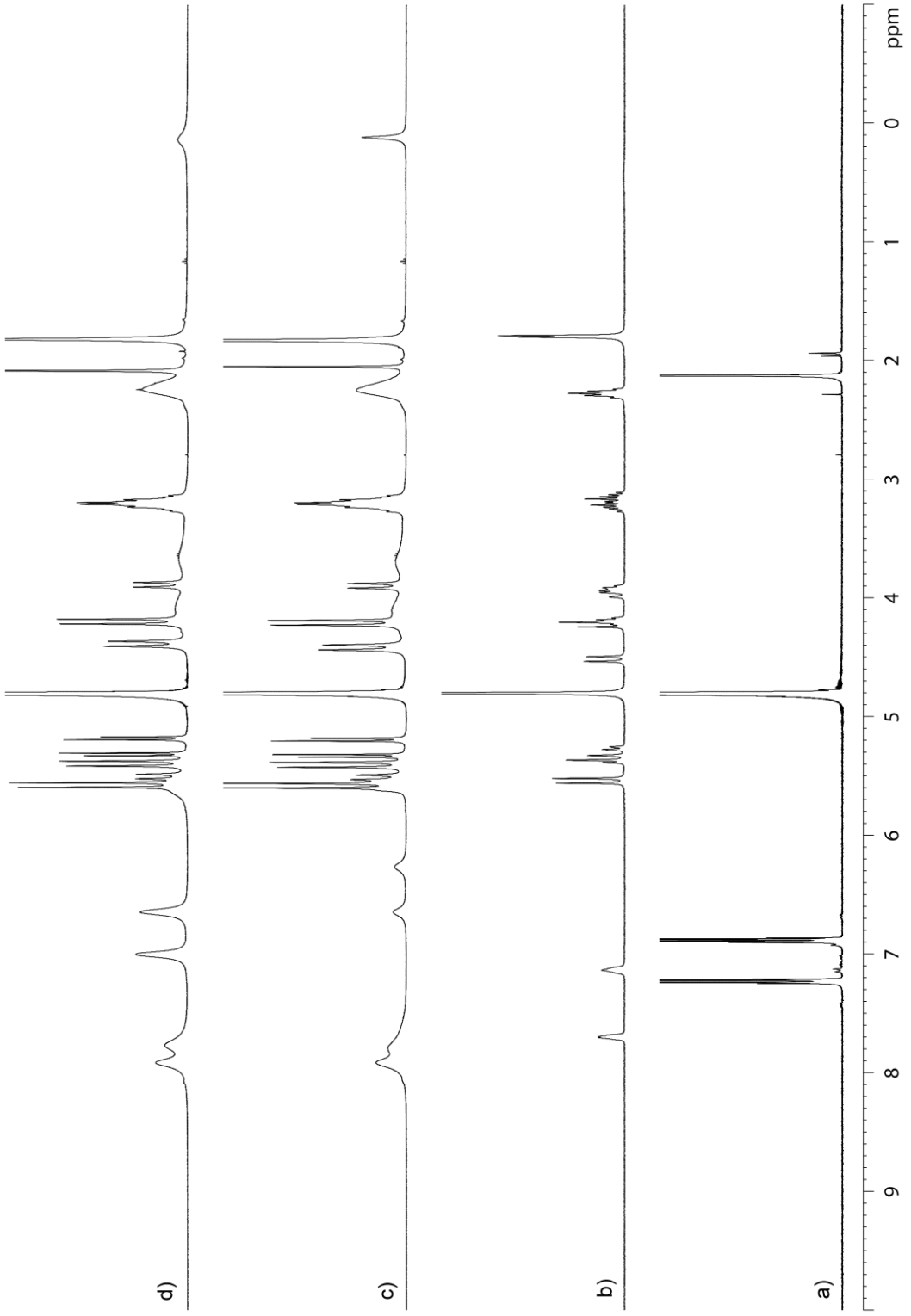

Figure II-S33. ^{1}H NMR spectra recorded (400 MHz, RT, D_2O) for a) **II-8**, b) **II-2**, c) an equimolar mixture of **II-2** and **II-8** (5 mM), and d) a 1:2 mixture of **II-2** (5 mM) and **II-8** (10 mM).

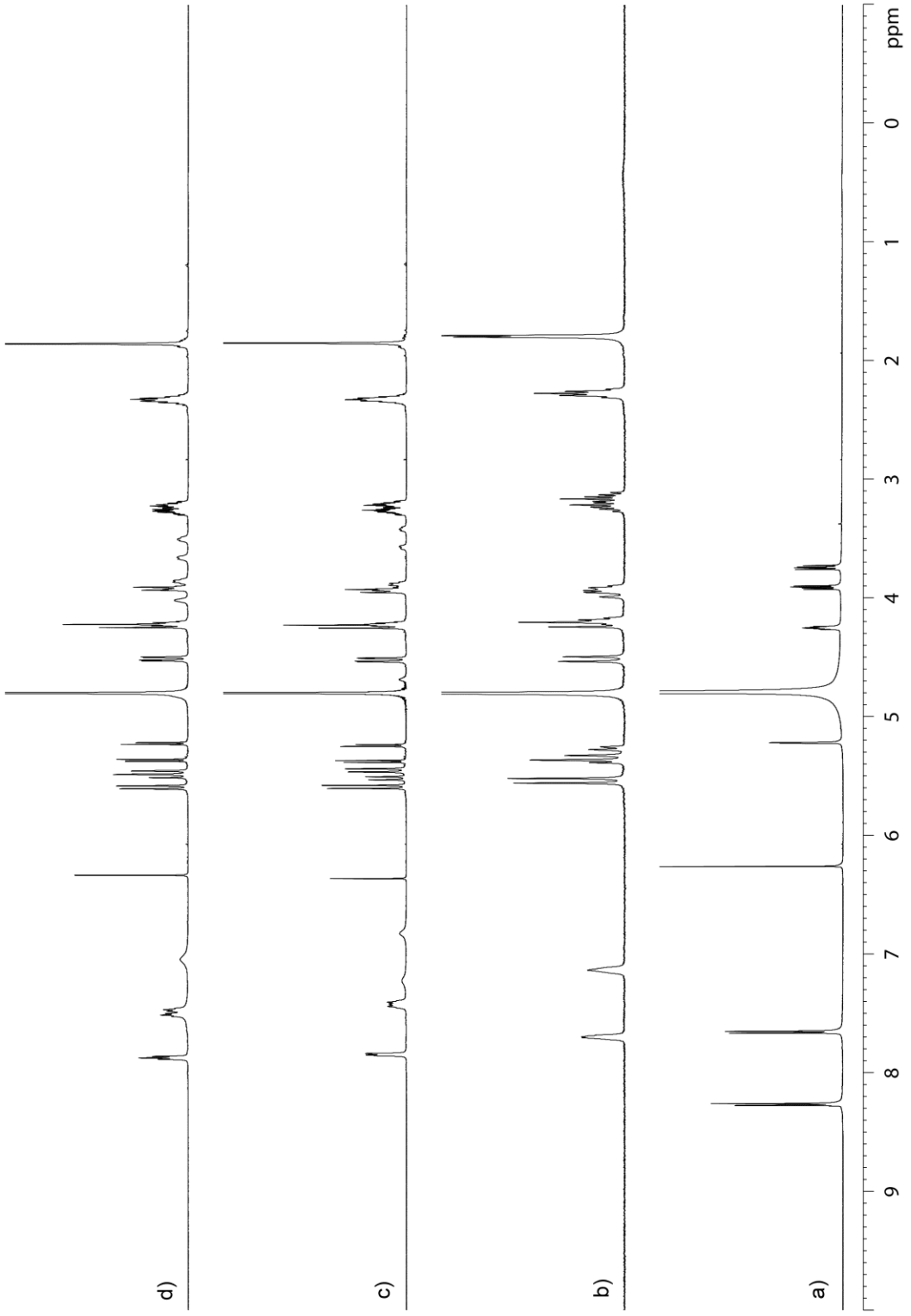

Figure II-S34. ^{1}H NMR spectra recorded (400 MHz, RT, D_2O) for a) **II-9**, b) **II-2**, c) an equimolar mixture of **II-2** and **II-9** (5 mM), and d) a 1:2 mixture of **II-2** (5 mM) and **II-9** (10 mM).

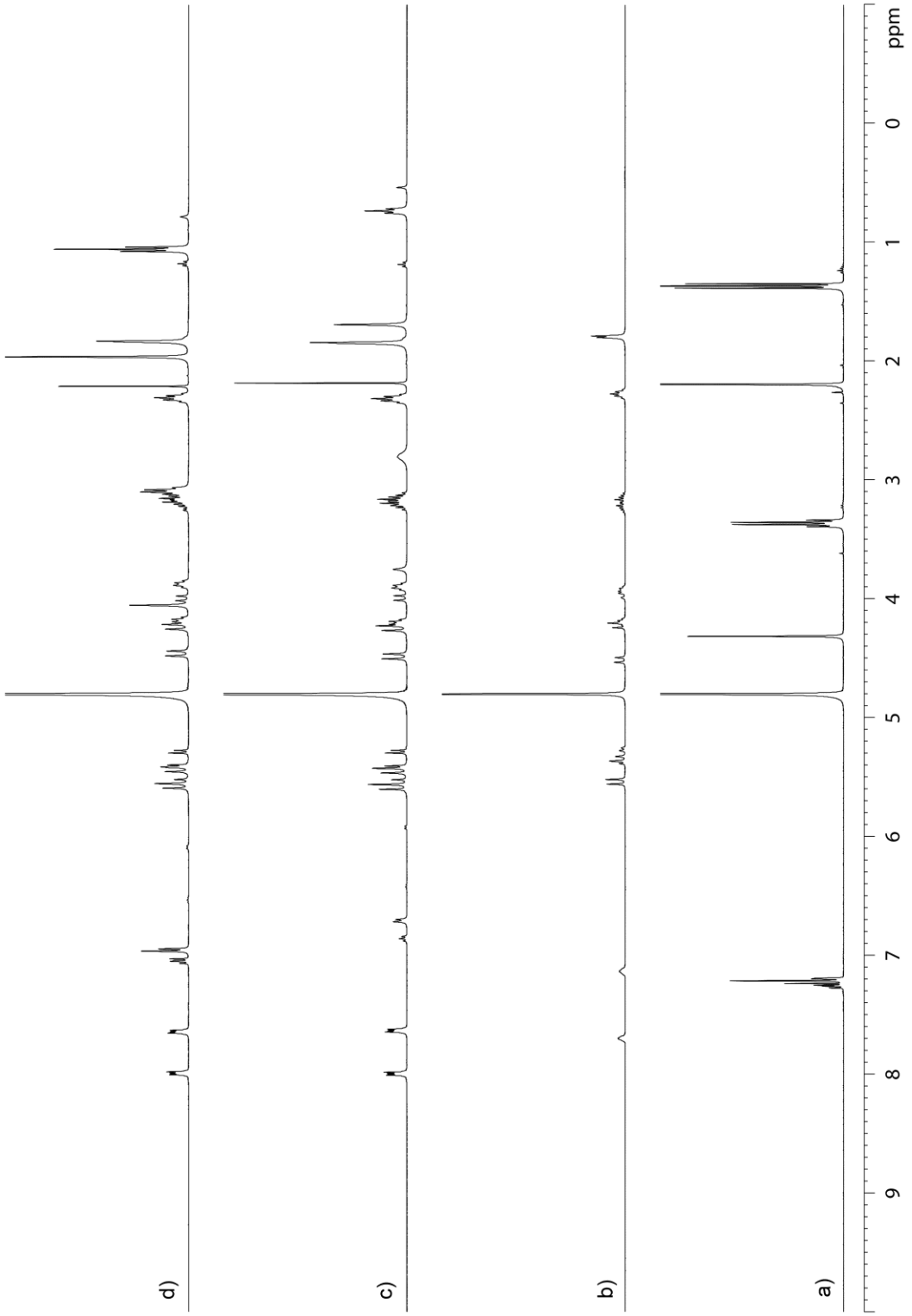

Figure II-S35. ^{1}H NMR spectra recorded (400 MHz, RT, D_2O) for a) **II-10**, b) **II-2**, c) an equimolar mixture of **II-2** and **II-10** (4 mM), and d) a 1:2 mixture of **II-2** (4 mM) and **II-10** (8 mM).

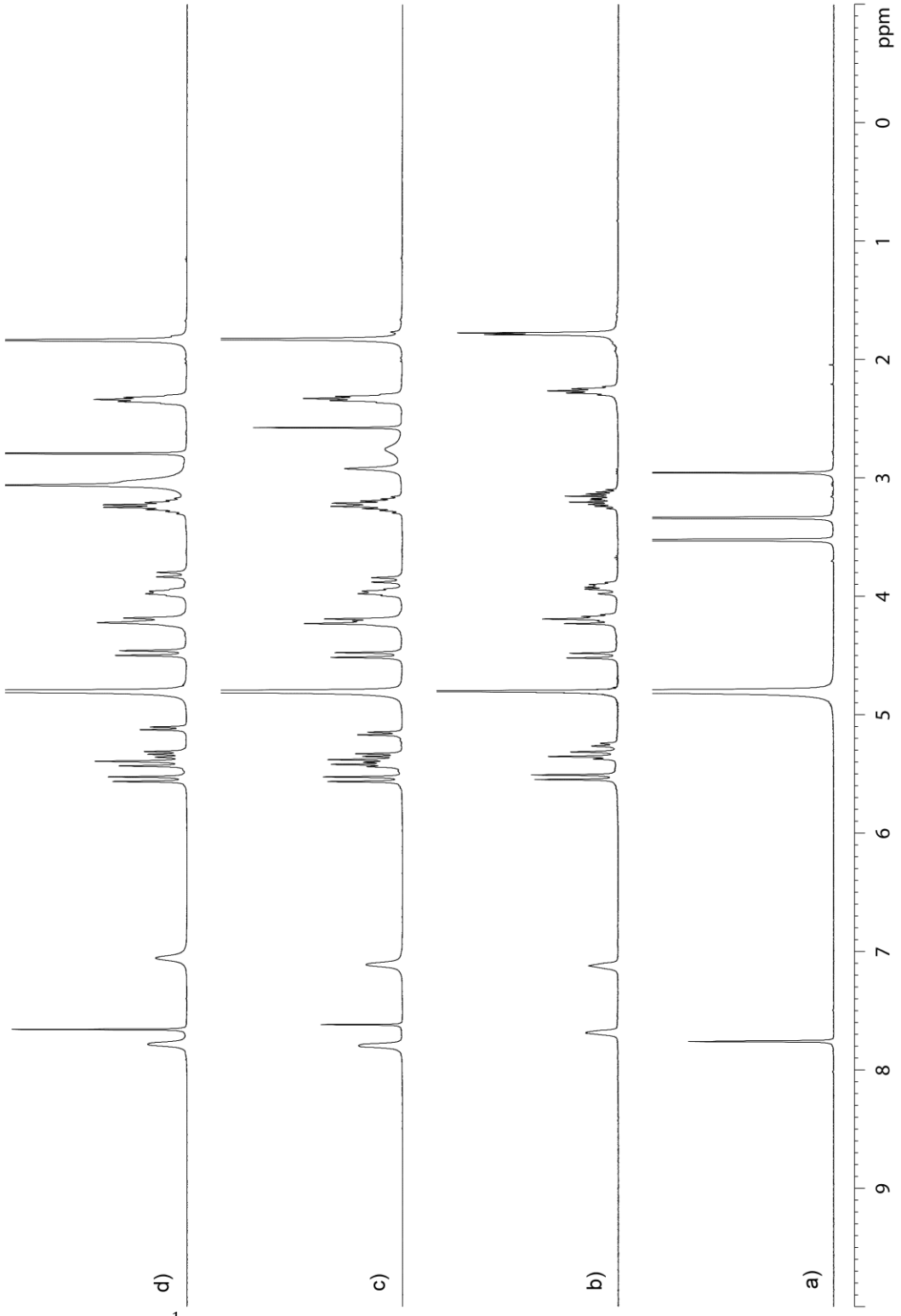

Figure II-S36. ^{1}H NMR spectra recorded (400 MHz, RT, D_2O) for a) **II-11**, b) **II-2**, c) an equimolar mixture of **II-2** and **II-11** (4 mM), and d) a 1:2 mixture of **II-2** (4 mM) and **II-11** (8 mM).

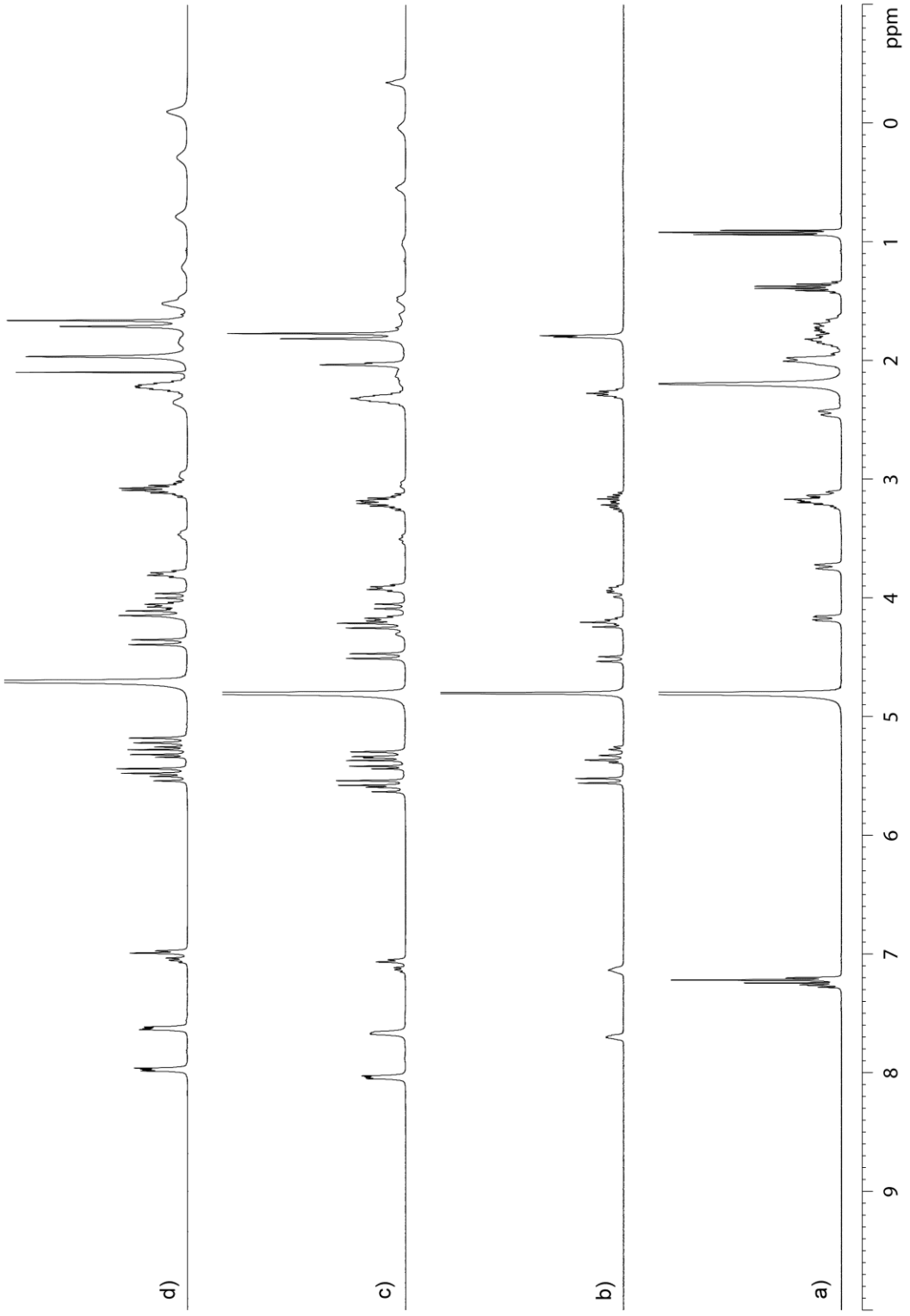

Figure II-S37. ^{1}H NMR spectra recorded (400 MHz, RT, D_2O) for a) **II-12**, b) **II-2**, c) an equimolar mixture of **II-2** and **II-12** (4 mM), and d) a 1:2 mixture of **II-2** (4 mM) and **II-12** (8 mM).

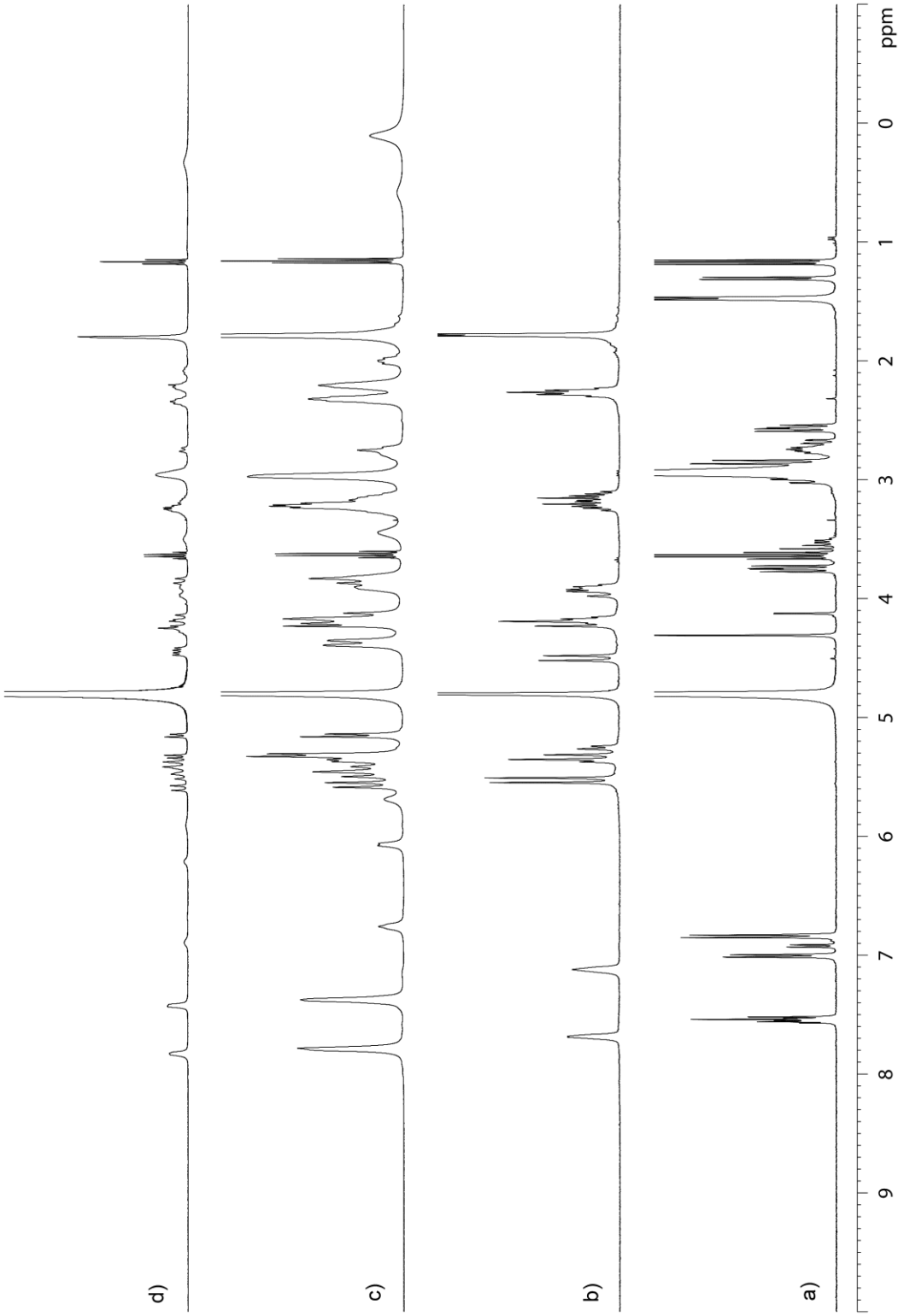

Figure II-S38. ^{1}H NMR spectra recorded (400 MHz, RT, D_2O) for a) **II-13**, b) **II-2**, c) an equimolar mixture of **II-2** and **II-13** (12.5 mM), and d) a 1:2 mixture of **II-2** (4 mM) and **II-13** (8 mM).

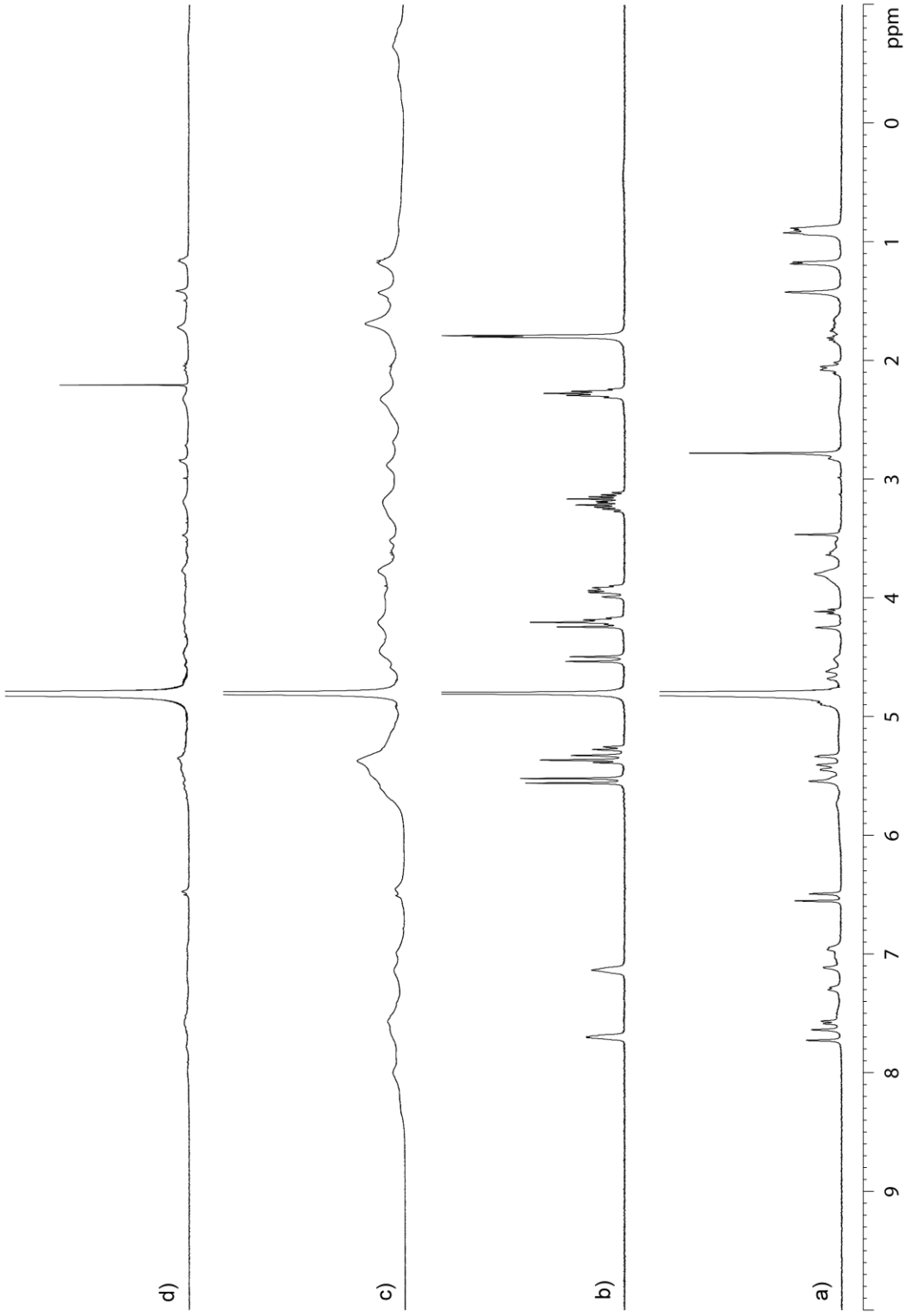

Figure II-S39. ^{1}H NMR spectra recorded (400 MHz, RT, D_2O) for a) **II-14**, b) **II-2**, c) an equimolar mixture of **II-2** and **II-14** (4 mM), and d) a 1:2 mixture of **II-2** (1 mM) and **II-14** (2 mM).

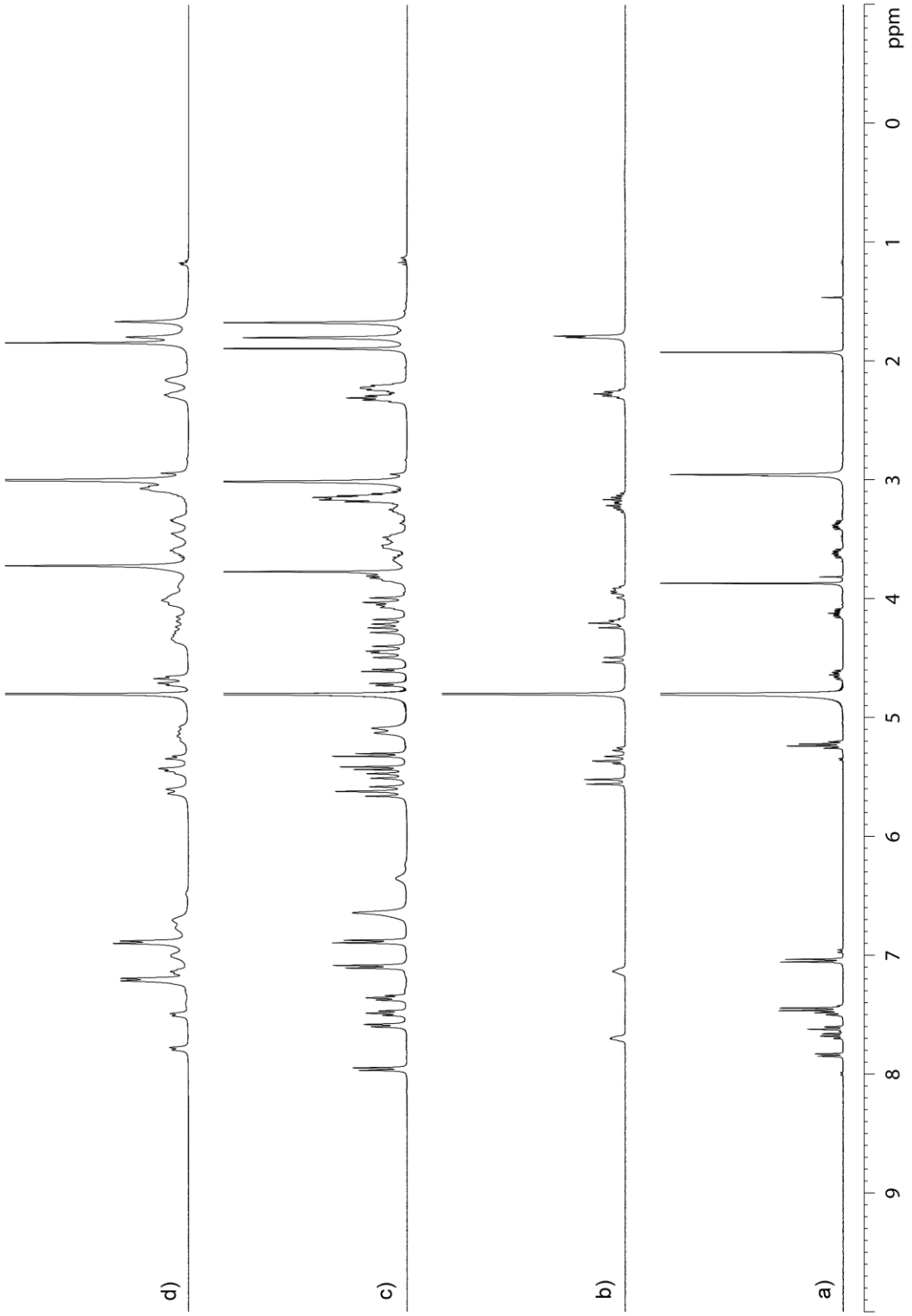

Figure II-S40. ^{1}H NMR spectra recorded (400 MHz, RT, D_2O) for a) **II-15**, b) **II-2**, c) an equimolar mixture of **II-2** and **II-15** (12.5 mM), and d) a 1:2 mixture of **II-2** (12.5 mM) and **II-15** (25 mM).

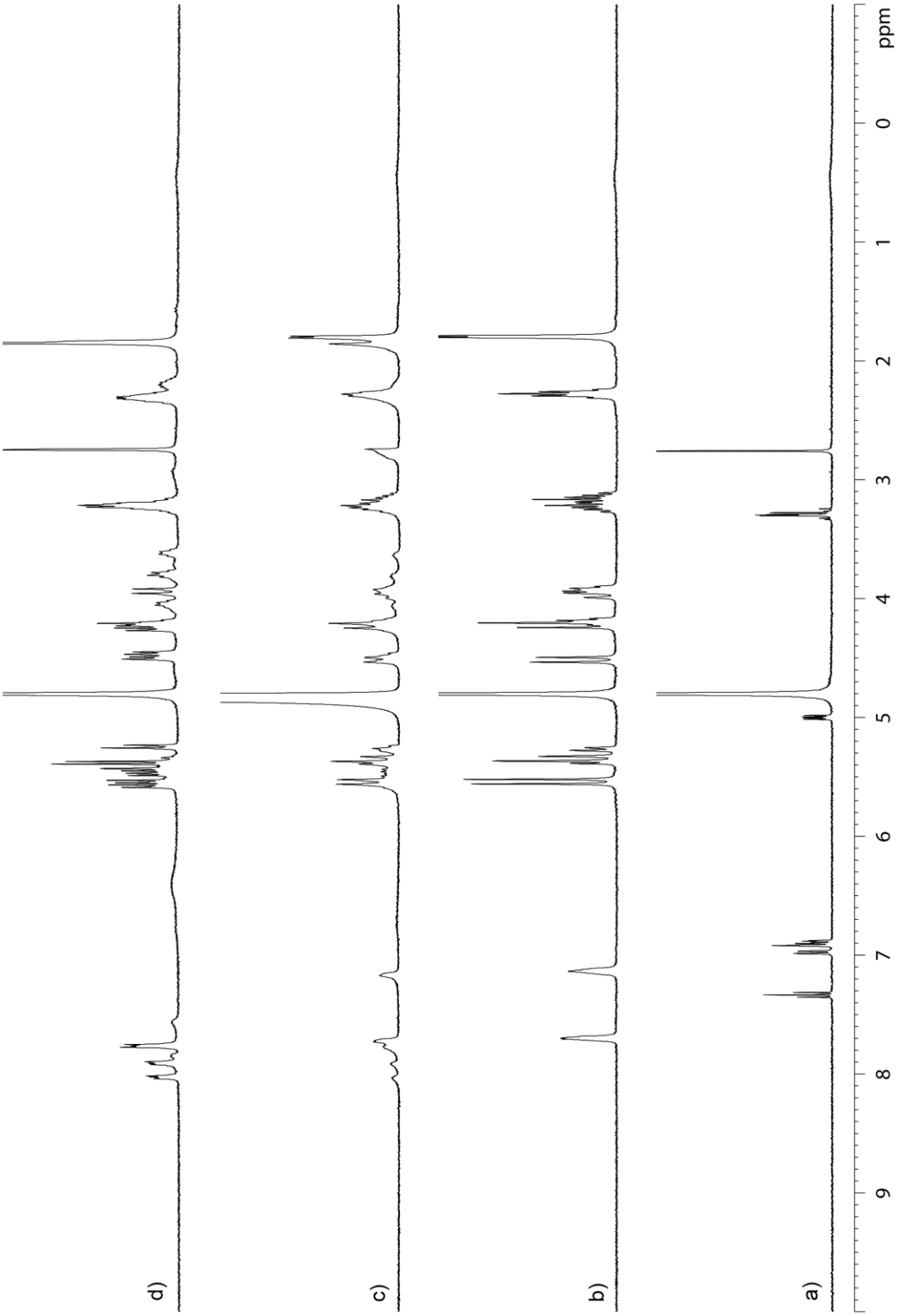

Figure II-S41. ^{1}H NMR spectra recorded (400 MHz, RT, D_2O) for a) **II-16**, b) **II-2**, and c) an equimolar mixture of **II-2** and **II-16** (2 mM), and d) a 1:2 mixture of **II-2** (0.7 mM) and **II-16** (1.3 mM).

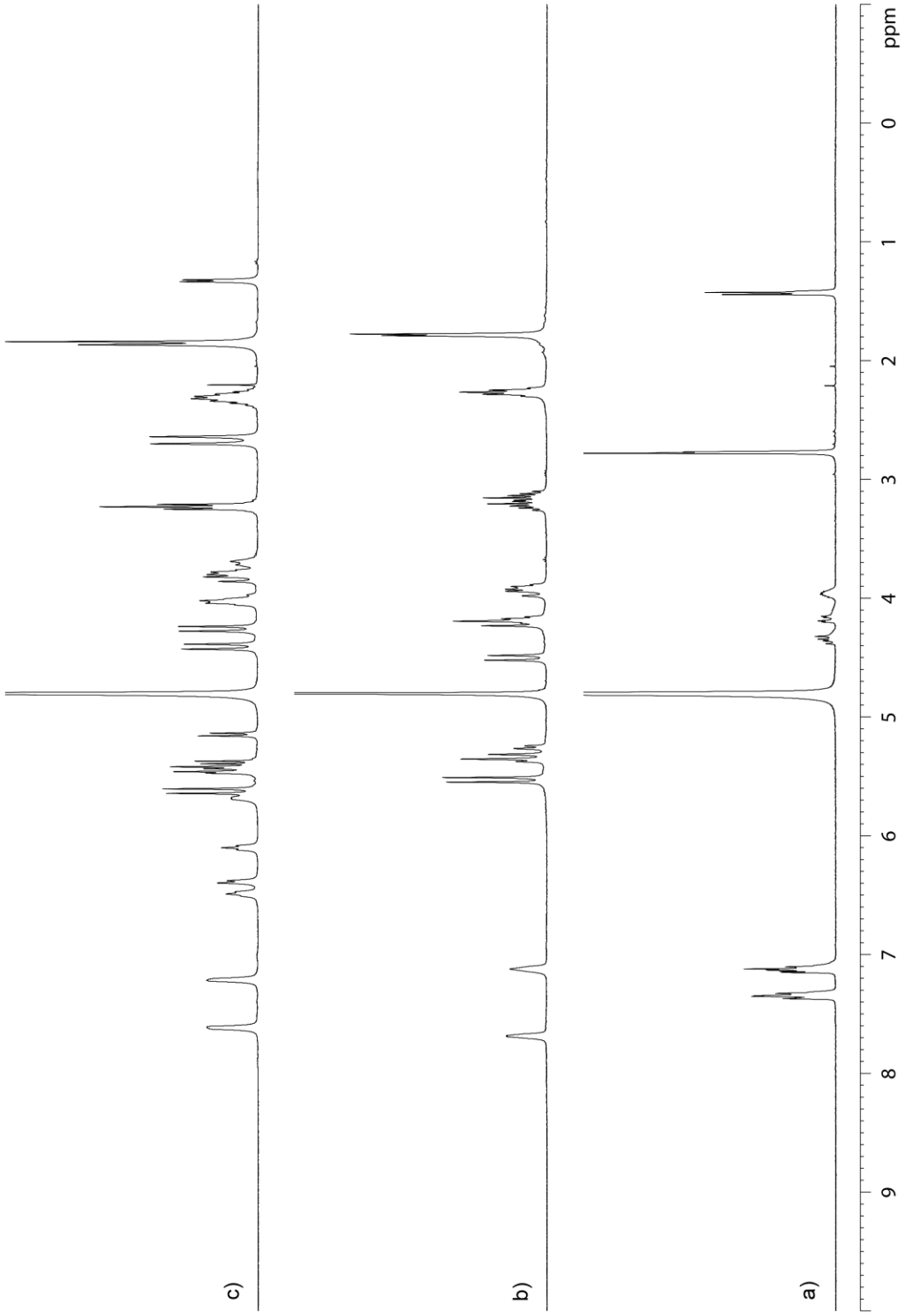

Figure II-S42. ^{1}H NMR spectra recorded (400 MHz, RT, D_2O) for a) **II-17**, b) **II-2**, and c) an equimolar mixture of **II-2** and **II-17** (4 mM).

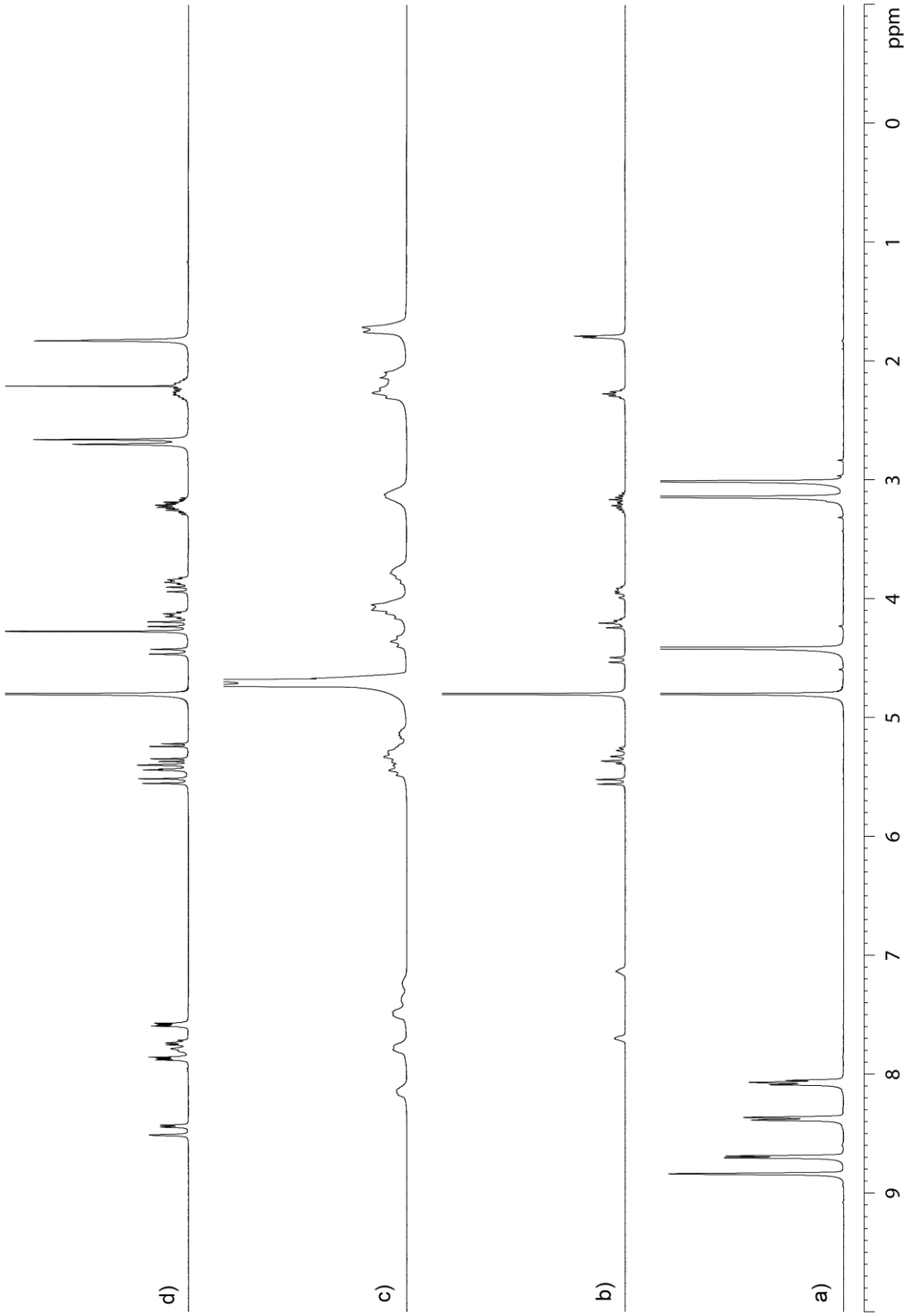

Figure II-S43. ^{1}H NMR spectra recorded (400 MHz, RT, D_2O) for a) **II-18**, b) **II-2**, c) an equimolar mixture of **II-2** and **II-18** (4 mM), and d) a 1:2 mixture of **II-2** (4 mM) and **II-18** (8 mM).

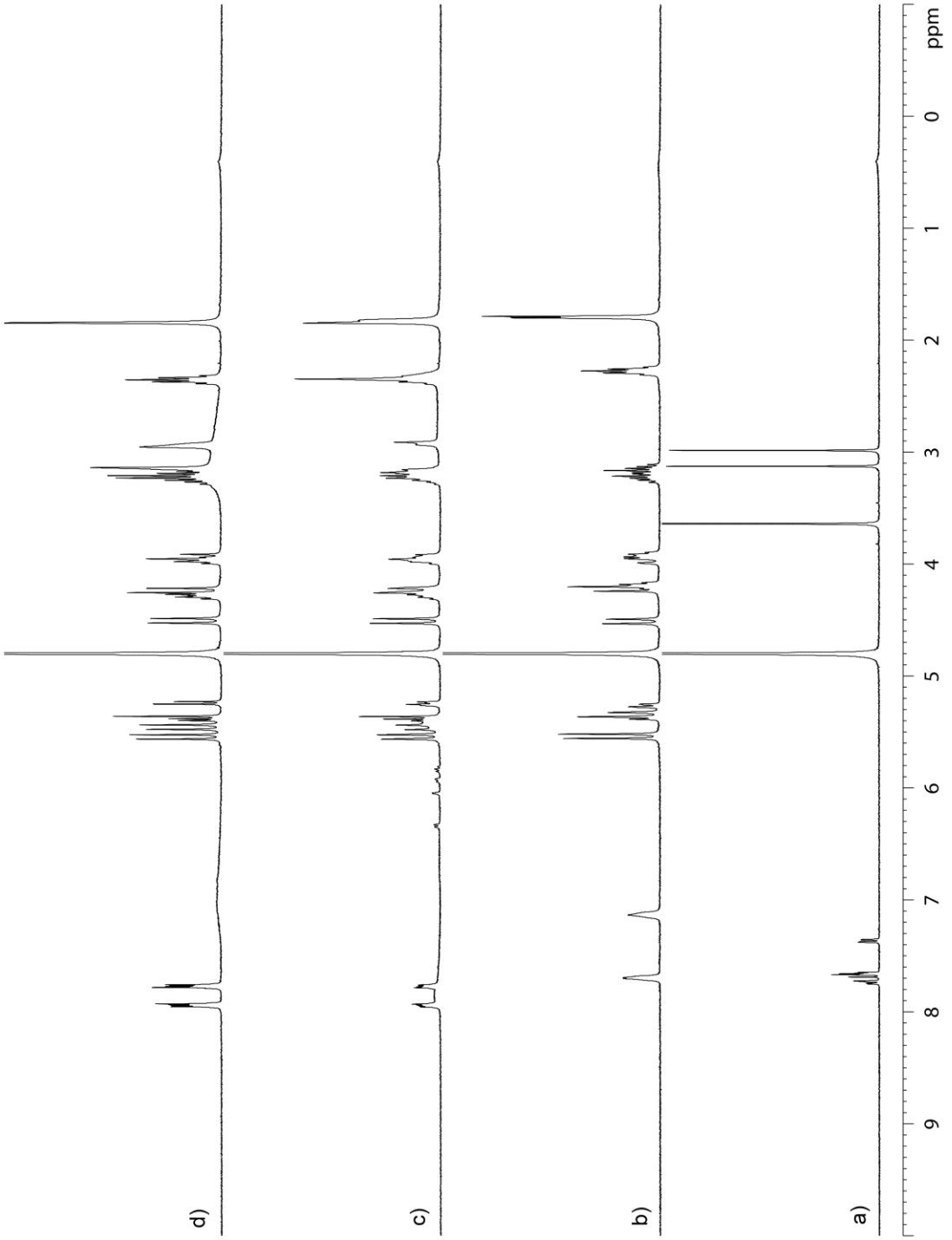

Figure II-S44. ^{1}H NMR spectra recorded (400 MHz, RT, D_2O) for a) **II-19**, b) **II-2**, c) an equimolar mixture of **II-2** and **II-19** (4 mM), and d) a 1:2 mixture of **II-2** (4 mM) and **II-19** (8 mM).

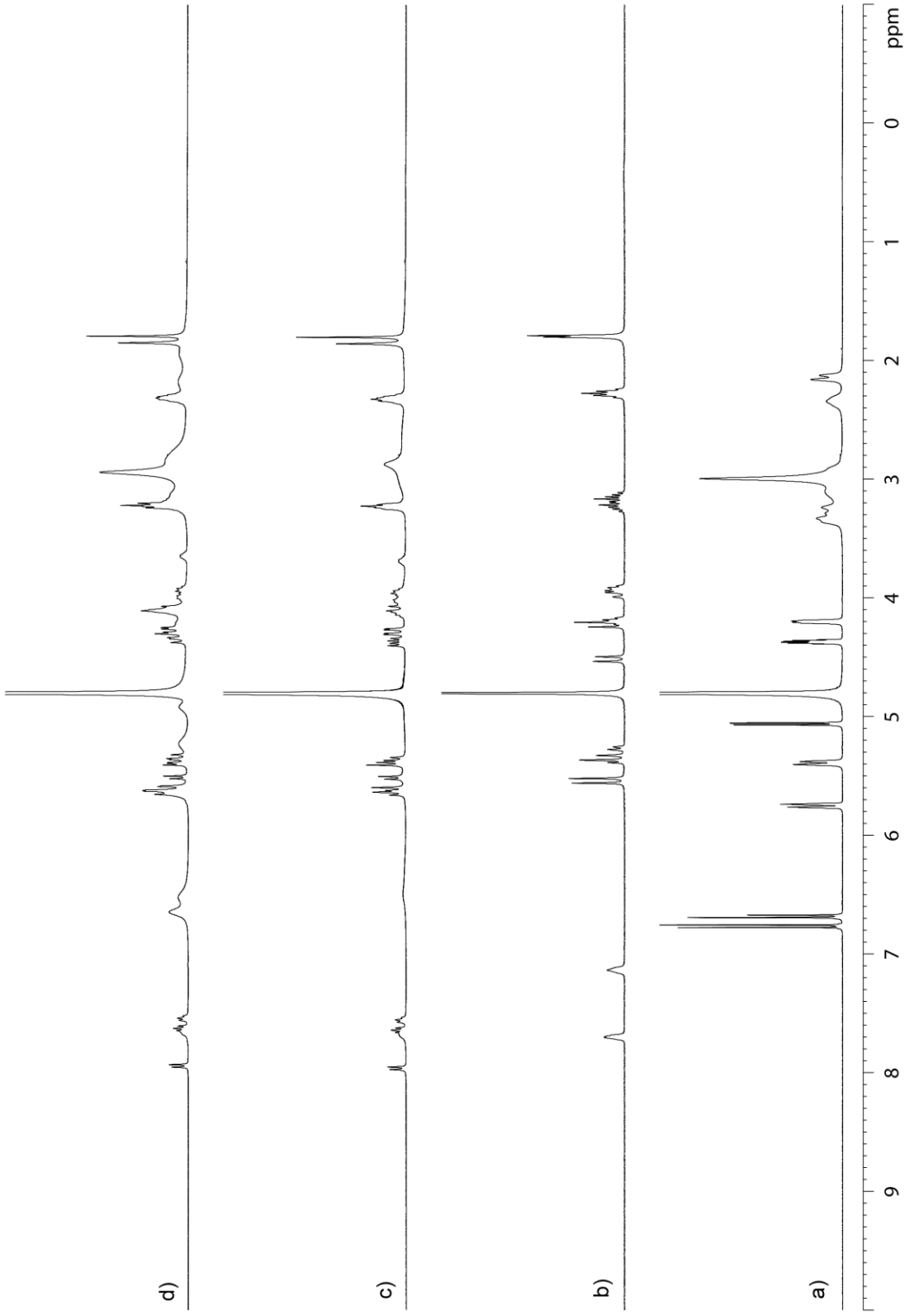

Figure II-S45. ^{1}H NMR spectra recorded (400 MHz, RT, D_2O) for a) **II-20**, b) **II-2**, c) an equimolar mixture of **II-2** and **II-20** (5 mM), and d) a 1:2 mixture of **II-2** (5 mM) and **II-20** (10 mM).

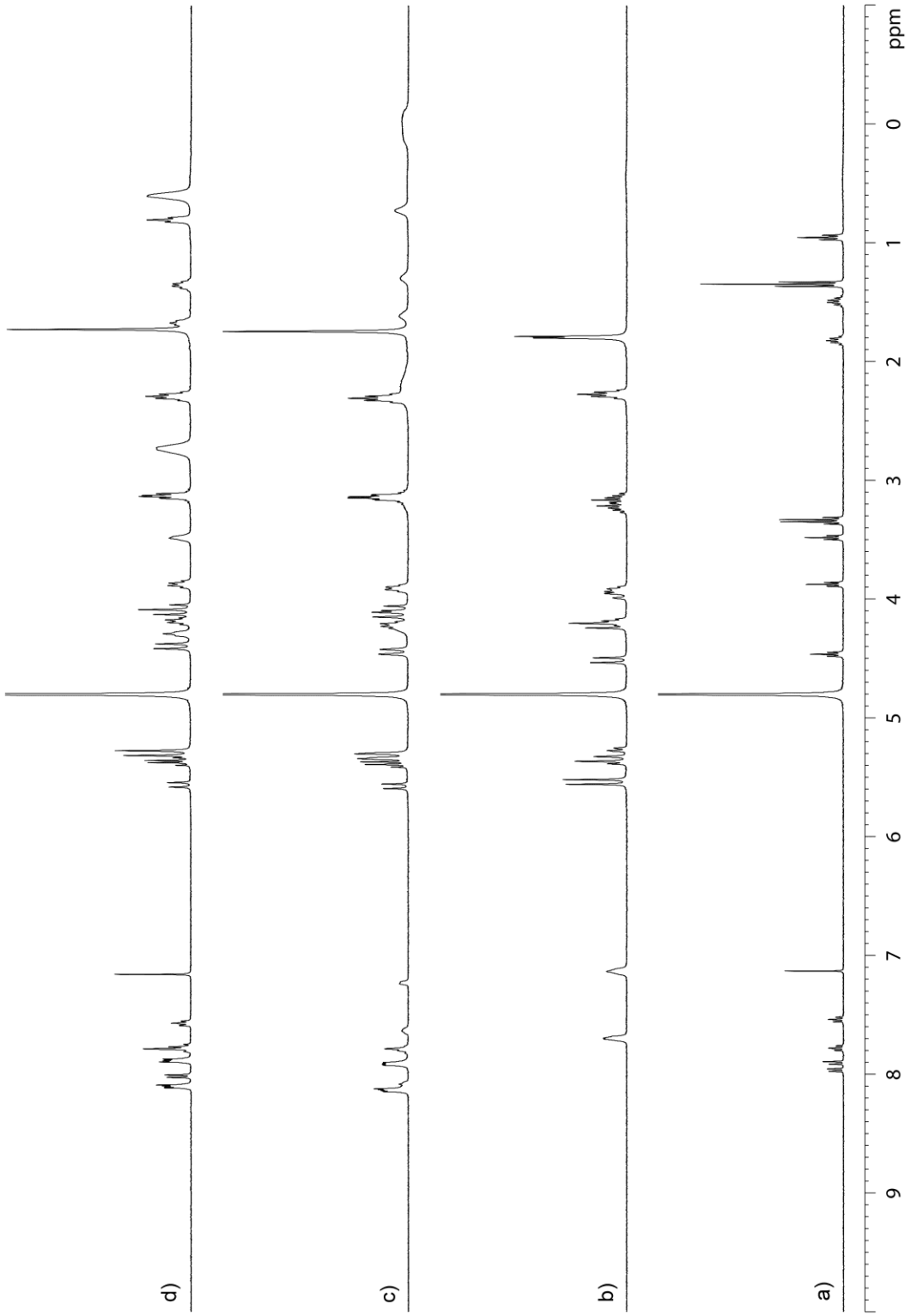

Figure II-S46. ^{1}H NMR spectra recorded (400 MHz, RT, D_2O) for a) **II-21**, b) **II-2**, and c) an equimolar mixture of **II-2** and **II-21** (4 mM), and d) a 1:2 mixture of **II-2** (2 mM) and **II-21** (4 mM).

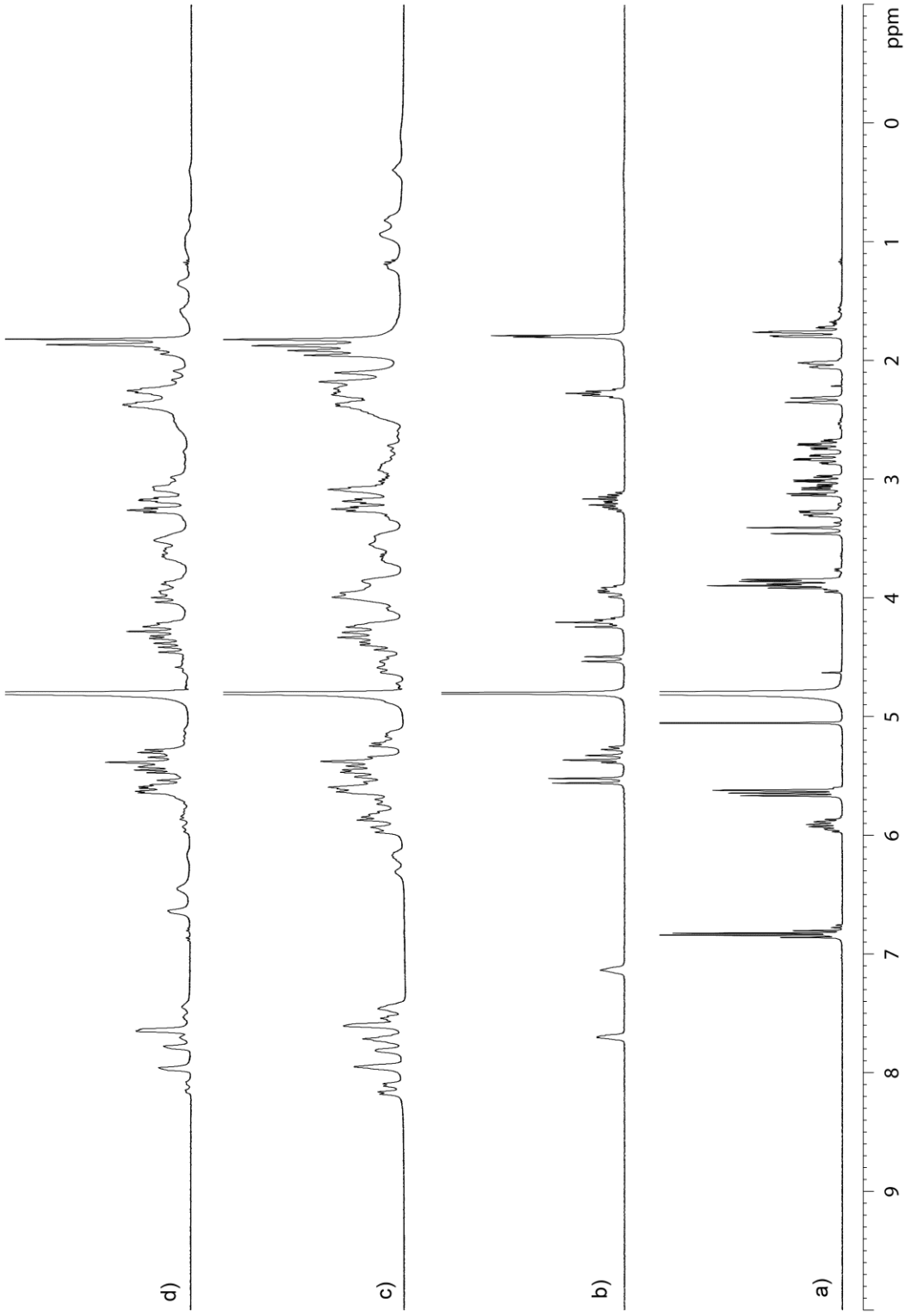

Figure II-47. ^{1}H NMR spectra recorded (400 MHz, RT, D_2O) for a) **II-22**, b) **II-2**, c) an equimolar mixture of **II-2** and **II-22** (12.5 mM), and d) a 1:2 mixture of **II-2** (6.25 mM) and **II-22** (12.5 mM).

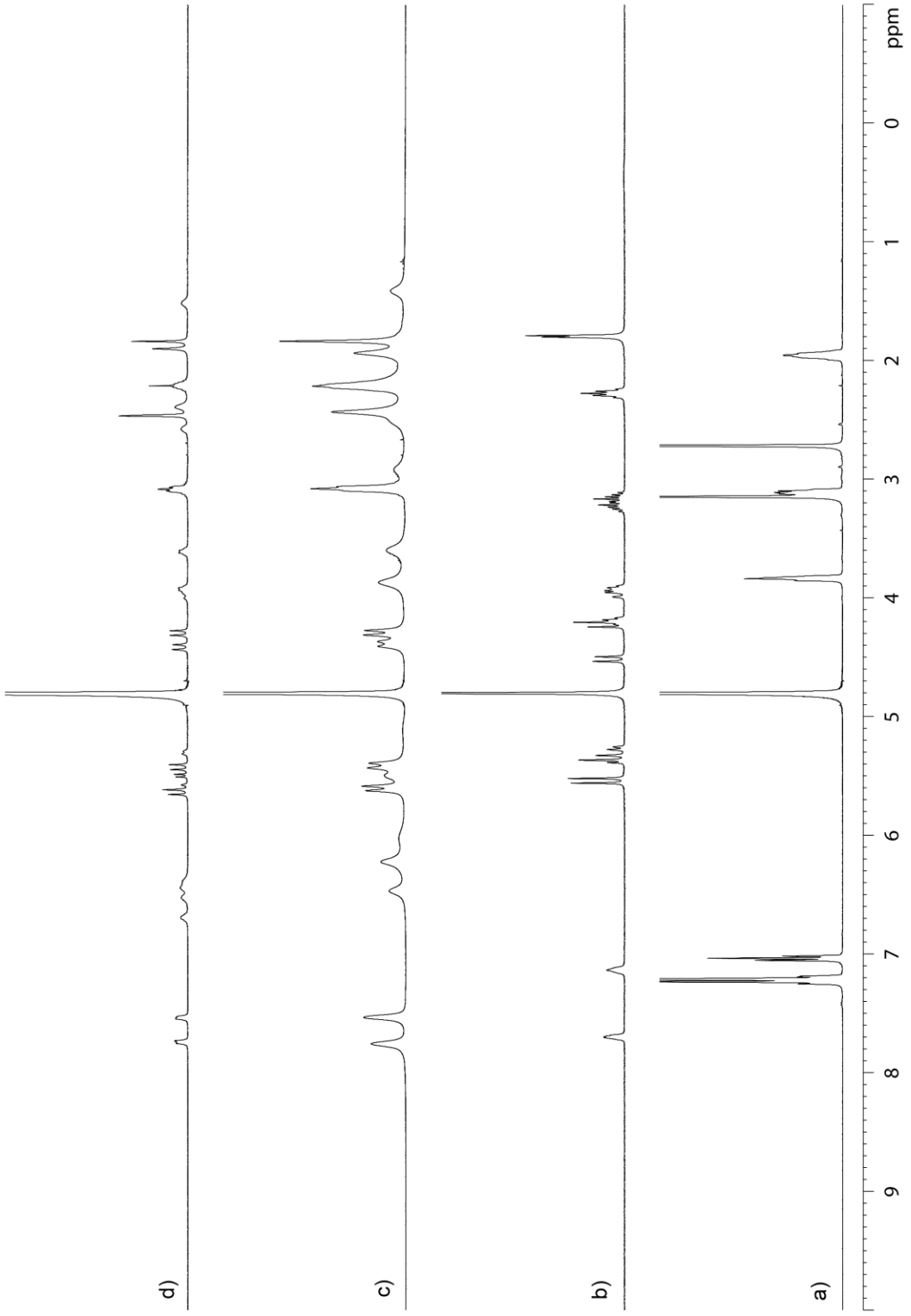

Figure II-S48. ^{1}H NMR spectra recorded (400 MHz, RT, D_2O) for a) **II-23**, b) **II-2**, c) an equimolar mixture of **II-2** and **II-23** (5 mM), and d) a 1:2 mixture of **II-2** (5 mM) and **II-23** (10 mM).

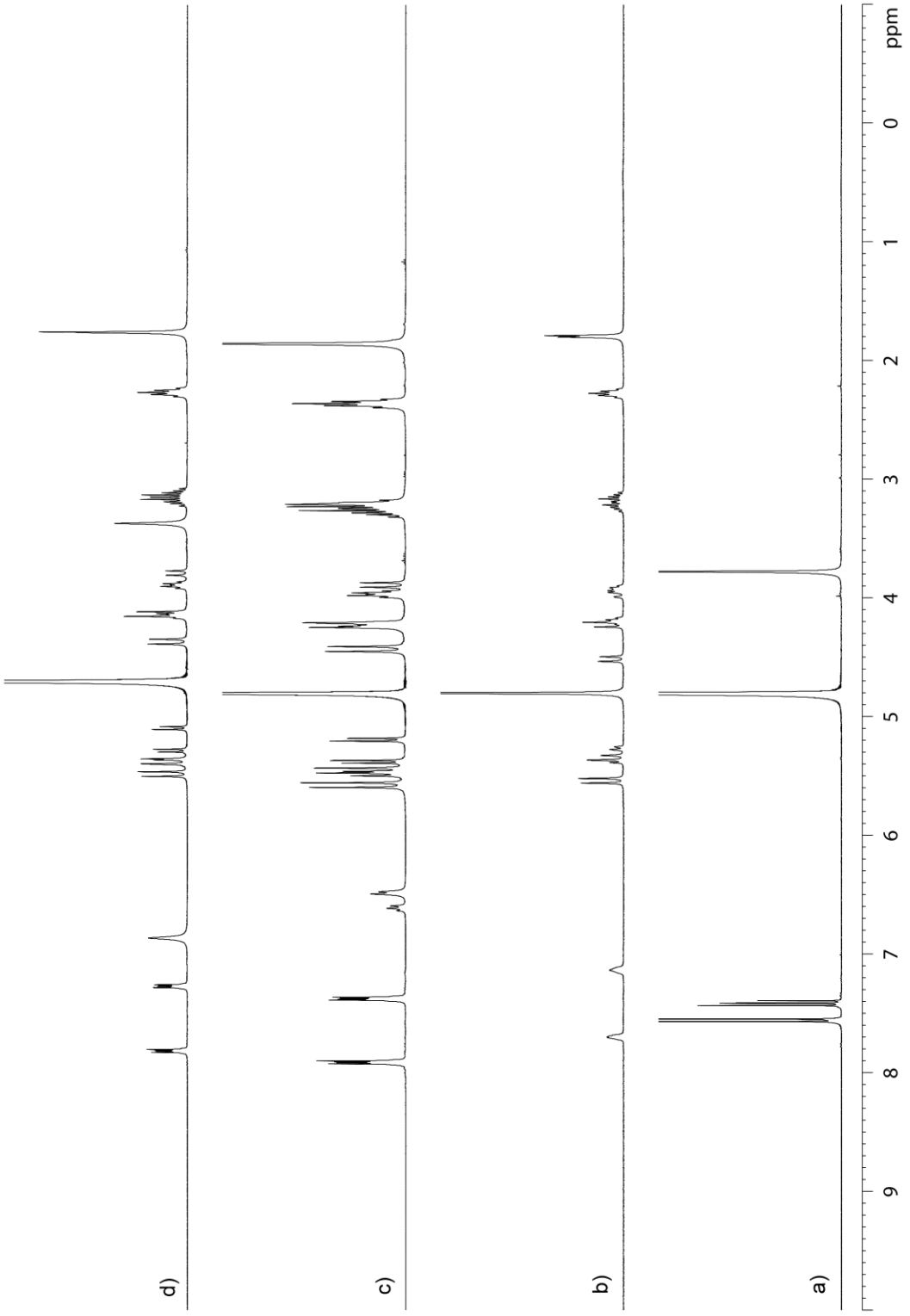

Figure II-S49. ^{1}H NMR spectra recorded (400 MHz, RT, D_2O) for a) **II-24**, b) **II-2**, c) an equimolar mixture of **II-2** and **II-24** (5 mM), and d) a 1:2 mixture of **II-2** (5 mM) and **II-24** (10 mM).

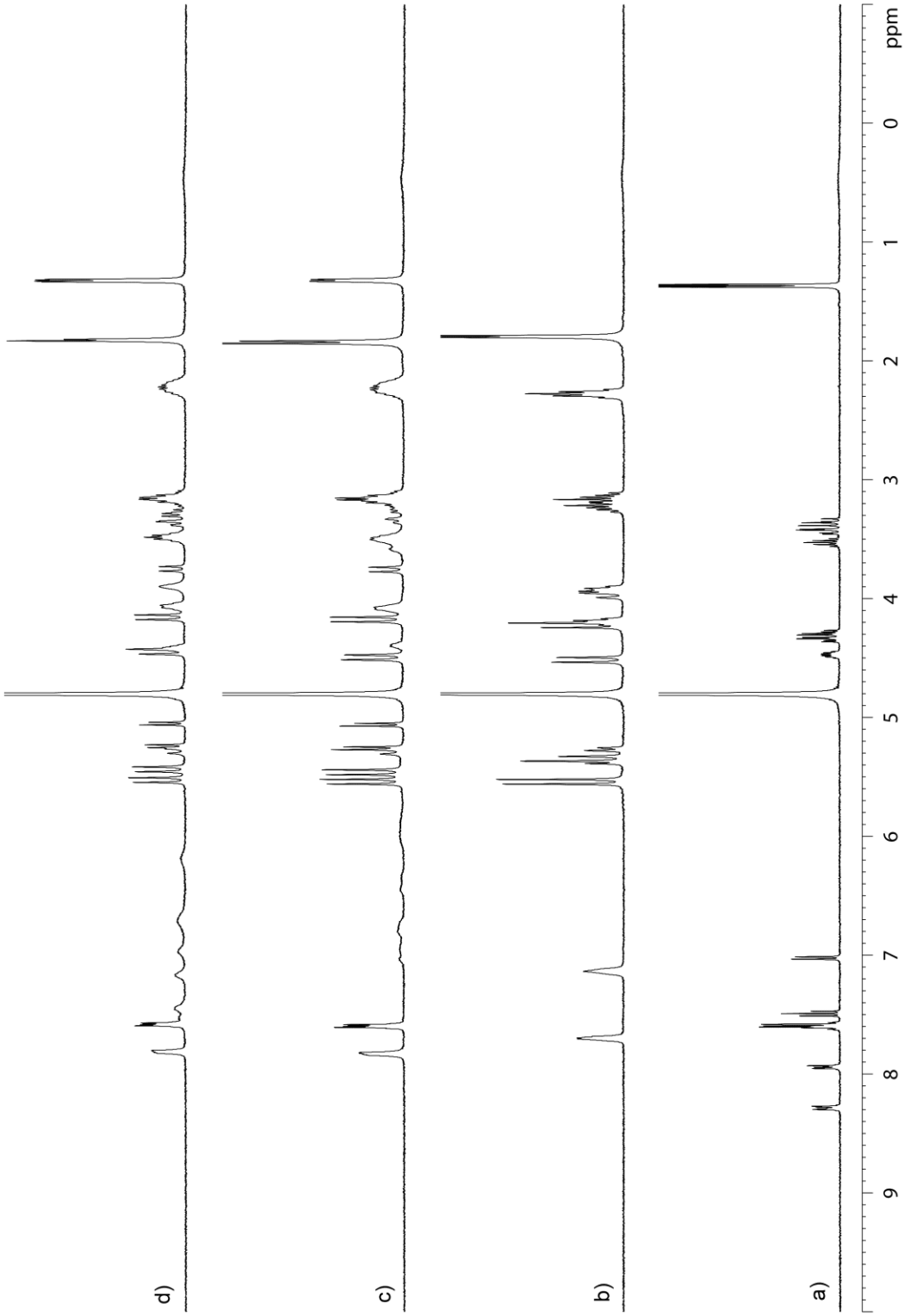

Figure II-S50. ^{1}H NMR spectra recorded (400 MHz, RT, D_2O) for a) **II-25**, b) **II-2**, and c) an equimolar mixture of **II-2** and **II-25** (2 mM), and d) a 1:2 mixture of **II-2** (0.7 mM) and **II-25** (1.3 mM).

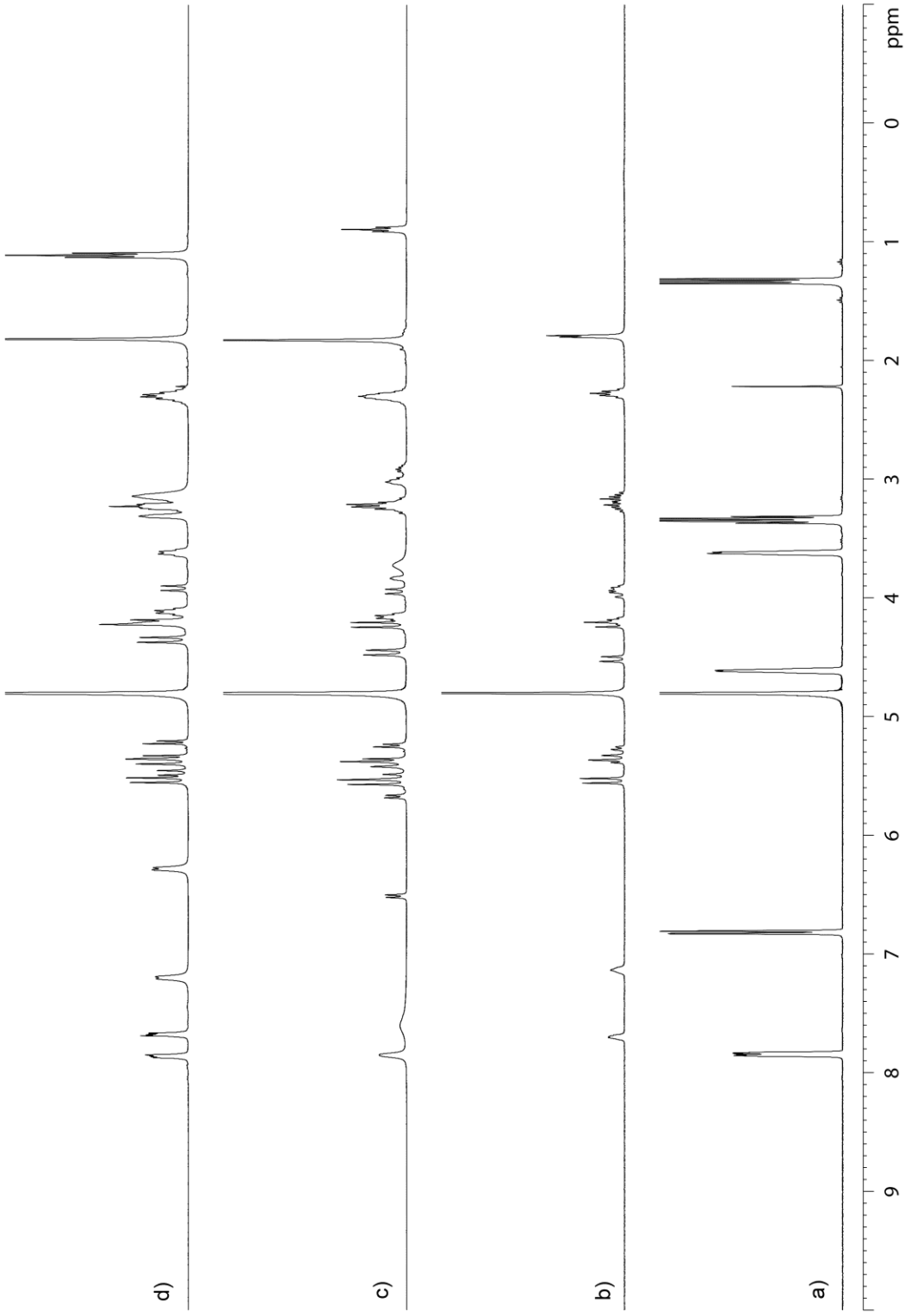

Figure II-S51. ^{1}H NMR spectra recorded (400 MHz, RT, D_2O) for a) **II-26**, b) **II-2**, c) an equimolar mixture of **II-2** and **II-26** (4 mM), and d) a 1:2 mixture of **II-2** (4 mM) and **II-26** (8 mM).

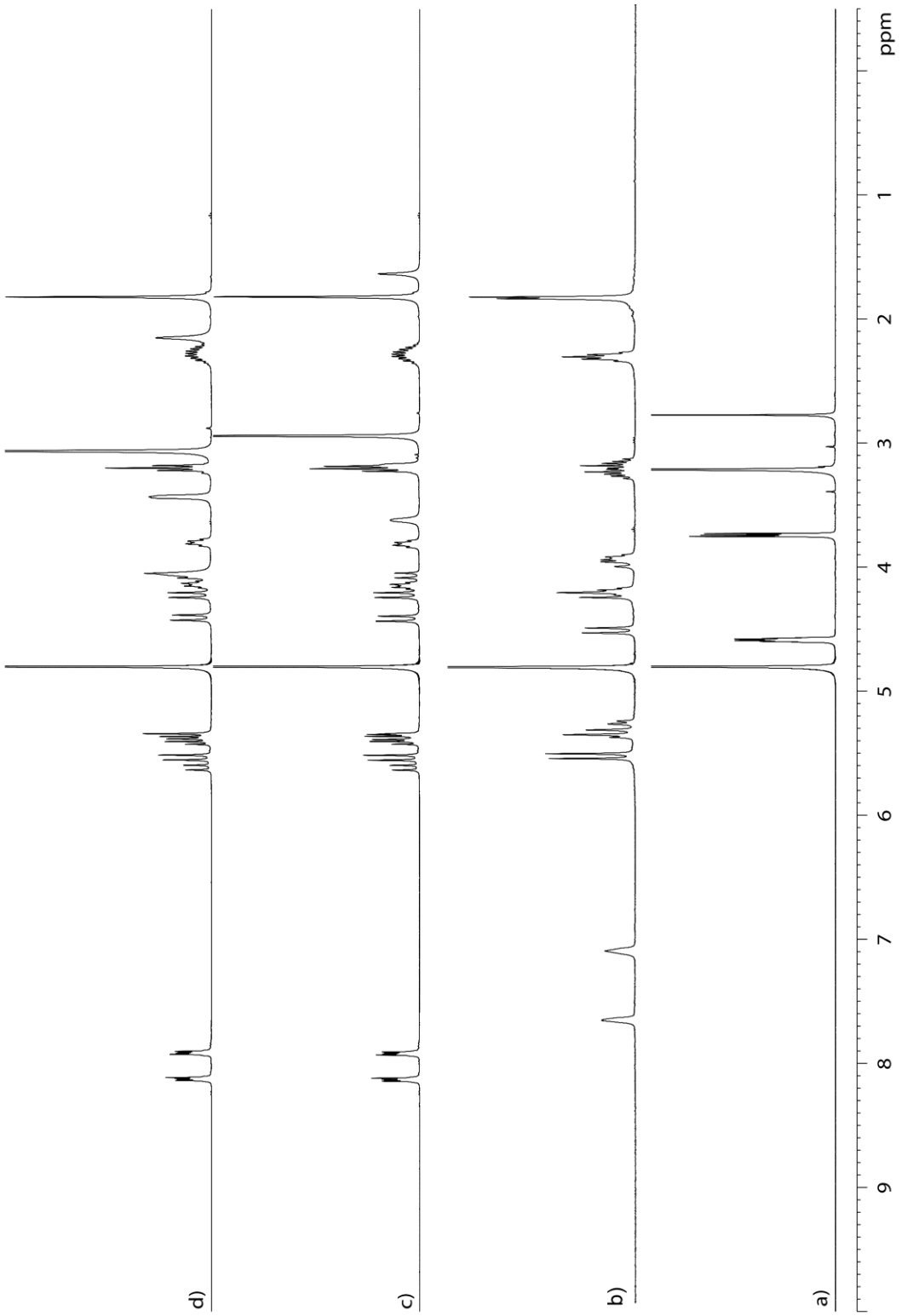

Figure II-S52. ^{1}H NMR spectra recorded (400 MHz, RT, D_2O) for a) **II-27**, b) **II-2**, c) an equimolar mixture of **II-2** and **II-27** (5 mM), and d) a 1:2 mixture of **II-2** (5 mM) and **II-27** (10 mM).

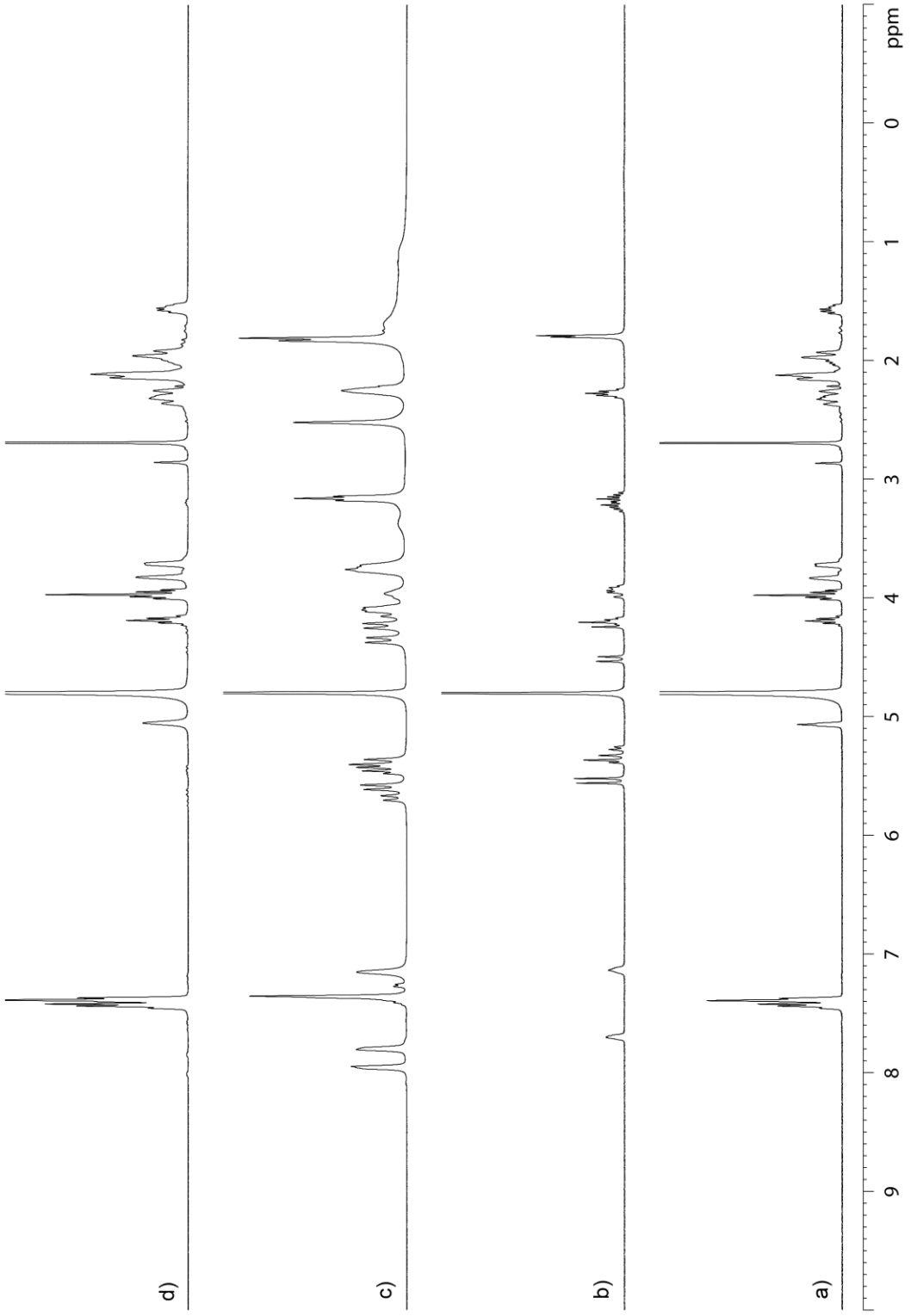

Figure II-S53. ^{1}H NMR spectra recorded (400 MHz, RT, D_2O) for a) **II-28**, b) **II-2**, c) an equimolar mixture of **II-2** and **II-28** (12.5 mM), and d) a 1:2 mixture of **II-2** (12.5 mM) and **II-28** (25 mM).

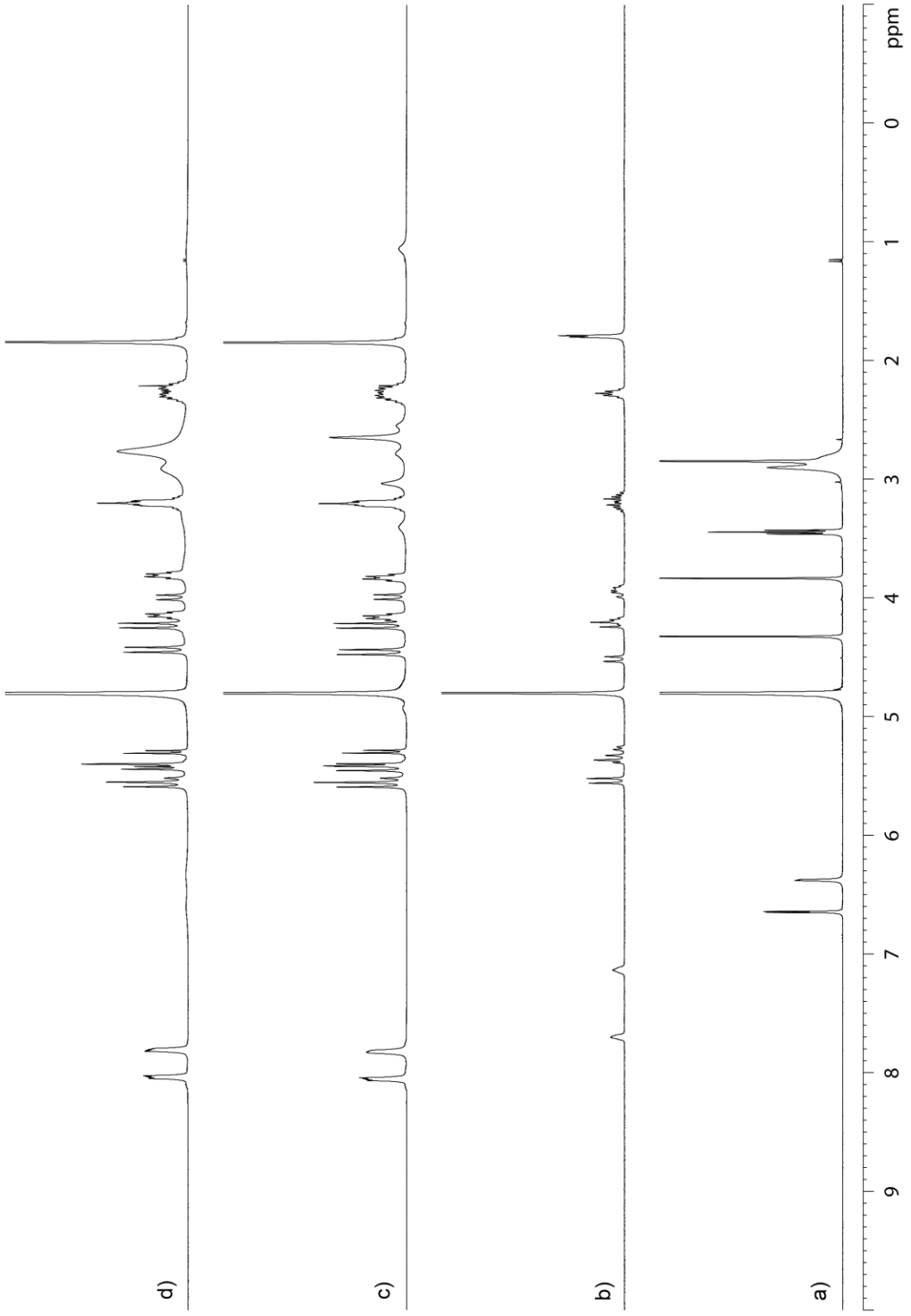

Figure II-S54. ^{1}H NMR spectra recorded (400 MHz, RT, D_2O) for a) **II-29**, b) **II-2**, c) an equimolar mixture of **II-2** and **II-29** (5 mM), and d) a 1:2 mixture of **II-2** (5 mM) and **II-29** (10 mM).

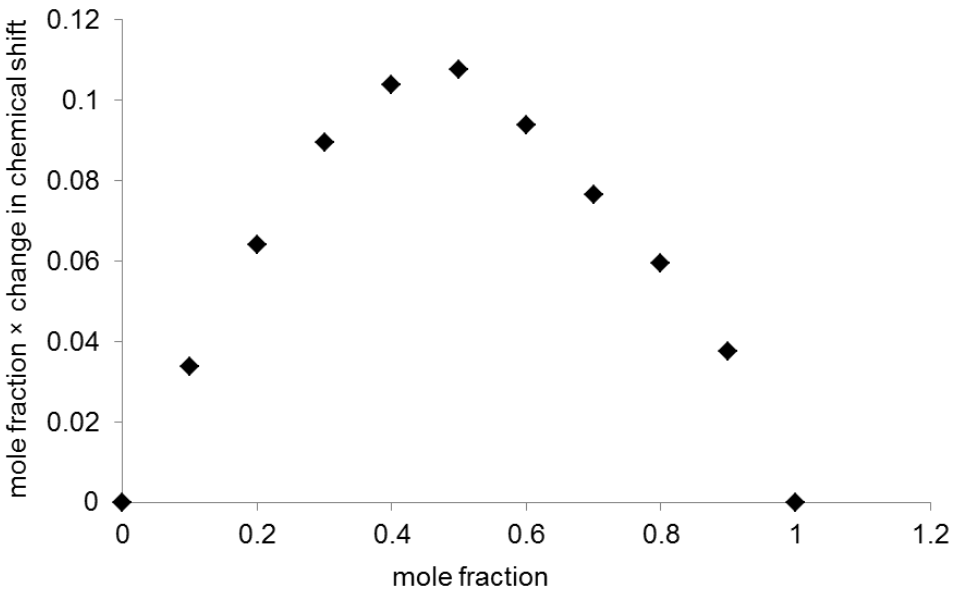

Figure II-S55. Job plot establishing 1:1 binding of **II-6** (0 - 1 mM) with **II-2** (0 - 1 mM) based on change in chemical shift of ^{1}H NMR (400 MHz, D_2O).

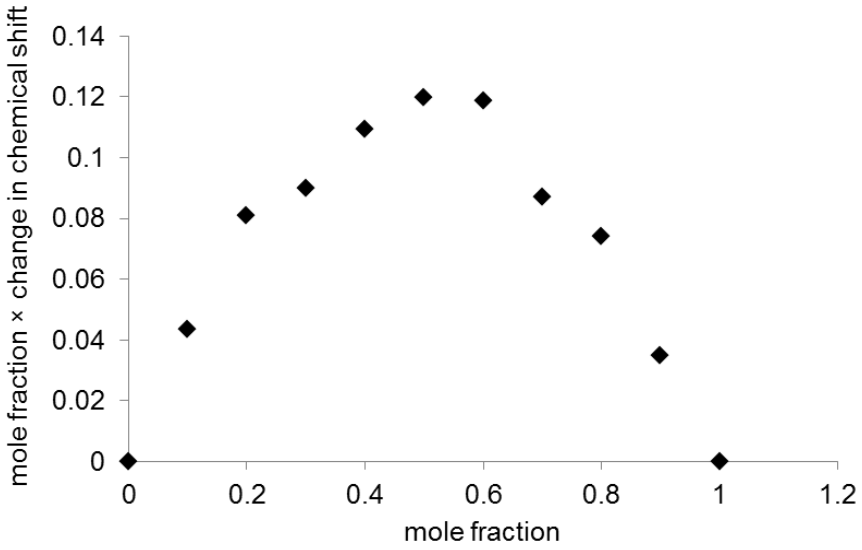

Figure II-S56. Job plot establishing 1:1 binding of **II-7** (0 - 1 mM) with **II-2** (0 - 1 mM) based on change in chemical shift of ^{1}H NMR (400 MHz, D_2O).

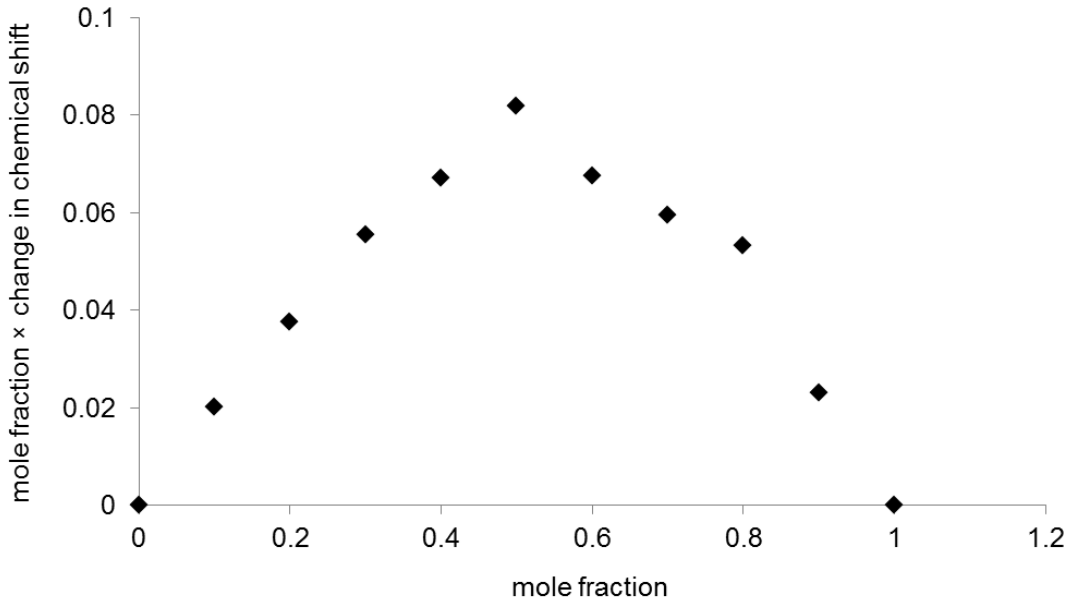

Figure II-S57. Job plot establishing 1:1 binding of **II-13** (0 - 1 mM) with **II-2** (0 - 1 mM) based on change in chemical shift of ^{1}H NMR (400 MHz, D_2O).

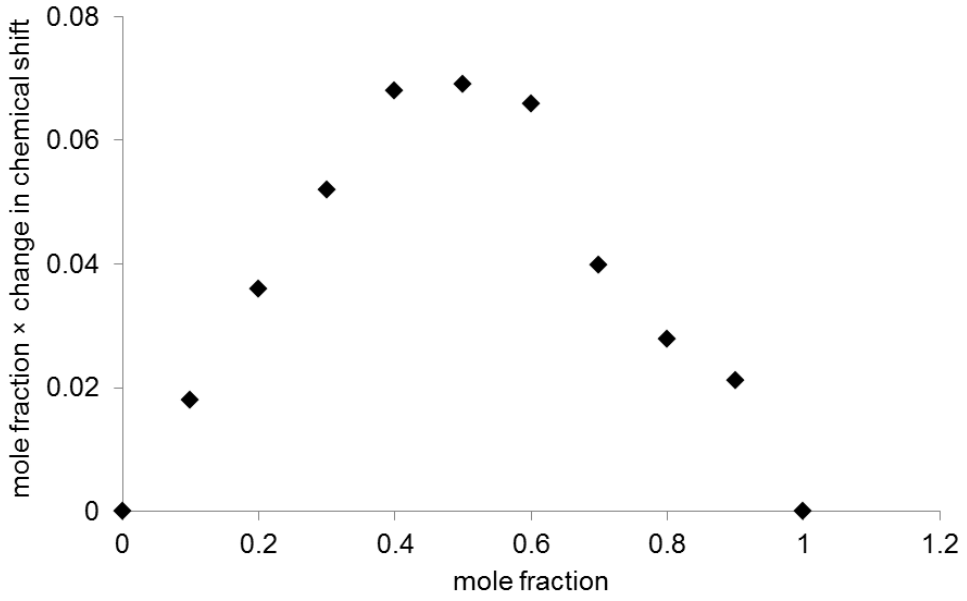

Figure II-S58. Job plot establishing 1:1 binding of **II-15** (0 - 1 mM) with **II-2** (0 - 1 mM) based on change in chemical shift of ^{1}H NMR (400 MHz, D_2O).

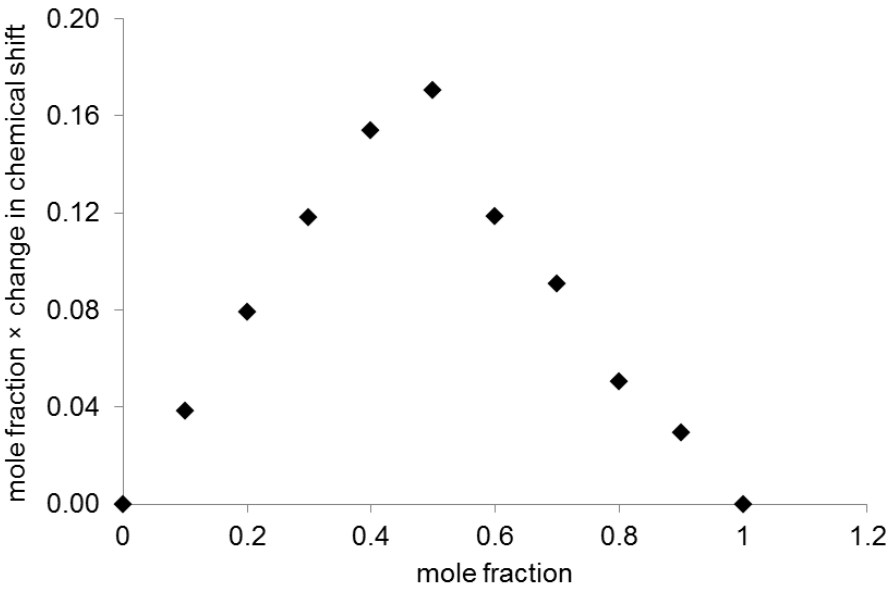

Figure II-S59. Job plot establishing 1:1 binding of **II-20** (0 - 1 mM) with **II-2** (0 - 1 mM) based on change in chemical shift of ^{1}H NMR (400 MHz, D_2O).

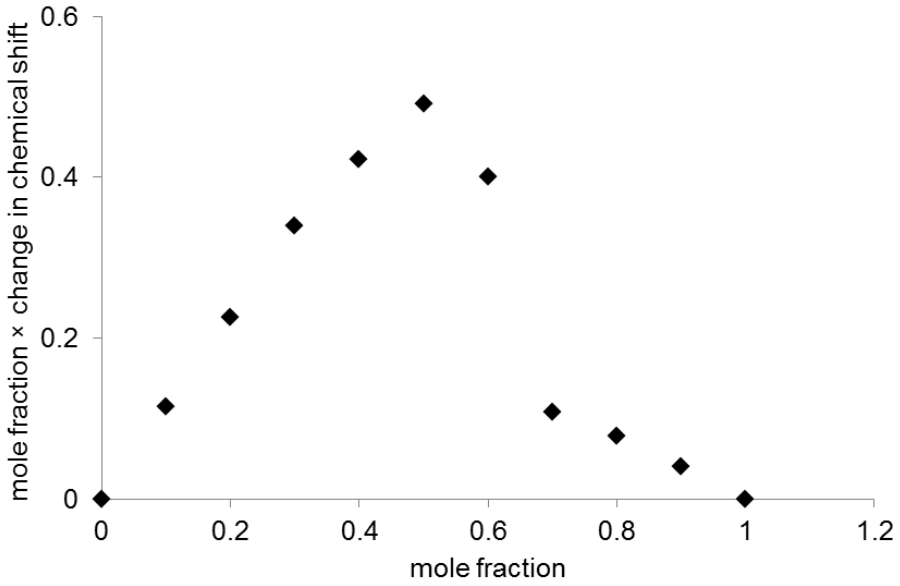

Figure II-S60. Job plot establishing 1:1 binding of **II-21** (0 - 1 mM) with **II-2** (0 - 1 mM) based on change in chemical shift of ^{1}H NMR (400 MHz, D_2O).

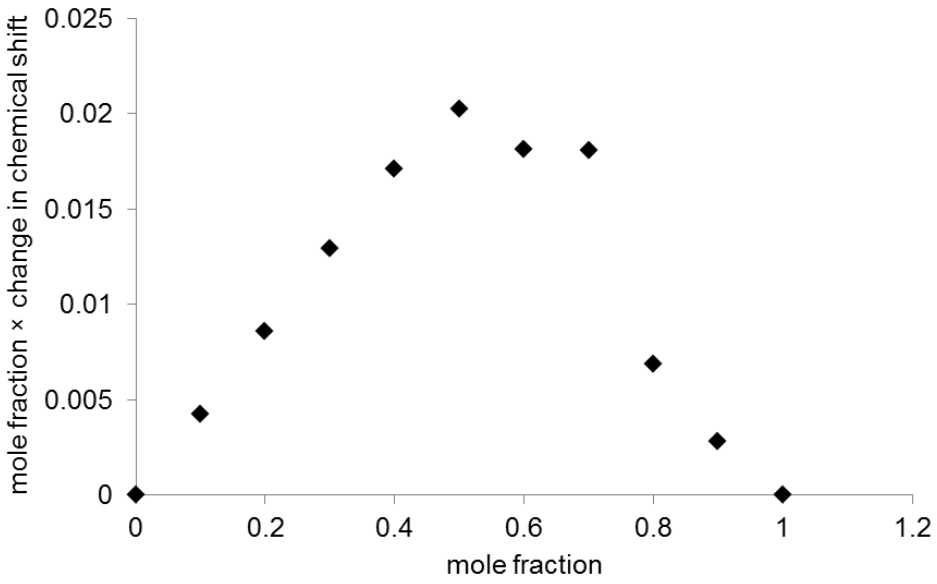

Figure II-S61. Job plot establishing 1:1 binding of **II-22** (0 - 1 mM) with **II-2** (0 - 1 mM) based on change in chemical shift of ^{1}H NMR (400 MHz, D_2O).

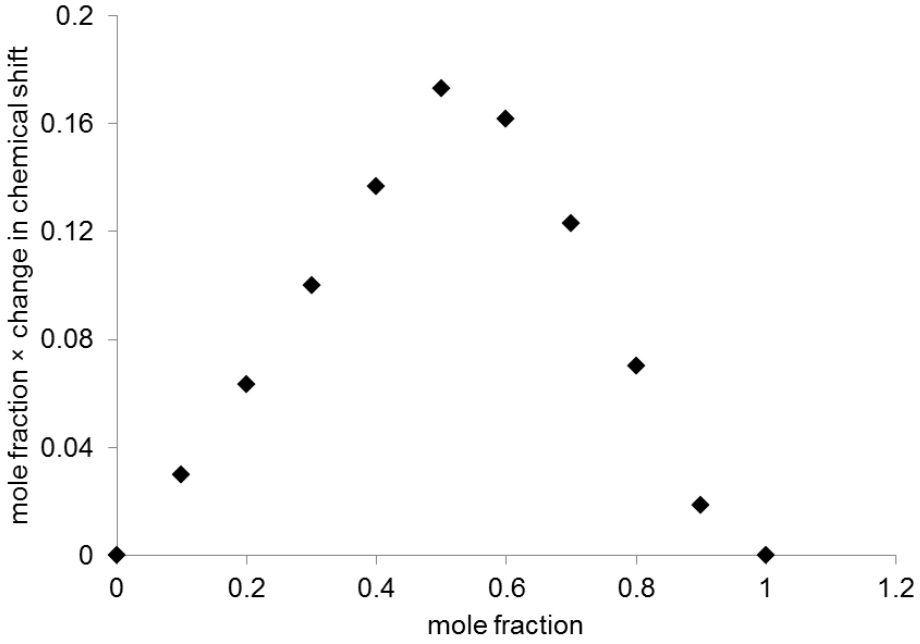

Figure II-S62. Job plot establishing 1:1 binding of **II-23** (0 - 1 mM) with **II-2** (0 - 1 mM) based on change in chemical shift of ^{1}H NMR (400 MHz, D_2O).

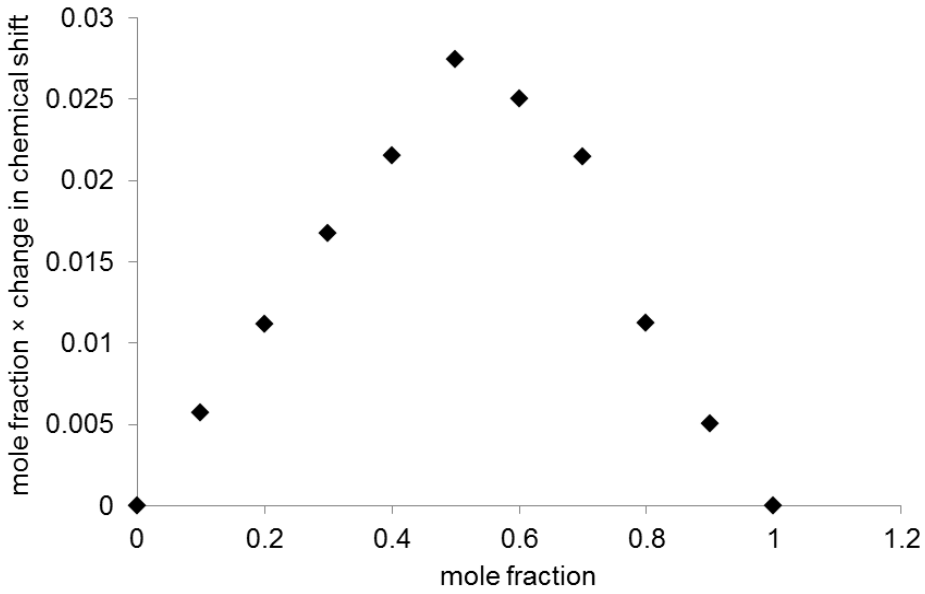

Figure II-S63. Job plot establishing 1:1 binding of **II-28** (0 - 1 mM) with **II-2** (0 - 1 mM) based on change in chemical shift of ^{1}H NMR (400 MHz, D_2O).

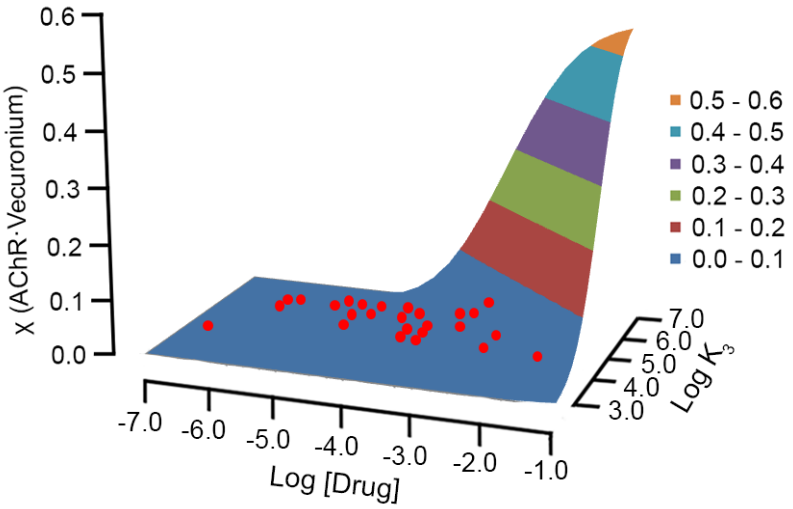

Figure II-S64. Three dimensional surface plot of the equilibrium mole fraction of AChR•vecuronium versus log [Drug] and log K_3 for vecuronium at [Vecuronium] = [AChR] = 27 μM, [**II-2**] = 54 μM (2 eqv.), $K_1 = 10^5$ M^{-1}, $K_2 = 1.6 \times 10^9$ M^{-1}. The red dots mark the points corresponding to each of the 27 drugs (**II-3** – **II-29**).

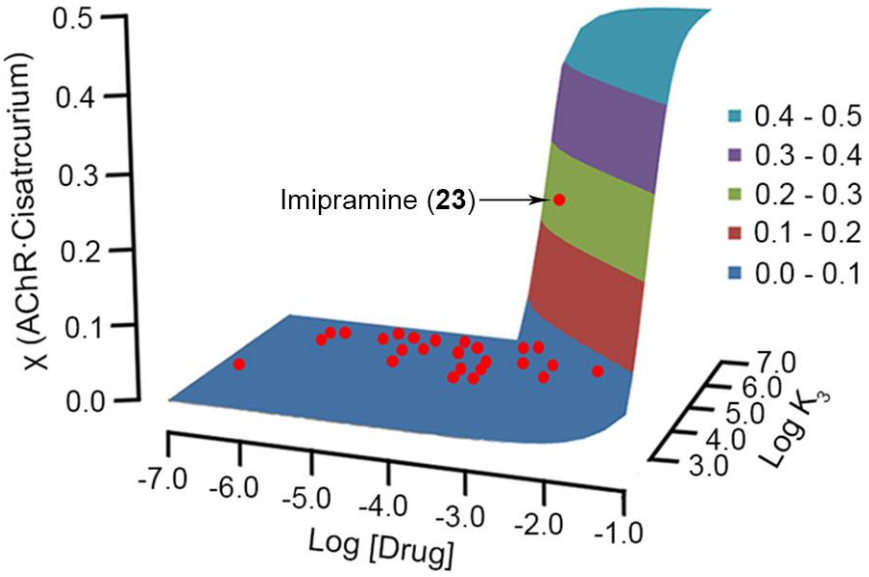

Figure II-S65. Three dimensional surface plot of the equilibrium mole fraction of AChR•cisatracurium versus log [Drug] and log K_3 at [Cisatracurium] = [AChR] = 18 μM, [**II-2**] = 576 μM (32 eqv.), $K_1 = 10^5$ M^{-1}, $K_2 = 4.8 \times 10^6$ M^{-1}. The red dots mark the points corresponding to each of the 27 drugs (**II-3** – **II-29**).

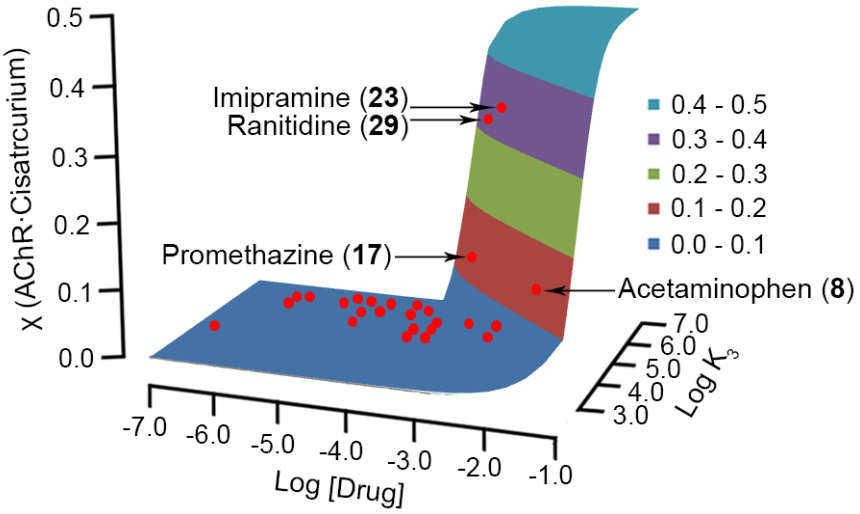

Figure II-S66. Three dimensional surface plot of the equilibrium mole fraction of AChR•cistracurium versus log [Drug] and log K_3 at [Cisatracurium] = [AChR] = 18 μM, [**II-2**] = 288 μM (16 eqv.), $K_1 = 10^5$ M^{-1}, $K_2 = 4.8 \times 10^6$ M^{-1}. The red dots mark the points corresponding to each of the 27 drugs (**II-3** – **II-29**).

Study of Hoffmann Degradation of Cisatracurium.

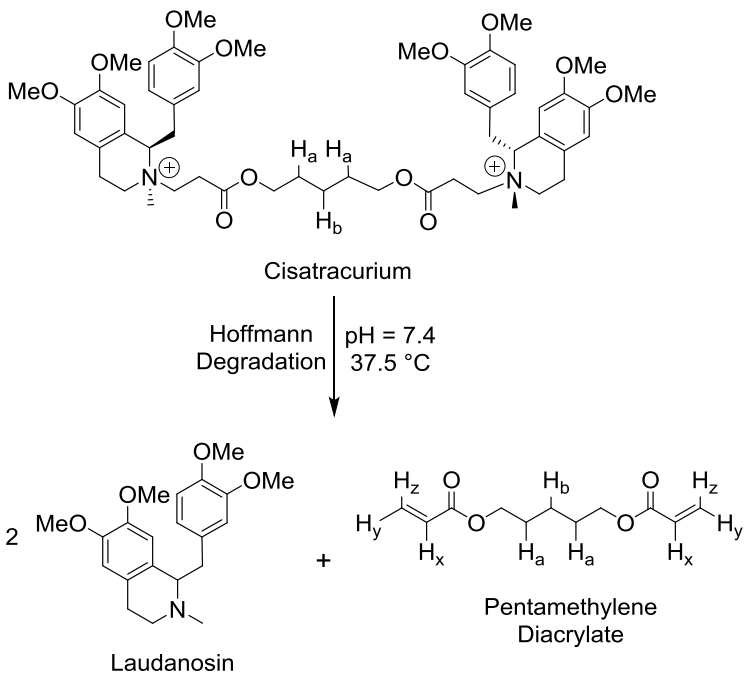

Figure II-S67. Probable pathway for the Hoffmann degradation of cisatracurium to laudanosin and pentamethylene diacrylate.

The Hoffmann degradation of cisatracurium was studied in the Krebs-Henseleit buffer (pH = 7.4, 37.5 °C), using ^{1}H-NMR. The Krebs-Henseleit buffer consisted of the following dissolved in deuterium oxide (D_2O): monopotassium phosphate (1.0 mM), magnesium sulphate heptahydrate (0.6 mM), potassium chloride (5.0 mM), sodium bicarbonate (30.0 mM), α-D-glucose monohydrate (20.0 mM), sodium chloride (118 mM), and calcium chloride (2.5 mM).

Figure II-S67 shows the most probable pathway for the degradation of cisatracurium to form laudanosin and pentamethylene diacrylate.

A 3.5 mM solution of cisatracurium in Krebs-Henseleit buffer was monitored by ^{1}H NMR every 10 min for 1 hour, and then hourly for 5 h. The last reading was taken 24 hours after the solution was prepared.

The conversion of cisatracurium into pentamethylene diacrylate was monitored by the appearance of its characteristic alkene proton peaks: H_x (2H, 6.35 ppm), H_y (2H, 6.13 ppm), and H_z (2H, 6.56 ppm), which increased in intensity over time. The peaks for H_a (4H, 1.90 ppm) and H_b (2H, 1.63 ppm) in cisatracurium overlap with those of pentamethylene diacrylate; hence their integrals represent the total concentration of cisatracurium added. These integrals can be compared to those of H_x, H_y, and H_z to quantify the extent of degradation with time.

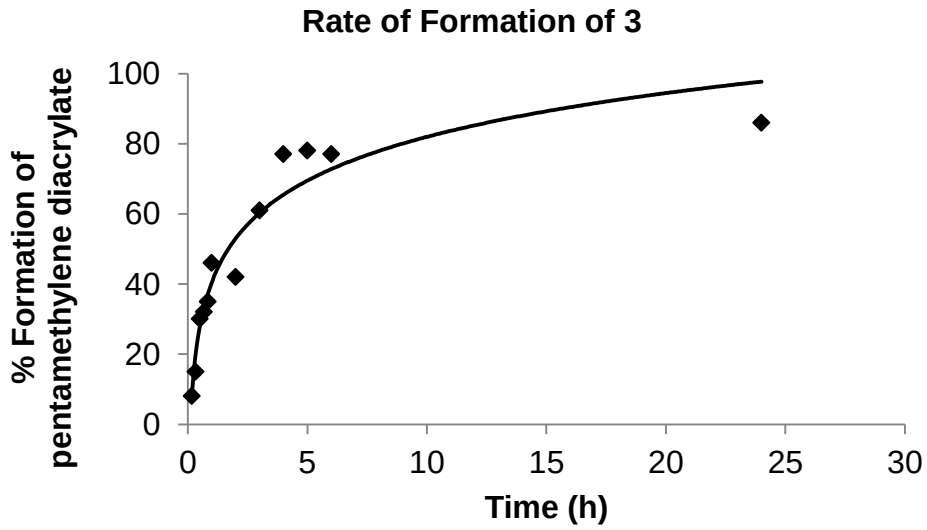

Figure II-S68. Plot of the formation of pentamethylene diacrylate over 24 h.

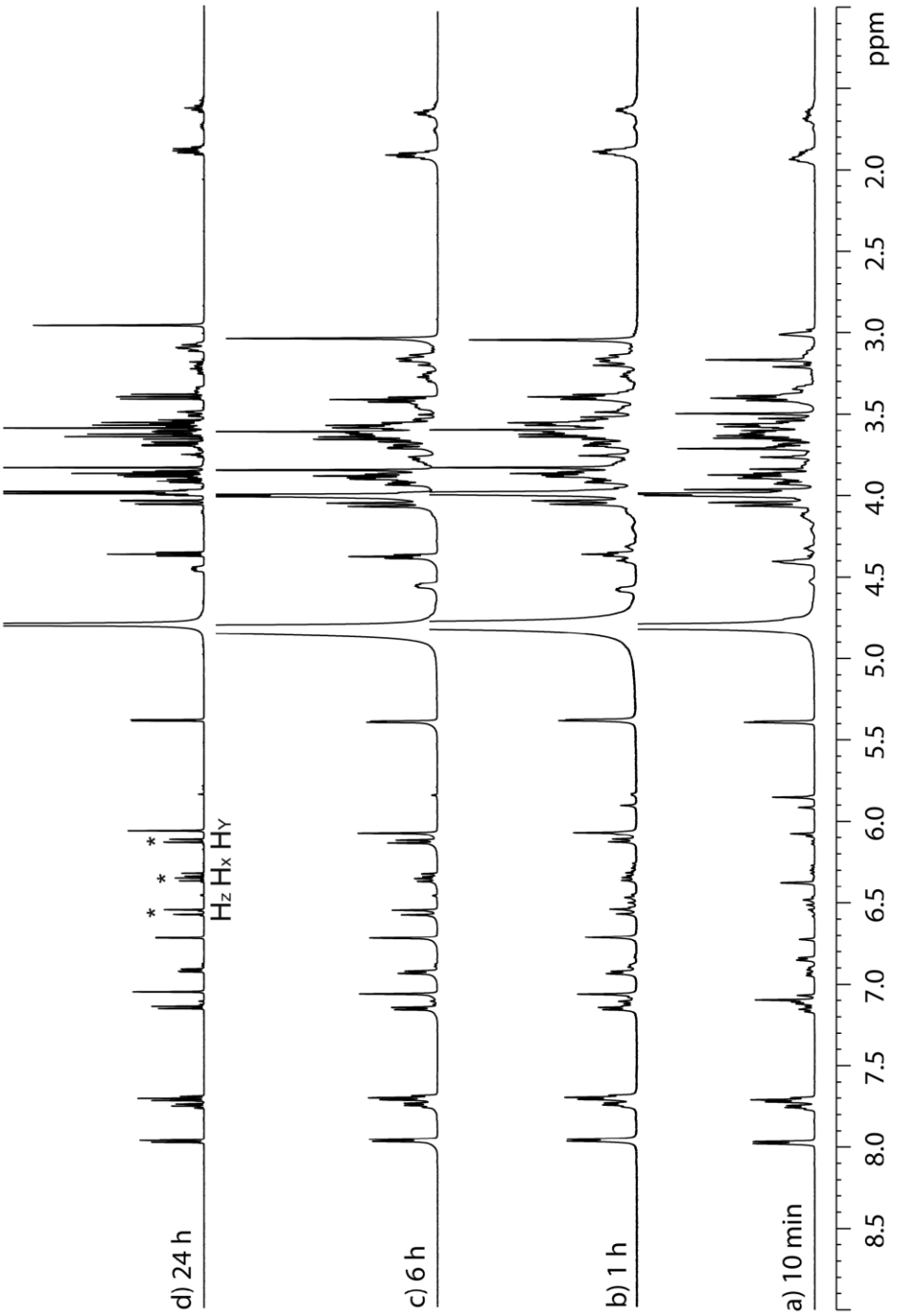

Figure II-S69. ^{1}H NMR spectra recorded (600 MHz, 37.5 °C, Krebs-Henseleit buffer in D_2O at pH = 7.4) for 3.5 mM cisatracurium at: a) 10 min, b) 1 h, c) 6 h, and d) 24 h.

Appendix 2

Molecular Containers Bind Drugs of Abuse in Vitro and Reverse the Hyperlocomotive Effect of Methamphetamine in Rats

Shweta Ganapati,[a] Stephanie Grabitz,[b] Steven Murkli,[a] Flora Scheffenbichler [b], Maíra I. Rudolph, [b] Peter Y. Zavalij, [a] Matthias Eikermann,[b] and Lyle Isaacs*[a]*

[a]Department of Chemistry and Biochemistry, University of Maryland, College Park, MD 20742 and [b]Department of Anesthesia, Critical Care and Pain Medicine, Massachusetts General Hospital, and Harvard Medical School, 55 Fruit Street, Boston, Massachusetts 02114

Supporting Information

Table of Contents **Pages**

General experimental details	168
^{1}H NMR based binding studies between various hosts and guests	169-203
Procedures and binding models for UV/Vis titrations	204-205
UV/Vis spectra and plots of absorbance data for K_a determination for various guests and hosts	206-215
Procedure and binding model for ^{1}H NMR titrations	216
^{1}H NMR stack plots and plots of chemical shift data for K_a determination by direct ^{1}H NMR titration	217-225
Procedure for K_a determination by ITC	226
ITC data for K_a determination for various guests and hosts	227-243
Job plots of selected hosts with methamphetamine	244
Details of the *in vivo* experiments	245-247

General experimental details.

Drugs used for measuring binding constants, host p-sulfo calix[4]arene, and hydroxypropyl β-cyclodextrin (HP-β-CD) were purchased from commercial suppliers and used without further purification. Calabadion 1, Calabadion 2, and CB[7] were prepared according to the literature procedures.[40,108] ^{1}H NMR spectra were measured on Bruker instruments operating at 400 or 600 MHz. UV/Vis spectra were measured on a Varian Cary 100 UV spectrophotometer. ITC data was collected on a Malvern Microcal PEAQ-ITC instrument.

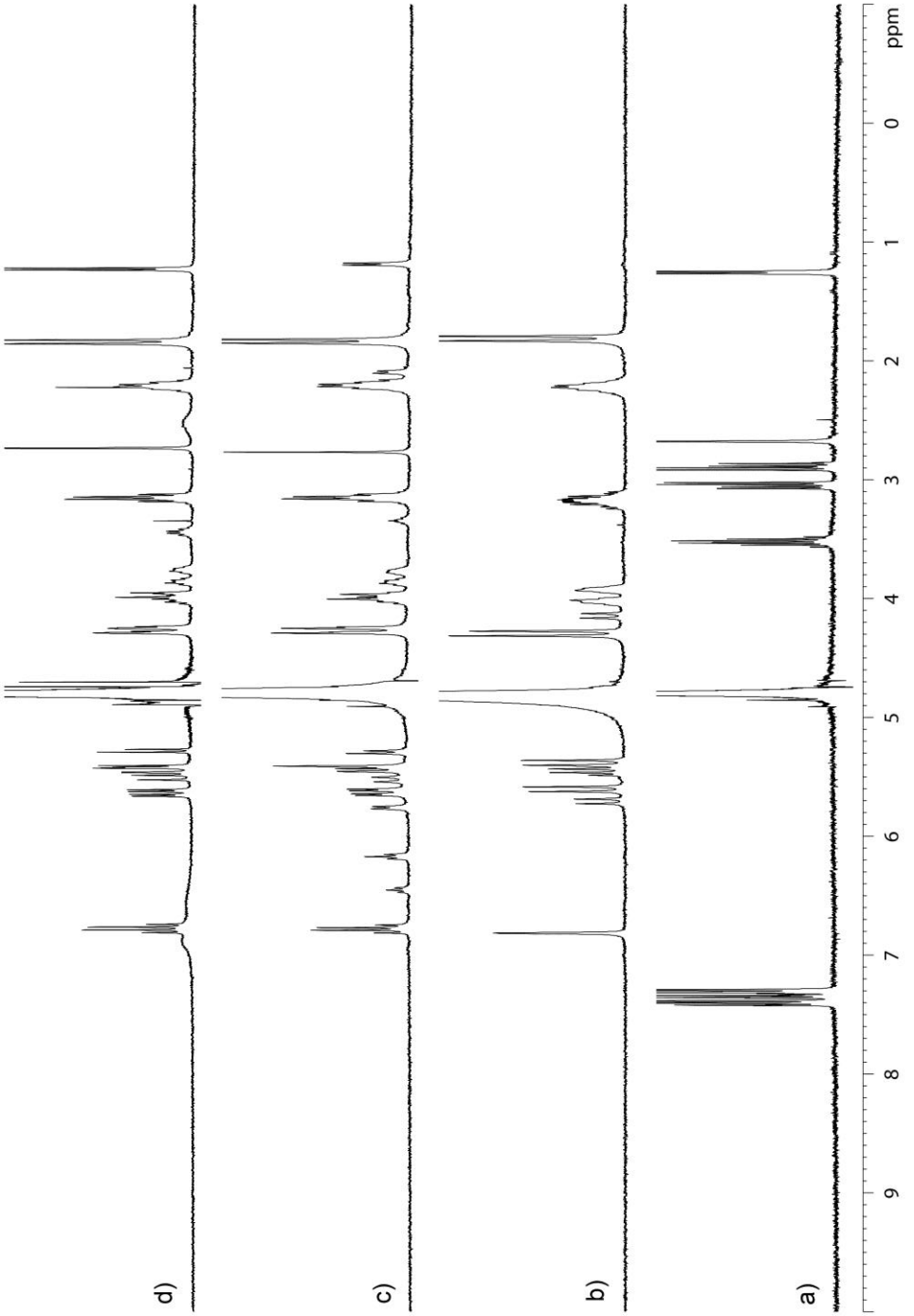

Figure III-S1. ^{1}H NMR spectra recorded (400 MHz, RT, D_2O) for: a) methamphetamine, b) Calabadion 1, c) an equimolar mixture of methamphetamine and Calabadion 1 (1 mM), and d) a 2:1 mixture of methamphetamine (2 mM) and Calabadion 1 (1 mM).

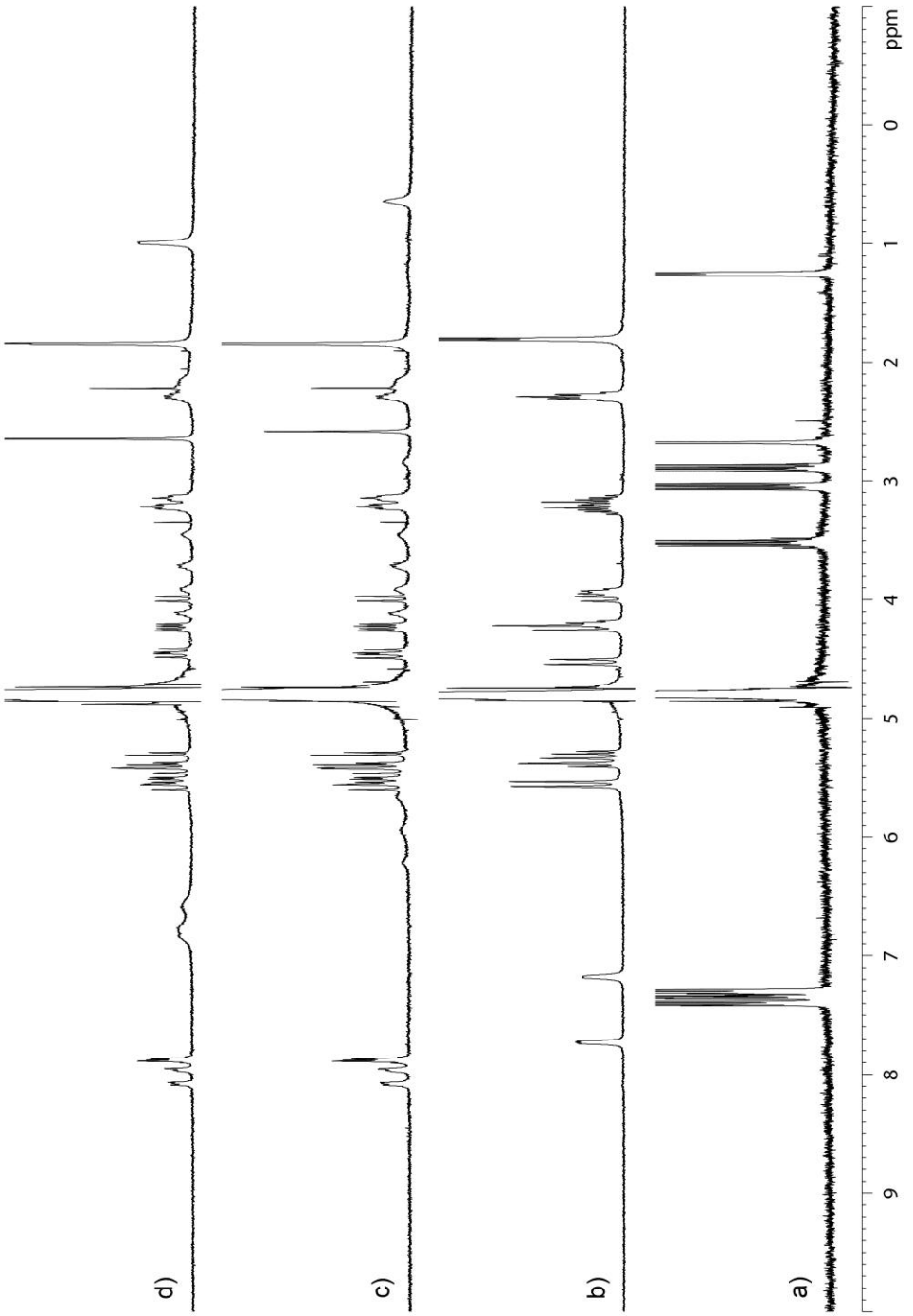

Figure III-S2. ^{1}H NMR spectra recorded (400 MHz, RT, D_2O) for: a) methamphetamine, b) Calabadion 2, c) an equimolar mixture of methamphetamine and Calabadion 2 (2 mM), and d) a 2:1 mixture of methamphetamine (2 mM) and Calabadion 2 (1 mM).

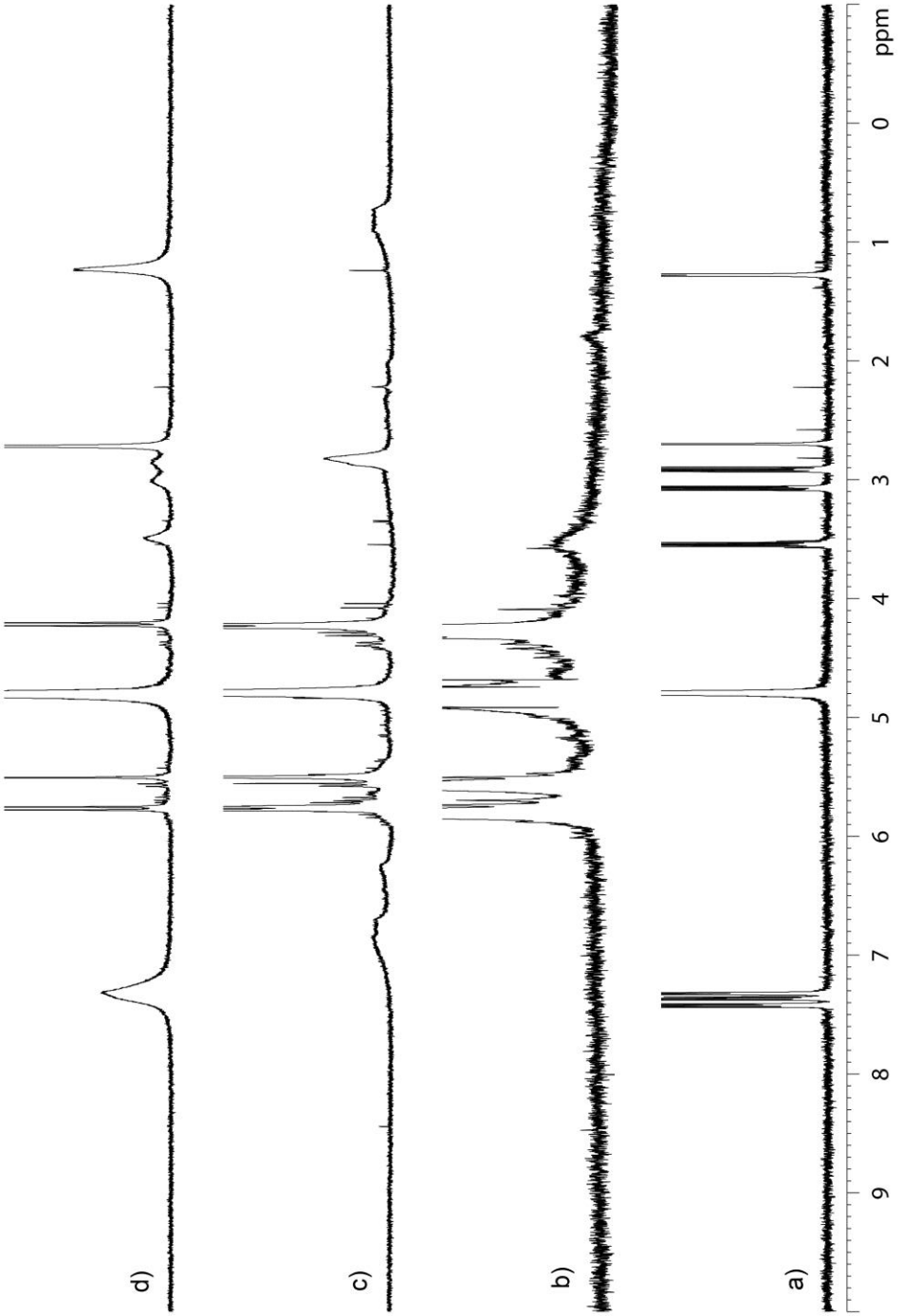

Figure III-S3. ^{1}H NMR spectra recorded (400 MHz, RT, D_2O) for: a) methamphetamine, b) CB[7], c) an equimolar mixture of methamphetamine and CB[7] (2 mM), and d) a 2:1 mixture of methamphetamine (2 mM) and CB[7] (1 mM).

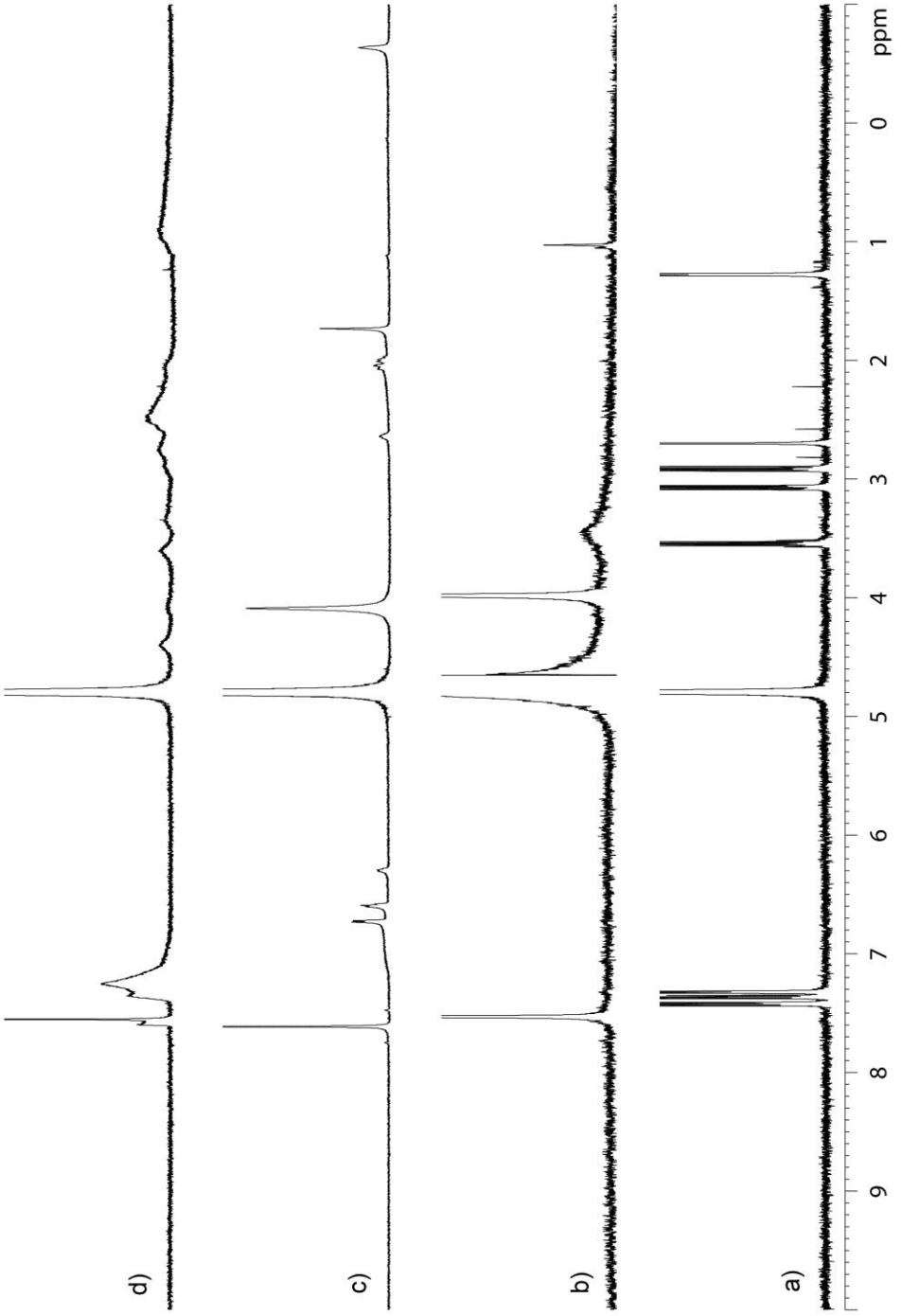

Figure III-S4. ^{1}H NMR spectra recorded (400 MHz, RT, D_2O) for: a) methamphetamine, b) p-sulfo calix[4]arene, c) an equimolar mixture of methamphetamine and p-sulfo calix[4]arene (2 mM), and d) a 2:1 mixture of methamphetamine (2 mM) and p-sulfo calix[4]arene (1 mM).

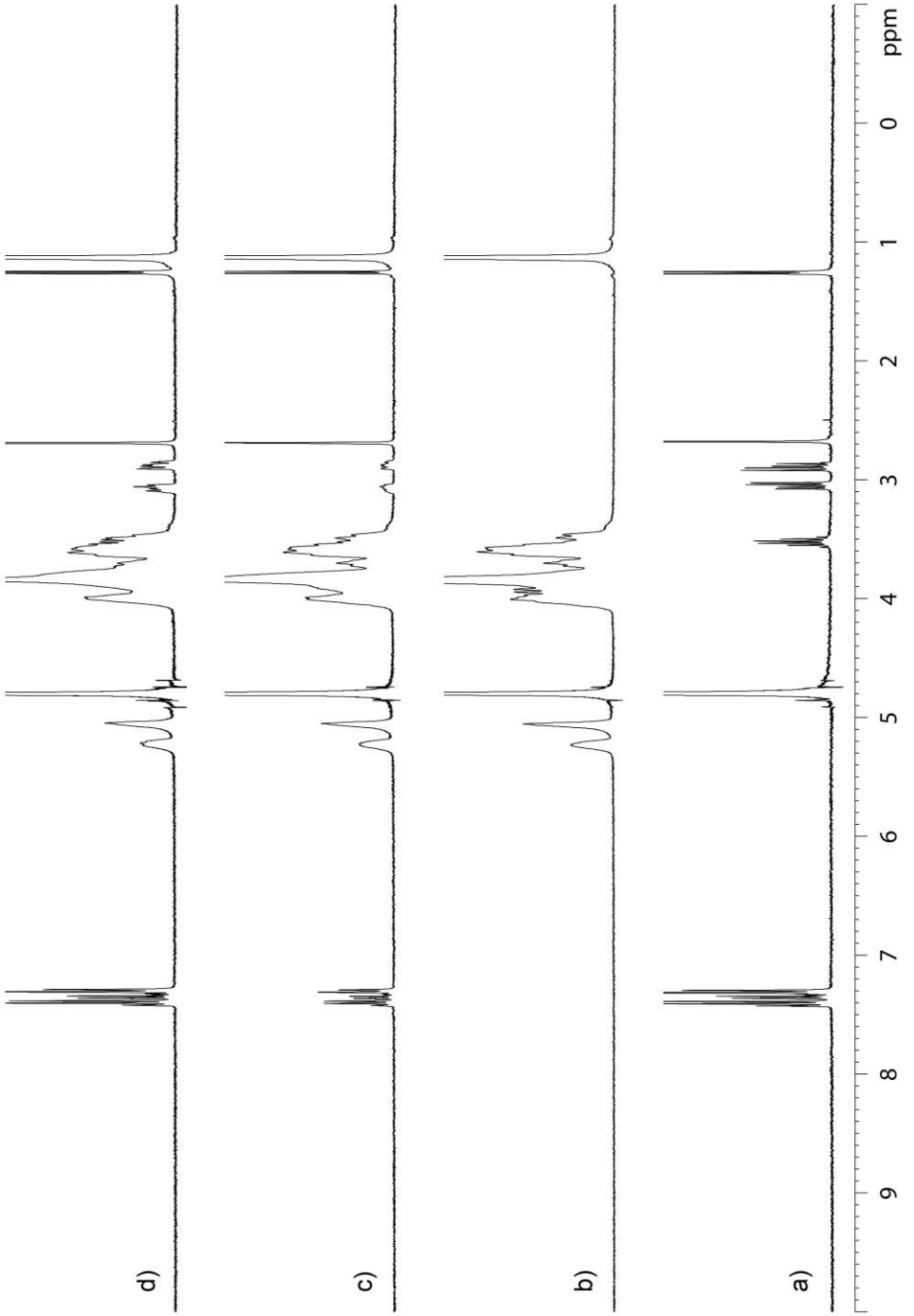

Figure III-S5. ^{1}H NMR spectra recorded (400 MHz, RT, D_2O) for: a) methamphetamine, b) HP-β-CD, c) an equimolar mixture of methamphetamine and HP-β-CD (1 mM), and d) a 2:1 mixture of methamphetamine (2 mM) and HP-β-CD (1 mM).

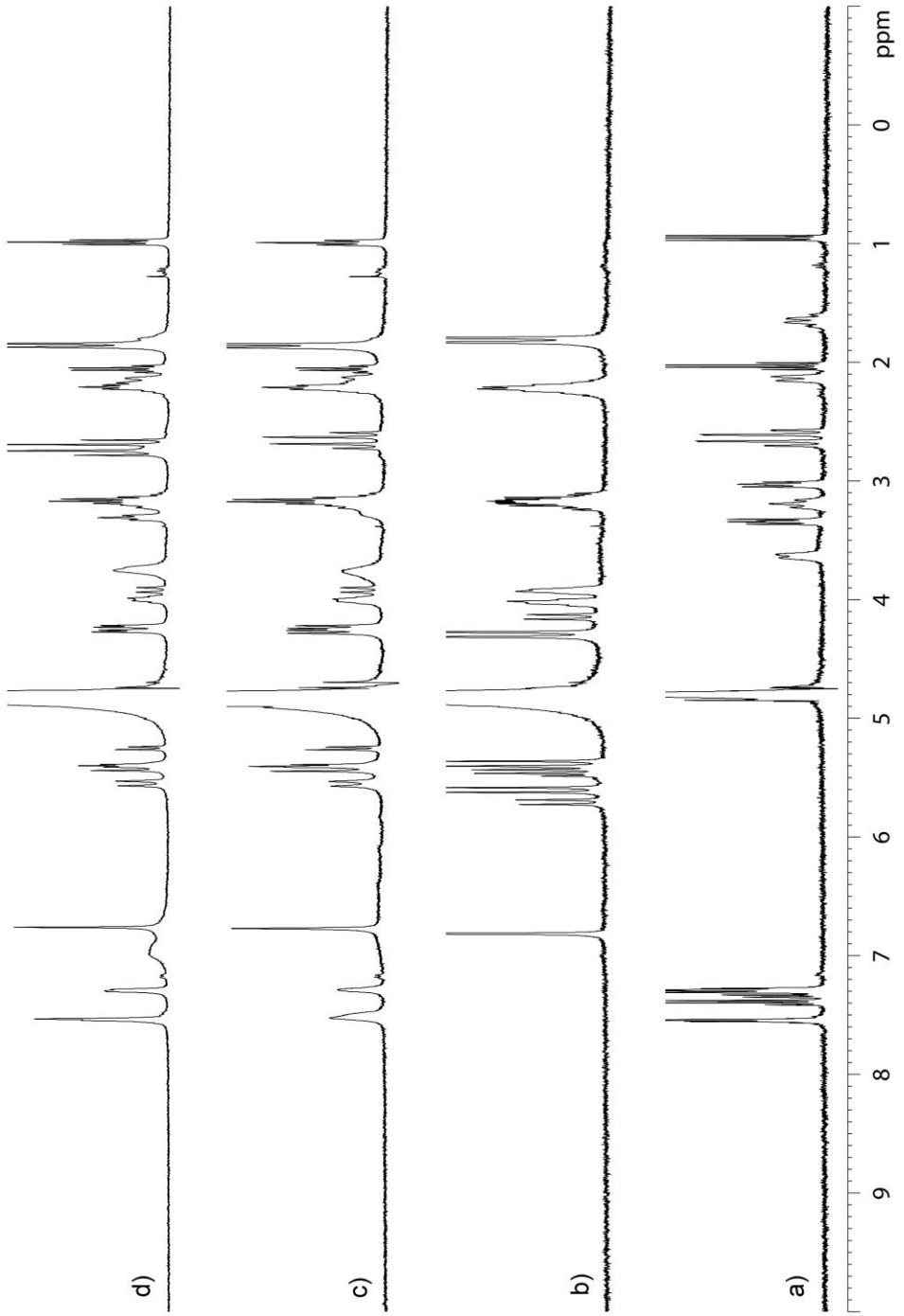

Figure III-S6. ^{1}H NMR spectra recorded (400 MHz, RT, D_2O) for: a) fentanyl, b) Calabadion 1, c) an equimolar mixture of fentanyl and Calabadion 1 (1 mM), and d) a 2:1 mixture of fentanyl (2 mM) and Calabadion 1 (1 mM).

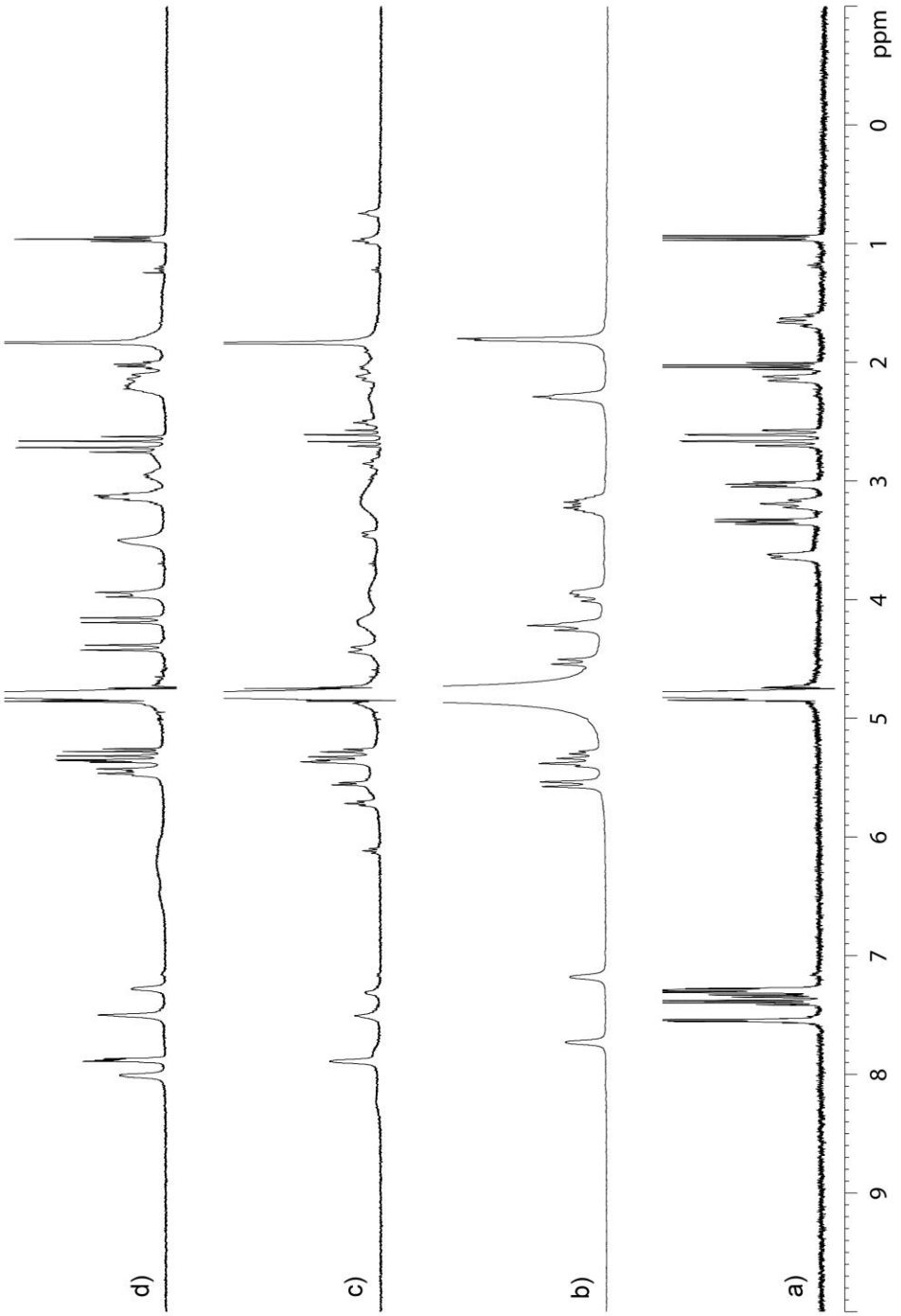

Figure III-S7. ^{1}H NMR spectra recorded (400 MHz, RT, D_2O) for: a) fentanyl, b) Calabadion 2, c) an equimolar mixture of fentanyl and Calabadion 2 (1 mM), and d) a 2:1 mixture of fentanyl (2 mM) and Calabadion 2 (1 mM).

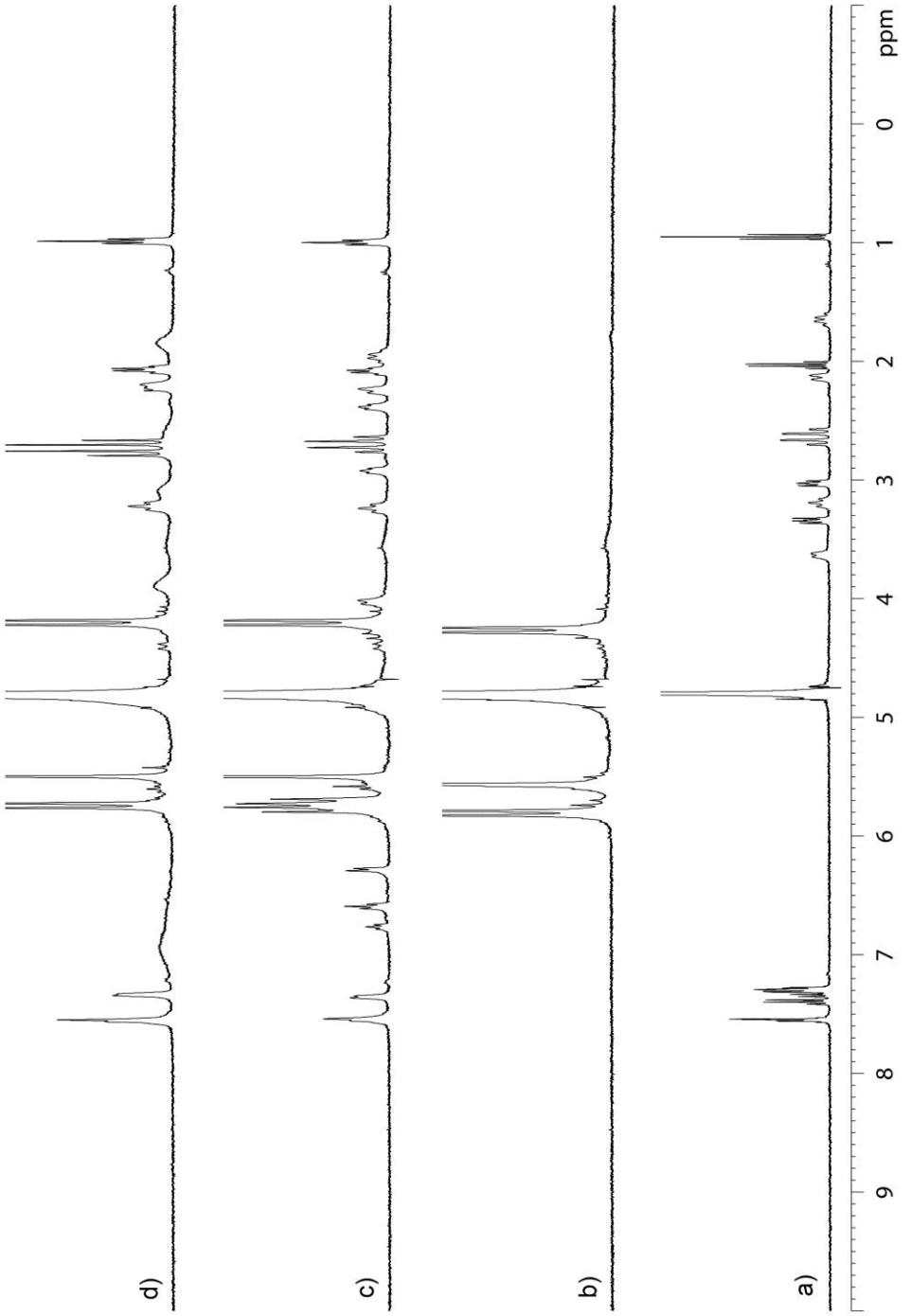

Figure III-S8. ^{1}H NMR spectra recorded (400 MHz, RT, D_2O) for: a) fentanyl, b) CB[7], c) an equimolar mixture of methamphetamine and fentanyl (1 mM), and d) a 2:1 mixture of fentanyl (2 mM) and CB[7] (1 mM).

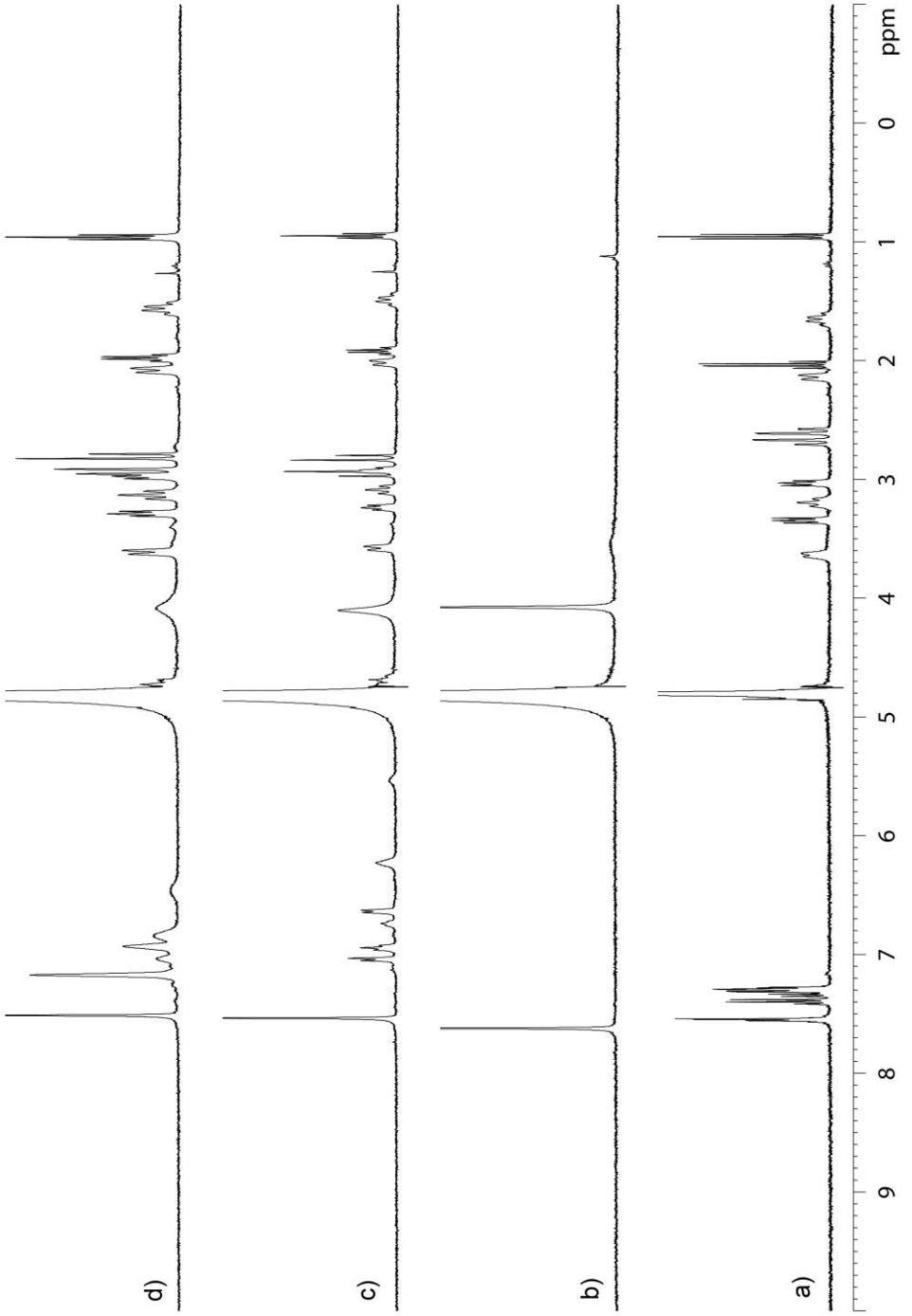

Figure III-S9. ^{1}H NMR spectra recorded (400 MHz, RT, D_2O) for: a) fentanyl, b) p-sulfo calix[4]arene, c) an equimolar mixture of fentanyl and p-sulfo calix[4]arene (1 mM), and d) a 2:1 mixture of fentanyl (2 mM) and p-sulfo calix[4]arene (1 mM).

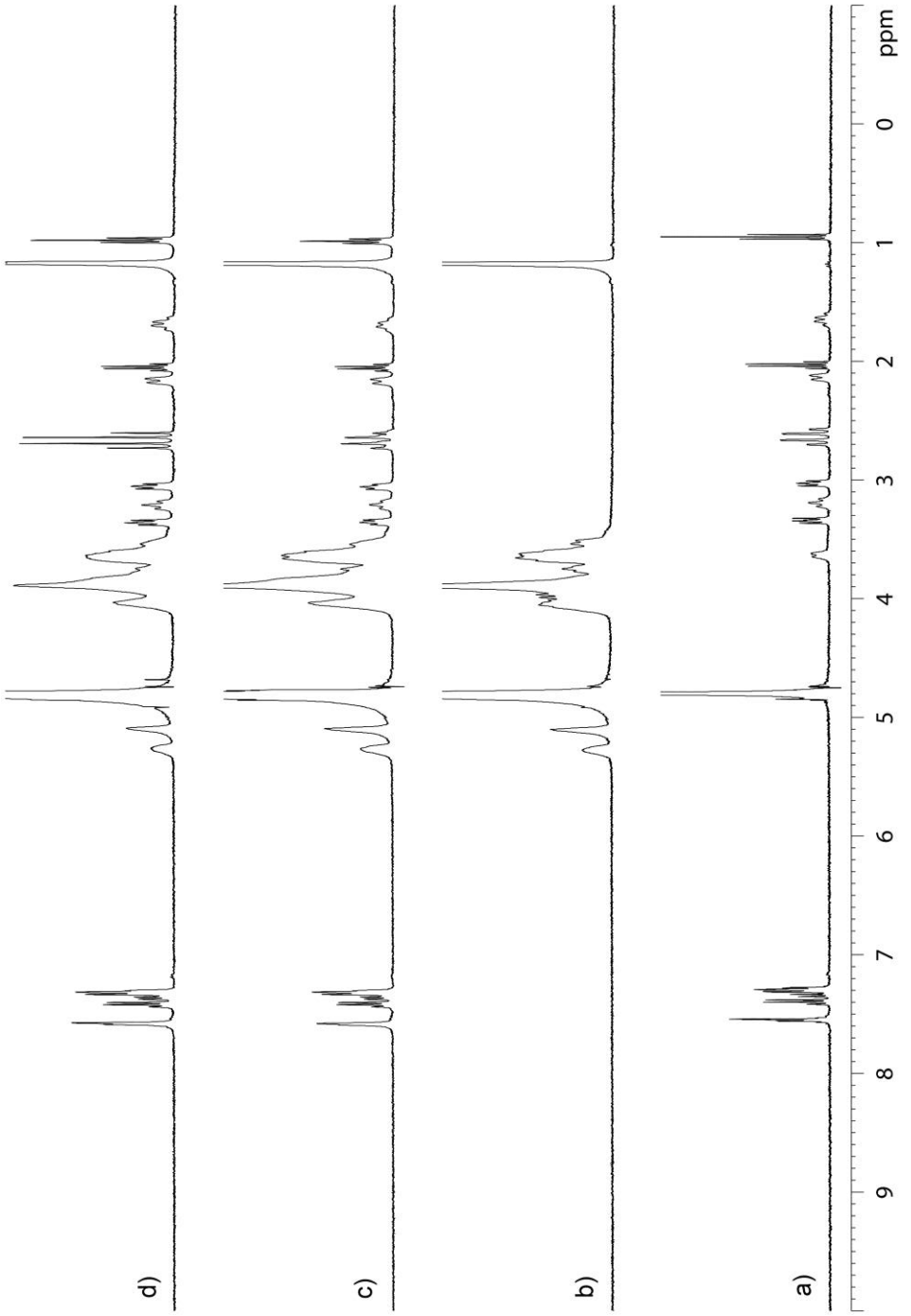

Figure III-S10. ^{1}H NMR spectra recorded (400 MHz, RT, D_2O) for: a) fentanyl, b) HP-β-CD, c) an equimolar mixture of fentanyl and HP-β-CD (1 mM), and d) a 2:1 mixture of fentanyl (2 mM) and HP-β-CD (1 mM).

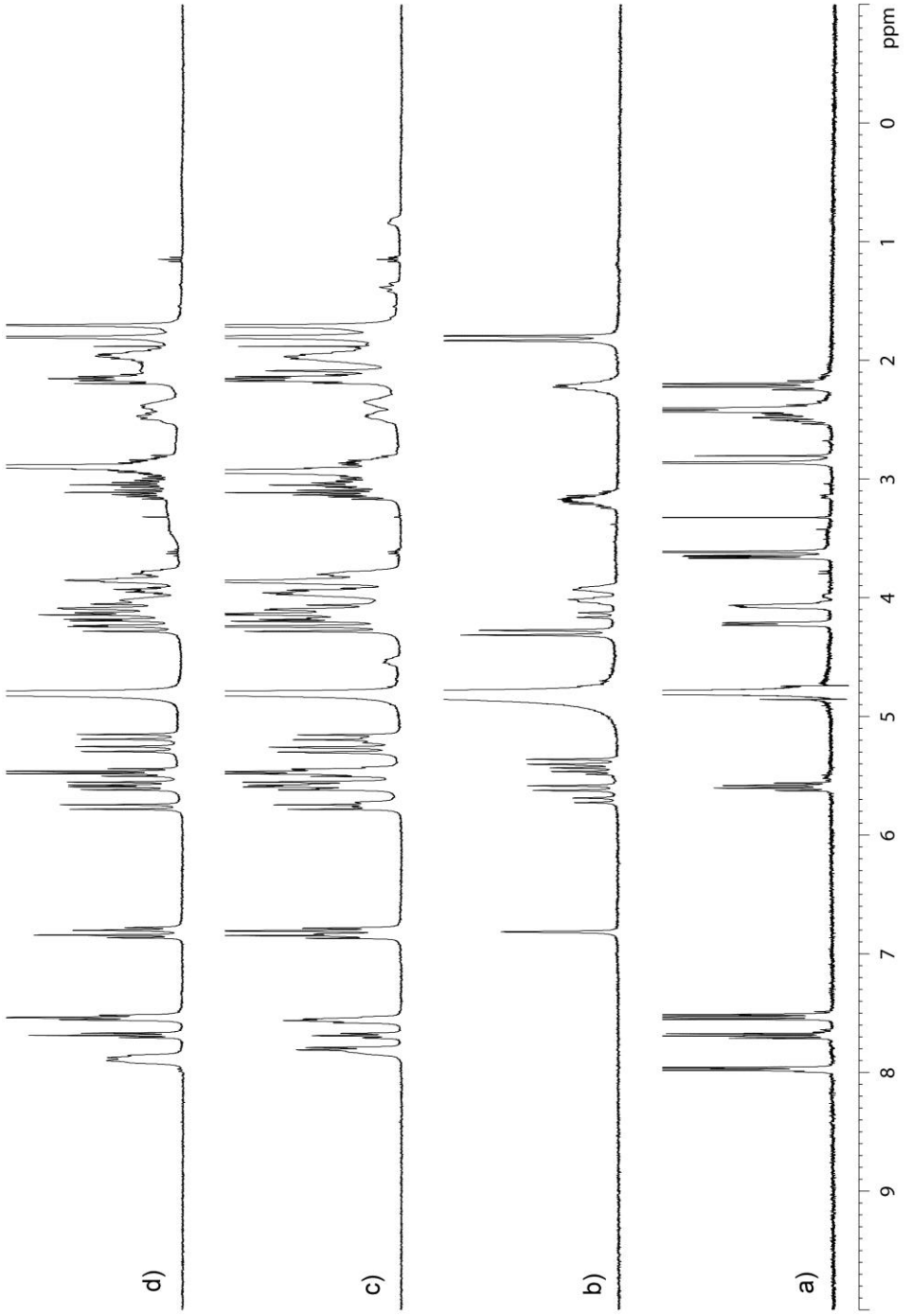

Figure III-S11. ^{1}H NMR spectra recorded (400 MHz, RT, D_2O) for: a) cocaine, b) Calabadion 1, c) an equimolar mixture of cocaine and Calabadion 1 (2 mM), and d) a 2:1 mixture of cocaine (2 mM) and Calabadion 1 (1 mM).

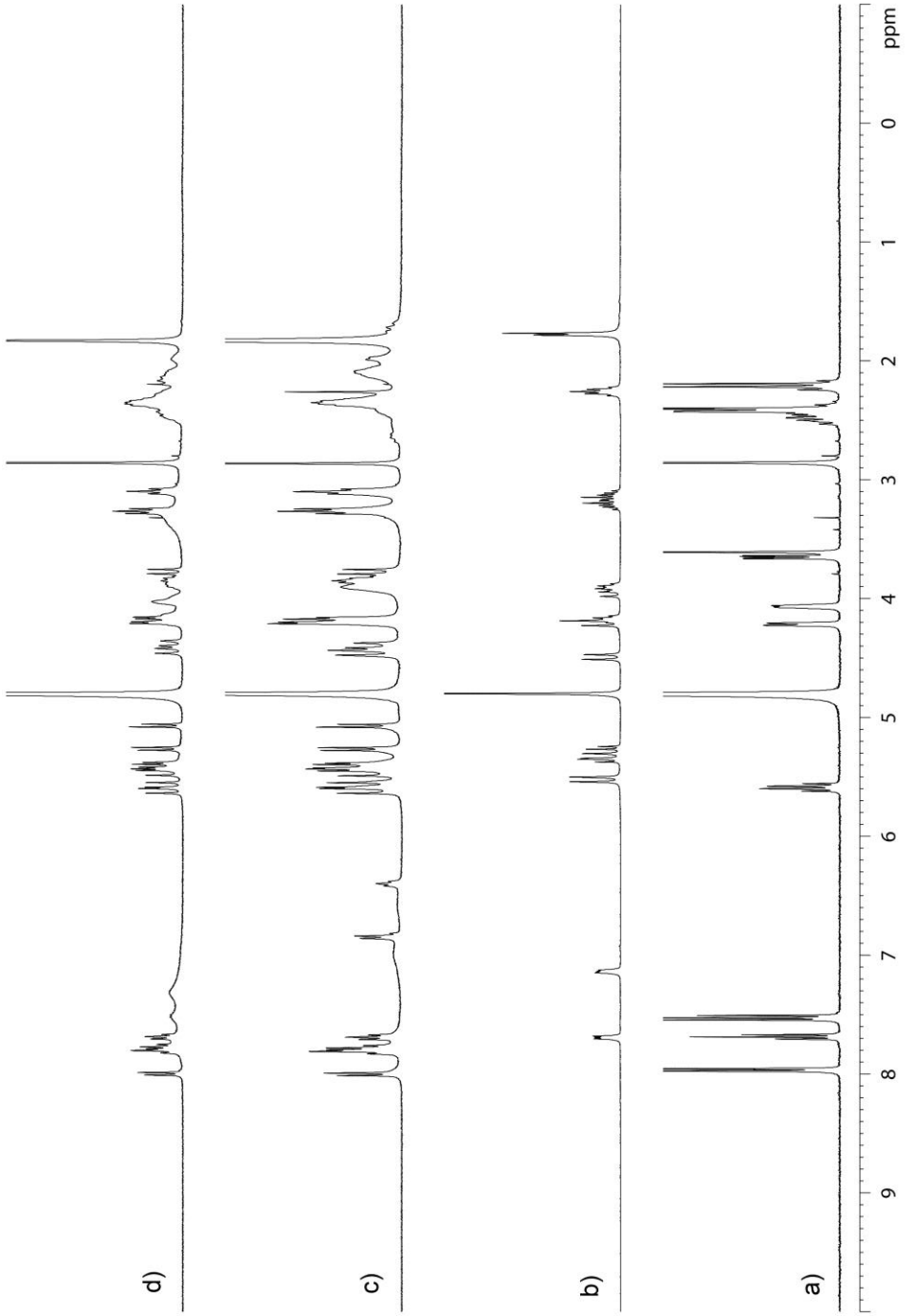

Figure III-S12. ^{1}H NMR spectra recorded (400 MHz, RT, D_2O) for: a) cocaine, b) Calabadion 2, c) an equimolar mixture of cocaine and Calabadion 2 (2 mM), and d) a 2:1 mixture of cocaine (2 mM) and Calabadion 2 (1 mM).

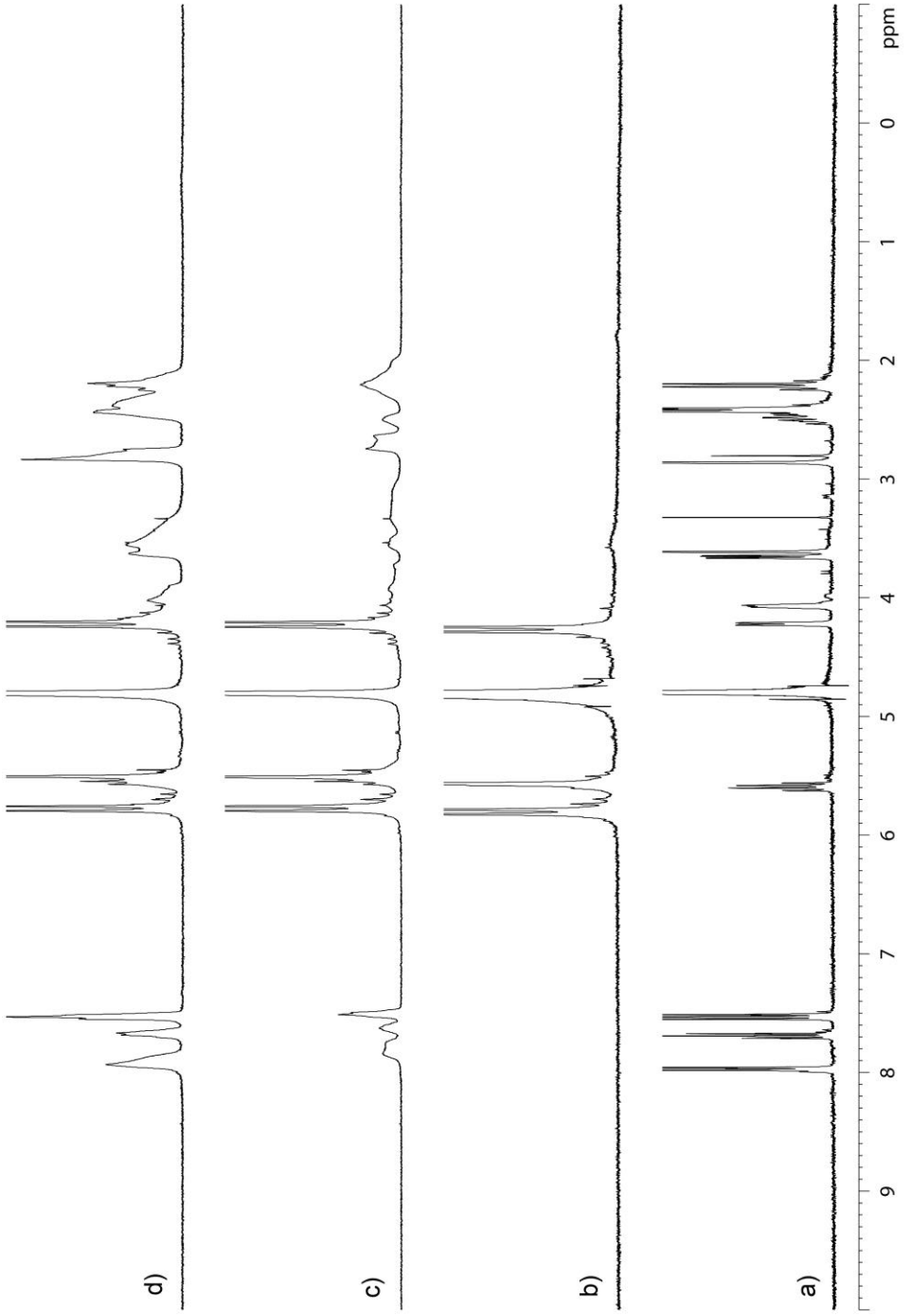

Figure III-S13. ^{1}H NMR spectra recorded (400 MHz, RT, D_2O) for: a) cocaine, b) CB[7], c) an equimolar mixture of cocaine and CB[7] (2 mM), and d) a 2:1 mixture of cocaine (2 mM) and CB[7] (1 mM).

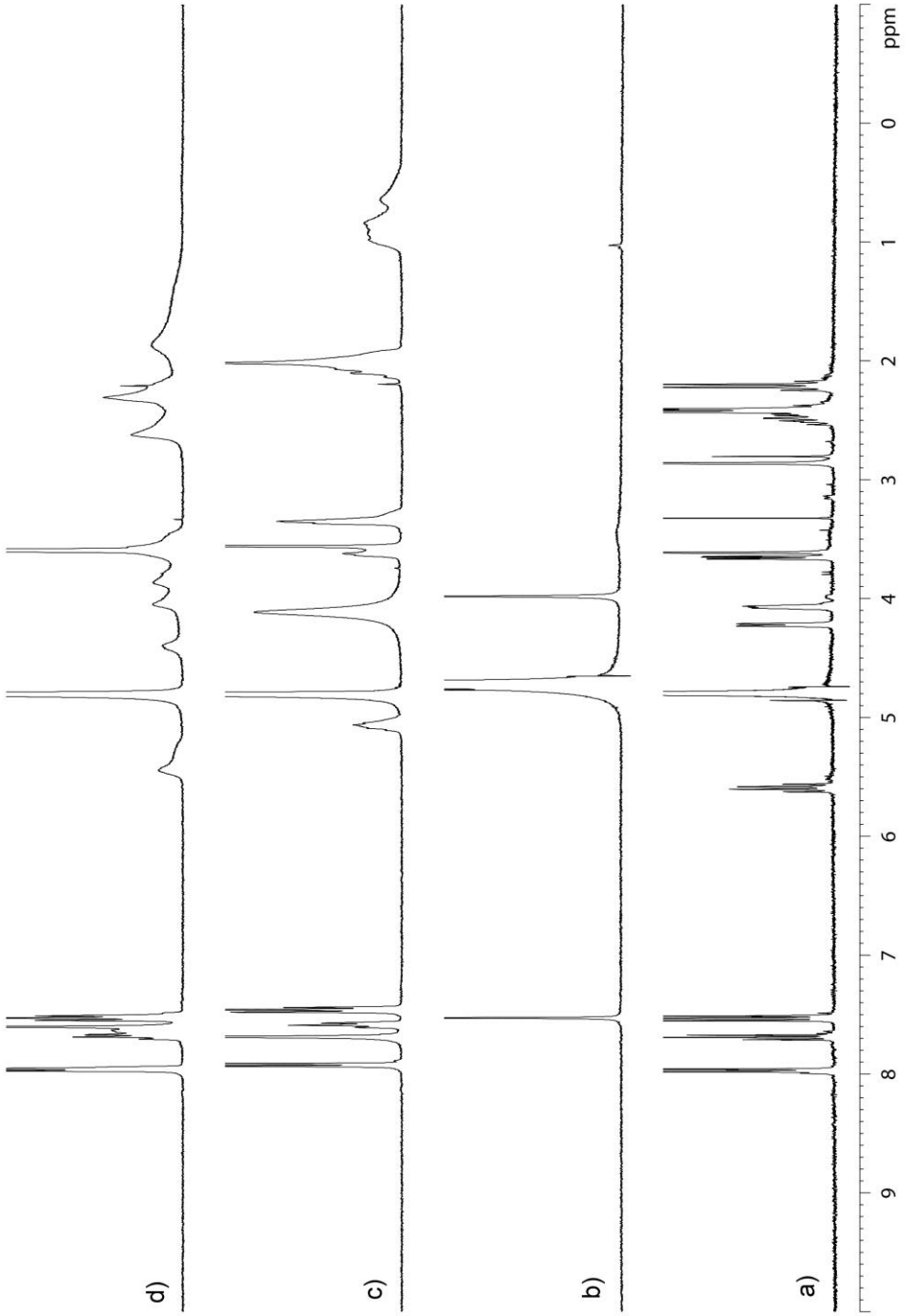

Figure III-S14. ^{1}H NMR spectra recorded (400 MHz, RT, D_2O) for: a) cocaine, b) p-sulfo calix[4]arene, c) an equimolar mixture of cocaine and p-sulfo calix[4]arene (2 mM), and d) a 2:1 mixture of cocaine (2 mM) and p-sulfo calix[4]arene (1 mM).

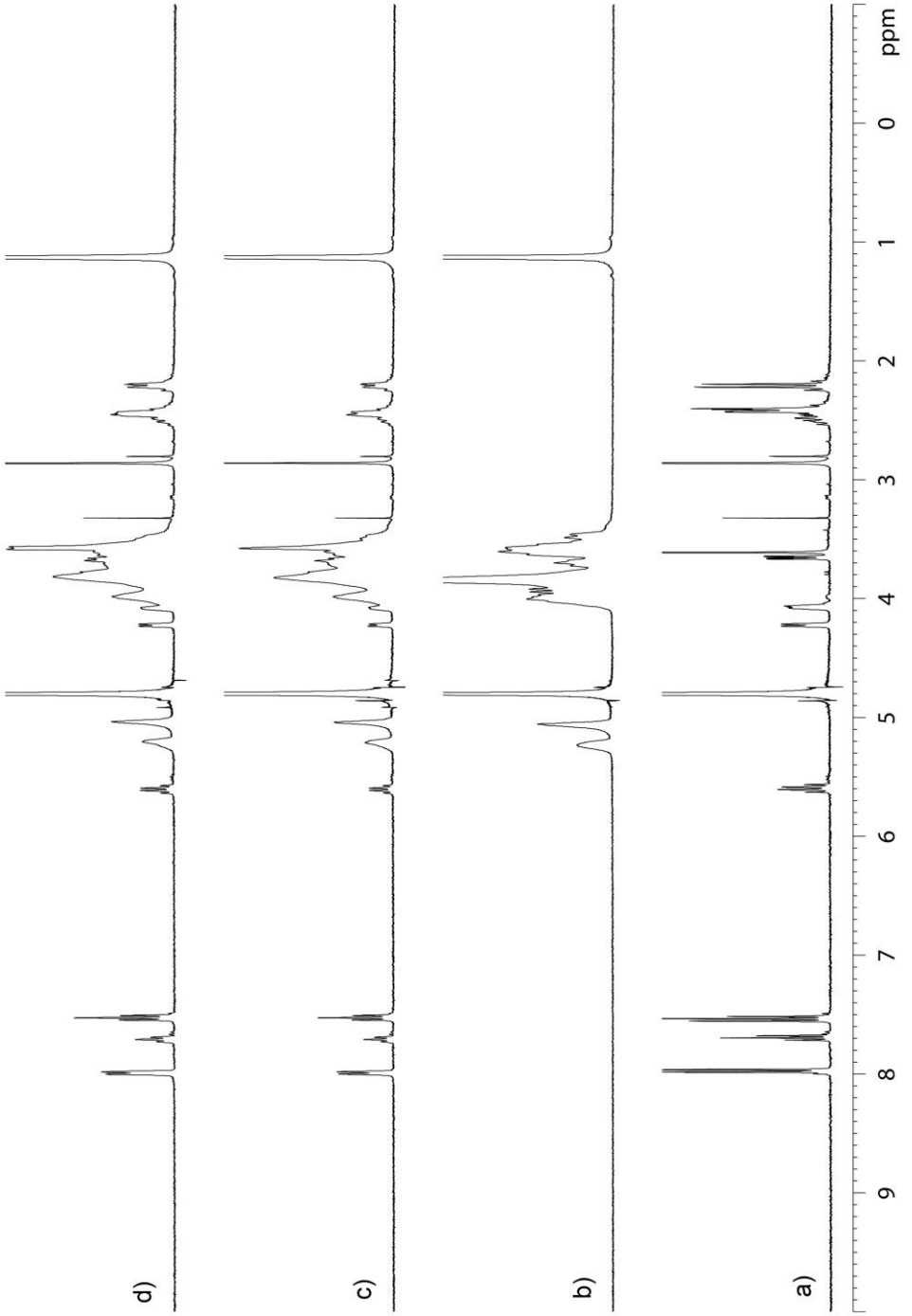

Figure III-S15. ^{1}H NMR spectra recorded (400 MHz, RT, D_2O) for: a) cocaine, b) HP-β-CD, c) an equimolar mixture of cocaine and HP-β-CD (1 mM), and d) a 2:1 mixture of cocaine (2 mM) and HP-β-CD (1 mM).

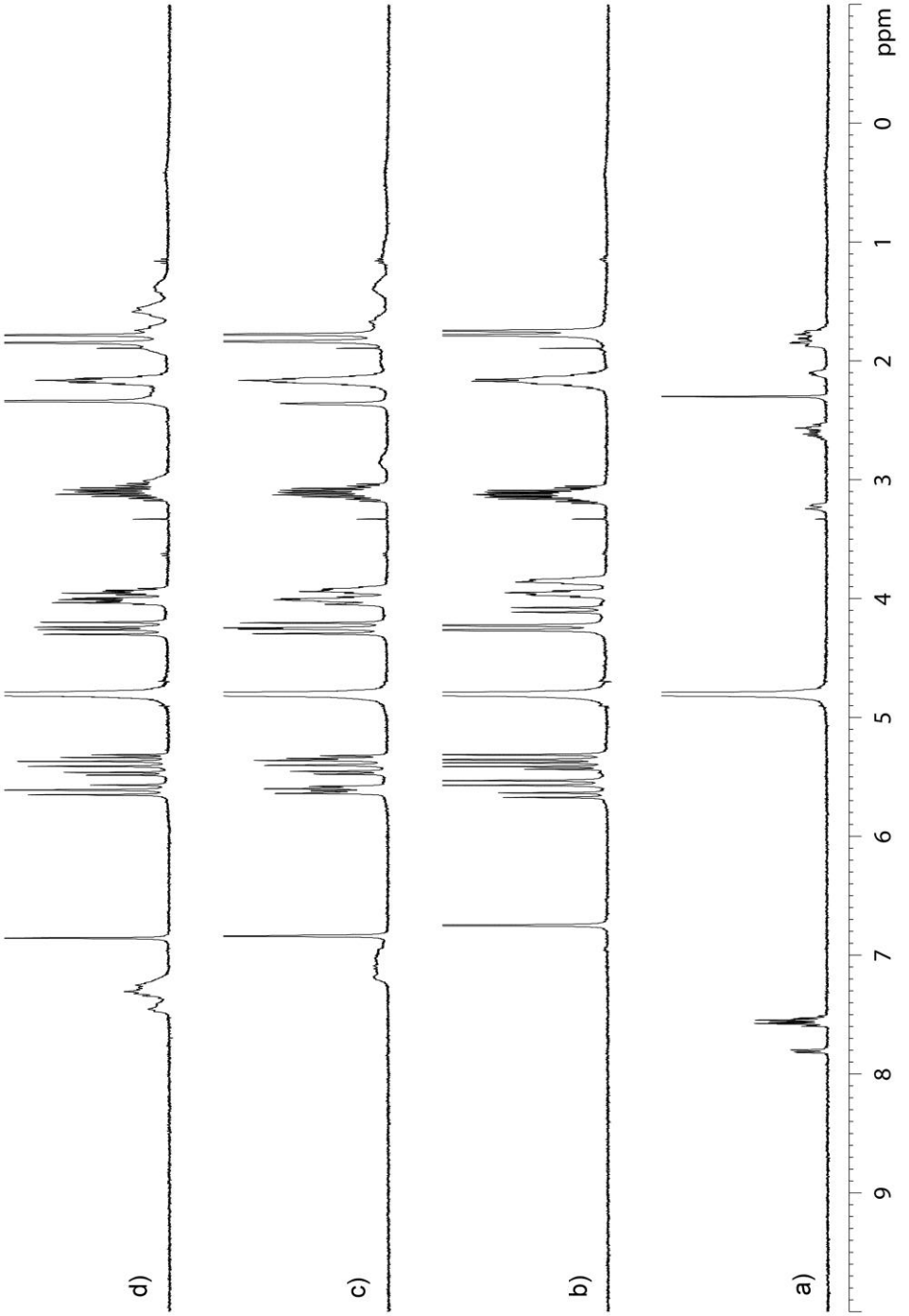

Figure III-S16. ^{1}H NMR spectra recorded (400 MHz, RT, D_2O) for: a) ketamine, b) Calabadion 1, c) an equimolar mixture of ketamine and Calabadion 1 (1 mM), and d) a 2:1 mixture of ketamine (2 mM) and Calabadion 1 (1 mM).

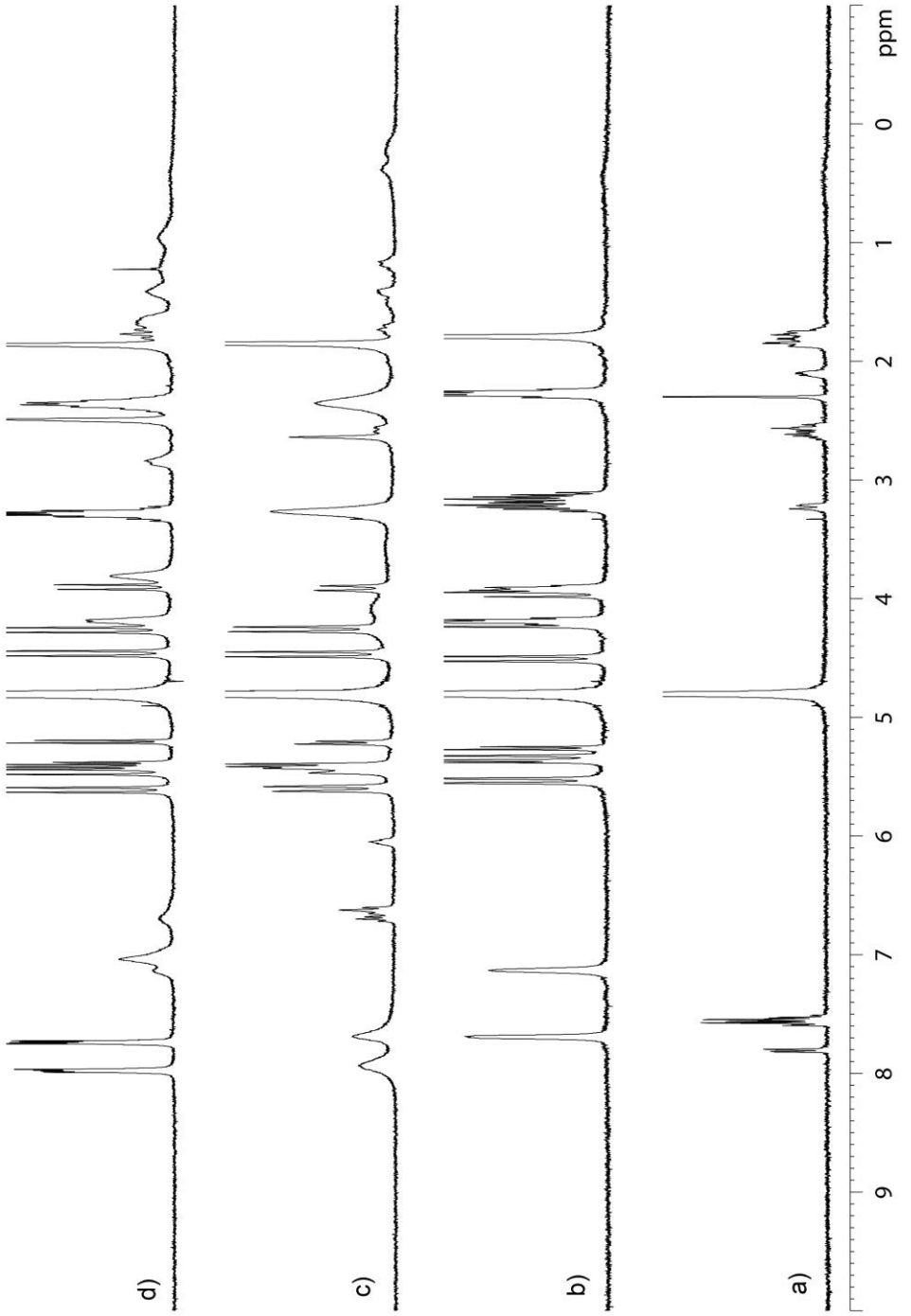

Figure III-S17. ^{1}H NMR spectra recorded (400 MHz, RT, D_2O) for: a) ketamine, b) Calabadion 2, c) an equimolar mixture of ketamine and Calabadion 2 (1 mM), and d) a 2:1 mixture of ketamine (2 mM) and Calabadion 2 (1 mM).

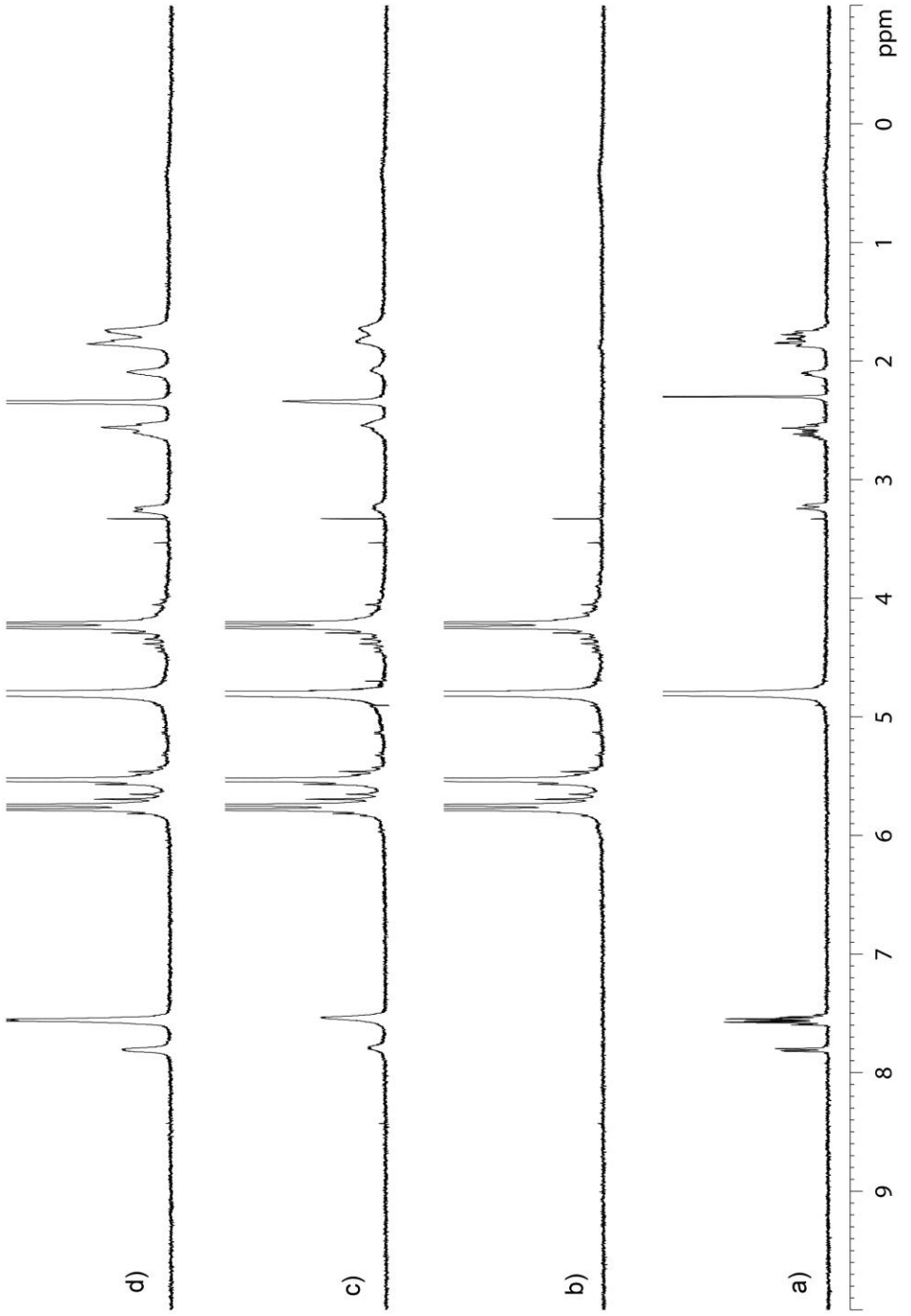

Figure III-S18. ^{1}H NMR spectra recorded (400 MHz, RT, D_2O) for: a) ketamine, b) CB[7], c) an equimolar mixture of ketamine and fentanyl (1 mM), and d) a 2:1 mixture of ketamine (2 mM) and CB[7] (1 mM).

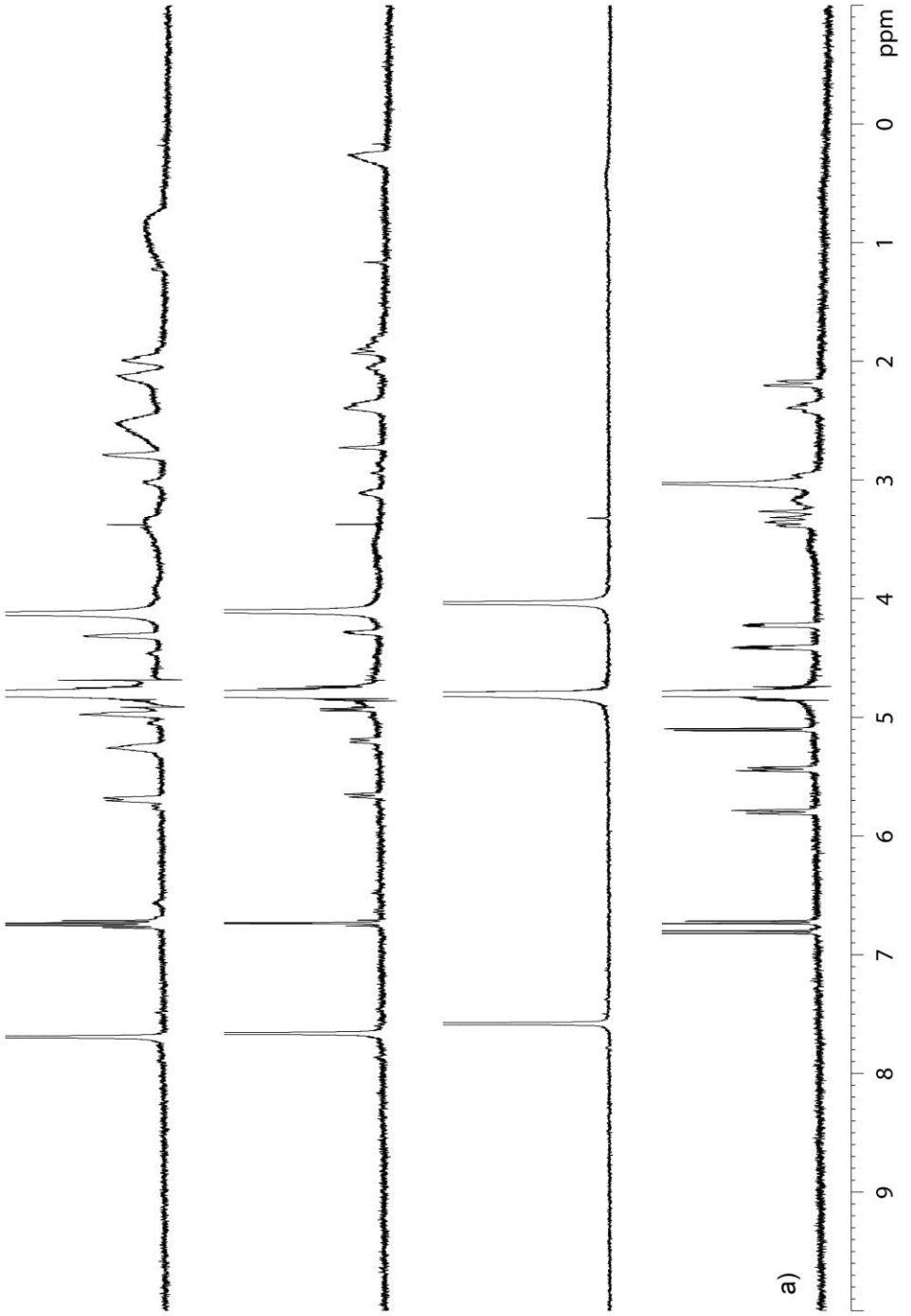

Figure III-S19. ^{1}H NMR spectra recorded (400 MHz, RT, D_2O) for: a) ketamine, b) p-sulfo calix[4]arene, c) an equimolar mixture of ketamine and p-sulfo calix[4]arene (1 mM), and d) a 2:1 mixture of ketamine (2 mM) and p-sulfo calix[4]arene (1 mM).

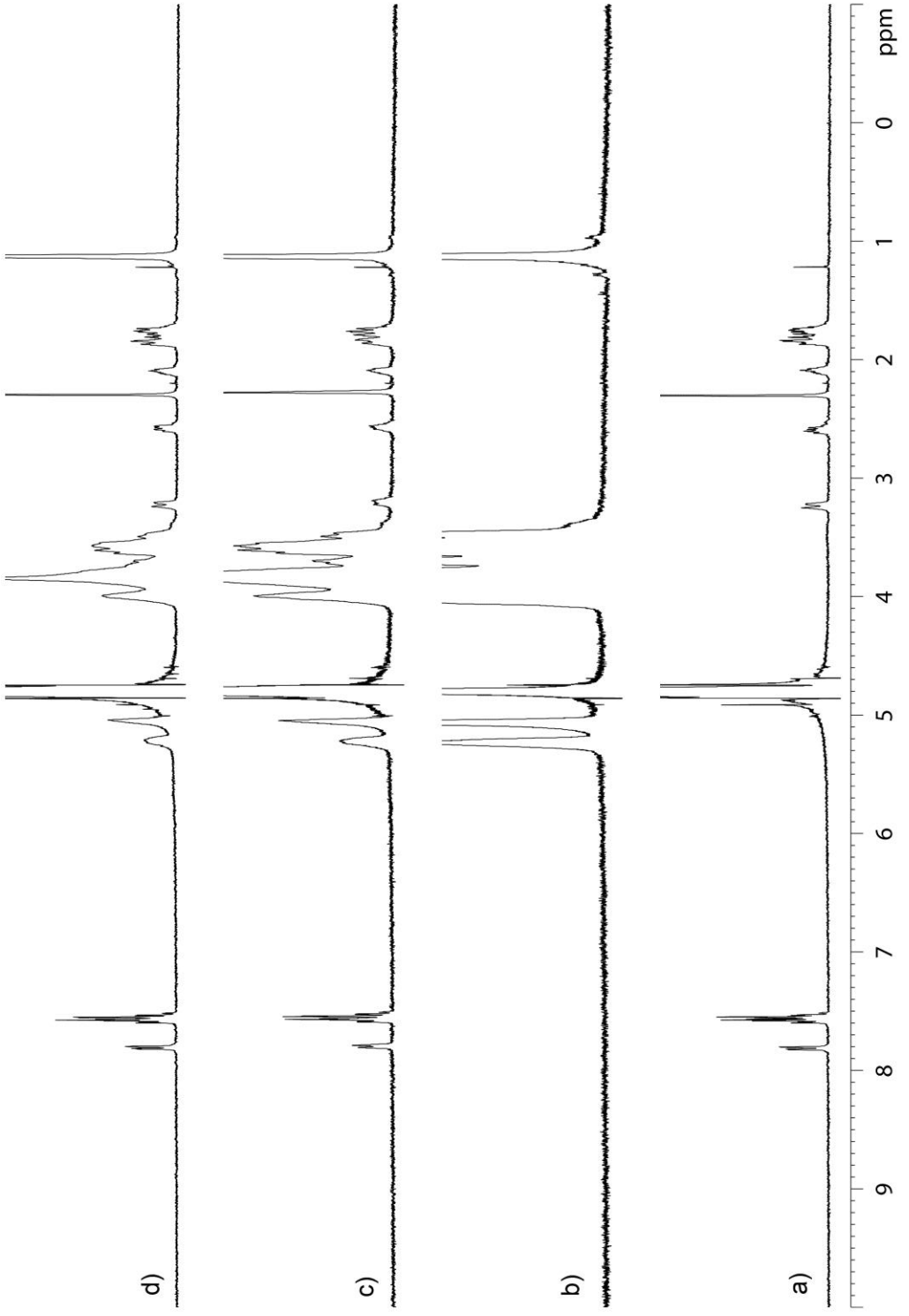

Figure III-S20. ^{1}H NMR spectra recorded (400 MHz, RT, D_2O) for: a) ketamine, b) HP-β-CD, c) an equimolar mixture of ketamine and HP-β-CD (1 mM), and d) a 2:1 mixture of ketamine (2 mM) and HP-β-CD (1 mM).

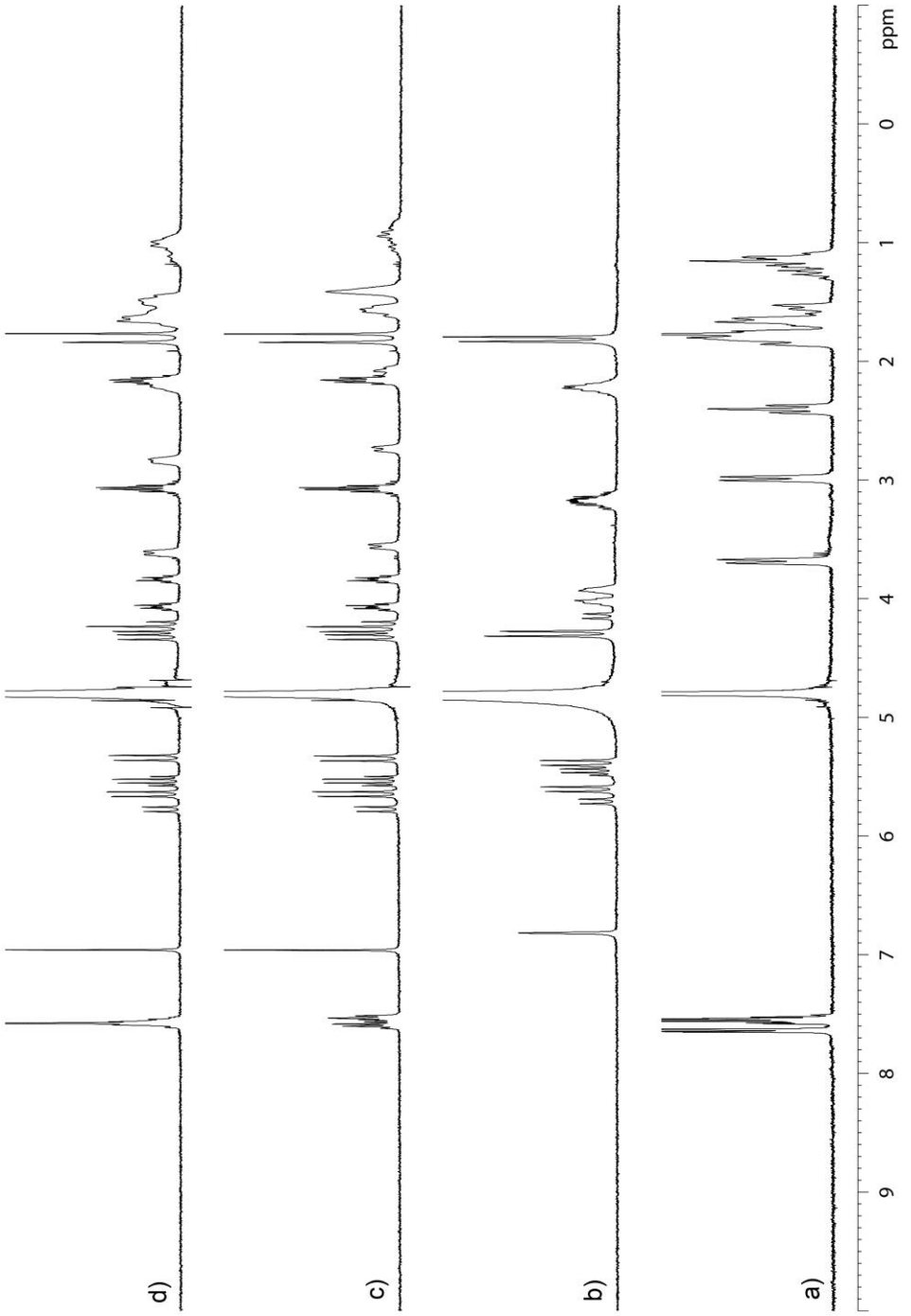

Figure III-S21. ^{1}H NMR spectra recorded (400 MHz, RT, D_2O) for: a) phencyclidine, b) Calabadion 1, c) an equimolar mixture of phencyclidine and Calabadion 1 (2 mM), and d) a 2:1 mixture of phencyclidine (2 mM) and Calabadion 1 (1 mM).

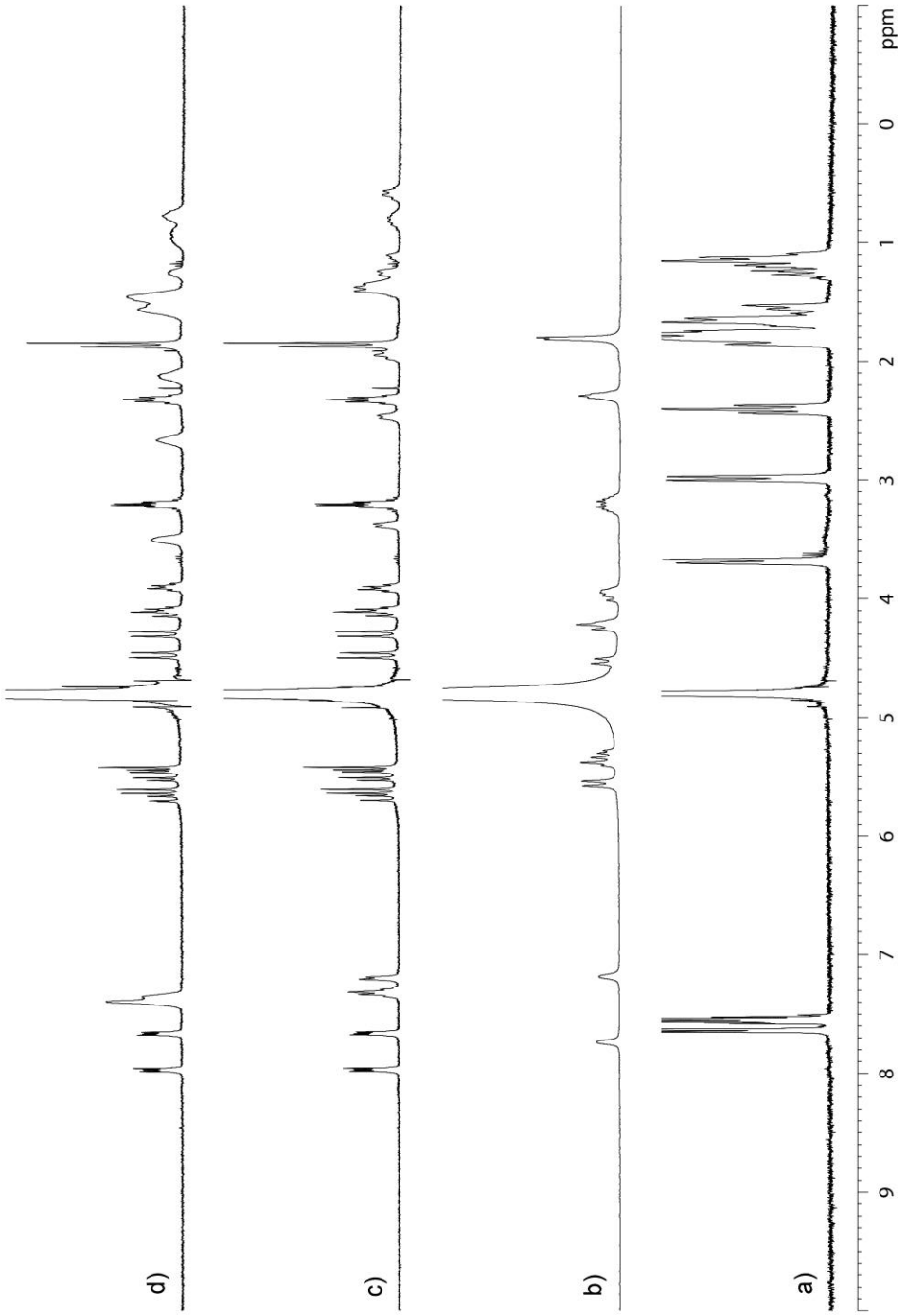

Figure III-S22. ^{1}H NMR spectra recorded (400 MHz, RT, D_2O) for: a) phencyclidine, b) Calabadion 2, c) an equimolar mixture of phencyclidine and Calabadion 2 (2 mM), and d) a 2:1 mixture of phencyclidine (2 mM) and Calabadion 2 (1 mM).

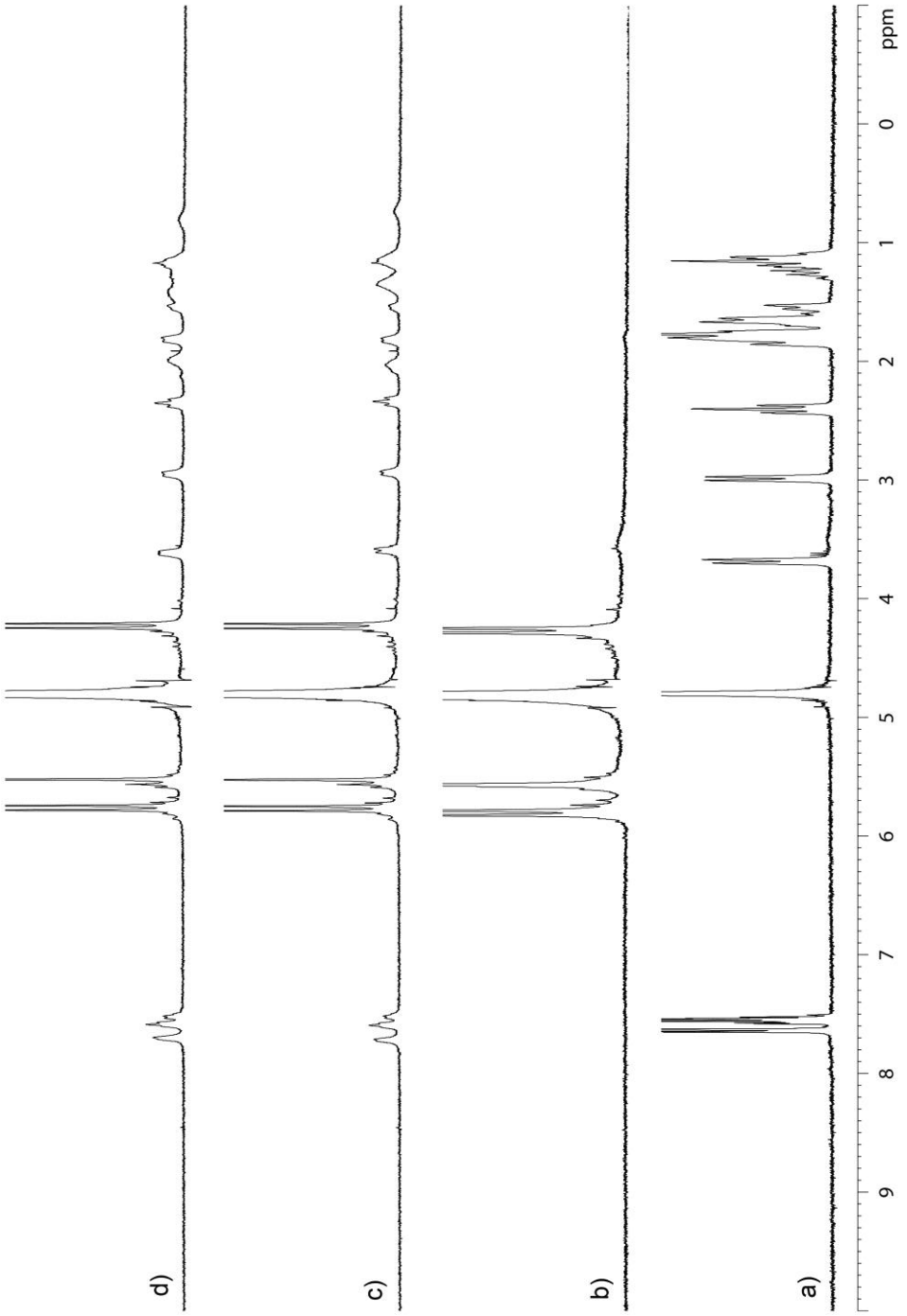

Figure III-S23. ^{1}H NMR spectra recorded (400 MHz, RT, D_2O) for: a) phencyclidine, b) CB[7], c) an equimolar mixture of phencyclidine and CB[7] (2 mM), and d) a 2:1 mixture of phencyclidine (2 mM) and CB[7] (1 mM).

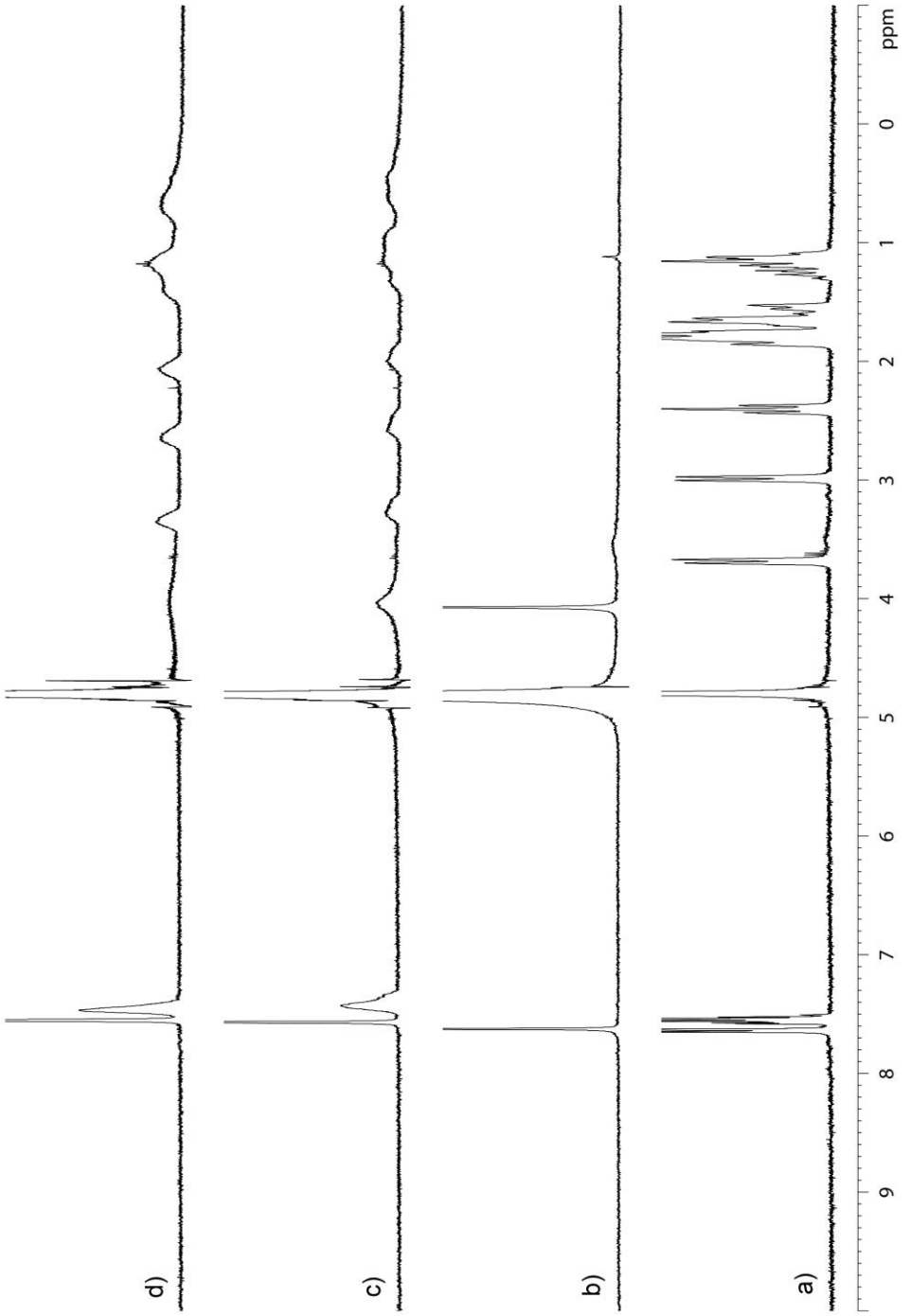

Figure III-S24. ^{1}H NMR spectra recorded (400 MHz, RT, D_2O) for: a) phencyclidine, b) p-sulfo calix[4]arene, c) an equimolar mixture of phencyclidine and p-sulfo calix[4]arene (2 mM), and d) a 2:1 mixture of phencyclidine (2 mM) and p-sulfo calix[4]arene (1 mM).

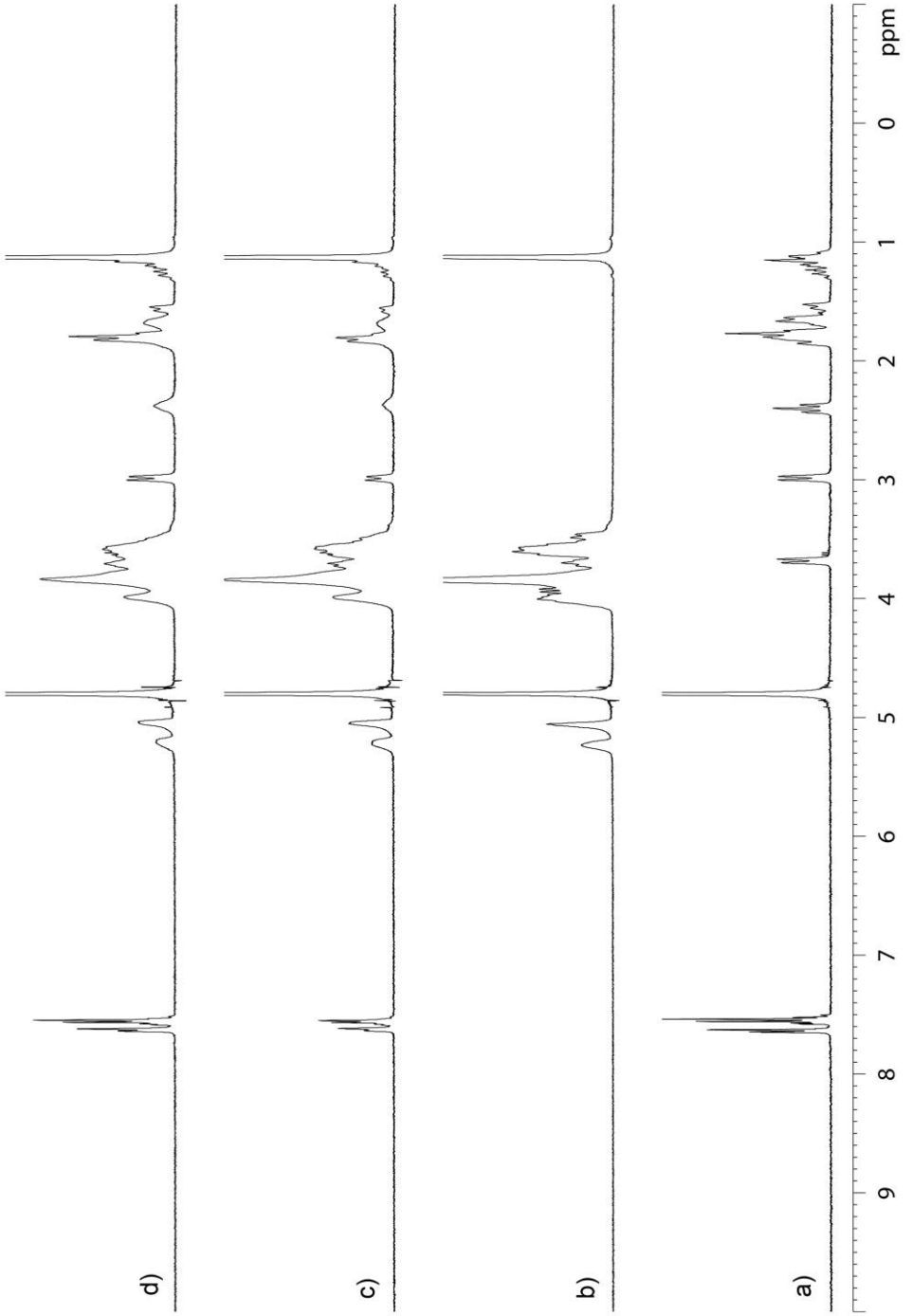

Figure III-S25. ^{1}H NMR spectra recorded (400 MHz, RT, D_2O) for: a) phencyclidine, b) HP-β-CD, c) an equimolar mixture of phencyclidine and HP-β-CD (1 mM), and d) a 2:1 mixture of phencyclidine (2 mM) and HP-β-CD (1 mM).

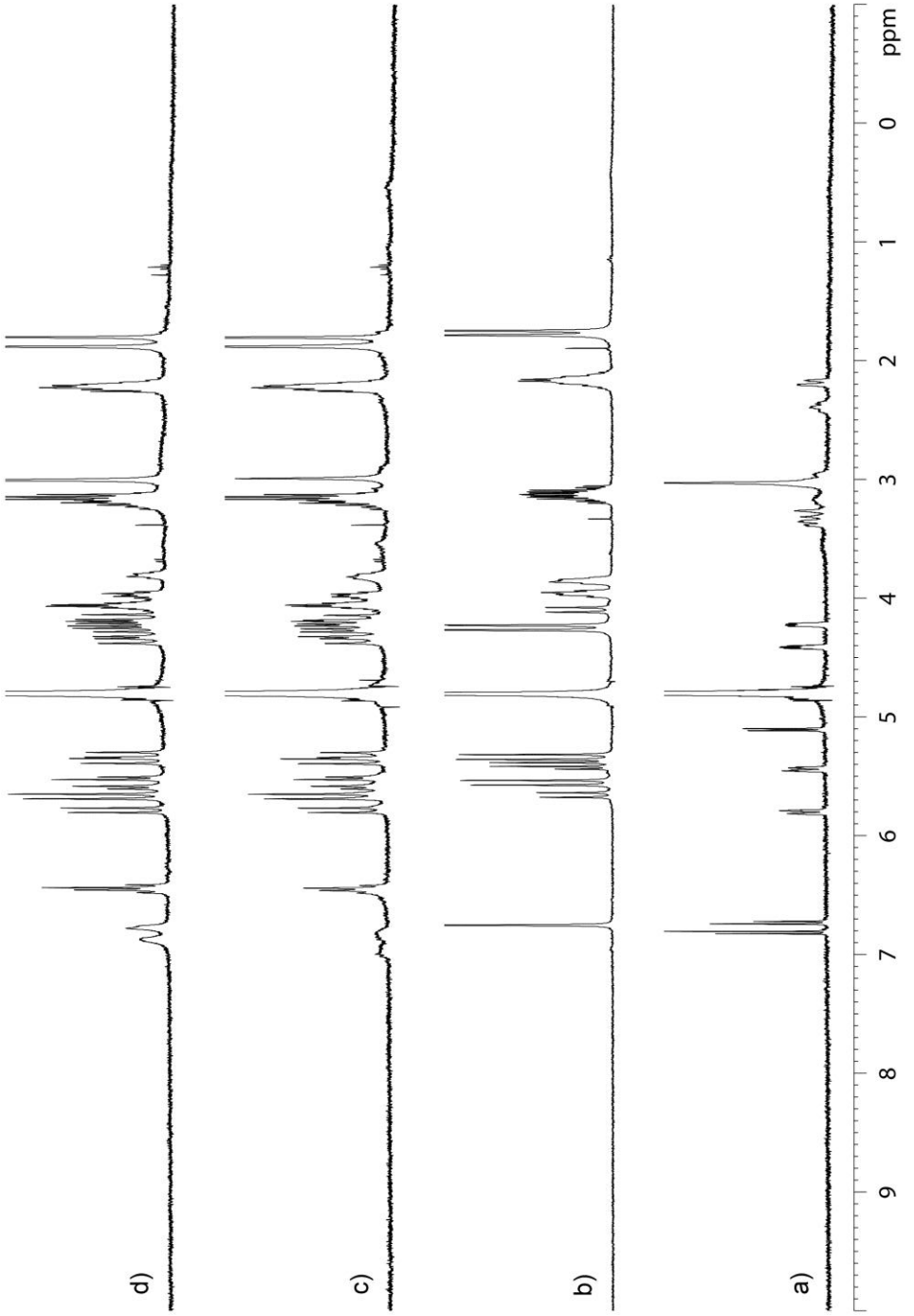

Figure III-S26. ^{1}H NMR spectra recorded (400 MHz, RT, D_2O) for: a) morphine, b) Calabadion 1, c) an equimolar mixture of morphine and Calabadion 1 (2 mM), and d) a 2:1 mixture of morphine (2 mM) and Calabadion 1 (1 mM).

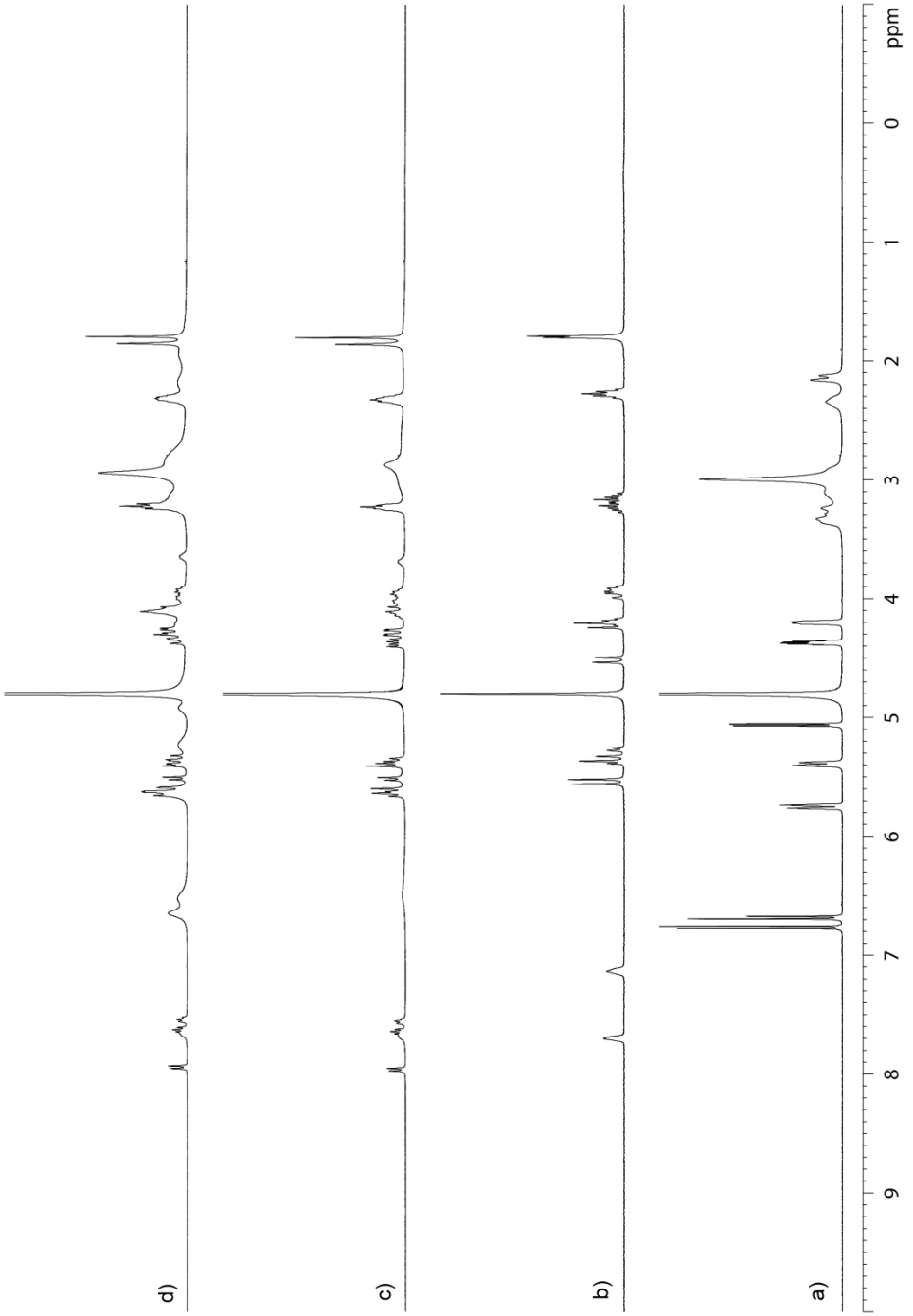

Figure III-S27. ^{1}H NMR spectra recorded (400 MHz, RT, D_2O) for: a) morphine, b) Calabadion 2, c) an equimolar mixture of morphine and Calabadion 2 (2 mM), and d) a 2:1 mixture of morphine (2 mM) and Calabadion 2 (1 mM).

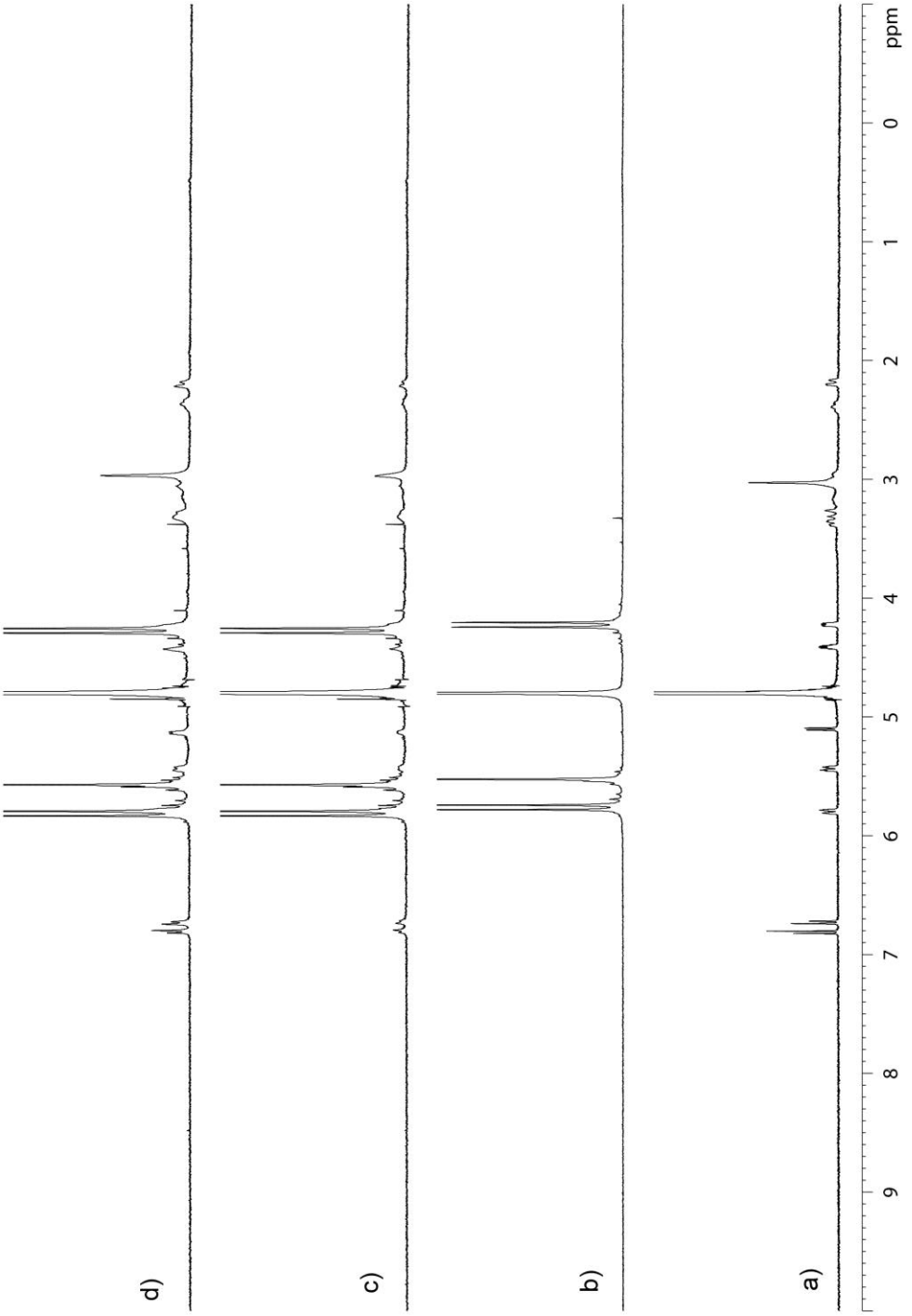

Figure III-S28. ^{1}H NMR spectra recorded (400 MHz, RT, D_2O) for: a) morphine, b) CB[7], c) an equimolar mixture of morphine and CB[7] (2 mM), and d) a 2:1 mixture of morphine (2 mM) and CB[7] (1 mM).

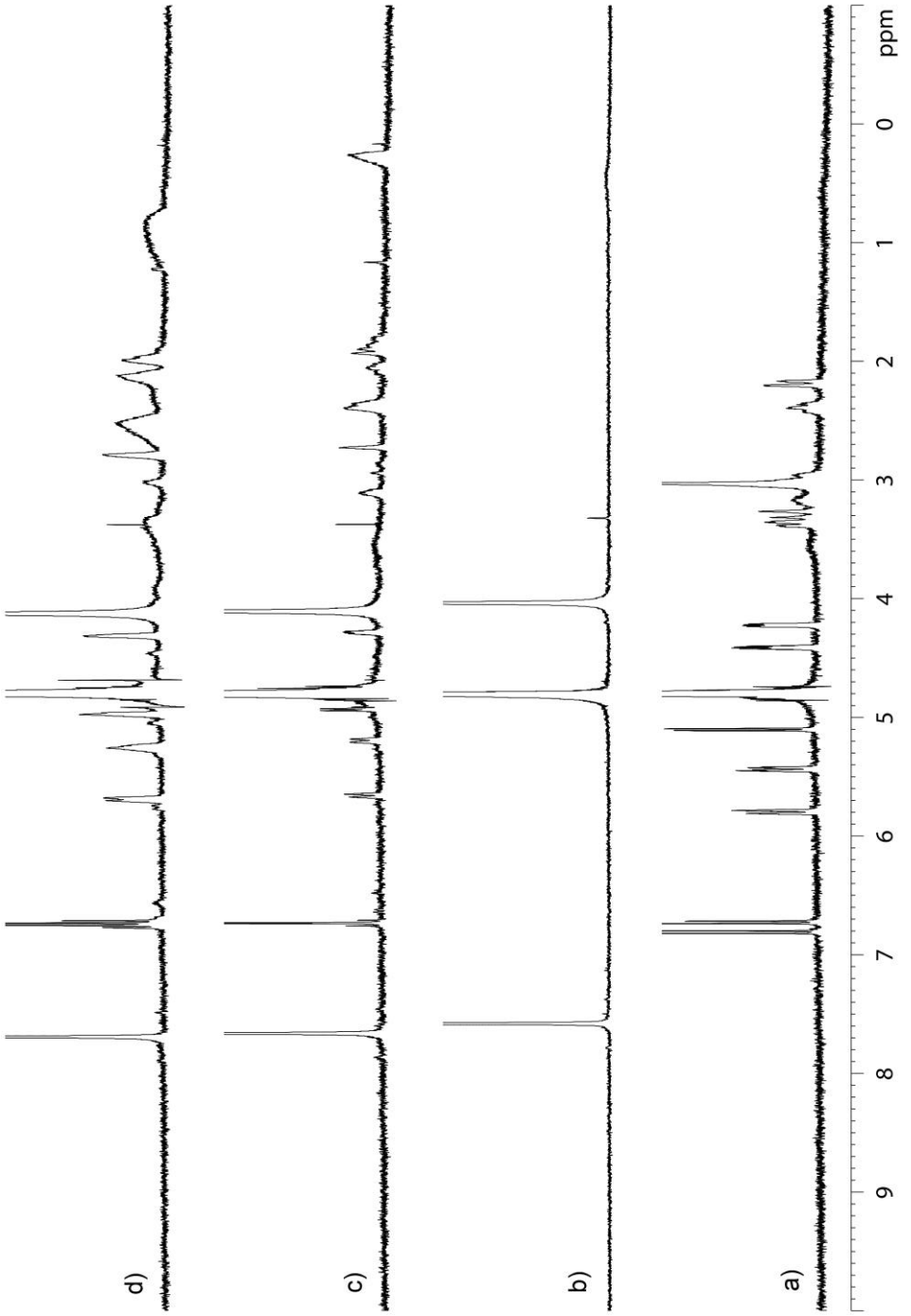

Figure III-S29. ^{1}H NMR spectra recorded (400 MHz, RT, D_2O) for: a) morphine, b) p-sulfo calix[4]arene, c) an equimolar mixture of morphine and p-sulfo calix[4]arene (2 mM), and d) a 2:1 mixture of morphine (2 mM) and p-sulfo calix[4]arene (1 mM).

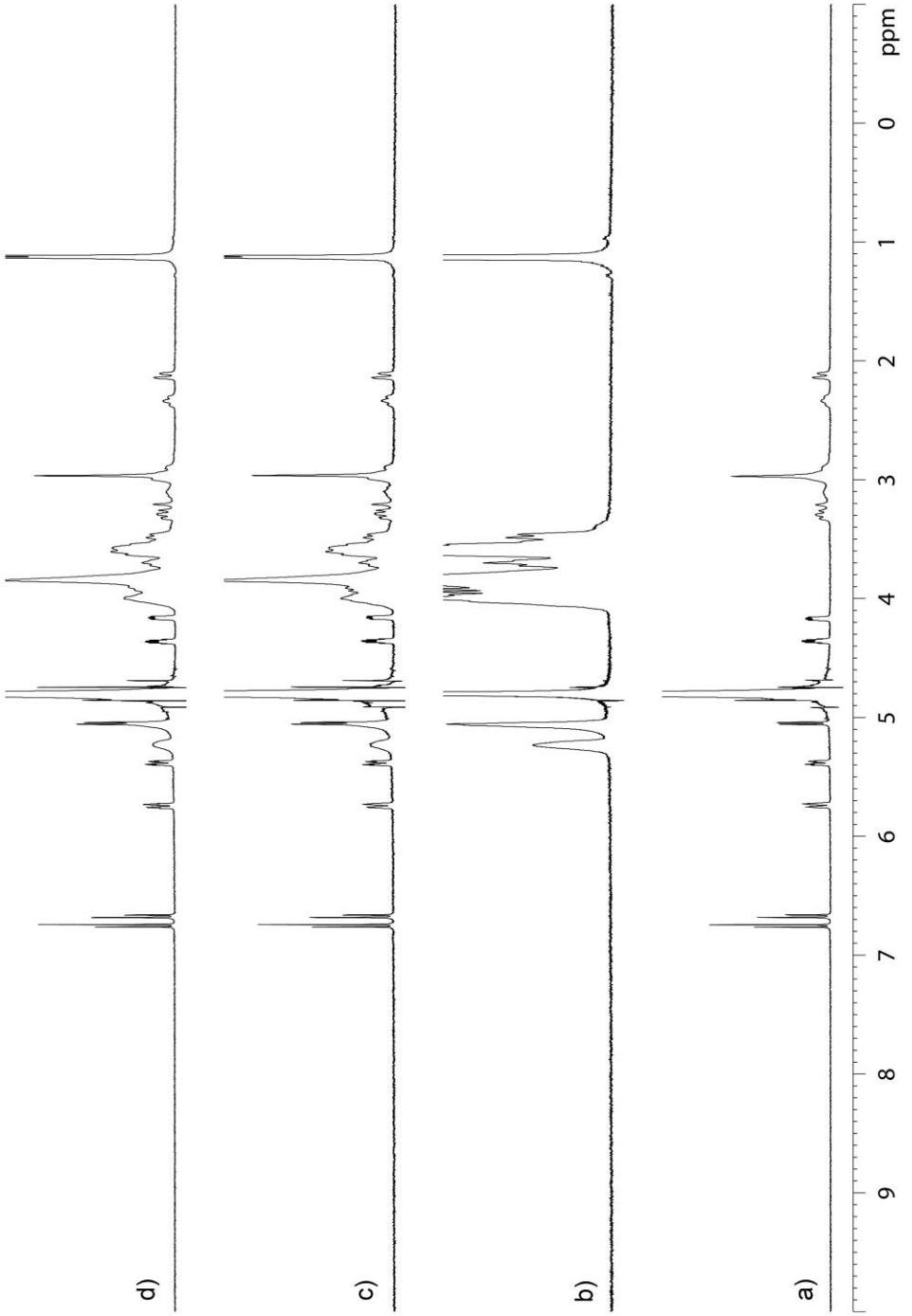

Figure III-S30. ^{1}H NMR spectra recorded (400 MHz, RT, D_2O) for: a) morphine, b) HP-β-CD, c) an equimolar mixture of morphine and HP-β-CD (1 mM), and d) a 2:1 mixture of morphine (2 mM) and HP-β-CD (1 mM).

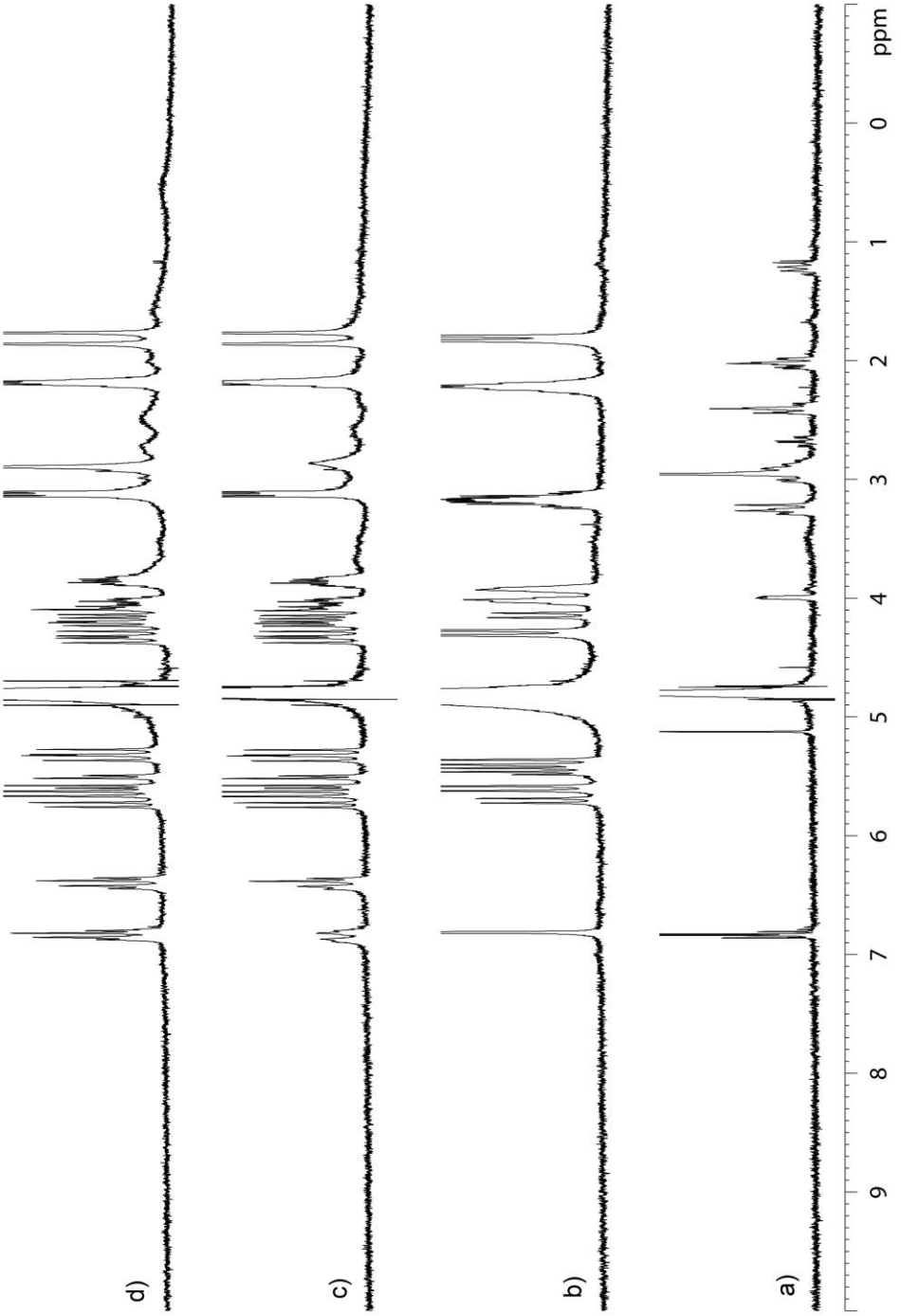

Figure III-S31. ^{1}H NMR spectra recorded (400 MHz, RT, D_2O) for: a) hydromorphone, b) Calabadion 1, c) an equimolar mixture of hydromorphone and Calabadion 1 (1 mM), and d) a 2:1 mixture of f hydromorphone (2 mM) and Calabadion 1 (1 mM).

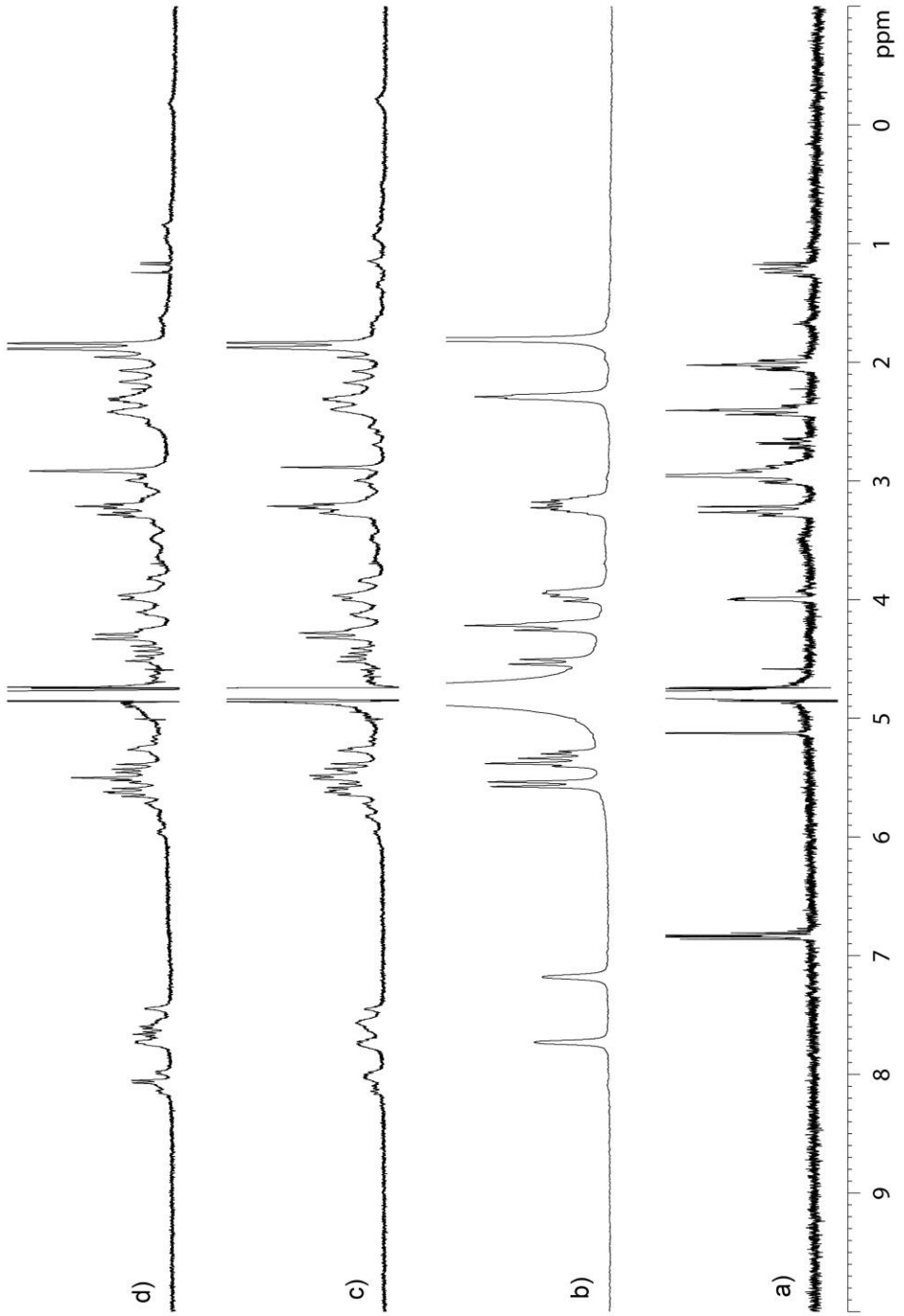

Figure III-S32. ^{1}H NMR spectra recorded (400 MHz, RT, D_2O) for: a) hydromorphone, b) Calabadion 2, c) an equimolar mixture of hydromorphone and Calabadion 2 (1 mM), and d) a 2:1 mixture of hydromorphone (2mM) and Calabadion 2 (1 mM).

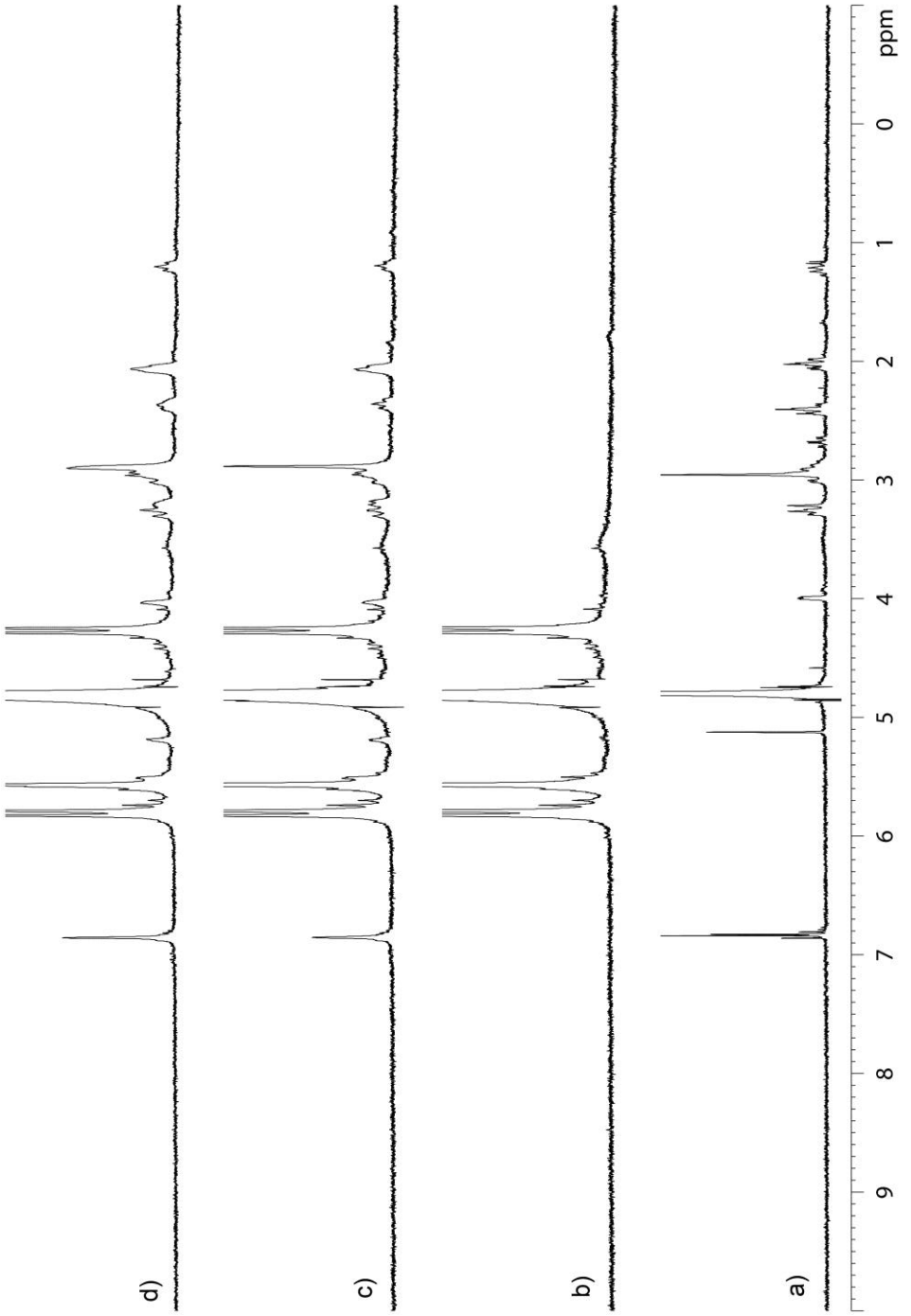

Figure III-S33. ^{1}H NMR spectra recorded (400MHz, RT, D_2O) for: a) hydromorphone, b) CB[7], c) an equimolar mixture of hydromorphone and fentanyl (1 mM), and d) a 2:1 mixture of hydromorphone (2 mM) and CB[7] (1 mM).

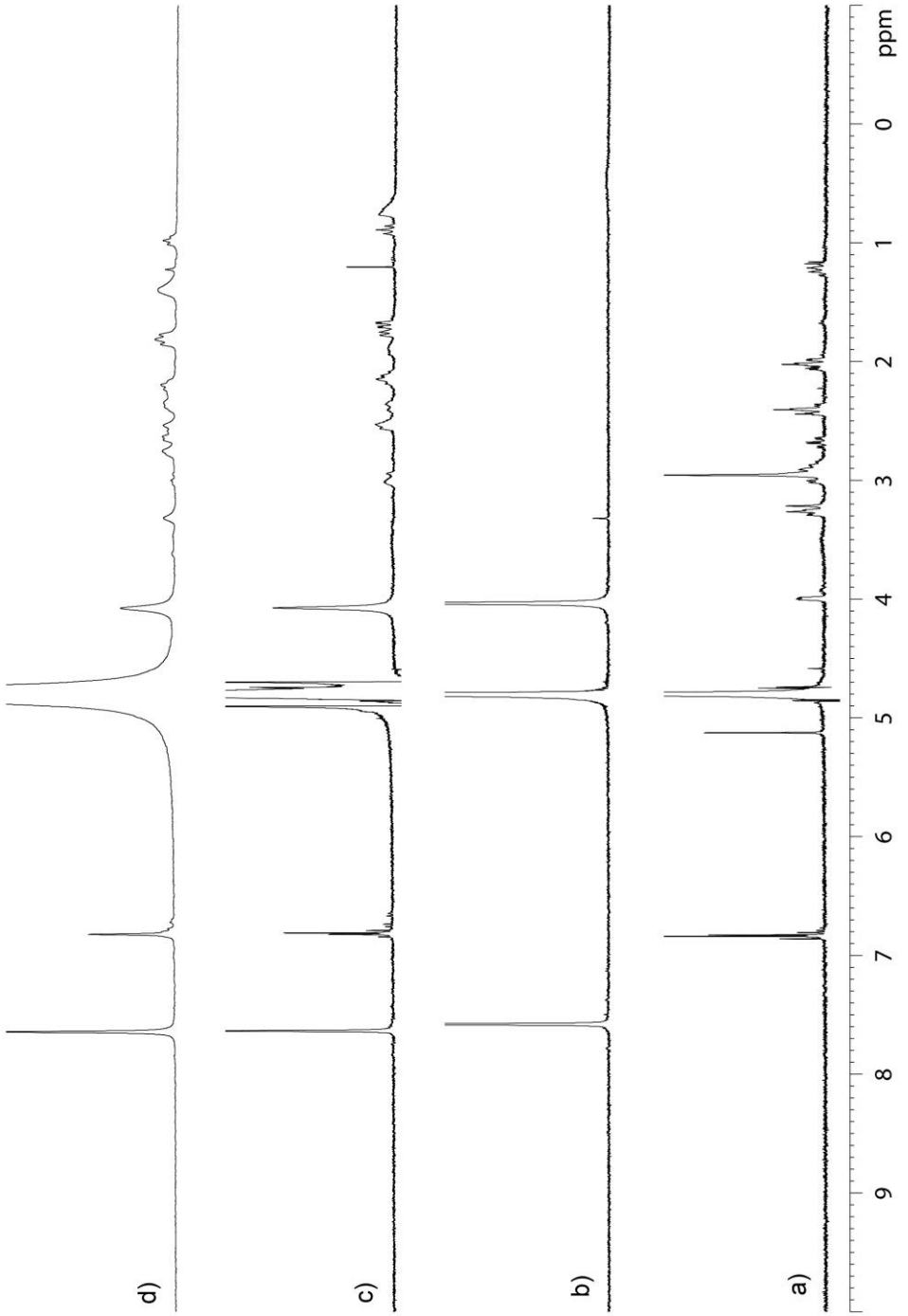

Figure III-S34. ^{1}H NMR spectra recorded (400 MHz, RT, D_2O) for: a) hydromorphone, b) p-sulfo calix[4]arene, c) an equimolar mixture of hydromorphone and p-sulfo calix[4]arene (1 mM), and d) a 2:1 mixture of hydromorphone (2 mM) and p-sulfo calix[4]arene (1 mM).

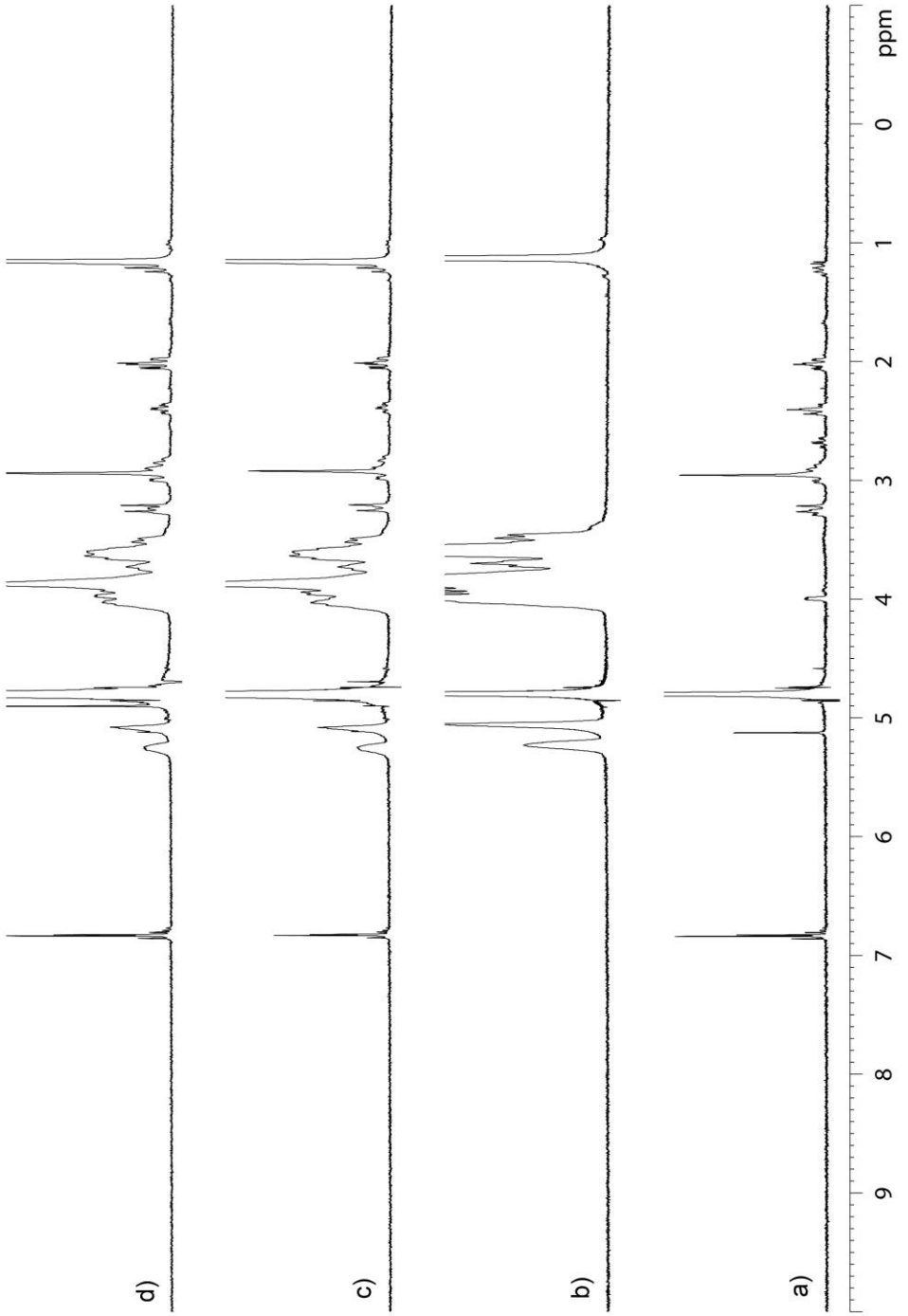

Figure III-S35. ^{1}H NMR spectra recorded (400 MHz, RT, D_2O) for: a) hydromorphone, b) HP-β-CD, c) an equimolar mixture of hydromorphone and HP-β-CD (1 mM), and d) a 2:1 mixture of hydromorphone (2 mM) and HP-β-CD (1 mM).

Determination of K_a between hosts Calabadion 1 and Calabadion 2 and various drugs of abuse using UV/Vis spectroscopy.

K_a values up to 10^4 M^{-1} can be measured by direct ^1H NMR titration. For values that exceed this level it is necessary to use other techniques such as UV/Vis, fluorescence, or isothermal titration calorimetry. UV/Vis spectroscopy was used in this work.

In order to determine the K_a value for Calabadion 1 and Calabadion 2 toward UV/Vis inactive drugs of abuse, an indicator displacement assay involving the addition of drug to a solution of host and dye rhodamine 6G was used. The change in UV/Vis absorbance as a function of drug concentration was fitted to a competitive binding model which allowed determination of the K_a values. The known K_a values between Calabadion1•rhodamine 6G (4.8×10^5 M^{-1}) and Calabadion 2 •rhodamine 6G (2.3×10^6 M^{-1}) were used as inputs in the competitive binding model.[48]

Competitive Binding (Indicator Displacement) Model Used to Determine Values of Ka with MicroMath Scientist

```
// MicroMath Scientist Model File
IndVars: ConcAntot
DepVars: Absorb
Params: ConcHtot, ConcGtot, Khg, Kha, AbsorbMax, AbsorbMin
Khg = ConcHG / (ConcH * ConcG)
Kha = ConcHAn / (ConcH * ConcAn)
Absorb = AbsorbMin + (AbsorbMax-AbsorbMin)*(ConcHG/ConcGtot)
ConcHtot = ConcH + ConcHG + ConcHAn
ConcGtot = ConcHG + ConcG
ConcAntot = ConcAn + ConcHAn
0 < ConcHG < ConcHtot
0 < ConcH < ConcHtot
0 < ConcG < ConcGtot
0 < ConcAn < ConcAntot
***
```

```
// MicroMath Scientist Model File
IndVars: ConcAntot
DepVars: Absorb1, Absorb2
Params:Khg, Kha, AbsorbMax1, AbsorbMin1, AbsorbMax2, AbsorbMin2
Khg = ConcHG / (ConcH * ConcG)
Kha = ConcHAn / (ConcH * ConcAn)
Absorb1 = AbsorbMin1 + (AbsorbMax1-AbsorbMin1)*(ConcHG/0.00001)
Absorb2 = AbsorbMin2 + (AbsorbMax2-AbsorbMin2)*(ConcHG/0.00001)
0.00001 = ConcH + ConcHG + ConcHAn
0.00001= ConcHG + ConcG
ConcAntot = ConcAn + ConcHAn
0 < ConcHG < 0.00001
0 < ConcH < 0.00001
0 < ConcG < 0.00001
0 < ConcAn < ConcAntot
```

a)

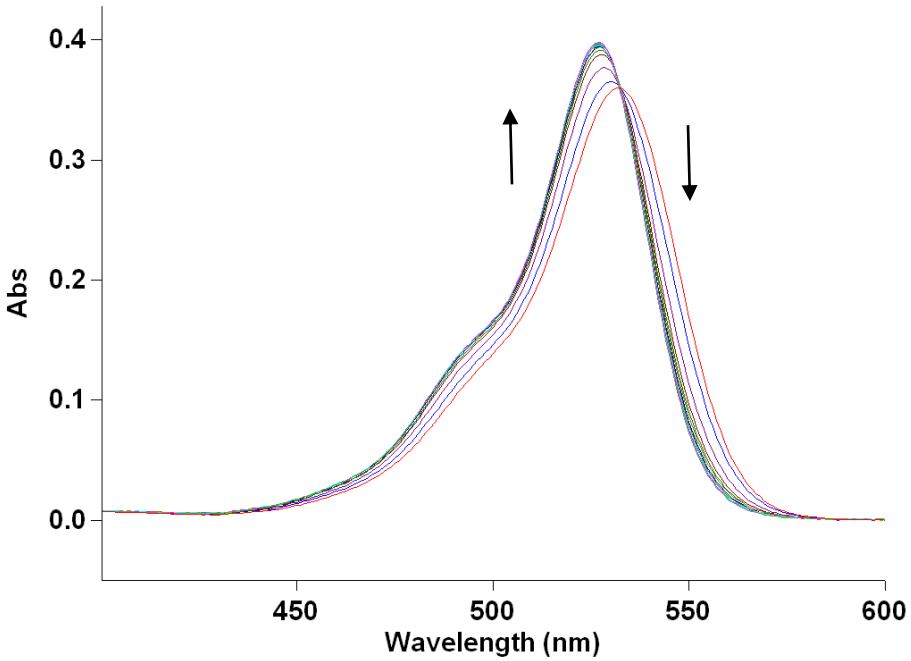

b)

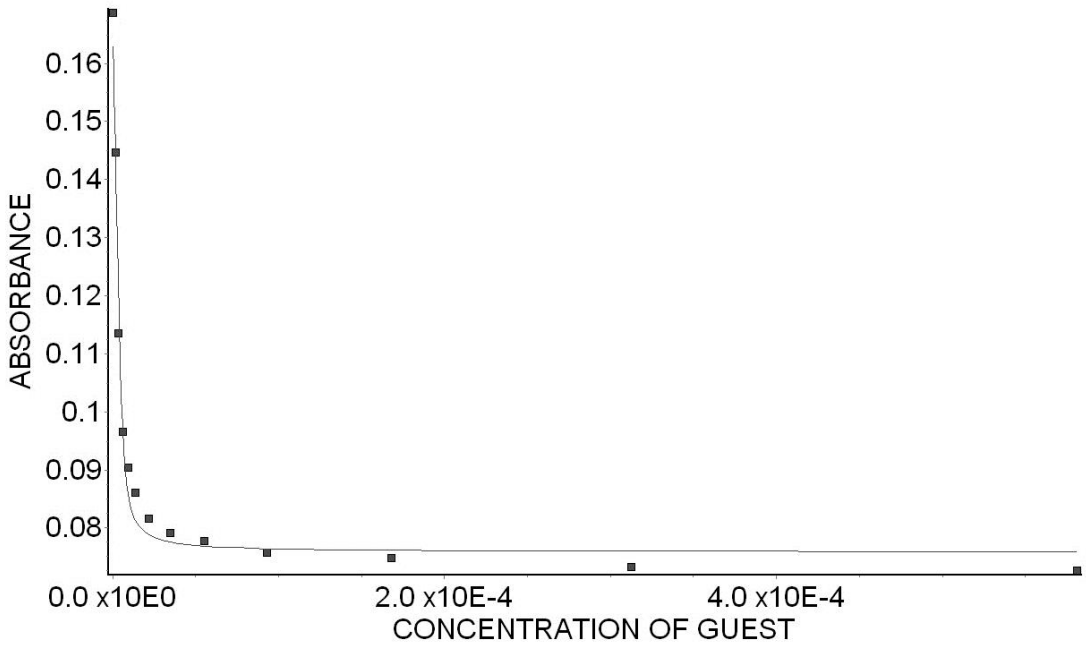

Figure III-S36. a) UV/Vis spectra from the titration of Calabadion 1 (5.02 µM) and rhodamine 6G (4.97 µM) with guest methamphetamine (0 – 581 µM) in 20 mM NaH_2PO_4 buffer (pH 7.4); b) plot of the A_{550} as a function of methamphetamine concentration. The solid line represents the best non-linear fit of the data to a 1:1 binding model ($K_a = (7.5 \pm 2.9) \times 10^6\ M^{-1}$).

a)

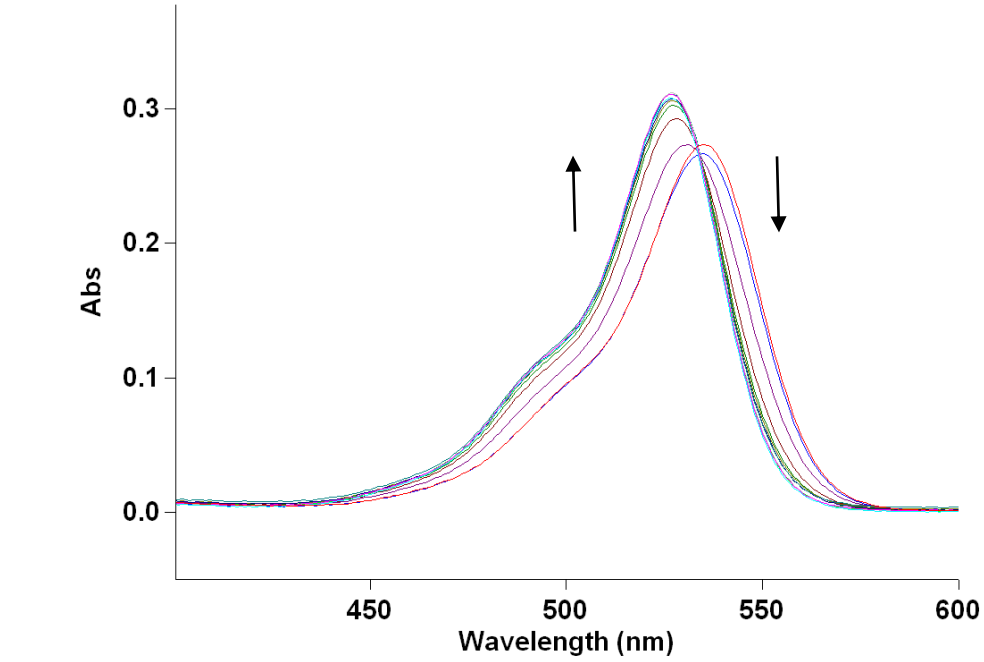

b)

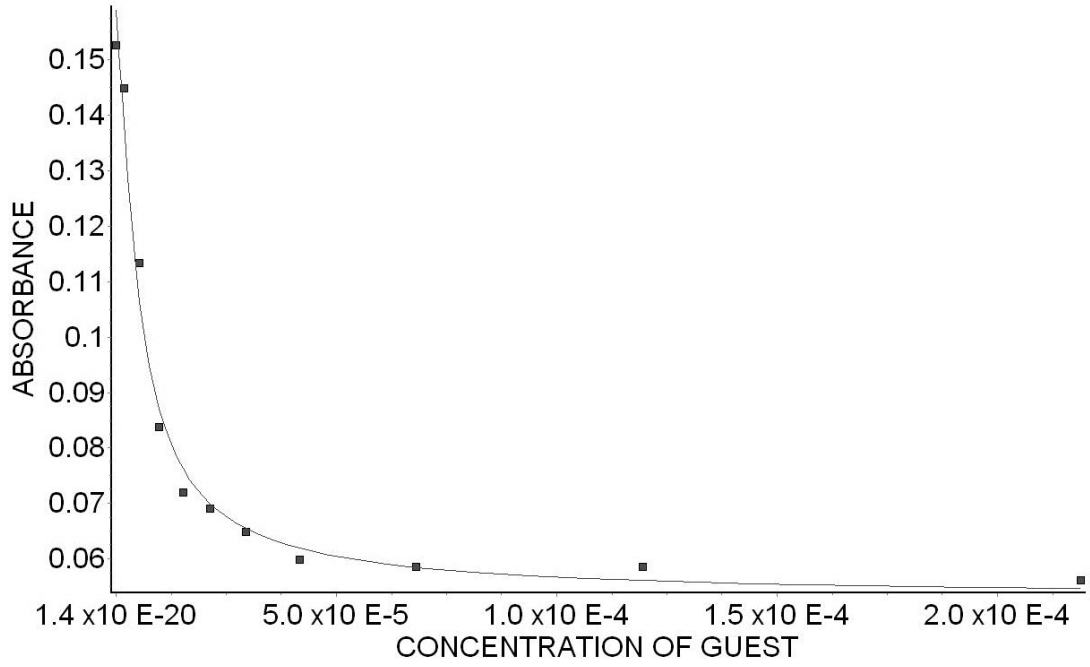

Figure III-S37. a) UV/Vis spectra from the titration of Calabadion 2 (4.97 µM) and rhodamine 6G (4.97 µM) with guest methamphetamine (0 – 219 µM) in 20 mM NaH_2PO_4 buffer (pH 7.4); b) plot of the A_{550} as a function of methamphetamine concentration. The solid line represents the best non-linear fit of the data to a 1:1 binding model ($K_a = (4.3 \pm 1.0) \times 10^6\ M^{-1}$).

a)

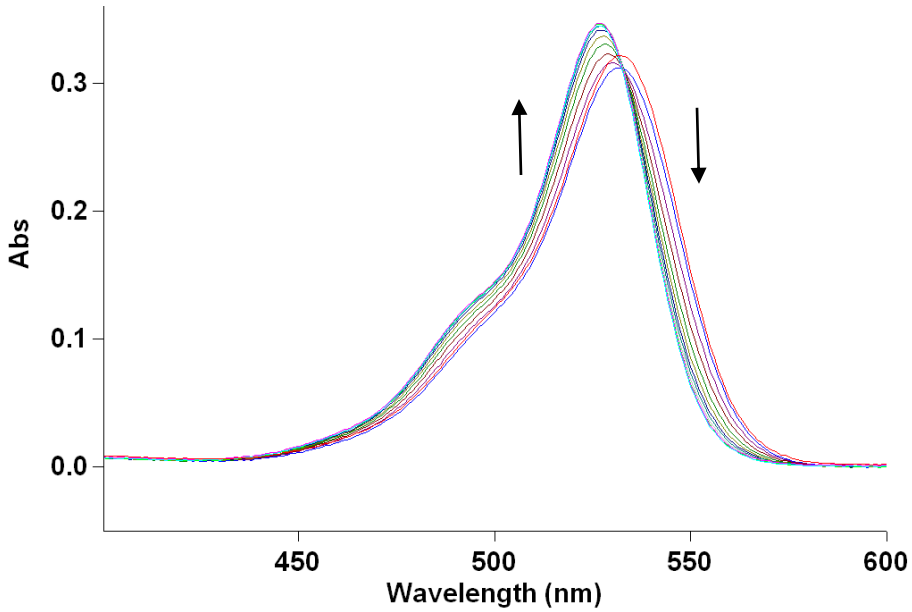

b)

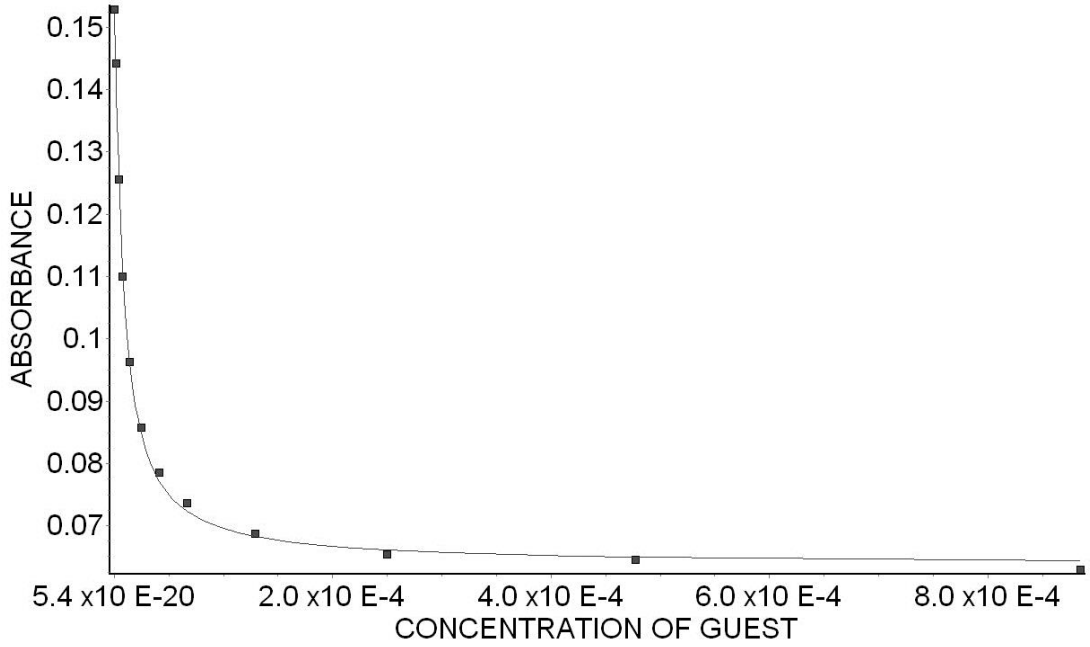

Figure III-S38. a) UV/Vis spectra from the titration of Calabadion 1 (5.02 µM) and rhodamine 6G (4.97 µM) with guest cocaine (0 – 885 µM) in 20 mM NaH_2PO_4 buffer (pH 7.4); b) plot of the A_{550} as a function of cocaine concentration. The solid line represents the best non-linear fit of the data to a 1:1 binding model (K_a = (6.6 ± 0.4) x 10^5 M^{-1}).

a)

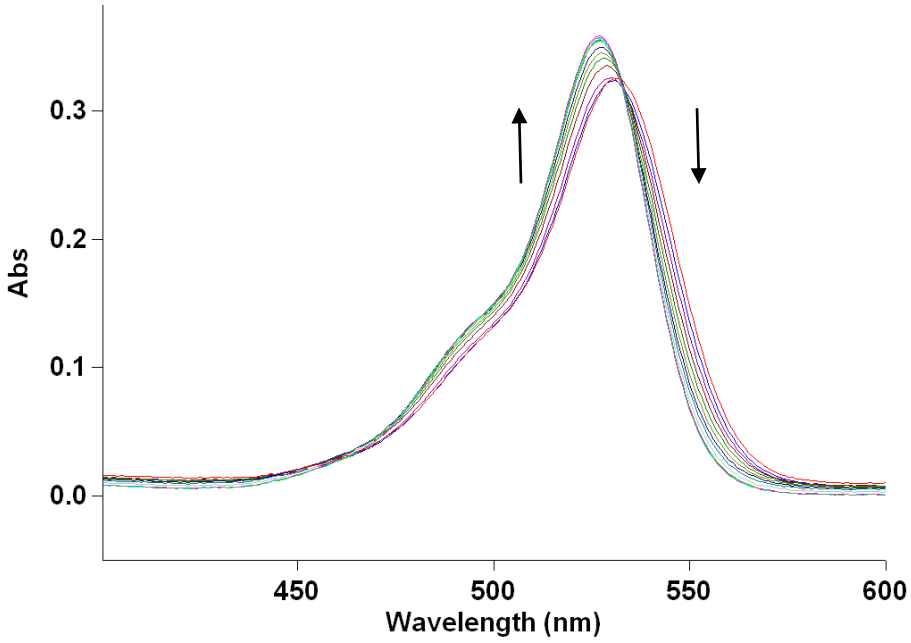

b)

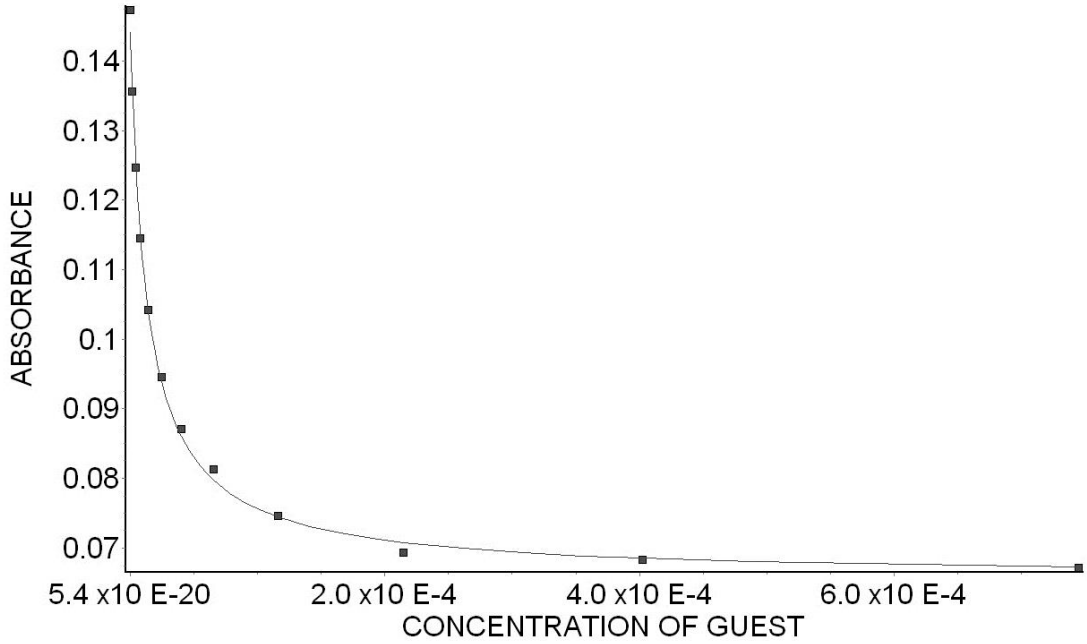

Figure III-S39. a) UV/Vis spectra from the titration of Calabadion 2 (4.97 µM) and rhodamine 6G (4.97 µM) with guest cocaine (0 – 745 µM) in 20 mM NaH_2PO_4 buffer (pH 7.4); b) plot of the A_{550} as a function of cocaine concentration. The solid line represents the best non-linear fit of the data to a 1:1 binding model (K_a = (1.0 ± 0.1) x 10^6 M^{-1}).

a)

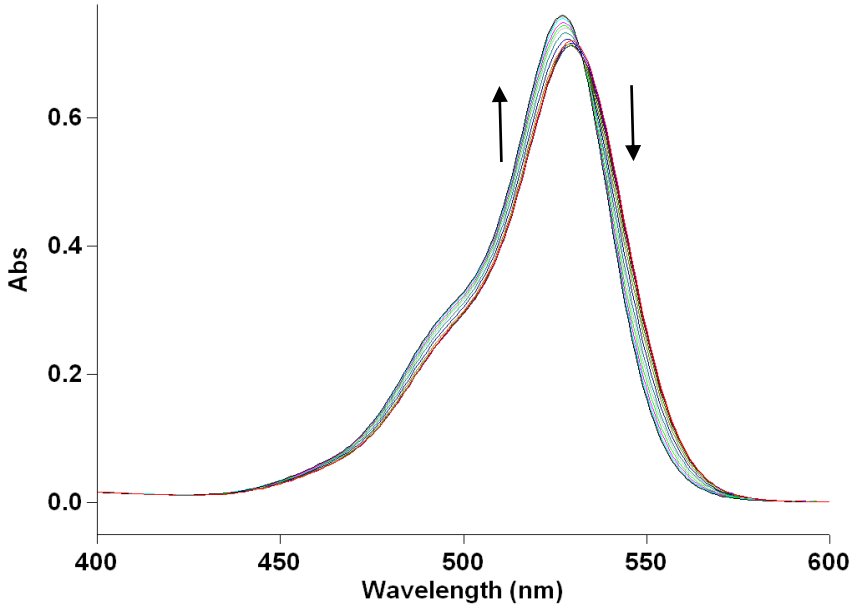

b)

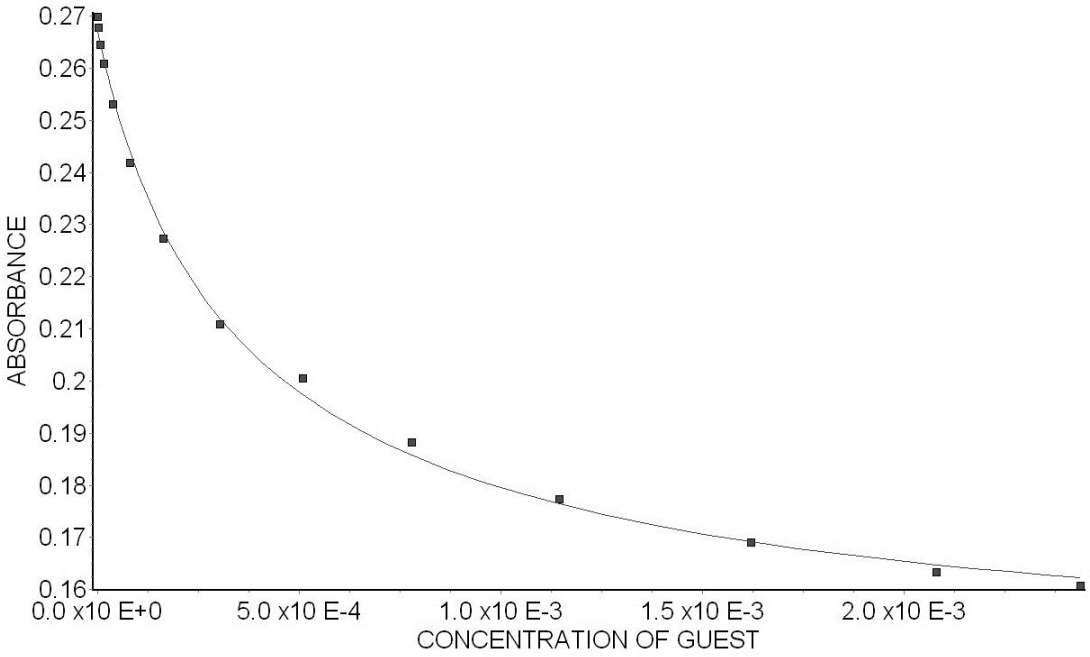

Figure 40. a) UV/Vis spectra from the titration of Calabadion 1 (5.01 µM) and rhodamine 6G (4.96 µM) with ketamine (0 – 2.44 mM) in 20 mM NaH_2PO_4 buffer (pH = 7.4); b) plot of the A_{550} as a function of the concentration of ketamine. The solid line represents the best non-linear fit of the data to a competitive binding model ($K_a = (1.1 \pm 0.1) \times 10^4\ M^{-1}$).

a)

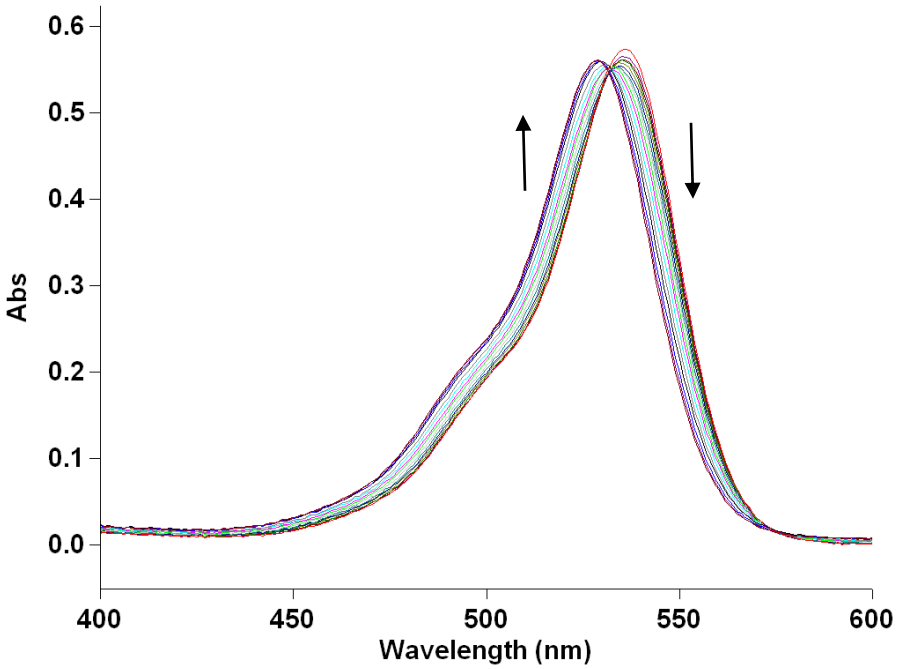

b)

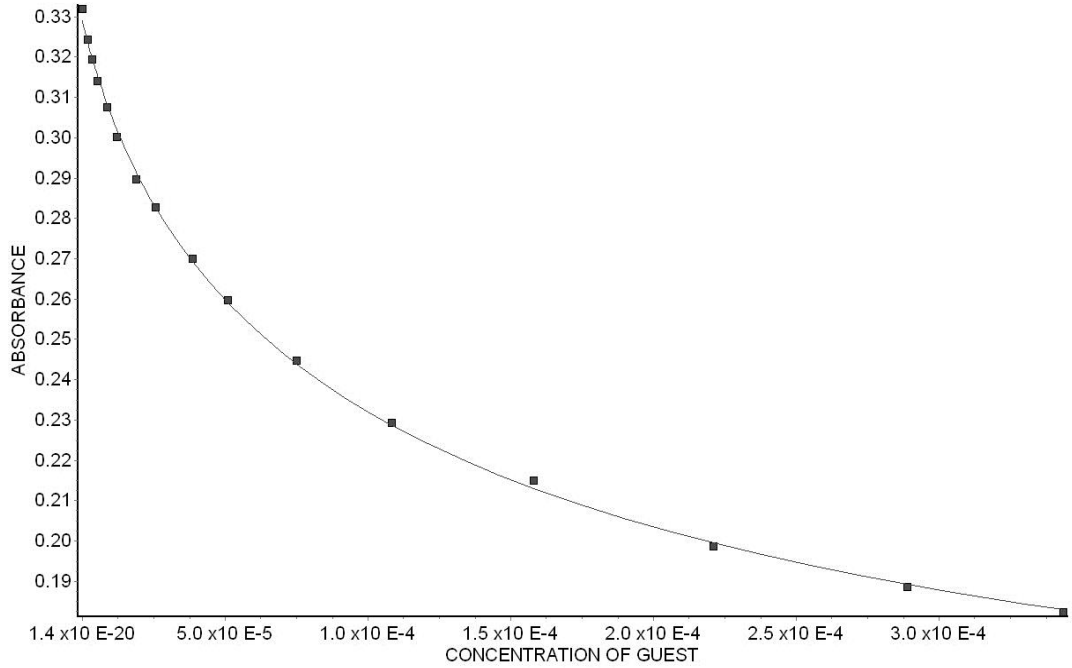

Figure 41. a) UV/Vis spectra from the titration of Calabadion 2 (9.18 µM) and rhodamine 6G (10.00 µM) with ketamine (0 – 0.35 mM) in 20 mM NaH_2PO_4 buffer (pH = 7.4); b) plot of the A_{550} as a function of the concentration of ketamine. The solid line represents the best non-linear fit of the data to a competitive binding model ($K_a = (1.8 \pm 0.1) \times 10^5\ M^{-1}$).

a)

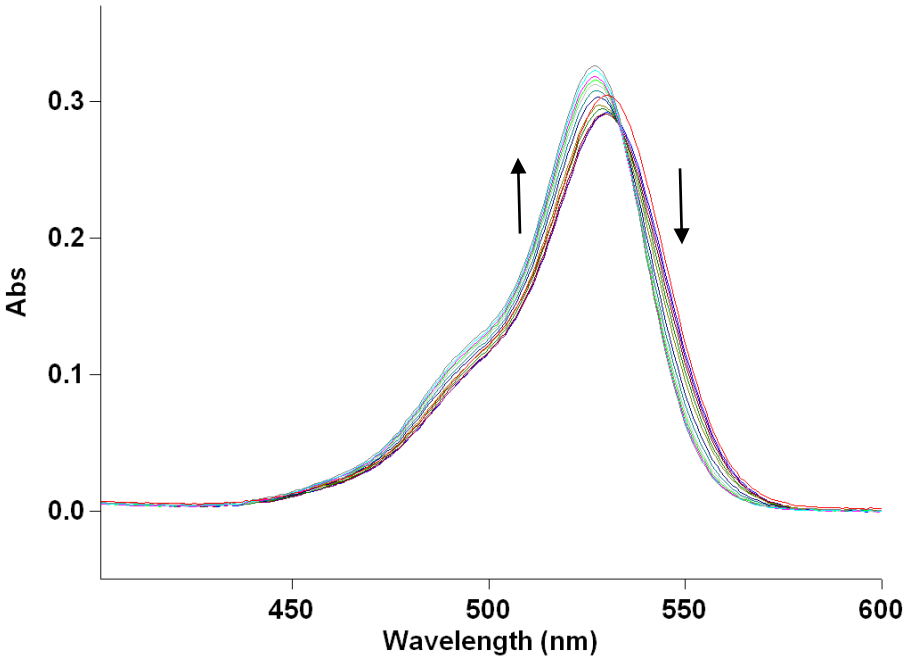

b)

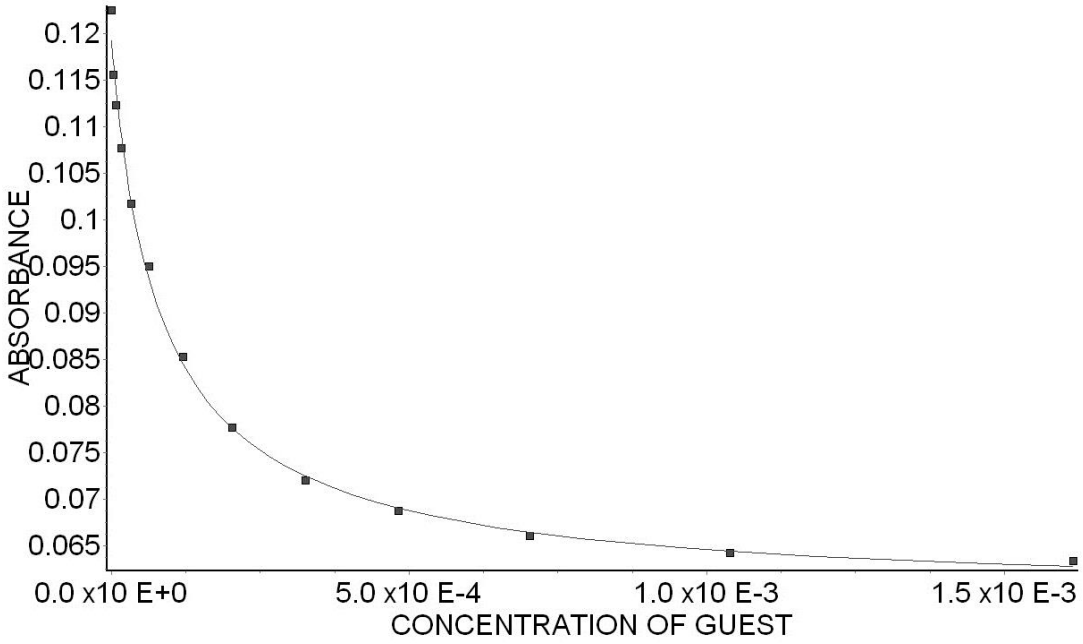

Figure III-S42. a) UV/Vis spectra from the titration of Calabadion 1 (5.02 µM) and rhodamine 6G (4.97 µM) with guest phencyclidine (0 – 1.62 mM) in 20 mM NaH_2PO_4 buffer (pH 7.4); b) plot of the A_{550} as a function of phencyclidine concentration. The solid line represents the best non-linear fit of the data to a 1:1 binding model ($K_a = (4.7 \pm 0.5) \times 10^4\ M^{-1}$).

a)

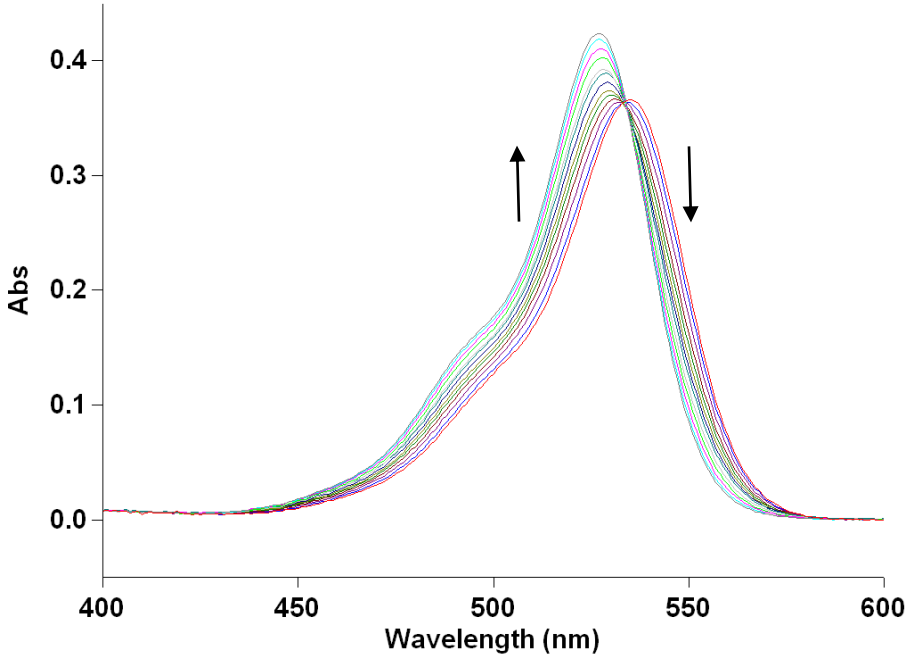

b)

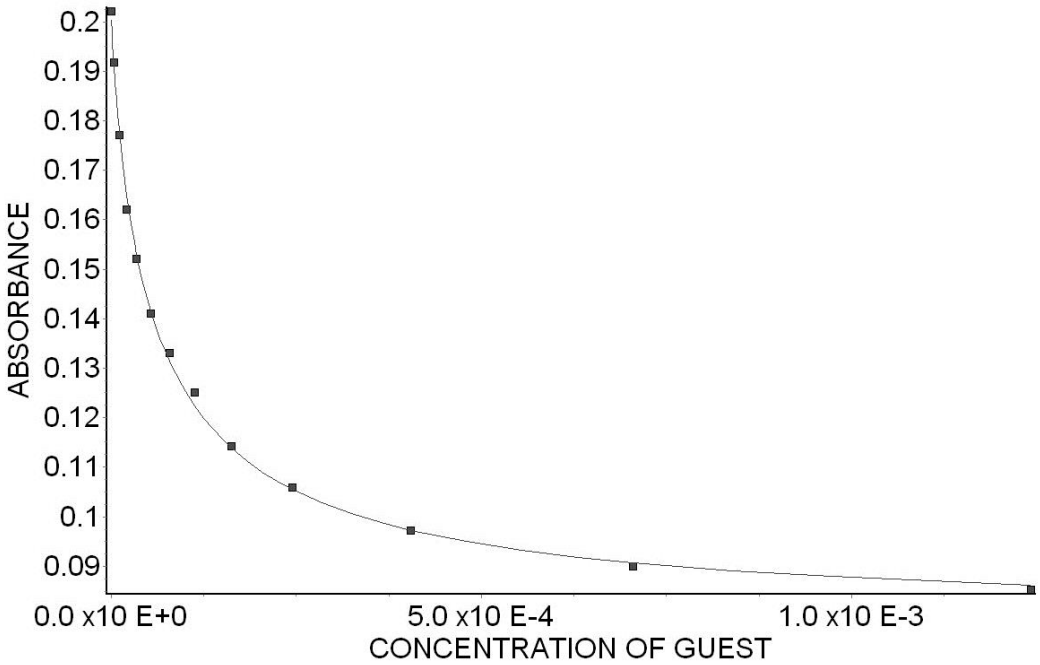

Figure III-S43. a) UV/Vis spectra from the titration of Calabadion 2 (4.97 µM) and rhodamine 6G (4.97 µM) with guest phencyclidine (0 – 1.24 mM) in 20 mM NaH_2PO_4 buffer (pH 7.4); b) plot of the A_{550} as a function of phencyclidine concentration. The solid line represents the best non-linear fit of the data to a 1:1 binding model (K_a = (2.1 ± 0.1) x 10^5 M^{-1}).

a)

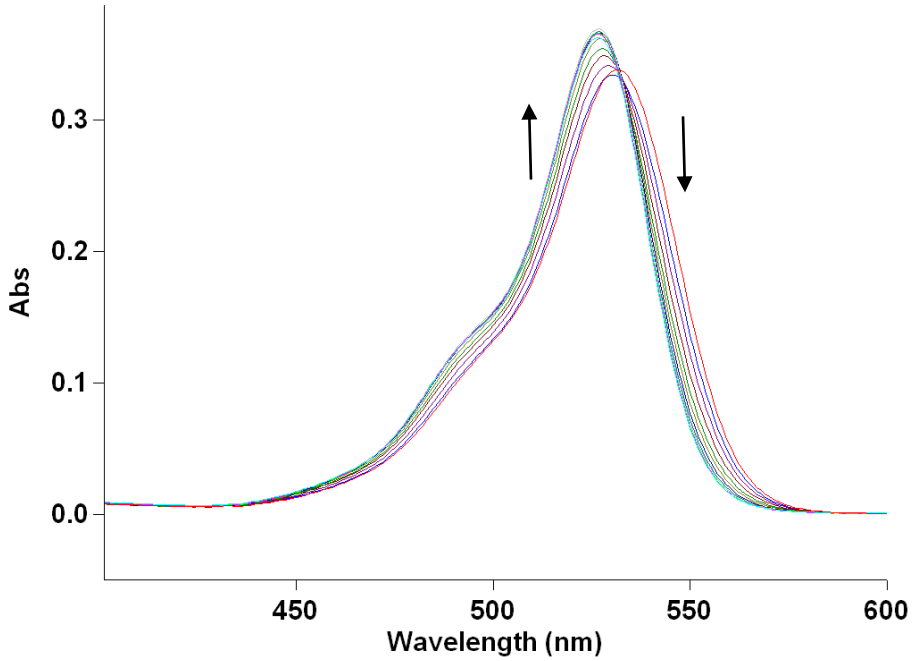

b)

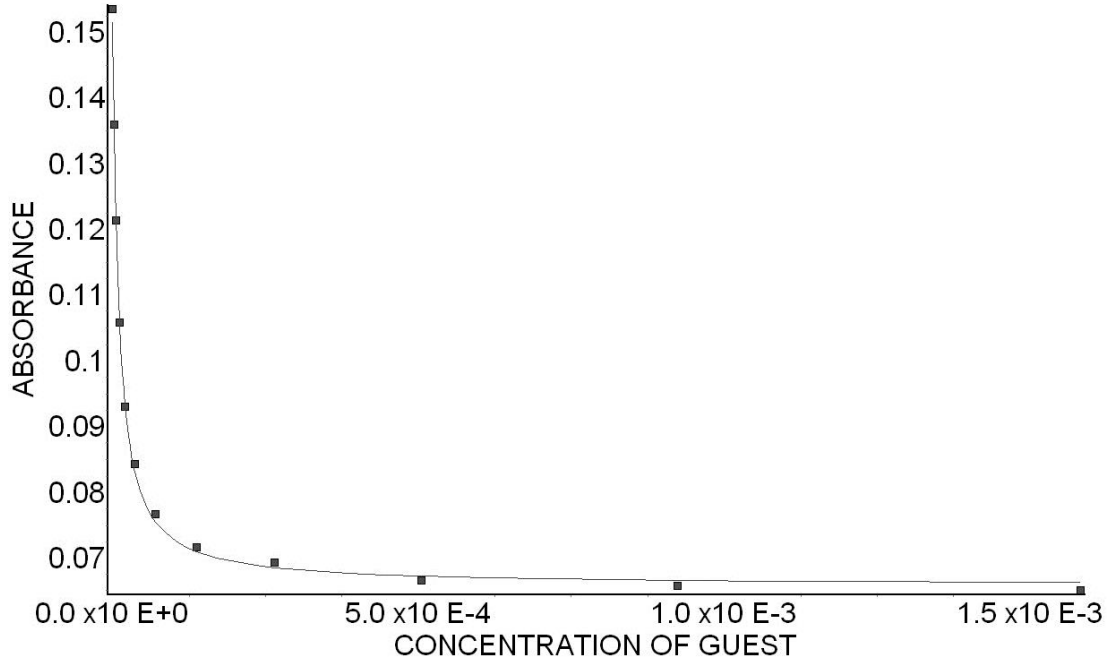

Figure III-S44. a) UV/Vis spectra from the titration of Calabadion 1 (5.00 µM) and rhodamine 6G (5.01 µM) with guest morphine (0 – 1.58 mM) in 20 mM NaH_2PO_4 buffer (pH 7.4); b) plot of the A_{550} as a function of morphine concentration. The solid line represents the best non-linear fit of the data to a 1:1 binding model (K_a = (5.3 ± 0.3) x 10^5 M^{-1}).

a)

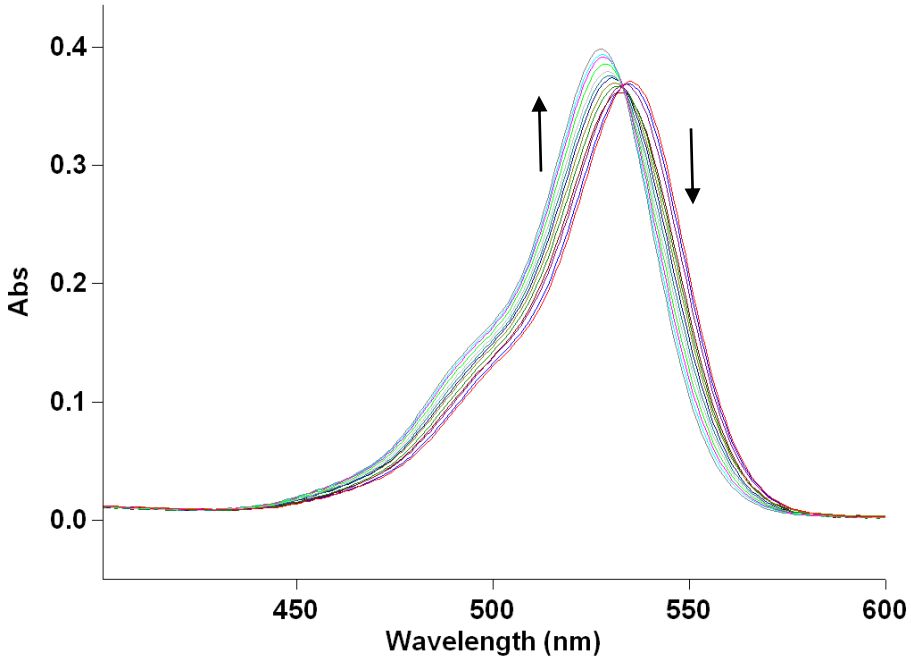

b)

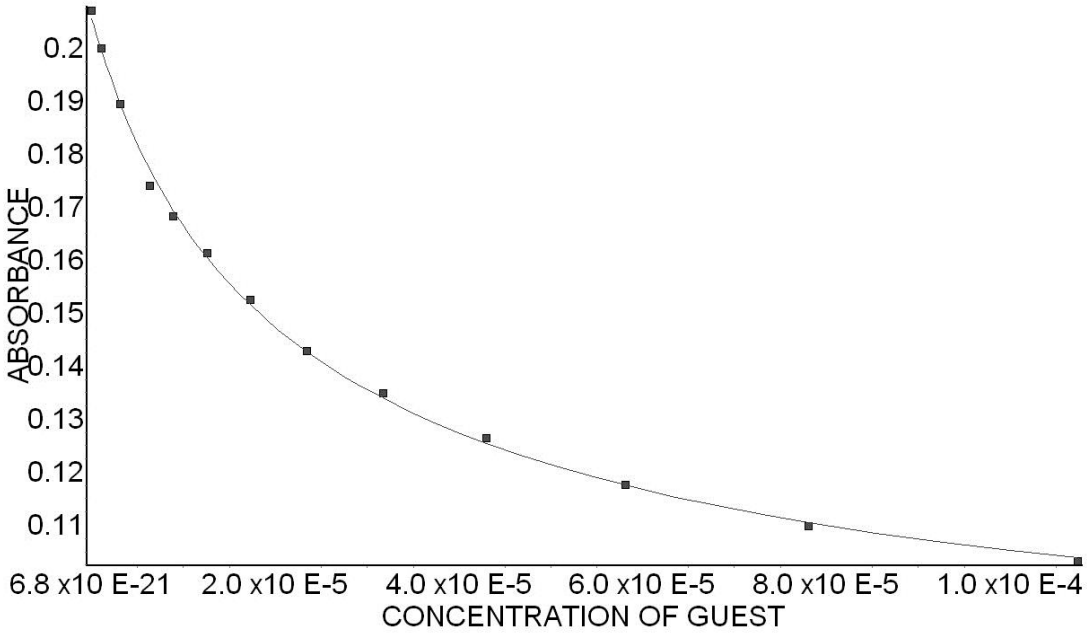

Figure III-S45. a) UV/Vis spectra from the titration of Calabadion 2 (5.07 µM) and rhodamine 6G (5.01 µM) with guest morphine (0 – 107 µM) in 20 mM NaH_2PO_4 buffer (pH 7.4); b) plot of the A_{550} as a function of morphine concentration. The solid line represents the best non-linear fit of the data to a 1:1 binding model (K_a = (5.3 ± 0.4) x 10^5 M^{-1}).

Determination of K_a between hosts CB[7] and p-sulfo calix[4]arene and various drugs of abuse using ^{1}H NMR.

The K_a values of complexes which were less than 10^4 M^{-1} were determined by direct ^{1}H NMR titrations. The concentration of either the host or guest was kept constant while varying the concentration of the other component. The change in chemical shift of a selected signal of the species whose concentration was fixed was monitored. The change in chemical shift as a function of the concentration of the species being varied was fitted to a 1:1 binding model to determine the K_a.

1:1 Binding Model for NMR

// Micromath Scientist Model File
// 1:1 Host:Guest binding model
//This model assumes the guest concentration is fixed and host concentration is varied
IndVars: ConcHostTot
DepVars: SpectroscopicSignal
Params: Ka, ConcGuestTot, SpectroscopicSignalMin, SpectroscopicSignalMax
Ka = ConcHostGuest/(ConcHostFree*ConcGuestFree)
ConcHostTot=ConcHostFree + ConcHostGuest
ConcGuestTot=ConcGuestFree + ConcHostGuest
SpectroscopicSignal = SpectroscopicSignalMin + (SpectroscopicSignalMax - SpectroscopicSignalMin) * (ConcHostGuest/ConcGuestTot)
//Constraints
0 < ConcHostFree < ConcHostTot
0 < Ka
0 < ConcGuestFree < ConcGuestTot
0 < ConcHostGuest < ConcHostTot
***

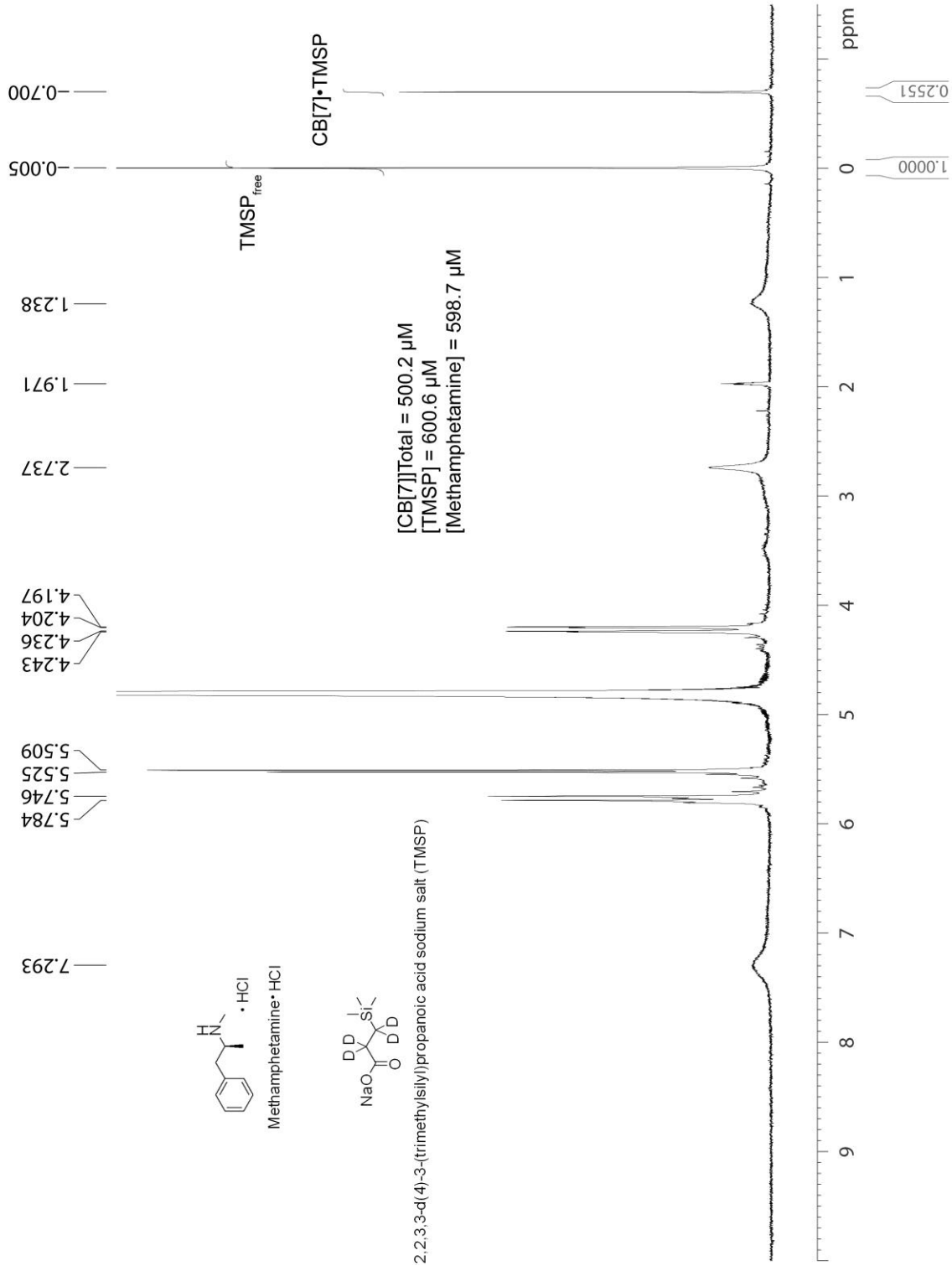

Figure III-S46. One of the ^{1}H NMR (600 MHz) spectra used in the determination of K_{rel} for CB[7]•methamphetamine and CB[7]•TMSP.

Sample Determination of K_{rel} for the Competition between TMSP and Methamphetamine for CB[7].

Equation 1 was used to determine K_{rel} for the competition of TMSP and methamphetamine for CB[7]. For this purpose, a solution containing CB[7] (500.2 μM), TMSP (600.6 μM), and methamphetamine (598.7 μM) was prepared and allowed to reach equilibrium (Figure III-S46). Next the relative concentrations of $TMSP_{free}$ and CB[7]•TMSP were determined by integration of the appropriate resonances in the ^{1}H NMR spectrum (Figure III-S46: $TMSP_{free}$: -0.005 ppm; CB[7]•TMSP: -0.700 ppm). Using the relative concentrations and the mass balance expression (equation 2) $[TMSP]_{free}$ = 478.5 μM and [CB[7]•TMSP] = 122.1 μM were calculated. Equation 3 was then used to calculate [CB[7]•methamphetamine] = 378.1 μM using the known value of CB[7]•TMSP.[18] Lastly, equation 4 was used to calculate $[methamphetamine]_{free}$ = 220.6 μM using the known value of [CB[7]•TMSP].

$$K_{rel} = ([CB[7]\bullet\ Methamphetamine][TMSP]_{free}) / ([CB[7]\bullet TMSP][methamphetamine]_{free}) \quad (1)$$

$$[TMSP]_{Total} = 600.6\ \mu M = [TMSP]_{free} + [CB[7]\bullet TMSP] \quad (2)$$

$$[CB[7]]_{Total} = 500.2\ \mu M = [CB[7]\bullet TMSP] + [CB[7]\bullet methamphetamine] \quad (3)$$

$$[methamphetamine]_{Total} = 598.7\ \mu M = [methamphetamine]_{free} + [CB[7]\bullet\ methamphetamine] \quad (4)$$

Substitution of the values of [CB[7]•TMSP], $[TMSP]_{free}$, [CB[7]•methamphetamine], and $[methamphetamine]_{free}$ into equation 1 gave K_{rel} = 6.72. These determinations were done in triplicate from independently prepared stock solutions and the average values were used in the calculations of K_a. In

preparing the solutions for the above determinations a small excess of TMSP was used to ensure there is no free CB[7]. The K_a for CB[7]•methamphetamine was calculated using the average K_{rel} and the known value of CB[7]•TMSP ((1.82 ± 0.22) × 10^7 M^{-1}). [18]

a)

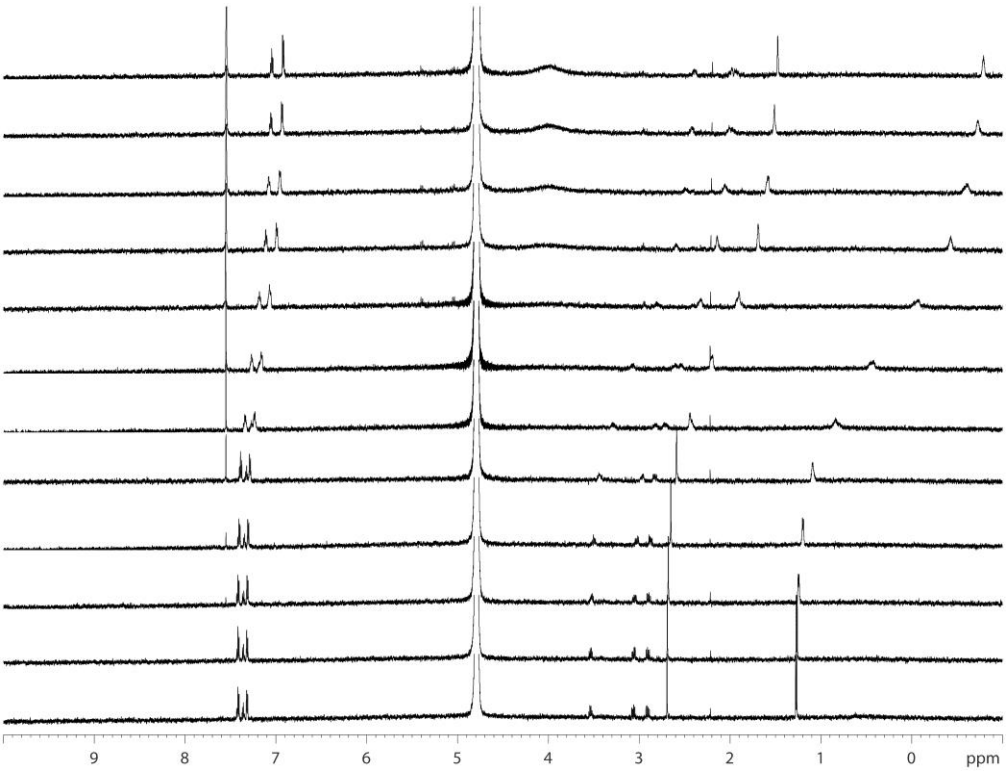

b)

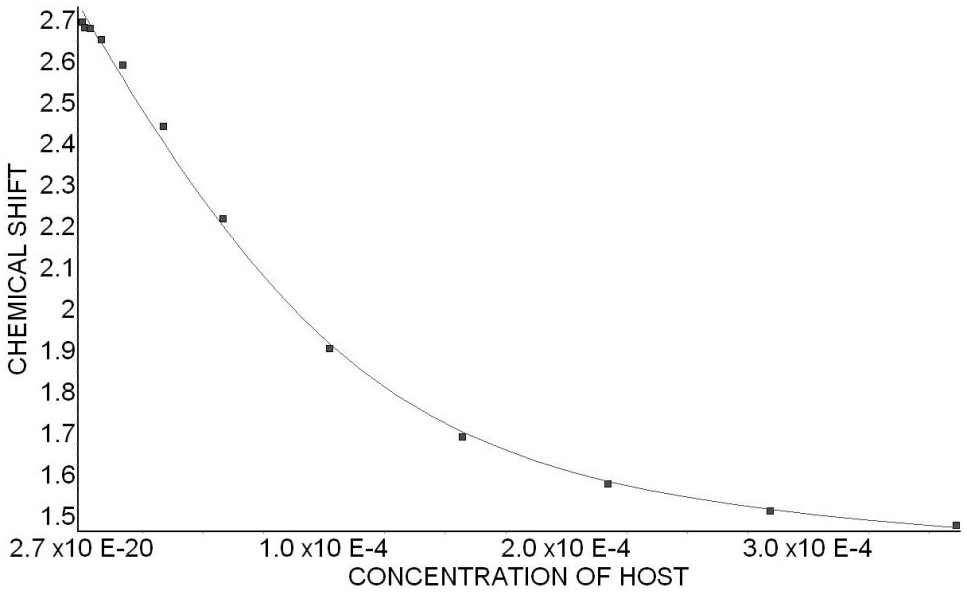

Figure III-S47. a) ^{1}H NMR stack plot from the titration of methamphetamine (111 µM) with host p-sulfo calix[4]arene (0 – 361 µM) in 20 mM NaH_2PO_4 buffer (pD 7.4); b) plot of the change in chemical shift of methamphetamine at 2.70 ppm as a function of p-sulfo calix[4]arene concentration. The solid line represents the best non-linear fit of the data to a 1:1 binding model ($K_a = (3.8 \pm 0.6) \times 10^4$ M^{-1}).

a)

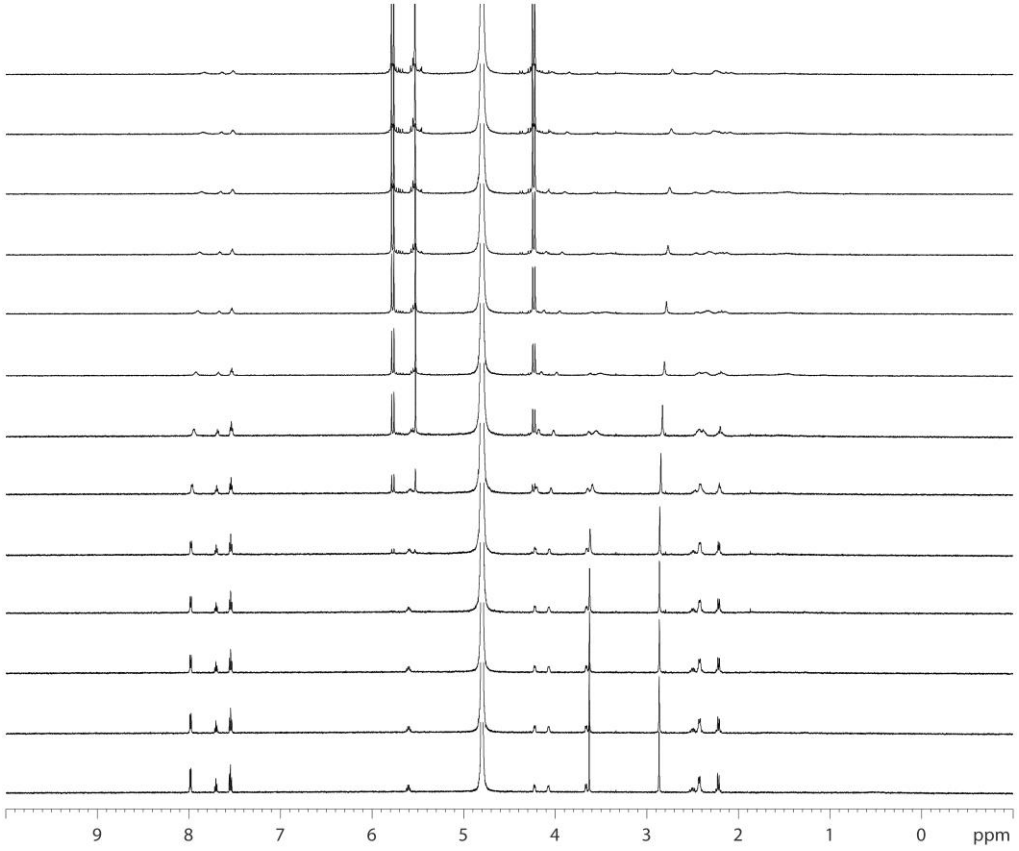

b)

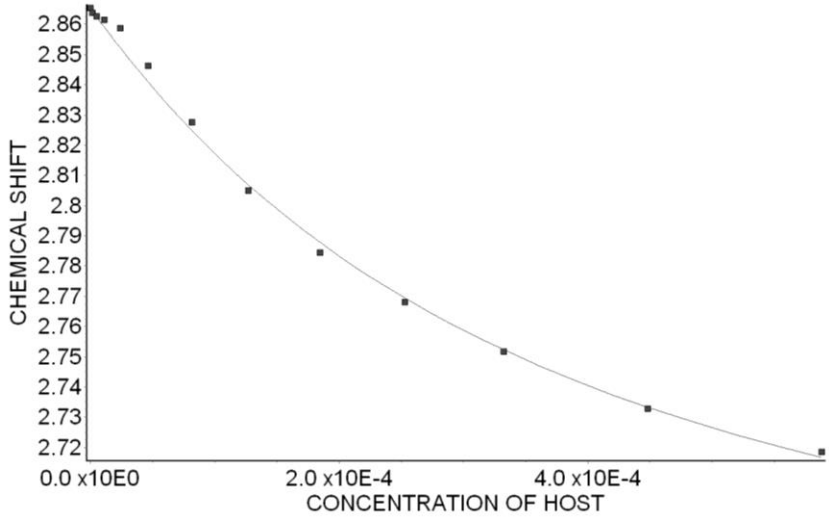

Figure III-S48. a) ^{1}H NMR stack plot from the titration of cocaine (103 µM) with host CB[7] (0 – 588 µM) in 20 mM NaH_2PO_4 buffer (pD 7.4); b) plot of the change in chemical shift of cocaine at 2.87 ppm as a function of CB[7] concentration. The solid line represents the best non-linear fit of the data to a 1:1 binding model ($K_a = (2.3 \pm 0.2) \times 10^3\ M^{-1}$).

a)

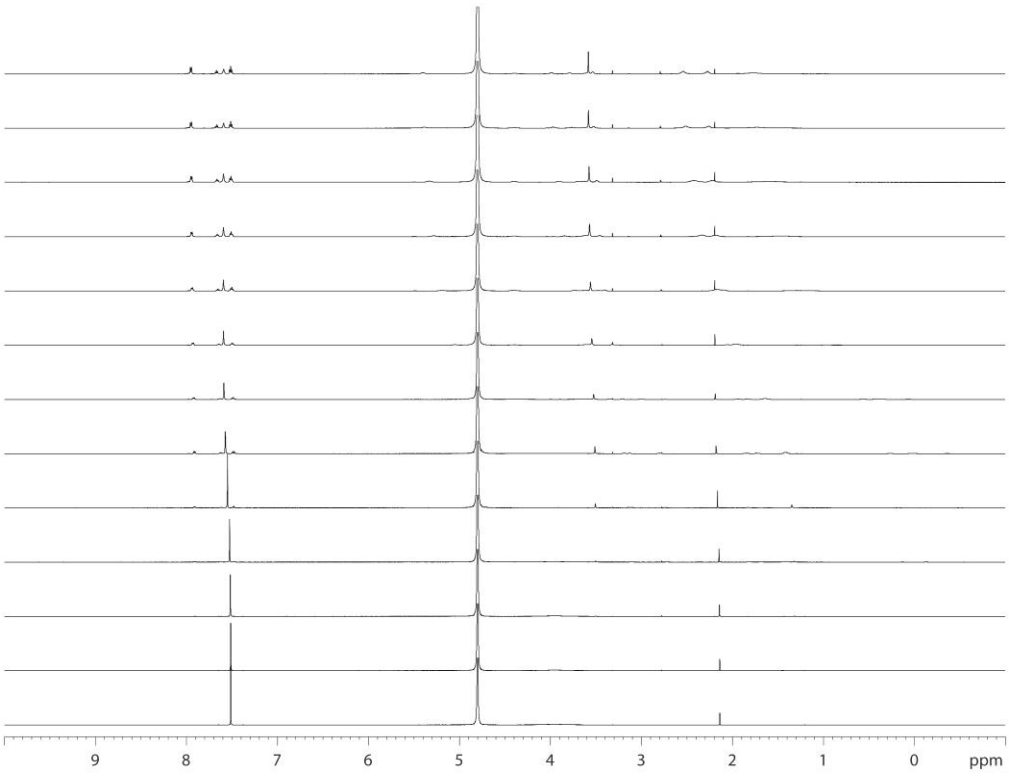

b)

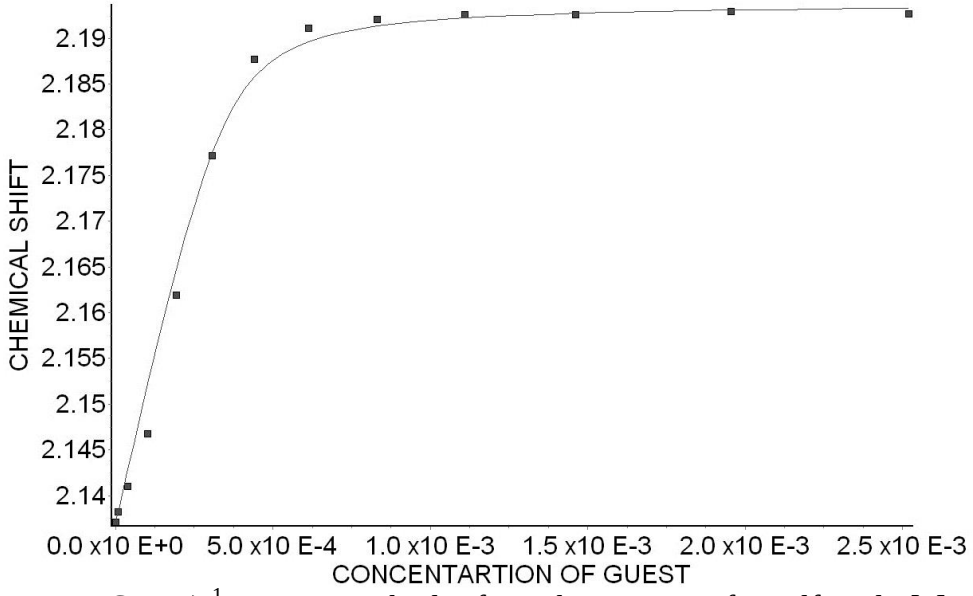

Figure III-S49. a) ^{1}H NMR stack plot from the titration of p-sulfo calix[4]arene (350 µM) with guest cocaine (0 – 2.52 mM) in 20 mM NaH_2PO_4 buffer (pD 7.4); b) plot of the change in chemical shift of p-sulfo calix[4]arene at 2.14 ppm as a function of cocaine concentration. The solid line represents the best non-linear fit of the data to a 1:1 binding model ($K_a = (4.3 \pm 1.5) \times 10^4\ M^{-1}$).

a)

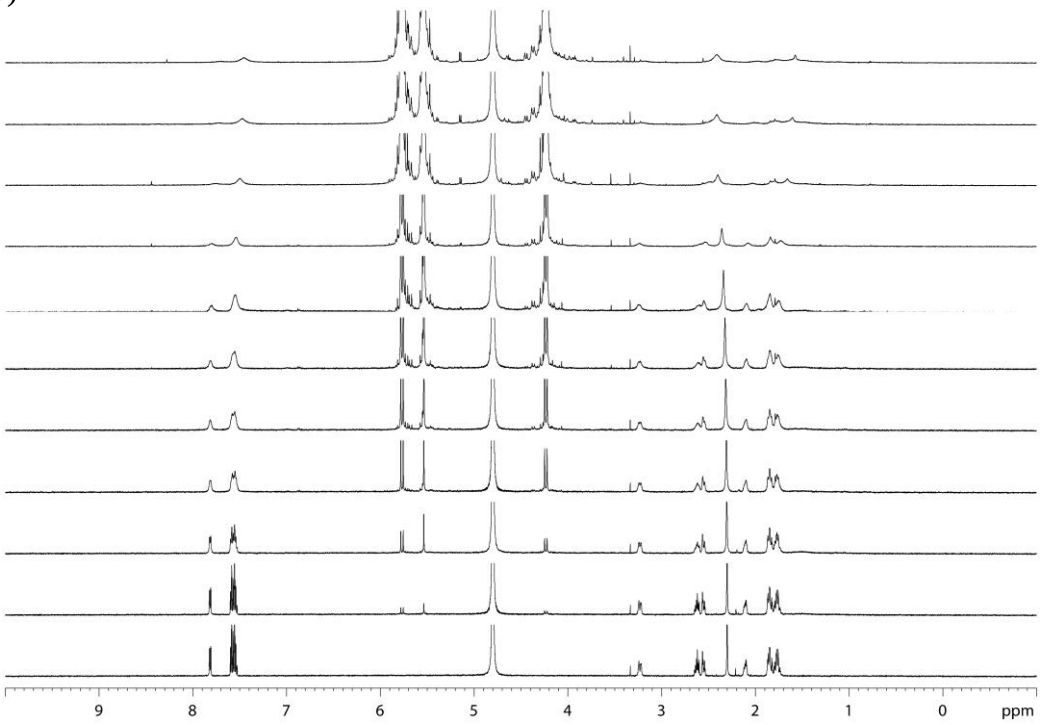

b)

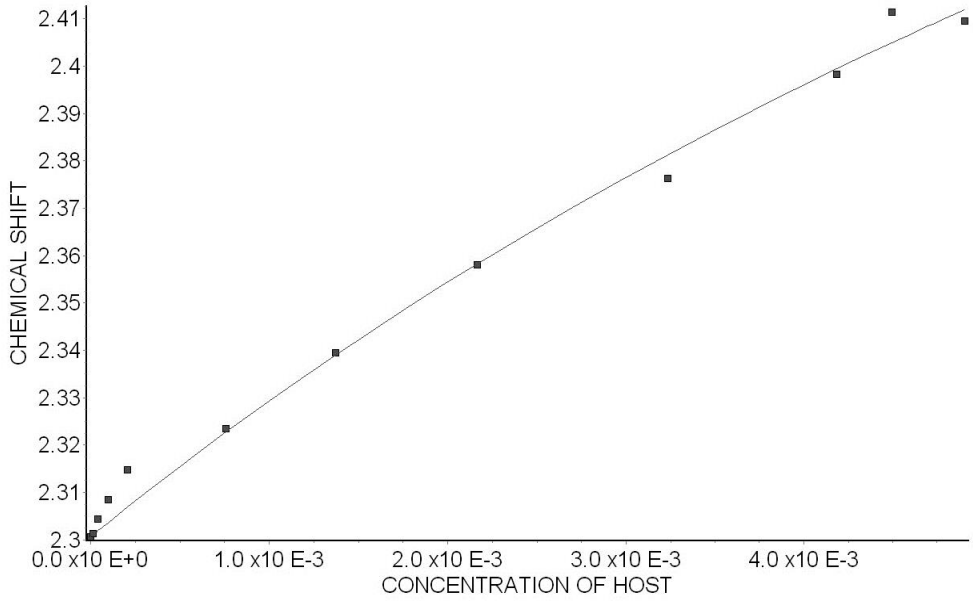

Figure III-S50. (A) ^{1}H NMR (600 MHz) stack plot from the titration of ketamine (1.00 mM) with host CB[7] (0 – 4.9 mM) in 20 mM NaH_2PO_4 buffered (pH = 7.4) D_2O; (B) plot of the chemical shift at 2.3 ppm as a function of host CB[7] concentration. The solid line represents the best non-linear fit of the data to a 1:1 model (K_a = (6.4 ± 1.2) x 10^2 M^{-1}).

a)

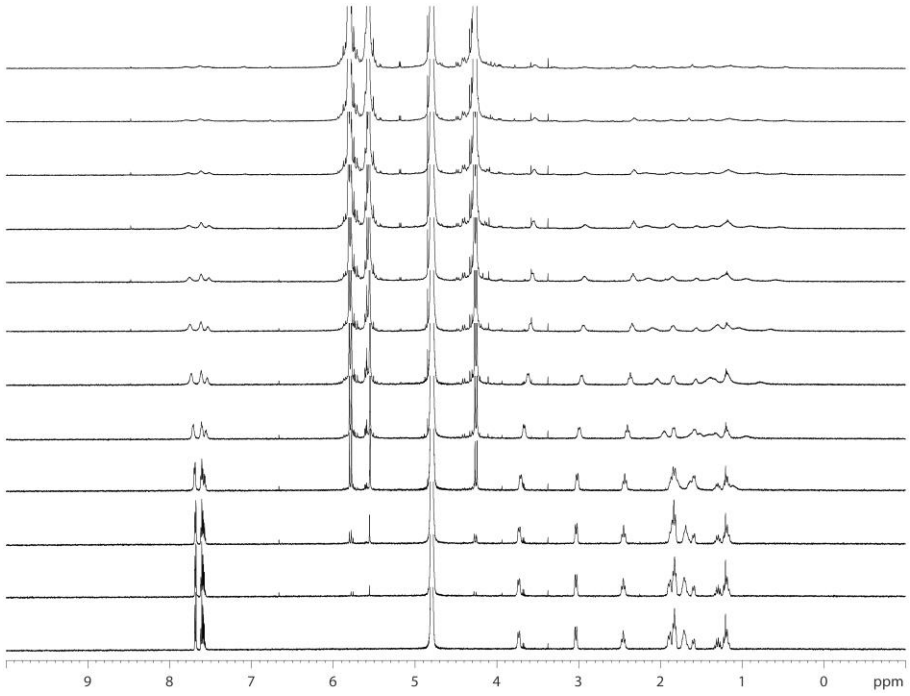

b)

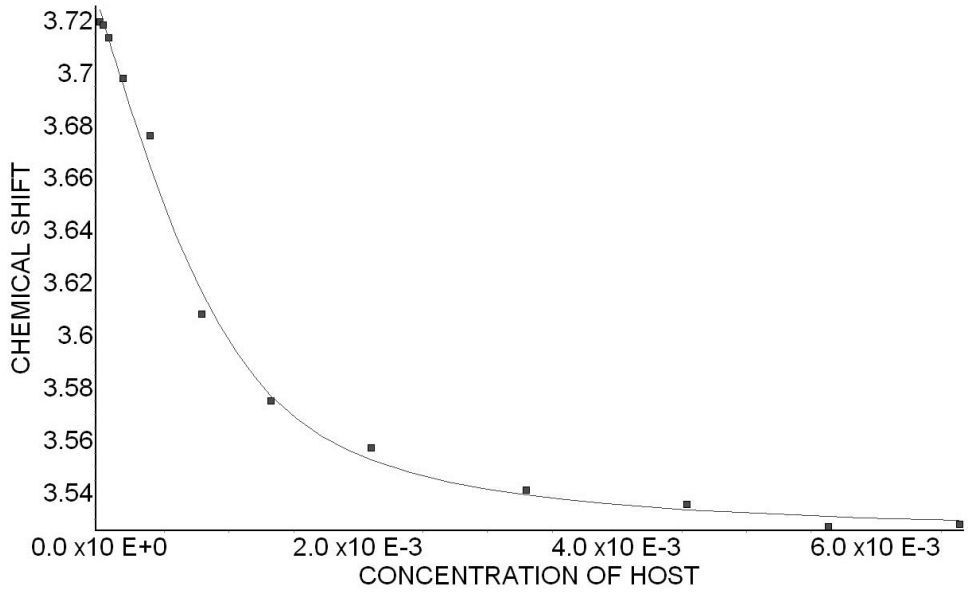

Figure III-S51. a) ^{1}H NMR stack plot from the titration of phencyclidine (1.00 mM) with host CB[7] (0 – 6.64 mM) in 20 mM NaH_2PO_4 buffer (pD 7.4); b) plot of the change in chemical shift of phencyclidine at 3.72 ppm as a function of CB[7]. The solid line represents the best non-linear fit of the data to a 1:1 model ($K_a = (4.4 \pm 0.9) \times 10^3\ M^{-1}$).

a)

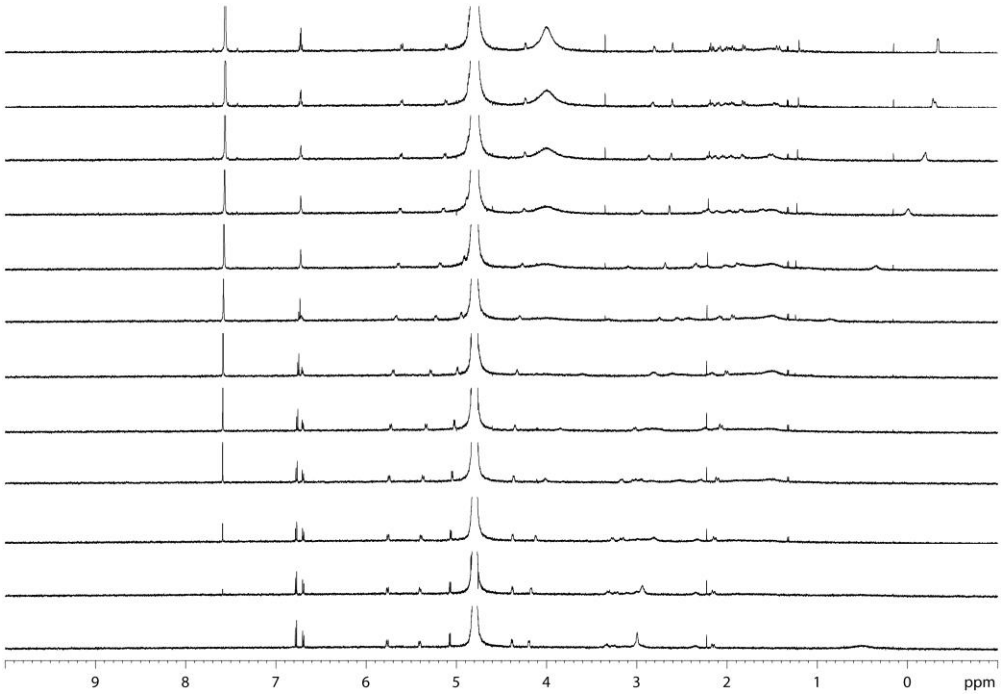

b)

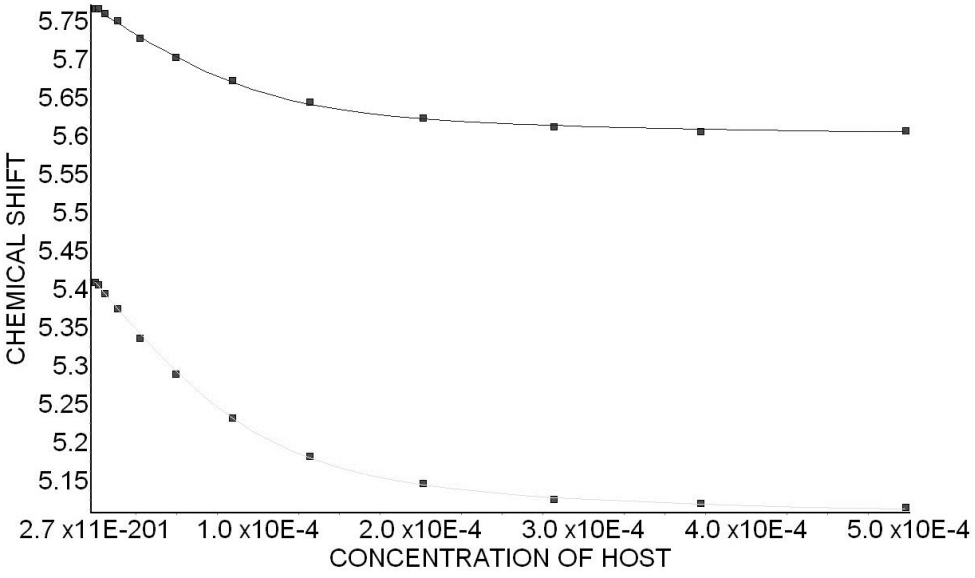

Figure III-S52. a) ^{1}H NMR stack plot from the titration of morphine (100 µM) with host p-sulfo calix[4]arene (0 – 498 µM) in 20 mM NaH_2PO_4 buffer (pD 7.4); b) plot of the change in chemical shift of morphine at 5.41 ppm and 5.77 ppm as a function of p-sulfo calix[4]arene concentration. The solid line represents the best non-linear fit of the data to a 1:1 binding model ($K_a = (4.9 \pm 0.3) \times 10^4\ M^{-1}$).

Determination of K_a between various hosts and drugs of abuse using Isothermal Titration Calorimetry (ITC).

All ITC experiments were conducted in the 200 μL working volume of the sample cell of the PEAQ ITC instrument. We used an injection syringe of 40 μL capacity. In each case, the host and guest solutions were prepared in a 20 mM NaH_2PO_4 buffer (pH 7.4). The sample cell was filled to capacity (200 μL) with the host solution and the guest solution was titrated in (first injection = 0.4μL, subsequent 18 injections = 2 μL). In case of Figure III-S61 and III-S69 two sets of 19 injections were concatenated to obtain the binding isotherm. The binding data was fitted using the 1:1 binding model in MicroCal PEAQ-ITC analysis software.

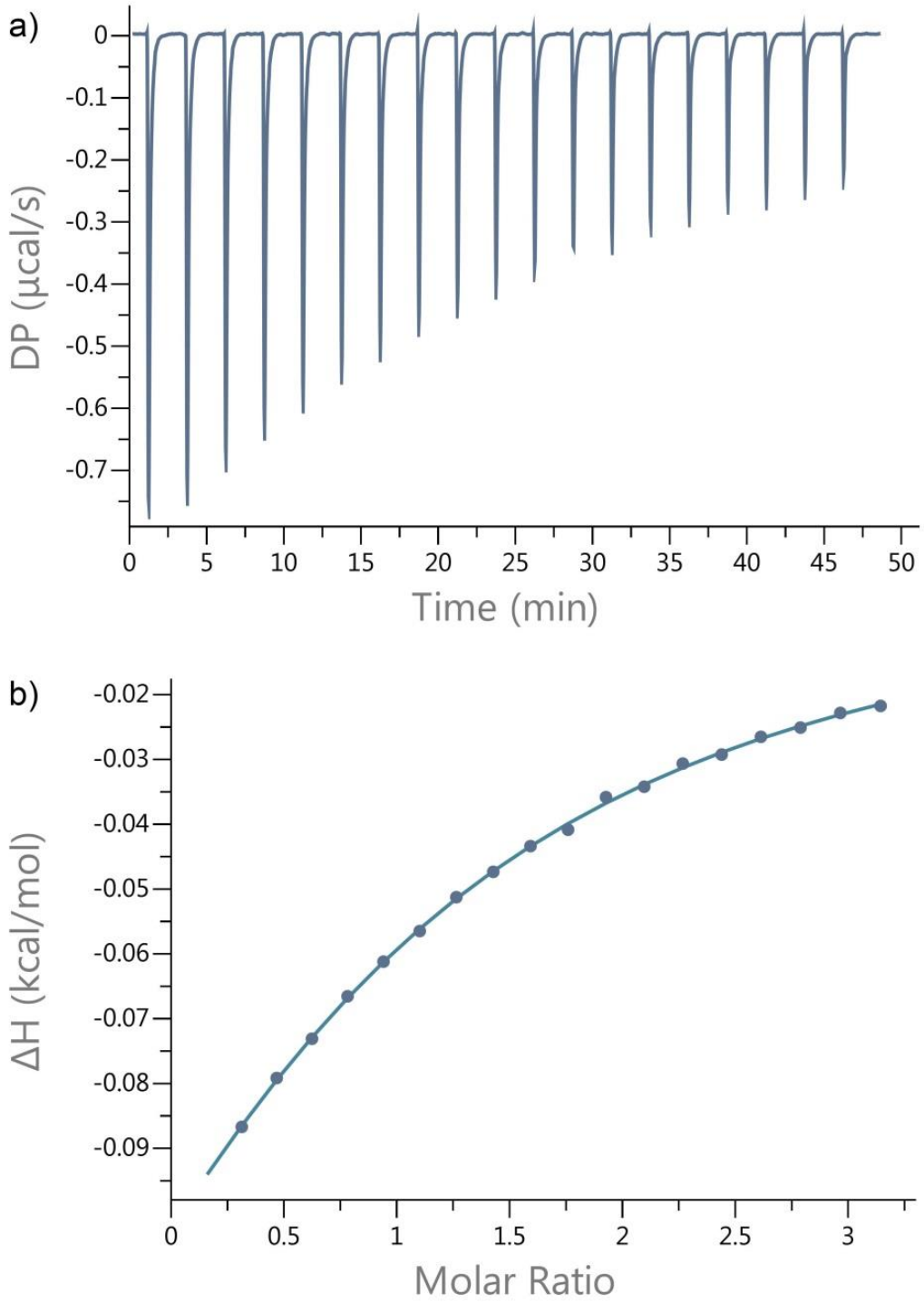

Figure III-S53. a) Plot of DP vs time from the titration of HP-β-CD (3.01 mM) and with guest methamphetamine (46.9 mM) in 20 mM NaH_2PO_4 buffer (pH 7.4); b) plot of the ΔH as a function of molar ratio. The solid line represents the best non-linear fit of the data to a 1:1 binding model (K_a = (1.9 ± 0.3) x 10^2 M^{-1}, ΔH = -0.26 ± 0.07 kcal/mol, -TΔS = -2.86 kcal/mol).

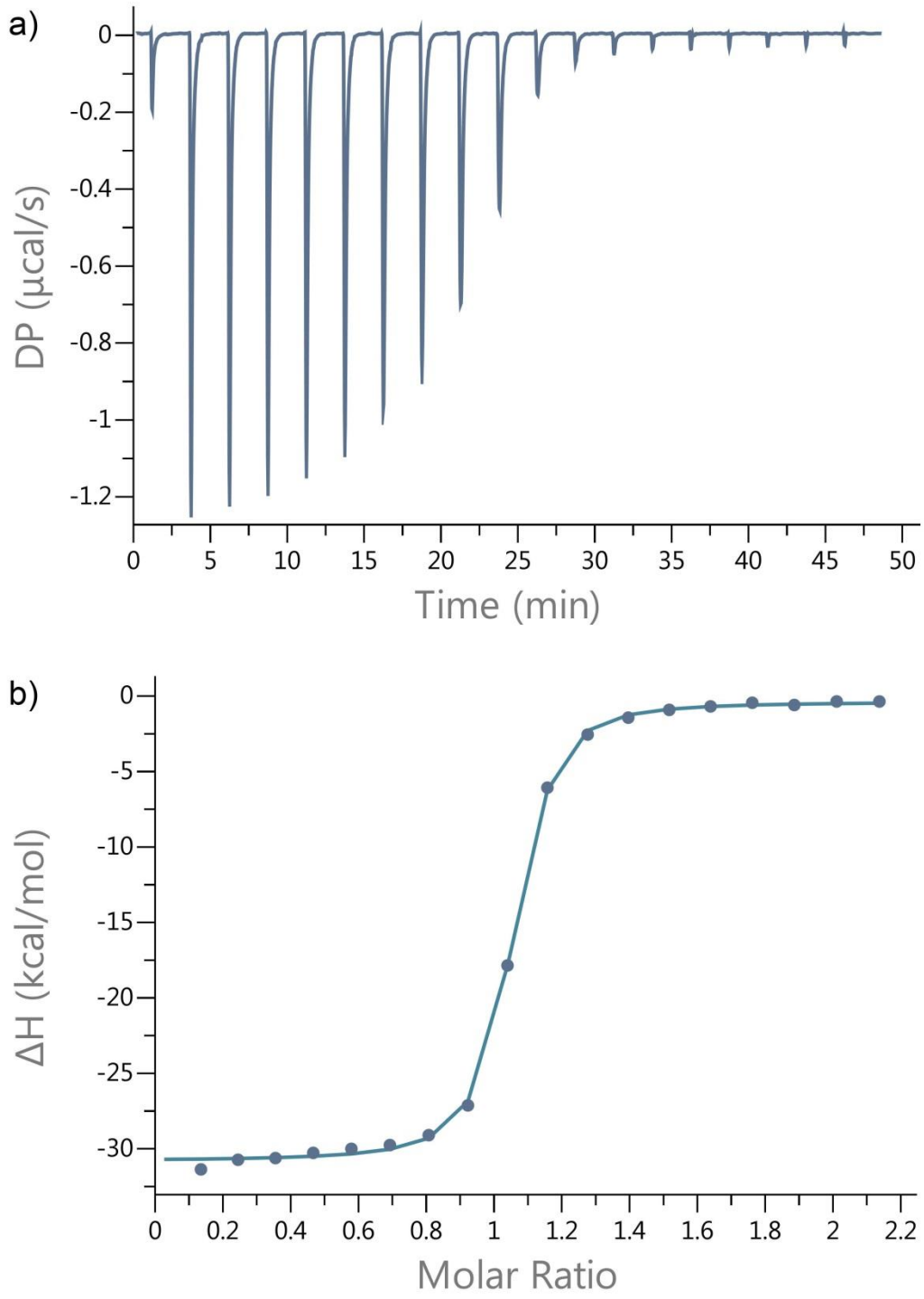

Figure III-S54. a) Plot of DP vs time from the titration of CB[7] (18.0 µM) and with guest fentanyl (0.20 mM) in 20 mM NaH_2PO_4 buffer (pH 7.4); b) plot of the ΔH as a function of molar ratio. The solid line represents the best non-linear fit of the data to a 1:1 binding model (K_a = (1.8 ± 0.1) x 10^7 M^{-1}, ΔH = - 30.4 ± 0.17 kcal/mol, -TΔS = 20.5 kcal/mol).

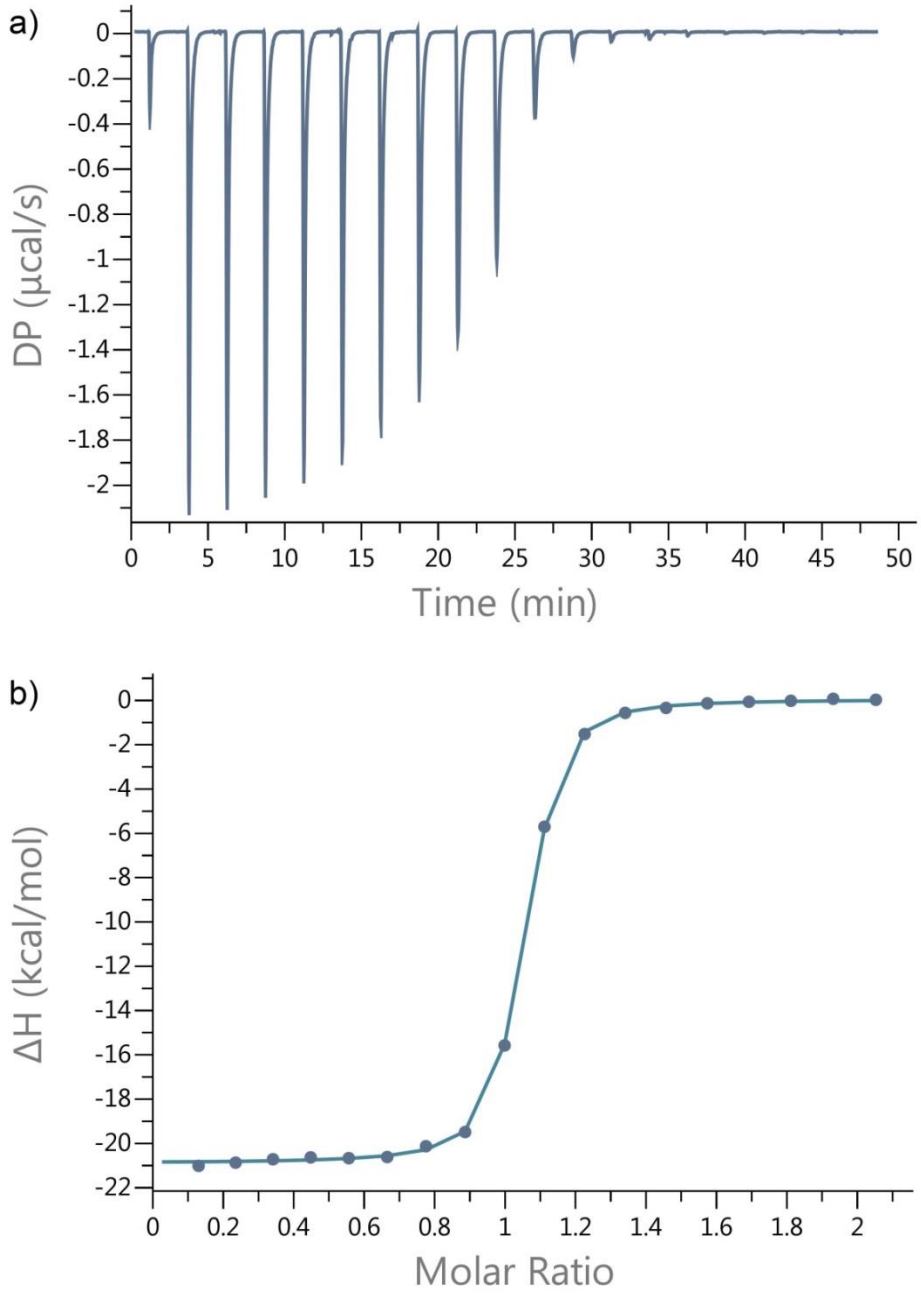

Figure III-S55. a) Plot of DP vs time from the titration of Calabadion 1 (46.8 µM) and with guest fentanyl (0.499 mM) in 20 mM NaH_2PO_4 buffer (pH 7.4); b) plot of the ΔH as a function of molar ratio. The solid line represents the best non-linear fit of the data to a 1:1 binding model (K_a = (1.1 ± 0.04) x 10^7 M^{-1}, ΔH = -20.9 ± 0.06 kcal/mol, -TΔS = 3.99 kcal/mol).

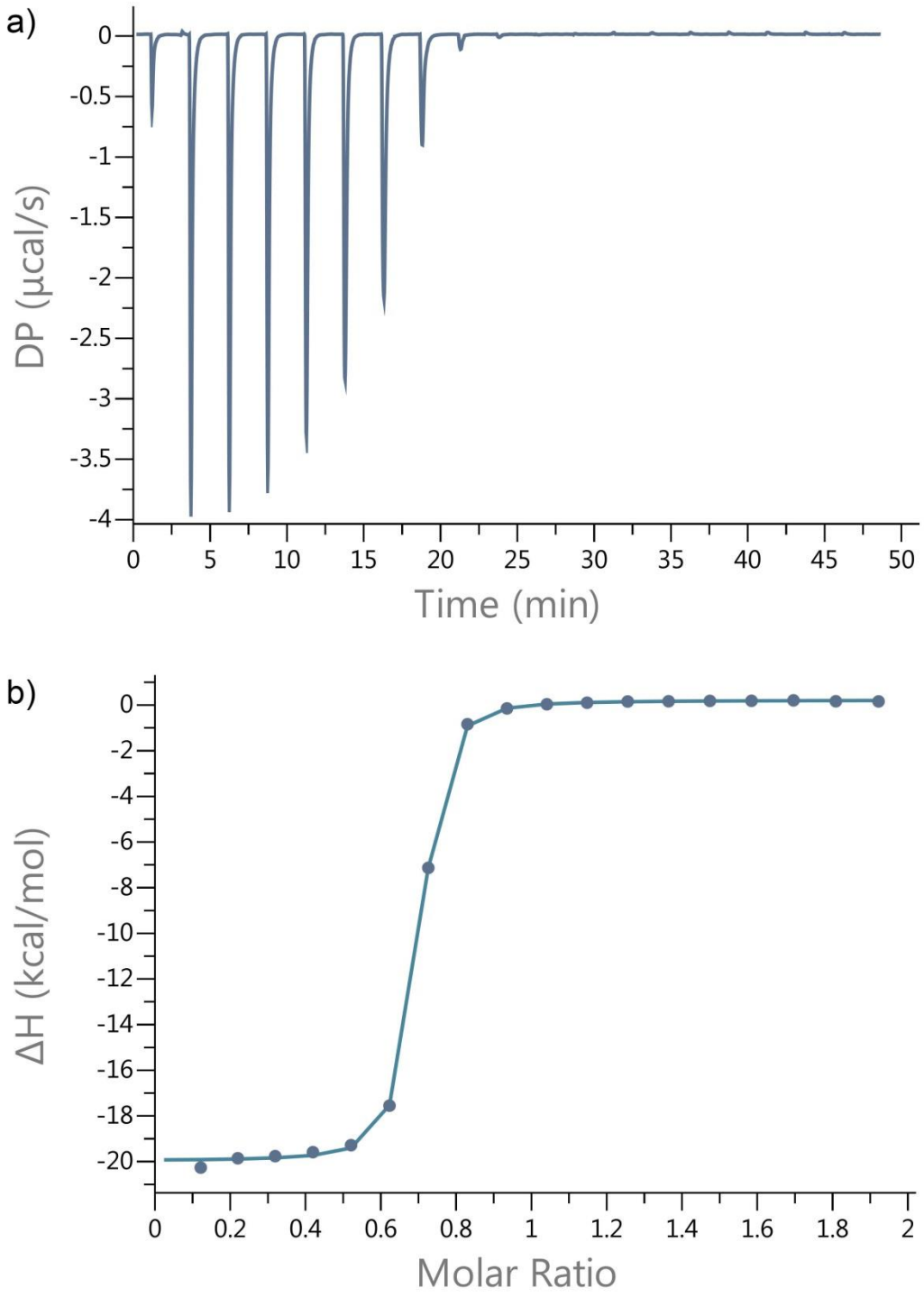

Figure III-S57. a) Plot of DP vs time from the titration of Calabadion 2 (100 µM) and with guest fentanyl (1.00 mM) in 20 mM NaH_2PO_4 buffer (pH 7.4); b) plot of the ΔH as a function of molar ratio. The solid line represents the best non-linear fit of the data to a 1:1 binding model (K_a = (7.6 ± 0.5) x 10^6 M^{-1}, ΔH = - 20.2 ± 0.07 kcal/mol, -TΔS = 10.8 kcal/mol).

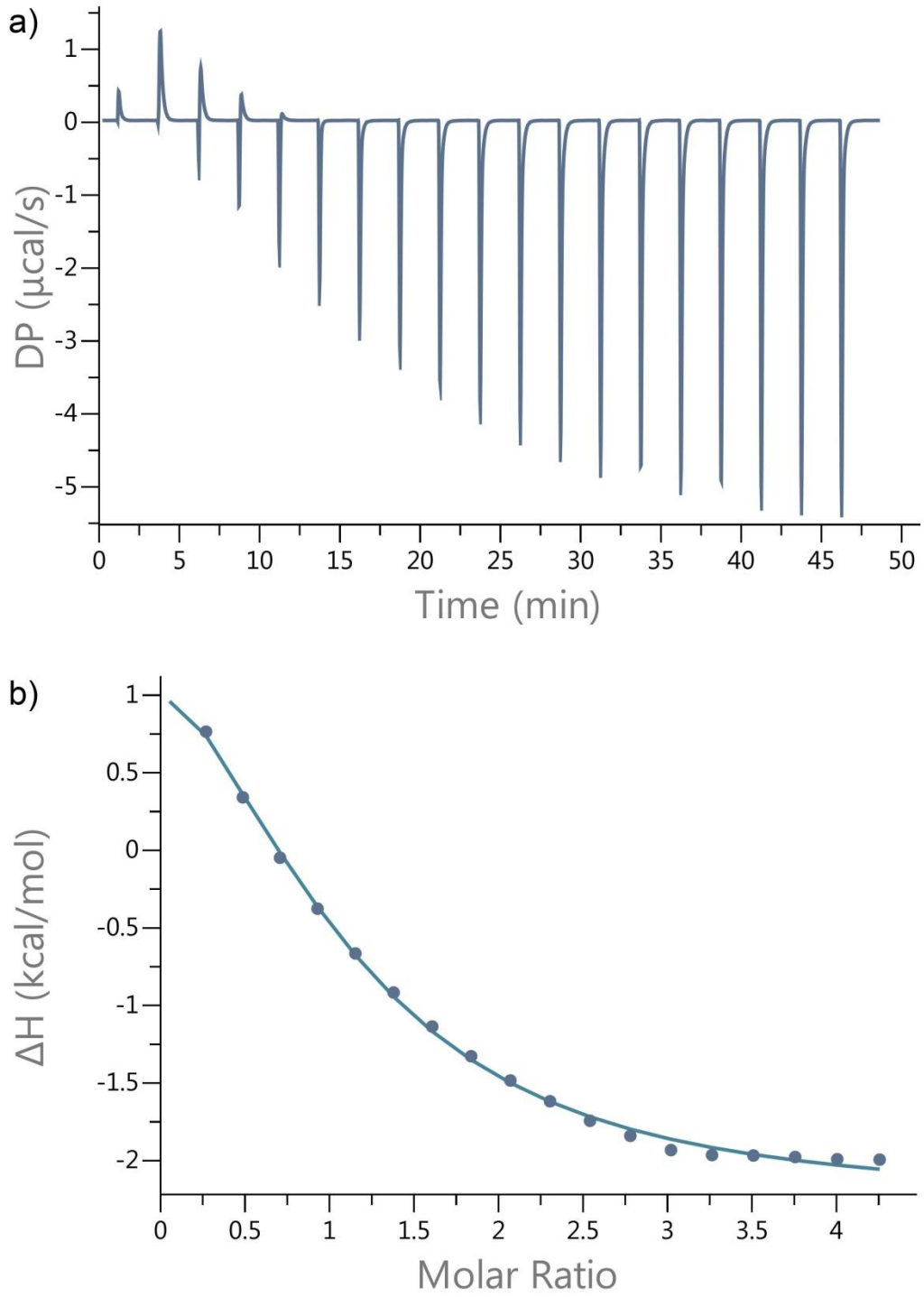

Figure III-S58. a) Plot of DP vs time from the titration of HP-β-CD (506 µM) and with guest fentanyl (11.2 mM) in 20 mM NaH_2PO_4 buffer (pH 7.4); b) plot of the ΔH as a function of molar ratio. The solid line represents the best non-linear fit of the data to a 1:1 binding model (K_a = (3.0 ± 0.5) x 10^3 M^{-1}, ΔH = 5.38 ± 0.58 kcal/mol, -TΔS = -10.1 kcal/mol).

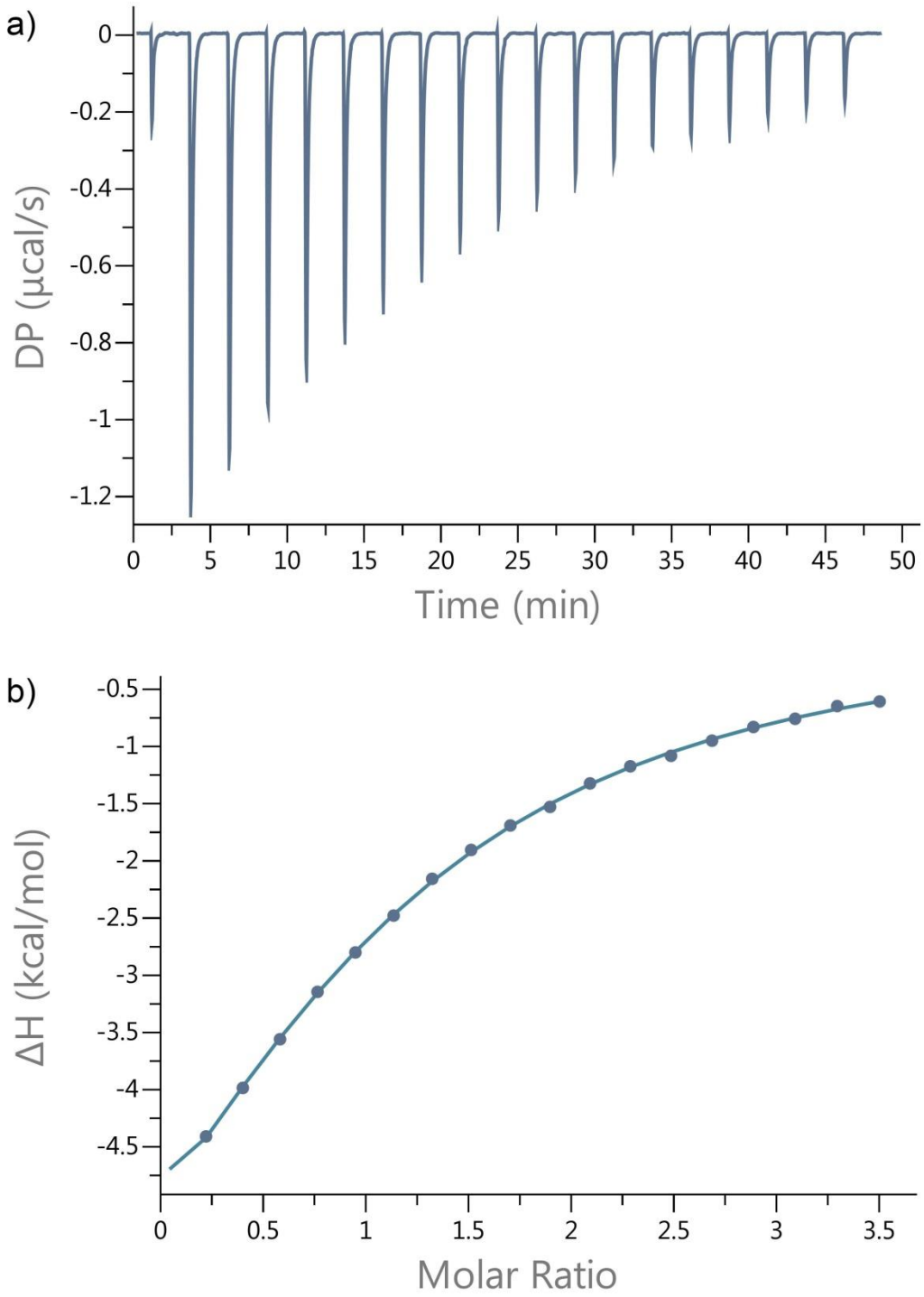

Figure III-S59. a) Plot of DP vs time from the titration of p-sulfo calix[4]arene (82.4 µM) and with guest fentanyl (1.50 mM) in 20 mM NaH_2PO_4 buffer (pH 7.4); b) plot of the ΔH as a function of molar ratio. The solid line represents the best non-linear fit of the data to a 1:1 binding model (K_a = (1.1 ± 0.1) x 10^4 M^{-1}, ΔH = - 9.99 ± 0.73 kcal/mol, -TΔS = -4.45 kcal/mol).

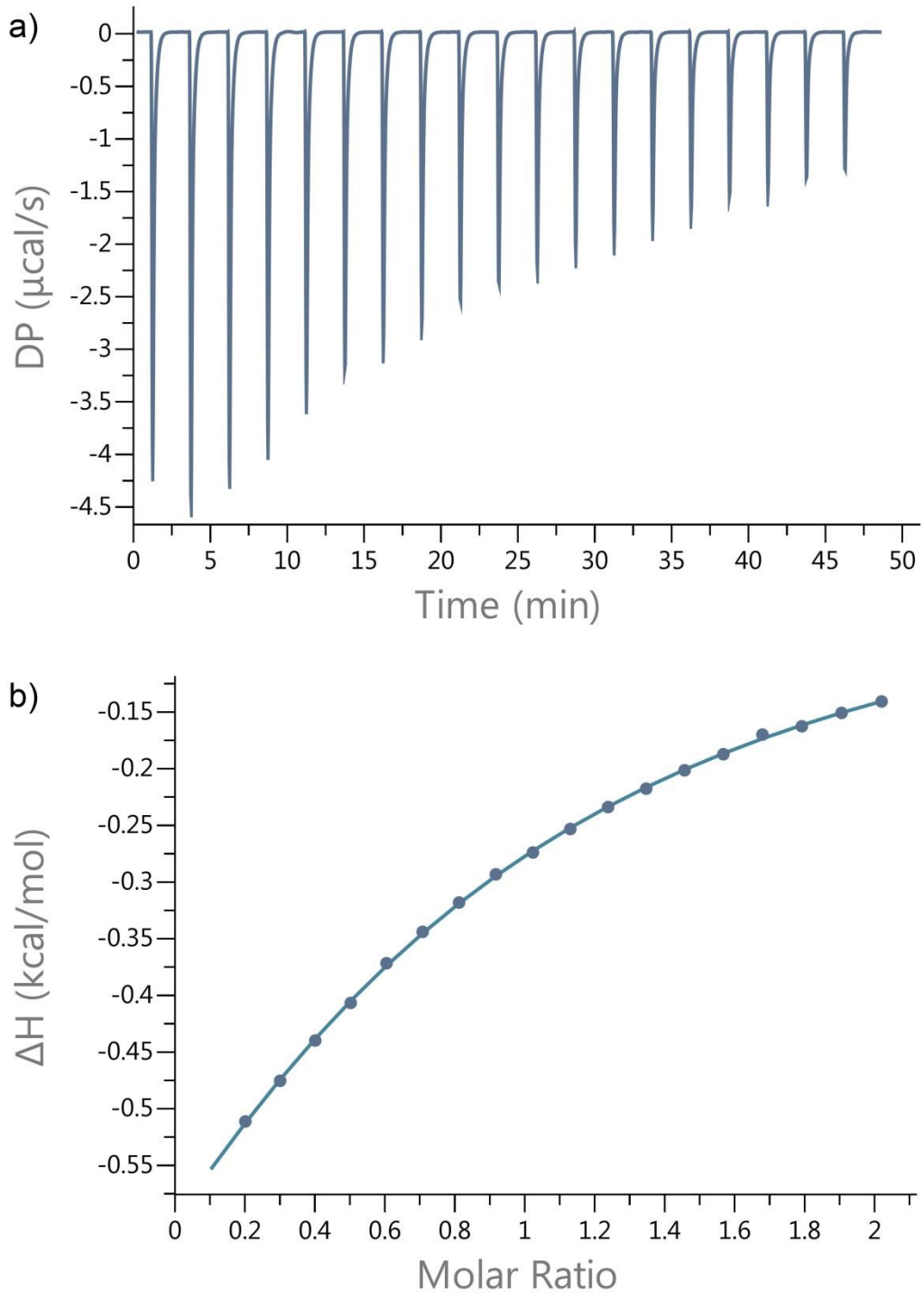

Figure III-S60. a) Plot of DP vs time from the titration of HP-β-CD(4.69 mM) and with guest cocaine (47.0 mM) in 20 mM NaH_2PO_4 buffer (pH 7.4); b) plot of the ΔH as a function of molar ratio. The solid line represents the best non-linear fit of the data to a 1:1 binding model (K_a = (1.7 ± 0.3) x 10^2 M^{-1}, ΔH = - 1.60 ± 0.32 kcal/mol, -TΔS = -1.43 kcal/mol).

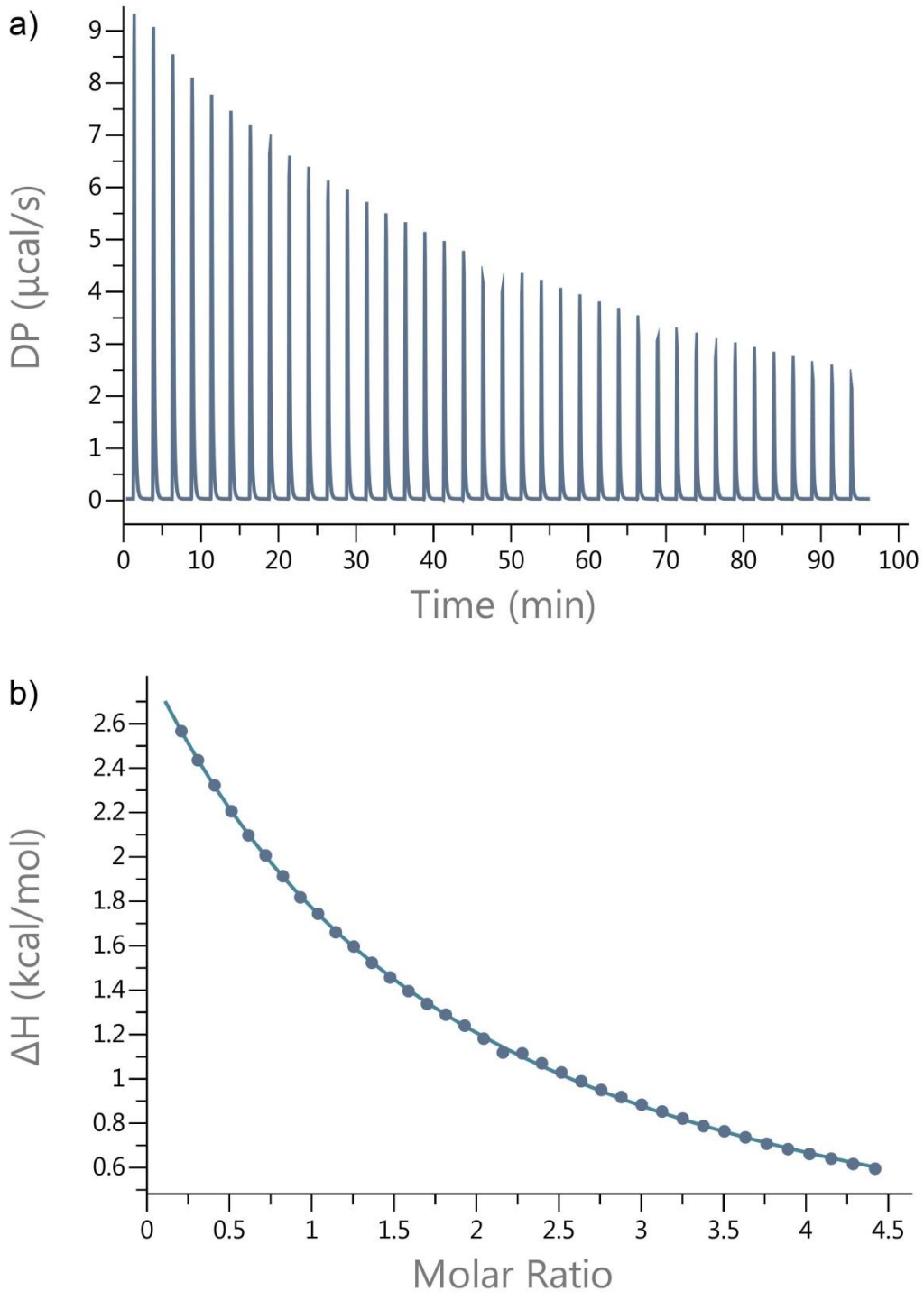

Figure III-S61. a) Plot of DP vs time from the titration of HP-β-CD (1.8 mM) and with guest ketamine (18.2 mM) in 20 mM NaH_2PO_4 buffer (pH 7.4); b) plot of the ΔH as a function of molar ratio. The solid line represents the best non-linear fit of the data to a 1:1 binding model (K_a = (1.1 ± 0.2) x 10^2 M^{-1}).

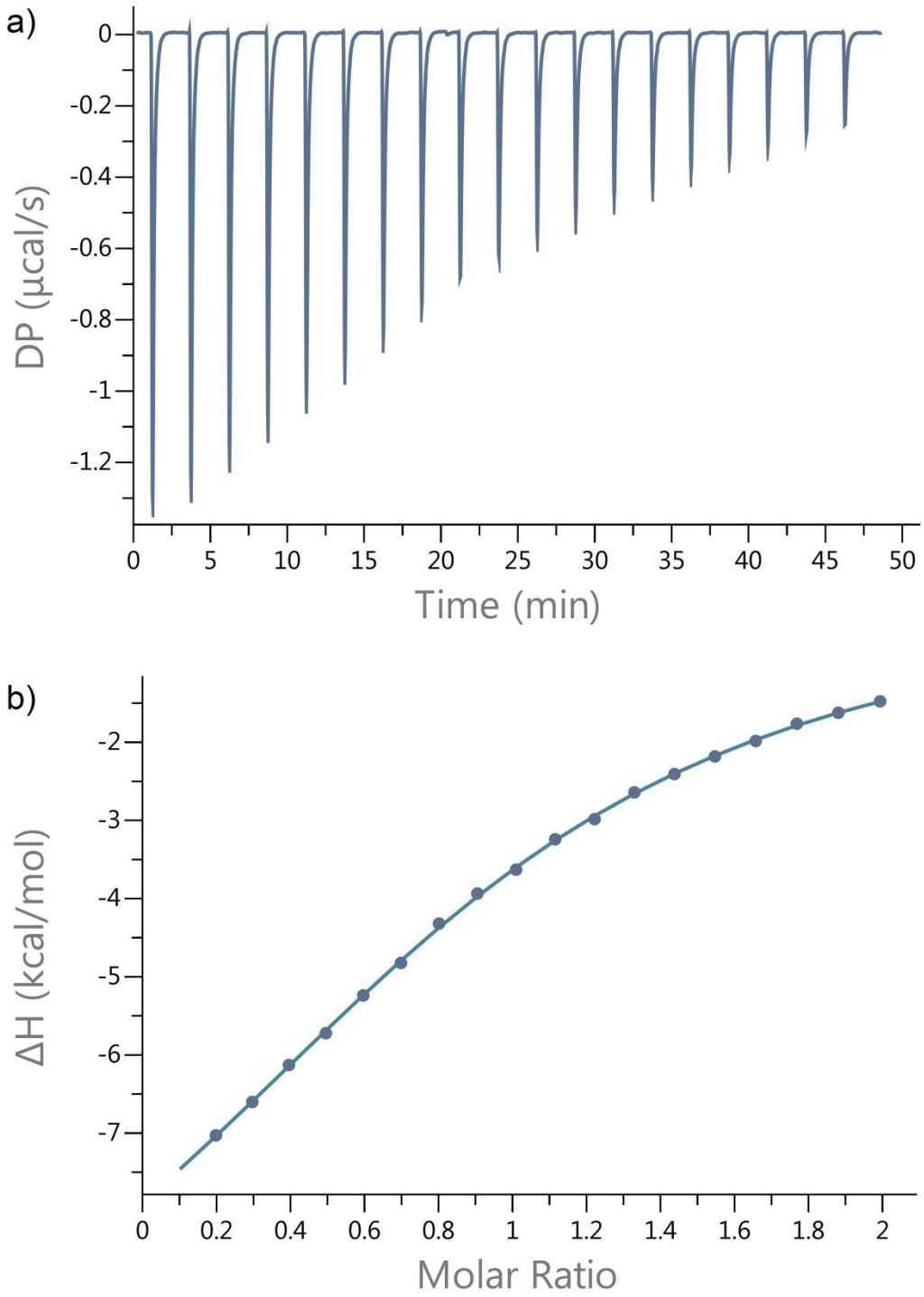

Figure III-S62. a) Plot of DP vs time from the titration of *p*-sulfo calix[4]arene (101 µM) and with guest ketamine (1.00 mM) in 20 mM NaH_2PO_4 buffer (pH 7.4); b) plot of the ΔH as a function of molar ratio. The solid line represents the best non-linear fit of the data to a 1:1 binding model (K_a = (2.0 ± 0.2)x 10^4 M^{-1}, ΔH = - 11.6 ± 0.58 kcal/mol, -TΔS = 5.75 kcal/mol).

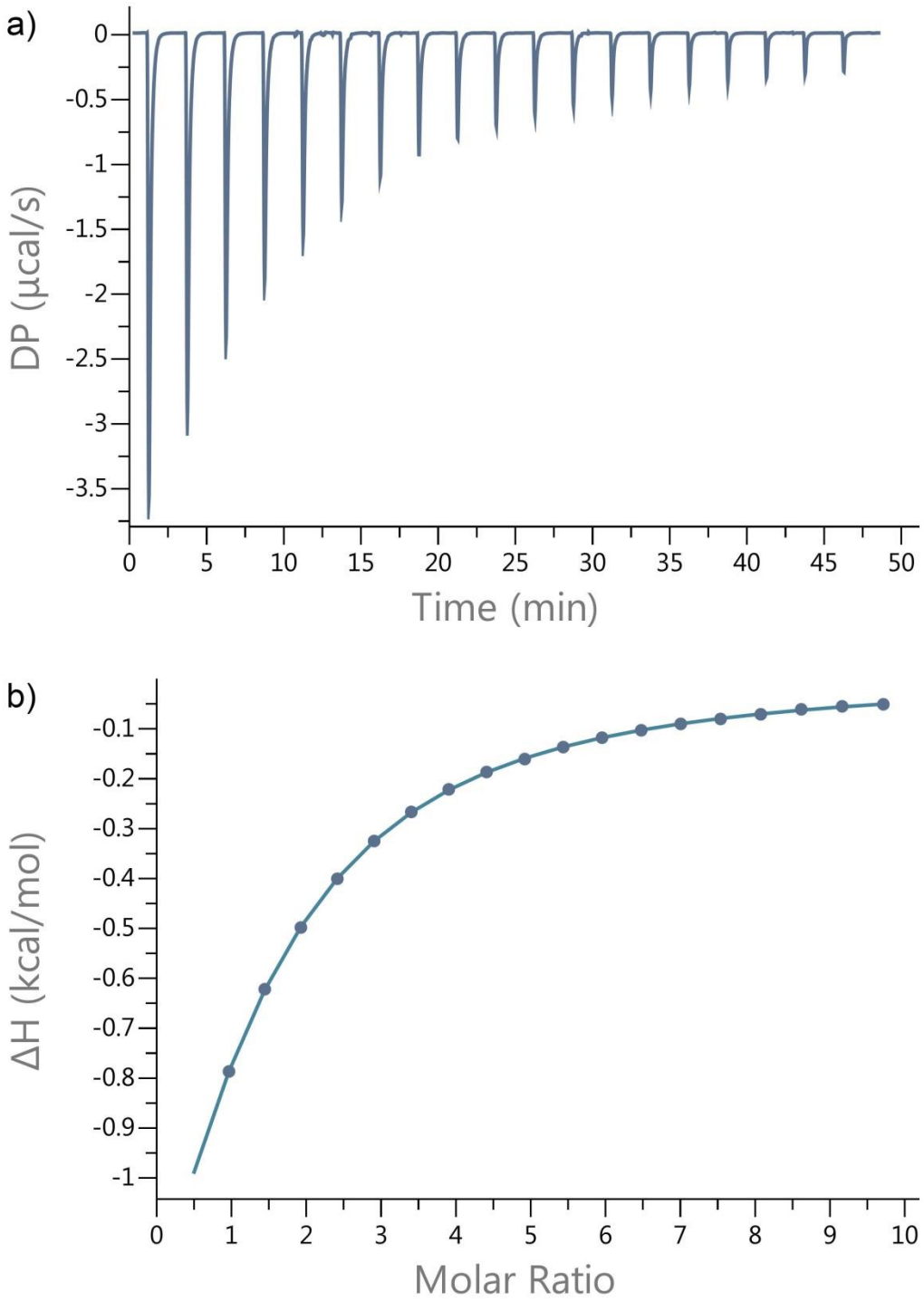

Figure III-S63. a) Plot of DP vs time from the titration of HP-β-CD (502 µM) and with guest phencyclidine (24.2 mM) in 20 mM NaH_2PO_4 buffer (pH 7.4); b) plot of the ΔH as a function of molar ratio. The solid line represents the best non-linear fit of the data to a 1:1 binding model (K_a = (1.0 ± 0.03) x 10^3 M^{-1}, ΔH = -3.22 ± 0.15 kcal/mol, -TΔS = -0.899 kcal/mol).

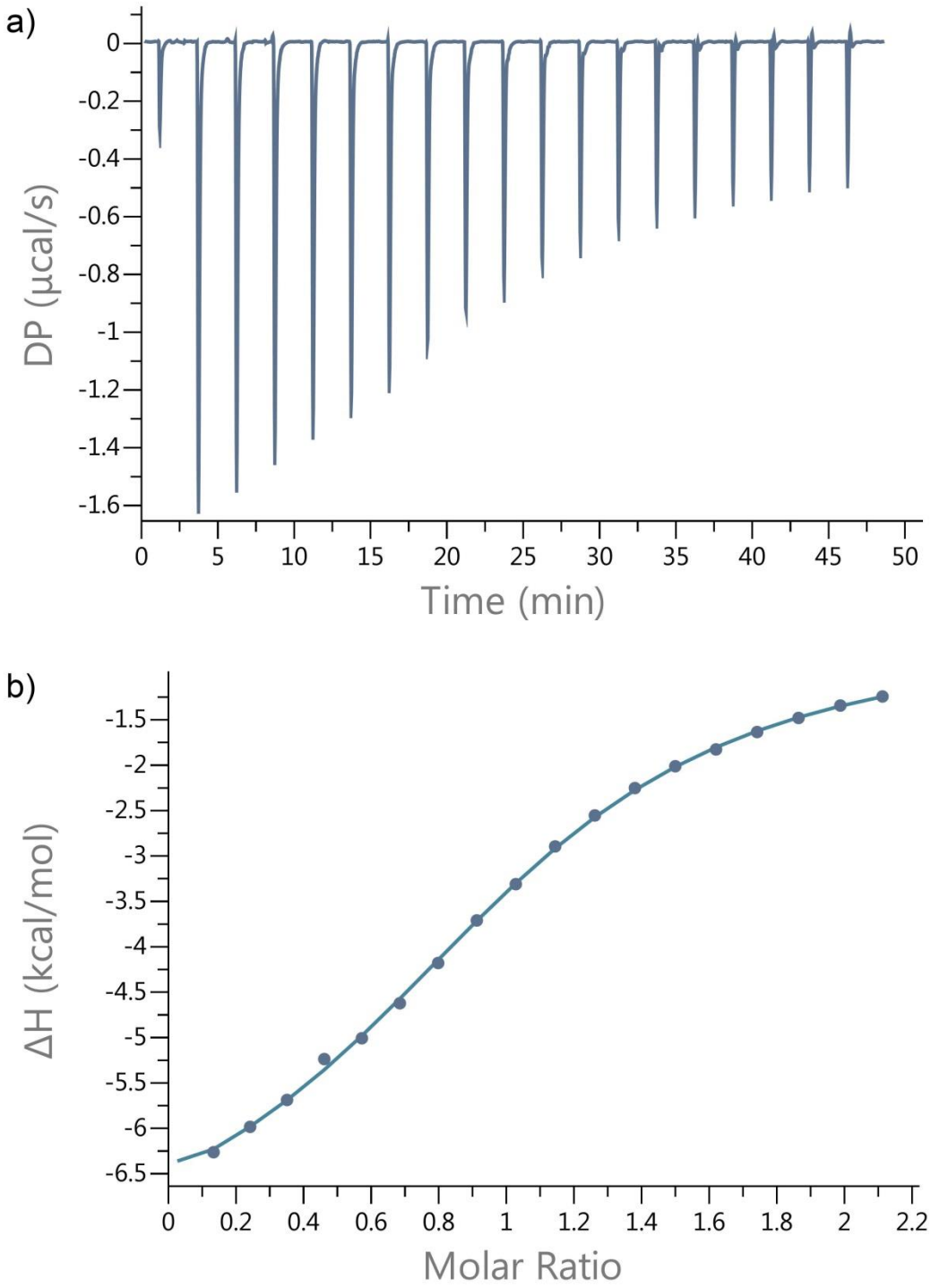

Figure III-S64. a) Plot of DP vs time from the titration of calix[4]arene (101 µM) and with guest phencyclidine (1.11 mM) in 20 mM NaH_2PO_4 buffer (pH 7.4); b) plot of the ΔH as a function of molar ratio. The solid line represents the best non-linear fit of the data to a 1:1 binding model (K_a = (4.5 ± 0.3) x 10^4 M^{-1}, ΔH = -7.07 ± 0.27 kcal/mol, -TΔS = 0.724 kcal/mol).

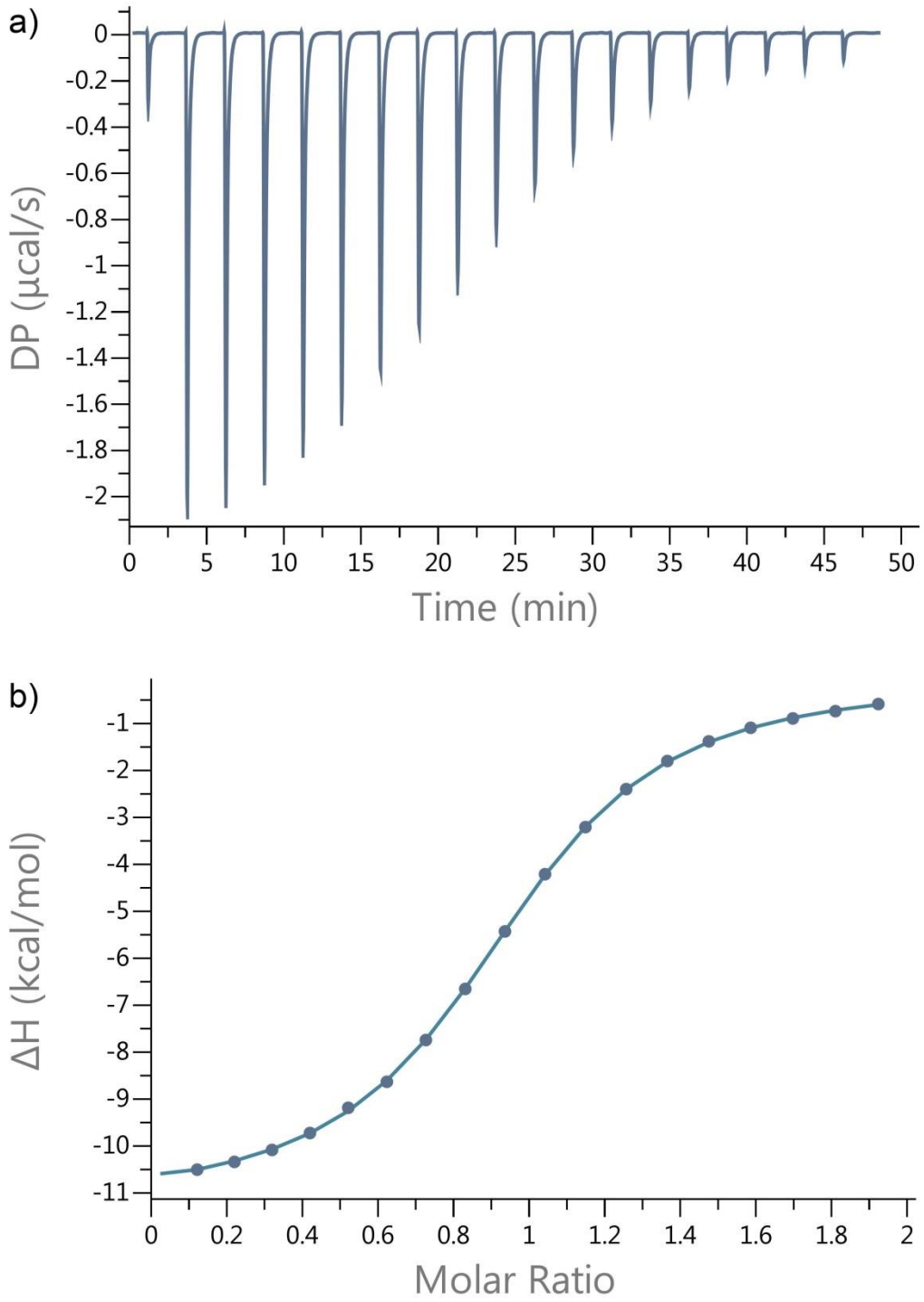

Figure III-S65. a) Plot of DP vs time from the titration of Calabadion 1 (100 µM) and with guest hydromorphone (1.00 mM) in 20 mM NaH_2PO_4 buffer (pH 7.4); b) plot of the ΔH as a function of molar ratio. The solid line represents the best non-linear fit of the data to a 1:1 binding model (K_a = (1.8 ± 0.03) x 10^5 M^{-1}, ΔH = -11.20 ± 0.04 kcal/mol, -TΔS = 3.99 kcal/mol).

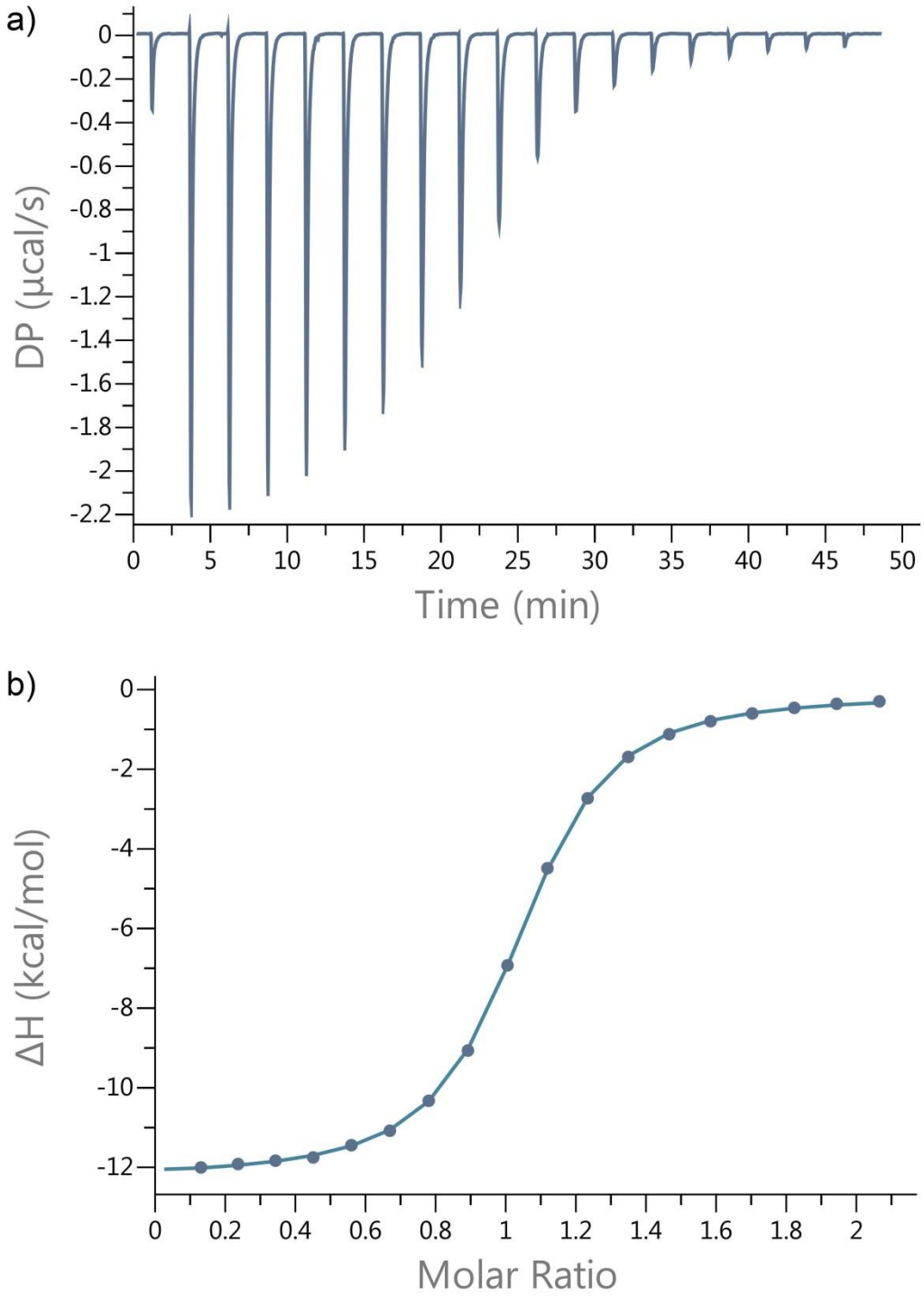

Figure III-S66. a) Plot of DP vs time from the titration of Calabadion 2 (87 µM) and with guest hydromorphone (0.934 mM) in 20 mM NaH_2PO_4 buffer (pH 7.4); b) plot of the ΔH as a function of molar ratio. The solid line represents the best non-linear fit of the data to a 1:1 binding model (K_a = (6.8 ± 0.1) x 10^5 M^{-1}, ΔH = - 12.1 ± 0.03 kcal/mol, -TΔS = 4.16 kcal/mol).

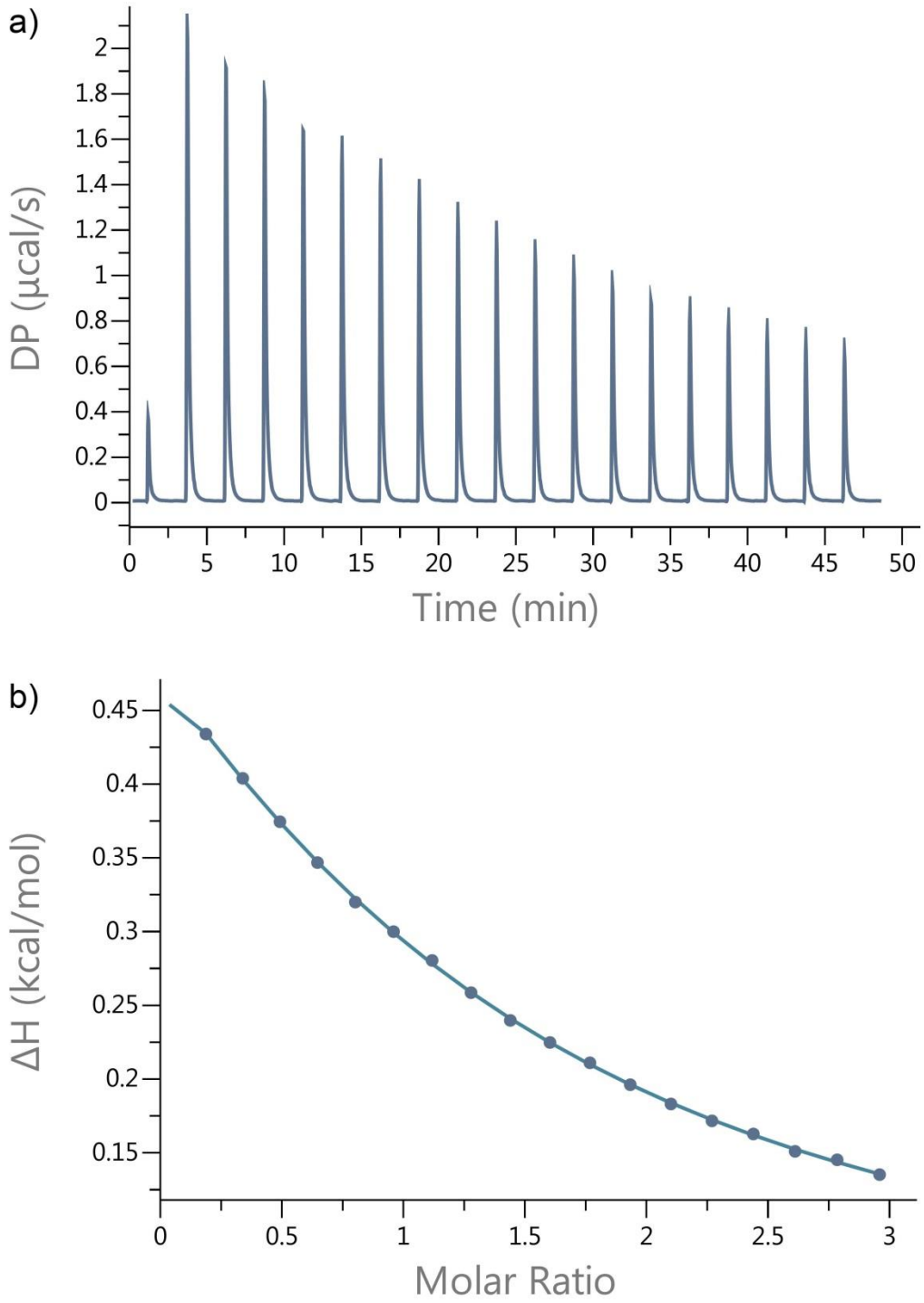

Figure III-S67. a) Plot of DP vs time from the titration of HP-β-CD (1.7 mM) and with guest hydromorphone (26.2 mM) in 20 mM NaH_2PO_4 buffer (pH 7.4); b) plot of the ΔH as a function of molar ratio. The solid line represents the best non-linear fit of the data to a 1:1 binding model (K_a = (2.8 ± 0.5) x 10^2 M^{-1}, ΔH = 1.35 ± 0.27 kcal/mol, -TΔS = -4.68 kcal/mol).

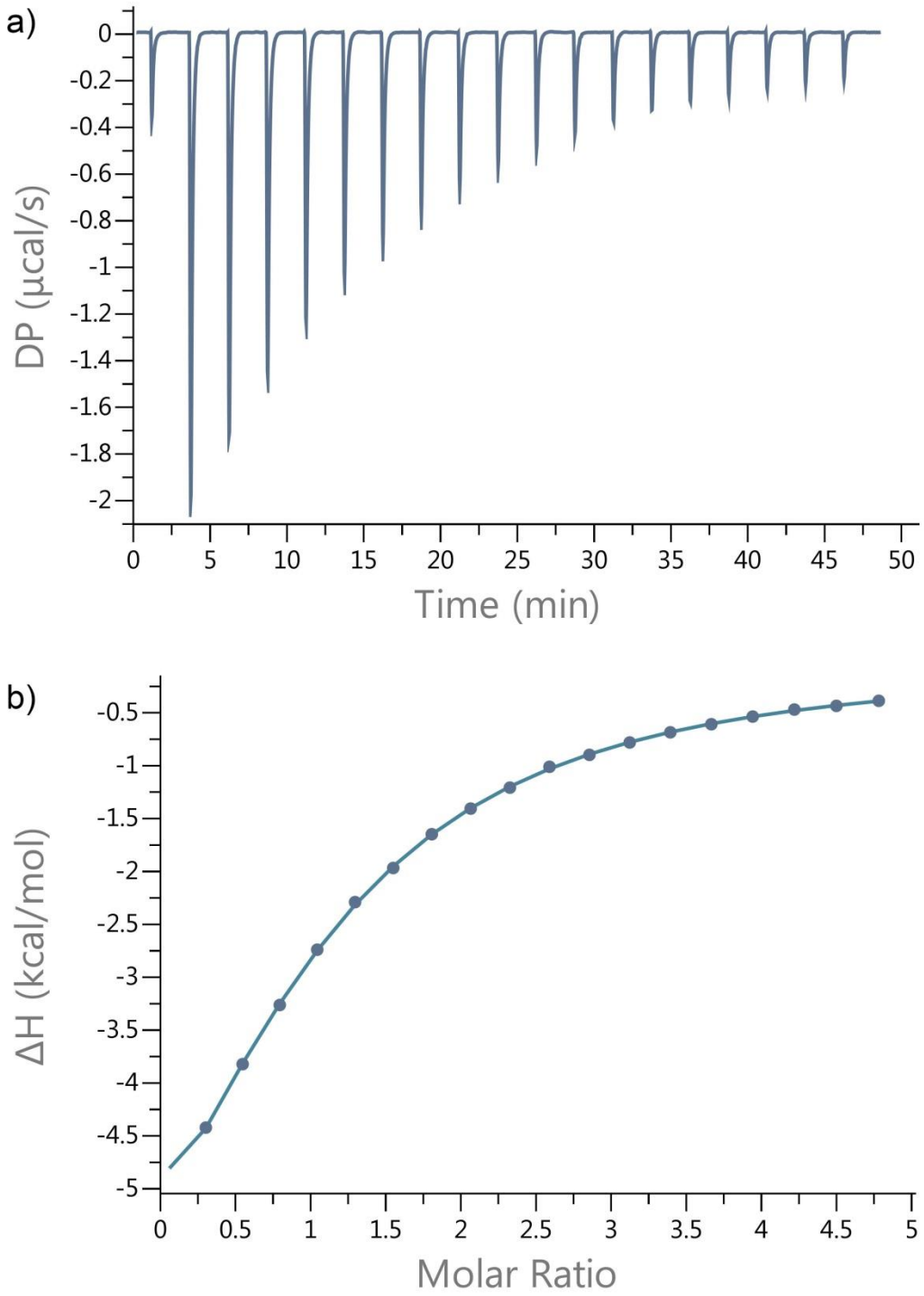

Figure III-S68. a) Plot of DP vs time from the titration of *p*-sulfo calix[4]arene (101 µM) and with guest hydromorphone (2.51 mM) in 20 mM NaH_2PO_4 buffer (pH 7.4); b) plot of the ΔH as a function of molar ratio. The solid line represents the best non-linear fit of the data to a 1:1 binding model (K_a = (1.0 ± 0.04) x 10^4 M^{-1}, ΔH = -9.52 ± 0.33 kcal/mol, -TΔS = 4.04 kcal/mol).

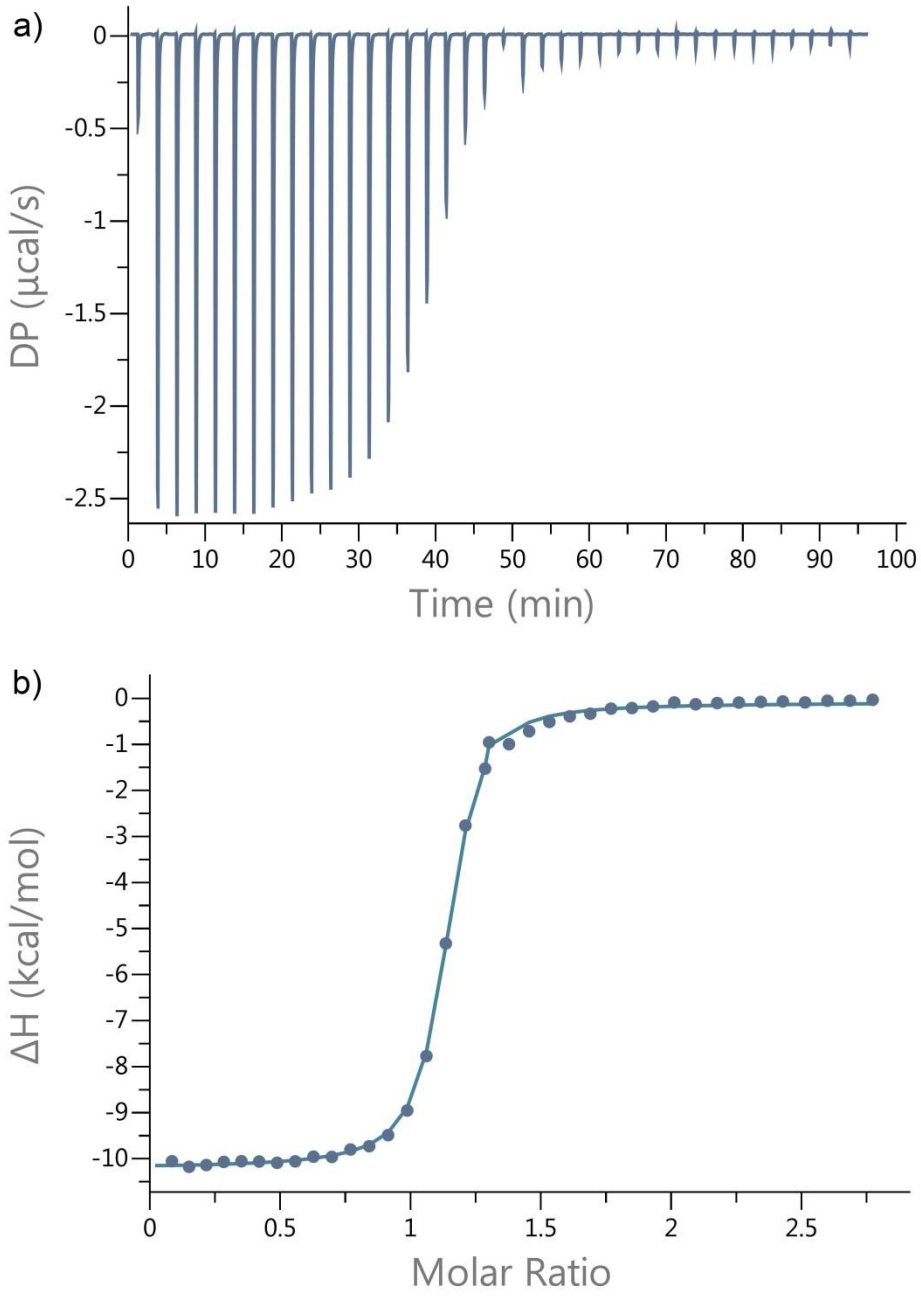

Figure III-S69. a) Plot of DP vs time from the titration of Calabadion 2 (150 µM) and with guest methamphetamine (1.0 mM) in 20 mM NaH_2PO_4 buffer (pH 7.4); b) plot of the ΔH as a function of molar ratio. The solid line represents the best non-linear fit of the data to a 1:1 binding model (K_a = (2.0 ± 0.1) x 10^6 M^{-1}, ΔH = - 10.0 ± 0.04 kcal/mol, -TΔS = 1.45 kcal/mol).

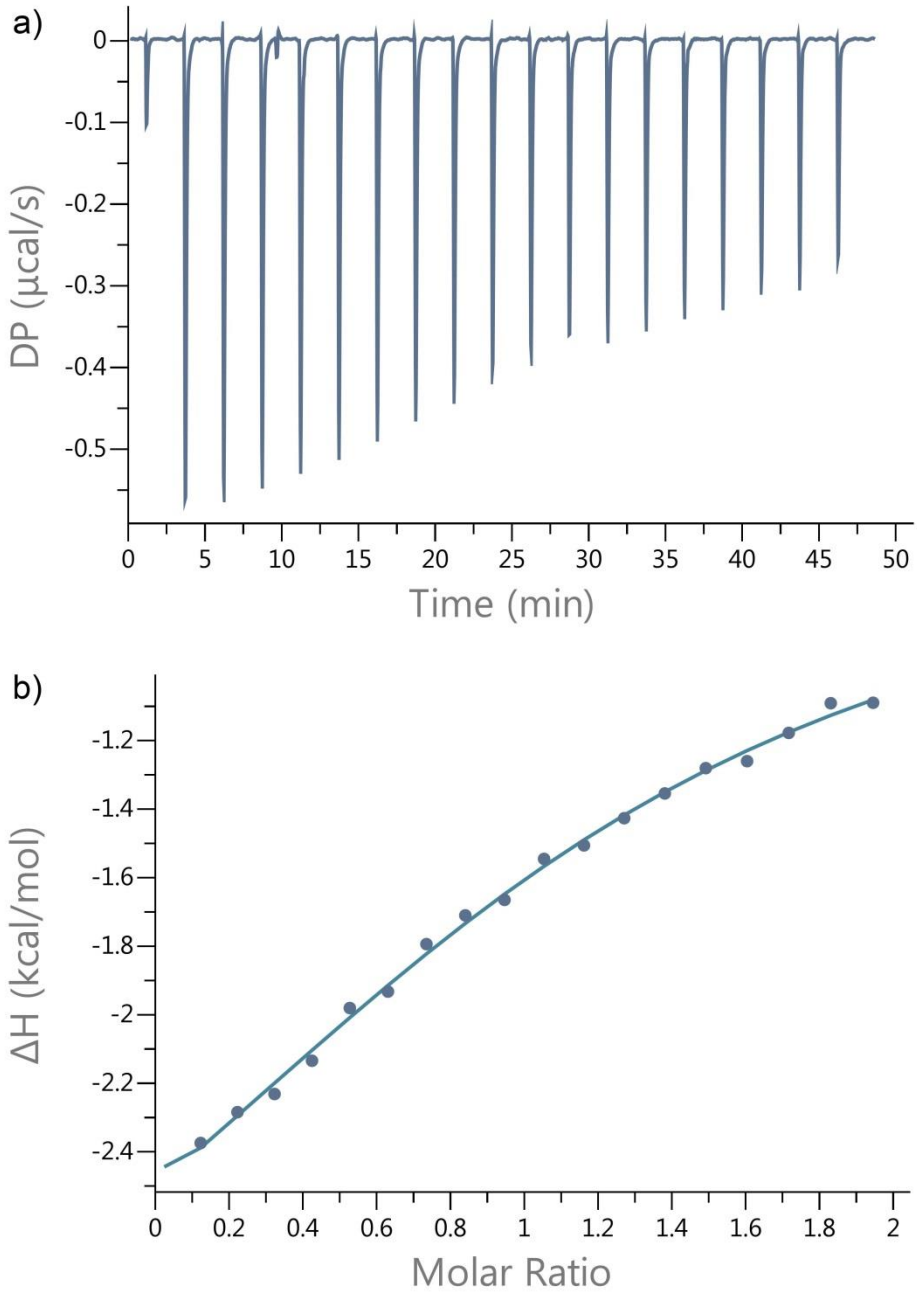

Figure III-S70. a) Plot of DP vs time from the titration of *p*-sulfo calix[4]arene (98.9 µM) and with guest methamphetamine (1.0 mM) in 20 mM NaH_2PO_4 buffer (pH 7.4); b) plot of the ΔH as a function of molar ratio. The solid line represents the best non-linear fit of the data to a 1:1 binding model (K_a = (1.3 ± 0.6) x 10^4 M^{-1}, ΔH = - 3.16 ± 0.84 kcal/mol, -TΔS = -2.45 kcal/mol).

Job plots of selected hosts with methamphetamine showing 1:1 binding.

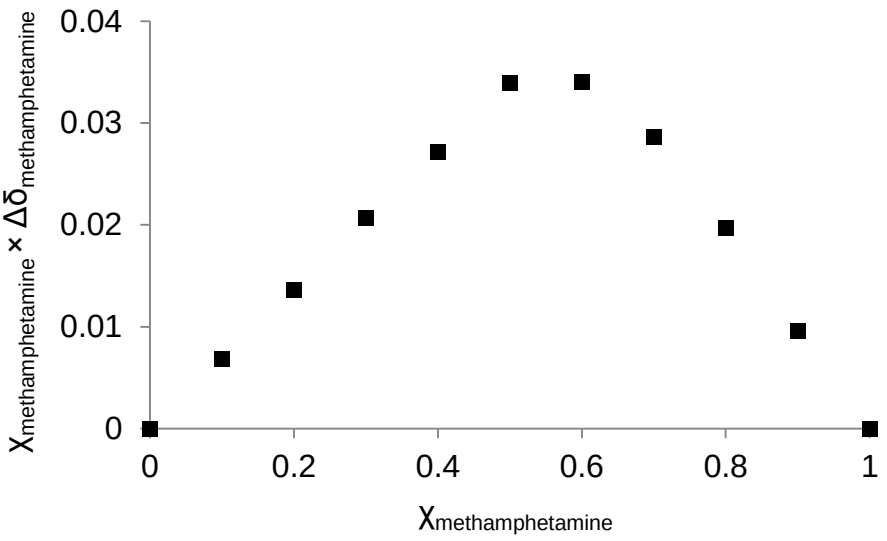

Figure III-S71. Job plot establishing 1:1 binding of methamphetamine (0-10 mM) with Calabadion 1 (0-10 mm) based on change in ^{1}H NMR chemical shift of methyl resonance of methamphetamine at 2.69 ppm (400 MHz, D_2O).

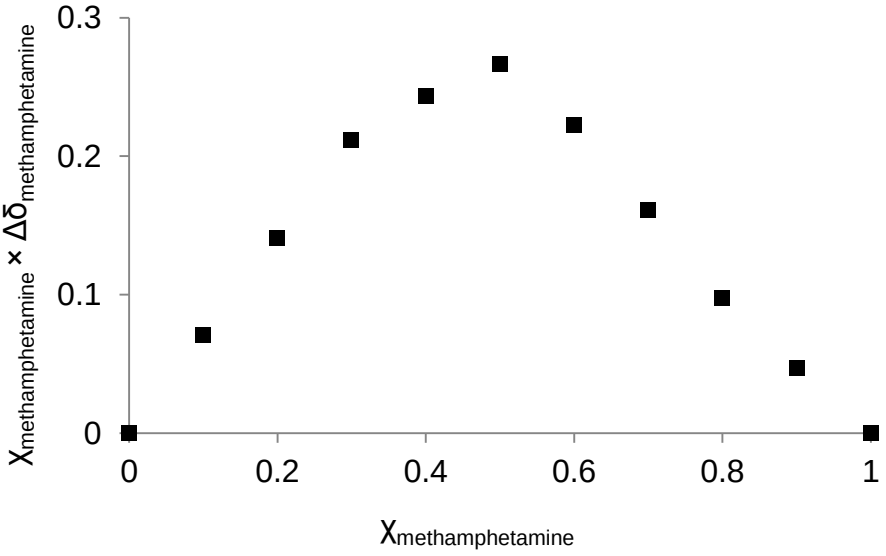

Figure III-S72. Job plot establishing 1:1 binding of methamphetamine (0-10 mM) with Calabadion 2 (0-10 mm) based on change in ^{1}H NMR chemical shift of methyl resonance of methamphetamine at 1.27 ppm (400 MHz, D_2O).

Details of the *in vivo* experiments.

Care and Use of Animals.

All experiments involving rats (21 male Sprague-Dawley rats, weight, mean ± SD: 288 ± 14 g) were conducted after approval was obtained from the Subcommittee on Research Animal Care at Massachusetts General Hospital, Boston, MA (Protocol 2011N00181). Experiments were conducted at the research laboratories of the Massachusetts General Hospital, Boston, Massachusetts. All institutional guidelines for animal care and usage for research purposes were followed.

General surgical procedures.

All animals were anesthetized (5% isoflurane for inducation; 1.5% isoflurane for maintenance in 70% N_2O/ 30% O_2) for placement of a tail vein intravenous catheter (24 gauge; 19 mm). Rectal temperature was kept stable/ steady at 37.0±0.1°C using a thermostatic heating pad (FHC, Bowdoinham, ME). After placement of the catheter the isoflurane anesthesia was stopped and 30 minutes were given to the animal to regain full consciousness. The venous catheter was removed after completion of the injections prior to any behavioral testing. All animals were tested repeatedly with 72h of break to allow recreation between the experiments.

Behavioral Testing

All animals were placed within one minute after the last injection in the center of a 100 cm × 100 cm × 40 cm open field for a total time of 20 minutes. The rat's

activity in the open field was videotaped while it was left undisturbed in the testing room.

The primary endpoint, total distance traveled in the open field, was quantified using the video tracking software ANY-maze (version 4.5, Stoelting, Wood Dale, IL, USA).

Statistical Analysis

Values are given in percent of the placebo + methamphetamine activity level and reported as mean ± standard error of the mean unless otherwise specified. Statistical analysis was performed using SPSS 22.0 (SPSS Inc. Chicago, IL).

To evaluate the effect of the testing drugs on locomotor activity, we built multiple mixed linear models (MLM) with an identity link function for normally distributed probability and defined the intercept as random effects.

Using the previously described MLM, we tested for a fixed main effect of placebo + methamphetamine vs. baseline on locomotor activity to evaluate if methamphetamine induces hyperlocomotion.

The testing drug's ability to reverse methamphetamine induced hyperlocomotion at different doses was determined by testing the fixed main effect of high dose + methamphetamine vs. placebo + methamphetamine and low dose + methamphetamine vs. placebo + methamphetamine on locomotor activity, respectively.

In order to ensure that the testing compound itself does not interfere with the outcome, we assessed the sole effect of the testing compound at the higher dose on locomotion and compared it to the baseline.

To evaluate if Calabadion 2's reversal effect is modified by the time of administration (indication) we used the same MLM as previously described and tested for the fixed interaction effect of indication and Calabadion 2 dose ("prevention/treatment" x "Calabadion 2 dose").

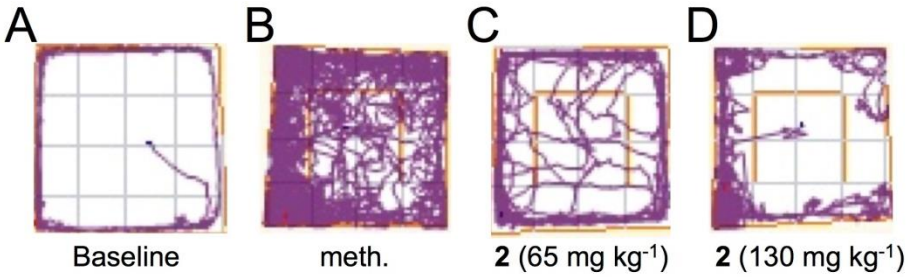

Figure III-S73. Tracking plots illustrating the traveled distance of one rat within 20 minutes in the open field: A) Baseline, no methamphetamine given, B) Following methamphetamine (0.3 mg kg^{-1}) + placebo, C) Following methamphetamine (0.3 mg kg^{-1}) + Calabadion 2 (65 mg kg^{-1}), and D) Following methamphetamine (0.3 mg kg^{-1}) + Calabadion 2 (130 mg kg^{-1}). Calabadion dose-dependently ameliorated methamphetamine–induced hyperlocomotion.

Appendix 3

Synthesis and Molecular Recognition Properties of Acyclic Cucurbit[n]urils with Alkyl Linkers

Shweta Ganapati,[a] *and Lyle Isaacs**[a]

[a]Department of Chemistry and Biochemistry, University of Maryland, College Park, MD 20742

Supporting Information

Table of Contents **Pages**

General experimental details 249

Synthetic procedures and characterization data 250-276

^{1}H NMR stack plots for the interaction between various hosts and guests 277-296

ITC data for K_a determination for various guests and hosts 297-317

General Experimental Details. Starting materials were purchased from commercial suppliers and were used without further purification or were prepared by literature procedures. Compound **1** and **5** were prepared according to literature procedures.[40] The synthesis of **IV-3a**, **IV-3b**, and **IV-3c** from dibromoalkanes and hydroquinone were performed by procedures similar to those reported in the literature.[106,107] The characterization data matches the reported data.

Melting points were measured on a Meltemp apparatus in open capillary tubes and are uncorrected. IR spectra were measured on a JASCO FT/IR 4100 spectrometer and are reported in cm^{-1}. NMR spectra were measured on Bruker spectrometers operating at 400 or 600 MHz for ^{1}H and 200 MHz for ^{13}C NMR. ITC data was collected on a Malvern Microcal PEAQ-ITC instrument. Mass spectrometry was performed using a JEOL AccuTOF electrospray instrument (ESI).

Synthetic Procedures and Characterization Data.

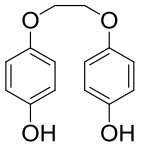

Compound IV-3a. A mixture of hydroquinone (17.55 g, 159 mmol) and potassium carbonate (44.00 g, 318 mmol) in acetonitrile (123 mL) was heated to 85 °C under N_2. 1,2-dibromoethane (3.0 g, 1.4 mL, 15.9 mmol) was added dropwise and the reaction was stirred for 12 h. The reaction mixture was cooled and filtered and the filtrate was evaporated under reduced pressure to obtain the crude solid product. This crude product was washed with water (375 mL) and recrystallized from ethanol (75 mL) to obtain **IV-3a** as an off white solid (0.51 g, 2.1 mmol, 13%). M.p. = 212-214 °C. IR (ATR, cm^{-1}): 3365w(br), 2943 w, 1512s, 1452m, 1373w, 1268w, 1211s, 1109 m, 1081w, 1070m, 1011w, 954s, 943w, 831s, 813m, 756s. ^{1}H NMR (600 MHz, DMSO): 8.91 (s, 2H), 6.78 (d, *J* = 8.9, 4H), 6.67 (d, *J* = 8.9, 4H), 4.14 (s, 4H). ^{13}C NMR (150 MHz, DMSO, 1,4-dioxane as internal reference): δ 151.4, 151.2, 115.8, 115.5, 67.0. High-Res MS (ESI): *m/z* 245.0825 ($[M - H]^-$), calculated for $C_{14}H_{13}O_4^-$ 245.0814.

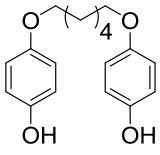

Compound IV-3b. A mixture of hydroquinone (27.10 g, 246 mmol) and potassium carbonate (68.00 g, 492 mmol) in acetonitrile (190 mL) was heated to 85 °C under N_2. 1,6-dibromohexane (6.0 g, 3.8 mL, 24.6 mmol) was added dropwise and the reaction was stirred for 12 h. The reaction mixture was cooled and filtered and the filtrate was evaporated under reduced pressure to obtain the crude solid product. This crude product was washed with water (500 mL) and recrystallized from ethanol (100 mL) to obtain

IV-3b as an off white solid (3.66 g, 12.3 mmol, 50%). M.p. = 178-180 °C. IR (ATR, cm^{-1}): 3381w(br), 2944w, 2866w, 1506s, 1477m, 1452m, 1395w, 1374m, 1299m, 1221s, 1167m, 1104s, 1072w, 1022s, 826s, 806m, 763s, 732m. ^{1}H NMR (600 MHz, DMSO): 8.85 (s, 2H), 6.72 (d, *J* = 8.9, 4H), 6.65 (d, *J* = 8.9, 4H), 3.84 (t, *J* = 6.5, 4H), 1.72-1.63 (m, 4H), 1.48-1.38 (m, 4H). ^{13}C NMR (150 MHz, DMSO): δ 151.5, 151.1, 115.7, 115.3, 67.8, 28.8, 25.4. High-Res MS (ESI): *m/z* 301.1443 ($[M - H]^-$), calculated for $C_{18}H_{21}O_4^-$ 301.1440.

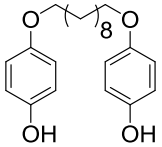

Compound IV-3c. A mixture of hydroquinone (11.00 g, 100 mmol) and potassium carbonate (27.64 g, 200 mmol) in acetonitrile (160 mL) was heated to 85 °C under N_2. 1,10-dibromodecane (3 g, 2.2 mL, 10 mmol) was added dropwise and the reaction was stirred for 12 h. The reaction mixture was cooled and filtered and the filtrate was evaporated under reduced pressure to obtain the crude solid product. This crude product was washed with water (500 mL) and recrystallized from ethanol (75 mL) to obtain **IV-3c** as an off white solid (1.18 g, 3.3 mmol, 33%). M.p. = 146-148 °C. IR (ATR, cm^{-1}): 3420w(br), 2931w, 2917w, 2852w, 1509m, 1473w, 1451w, 1395w, 1371w, 1299w, 1227s, 1168w, 1104w, 1048w, 822s, 767s. ^{1}H NMR (600 MHz, DMSO): 8.84 (s, 2H), 6.72 (d, *J* = 8.9, 4H), 6.65 (d, *J* = 8.9, 4H), 3.82 (t, *J* = 6.5, 4H), 1.64 (p, *J* = 7.0, 4H), 1.41-1.34 (m, 4H), 1.34-1.22 (m, 8H). ^{13}C NMR (150 MHz, DMSO, 1, 4-dioxane as internal reference): δ 151.5, 151.0, 115.6, 115.3, 67.8, 28.9, 28.8, 28.7, 25.5. High-Res MS (ESI): *m/z* 357.2080 ($[M - H]^+$), calculated for $C_{22}H_{29}O_4^-$ 357.2066.

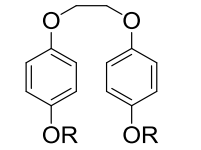

R = $(CH_2)_3SO_3Na$

Compound IV-4a. A solution of 1,3-propanesultone (1.34 g, 11 mmol) in 1,4-dioxane (11 mL) was added to a solution of **IV-3a** (1.2 g, 4.1 mmol) in aqueous sodium hydroxide solution (10 wt%, 9 mL). This mixture was stirred at RT for 12 h and then filtered to collect the crude solid. The crude product was washed with acetone (30 mL). The filtered solid was dissolved in hot water (15 mL) and precipitated with ethanol (30 mL) to obtain the off white solid **IV-4a** (1.91 g, 3.6 mmol, 87%). M.p. > 300 °C. IR (ATR, cm^{-1}): 3422w(br), 2942w, 2520w, 1512s, 1450w, 1285w, 1201s, 1053s, 943m, 758m, 734m. ^1H NMR (600 MHz, D_2O): 7.06-7.04 (m, 4H), 7.04-7.02 (m, 4H), 4.37 (s, 4H), 4.18 (t, *J* = 6.3, 4H), 3.13-3.09 (m, 4H), 2.25-2.18 (m, 4H). ^{13}C NMR (150 MHz, D_2O, 1, 4-dioxane as internal reference): δ 152.3, 151.9, 115.9, 115.8, 67.0, 66.7, 47.3, 23.8. High-Res MS (ESI): *m/z* 489.0882 ($[M - 2Na + H]^-$), calculated for $C_{20}H_{25}O_{10}S_2^-$ 489.0889.

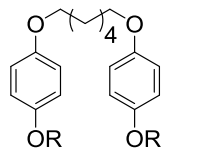

R = $(CH_2)_3SO_3Na$

Compound IV-4b. A solution of 1,3-propanesultone (7.7 g, 63 mmol) in tetrahydrofuran (152 mL) was added to a solution of **IV-3b** (7.6 g, 25.2 mmol) in aqueous sodium hydroxide solution (10 wt%, 76 mL). This mixture was stirred at RT for 12 h and then filtered to collect the crude solid. The crude product was washed with acetone (200 mL). The filtered solid was dissolved in hot water (100 mL) and precipitated with ethanol (200 mL) to obtain the off white solid **IV-4b** (11.5 g, 9.4 mmol, 77%). M.p. > 300 °C. IR (ATR, cm^{-1}): 2941w, 2905w, 2870w, 1508s, 1475m, 1399w, 1289w, 1220s, 1188s, 1170s, 1115m, 1050s, 1031s, 830s, 805m, 767s, 755m,

734m. ^{1}H NMR (600 MHz, D_2O): 7.03-7.00 (m, 4H), 7.00-6.98 (m, 4H), 4.16 (t, *J* = 6.3, 4H), 4.07 (t, *J* = 6.5, 4H), 3.13-3.07 (m, 4H), 2.24-2.16 (m, 4H), 1.82-1.75 (m, 4H), 1.54-1.50 (m, 4H). ^{13}C NMR (150 MHz, DMSO, 1,4-dioxane as internal reference): δ 152.6, 115.3, 115.3, 67.8, 67.1, 48.0, 28.8, 25.4. High-Res MS (ESI): m/z 545.1519 ([M - 2Na +H]$^-$), calculated for $C_{24}H_{33}O_{10}S_2^-$ 545.1515.

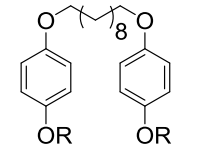

R = $(CH_2)_3SO_3Na$

Compound IV-4c. A solution of 1,3-propanesultone (1.00 g, 8.25 mmol) in tetrahydrofuran (20 mL) was added to a solution of **IV-3c** (1.2 g, 3.3 mmol) in aqueous sodium hydroxide solution (10 wt%, 10 mL). This mixture was stirred at RT for 12 h and then filtered to collect the crude solid. The crude product was washed with acetone (30 mL). The filtered solid was dissolved in hot water (15 mL) and precipitated with ethanol (30 mL) to obtain the off white solid **IV-4c** (1.0 g, 1.6 mmol, 47%). M.p. > 300 °C. IR (ATR, cm^{-1}): 2935w, 2924w, 2853w, 1508s, 1475m, 1396w, 1289w, 1217s, 1115w, 1046s, 1029s, 827s, 768m, 731m. ^{1}H NMR (600 MHz, DMSO, 1, 4-dioxane as internal reference): 7.02-7.00 (m, 4H), 7.00-6.98(m, 4H), 4.14 (t, *J* = 6.3, 4H), 4.05 (t, *J* = 6.5 4H), 3.11-3.07 (m, 4H), 2.23-2.16 (m, 4H), 1.74 (p, *J* = 6.9, 4H), 1.44 (p *J* = 7.3, 4H), 1.39-1.30 (m, 8H). ^{13}C NMR (150 MHz, DMSO, 1, 4-dioxane as internal reference): δ 152.6, 152.6, 115.3, 115.2, 67.8, 67.1, 48.0, 29.0, 28.9, 28.8, 25.5, 25.4. High-Res MS (ESI): m/z 601.2131 ([M - 2Na +H]$^-$), calculated for $C_{28}H_{40}NaO_{10}S_2^-$ 601.2141.

Compound IV-2a. Compound **IV-4a** (1.8 g, 3.4 mmol) was added to a solution of **IV-5** (1.3 g, 1.7 mmol) in a mixture of trifluoroacetic acid (130

mL) and acetic anhydride (130 mL). This solution was stirred and heated at 70 °C for 3 h. The reaction mixture was cooled to room temperature, treated with methanol (130 mL), and the solvent was removed under reduced pressure to obtain the crude product. The crude product was washed three times with a mixture of water (50 mL) and acetone (100 mL). The dark orange colored solid obtained was loaded onto a Dowex® 1X2 chloride form, 200-400 mesh ion exchange resin (50 g). The column was eluted with increasing concentrations of hydrochloric acid (HCl) starting from plain water (750 mL) to 6M HCl (750 mL) to 12 M HCl (300 mL). The eluted fractions were analyzed by ^{1}H NMR and the almost pure compound **IV-2a** was obtained in the fractions eluted with 12 M HCl. This fraction was dried under reduced pressure and washed with a mixture of water and methanol (1:1, v/v, 100 mL). Finally, the solid obtained was dissolved in water and the pH of the solution was adjusted to 7 using aqueous sodium hydroxide (1M). The solvent was removed under reduced pressure and the solid was further dried under high vacuum to obtain pure **IV-2a** as a light orange solid (0.72 g, 0.56 mmol, 33%). M.p. > 300 °C. IR (ATR, cm^{-1}): 3447w (br), 1712s, 1466s, 1422m, 1377m, 1317s, 1228s, 1182s, 1084m, 1036s, 974m, 926w, 794s, 760s, 731m. ^{1}H NMR (600 MHz, D_2O): 7.17 (d, *J* = 9.0, 2H), 7.05 (d, *J* = 9.0, 2H), 5.63 (d, *J* = 15.5, 2H), 5.54 (d, *J* = 15.5, 2H), 5.50 - 5.42 (m, 8H), 5.26 (d, *J* = 16.4, 2H), 4.47 (d of d, *J* = 5.4, 2H), 4.33 (d, *J* = 16.4, 2H), 4.31 (d, *J* = 15.7, 2H), 4.27 – 4.24 (m, 4H), 4.19 – 4.14 (m, 6H), 3.87 (d of d, *J* = 5.4, 2H), 3.29-

3.13 (m, 4H), 2.30 (p, J = 7.2, 4H), 1.76 (s, 6H), 1.75 (s, 6H). ^{13}C NMR (125 MHz, D_2O, 1, 4-dioxane as internal reference): δ 157.3, 156.2, 155.9, 154.5, 151.2, 149.0, 127.8, 127.7, 117.9, 113.9, 81.4, 78.9, 77.4, 71.1, 70.8, 70.6, 68.0, 51.8, 47.9, 47.7, 47.5, 35.4, 33.7, 24.2, 14.5, 13.7. High-Res MS (ESI): m/z 616.1650 ([M - 2Na]$^{2-}$), calculated for $C_{50}H_{56}N_{16}O_{18}S_2^{2-}$ 616.1700.

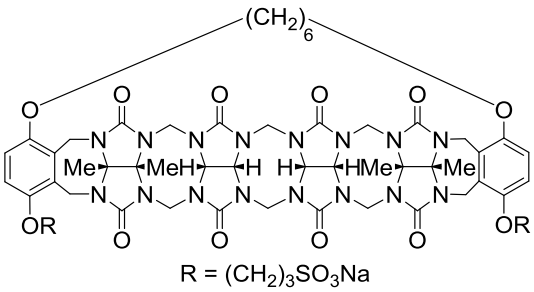

Compound IV-2b. Compound **IV-4b** (2.0s g, 3.4 mmol) was added to a solution of **IV-5** (1.3 g, 1.7 mmol) in a mixture of trifluoroacetic acid (130 mL) and acetic anhydride (130 mL). This solution was stirred and heated at 70 °C for 3 h. The reaction mixture was cooled to room temperature, treated with methanol (130 mL), and the solvent was removed under reduced pressure to obtain the crude product. The crude product was washed three times with a mixture of water (50 mL) and acetone (100 mL). The dark orange colored solid obtained was loaded onto a Dowex® 1X2 chloride form, 200-400 mesh ion exchange resin (50 g). The column was eluted with increasing concentrations of hydrochloric acid (HCl) starting from plain water (750 mL) to 6M HCl (750 mL) to 12 M HCl (300 mL). The eluted fractions were analyzed by ^{1}H NMR and the almost pure compound **IV-2b** was obtained in the fractions eluted with 12 M HCl. This fraction

was dried under reduced pressure and washed with a mixture of water and methanol (1:1, v/v, 100 mL). Finally, the solid obtained was dissolved in water and the pH of the solution was adjusted to 7 using aqueous sodium hydroxide (1M). The solvent was removed under reduced pressure and the solid was further dried under high vacuum to obtain pure **IV-2b** as a light yellow solid (0.30 g, 0.56 mmol, 13%). M.p. > 300 °C. IR (ATR, cm^{-1}): 3449w (br), 2939w, 1719s, 1464m, 1425w, 1378w, 1314m, 1230m, 1181m, 1084m, 1036s, 972m, 924w, 797s, 758m, 730w. ^{1}H NMR (600 MHz, D_2O): 7.01-6.96 (m, 4H), 5.72 (d, *J* = 15.4, 1H), 5.57 (d, *J* = 15.4, 1H), 5.56 (d, *J* = 15.7, 2H), 5.53 (d, *J* = 15.7, 2H), 5.46 (d, *J* = 9.0, 2H), 5.38 (d, *J* = 16.4, 2H), 5.37 (d, *J* = 9.1, 4H), 5.25 (d, *J* = 16.4, 2H), 4.36 (d, *J* = 15.7, 2H), 4.32 (d, *J* = 16.4, 2H), 4.24 – 4.12 (m, 4H), 4.22 (d, *J* = 15.7, 2H), 4.16 (d, *J* = 15.4, 1H), 4.13 (d, *J* = 16.4, 2H), 4.03 (d, *J* = 15.4, 1H), 3.90-3.76 (m, 4H), 3.127-3.11 (m, 4H), 2.34-2.23 (m, 4H), 1.76 (s, 6H), 1.75 (s, 6H), 1.39-1.26 (m, 4H), 1.18-1.09 (m, 2H), 1.05-0.95 (m, 2H). ^{13}C NMR (150 MHz, DMSO, 1, 4-dioxane as internal reference): δ 156.0, 155.2, 154.8, 154.1, 150.2, 150.0, 127.8, 126.6, 113.9, 113.5, 77.3, 76.9, 70.5, 70.2, 69.5, 68.5, 64.6, 59.2, 48.5, 48.3, 48.0, 35.7, 34.4, 28.0, 25.6, 24.0, 16.8, 15.0. High-Res MS (ESI): m/z 644.2016 ($[M - 2Na]^{2-}$), calculated for $C_{54}H_{64}N_{16}O_{18}S_2^{2-}$ 644.2013.

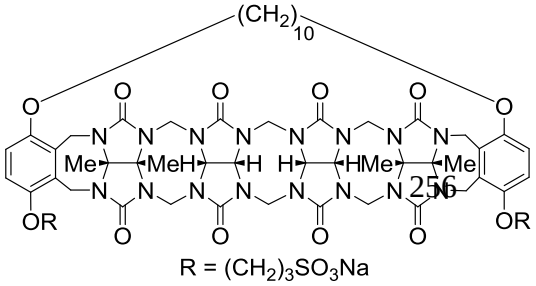

Compound IV-2c. Compound **IV-4c** (1.7 g, 2.6 mmol) was

added to a solution of **IV-5** (1.0 g, 1.3 mmol) in a mixture of trifluoroacetic acid (100 mL) and acetic anhydride (100 mL). This solution was stirred and heated at 70 °C for 3 h. The reaction mixture was cooled to room temperature, treated with methanol (100 mL), and the solvent was removed under reduced pressure to obtain the crude product. The crude product was washed three times with a mixture of water (50 mL) and acetone (100 mL). The dark orange colored solid obtained was loaded onto a Dowex® 1X2 chloride form, 200-400 mesh ion exchange resin (50 g). The column was eluted with increasing concentrations of hydrochloric acid (HCl) starting from plain water (750 mL) to 6M HCl (750 mL) to 12 M HCl (300 mL). The eluted fractions were analyzed by ^{1}H NMR and the almost pure compound **IV-2c** was obtained in the fractions eluted with 12 M HCl. This fraction was dried under reduced pressure and washed with a mixture of water and methanol (1:1, v/v, 100 mL). Finally, the solid obtained was dissolved in water and the pH of the solution was adjusted to 7 using aqueous sodium hydroxide (1M). The solvent was removed under reduced pressure and the solid was further dried under high vacuum to obtain pure **IV-2c** as an off white solid (0.47 g, 0.34 mmol, 26%). M.p. > 300 °C. IR (ATR, cm^{-1}): 3435w (br), 2930w, 1721s, 1463s, 1425m, 1378m, 1313m, 1230s, 1181s, 1085m, 1037s, 972m, 924w, 823m, 797s, 757m, 731m. ^{1}H NMR (600 MHz, D_2O): 7.10-6.98 (m, 4H), 5.72 (d, *J* = 15.2, 1H), 5.64 (d, *J* = 15.2, 1H), 5.59 (d, *J* = 15.7, 2H), 5.56 (d, *J* = 15.7, 2H),5.45 (d, *J* = 9.0, 2H), 5.45 (d, *J* = 16.5, 2H), 5.40 (d, *J* = 9.0, 2H), 5.31

(d, *J* = 16.5, 2H), 4.31 (d, *J* = 15.7, 2H), 4.23 (d, *J* = 15.7, 2H), 4.20 – 4.08 (m, 11H), 4.06 (d, J = 15.2, 1H), 4.01-3.93 (m, 2H), 3.28-3.09 (m, 4H), 2.35-2.22 (m, 4H), 1.78 (s, 6H), 1.74 (s, 6H), 1.58-1.46 (m, 2H), 1.40-1.27 (m, 2H), 1.12-0.93 (m, 4H), 0.91-0.75 (m, 6H), 0.75-0.65 (m, 2H). ^{13}C NMR (150 MHz, DMSO, 1, 4-dioxane as internal reference): δ 156.1, 155.2, 154.6, 154.0, 150.2, 150.1, 128.1, 114.0, 113.6, 113.5, 77.5, 76.4, 70.7, 70.4, 69.8, 68.6, 64.6, 59.2, 48.4, 48.3, 48.2, 34.7, 34.5, 28.5, 27.2, 27.1, 25.6, 24.2, 16.6, 15.7.High-Res MS (ESI): m/z 672.2341 ([M - 2Na]$^{2-}$), calculated for $C_{58}H_{72}N_{16}O_{18}S_2^{2-}$ 672.2326.

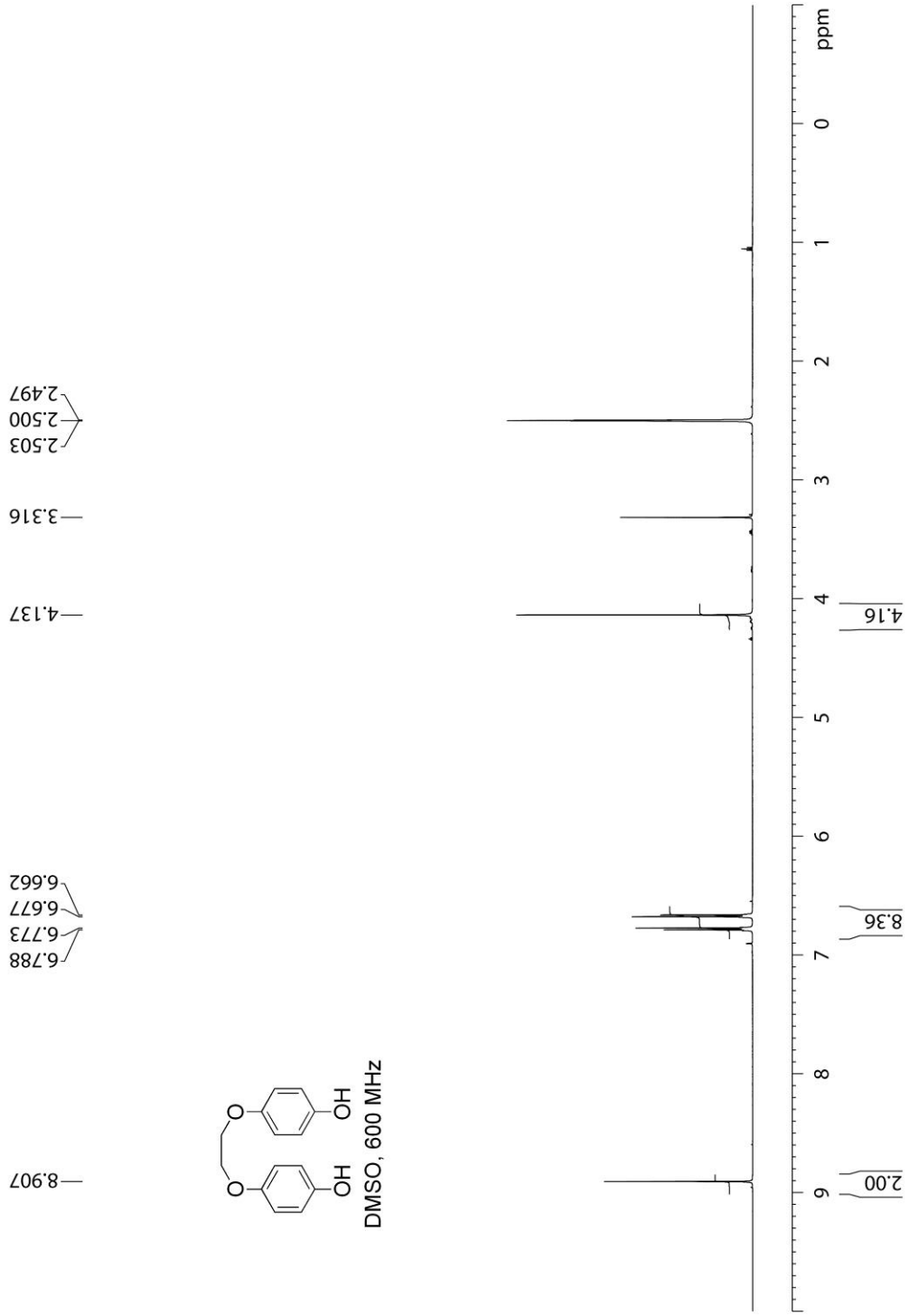

Figure IV-S1. ^{1}H NMR spectra (600 MHz, DMSO) recorded for **IV-3a**.

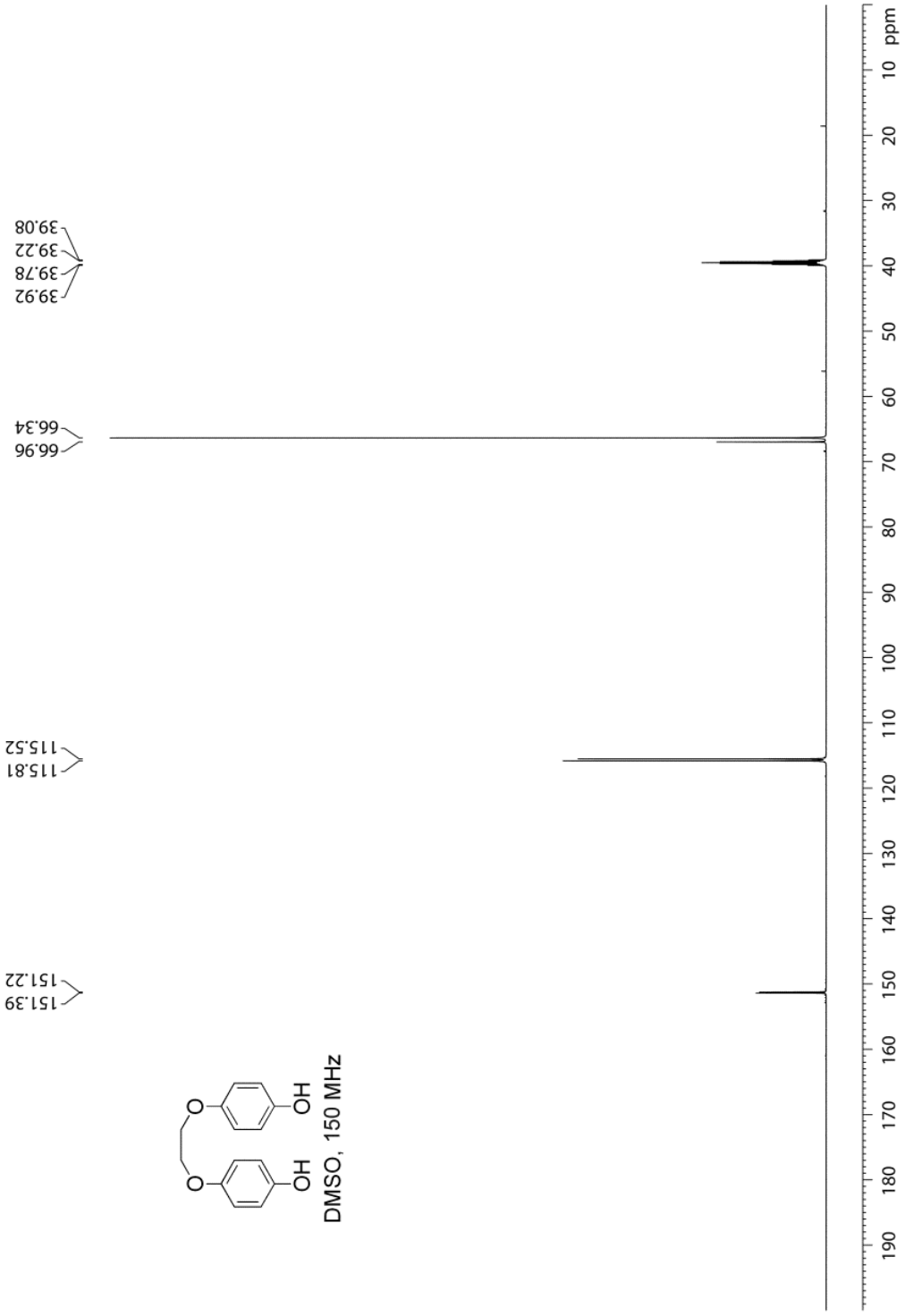

Figure IV-S2. ^{13}C NMR spectra (150 MHz, DMSO, 1, 4-dioxane as internal reference) recorded for **IV-3a**.

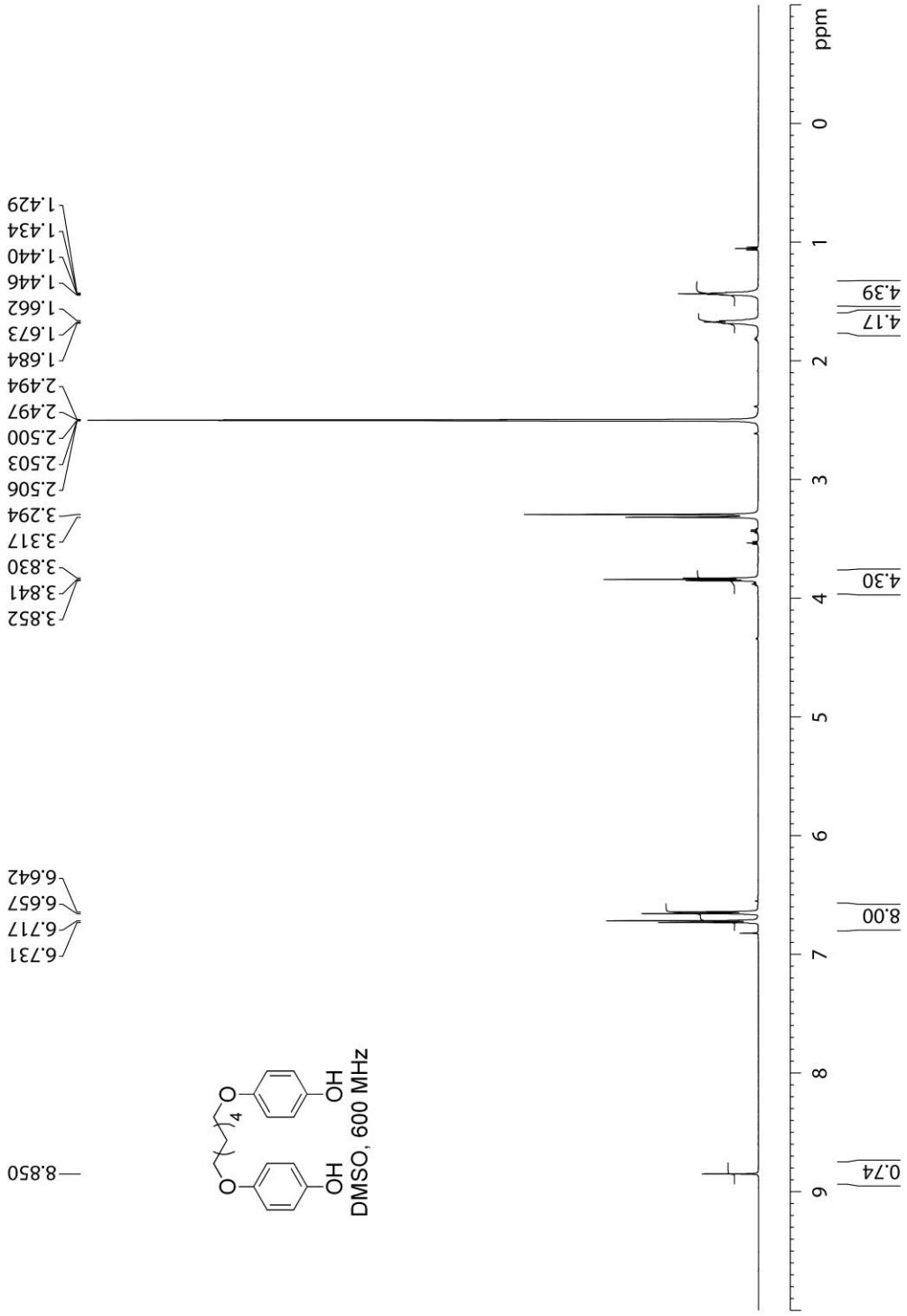

Figure IV-S3. ^{1}H NMR spectra (600 MHz, DMSO) recorded for **IV-3b**.

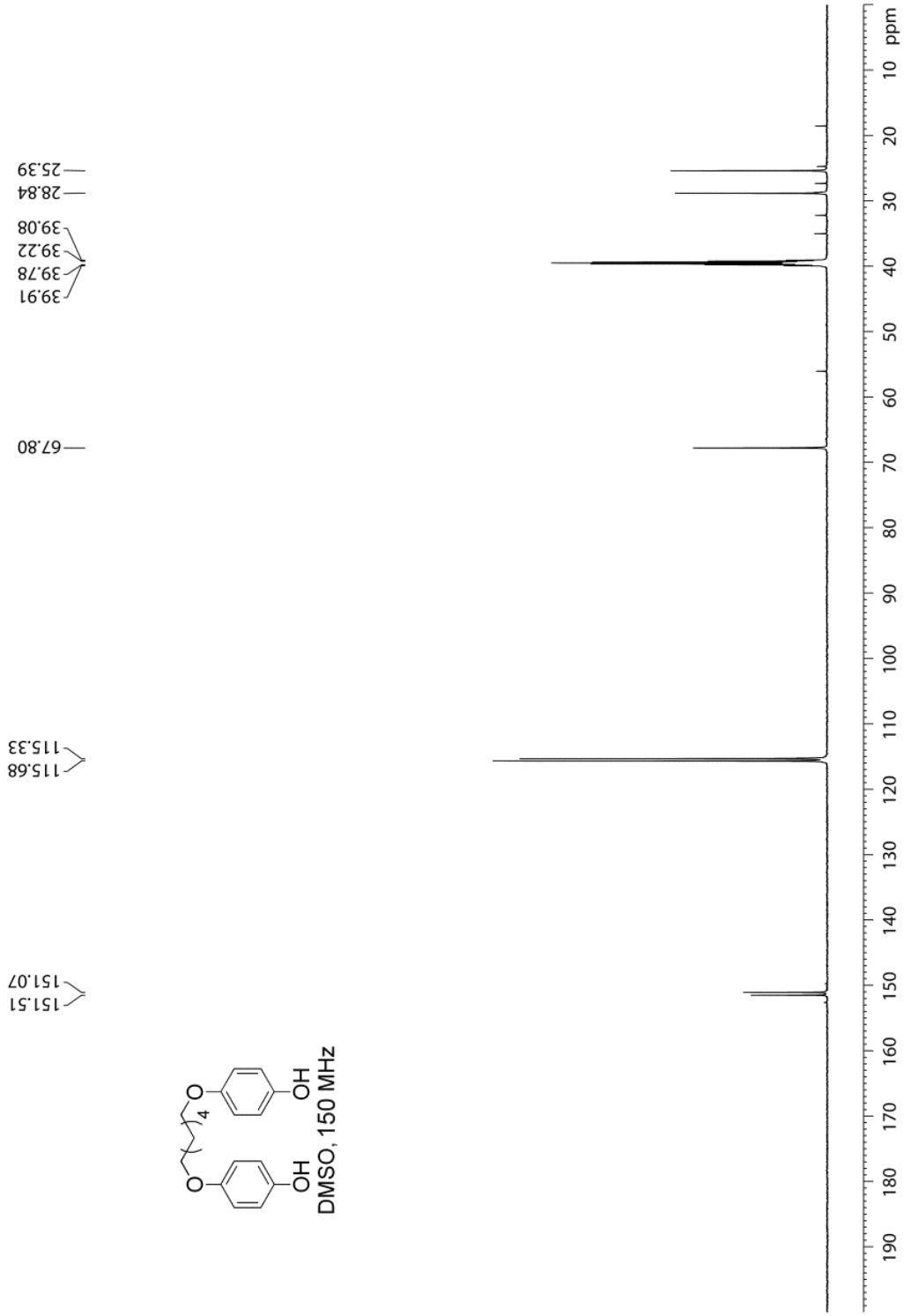

Figure IV-S4. ^{13}C NMR spectra (150 MHz, DMSO) recorded for **IV-3b**.

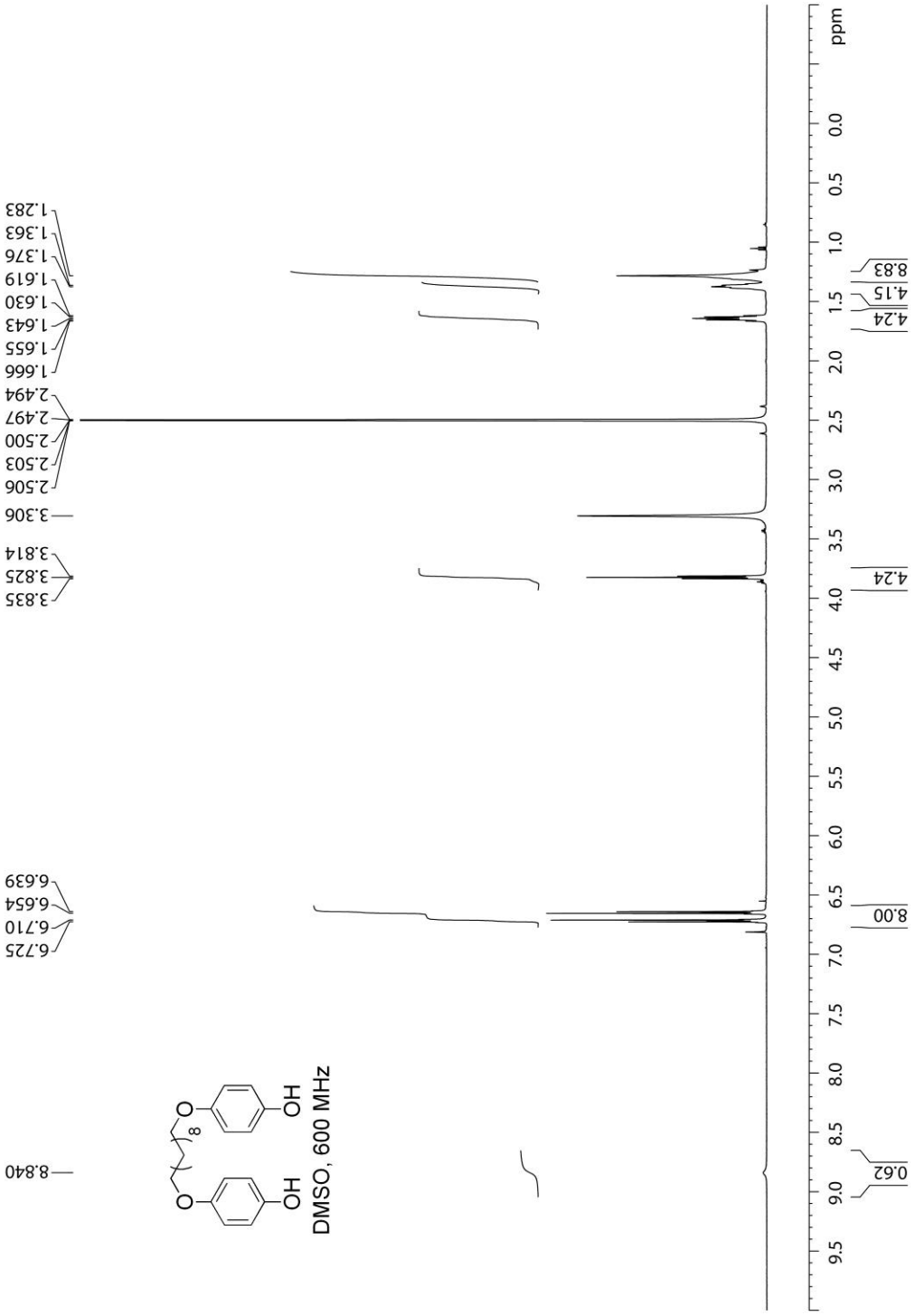

Figure IV-S5. ^{1}H NMR spectra (600 MHz, DMSO) recorded for **IV-3c**.

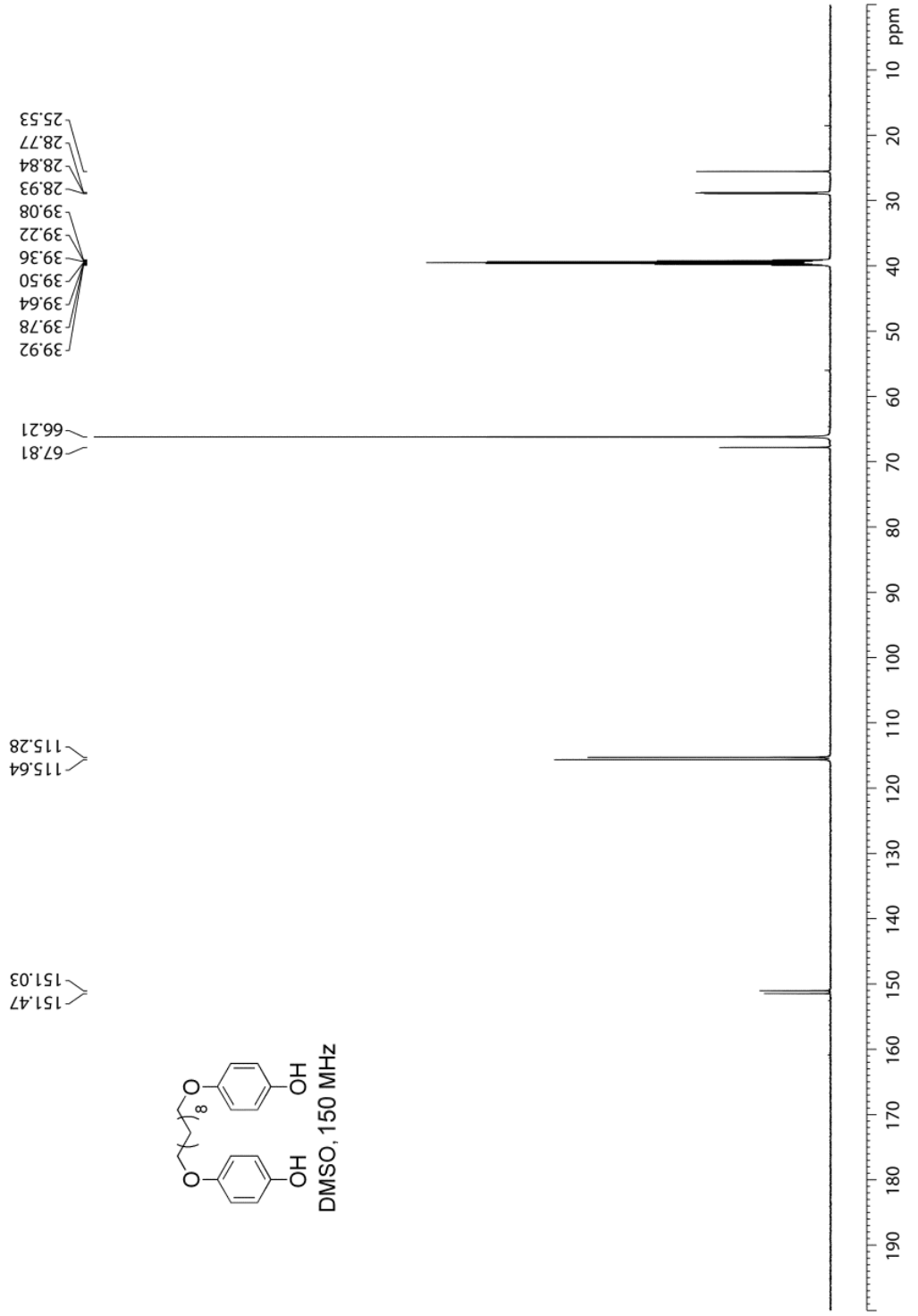

Figure IV-S6. ^{13}C NMR spectra (150 MHz, DMSO, 1, 4-dioxane as internal reference) recorded for **IV-3c**.

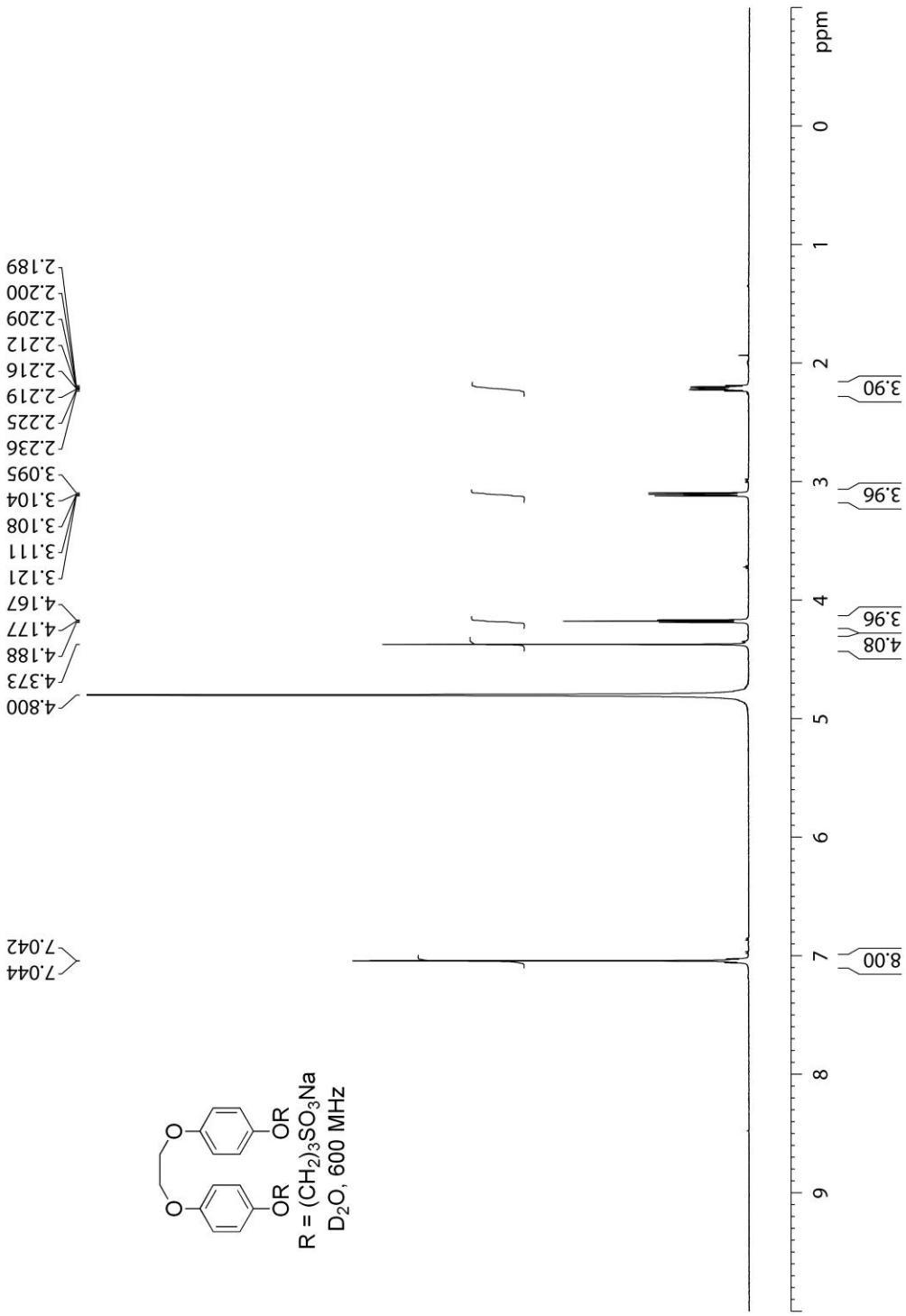

Figure IV-S7. ^{1}H NMR spectra (600 MHz, D_2O) recorded for **IV-4a**.

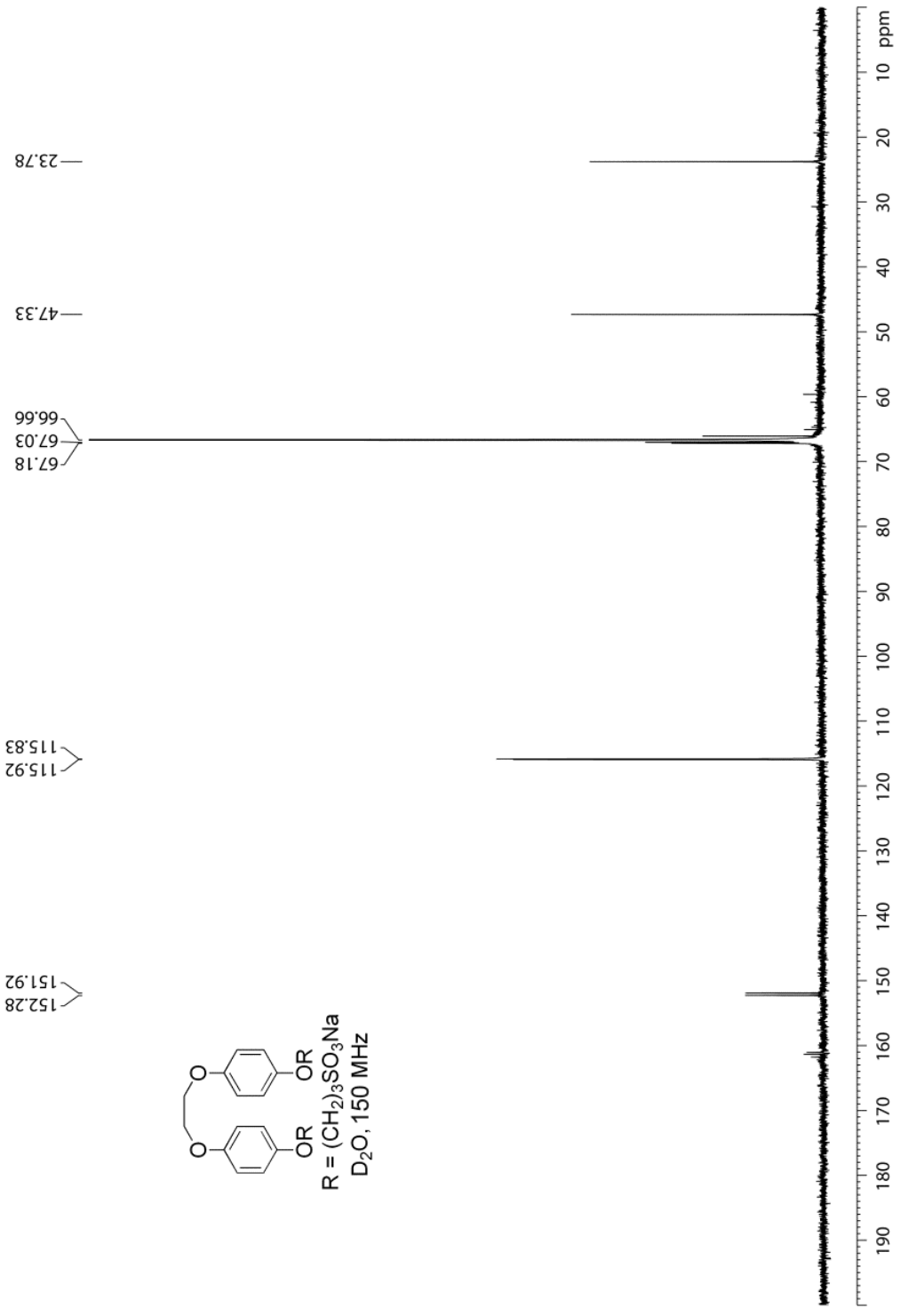

Figure IV-S8. ^{13}C NMR spectra (150 MHz, D_2O, 1, 4-dioxane as internal reference) recorded for **IV-4a**.

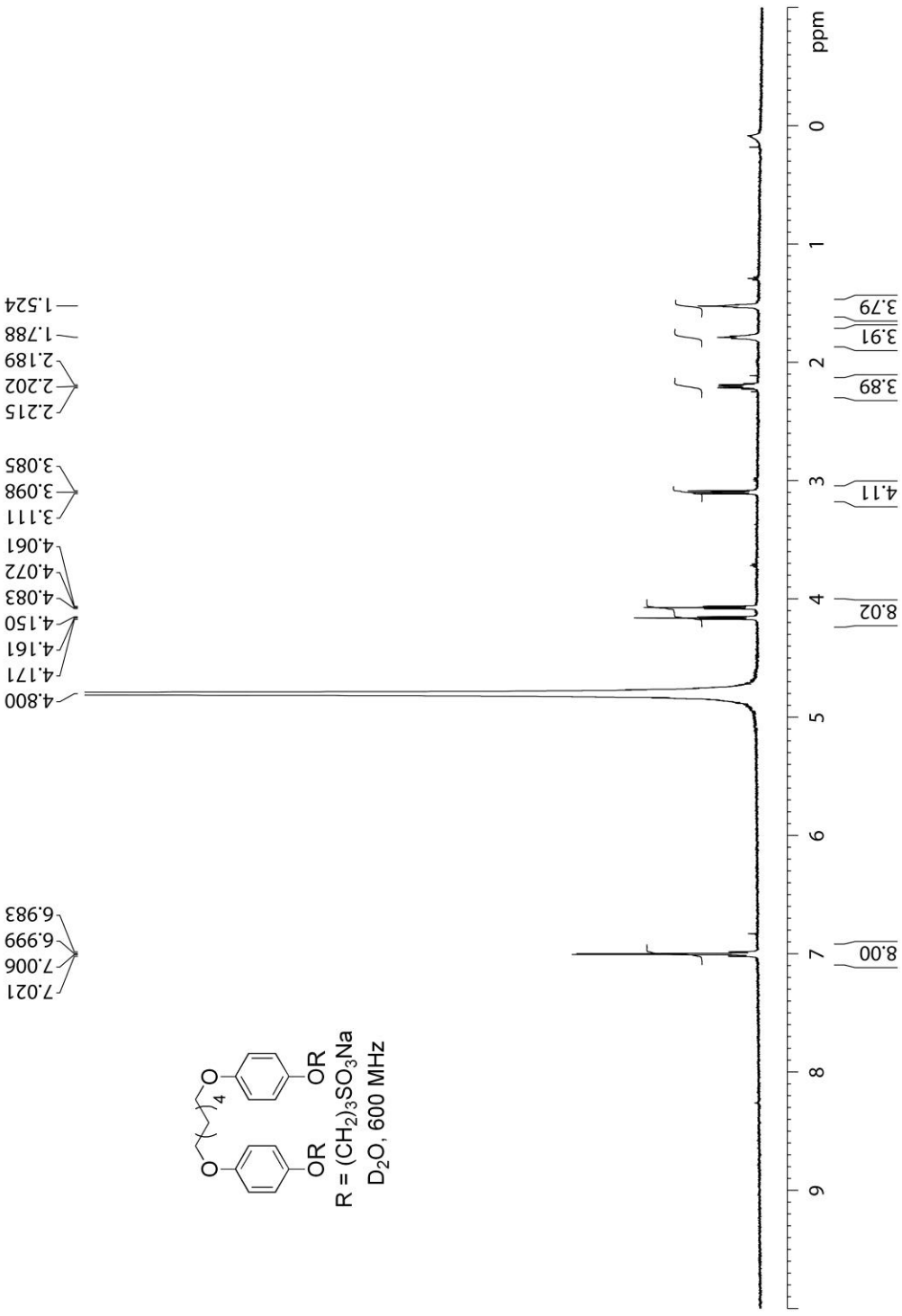

Figure IV-S9. ^{1}H NMR spectra (600 MHz, D_2O) recorded for **IV-4b**.

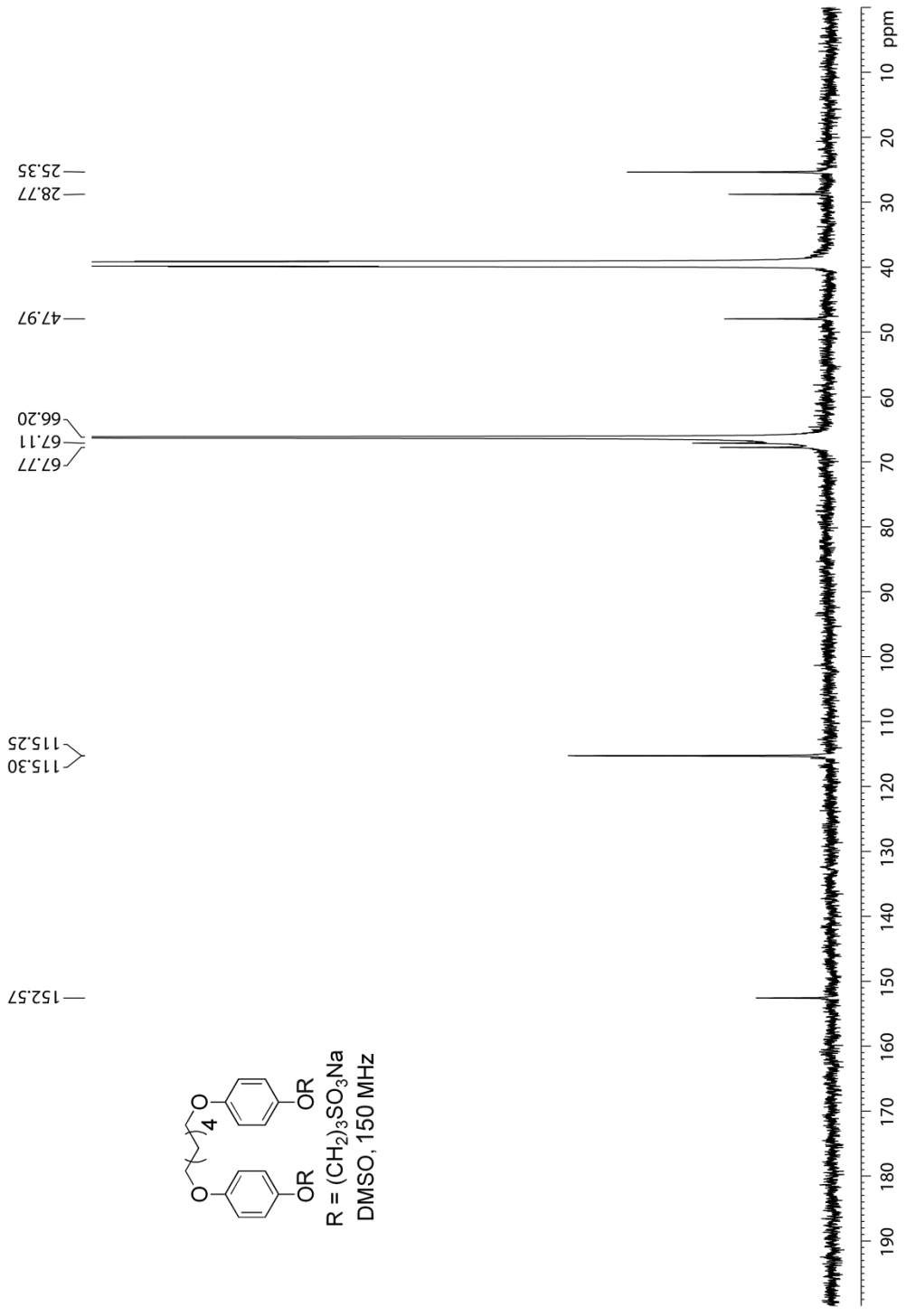

Figure IV-S10. ^{13}C NMR spectra (150 MHz, DMSO, 1, 4-dioxane as internal reference) recorded for **IV-4b**.

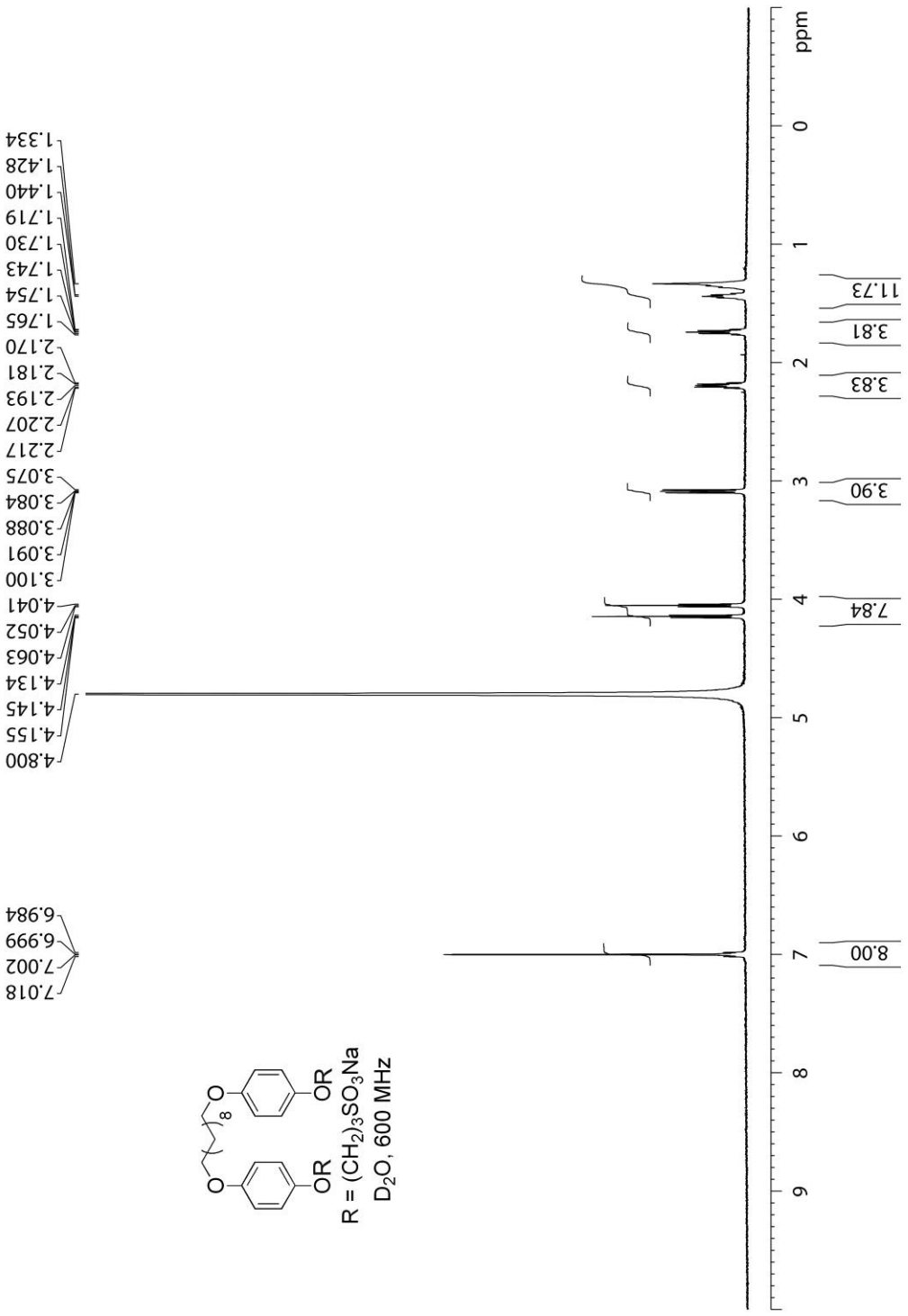

Figure IV-S11. ^{1}H NMR spectra (600 MHz, D_2O) recorded for **IV-4c**.

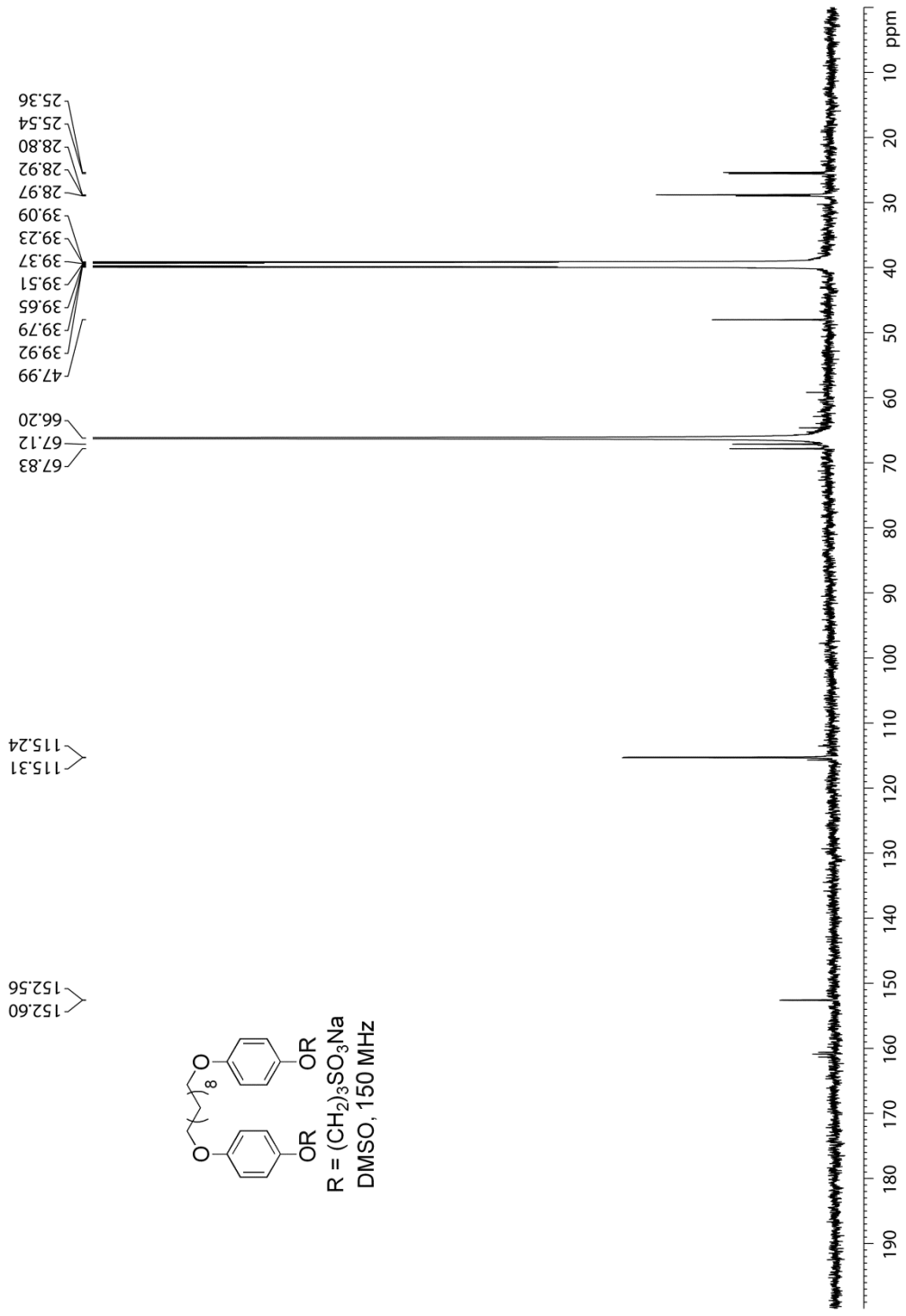

Figure IV-S12. ^{13}C NMR spectra (150 MHz, DMSO, 1, 4-dioxane as internal reference) recorded for **IV-4c**.

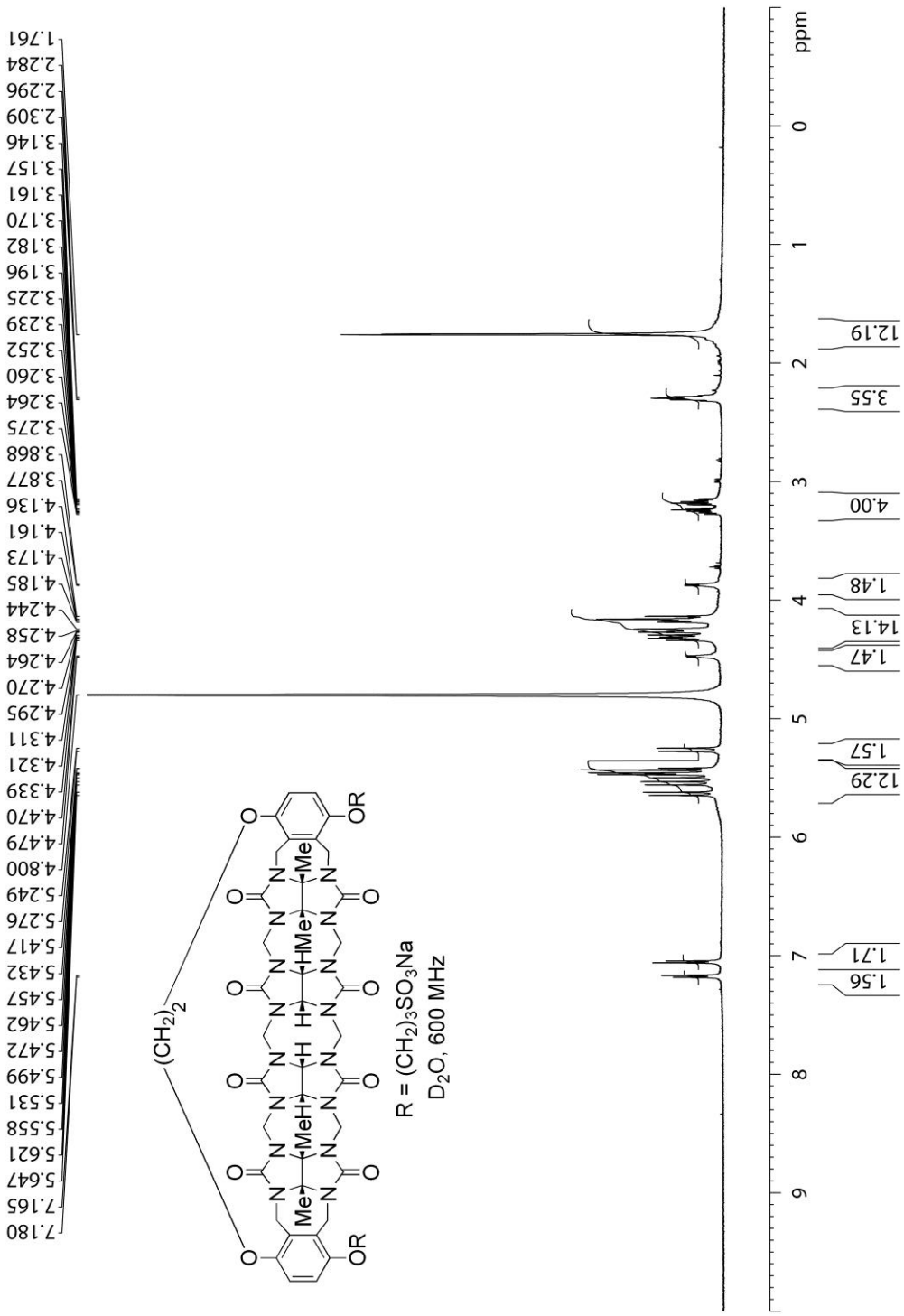

Figure IV-S13. ^{1}H NMR spectra (600 MHz, D_2O) recorded for **IV-2a**.

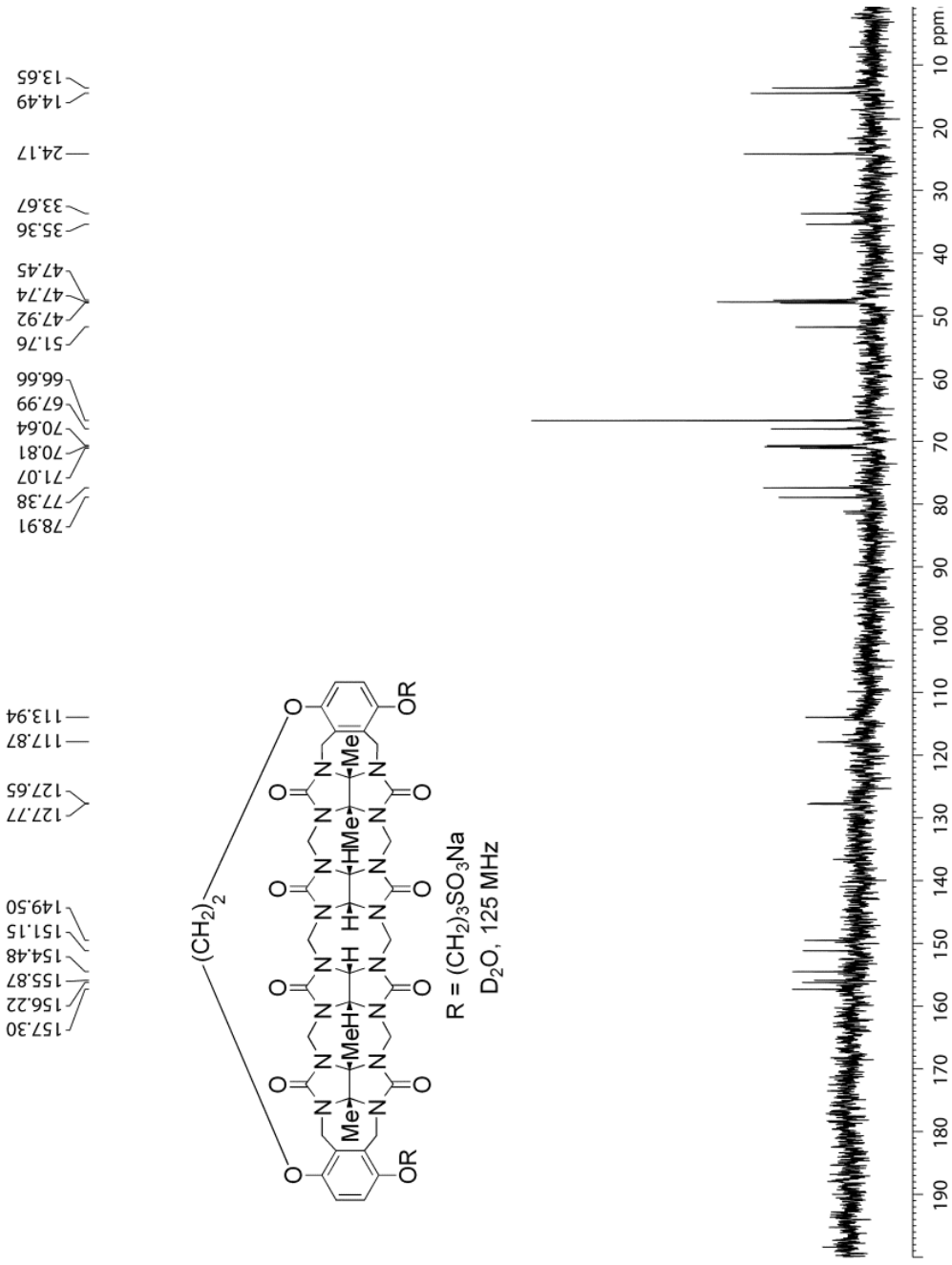

Figure IV-S14. ^{13}C NMR spectra (125 MHz, D_2O, 1, 4-dioxane as internal reference) recorded for **IV-2a**.

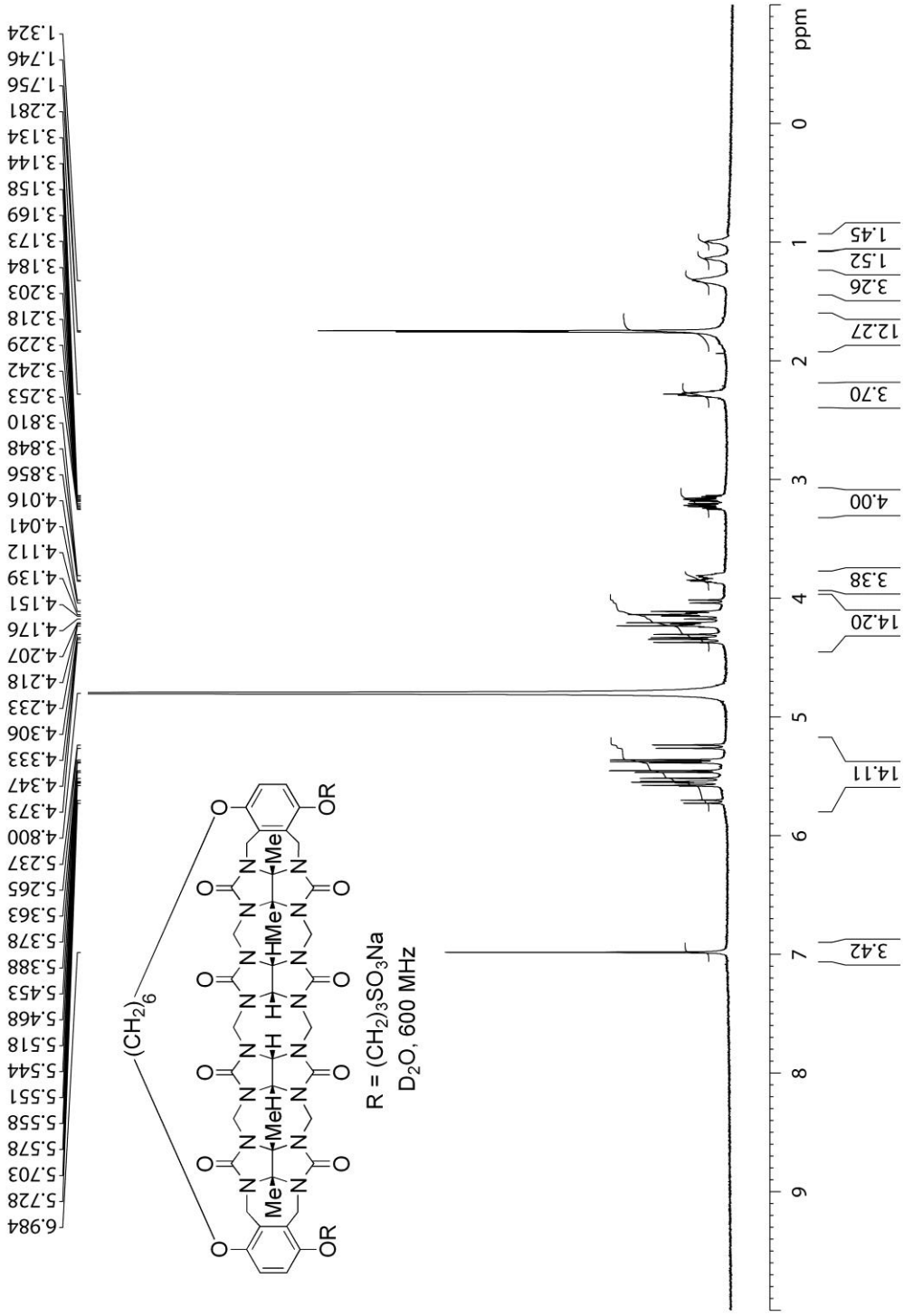

Figure IV-S15. ^{1}H NMR spectra (600 MHz, D_2O) recorded for **IV-2b**.

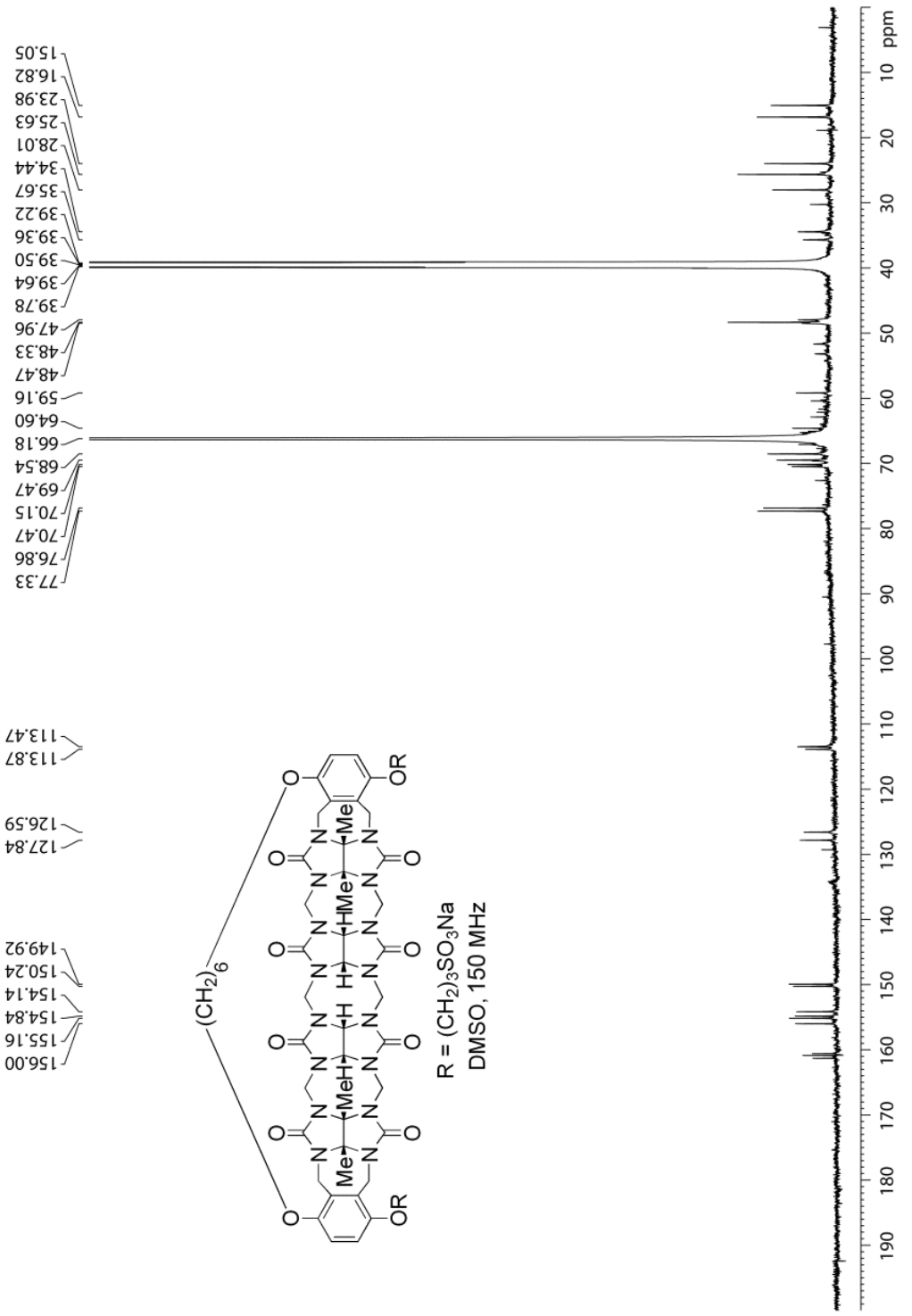

Figure IV-S16. ^{13}C NMR spectra (150 MHz, DMSO, 1, 4-dioxane as internal reference) recorded for **IV-2b**.

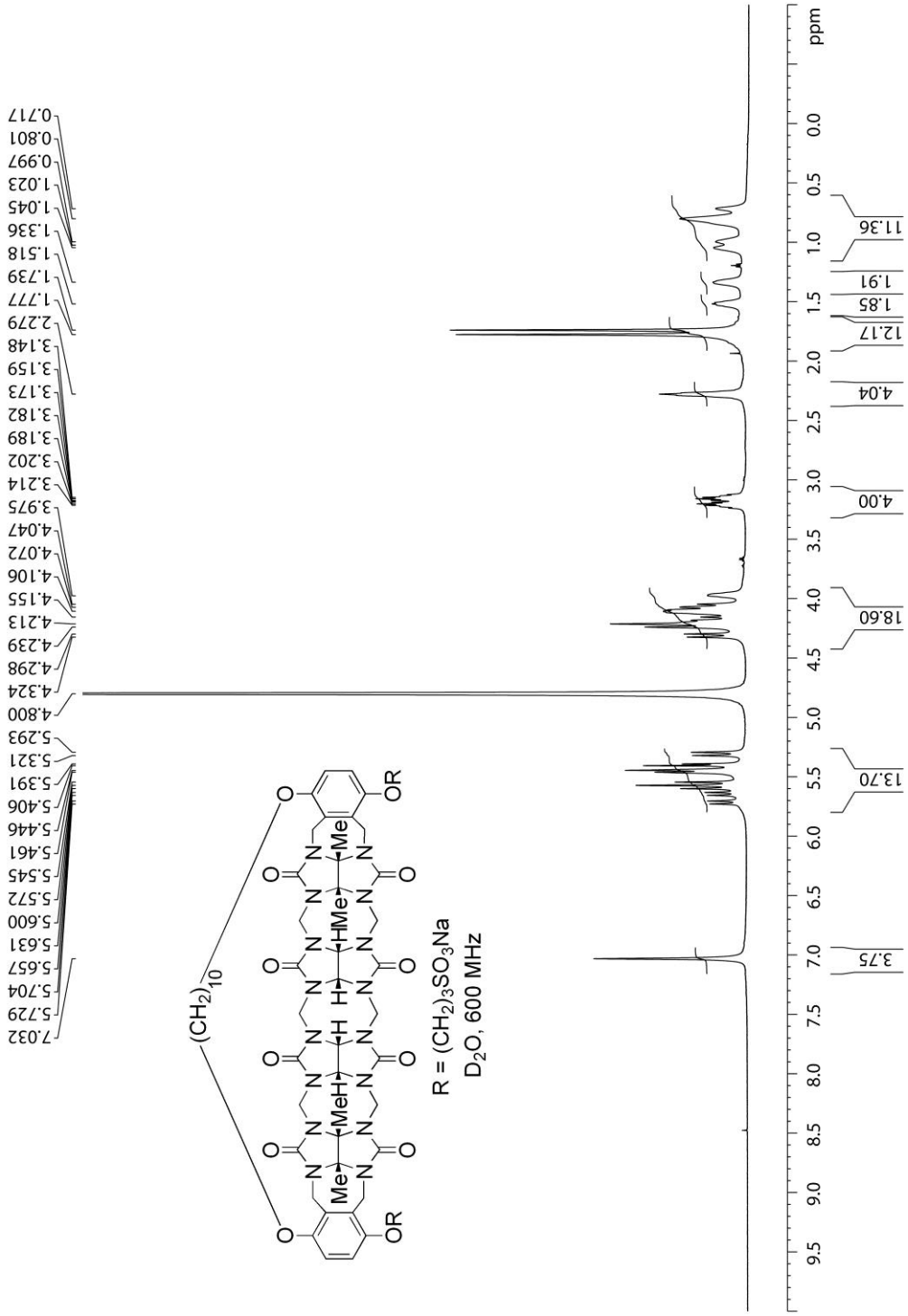

Figure IV-S17. ^{1}H NMR spectra (600 MHz, D_2O) recorded for **IV-2c**.

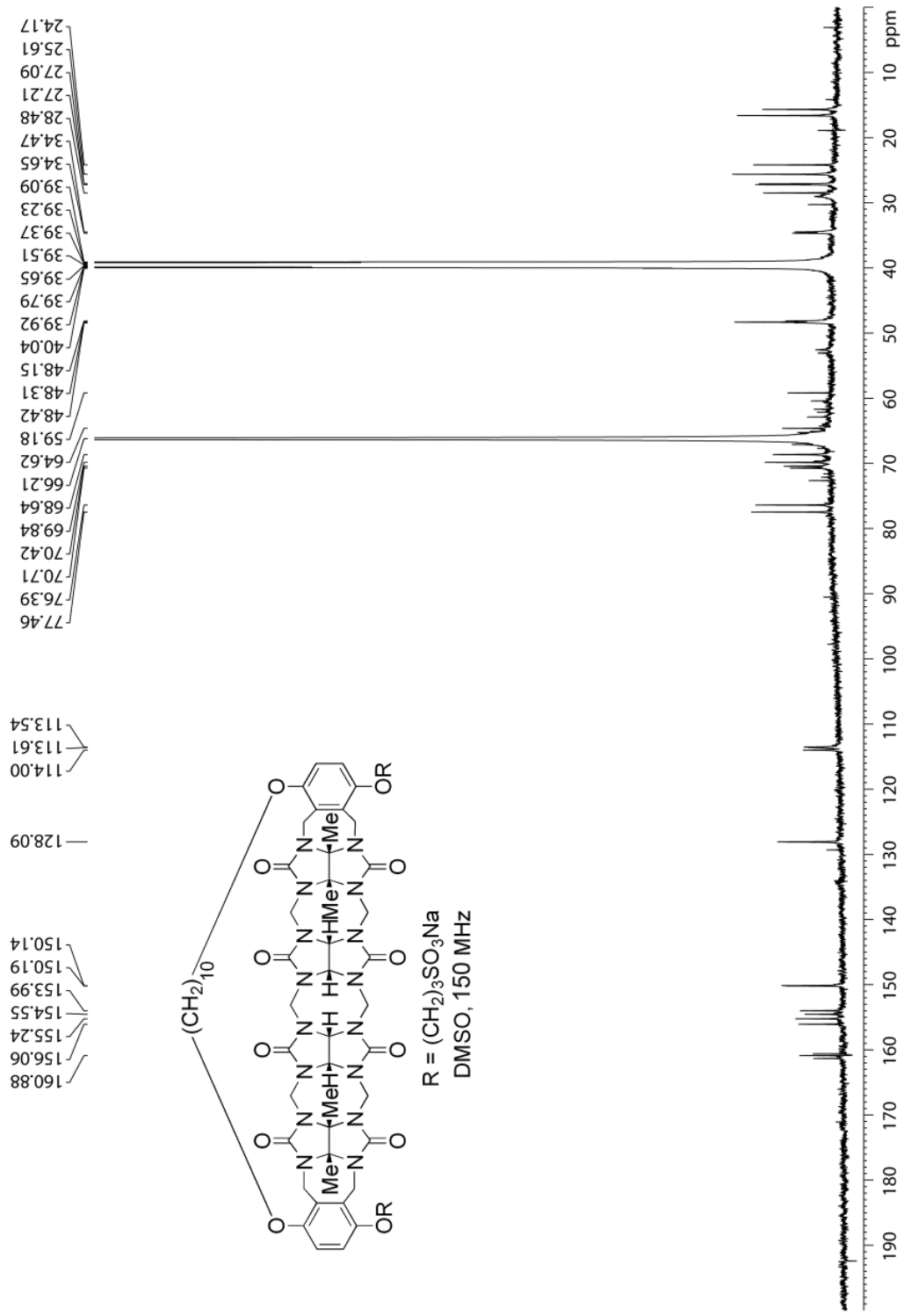

Figure IV-S18. ^{13}C NMR spectra (150 MHz, DMSO, 1, 4-dioxane as internal reference) recorded for **IV-2c**.

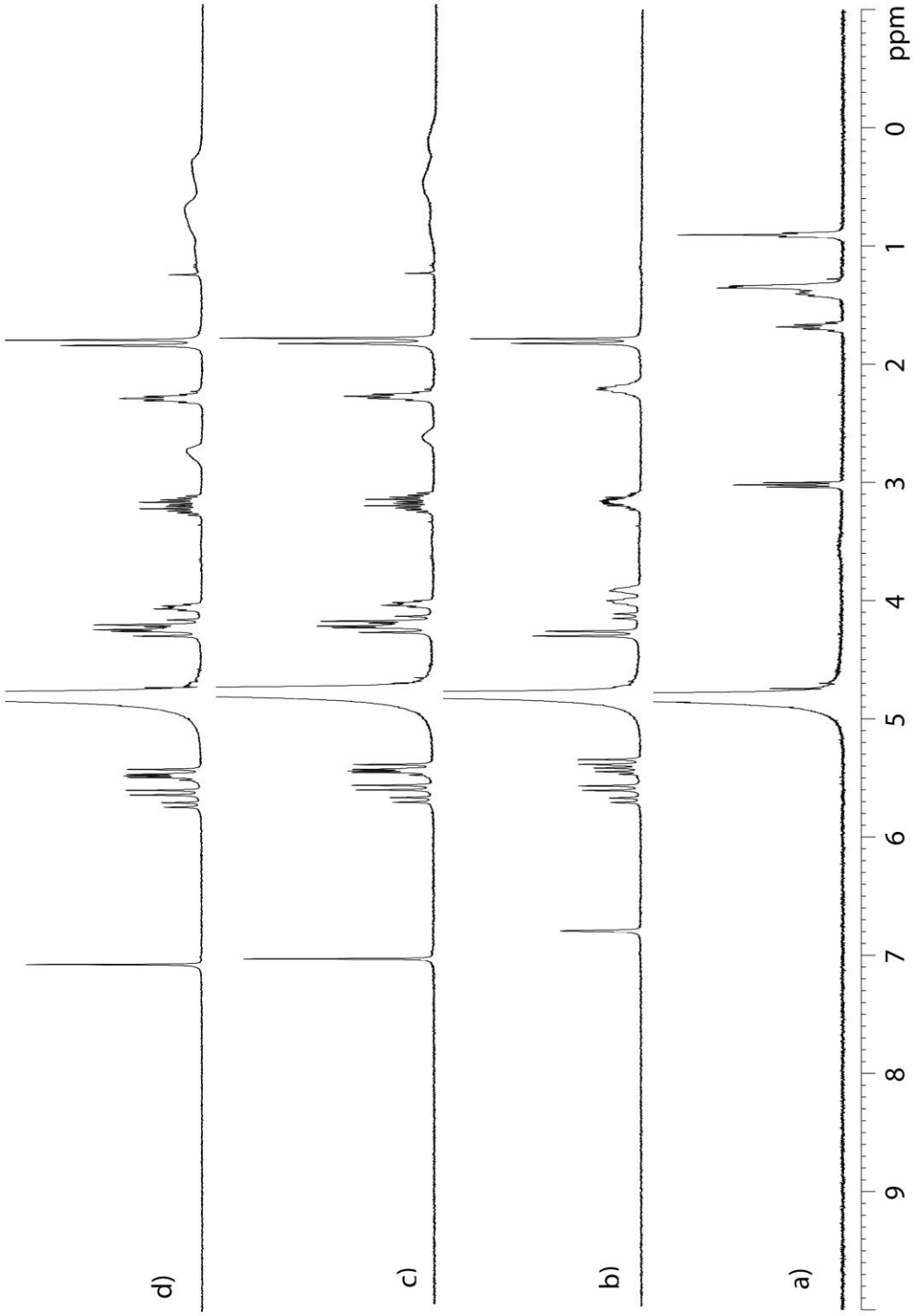

Figure IV-S19. ^{1}H NMR spectra recorded (400 MHz, RT, D_2O) for a) **IV-6**, b) **IV-1**, c) an equimolar mixture of **IV-6** and **IV-1** (1 mM), and d) a 2:1 mixture of **IV-6** (2 mM) and **IV-1**(1 mM).

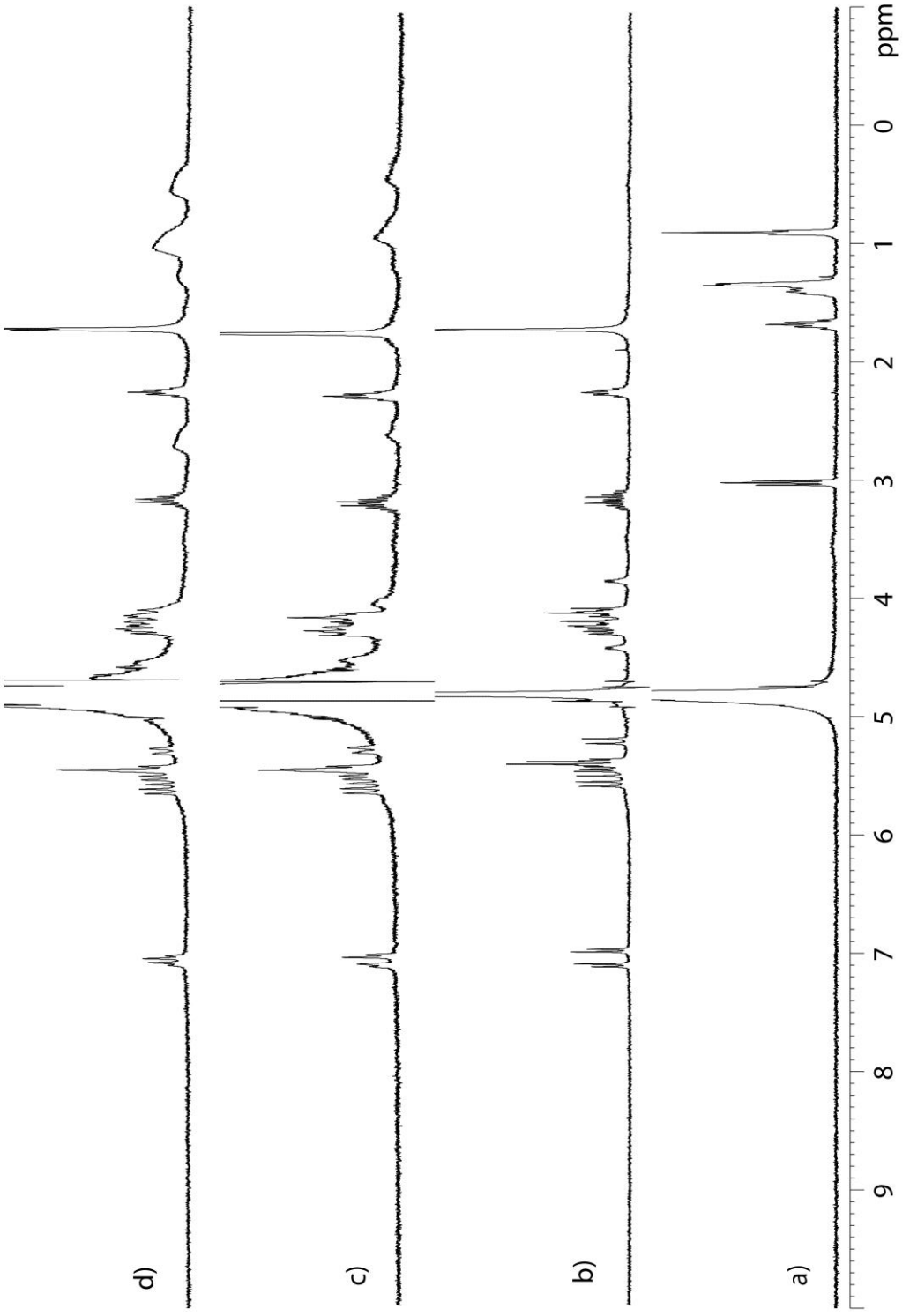

Figure IV-S20. ^{1}H NMR spectra recorded (400 MHz, RT, D_2O) for a) **IV-6**, b) **IV-2a**, c) an equimolar mixture of **IV-6** and **IV-2a** (0.5 mM), and d) a 2:1 mixture of **IV-6** (1 mM) and **IV-2a** (0.5 mM).

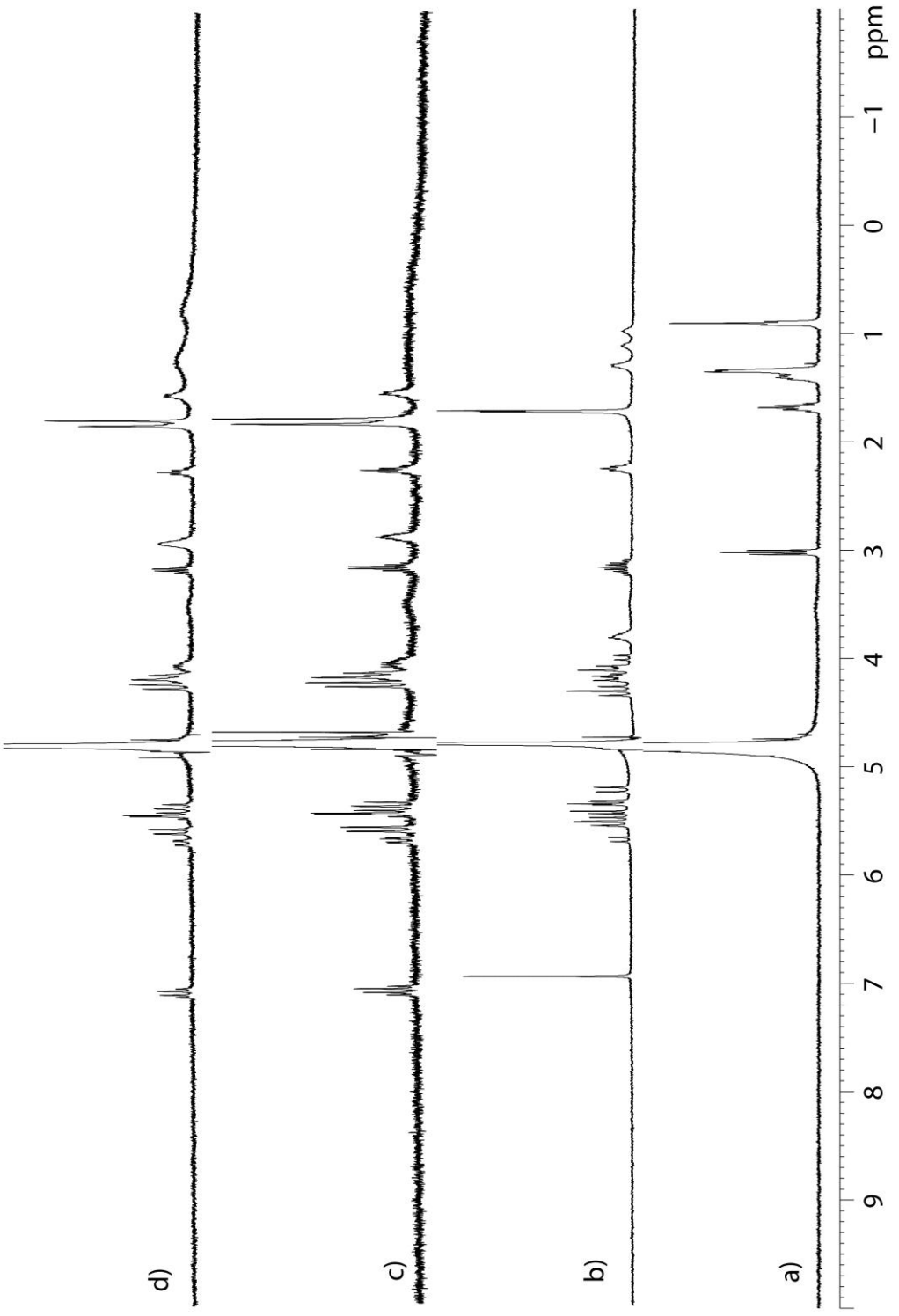

Figure IV-S21. ^{1}H NMR spectra recorded (400 MHz, RT, D_2O) for a) **IV-6**, b) **IV-2b**, c) an equimolar mixture of **IV-6** and **IV-2b** (0.5 mM), and d) a 2:1 mixture of **IV-6** (1 mM) and **IV-2b** (0.5 mM).

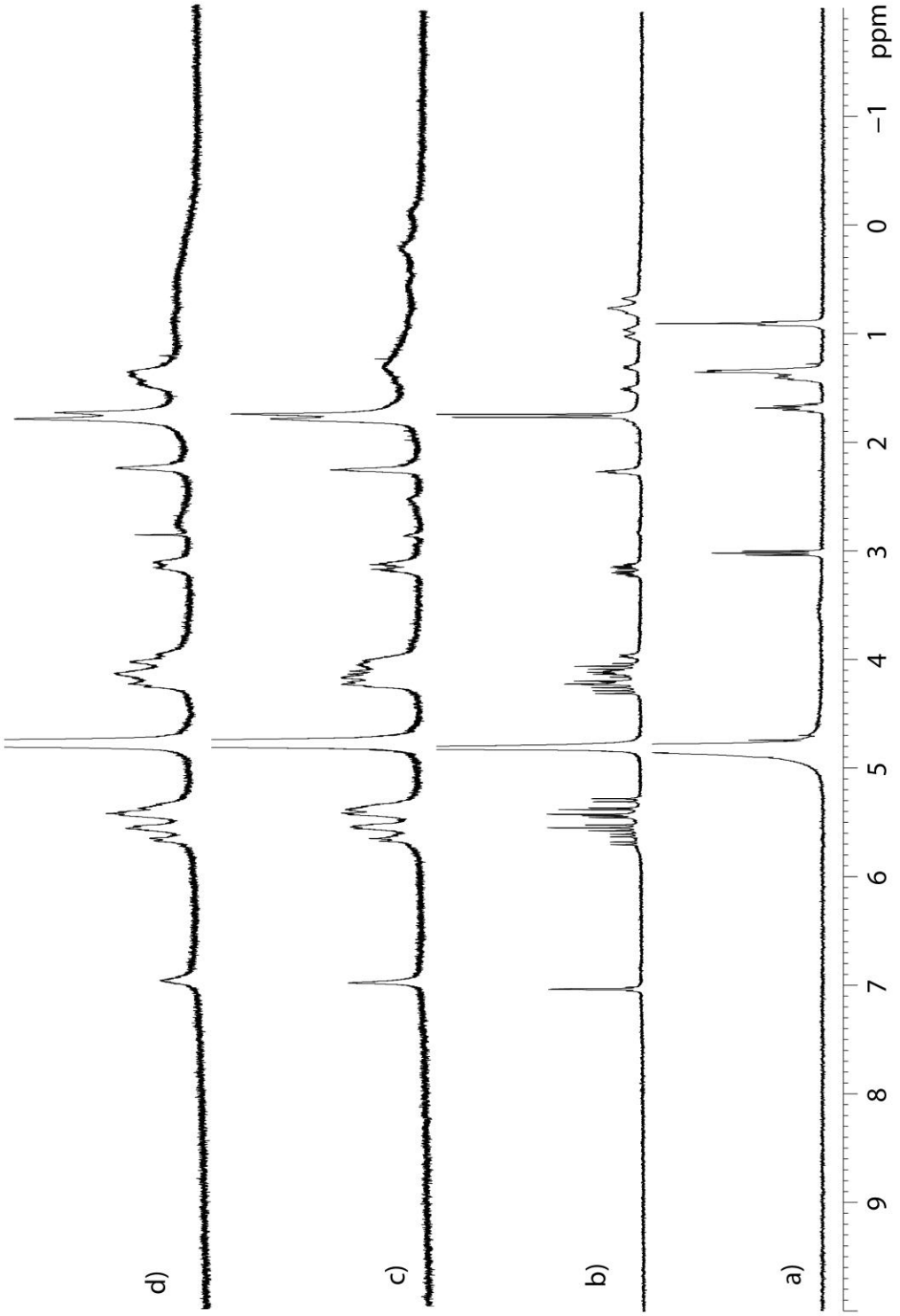

Figure IV-S22. ^{1}H NMR spectra recorded (400 MHz, RT, D_2O) for a) **IV-6**, b) **IV-2c**, c) an equimolar mixture of **IV-6** and **IV2c** (0.3 mM), and d) a 2:1 mixture of **IV-6** (0.6 mM) and **IV-2c** (0.3 mM).

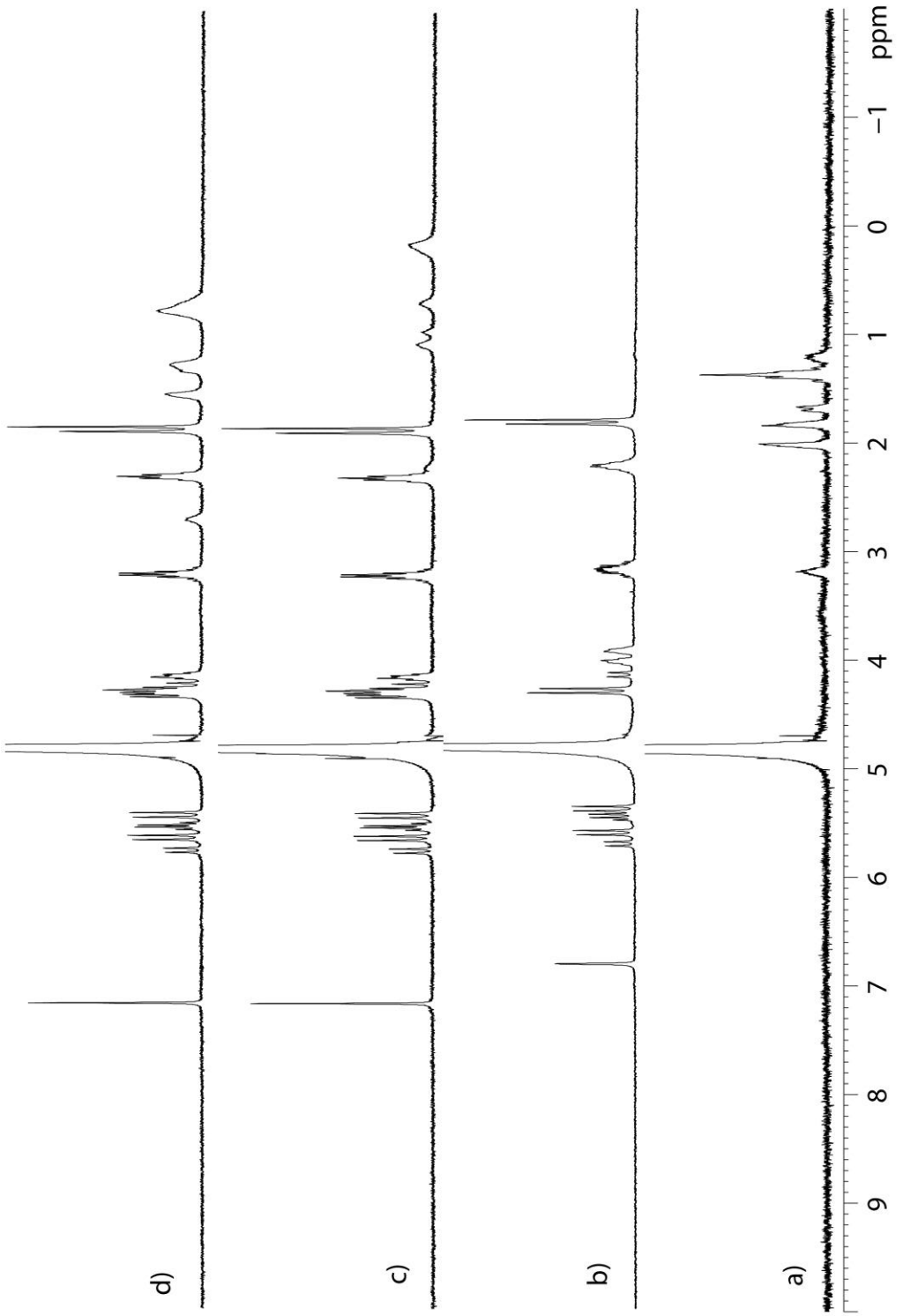

Figure IV-S23. ^{1}H NMR spectra recorded (400 MHz, RT, D_2O) for a) **IV-7**, b) **IV-1**, c) an equimolar mixture of **IV-7** and **IV-1** (1 mM), and d) a 2:1 mixture of **IV-7** (2 mM) and **IV-1** (1 mM).

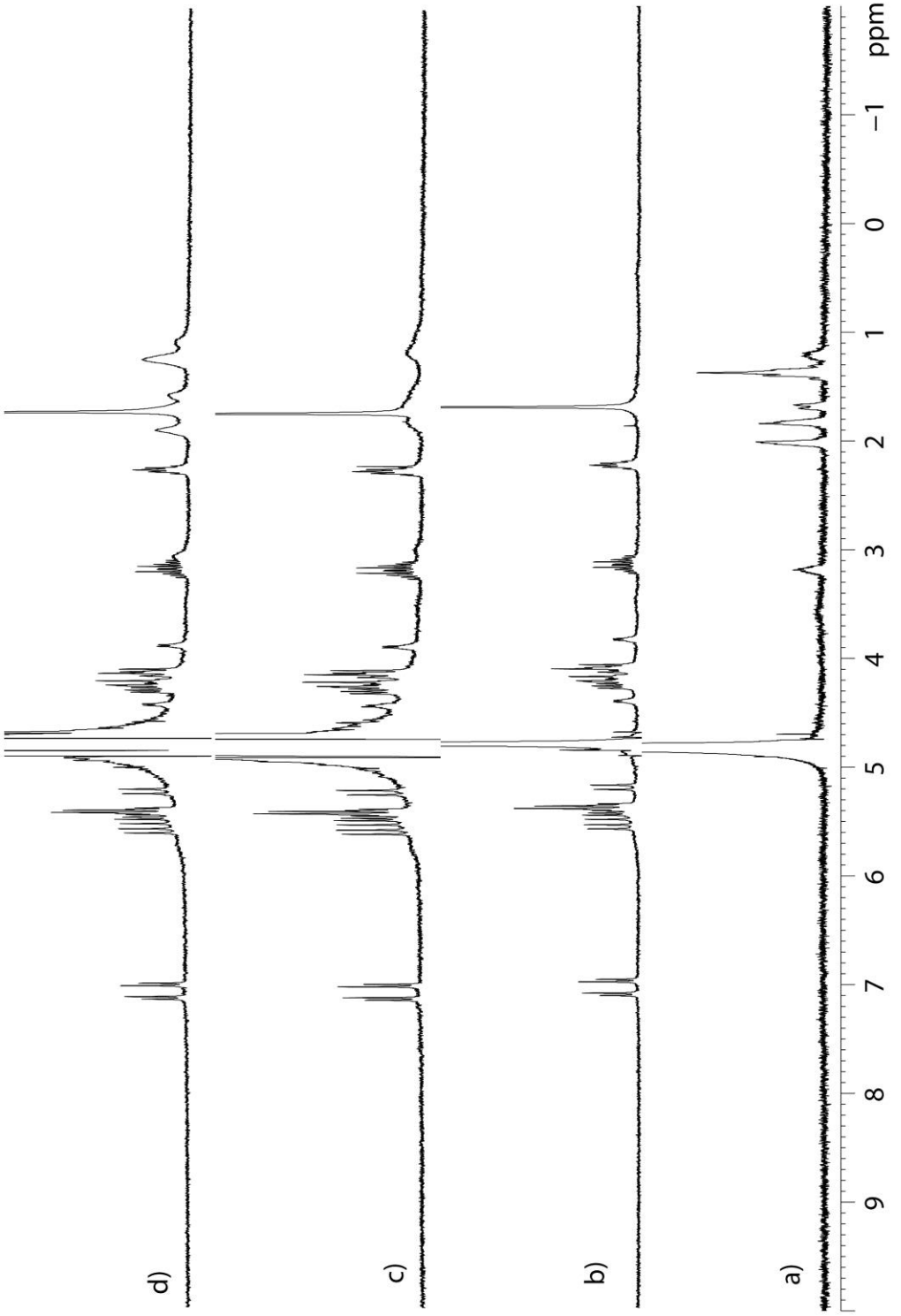

Figure IV-S24. ^{1}H NMR spectra recorded (400 MHz, RT, D_2O) for a) **IV-7**, b) **IV-2a**, c) an equimolar mixture of **IV-7** and **IV-2a** (0.5 mM), and d) a 2:1 mixture of **IV-7** (1 mM) and **IV-2a** (0.5 mM).

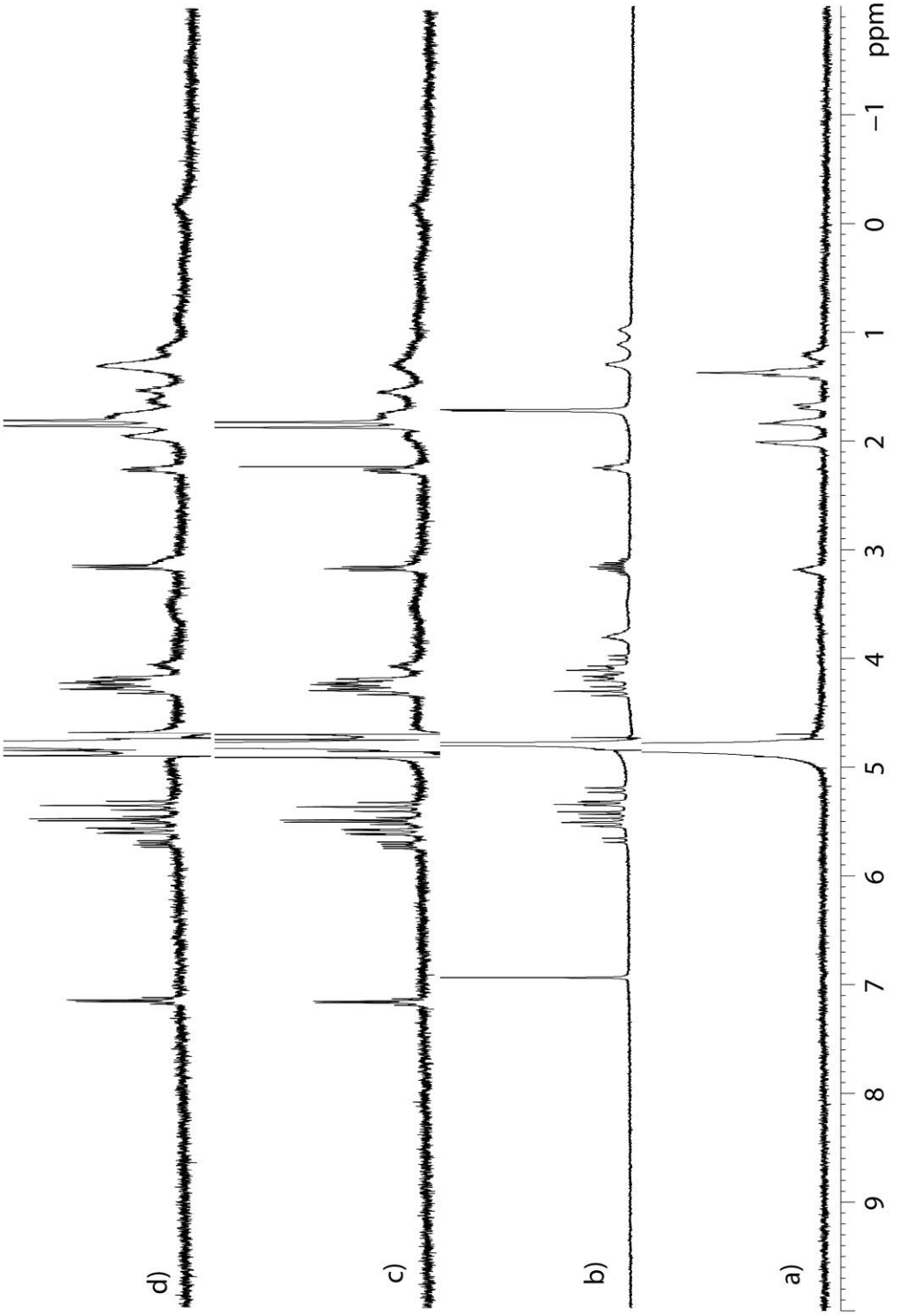

Figure IV-S25. ^{1}H NMR spectra recorded (400 MHz, RT, D_2O) for a) **IV-7**, b) **IV-2b**, c) an equimolar mixture of **IV-7** and **IV-2b** (0.5 mM), and d) a 2:1 mixture of **IV-7** (1 mM) and **IV-2b** (0.5 mM).

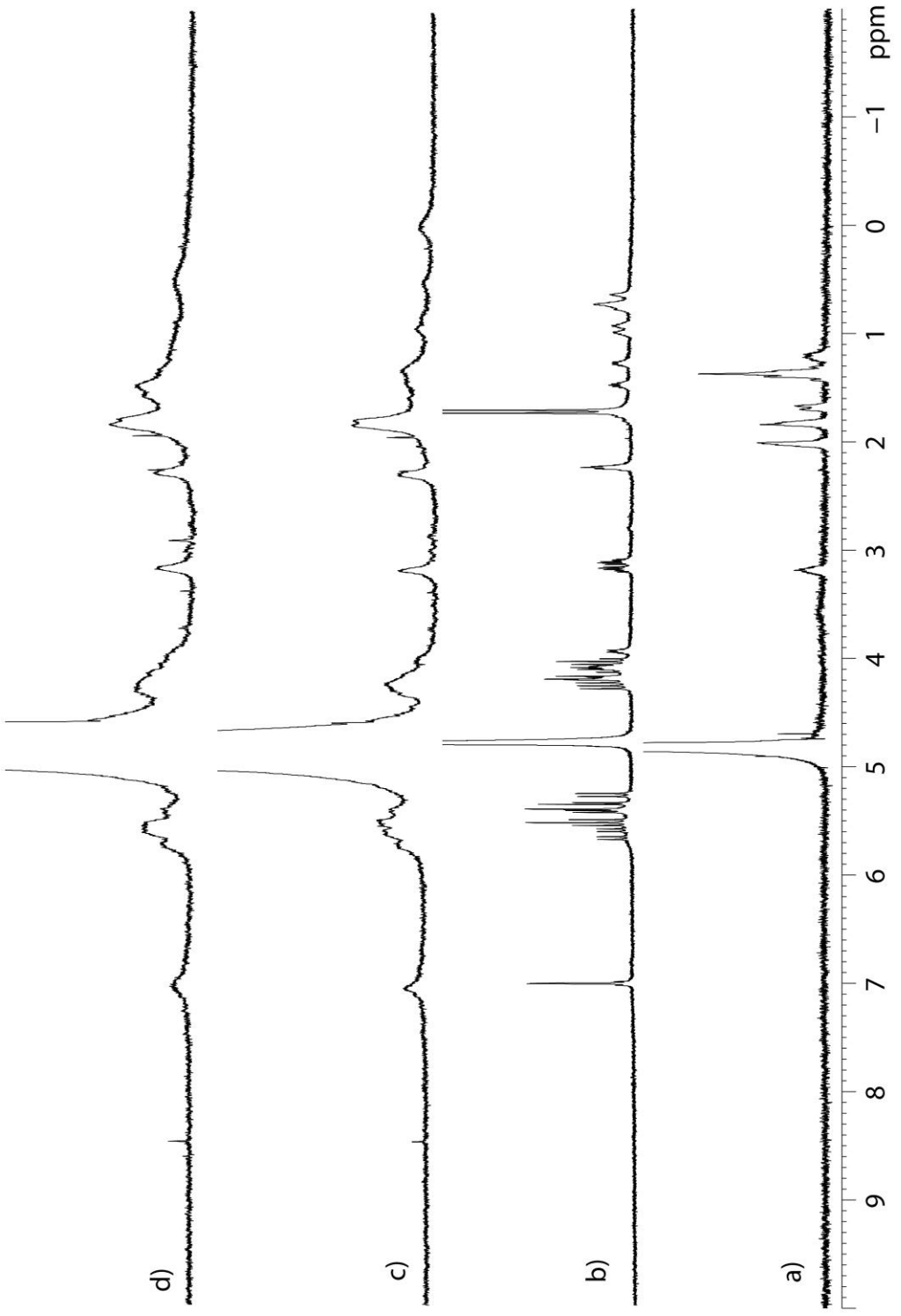

Figure IV-S26. ^{1}H NMR spectra recorded (400 MHz, RT, D_2O) for a) **IV-7**, b) **IV-2c**, c) an equimolar mixture of **IV-7** and **IV-2c** (1 mM), and d) a 2:1 mixture of **IV-7** (2 mM) and **IV-2c** (1 mM).

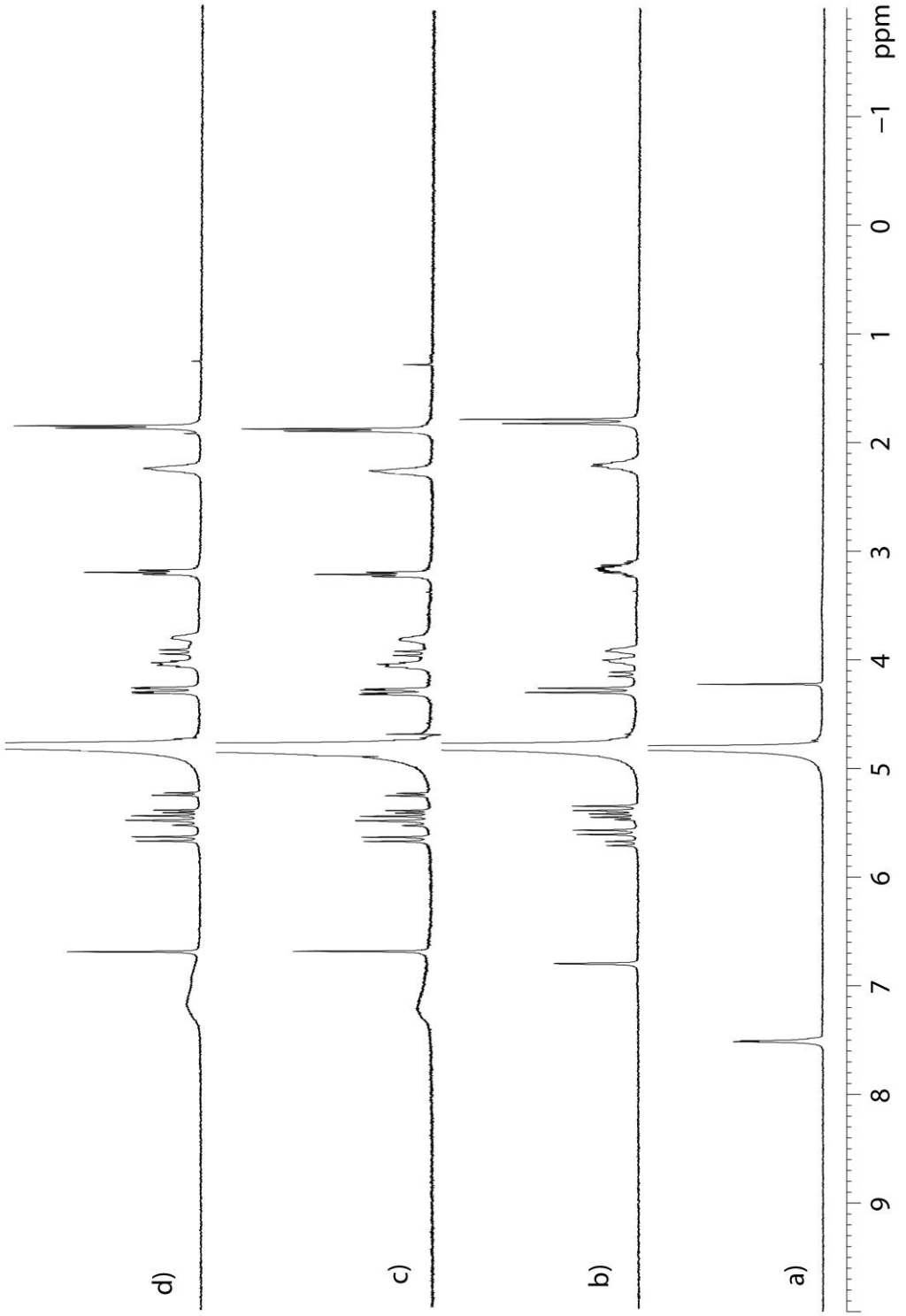

Figure IV-S27. ^{1}H NMR spectra recorded (400 MHz, RT, D_2O) for a) **IV-8**, b) **IV-1**, c) an equimolar mixture of **IV-8** and **IV-1** (1 mM), and d) a 2:1 mixture of **IV-8** (2 mM) and **IV-1** (1 mM).

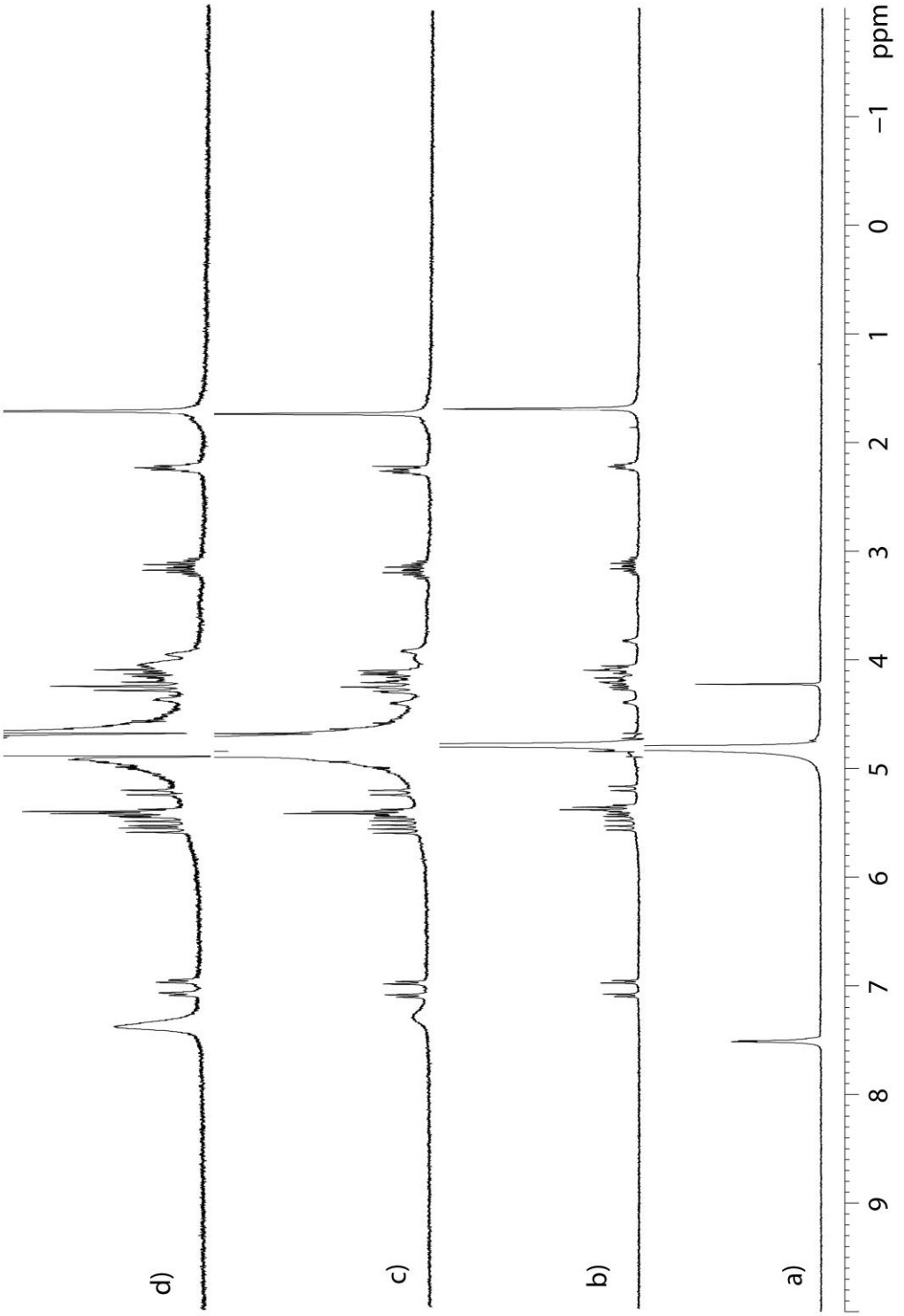

Figure IV-S28. ^{1}H NMR spectra recorded (400 MHz, RT, D_2O) for a) **IV-8**, b) **IV-2a**, c) an equimolar mixture of **IV-8** and **IV-2a** (0.5 mM), and d) a 2:1 mixture of **IV-8** (1 mM) and **IV-2a** (0.5 mM).

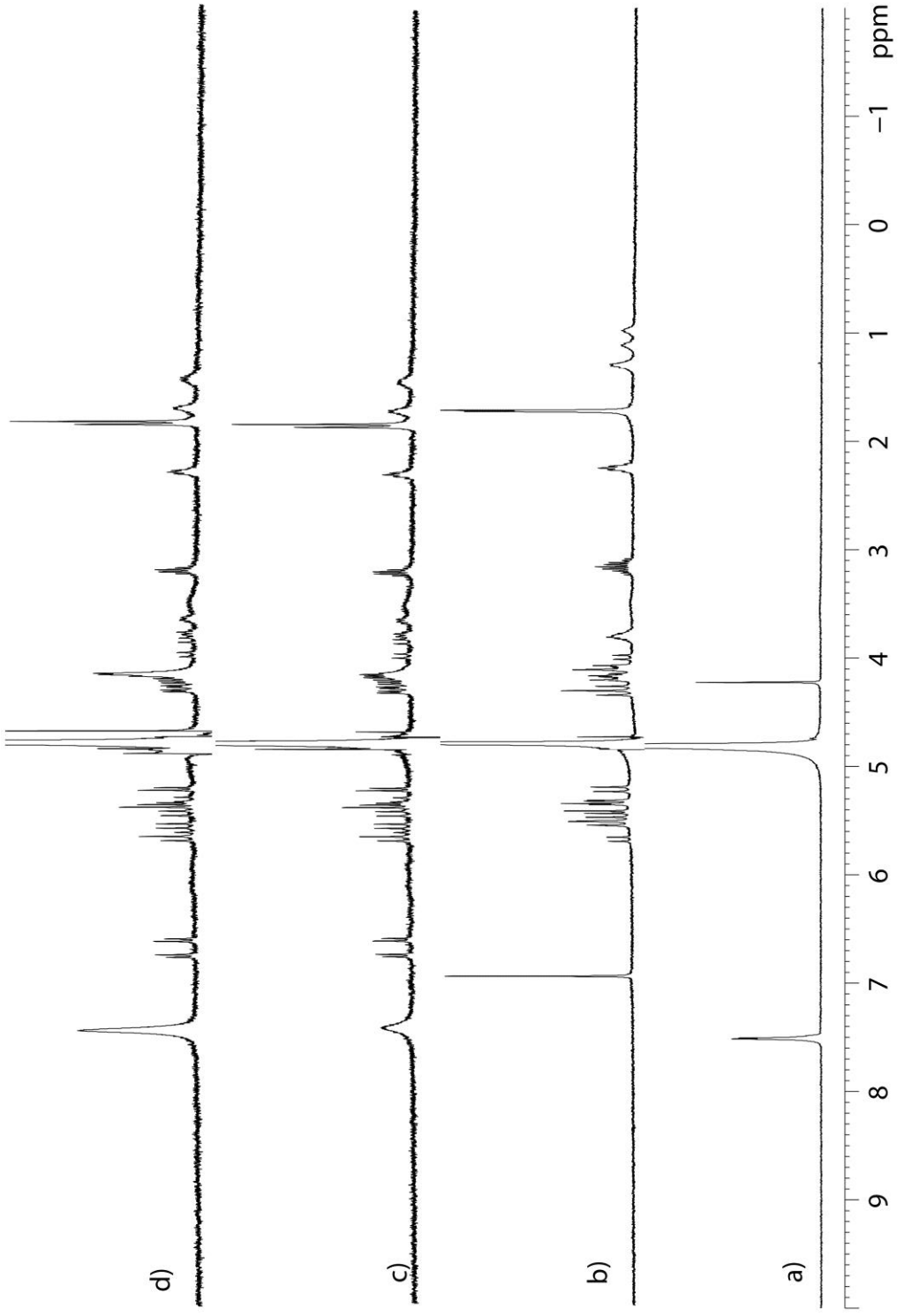

Figure IV-S29. ^{1}H NMR spectra recorded (400 MHz, RT, D_2O) for a) **IV-8**, b) **IV-2b**, c) an equimolar mixture of **IV-8** and **IV-2b** (0.5 mM), and d) a 2:1 mixture of **IV-8** (1 mM) and **IV-2b** (0.5 mM).

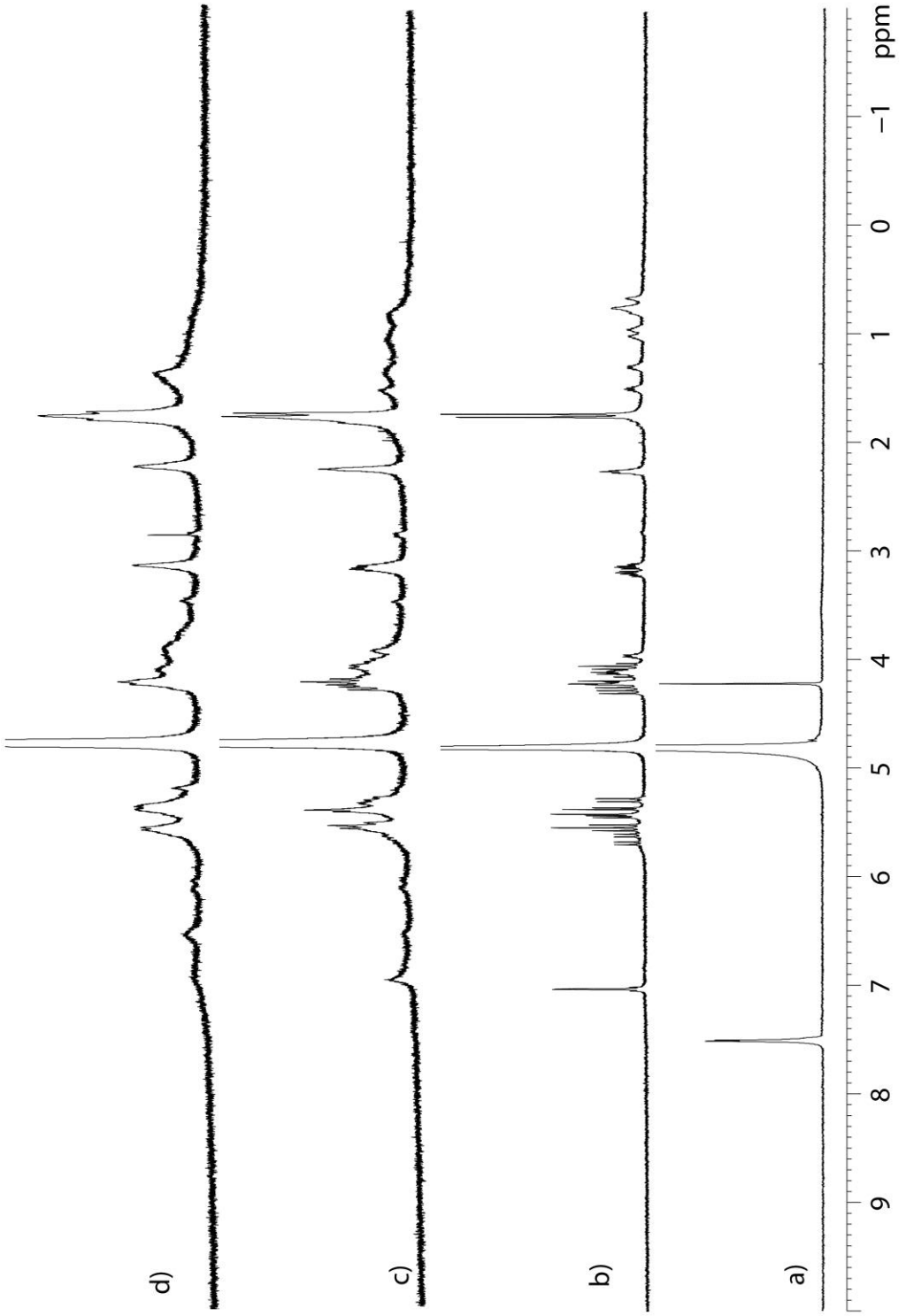

Figure IV-S30. ^{1}H NMR spectra recorded (400 MHz, RT, D_2O) for a) **IV-8**, b) **IV-2c**, c) an equimolar mixture of **IV-8** and **IV-2c** (0.3 mM), and d) a 2:1 mixture of **IV-8** (0.6 mM) and **IV-2c** (0.3 mM).

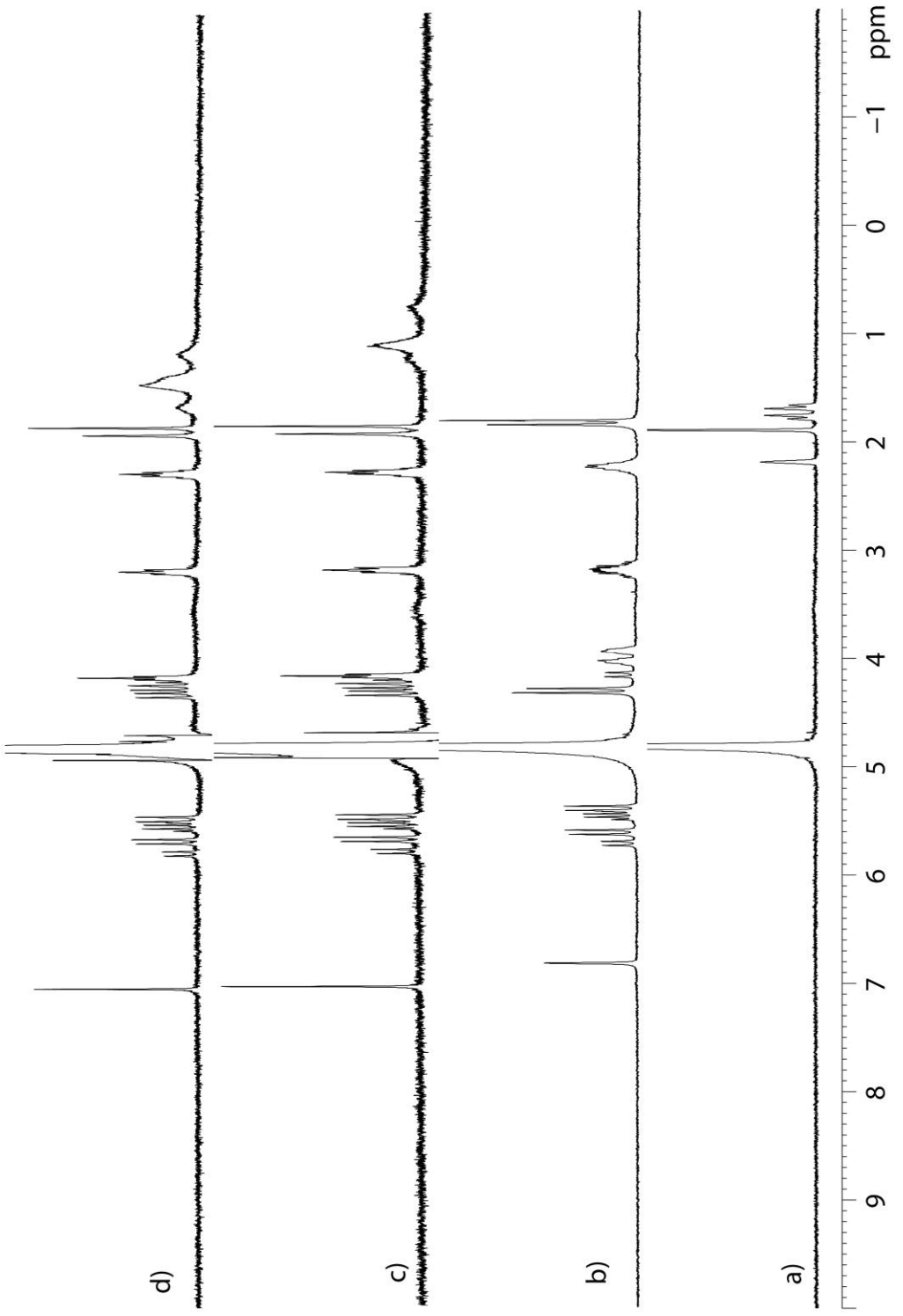

Figure IV-S31. ^{1}H NMR spectra recorded (400 MHz, RT, D_2O) for a) **IV-9**, b) **IV-1**, c) an equimolar mixture of **IV-9** and **IV-1** (0.5 mM), and d) a 2:1 mixture of **IV-9** (1.0 mM) and **IV-1** (0.5 mM).

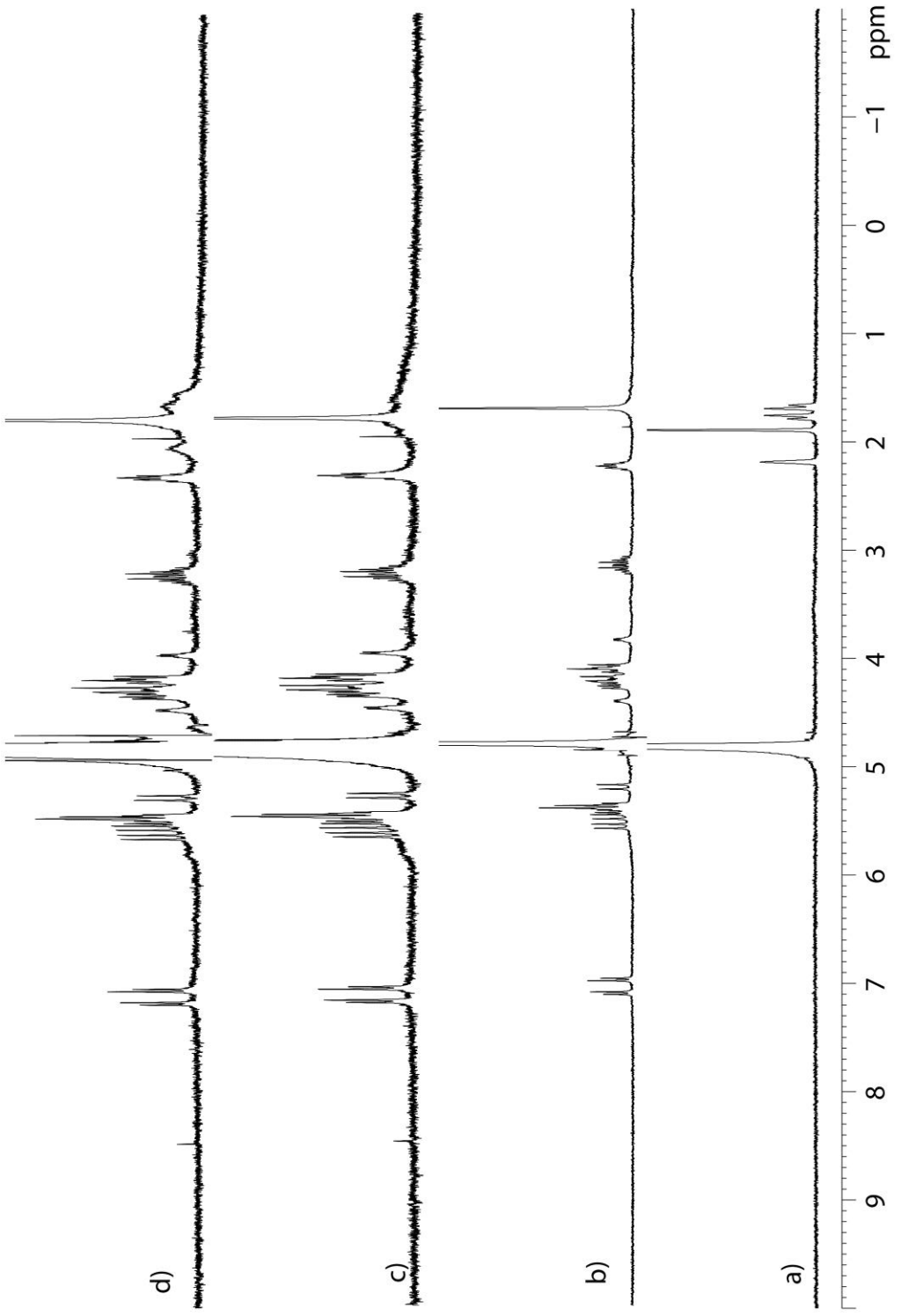

Figure IV-S32. ^{1}H NMR spectra recorded (400 MHz, RT, D_2O) for a) **IV-9**, b) **IV-2a**, c) an equimolar mixture of **IV-9** and **IV-2a** (0.5 mM), and d) a 2:1 mixture of **IV-9** (1.0 mM) and **IV-2a** (0.5 mM).

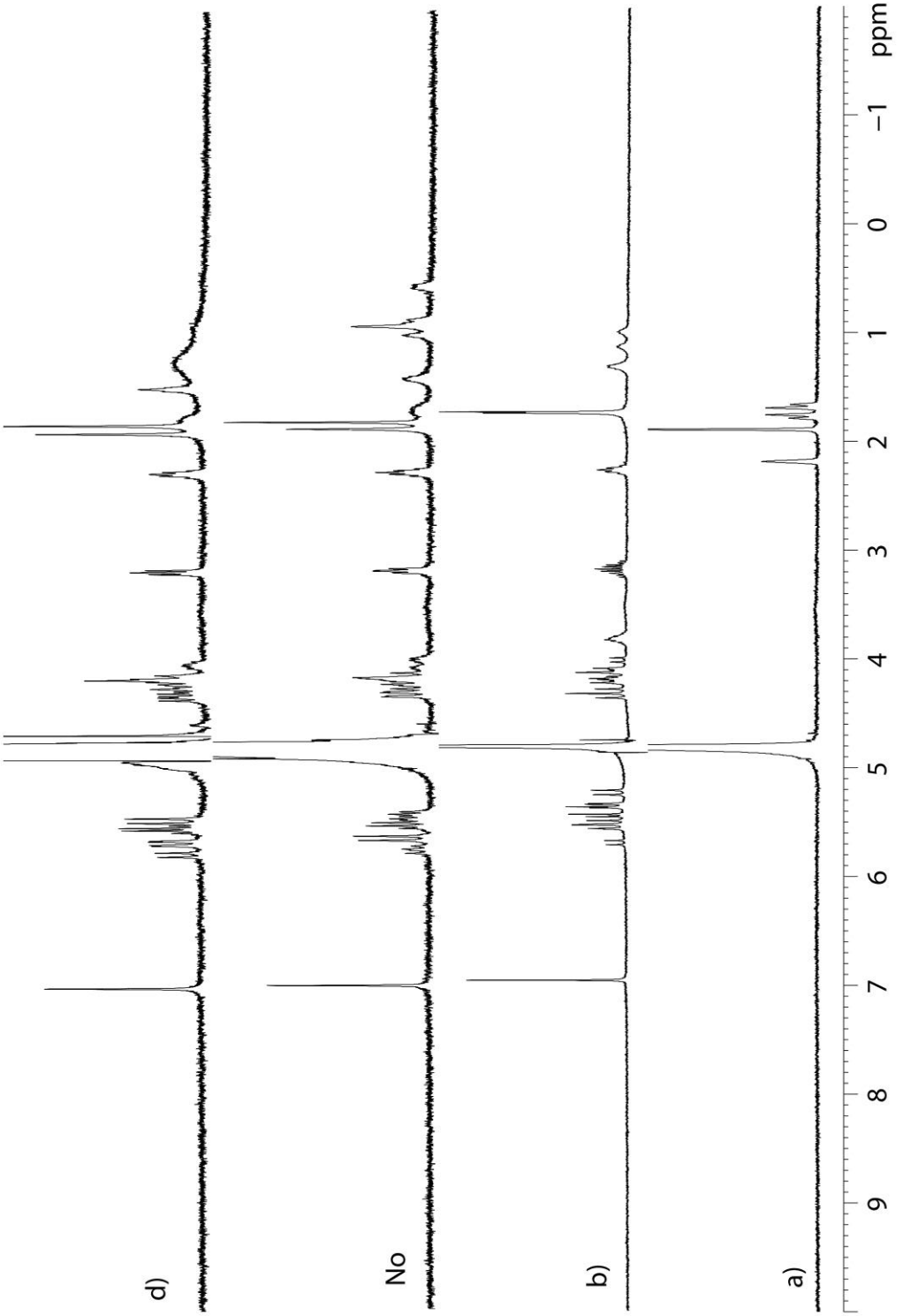

Figure IV-S33. ^{1}H NMR spectra recorded (400 MHz, RT, D_2O) for a) **IV-9**, b) **IV-2b**, c) an equimolar mixture of **IV-9** and **IV-2b** (0.5 mM), and d) a 2:1 mixture of **IV-9** (1.0 mM) and **IV-2b** (0.5 mM).

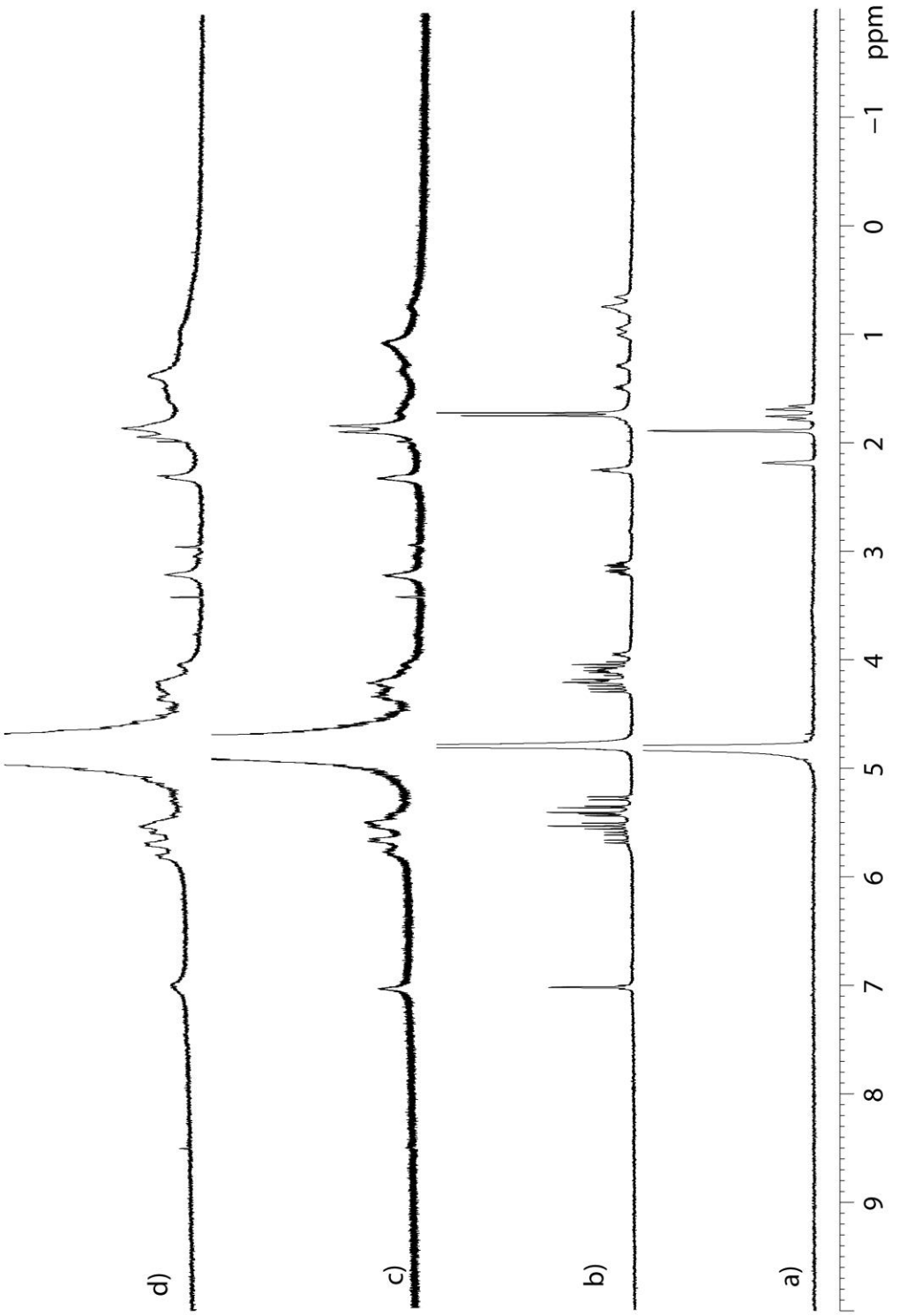

Figure IV-S34. ^{1}H NMR spectra recorded (600 MHz, RT, D_2O) for a) **IV-9**, b) **IV-2c**, c) an equimolar mixture of **IV-9** and **IV-2c** (0.25 mM), and d) a 2:1 mixture of **IV-9** (0.5 mM) and **IV-2c** (0.25 mM).

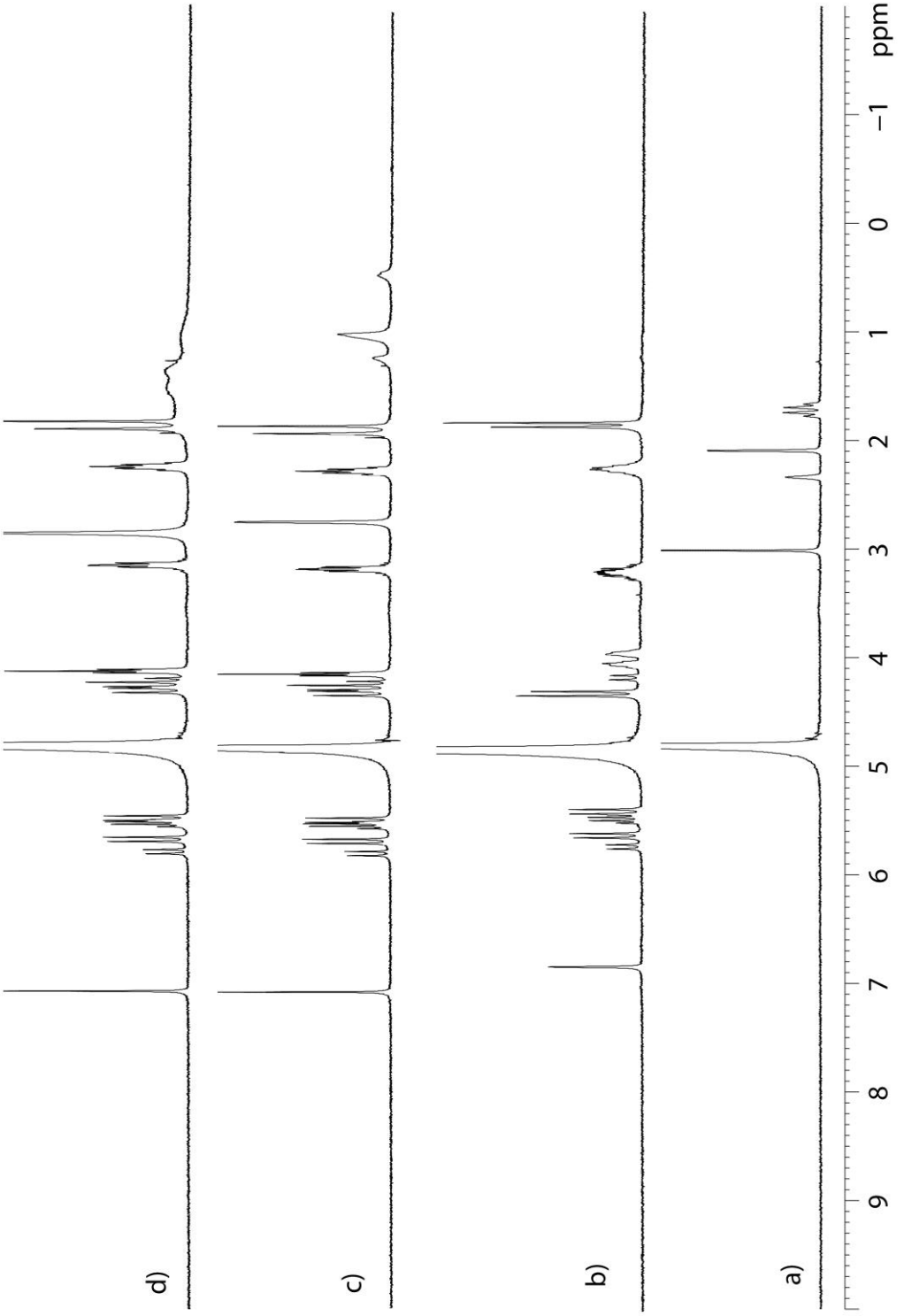

Figure IV-S35. ^{1}H NMR spectra recorded (400 MHz, RT, D_2O) for a) **IV-10**, b) **IV-1**, c) an equimolar mixture of **IV-10** and **IV-1** (1 mM), and d) a 2:1 mixture of **IV-10** (2 mM) and **IV-1**(1 mM).

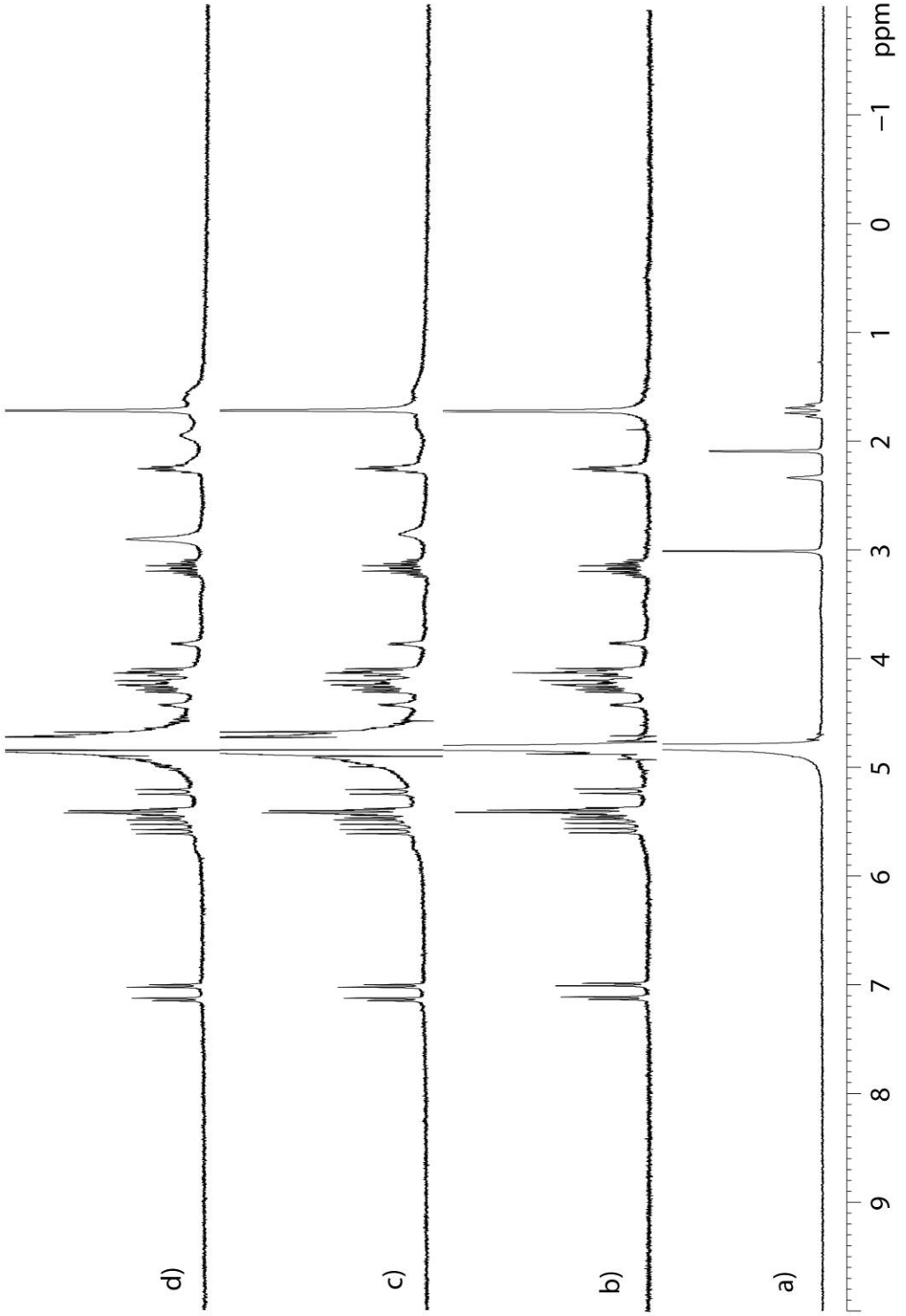

Figure IV-S36. ^{1}H NMR spectra recorded (400 MHz, RT, D_2O) for a) **IV-10**, b) **IV-2a**, c) an equimolar mixture of **IV-10** and **IV-2a** (0.5 mM), and d) a 2:1 mixture of **IV-10** (1 mM) and **IV-2a** (0.5 mM).

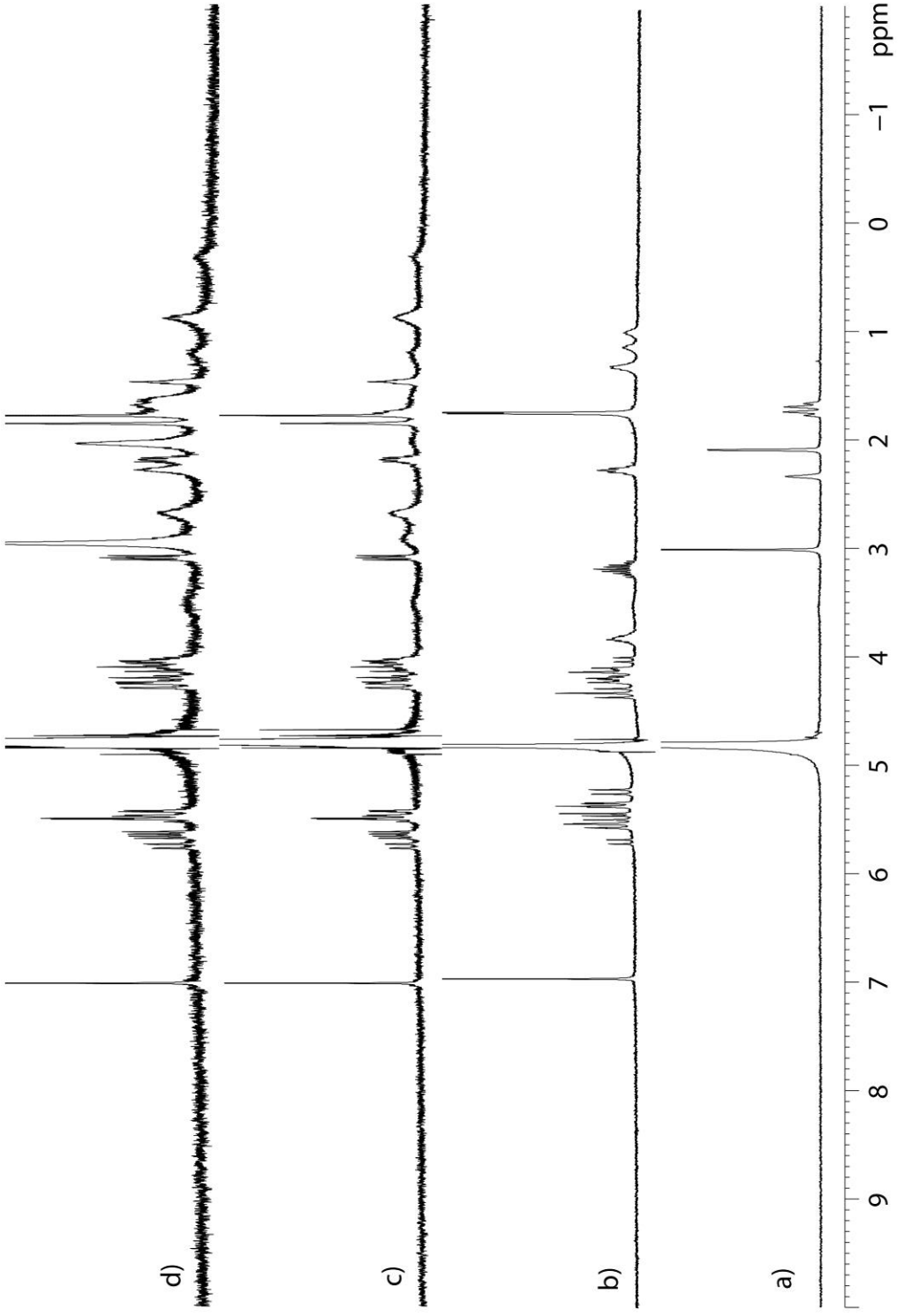

Figure IV-S37. ^{1}H NMR spectra recorded (400 MHz, RT, D_2O) for a) **IV-10**, b) **IV-2b**, c) an equimolar mixture of **IV-10** and **IV-2b** (0.5 mM), and d) a 2:1 mixture of **IV-10** (1 mM) and **IV-2b** (0.5 mM).

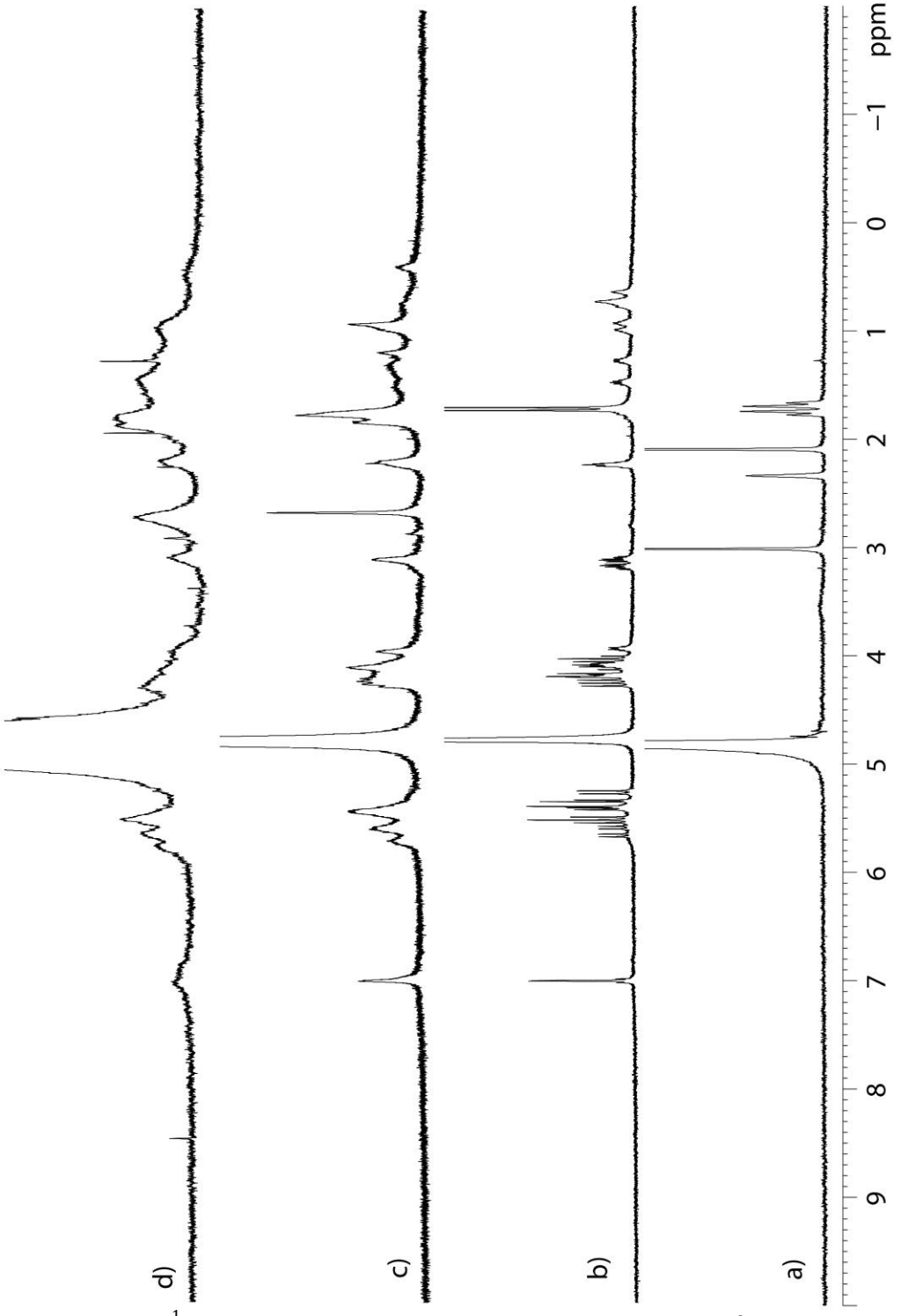

Figure IV-S38. ^{1}H NMR spectra recorded (400 MHz, RT, D_2O) for a) **IV-10**, b) **IV-2c**, c) an equimolar mixture of **IV-10** and **IV-2c** (1 mM), and d) a 2:1 mixture of **IV-10** (2 mM) and **IV-2c** (1 mM).

Determination of K_a between various hosts guests using Isothermal Titration Calorimetry (ITC).

All ITC experiments were conducted in the 200 μL working volume of the sample cell of the PEAQ ITC instrument. We used an injection syringe of 40 μL capacity. In each case, the host and guest solutions were prepared in a 20 mM NaH_2PO_4 buffer (pH 7.4). The sample cell was filled to capacity (200 μL) with the host solution and the guest solution was titrated in (first injection = 0.4μL, subsequent 18 injections = 2 μL). In case of Figures IV-S40, IV-S42, IV-S48 and IV-S56 two sets of 19 injections were concatenated to obtain the binding isotherm. In case of Figure IV-S50 the first set of 19 injections was followed by an additional 26.4 μL of titrant added over 10 injections and these 29 injections were concatenated to obtain the binding isotherm. The binding data was fitted using the 1:1 binding model in MicroCal PEAQ-ITC analysis software.

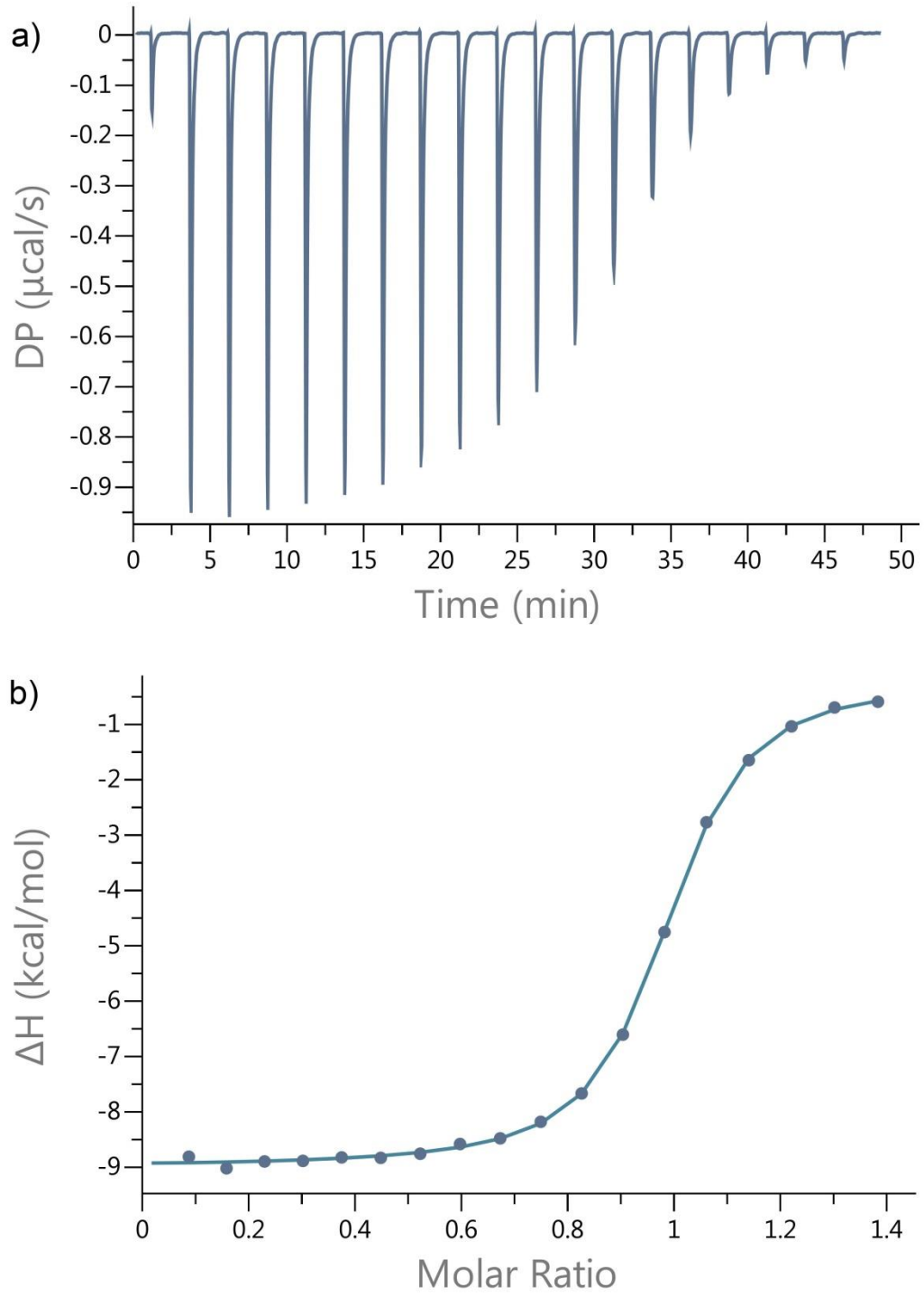

Figure IV-S39. a) Plot of DP vs time from the titration of **IV-1** (70.5 µM) with guest **IV-6** (0.507 mM) in 20 mM NaH_2PO_4 buffer (pH 7.4); b) plot of the ΔH as a function of molar ratio. The solid line represents the best non-linear fit of the data to a 1:1 binding model (K_a = (2.4 ± 0.1) × 10^6 M^{-1}, ΔH = - 8.7 ± 0.05 kcal/mol, N = 0.95).

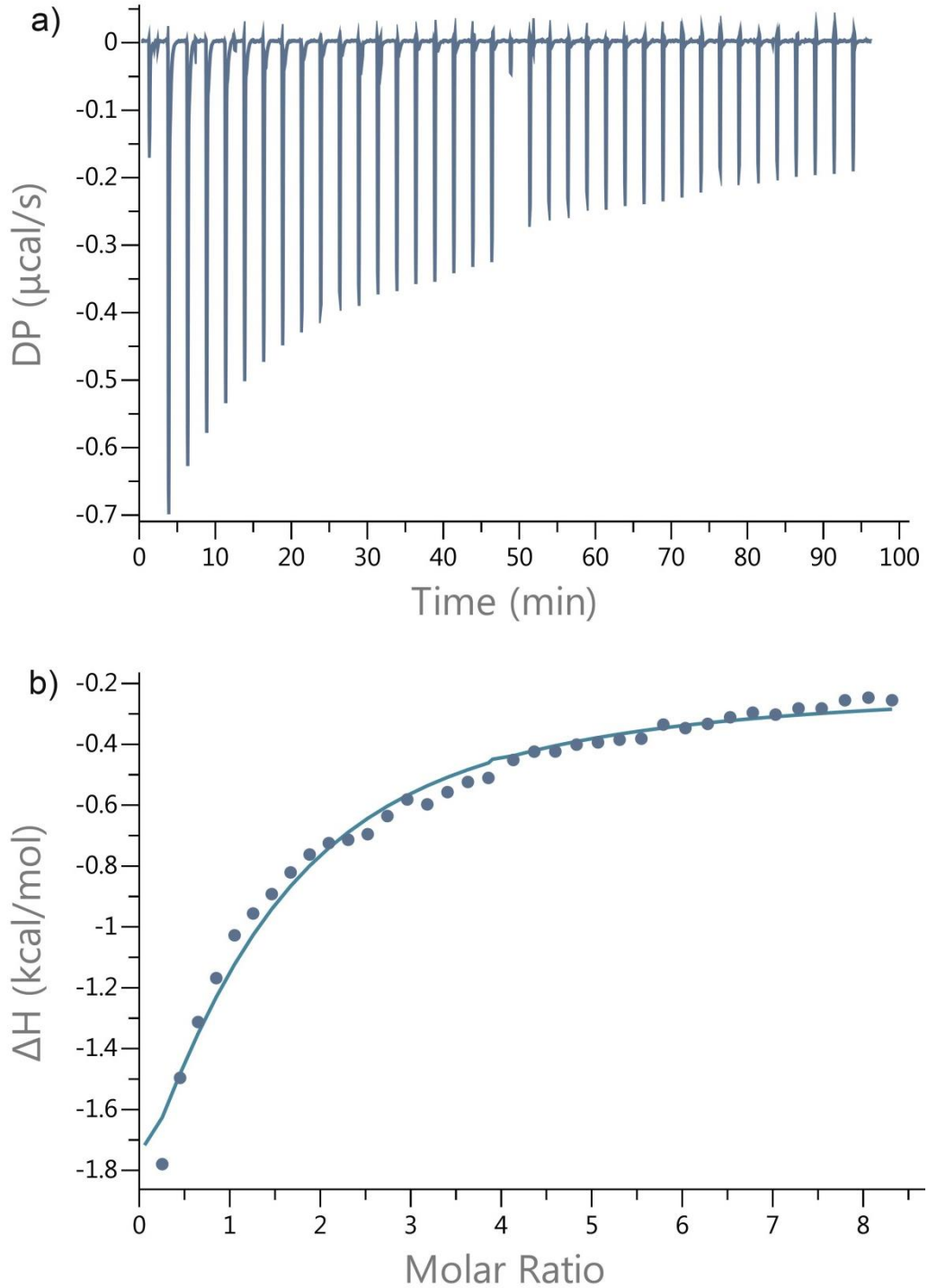

Figure IV-S40. a) Plot of DP vs time from the titration of **IV-2a** (100 µM) with guest **IV-6** (2.00 mM) in 20 mM NaH_2PO_4 buffer (pH 7.4); b) plot of the ΔH as a function of molar ratio. The solid line represents the best non-linear fit of the data to a 1:1 binding model (K_a = (6.2 ± 0.9) × 10^3 M^{-1}, ΔH = - 3.94 ± 0.35 kcal/mol, N = 1.00).

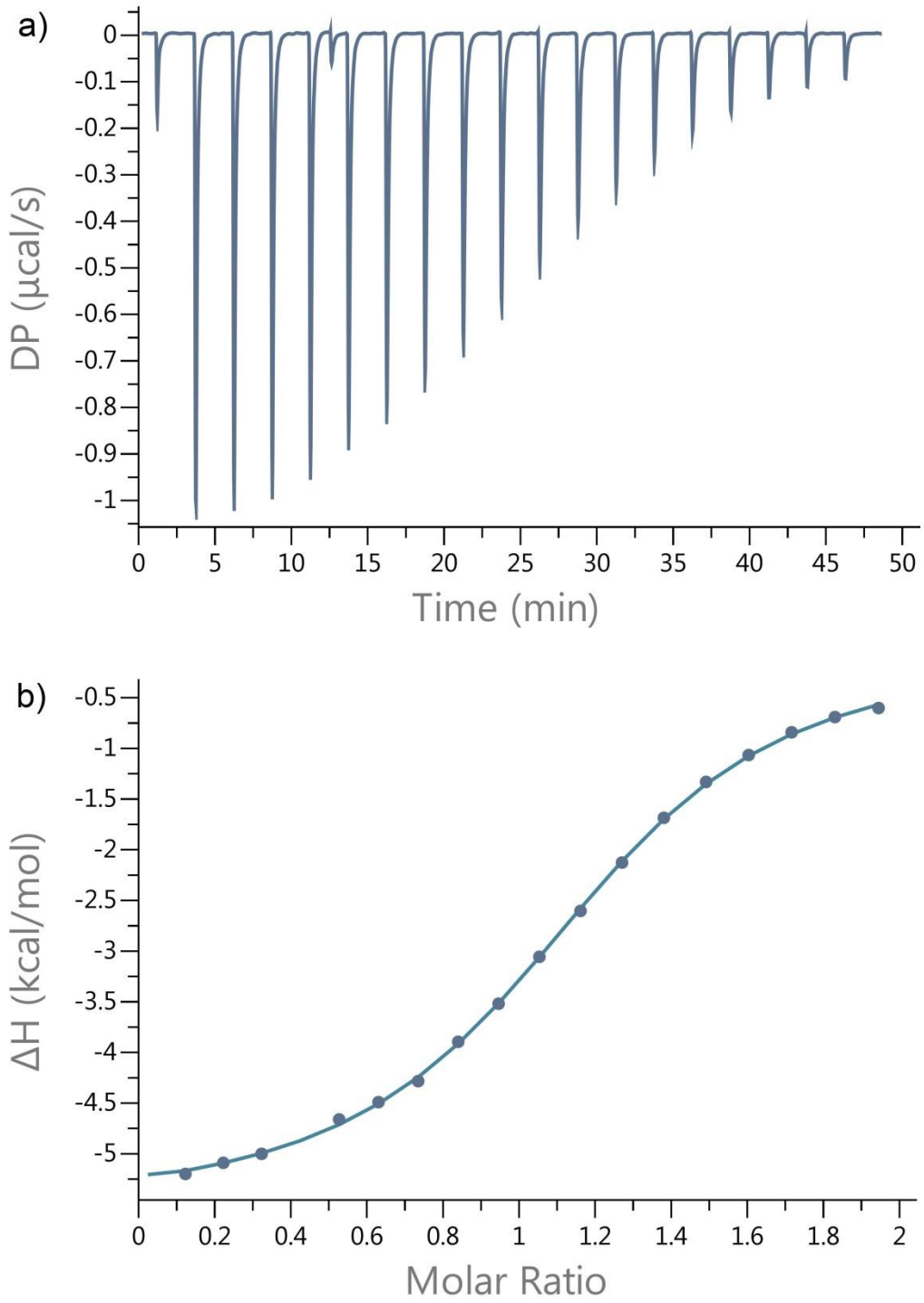

Figure IV-S41. a) Plot of DP vs time from the titration of **IV-2b** (0.1 mM) with guest **IV-6** (1.0 mM) in 20 mM NaH_2PO_4 buffer (pH 7.4); b) plot of the ΔH as a function of molar ratio. The solid line represents the best non-linear fit of the data to a 1:1 binding model (K_a = (1.3 ± 0.05) × 10^5 M^{-1}, ΔH = - 5.5 ± 0.06 kcal/mol, N = 1.16).

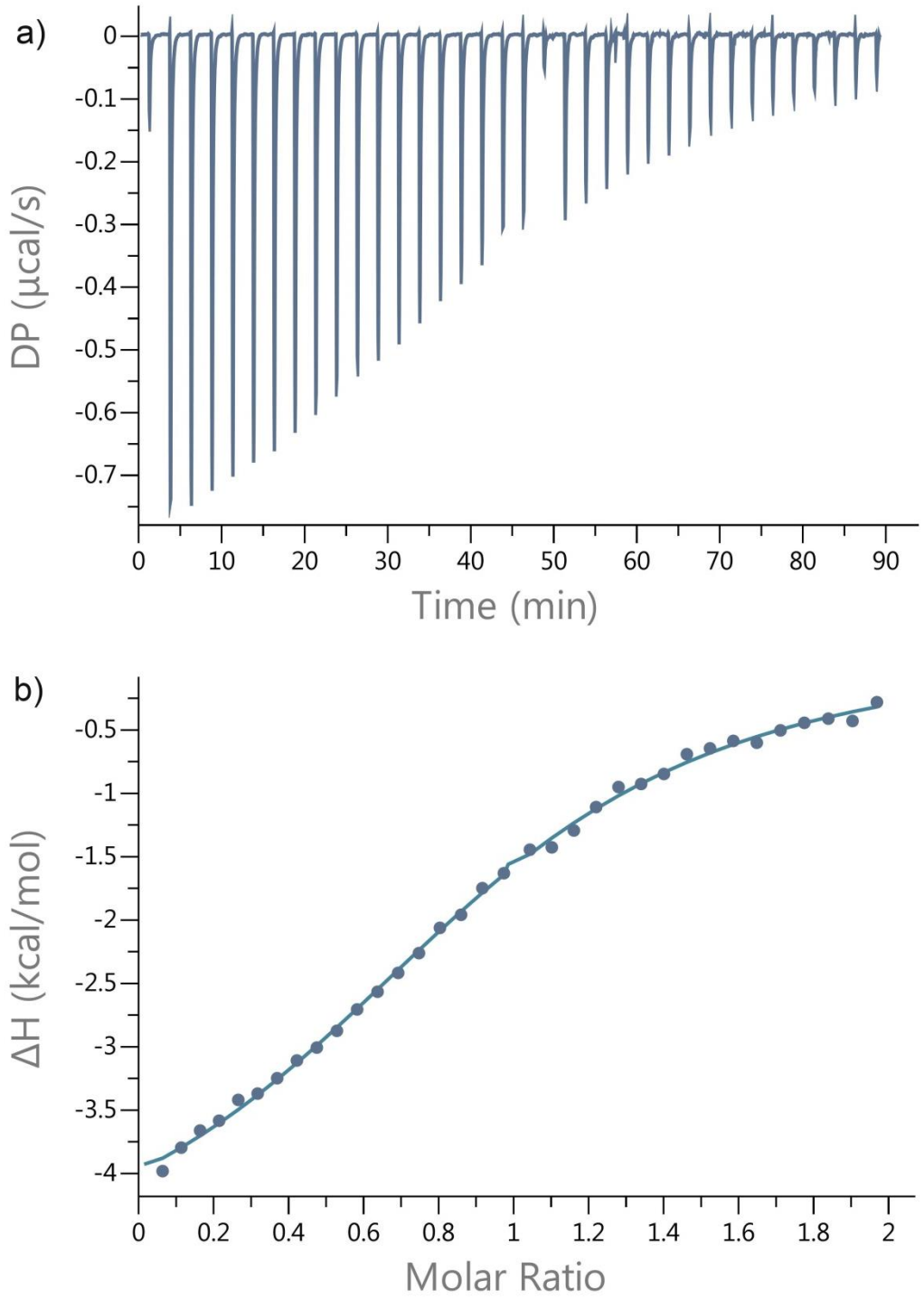

Figure IV-S42. a) Plot of DP vs time from the titration of **IV-2c** (0.2 mM) with guest **IV-6** (1.01 mM) in 20 mM NaH_2PO_4 buffer (pH 7.4); b) plot of the ΔH as a function of molar ratio. The solid line represents the best non-linear fit of the data to a 1:1 binding model ($K_a = (2.3 \pm 0.2) \times 10^4$, ΔH = - 4.98 ± 0.16 kcal/mol, N = 0.97).

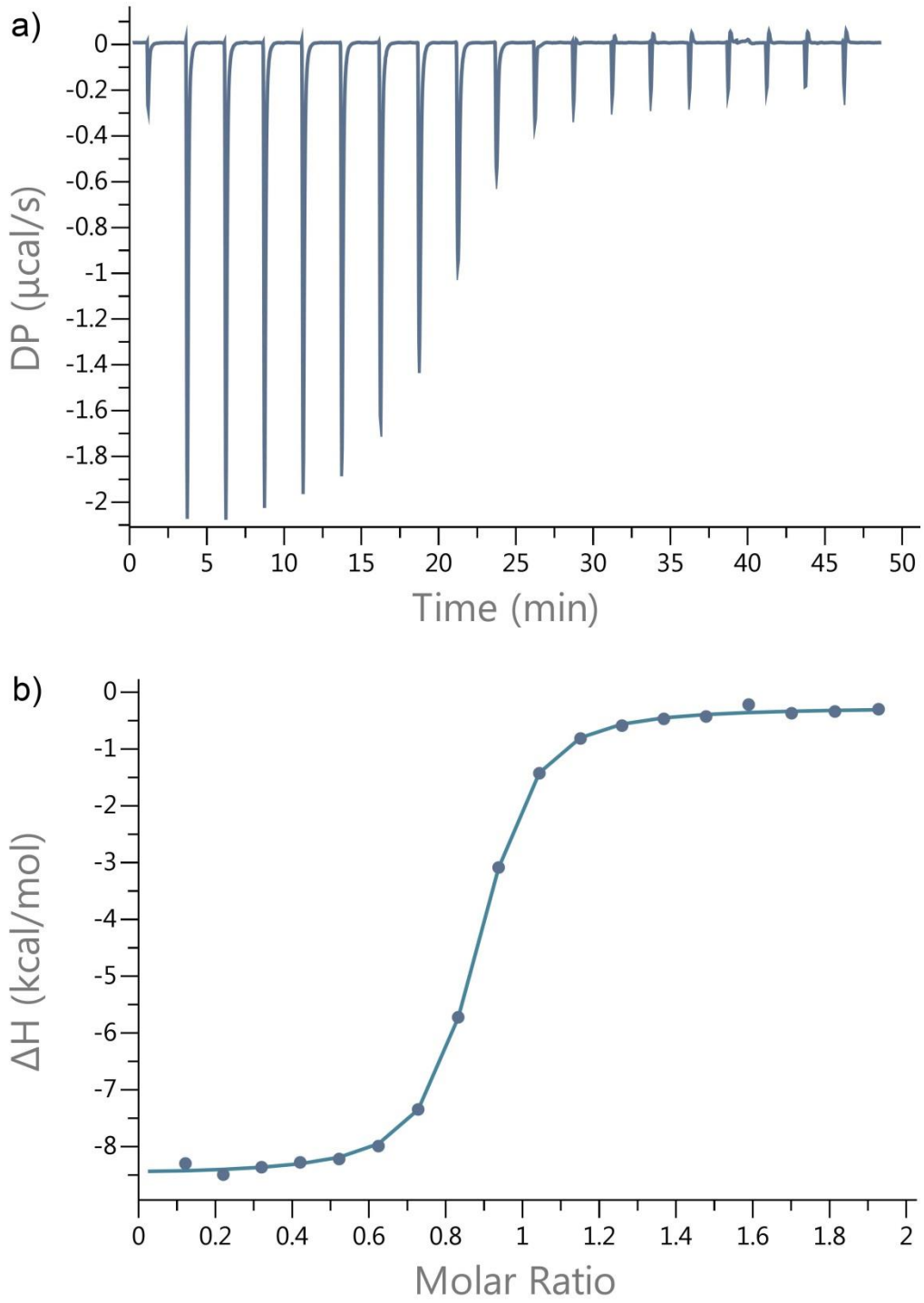

Figure IV-S43. a) Plot of DP vs time from the titration of **IV-1** (0.1 mM) with guest **IV-7** (1.0 mM) in 20 mM NaH_2PO_4 buffer (pH 7.4); b) plot of the ΔH as a function of molar ratio. The solid line represents the best non-linear fit of the data to a 1:1 binding model ($K_a = (1.7 \pm 0.1) \times 10^6$ M^{-1}, ΔH = - 8.2 ± 0.04 kcal/mol, N = 0.84).

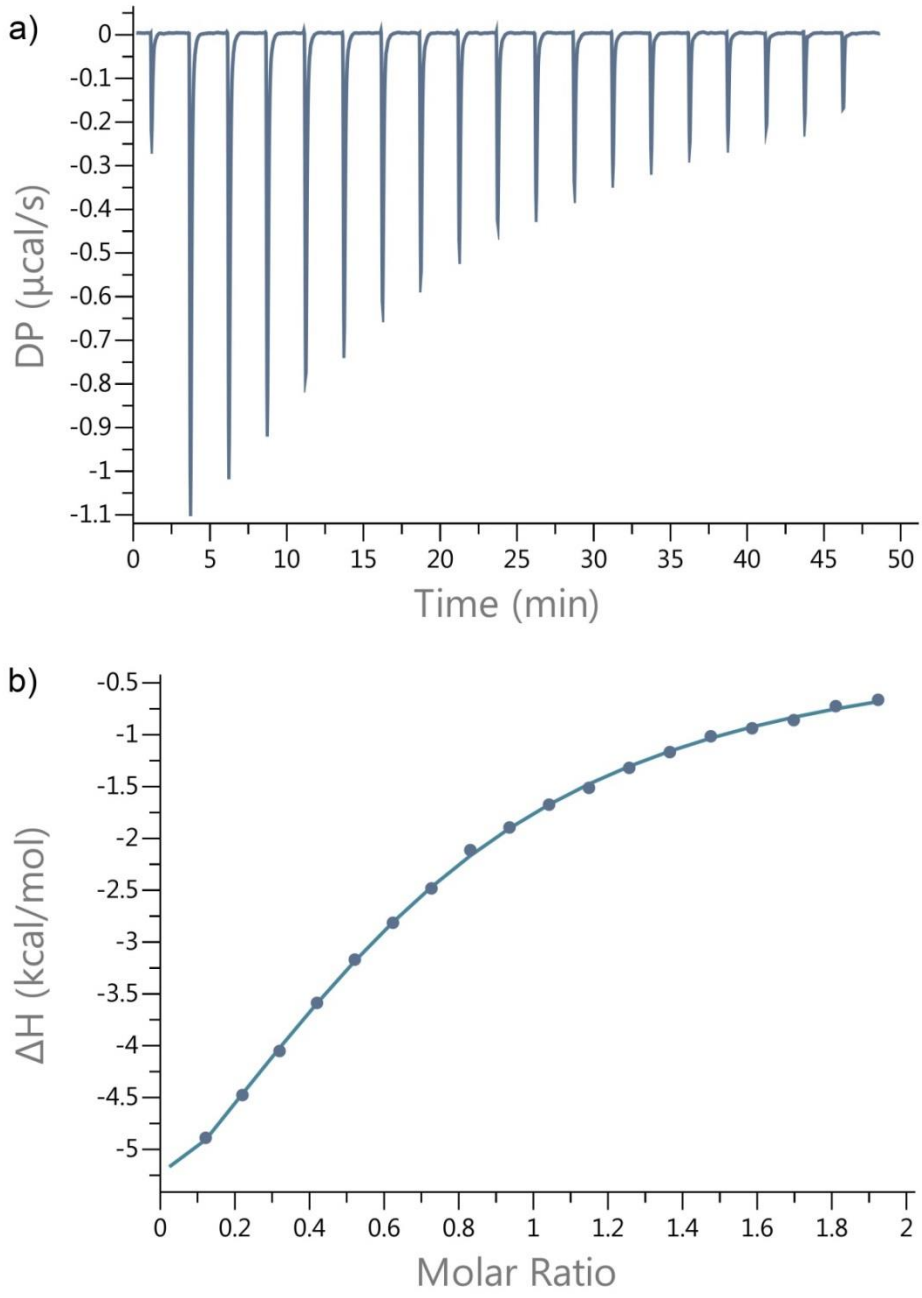

Figure IV-S44. a) Plot of DP vs time from the titration of **IV-2a** (0.1 mM) with guest **IV-7** (1.0 mM) in 20 mM NaH_2PO_4 buffer (pH 7.4); b) plot of the ΔH as a function of molar ratio. The solid line represents the best non-linear fit of the data to a 1:1 binding model ($K_a = (2.3 \pm 0.2) \times 10^4\ M^{-1}$, ΔH = - 8.7 ± 0.5 kcal/mol, N = 0.62).

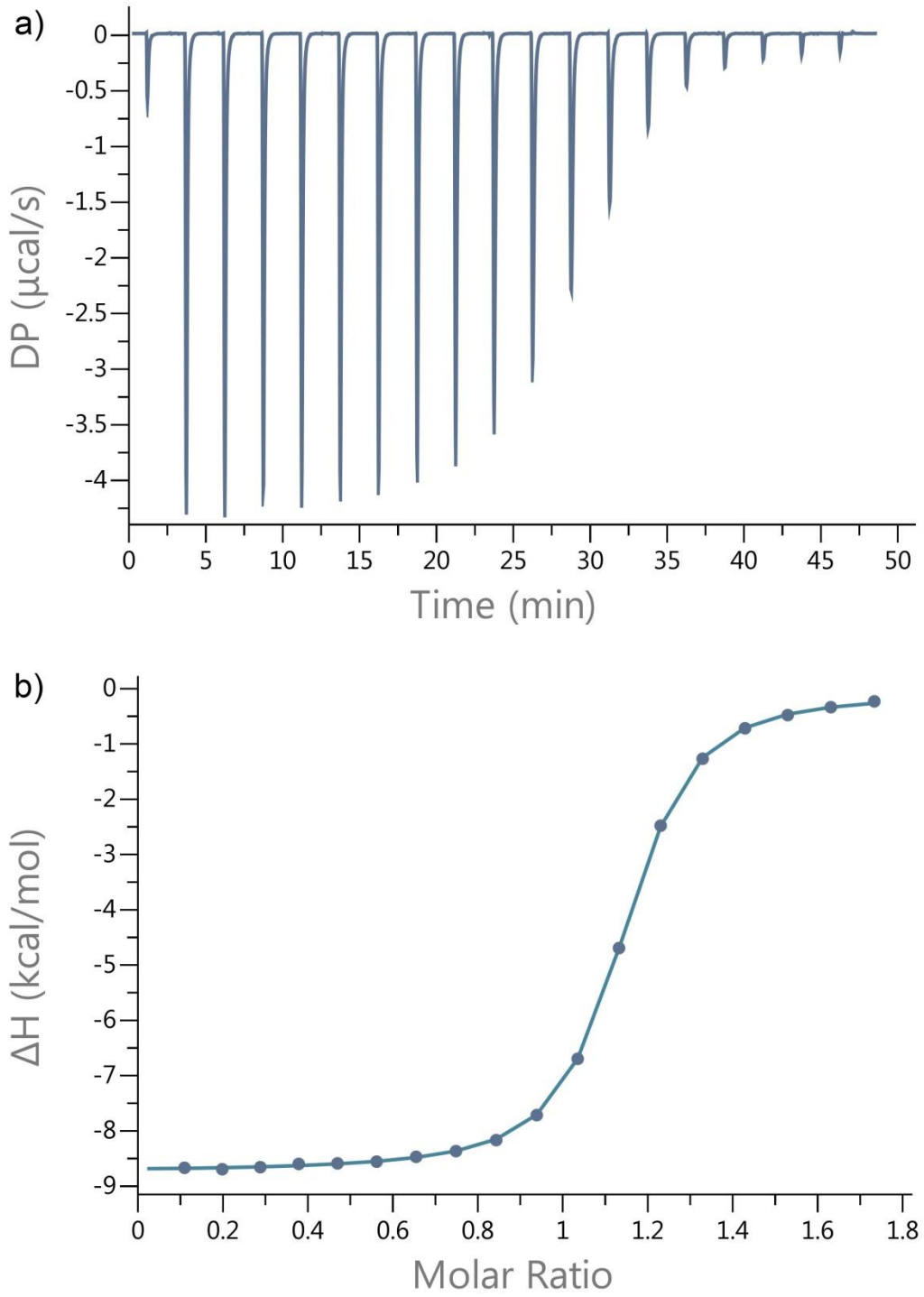

Figure IV-S45. a) Plot of DP vs time from the titration of **IV-2b** (0.2 mM) with guest **IV-7** (2.0 mM) in 20 mM NaH_2PO_4 buffer (pH 7.4); b) plot of the ΔH as a function of molar ratio. The solid line represents the best non-linear fit of the data to a 1:1 binding model (K_a = (7.9 ± 0.1) × 10^5 M^{-1}, ΔH = - 8.62 ± 0.02 kcal/mol, N = 1.10).

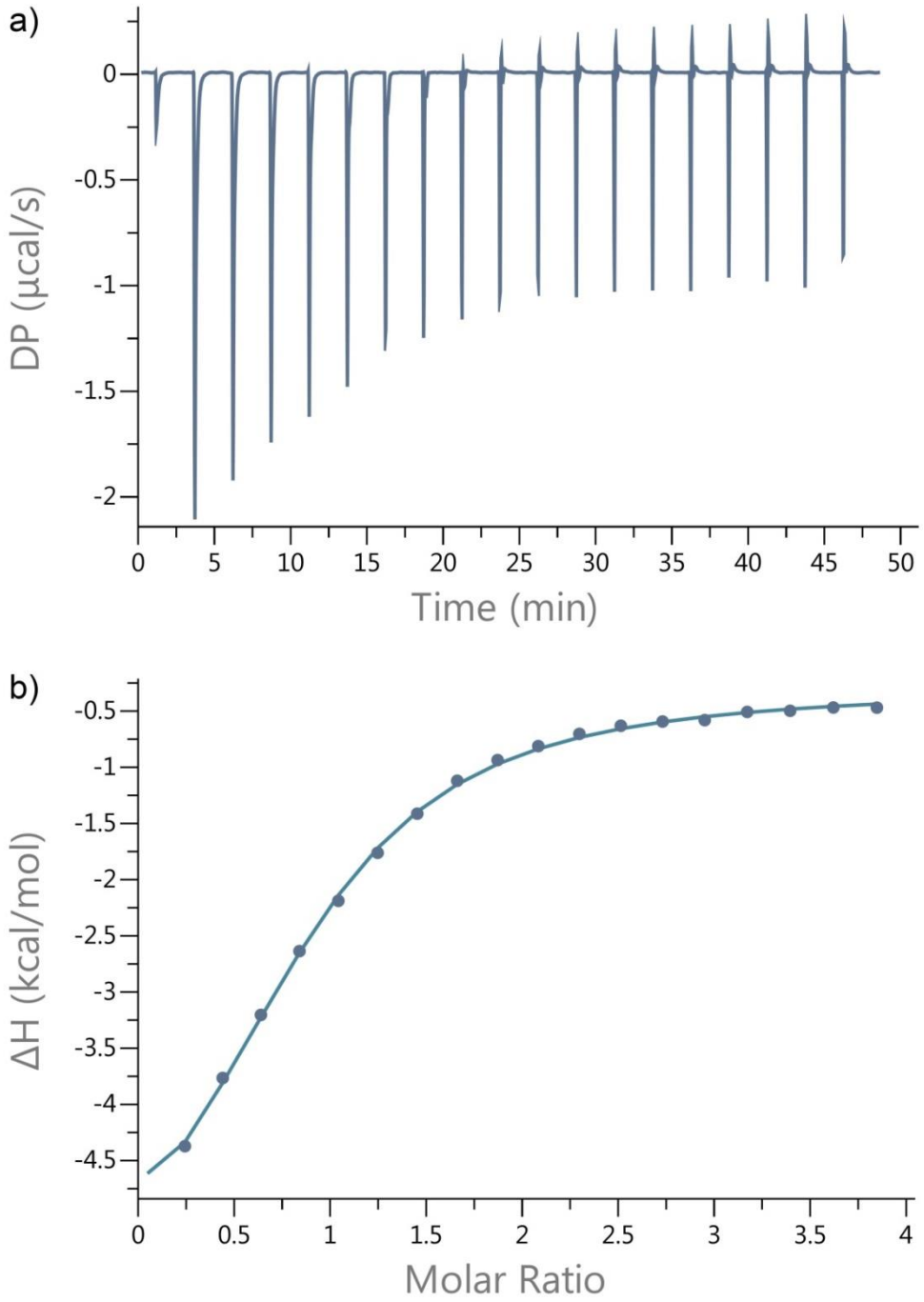

Figure IV-S46. a) Plot of DP vs time from the titration of **IV-2c** (0.1 mM) with guest **IV-7** (2.0 mM) in 20 mM NaH_2PO_4 buffer (pH 7.4); b) plot of the ΔH as a function of molar ratio. The solid line represents the best non-linear fit of the data to a 1:1 binding model ($K_a = (3.2 \pm 0.3) \times 10^4\ M^{-1}$, $\Delta H = -6.0 \pm 0.23$ kcal/mol, N = 0.84).

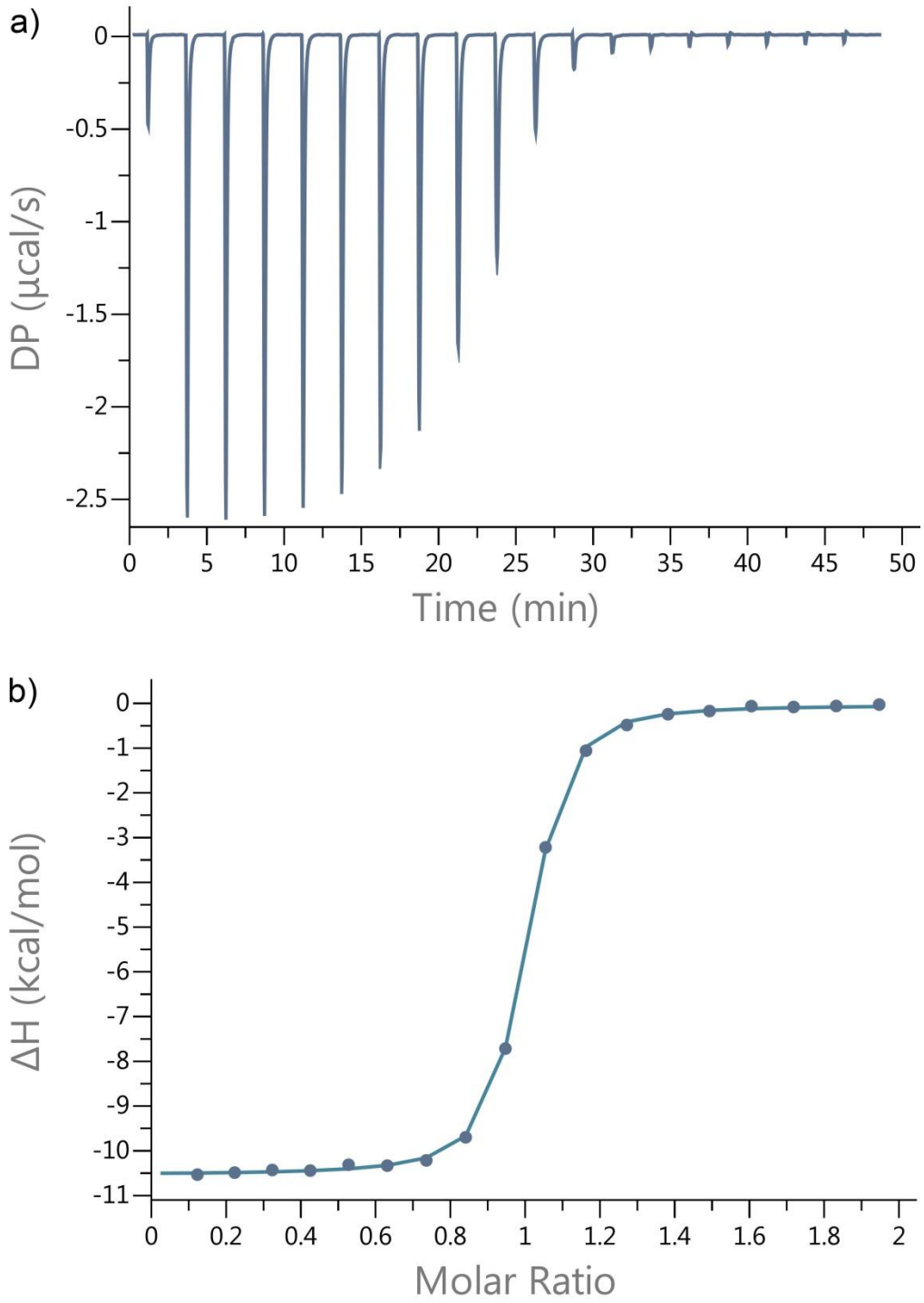

Figure IV-S47. a) Plot of DP vs time from the titration of **IV-1** (0.1 mM) with guest **IV-8** (1.0 mM) in 20 mM NaH_2PO_4 buffer (pH 7.4); b) plot of the ΔH as a function of molar ratio. The solid line represents the best non-linear fit of the data to a 1:1 binding model (K_a = (3.9± 0.2) × 10^6 M^{-1}, ΔH = - 10.5 ± 0.03 kcal/mol, N = 0.95).

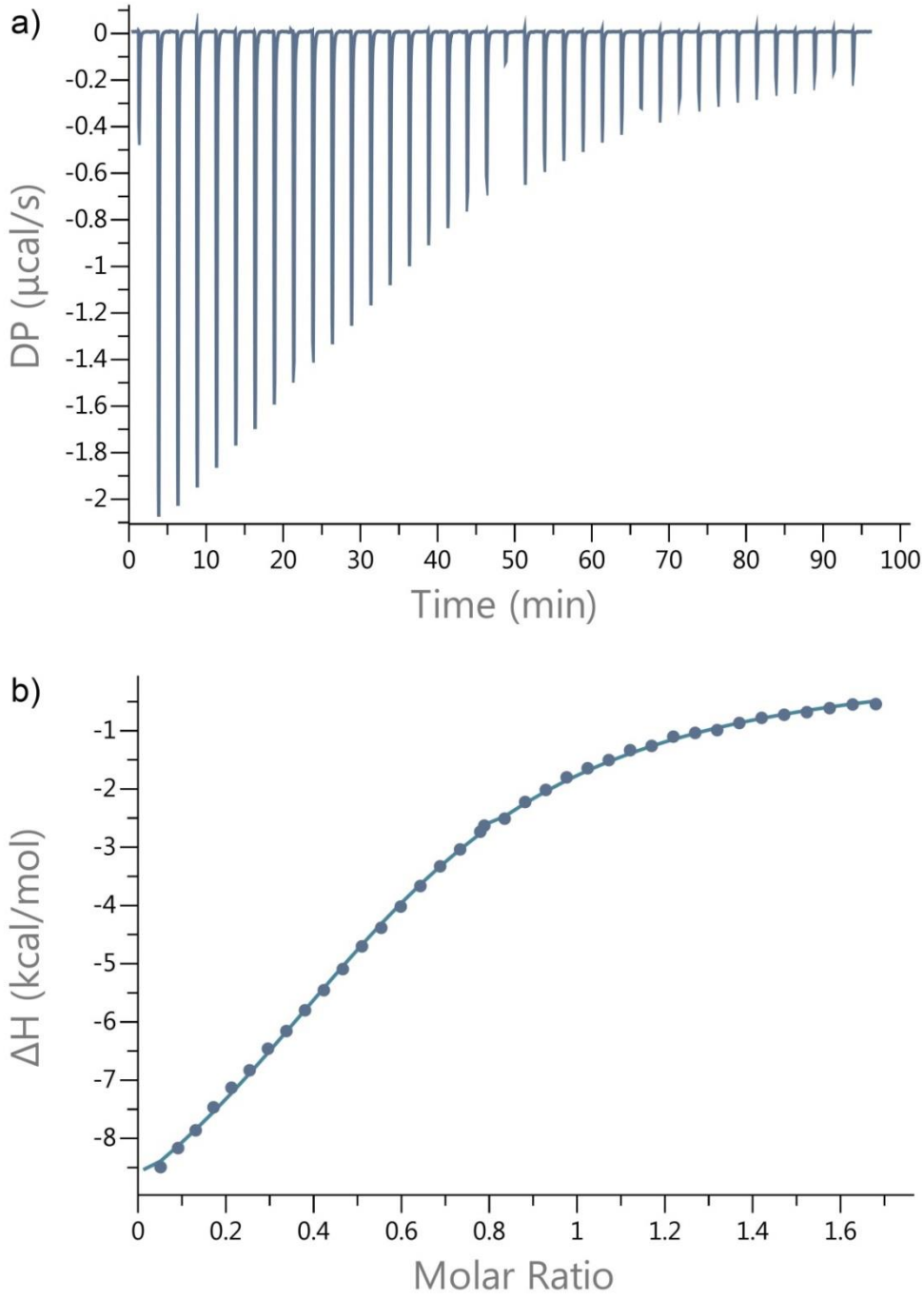

Figure IV-S48. a) Plot of DP vs time from the titration of **IV-2a** (0.25 mM) with guest **IV-8** (1.0 mM) in 20 mM NaH_2PO_4 buffer (pH 7.4); b) plot of the ΔH as a function of molar ratio. The solid line represents the best non-linear fit of the data to a 1:1 binding model ($K_a = (2.1 \pm 0.1) \times 10^4$ M^{-1}, ΔH = - 11.3 ± 0.19 kcal/mol, N = 0.61).

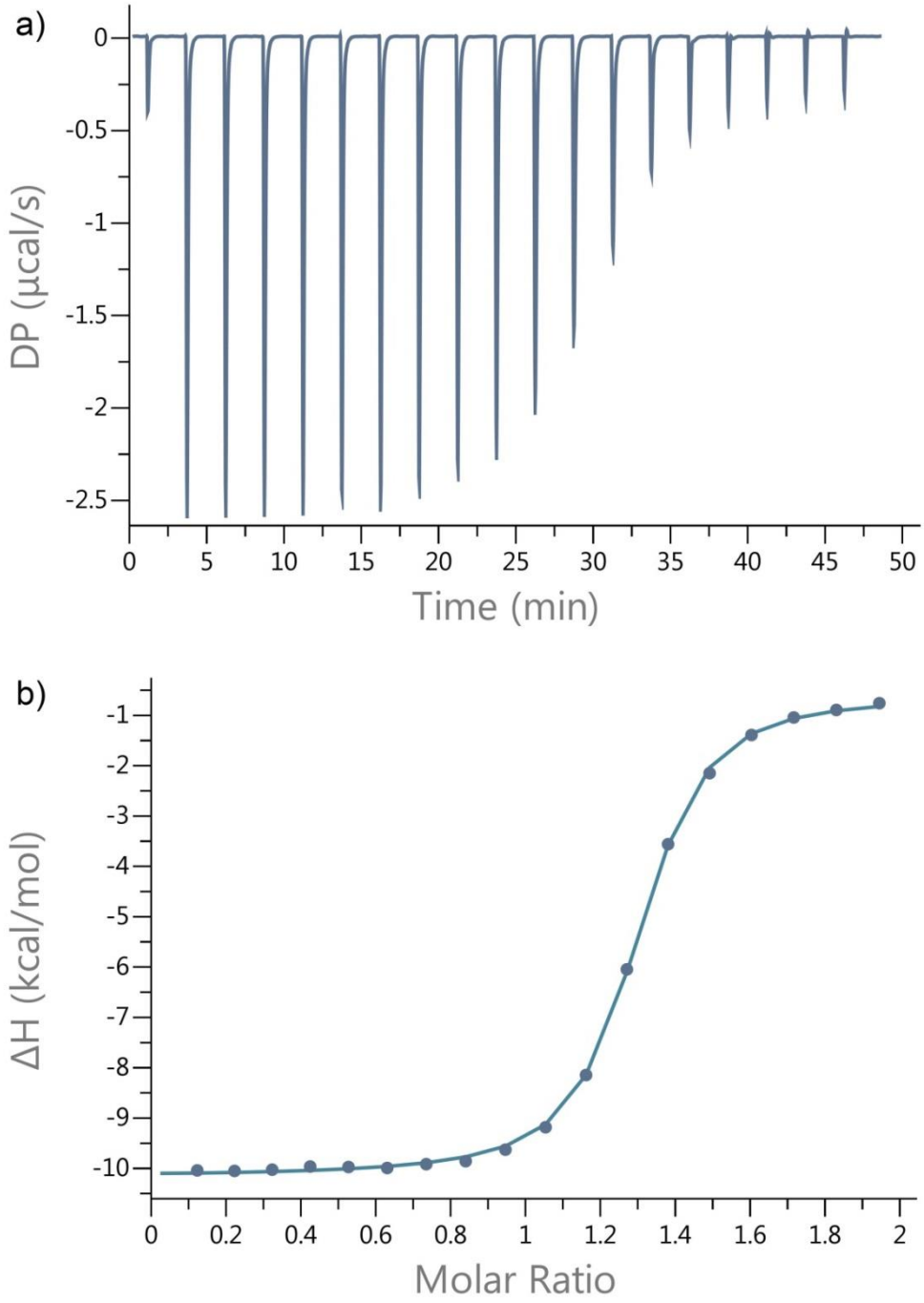

Figure IV-S49. a) Plot of DP vs time from the titration of **IV-2b** (0.1 mM) with guest **IV-8** (1.0 mM) in 20 mM NaH_2PO_4 buffer (pH 7.4); b) plot of the ΔH as a function of molar ratio. The solid line represents the best non-linear fit of the data to a 1:1 binding model ($K_a = (1.6 \pm 0.1) \times 10^6$ M^{-1}, $\Delta H = -9.5 \pm 0.05$ kcal/mol, N = 1.25).

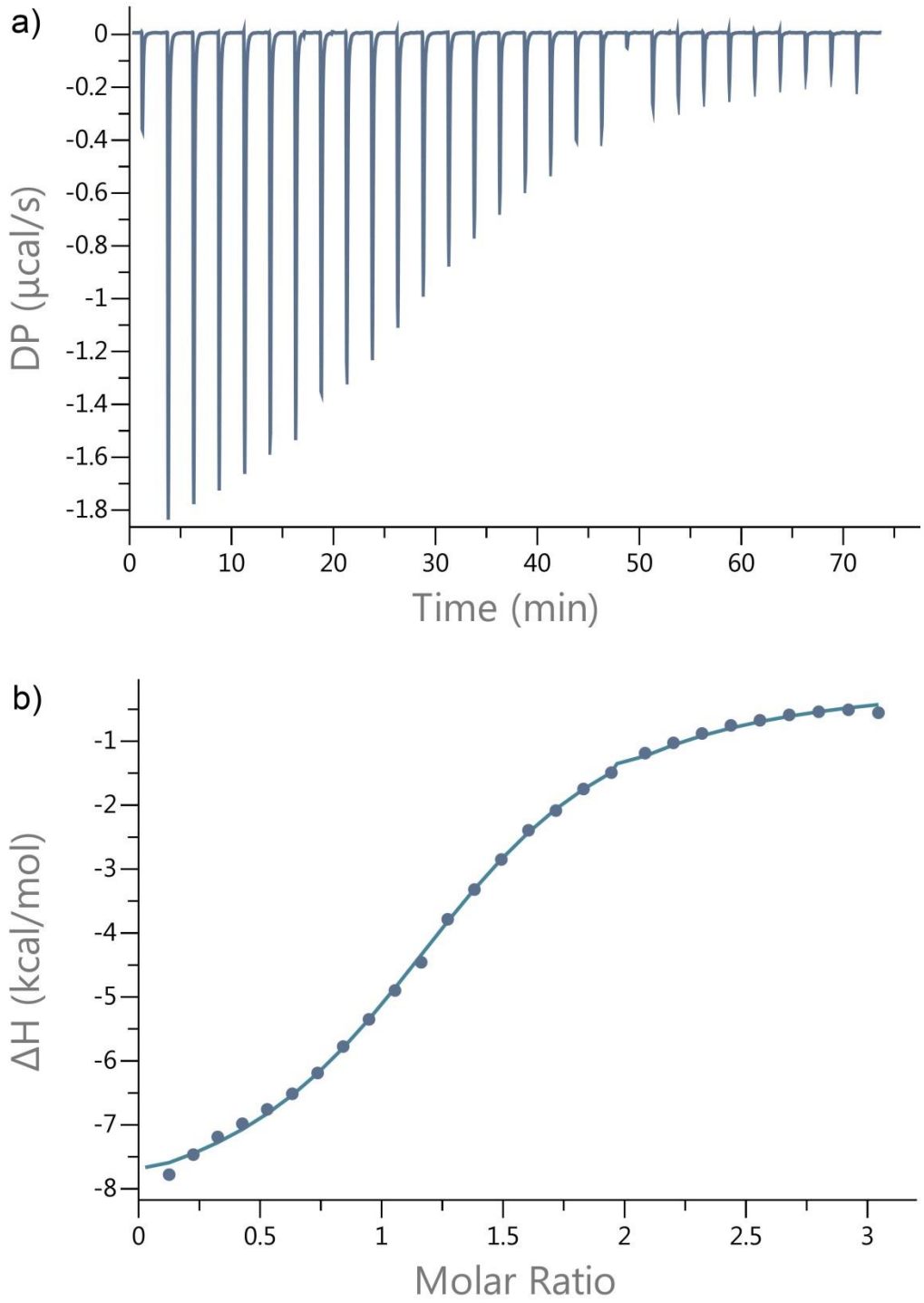

Figure IV-S50. a) Plot of DP vs time from the titration of **IV-2c** (0.1 mM) with guest **IV-8** (1.0 mM) in 20 mM NaH_2PO_4 buffer (pH 7.4); b) plot of the ΔH as a function of molar ratio. The solid line represents the best non-linear fit of the data to a 1:1 binding model ($K_a = (7.1 \pm 0.4) \times 10^4\ M^{-1}$, ΔH = - 8.5 ± 0.12 kcal/mol, N = 1.30).

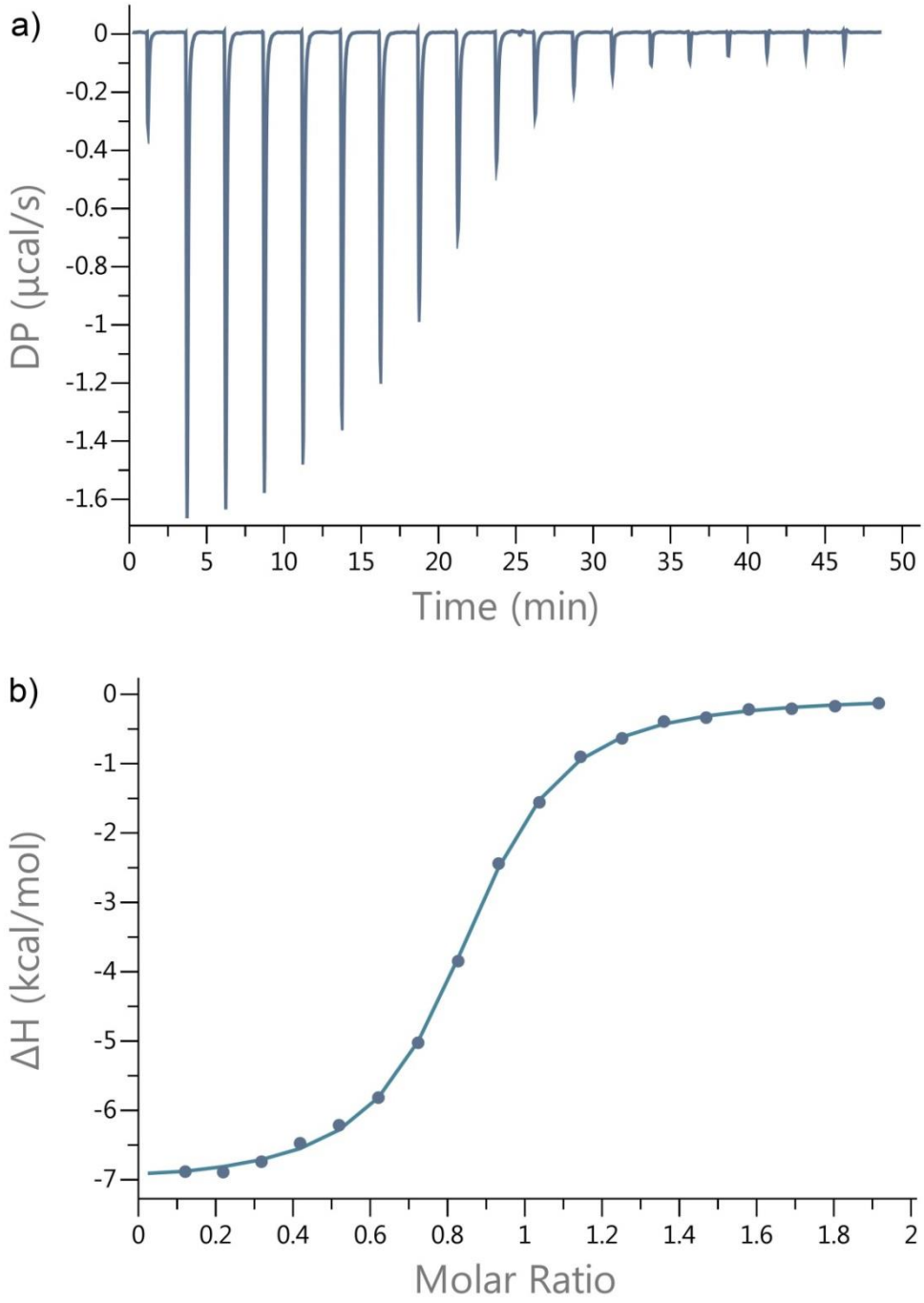

Figure IV-S51. a) Plot of DP vs time from the titration of **IV-1** (0.1 mM) with guest **IV-9** (1.0 mM) in 20 mM NaH_2PO_4 buffer (pH 7.4); b) plot of the ΔH as a function of molar ratio. The solid line represents the best non-linear fit of the data to a 1:1 binding model ($K_a = (4.9 \pm 0.2) \times 10^5\ M^{-1}$, ΔH = - 7.1 ± 0.05 kcal/mol, N = 0.82).

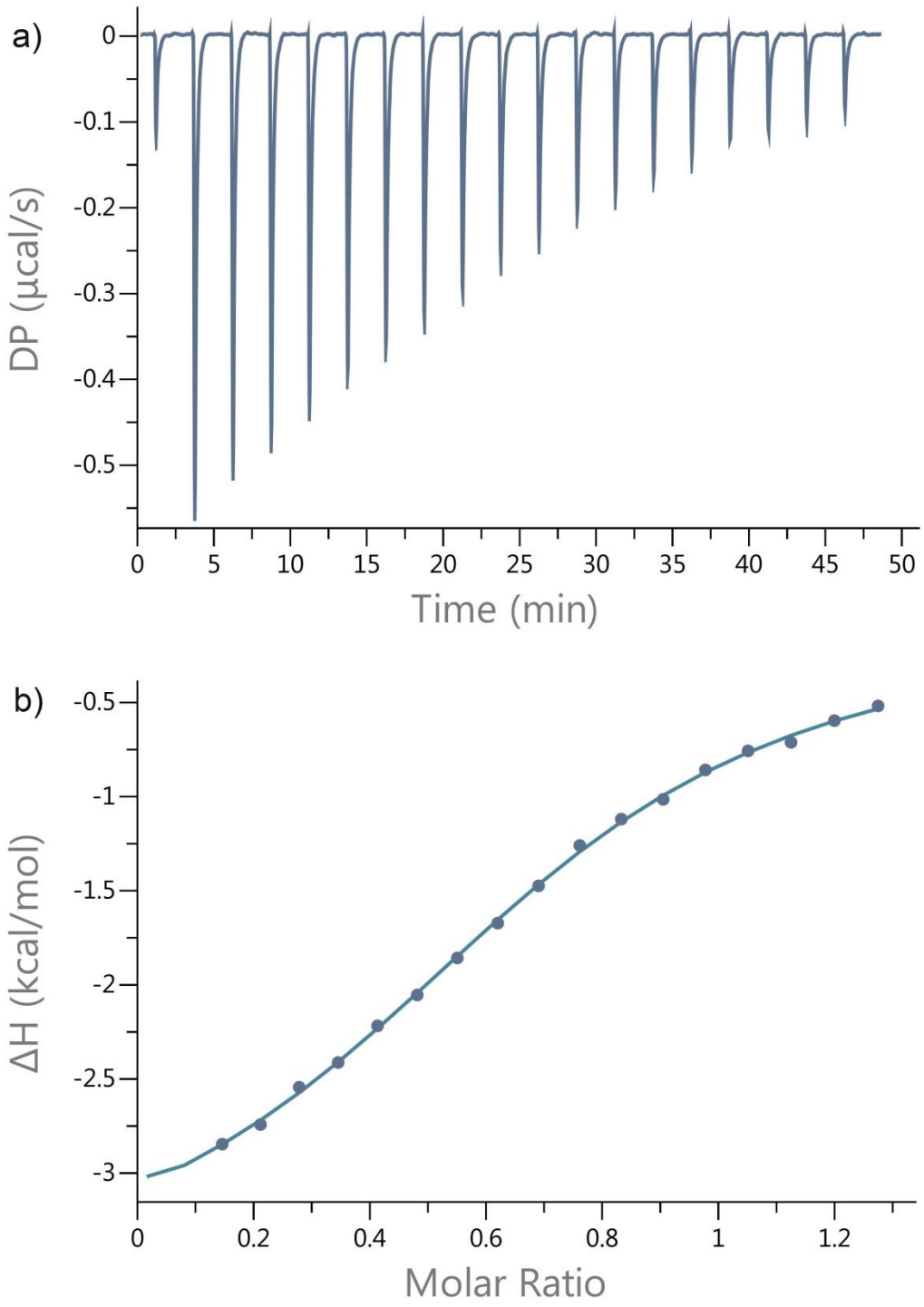

Figure IV-S52. a) Plot of DP vs time from the titration of **IV-2a** (0.15 mM) with guest **IV-9** (0.99 mM) in 20 mM NaH_2PO_4 buffer (pH 7.4); b) plot of the ΔH as a function of molar ratio. The solid line represents the best non-linear fit of the data to a 1:1 binding model (K_a = (2.7 ± 0.6) × 10^4 M^{-1}, ΔH = - 4.48 ± 0.48 kcal/mol, N = 0.69).

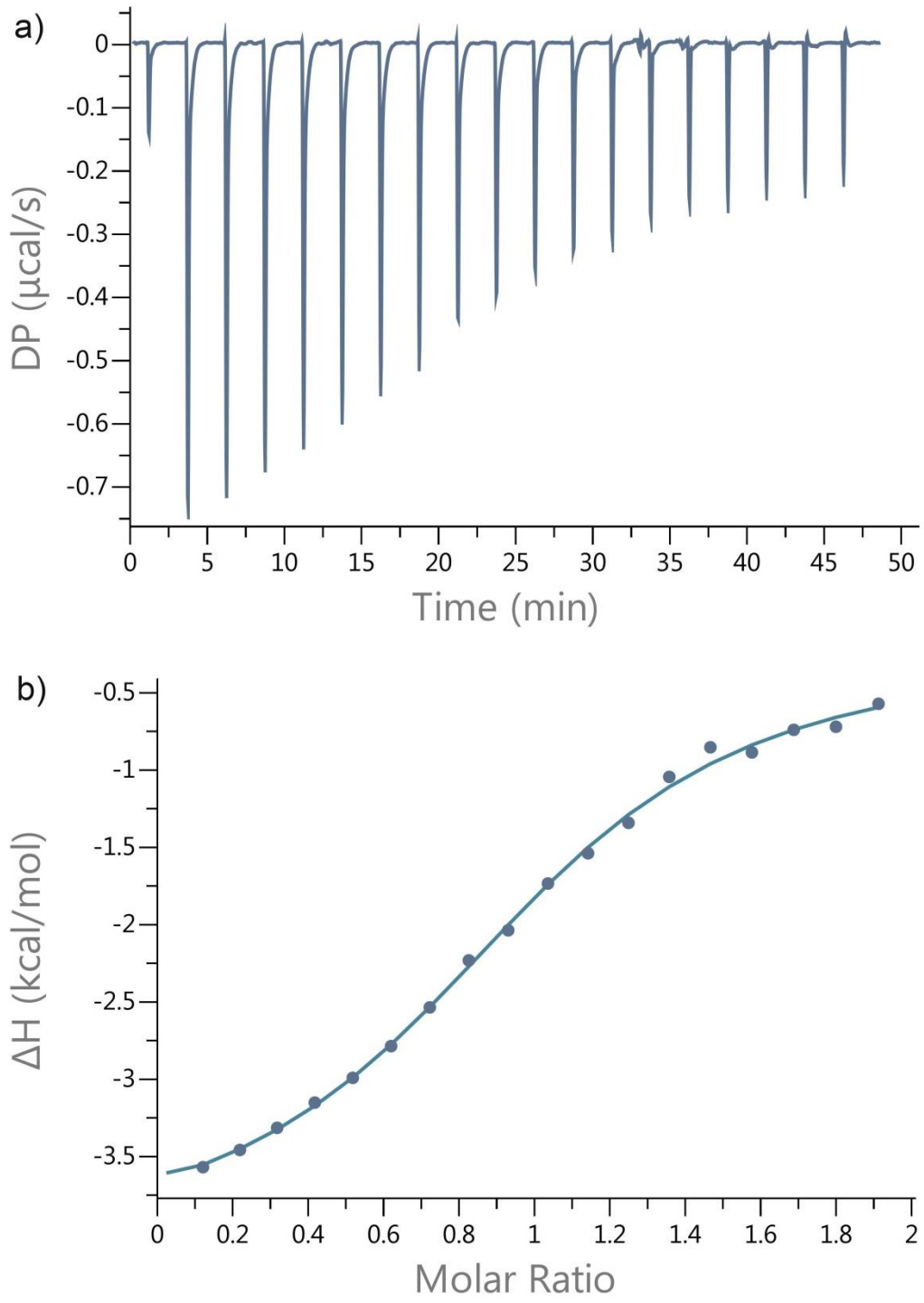

Figure IV-S53. a) Plot of DP vs time from the titration of **IV-2b** (0.10 mM) with guest **IV-9** (0.99 mM) in 20 mM NaH_2PO_4 buffer (pH 7.4); b) plot of the ΔH as a function of molar ratio. The solid line represents the best non-linear fit of the data to a 1:1 binding model (K_a = (7.2 ± 1.0) × 10^5 M^{-1}, ΔH = - 3.86 ± 0.17 kcal/mol, N = 0.98).

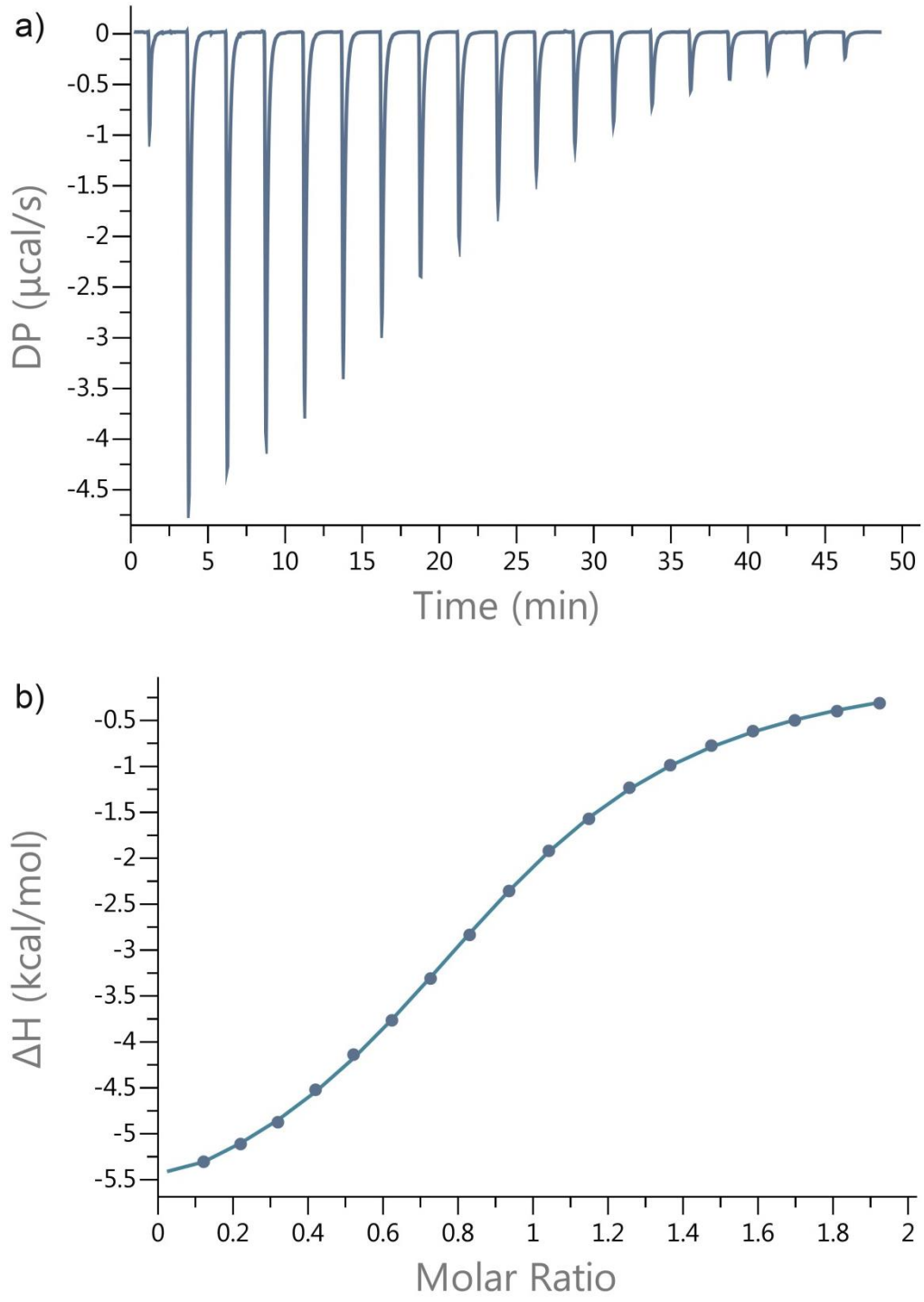

Figure IV-S54. a) Plot of DP vs time from the titration of **IV-2c** (0.50 mM) with guest **IV-9** (5.0 mM) in 20 mM NaH_2PO_4 buffer (pH 7.4); b) plot of the ΔH as a function of molar ratio. The solid line represents the best non-linear fit of the data to a 1:1 binding model (K_a = (1.5 ± 0.0) × 10^4 M^{-1}, ΔH = - 6.47 ± 0.06 kcal/mol, N = 0.88).

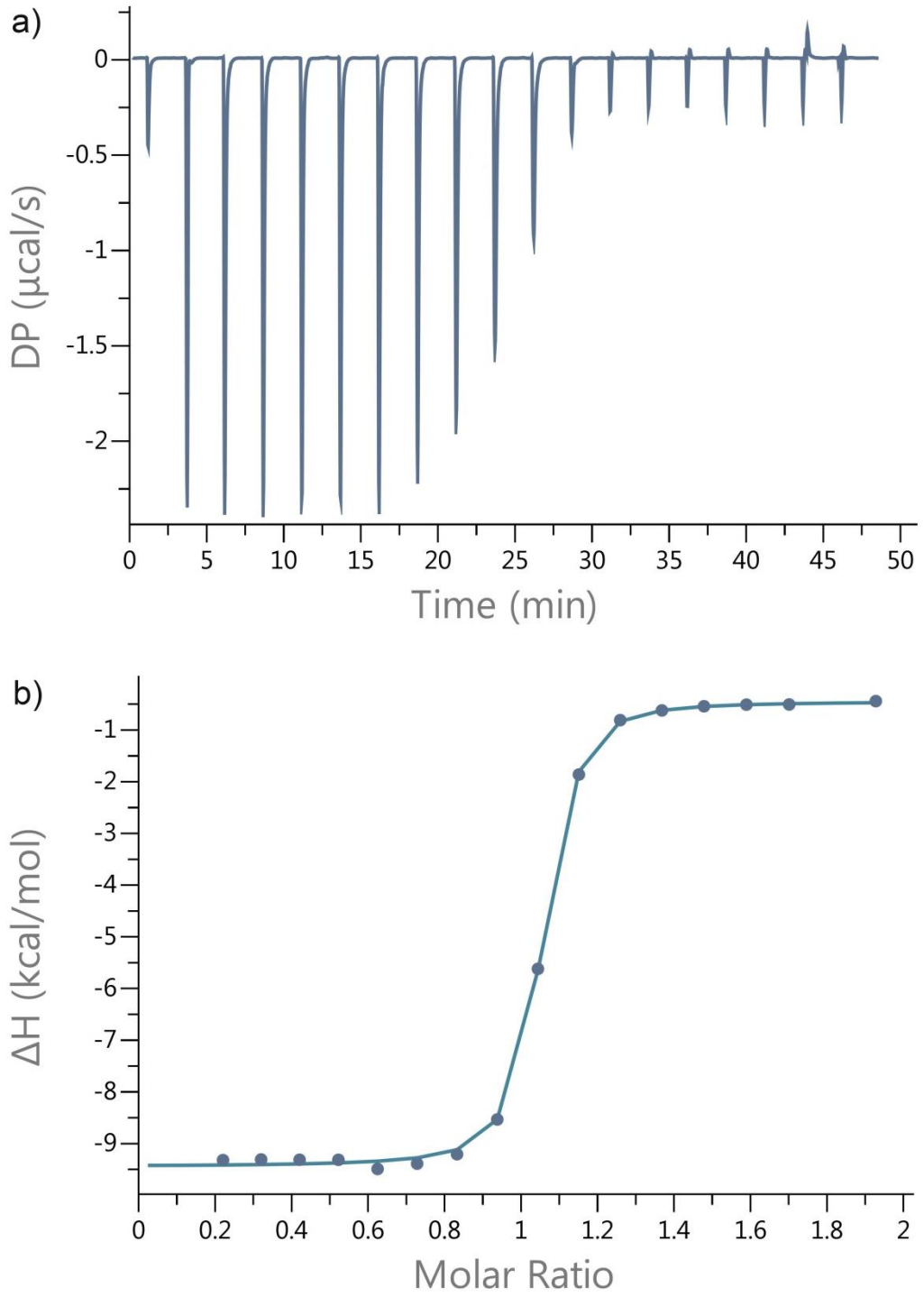

Figure IV-S55. a) Plot of DP vs time from the titration of **IV-1** (0.1 mM) with guest **IV-10** (1.0 mM) in 20 mM NaH_2PO_4 buffer (pH 7.4); b) plot of the ΔH as a function of molar ratio. The solid line represents the best non-linear fit of the data to a 1:1 binding model (K_a = (6.2 ± 0.6) × 10^6 M^{-1}, ΔH = - 9.0 ± 0.09 kcal/mol, N = 1.00).

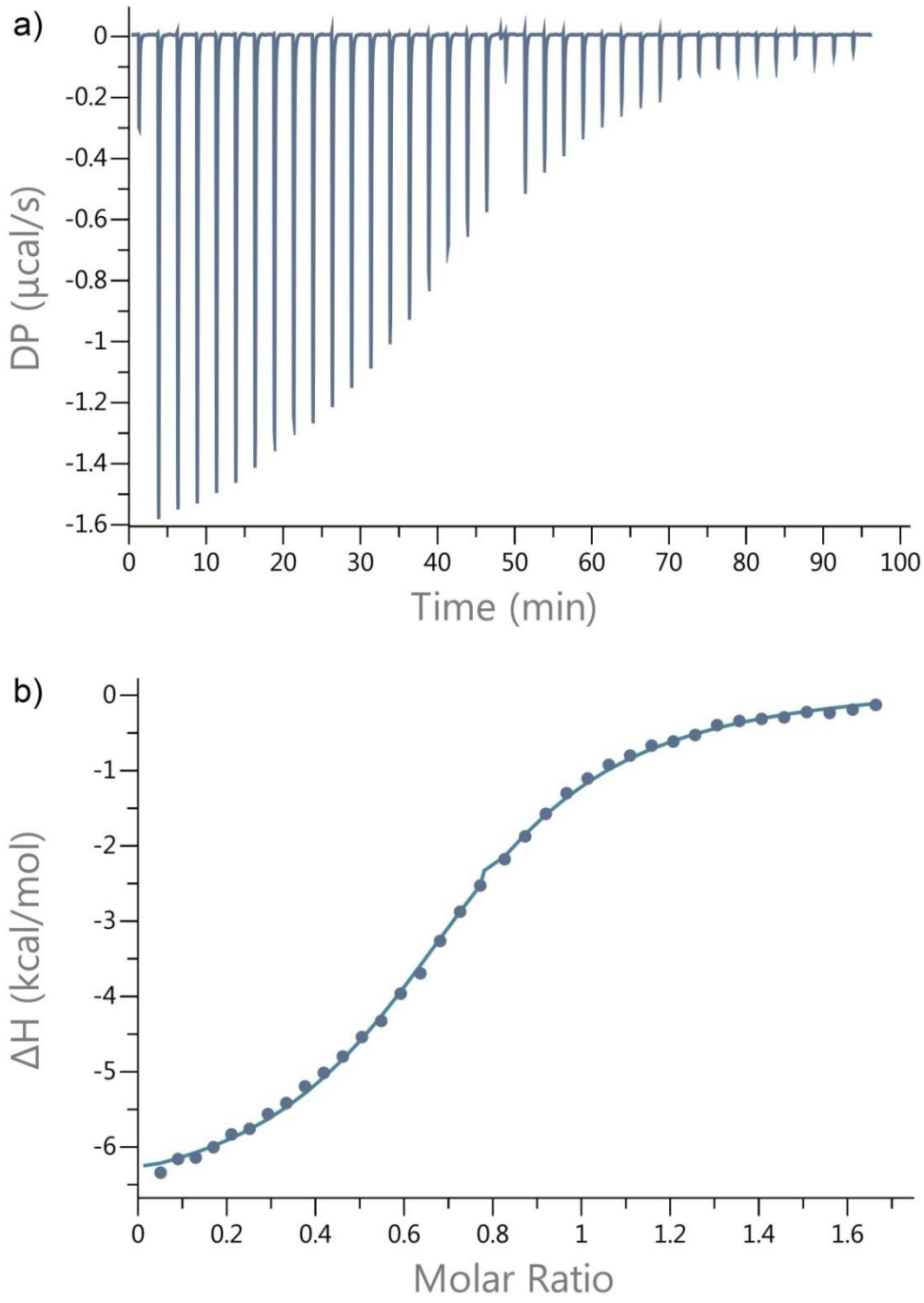

Figure IV-S56. a) Plot of DP vs time from the titration of **IV-2a** (0.25 mM) with guest **IV-10** (1.0 mM) in 20 mM NaH_2PO_4 buffer (pH 7.4); b) plot of the ΔH as a function of molar ratio. The solid line represents the best non-linear fit of the data to a 1:1 binding model ($K_a = (6.9 \pm 0.3) \times 10^4$ M^{-1}, ΔH = - 6.9 ± 0.07 kcal/mol, N = 0.73).

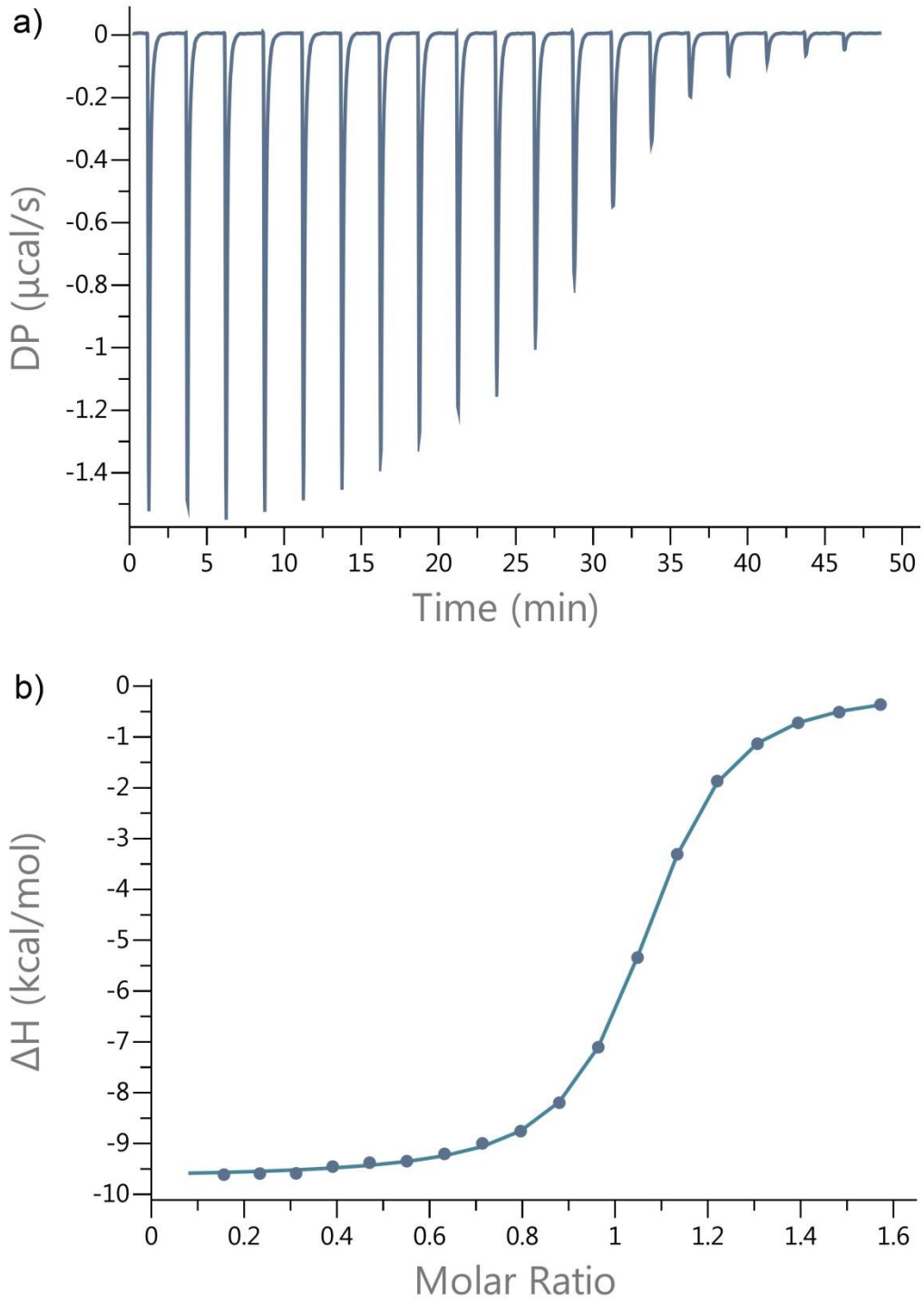

Figure IV-S57. a) Plot of DP vs time from the titration of **IV-2b** (0.1 mM) with guest **IV-10** (0.78 mM) in 20 mM NaH_2PO_4 buffer (pH 7.4); b) plot of the ΔH as a function of molar ratio. The solid line represents the best non-linear fit of the data to a 1:1 binding model (K_a = (1.3 ± 0.03) × 10^6 M^{-1}, ΔH = - 9.6 ± 0.04 kcal/mol, N = 1.03).

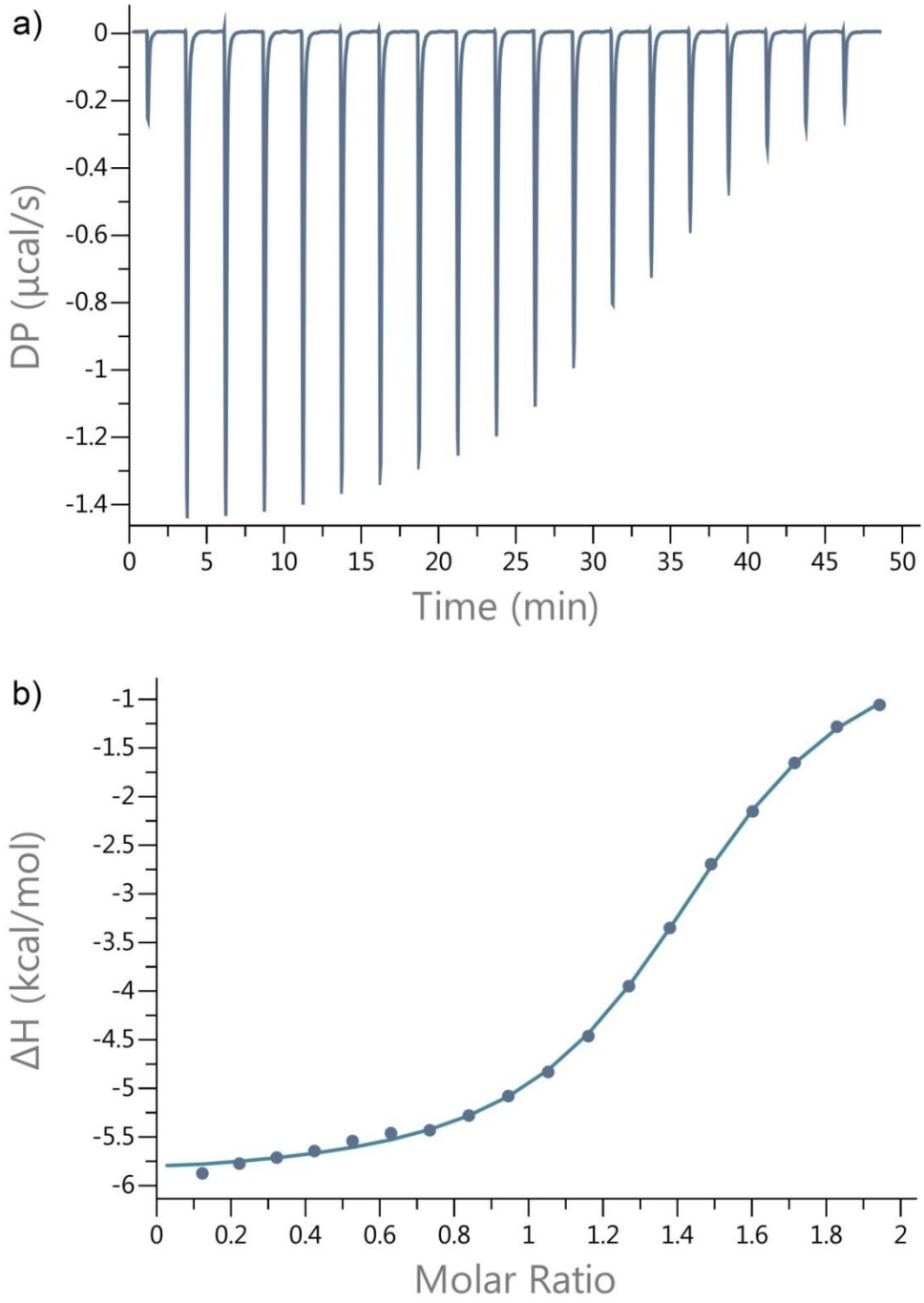

Figure IV-S58. a) Plot of DP vs time from the titration of **IV-2c** (0.1 mM) with guest **IV-10** (1.0 mM) in 20 mM NaH_2PO_4 buffer (pH 7.4); b) plot of the ΔH as a function of molar ratio. The solid line represents the best non-linear fit of the data to a 1:1 binding model ($K_a = (2.7 \pm 0.2) \times 10^5\ M^{-1}$, ΔH = - 5.7 ± 0.1 kcal/mol, N = 1.42).

Appendix 4

List of Publications

I am listed as an author in the following peer-reviewed articles:

1. Haerter, F.; Simons, J. C. P.; Foerster, U.; Moreno Duarte, I.; Diaz-Gil, D.; Ganapati, S.; Eikermann-Haerter, K.; Ayata, C.; Zhang, B.; Blobner, M.; Isaacs, L.; Eikermann, M., Comparative Effectiveness of Calabadion and Sugammadex to Reverse Non-depolarizing Neuromuscular-blocking Agents. *Anesthesiology* **2015**, *123*, 1337-1349.
2. Ganapati, S.; Zavalij, P. Y.; Eikermann, M.; Isaacs, L., In Vitro Selectivity of an Acyclic Cucurbit[n]uril Molecular Container towards Neuromuscular Blocking Agents Relative to Commonly Used Drugs. *Org. Biomol. Chem.* **2016**, *14*, 1277-1287.
3. Diaz-Gil, D.; Haerter, F.; Falcinelli, S.; Ganapati, S.; Hettiarachchi, G. K.; Simons, J. C. P.; Zhang, B.; Grabitz, S. D.; Moreno Duarte, I.; Cotten, J. F.; Eikermann-Haerter, K.; Deng, H.; Chamberlin, N. L.; Isaacs, L.; Briken, V.; Eikermann, M., A Novel Strategy to Reverse General Anesthesia by Scavenging with the Acyclic Cucurbit[n]uril-type Molecular Container Calabadion 2. *Anesthesiology* **2016**, *125*, 333-345.
4. Ganapati, S.; Grabitz, S. D.; Murkli, S.; Scheffenbichler, F.; Rudolph, M. I.; Zavalij, P. Y.; Eikermann, M.; Isaacs, L., Molecular Containers Bind Drugs of Abuse in Vitro and Reverse the Hyperlocomotive Effect of

Methamphetamine in Rats. *Chembiochem* **2017**, In press:

http://dx.doi.org/10.1002/cbic.201700289.

Bibliography

1. Lehn, J. M. *Science* **1993**, *260*, 1762-1763.
2. Frieden, E. *J. Chem. Educ.* **1975**, *52*, 754-761.
3. Pedersen, C. J. *J. Amer. Chem. Soc.* **1967**, *89*, 7017-7036.
4. Zarra, S.; Wood, D. M.; Roberts, D. A.; Nitschke, J. R. *Chem. Soc. Rev.* **2015**, *44*, 419-432.
5. Nimse, S. B.; Kim, T. *Chem. Soc. Rev.* **2013**, *42*, 366-386.
6. Del Valle, E. M. M. *Process Biochem.* **2004**, *39*, 1033-1046.
7. Lagona, J.; Mukhopadhyay, P.; Chakrabarti, S.; Isaacs, L. *Angew. Chem., Int. Ed.* **2005**, *44*, 4844-4870.
8. Cao, L.; Sekutor, M.; Zavalij, P. Y.; Mlinaric-Majerski, K.; Glaser, R.; Isaacs, L. *Angew. Chem., Int. Ed.* **2014**, *53*, 988-993.
9. Behrend, R.; Meyer, E.; Rusche, F. *Liebigs Ann.* **1905**, *339*, 1-37.
10. Freeman, W. A.; Mock, W. L.; Shih, N. Y. *J. Am. Chem. Soc.* **1981**, *103*, 7367-7368.
11. Day, A. I.; Blanch, R. J.; Arnold, A. P.; Lorenzo, S.; Lewis, G. R.; Dance, I. *Angew. Chem., Int. Ed.* **2002**, *41*, 275-277.
12. Kim, J.; Jung, I.-S.; Kim, S.-Y.; Lee, E.; Kang, J.-K.; Sakamoto, S.; Yamaguchi, K.; Kim, K. *J. Am. Chem. Soc.* **2000**, *122*, 540-541.
13. Cheng, X.-J.; Liang, L.-L.; Chen, K.; Ji, N.-N.; Xiao, X.; Zhang, J.-X.; Zhang, Y.-Q.; Xue, S.-F.; Zhu, Q.-J.; Ni, X.-L.; Tao, Z. *Angew. Chem., Int. Ed.* **2013**, *52*, 7252-7255.

14. Liu, S. M.; Zavalij, P. Y.; Isaacs, L. *J. Am. Chem. Soc.* **2005**, *127*, 16798-16799.

15. Isaacs, L.; Park, S. K.; Liu, S. M.; Ko, Y. H.; Selvapalam, N.; Kim, Y.; Kim, H.; Zavalij, P. Y.; Kim, G. H.; Lee, H. S.; Kim, K. *J. Am. Chem. Soc.* **2005**, *127*, 18000-18001.

16. Isaacs, L. *Isr. J. Chem.* **2011**, *51*, 578-591.

17. Nau, W. M.; Florea, M.; Assaf, K. I. *Isr. J. Chem.* **2011**, *51*, 559-577.

18. Liu, S. M.; Ruspic, C.; Mukhopadhyay, P.; Chakrabarti, S.; Zavalij, P. Y.; Isaacs, L. *J. Am. Chem. Soc.* **2005**, *127*, 15959-15967.

19. Lee, J. W.; Samal, S.; Selvapalam, N.; Kim, H.-J.; Kim, K. *Acc. Chem. Res.* **2003**, *36*, 621-630.

20. Cao, L. P.; Sekutor, M.; Zavalij, P. Y.; Mlinaric-Majerski, K.; Glaser, R.; Isaacs, L. *Angew. Chem., Int. Ed.* **2014**, *53*, 988-993.

21. Biedermann, F.; Scherman, O. A. *J. Phys. Chem. B* **2012**, *116*, 2842-2849.

22. Bardelang, D.; Udachin, K. A.; Leek, D. M.; Margeson, J. C.; Chan, G.; Ratcliffe, C. I.; Ripmeester, J. A. *Cryst. Growth Des.* **2011**, *11*, 5598-5614.

23. Malaspina, T.; Fileti, E.; Chaban, V. V. *J. Phys. Chem. B* **2016**, *120*, 7511-7516.

24. Flinn, A.; Hough, G. C.; Stoddart, J. F.; Williams, D. J. *Angew. Chem.* **1992**, *104*, 1550-1551.

25. Zhao, J.; Kim, H.-J.; Oh, J.; Kim, S.-Y.; Lee, J. W.; Sakamoto, S.; Yamaguchi, K.; Kim, K. *Angew. Chem., Int. Ed.* **2001**, *40*, 4233-4235.

26. Lewin, V.; Rivollier, J.; Coudert, S.; Buisson, D.-A.; Baumann, D.; Rousseau, B.; Legrand, F.-X.; Kourilova, H.; Berthault, P.; Dognon, J.-P.; Heck, M.-P.; Huber, G. *Eur. J. Org. Chem.* **2013**, *2013*, 3857-3865.

27. Lagona, J.; Mukhopadhyay, P.; Chakrabarti, S.; Isaacs, L. *Angew. Chem., Int. Ed.* **2005**, *44*, 4844-4870.

28. Jon, S. Y.; Selvapalam, N.; Oh, D. H.; Kang, J.-K.; Kim, S.-Y.; Jeon, Y. J.; Lee, J. W.; Kim, K. *J. Am. Chem. Soc.* **2003**, *125*, 10186-10187.

29. Lucas, D.; Minami, T.; Iannuzzi, G.; Cao, L.; Wittenberg, J. B.; Anzenbacher, P.; Isaacs, L. *J. Am. Chem. Soc.* **2011**, *133*, 17966-17976.

30. Vinciguerra, B.; Cao, L. P.; Cannon, J. R.; Zavalij, P. Y.; Fenselau, C.; Isaacs, L. *J. Am. Chem. Soc.* **2012**, *134*, 13133-13140.

31. Cao, L. P.; Hettiarachchi, G.; Briken, V.; Isaacs, L. *Angew. Chem., Int. Ed.* **2013**, *52*, 12033-12037.

32. Webber, M. J.; Appel, E. A.; Vinciguerra, B.; Cortinas, A. B.; Thapa, L. S.; Jhunjhunwala, S.; Isaacs, L.; Langer, R.; Anderson, D. G. *Proc. Natl. Acad. Sci. U. S. A.* **2016**, *113*, 14189-14194.

33. Bockus, A. T.; Smith, L. C.; Grice, A. G.; Ali, O. A.; Young, C. C.; Mobley, W.; Leek, A.; Roberts, J. L.; Vinciguerra, B.; Isaacs, L.; Urbach, A. R. *J. Am. Chem. Soc.* **2016**, *138*, 16549-16552.

34. Samanta, S. K.; Quigley, J.; Vinciguerra, B.; Briken, V.; Isaacs, L. *J. Am. Chem. Soc.* **2017**, *139*, 9066-9074.

35. Vinciguerra, B.; Zavalij, P. Y.; Isaacs, L. *Org. Lett.* **2015**, *17*, 5068-5071.

36. Ayhan, M. M.; Karoui, H.; Hardy, M.; Rockenbauer, A.; Charles, L.; Rosas, R.; Udachin, K.; Tordo, P.; Bardelang, D.; Ouari, O. *J. Am. Chem. Soc.* **2015**, *137*, 10238-10245.

37. Burnett, C. A.; Witt, D.; Fettinger, J. C.; Isaacs, L. *J. Org. Chem.* **2003**, *68*, 6184-6191.

38. Stancl, M.; Hodan, M.; Sindelar, V. *Org. Lett.* **2009**, *11*, 4184-4187.

39. Ma, D.; Zavalij, P. Y.; Isaacs, L. *J. Org. Chem.* **2010**, *75*, 4786-4795.

40. Ma, D.; Hettiarachchi, G.; Nguyen, D.; Zhang, B.; Wittenberg, J. B.; Zavalij, P. Y.; Briken, V.; Isaacs, L. *Nat. Chem.* **2012**, *4*, 503-510.

41. Shen, C.; Ma, D.; Meany, B.; Isaacs, L.; Wang, Y. H. *J. Am. Chem. Soc.* **2012**, *134*, 7254-7257.

42. Lu, X.; Isaacs, L. *Angew. Chem., Int. Ed.* **2016**, *55*, 8076-8080.

43. Zhang, B.; Zavalij, P. Y.; Isaacs, L. *Org. Biomol. Chem.* **2014**, *12*, 2413-2422.

44. Zhang, B.; Isaacs, L. *J. Med. Chem.* **2014**, *57*, 9554-9563.

45. Sigwalt, D.; Moncelet, D.; Falcinelli, S.; Mandadapu, V.; Zavalij, P. Y.; Day, A.; Briken, V.; Isaacs, L. *ChemMedChem* **2016**, *11*, 980-989.

46. Gilberg, L.; Zhang, B.; Zavalij, P. Y.; Sindelar, V.; Isaacs, L. *Org. Biomol. Chem.* **2015**, *13*, 4041-4050.

47. She, N.; Moncelet, D.; Gilberg, L.; Lu, X.; Sindelar, V.; Briken, V.; Isaacs, L. *Chem. Eur. J.* **2016**, *22*, 15270-15279.

48. Ma, D.; Zhang, B.; Hoffmann, U.; Sundrup, M. G.; Eikermann, M.; Isaacs, L. *Angew. Chem., Int. Ed.* **2012**, *51*, 11358-11362.

49. Raghavendra, T. *J. R. Soc. Med.* **2002**, *95*, 363-367.

50. Maybauer, D. M.; Geldner, G.; Blobner, M.; Puehringer, F.; Hofmockel, R.; Rex, C.; Wulf, H. F.; Eberhart, L.; Arndt, C.; Eikermann, M. *Anaesthesia* **2007**, *62*, 12-17.

51. Butterly, A.; Bittner, E. A.; George, E.; Sandberg, W. S.; Eikermann, M.; Schmidt, U. *Br. J. Anaesth.* **2010**, *105*, 304-309.

52. Meyer, M. J.; Bateman, B. T.; Kurth, T.; Eikermann, M. *BMJ* **2013**, *346*, f1460.

53. Adam, J. M.; Bennett, D. J.; Bom, A.; Clark, J. K.; Feilden, H.; Hutchinson, E. J.; Palin, R.; Prosser, A.; Rees, D. C.; Rosair, G. M.; Stevenson, D.; Tarver, G. J.; Zhang, M.-Q. *J. Med. Chem.* **2002**, *45*, 1806-1816.

54. Bom, A.; Bradley, M.; Cameron, K.; Clark, J. K.; Van Egmond, J.; Feilden, H.; MacLean, E. J.; Muir, A. W.; Palin, R.; Rees, D. C.; Zhang, M.-Q. *Angew. Chem., Int. Ed.* **2002**, *41*, 265-270.

55. Cameron, K. S.; Clark, J. K.; Cooper, A.; Fielding, L.; Palin, R.; Rutherford, S. J.; Zhang, M. Q. *Org. Lett.* **2002**, *4*, 3403-3406.

56. Naguib, M. *Anesth. Analg.* **2007**, *104*, 575-581.

57. Epemolu, O.; Bom, A.; Hope, F.; Mason, R. *Anesthesiology* **2003**, *99*, 632-637.

58. Sorgenfrei, I. F.; Norrild, K.; Larsen, P. B.; Stensballe, J.; Ostergaard, D.; Prins, M. E.; Viby-Mogensen, J. *Anesthesiology* **2006**, *104*, 667-674.

59. Duvaldestin, P.; Kuizenga, K.; Saldien, V.; Claudius, C.; Servin, F.; Klein, J.; Debaene, B.; Heeringa, M. *Anesth. Analg.* **2009**, *110*, 74-82.

60. Uzunova, V. D.; Cullinane, C.; Brix, K.; Nau, W. M.; Day, A. I. *Org. Biomol. Chem.* **2010**, *8*, 2037-2042.

61. Montes-Navajas, P.; Gonzalez-Bejar, M.; Scaiano, J. C.; Garcia, H. *Photochem. Photobiol. Sci.* **2009**, *8*, 1743-1747.

62. Macartney, D. H. *Future Med. Chem.* **2013**, *5*, 2075-2089.

63. Hoffmann, U.; Grosse-Sundrup, M.; Eikermann-Haerter, K.; Zaremba, S.; Ayata, C.; Zhang, B.; Ma, D.; Isaacs, L.; Eikermann, M. *Anesthesiology* **2013**, *119*, 317-325.

64. Haerter, F.; Simons, J. C. P.; Foerster, U.; Moreno Duarte, I.; Diaz-Gil, D.; Ganapati, S.; Eikermann-Haerter, K.; Ayata, C.; Zhang, B.; Blobner, M.; Isaacs, L.; Eikermann, M. *Anesthesiology* **2015**, *123*, 1337-1349.

65. Zwiers, A.; van den Heuvel, M.; Smeets, J.; Rutherford, S. *Clin. Drug Invest.* **2011**, *31*, 101-111.

66. Facing Addition in America: The Surgeon General's Report on Alcohol, Drugs, and Health, 2016. https://www.surgeongeneral.gov/library/2016alcoholdrugshealth/index.html (accessed April 6, **2017**).

67. Behavioral Health Trends in the United States. https://www.samhsa.gov/data/sites/default/files/NSDUH-FRR1-2014/NSDUH-FRR1-2014.pdf (accessed April 6, **2017**).

68. National Drug Threat Assessment 2011. http://www.justice.gov/archive/ndic/pubs44/44849/44849p.pdf (accessed April 6, **2017**).

69. Gorelick, D. A. *Future Med. Chem.* **2012**, *4*, 227-243.

70. Veilleux Jennifer, C.; Colvin Peter, J.; Anderson, J.; York, C.; Heinz Adrienne, J. *Clin. Psychol. Rev.* **2010**, *30*, 155-166.

71. Skolnick, P. *Trends Pharmacol. Sci.* **2015**, *36*, 628-635.

72. Montoya Ivan, D. *Adicciones* **2012,** *24*, 95-103.

73. Zhan, C.-G.; Zheng, F.; Landry, D. W. *J. Am. Chem. Soc.* **2003**, *125*, 2462-2474.

74. Xue, L.; Hou, S.; Yang, W.; Fang, L.; Zheng, F.; Zhan, C.-G. *Chem.-Biol. Interact.* **2013**, *203*, 57-62.

75. Shram, M. J.; Cohen-Barak, O.; Chakraborty, B.; Bassan, M.; Schoedel, K. A.; Hallak, H.; Eyal, E.; Weiss, S.; Gilgun, Y.; Sellers, E. M.; Faulknor, J.; Spiegelstein, O. *J. Clin. Psychopharmacol.* **2015**, *35*, 396-405.

76. Bremer, P. T.; Kimishima, A.; Schlosburg, J. E.; Zhou, B.; Collins, K. C.; Janda, K. D. *Angew. Chem., Int. Ed.* **2016**, *55*, 3772-3775.

77. Collins, K. C.; Schlosburg, J. E.; Bremer, P. T.; Janda, K. D. *J. Med. Chem.* **2016**, *59*, 3878-3885.

78. Kimishima, A.; Wenthur, C. J.; Zhou, B.; Janda, K. D. *ACS Chem. Biol.* **2017**, *12*, 36-40.

79. Gooyit, M.; Miranda, P. O.; Wenthur, C. J.; Ducime, A.; Janda, K. D. *ACS Chem. Neurosci.* **2017**, *8*, 468-472.

80. Kosten, T. R.; Domingo, C. B.; Shorter, D.; Orson, F.; Green, C.; Somoza, E.; Sekerka, R.; Levin, F. R.; Mariani, J. J.; Stitzer, M.; Tompkins, D. A.; Rotrosen, J.; Thakkar, V.; Smoak, B.; Kampman, K. *Drug Alcohol Depend.* **2014**, *140*, 42-47.

81. Stevens Misty, W.; Henry Ralph, L.; Owens, S. M.; Schutz, R.; Gentry, W. B. *MAbs* **2014**, *6*, 1649-1656.

82. Guo, D.-S.; Liu, Y. *Acc. Chem. Res.* **2014**, *47*, 1925-1934.

83. Pinalli, R.; Dalcanale, E. *Acc. Chem. Res.* **2013**, *46*, 399-411.

84. Biavardi, E.; Federici, S.; Tudisco, C.; Menozzi, D.; Massera, C.; Sottini, A.; Condorelli, G. G.; Bergese, P.; Dalcanale, E. *Angew. Chem., Int. Ed.* **2014**, *53*, 9183-9188.

85. Minami, T.; Esipenko, N. A.; Akdeniz, A.; Zhang, B.; Isaacs, L.; Anzenbacher, P. *J. Am. Chem. Soc.* **2013**, *135*, 15238-15243.

86. Mock, W. L.; Shih, N. Y. *J. Org. Chem.* **1986,** *51*, 4440-6.

87. Anslyn, E. V. *J. Org. Chem.* **2007,** *72*, 687-699.

88. Carpenter, W. *Exotic Animal Formulary*, 4th ed.; Elsevier, **2012**; Boston University Research Compliance Rat Formulary. http://www.bu.edu/orccommittees/iacuc/policies-andguidelines/ anesthesia-and-analgesia-in-research-animals/ rat-formulary/ (accessed November **2015**); University of California, San Francisco IACUC Rat Formulary. http://www.iacuc.ucsf.

edu/Proc/awRatFrm.asp (accessed November **2015**).

89. Rekharsky, M. V.; Mori, T.; Yang, C.; Ko, Y. H.; Selvapalam, N.; Kim, H.; Sobransingh, D.; Kaifer, A. E.; Liu, S. M.; Isaacs, L.; Chen, W.; Moghaddam, S.; Gilson, M. K.; Kim, K. M.; Inoue, Y. *Proc. Natl. Acad. Sci. U. S. A.* **2007**, *104*, 20737-20742.

90. Cao, L.; Isaacs, L. *Supramol. Chem.* **2014**, *26*, 251-258.

91. Mendes, P. *Comput. Appl. Biosci.* **1993**, *9*, 563-71.

92. Mendes, P. *Trends Biochem. Sci.* **1997**, *22*, 361-363.

93. Mendes, P.; Kell, D. B. *Bioinformatics* **1998**, *14*, 869-883.

94. Probst, R. J.; Lim, J. M.; Bird, D. N.; Pole, G. L.; Sato, A. K.; Claybaugh, J. R. *J. Am. Assoc. Lab. Anim. Sci.* **2006**, *45*, 49-52.

95. Diaz-Gil, D.; Haerter, F.; Falcinelli, S.; Ganapati, S.; Hettiarachchi, G. K.; Simons, J. C. P.; Zhang, B.; Grabitz, S. D.; Moreno Duarte, I.; Cotten, J. F.; Eikermann-Haerter, K.; Deng, H.; Chamberlin, N. L.; Isaacs, L.; Briken, V.; Eikermann, M. *Anesthesiology* **2016**, *125*, 333-345.

96. Ghale, G.; Nau, W. M. *Acc. Chem. Res.* **2014,** *47*, 2150-2159.

97. Ganapati, S.; Zavalij, P. Y.; Eikermann, M.; Isaacs, L. *Org. Biomol. Chem.* **2016**, *14*, 1277-1287; Isaacs, L.; Eikermann, M. Unpublished results, **2016**. The binding constants reported in reference 97 were reproduced by an independent contract research organization sponsored by Calabash Bioscience.

98. Gentry, W. B.; Ghafoor, A. U.; Wessinger, W. D.; Laurenzana, E. M.; Hendrickson, H. P.; Owens, S. M. *Pharmacol., Biochem. Behav.* **2004**, *79*, 751-760.

99. Hettiarachchi, G.; Samanta, S. K.; Falcinelli, S.; Zhang, B.; Moncelet, D.; Isaacs, L.; Briken, V. *Mol. Pharmaceutics* **2016**, *13*, 809-818.

100. Ganapati, S.; Grabitz, S. D.; Murkli, S.; Scheffenbichler, F.; Rudolph, M. I.; Zavalij, P. Y.; Eikermann, M.; Isaacs, L. *Chembiochem* **2017**, In press: http://dx.doi.org/10.1002/cbic.201700289 .

101. Hug, C. C., Jr.; Murphy, M. R. *Anesthesiology* **1981**, *55*, 369-375.

102. McClain, D. A.; Hug, C. C., Jr. *Clin. Pharmacol. Ther.* **1980**, *28*, 106-114.

103. Isaacs, L. *Acc. Chem. Res.* **2014**, *47*, 2052-2062.

104. Masson, E.; Ling, X.; Joseph, R.; Kyeremeh-Mensah, L.; Lu, X. *RSC Adv.* **2012**, *2*, 1213-1247.

105. Kim, K.; Selvapalam, N.; Ko, Y. H.; Park, K. M.; Kim, D.; Kim, J. *Chem. Soc. Rev.* **2007**, *36*, 267-279.

106. Caruso, U.; Pragliola, S.; Roviello, A.; Sirigu, A.; Iannelli, P. *Macromolecules* **1995**, *28*, 6089-6094.

107. Griffin, A. C.; Havens, S. J. *J. Polym. Sci., Polym. Phys. Ed.* **1981**, *19*, 951-969.

108. Huang, W.; Liu, S.; Isaacs L. in *Modern Supramolecular Chemistry: Strategies for Macrocycle Synthesis* (Eds.: Diederich, F.; Stang, P. J.; Tykwinski, R. K.), WILEY-VCH Verlag GmbH & Co. KGaA, Weinheim, **2008**, pp. 113-142.